Laser Shock Peening in Friction Stir Welded Joints with Lack of Penetration Defects

M. P. Leering

A thesis submitted to the Faculty of Engineering and the Built Environment, University of the Witwatersrand, Johannesburg, in fulfilment of the requirements for the degree of Master of Science in Engineering.

Johannesburg, May 2016

Declaration

I, Mitchell P. Leering declare that this thesis is my own, unaided work, except where otherwise acknowledged. It is being submitted for the degree of Master of Science in Engineering at the University of the Witwatersrand, Johannesburg. It has not been submitted before for any degree or examination at any other university.

Signed this 23rd day of May 2016

M. P. Leering

To Shannon, thank you for your unwavering love and support. Without you this would not have been possible. Love you forever!

Abstract

This experimental work was conducted in order to assess the influence of the application of Laser Shock Peening (LSP) to Friction Stir Welded (FSW) joints. LSP has the ability to potentially recover the reduction in joint mechanical properties that arose due to the presence of a common FSW defect known as Lack of Penetration (LOP). The material used throughout this study was 3 mm thick AA6082-T6 Aluminium. This specific material was selected due to its weldability and common use in the manufacturing of aircraft structures.

A 20 mm diameter, spiralled profile shoulder and 5 mm diameter, tapered, three facetted pin was used in the manufacturing of the FSW joints. Experimental assessment and optimisation of the FSW parameters window consisted of the varying the tool rotational speed from 630 to 1600 RPM, at five increments and the feed rate from 200 to 600 mm/min, 200 mm/min intervals. The joints were assessed on the overall quality, microstructure, ductility and static strength. The parameter combinations produced joints with ultimate tensile joint efficiencies which ranged from 48% to 74% that of the base material. The initial study showed that higher welding rates, typically associated with low feed rates, resulted in the highest quality joints. This was attributed to the sufficient thermal softening of the material during welding. The increased welding temperatures improved the joint formation, material flow and mechanical properties. Due to the elevated welding temperatures and material flow, substantial flash formation was observed on all joints manufactured with a welding rate of 5 rev/mm and higher. These results formed the foundation of the multi-objective optimisation in order to determine the most suitable parameters for this welding configuration. The optimisation simulation determined the optimum parameters to be, a tool rotational speed of 1433 RPM, feed rate of 196 mm/min and a welding rate of 7.3 rev/mm. Due to the fixed gearing of the CNC FSW machine the required tool rotational speed could not be achieved, thus, all FSW completed after the optimisation was completed at 1600 RPM, 200 mm/min and 8.00 rev/mm. This parameter combination produced a joint of high structural integrity, high ductility and with no visual sign of internal voids, defects or lack of penetration.

The performance of the defect free joint formed the foundation of the characterisation of the influence of intentionally introduced LOP defects. LOP was defined as a pre-initiated crack which formed at the root surface during the fabrication of a FSW joint. Controlled and consistent LOP was introduced into the joints, manufactured with welding parameters of 1600 RPM and 200 mm/min, by offsetting the welding tool in combinations of the normal and lateral directions relative to the joint line. The defects originated at the root surface and extended at various lengths through the thickness of the joints due to the numerous offsets. The defects lengths ranged from a few microns to as much as 954.5 μm. A number of defects affected as much as 43% of the joint thickness. The presence of the defects

negatively affected the joints structural static strength by as much as 9% to 27% (dependent on the size of the defect) and dynamic fatigue life of as much as 36%.

Laser Shock Peening (LSP) is a novel post manufacturing technique, which has been used to introduce compressive residual stresses within the near surface of the metallic components. A LSP processing was completed without a protective ablative coating (LSPwC), at a wavelength of 1064 nm and pulsed nano-second laser at 10 Hz. The characterisation of varying the laser power intensity and processed coverage to the base of FSW AA6082-T6 Aluminium was completed through extensive parameter window exploration. Factors such as the quality of the energy delivery, sample deflection, strain hardening, penetration of effects through the FSW joint thickness and the improvement of the fatigue life of the base material were used to define the appropriate parameters. A multi-objective optimisation strategy was implemented in the attempt to fully explore the regions between tested parameter combinations; to provide an optimum set of LSP parameters which would be used in combination of the optimum FSW parameters. The simulation predicted two optimum sets of parameters dependent on the desired outcome of either maximising component fatigue or LSP depth of penetration effect. Due to the nature of this research requiring both fatigue and penetration depth, a parameter set was selected based on parameters that would theoretically provide the maximum for both desired outcomes. The optimum power intensity and coverage was specified as 3.33 GW/cm^2 and 1067 $spots/cm^2$.

The optimum parameters of each process was combined in an attempt to recover the drop in fatigue life of the joints due to the presence of the LOP defect. LSP was capable of altering the near surface residual stress states of approximately 100 MPa tensile to -150 to -200 MPa compressive across the three measurement ranges. It was found that LSP had minimal effect on the fatigue life of the components in the low cycle fatigue due to the applied stress relaxing the introduced stress thus having minimal effect on the life of the joints. LSP was found to increase the fatigue life of the non-defective joints by as much as 68%. LSP showed a life improvement of approximately 20% in a joint which had a defect length of roughly 175µm. After the application of LSP the samples in the low cycle fatigue tended to fail at a closed cycles to failure as the non-defective unpeened samples. Application of a LSP to a FSW was found to shift the fracture position of the flawed components from the region of the defect to that of the Heat Affected Zone (HAZ) on the advancing side of the weld. It is suggested that, the shift in fracture position was due to critical relocation of the tensile stress during LSP into the HAZ on the advancing side. The results did not conclusively show that LSP was capable of recovering the effects of the LOP but was plausible that it could possible. This has been said due to some samples exhibiting an increase and due to the change in location of the fracture position.

Acknowledgements

- Prof. Claudia Polese, my supervisor for her constant support and encouragement to persevere. She so often gave of her precious time for advice and discussions in all realms of her expertise that has given me knowledge that not many are lucky enough to experience. She has given me opportunities one can only dream of and I will be eternally grateful.
- Mr Philip Haupt, my National Aerospace Centre supervisor for his support which plays an invaluable part in this research. I am always grateful for his never failing willingness to help and was always warmly welcomed which made discussions so motivational.
- Dr Furfari Domenico and Mr Marco Pacchione, my industry supervisors for their concerted support and without them this research would not have been possible.
- Mr Shaun Rieket, Mr Marius Van Wyk, Mr Lionel Claasens, Mr Andrew Heydenrych and Mr Tokkie Moller as well as all the staff of the WITS University Mechanical Engineering Workshop for their help in manufacturing throughout this research and their constant technical advice. I have learnt lifelong skills and I will always be appreciative for that.
- Mr Daniel Correia, I am extremely grateful for all your help and contributions regarding Friction Stir Welding and apparatus development.
- Mr Daniel Glaser, many thanks for all help and assistance with Laser Shock Peening, I appreciate all the time you have spent in my aid.
- Ms Bathusile Masina, for her much needed assistance in the laboratory, as well as all the staff of the National Laser Centre at the CSIR.
- Mr Pierre Rossouw, from the Council for Scientific and Industrial Research for performing the heat treatment of all manufactured tool pins and the kindness he showed in doing so.

Table of Contents

Table of Figures

Table of Tables

Nomenclature

Symbol	Meaning	Units
R	Tool Rotational Speed	RPM
V_F	Feed Rate	mm/min
T_{Dwell}	Dwell Time	s
P_{rate}	Plunge Rate	mm/min
$E_{beam\ energy}$	Energy	mJ
I_o	Power Intensity	GW/cm^2
τ	Pulse Width	µs
d_{spot}	Laser Spot Diameter	mm
v	Poisson's Ratio	-
${\sigma_y}^{dyn}$	Dynamic Yield Strength	MPa
x_{steps}	Steps of CNC	$mm/\sqrt{spots}$
S	Coverage	$Spots/cm^2$
v_{steps}	Speed of CNC	mm/min
f	Frequency or Repetition Rate	Hz
σ_r	Stress Range	MPa
σ_a	Stress Amplitude	MPa
σ_m	Mean Stress	MPa
R	Stress Ratio	-
A	Amplitude Ratio	-
F_X	Transverse Force	N
F_y	Longitudinal Force	N

F_Z	Normal Force	N
X_c	Peak Location / Centre	Degrees
X_{ce}	Peak Centre Error	Degrees
h	Plank's Constant	-
c	Speed of light	m/s

List of Acronyms

Friction Stir Welding (FSW)

Lack of Penetration (LOP)

Laser Shock Peening (LSP)

Non Destructive Methods (NDT)

Rotation per Minute (RPM)

Unaffected base material (BM)

Heat Affected Zone (HAZ)

Thermo-Mechanically Affected Zone (TMAZ)

Nugget Zone (NZ)

Compressive Residual Stress (CRS)

Laser Shock Peening with a Coating (LSPC)

Laser Shock Peening without a Coating (LSPwC)

Neodymium-Doped Yttrium Aluminium Garnet (Nd:YAG)

Full Width at Half Maximum (FWHM)

Laser Induced Breakdown (LIB)

Laser Absorption Wave (LAW)

Hugoniot Elastic Limit (HEL)

Design of Experiments (DOE)

Response Surface Methodology (RSM)

Multi-Objective Algorithm II (MOGA-II)

Adaptive Range Multi-Objective Genetic Algorithm (ARMOGA)

High Cycle Fatigue (HCF)

X-ray Diffraction (XRD)

Materials Characterisation by X-ray (MCX)

Data Acquisition (DAQ)

Council for Scientific and Industrial Research (CSIR)

CSIR National Laser Centre (NLC)

Ultimate Tensile Strength (UTS)

Potable Instrument Control Interpreter (PINCER)

University of the Witwatersrand (Wits)

Note:

1. From here on out FSW was used interchangeably as:
    a. Friction Stir Welded
    b. Friction Stir Welding
2. From here on out LSP was used interchangeably as:
    a. Laser Shock Peened
    b. Laser Shock Peening

1 Introduction

1.1 Background

Friction Stir Welding (FSW) is a solid state joining technique, invented in 1991 by The Welding Institute [1]. Since the invention of the process, the interest in solid state joining of materials has rapidly increased. World leading aircraft designers and manufacturers have shown great interest in the potential of using FSW as a viable and efficient metallic joining method for the construction of aircraft. The standard FSW method uses a solitary welding tool which interacts on a single side of two sheets of material. A backing bar, on the reverse side of the joining plates, was used to provide support to the clamped sheets during the welding process. At all times of this process, the tool should maintain a minimum distance of ± 0.05-0.2 mm from the backing bar; this is in order to prevent damage from occurring to the components used in the process.

An inherent defect associated with the standard FSW method is Lack of Penetration (LOP). This process defect is caused by the welding pin not entirely penetrating or not completing full penetration of the relevant thickness of the joining material, poor selection of welding parameters, poor design of the welding tool and misalignment of the tool or joining sheets. This defect causes a formation of a crack in the surface opposite to the tool entrance, known as the root surface. This defect has been found to drastically affect the mechanical properties of the welded joint.

Laser Shock Peening (LSP) is a surface process in which a high powered laser is used to induce favourable residual stresses in a metallic component. It is believed that LSP can be used to treat FSW joints to produce more robust and resilient welds. It has been identified that LSP will theoretically be able to recover the decrease in mechanical properties that were caused by the inherent nature of the welding process and any defects that were introduced.

1.2 Motivation for Research

With special attention within aircraft manufacturing industries, advancements in FSW has allowed for the possibilities for this state-of-the- art manufacturing technique to begin to replace the standard metal stiffened panel joint method in the construction of aircraft. It is predicted that this technology will allow for the removal of rivets and other fasteners that are commonly used on aircraft structures. The standard method of performing an FSW is preferred as it allows for welds to be completed at a faster rate, is the easiest to implement and requires a single tool for welding. Exact position accuracy is required during welding to ensure that a full weld is completed. The presence of a LOP defect as small as 0.2 mm can result in a 40% reduction in the fatigue life of the aluminium component [2]. Detection of these defects using standard Non Destructive Methods (NDT) increases cost and time of

manufacture of the constituent. Costs incured by companies by the scrapping of components due to manufacturing errors cannot be tolerated in an industry with such tight profit margins.

The replacement of classic riveting construction methods by FSW can result in considerable structural weight savings as overlapping material, doublers, crack stoppers, rivets and sealant can be avoided. The Eclipse Aviation Company released an aircraft which has been manufactured using FSW, where the skin and underlying aluminium structure were welded together using this technique. The aircraft gained full certification by the FAA in late September 2006. Figure 1.1 illustrates differences between the construction of the Eclipse 500 and slice of a standard commercial jet which had been built using the standard method [3].

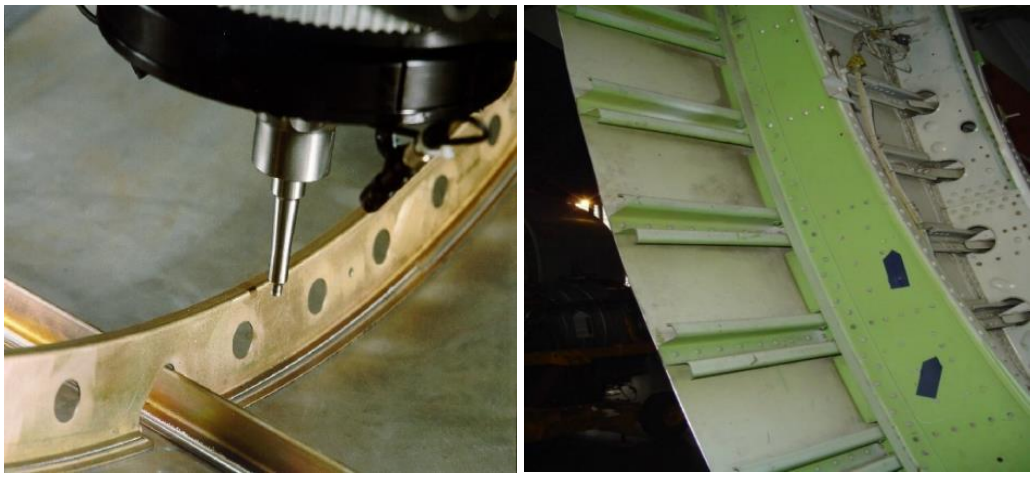

Figure 1.1 - Eclipse 500 Friction Stir Welded Fuselage and General Commercial Jet Fuselage Construction

The full implementation of FSW into the aviation manufacturing industry will reduce the time and cost of manufacture of an aircraft as numerous rivet holes are not required to be drilled and deburred, extensive material preparation and less material being used in the aircraft construction, the advantages of the replacement is clearly shown in Figure 1.2 [2].

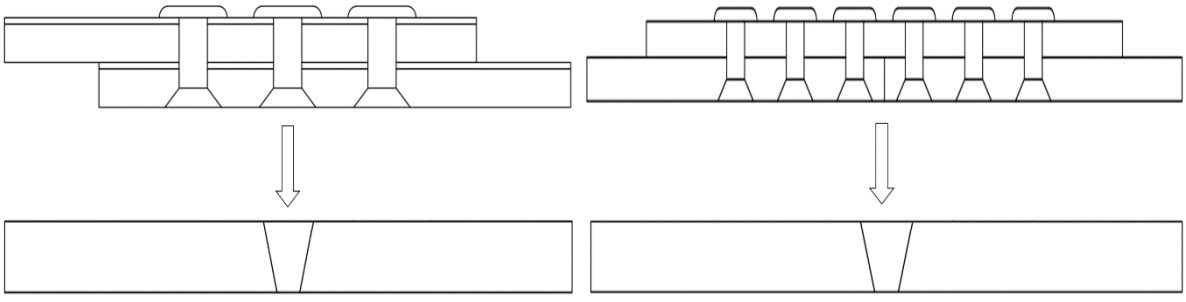

Figure 1.2 - Weight and Complexity Trade-off between Current Riveting Techniques and Friction Stir Welding

Figure 1.1 and Figure 1.2 provide a fairly clear indication of the benefits that can be achieved by replacing the conventional construction methods of metallic structures with FSW. Table 1.1 provides a weight breakdown for a typical longitudinal 3 rows of rivets splice as shown in Figure 1.2. This

table illustrates the results of significant weight reduction in aircraft structures due to the amendment of standard aircraft manufacturing technique.

Table 1.1 - Weight Penalty from a Longitudinal 3-row Rivet Splice

Component	Weight
Overlap of material	0.3 kg/m
Thickness increase	0.3 kg/m
Titanium crack stoppers	0.34 kg/m
Fasteners/sealant	0.05 kg/m
Total weight per meter	±1 kg/m

The introduction of FSW as an innovative welding technique for aluminium aircraft structures does possess some disadvantages and concerns which would have to be addressed:

1. The welding process is often not robust enough compared to other fusion or joining techniques to effectively deal with material sheet thickness variations.
2. Significant consideration on the clamping of components is required in order to prevent movement of the parts under the large downward welding force required for welding.
3. As with most welding techniques, the formation of welding defects is an ever present concern. The presence of the defect within the joint would all most always negatively affect the performance of the joint.
4. Due to the nature of the welding process, a unique joint microstructure is formed. Added to this, the welding process introduces significant residual stresses which can negatively affect the dynamic load carrying capabilities of a FSW part. A highly tensile residual stress state is extremely conducive to the growth of internal weld defects which could lead to premature failure of the joint.

Laser Shock Peening has been identified as an innovative technique to be used to successfully alter the residual stress profile in the FSW joint. By the application of LSP to key areas of the FSW joint it is anticipated that the compressive residual stress will be introduced into the joint. By combining FSW and LSP favourable compressive residual stresses can be introduced into the welded components. These stresses would then potentially improve the fatigue life of the various welded components. It is anticipated that by surrounding internal welding defects with large compressive residual stresses that this would potentially prevent or slow further growth of the detrimental defects.

2 Literature Survey

This section serves as a platform to present relevant topics that need to be elaborated on and considered in the completion of this research dissertation.

2.1 AA6082-T6 Aluminium Alloy Base Material Specifications

3 mm thick AA6082-T6 aluminium alloy was the base material used in this research. This material has the highest strength of all 6xxx series aluminium partnered with excellent corrosion resistance; it is used extensively in the aerospace industry. It has very good weld ability with standard aluminium techniques, but the strength is lowered in the welded zones. This material was solution heat treated and artificially aged. The material chemical composition is listed in Table 2.1 [4].

Table 2.1 - Chemical Composition of AA6082-T6 Aluminium

Element	Aluminium (Al)	Manganese (Mn)	Iron (Fe)	Magnesium (Mg)	Silicon (Si)	Copper (Cu)	Zinc (Zn)	Chromium (Cr)	Titanium (Ti)
Percentage	95.35 – 97.15%	0.4 - 1%	Less than 0.5%	0.6 – 1.2%	0.7 – 1.3%	Less than 0.1%	Less than 0.2%	Less than 0.25%	Less than 0.1%

The expected physical and mechanical properties of the base material are listed in Table 2.2 [4].

Table 2.2 - Physical and Mechanical Properties of AA6082-T6 Aluminium

Property	**Value**	**Units**
Density	2.7	g/cm^3
Hardness (Vickers)	95	HV
Ultimate Tensile Strength	290 – 310	MPa
Yield Tensile Strength	250 – 260	MPa
Elongation at Break	10	%
Thermal Conductivity	170	W/m.K
Melting Temperature	555	°C
Thermal Expansion	$24x10^{-6}$	/K

Figure 2.1 shows the experimental stress-strain curve of AA6082-T6 aluminium [5]. This figure will be used in the verification of the material that will be used in this research.

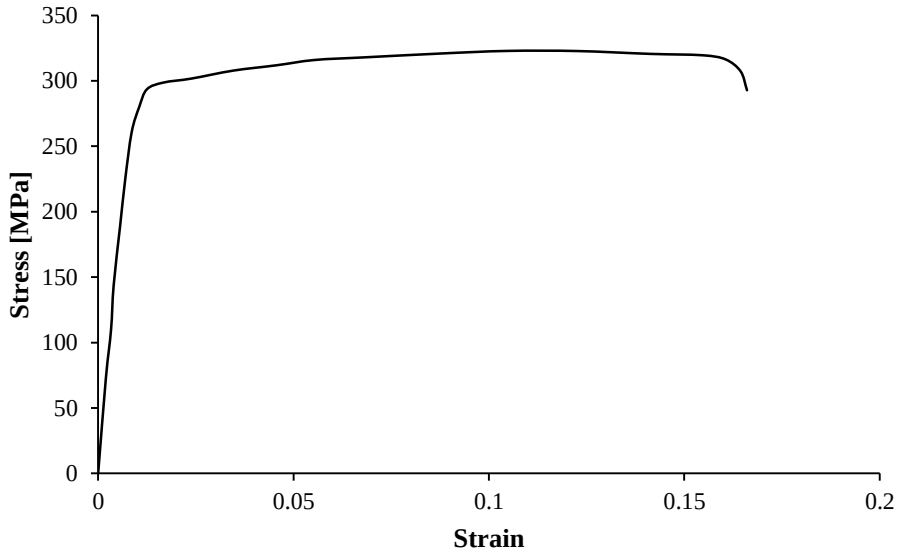

Figure 2.1 - Experimental Stress-Strain Profile of AA6082-T6 Aluminium

Figure 2.2 provides the expected fatigue life of the base material [6]. This data provides a good starting point for the loading and expected number of cycles that one should expect from the AA6082-T6 material being used in this research. In the medium stress amplitude range there is very little variation in fatigue life in the two material directions.

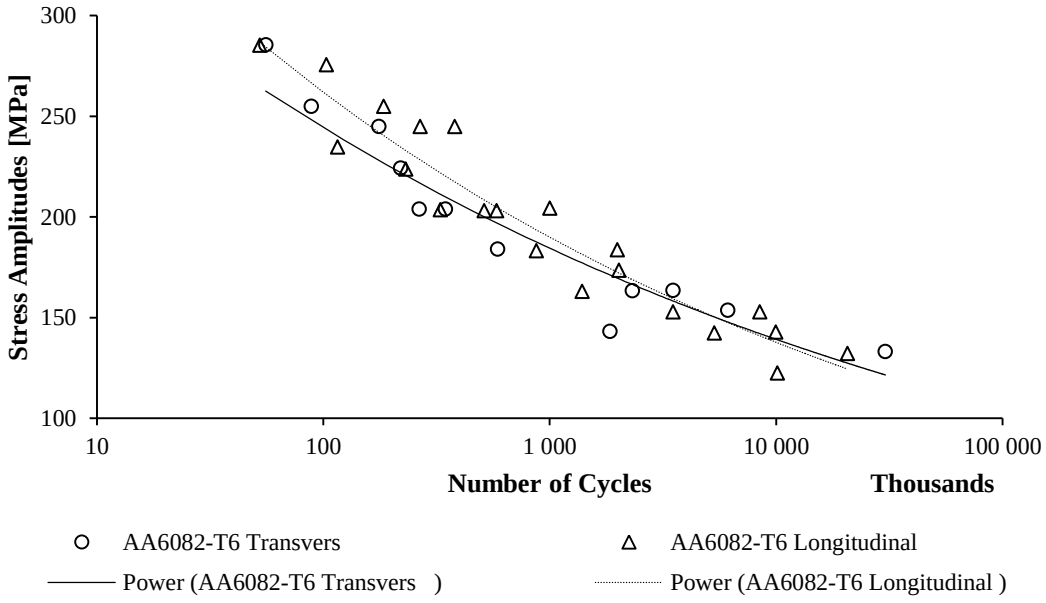

Figure 2.2 - S-N Fatigue Curve for AA6082-T6 Aluminium

2.2 Friction Stir Welding

In this solid state joining process two sheets of parent material are clamped and welded by a rotating tool which is plunged into the joining line of the plates. The tool locally heats the material due to friction resulting in a plasticised region forming around the tool. This softened material is then mechanically stirred under the pressure and rotation of the welding implement. On cooling of the joint, a solid-state weld is formed along the joint line. The process is always performed at temperatures lower than that of the melting point of the respective alloy being joined. This process has been used to form bonds between many difficult to weld materials such as aluminium. It has also been used to join dissimilar materials and is finding suitable applications in aerospace, naval and automotive manufacturing. FSW is capable of producing typical welds such as lap or butt joints. The process is recognised for the following significant advantages [7]:

- Improved joint strength and efficiency.
- Improved fatigue life of the joint.
- Cleaner more efficient form of welding as there are no fumes or consumables used and created in the process.
- Lower heat distortion and shrinkage of the joining components.

2.2.1 Friction Stir Welding Terminology

The following is a list of terminology that is commonly used in FSW:

- **Plunging Force:** The vertical force applied to the tool by the driving machine required to plunge and maintain the tool in the joining material as the tool travels.
- **Welding Tool:** Implement used to produce the frictional heat and complete the stirring function of the process.
- **Welding Direction:** The direction in which the tool moves along the joining line.
- **Retreating Side:** The region of the weld in which material is being pulled by the tool to be deposited. The tool rotational direction is opposite to the direction of the tool travel.
- **Advancing Side:** The regions of the weld where the material is being deposited thus form the bond. The tool rotation is in the same direction of the tool travel.

Figure 2.3 shows were the basic terminology is applied during the process [8]. A rudimentary view of the welding tool and material interaction has been illustrated in the figure.

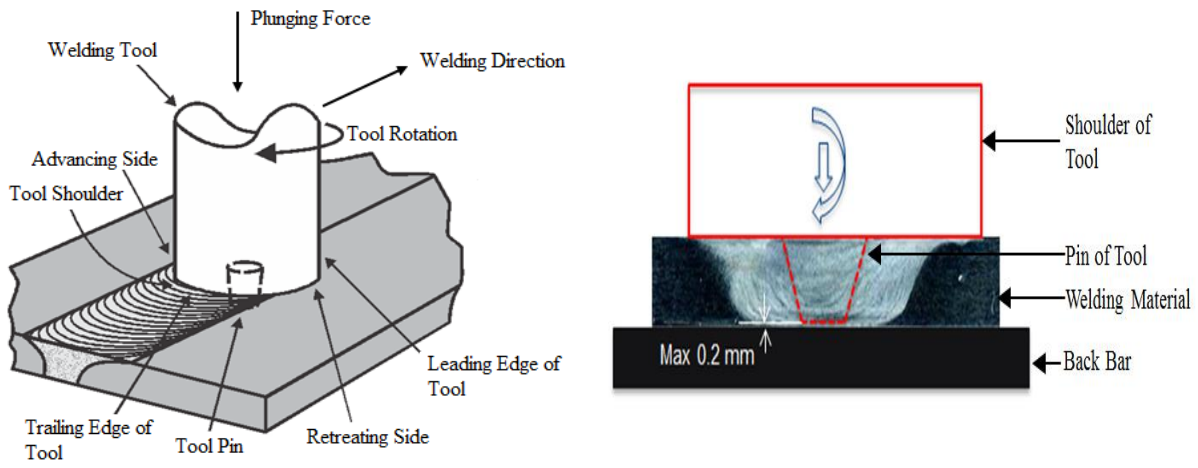

Figure 2.3 – Friction Stir Welding Terminology

2.2.2 Friction Stir Welding Process Phases

During the completion of any FSW application the following process will be completed. The method is outlined as follows:

1. Stage 1 - Rotation

This is the beginning stage at which point the tool spindle starts to rotate at the predetermined RPM. Once the spindle has achieved its set rotational speed it will remain at this point for the duration of the weld. Figure 2.4 indicates this stage of the process [9].

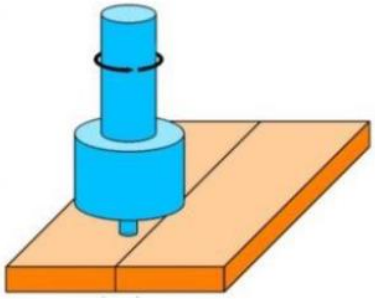

Figure 2.4 - Stage 1 of the Friction Stir Welding Process - Tool Rotation

2. Stage 2 - Plunge

The rotating tool is brought into contact with the surface of the welding plates. The tool is continuously driven into the plates at a constant rate. This action is similar to drilling as the tool will plunge until the shoulder of the tool achieves its required depth. Figure 2.5 indicated an example of this action.

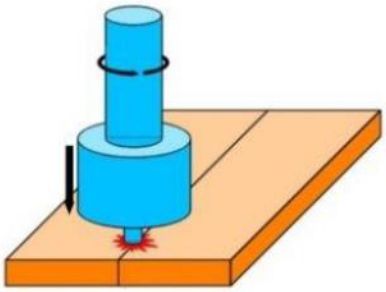

Figure 2.5 - Stage 2 of the Friction Stir Welding Process – Plunge of Tool

3. Stage 3 - Dwell

When the tool shoulder achieves the required plunge depth below the surface of the welding plates, the tool is allowed to rotate in a fixed position for a set period of time. The constant rotation of the tool produces a build-up of heat caused by frictional contact, resulting in a plasticised material. Figure 2.6 provides an example of this action.

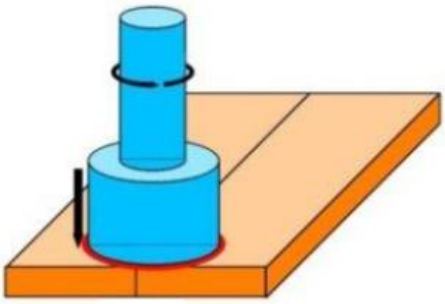

Figure 2.6 - Stage 3 of the Friction Stir Welding Process – Dwell

4. Stage 4 – Feed

Once sufficient heat has been produced the tool is then pulled (translated) along the joining line of the plates. The completion of this stage results in the completion of an FSW joint. Figure 2.7 indicates this action.

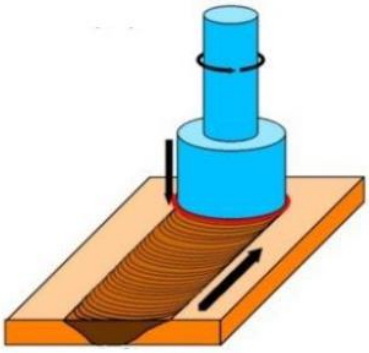

Figure 2.7 - Stage 4 of the Friction Stir Welding Process – Feeding of the Weld

Each stage gives rise to a specific process parameter that is required to be controlled and which has a dramatic influence on the resulting weld. Each of these parameters was discussed in the next section.

2.2.3 Friction Stir Welding Process Parameters

The process of FSW is controlled by a number of key parameters that should be monitored during welding. The following is a list the most important welding parameters:

- **Tool Rotation:** Rotation of the tool which results in the frictional heat and stirring of the material. Measured in revolutions per minute (RPM).
- **Plunge Depth:** Depth that the tool shoulder is forced below the top surface of the joining plates. Measured in millimetres (mm).
- **Plunge Rate:** The time taken for the tool to achieve its plunging depth, speed at which the tool is driven into the sheets of material. Measured in mm per second (mm/s).
- **Dwell Time:** The time that the tool remains stationary once reaching its required plunging depth. Measured in seconds (s).
- **Feed Rate:** The rate at which the tool transverse along the weld line. Measured in mm per minute (mm/min).
- **Weld Pitch Ratio (WPR):** The ratio between feed rate and RPM. Measured in millimetres per revolution (mm/rev).

The WPR has been found to be an acceptable method to define the plasticised material during welding as it can be used to define the range of hot and cold conditions of the weld [10]. The WPR can be calculated according to equation 2.1.

$$WPR = \frac{R}{V_F} \tag{2.1}$$

The following definitions gave an idea of the type of welding condition that will be obtained with the following ratios in Table 2.3. Experimental results have shown that the intermediate condition generally resulted in the best welds.

Table 2.3 - Weld Pitch Ratio Characterisation

Condition	WPR Range
Cold	<2
Intermediate	2 - 4
Hot	>4

2.2.4 Friction Stir Welding Tool Geometry and Welding Support Method

Since the invention of FSW, a number of variations of tool geometry have been used in an attempt to produce welds of ever increasing quality and efficiency. This process involves advanced material

movement which is directly related to the tool design, force control and temperature generation caused by the tool.

The tool is the governing factor in relation to how good a joint is and how quickly it can be produced. If the pin is offset or does not protrude far enough into the joining plates, a defective weld which has LOP will most likely result. All FSW tools are made of two vital components, a pin and a shoulder. The pin is the portion of the tool that is completely plunged into the joining material, in certain methods of welding the pin protrudes from the underside of the joining plates. The shoulder is general plunged only a few microns into the upper surface of the joining plates and must be in contact at all times to produce sufficient heat for the process as well as apply enough force to stir the plasticised material [11]. The relative size of the pin and shoulder are the two most important dimensions in the design of the welding tool. A number of tool pins and shoulders make use of complex features such as those shown in Figure 2.8 [11], [12]. The most commonly used shoulder feature is a scrolled profile as this draws in material from the outer circumference of the shoulder towards the pin. This feature eliminates the need for tilting the tool during welding.

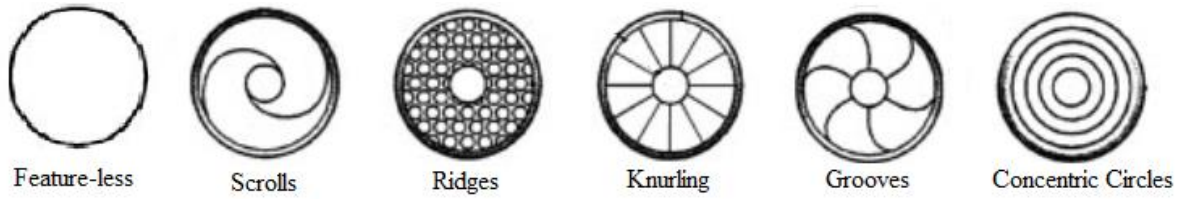

Figure 2.8 – Common Friction Stir Welding Shoulder Features

Generally, some form of profiling is applied to the pin to improve material movement. Common features are threading or chamfering/cut out portions of the pin to make distinct corners. A variety of pin profiles are shown in Figure 2.9. These profiles are used to improve the flow of material around the probe and reduce the loading on the tool [13]. Due to larger surface areas of the pin in contact with the joining material, tapered pins have been found to produce higher frictional heat during the welding process.

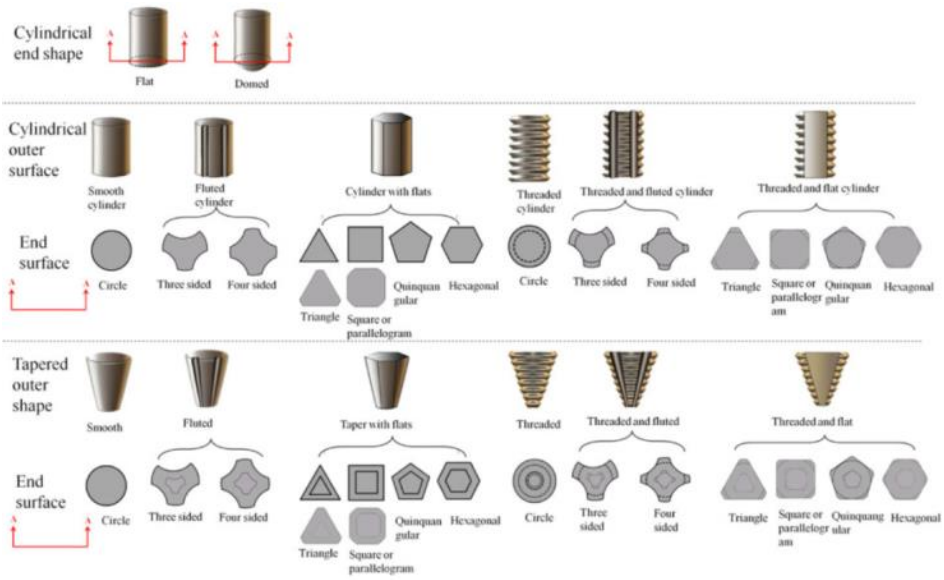

Figure 2.9 – Common Friction Stir Welding Pin Profiles

The complexity in which FSW is completed is attributed to the type of welding support method being performed and the overall set up of the apparatus being used. Researchers have attempted a wide variety of support systems in the attempt to produce a viable industrial process that is cost effective, repeatable and produces excellent quality welds. Methods such as backing bars, self-supporting, through thickness and bobbing pin welding are just a few methods that have been trailed and characterised by other researchers. The backing bar method will be further investigated as this is the most favourable method which will be employed in this research.

The Backing bar FSW method is the simplest and easiest method to perform high quality FSW. The apparatus set up is fairly simple and inexpensive due to the requirement of only one pin and shoulder tool set and some form of clamping set up. The welding plates are clamped to a backing plate, generally made of steel and the tool plunges a set distance into the welding plate. A distance of 0.1 to 0.2 mm is the general range from the tip of the pin to the backing plate. The gap ensures that the pin and the steel backing plate do not come into contact resulting in damage to the apertures and tool. Figure 2.10 shows a schematic of a standard FSW tool.

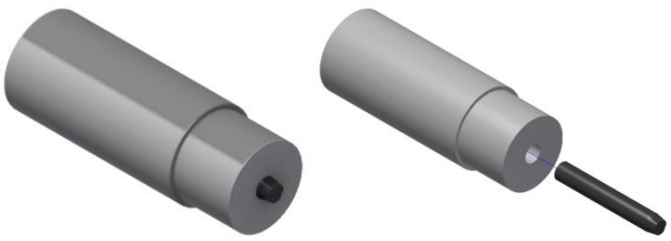

Figure 2.10 - Standard Friction Stir Welding Tool

All FSW completed at the University of the Witwatersrand is completed on a retrofitted Maho MH-C 700 CNC horizontal vertical tool roaming milling machine. This machine is located at the University of the Witwatersrand Barloworld Mechanical Engineering Laboratory. Figure 2.11 shows the CNC in its current operating state.

Figure 2.11 - Retrofitted Maho MH-C 700 CNC Friction Stir Welding Apparatus

Figure 2.12 shows the schematic setup of a backing bar FSW apparatus currently being used at the University of the Witwatersrand.

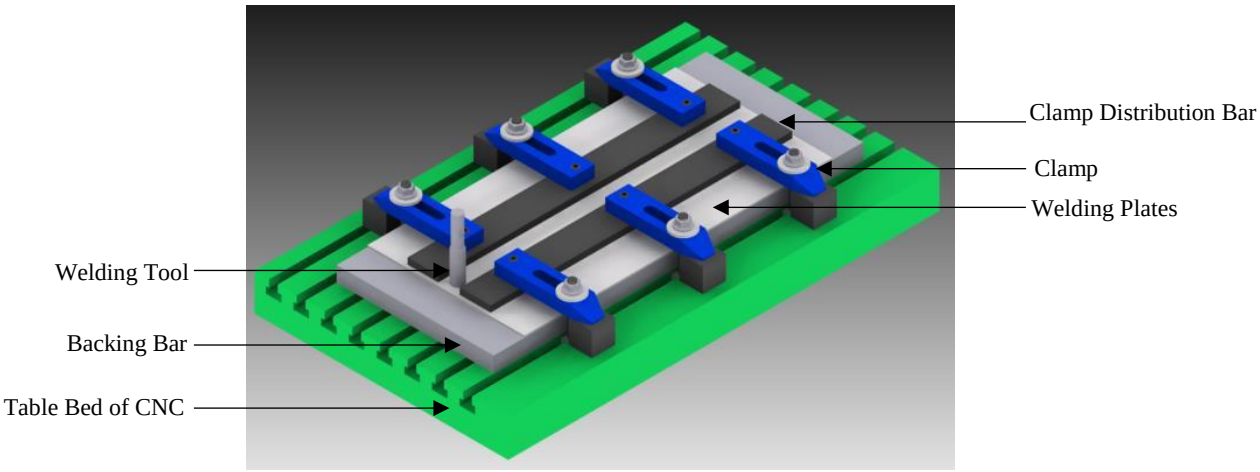

Figure 2.12 – Schematic of a Backing Bar Apparatus

Figure 2.13 shows an actuate representation of the apparatus in operation [14].

Figure 2.13 –Representation of the Backing bar Method

2.3 Friction Stir Welding Joints

Friction Stir Welding produces a unique joint which will be investigated further within this section.

2.3.1 Friction Stir Welded Joint Microstructure

The microstructure of an FSW joint has distinctive recrystallization areas which are caused by the intensive plastic deformation, heating and cooling rates and material flow resulting in four unique zones, these areas are listed below [11] and shown schematically in Figure 2.14 [15].

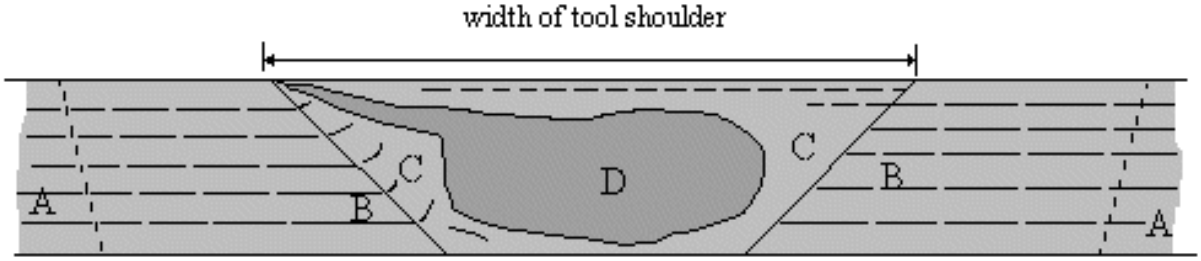

Figure 2.14 – Friction Stir Welded Joint Microstructure

A. **Unaffected base material (BM):** Material that has not been deformed by the welding process may have been exposed to thermal cycling, but there is no evidence of microstructure change.
B. **Heat Affected Zone (HAZ):** This zone is exposed to a thermal cycle, but does not undergo physical deformation. The HAZ maintains roughly the same grain structure as the parent material.
C. **Thermo-Mechanically Affected Zone (TMAZ):** This zone is unique to FSW as it undergoes thermal changes and mechanical deformation. This zone is a transition between the weld nugget and the parent material.

D. **Nugget Zone (NZ):** This is a region of extensive plastic deformation and thermal change due to frictional heat. The recrystallization of the grains results in a fine microstructure.

Each region of the weld presents distinct material properties, this is a characteristic of the type of material, the selected parameters and tool used for welding. Many researchers have shown that the HAZ on the advancing side of the weld was the weakest section as failure occurred there the most when static loading was applied [16]. The rotation of the tool is the major contributing factor for the asymmetric profile noted with FSW. The rotation causes a differential in temperature and material flow across the vertical centre of the tool axis thus producing the unique microstructure.

2.3.1.1 Microstructure Analysis of Friction Stir Welded AA6082-T6 Aluminium

The geometric size of the welds cross section of AA6082-T6 or any aluminium alloy for this matter will be dependent on the features of the welding tool and selected parameters. Typically the features and the boundaries between zones appear to be sharper on the advancing side of the weld due to the nature of FSW.

Various researchers have shown that the four distinct regions are clearly formed during FSW of AA6082-T6 [17]. The inhomogeneous welding nugget has been found to display a band "ring pattern" microstructure. This type of structure is associated with the tool design and the tool advance per revolution [18]. The ring patterns are clearly visible in the examples of typical FSW AA6082-T6 microstructures presented in Figure 2.15[16], [18]. In both profiles, the nugget area tapers through the thickness with the widest section being closest to the crown of the weld, due to the stirring effects of the shoulder. The rings in Figure 2.15.a are spaced approximately 20 to 30 μm wide and there were no grain size variations in the area between rings and out of the ringed area. The formation of the rings is due to complex material flow and rotation of the tool [19]. The grains in the nugget zone were found to be approximately 10μm for Figure 2.15.a and between 1 to 5 μm for Figure 2.15.b. The orientation of both sets of grains were in the typical equiaxed shape, a higher magnification of the spacing was shown in Figure 2.16 [18]. The refined recystallised grains are a function of high strain rates and elevated temperatures in that region.

a)

b)

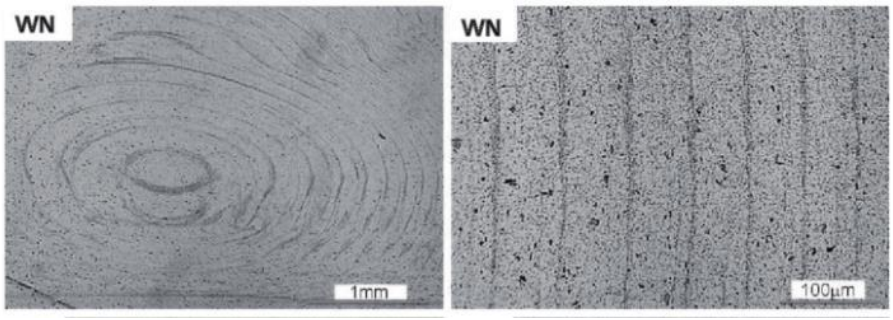

Figure 2.15 - Microstructure of AA6082-T6 Friction Stir Welded Joints

Comparing Figure 2.15 a to b one can see the influence of welding tool design, process parameters and sheet thickness as there is a clear variation in the grain size, weld bandwidth and material distribution. Figure 2.16 showed an example of the gran structure within the nugget region of a FSW joint manufactured in AA6082-T6.

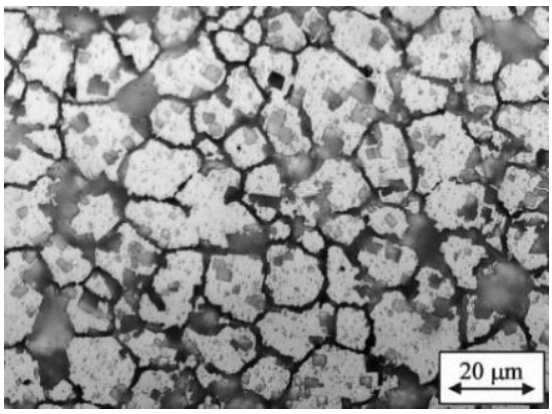

Figure 2.16 - Typical Equiaxed Grain Shape within the Nugget of an AA6082-T6 Friction Stir Welds

The boundary between the nugget and the TMAZ is a clear and sharp transition as the grains of the TMAZ are bent around the nugget zone. The large deformation within the TMAZ does not cause recrystallization of the grains but rather a deformation, elongation and rotation due to the applied strain. The three images of Figure 2.17 shows the transition between the nugget and TMAZ, image b

shows smaller equiaxed grains on the left-hand side of the image whilst larger rotated grains can be seen in the remain sections of the image [16], [18].

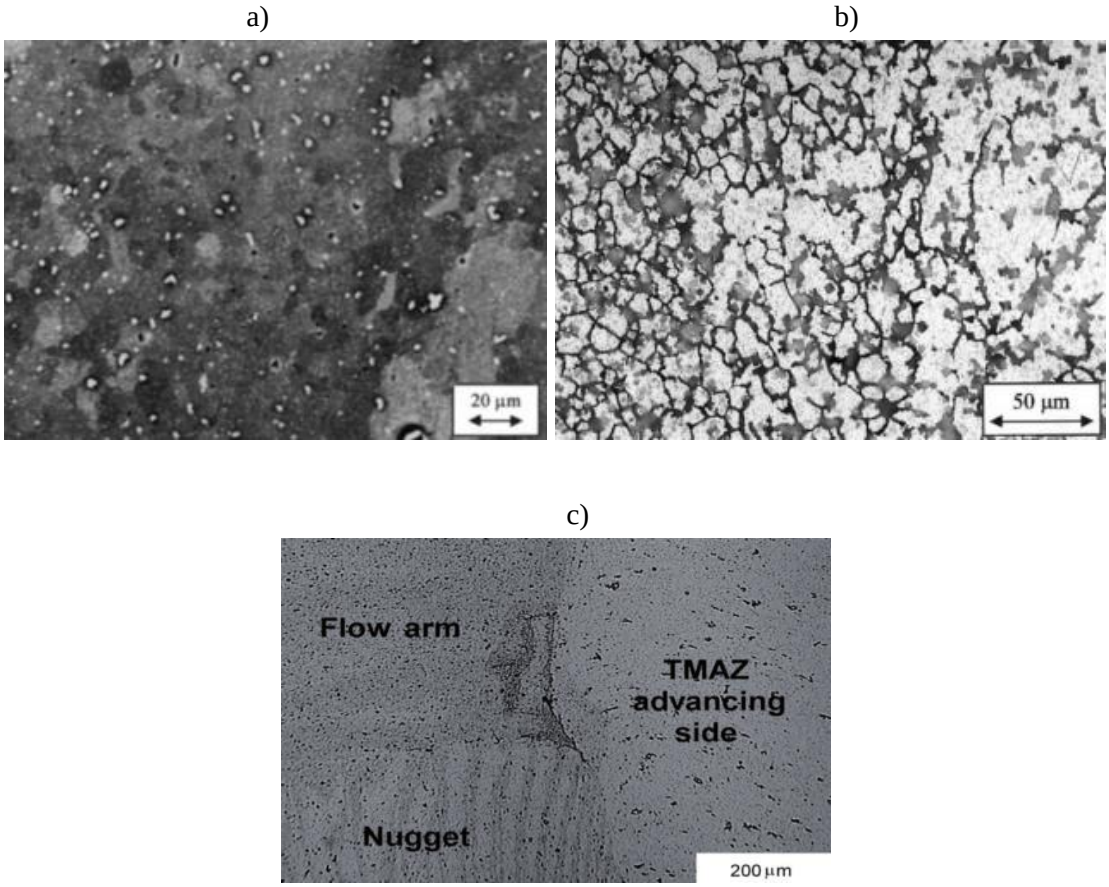

Figure 2.17 - Transition between Welding Nugget and Thermo-Mechanically Affected Zone

The HAZ has been found to be the weakest of all the regions within a FSW cross section. The microstructure in this region is extremely similar to that of the base material. The grains are typically overgrown due to the exposure of the welding heat [16]. Figure 2.18.a and b show the effects of the heat on the size of the grains whilst images c and d show the similarity between the HAZ and base material [16],[17].

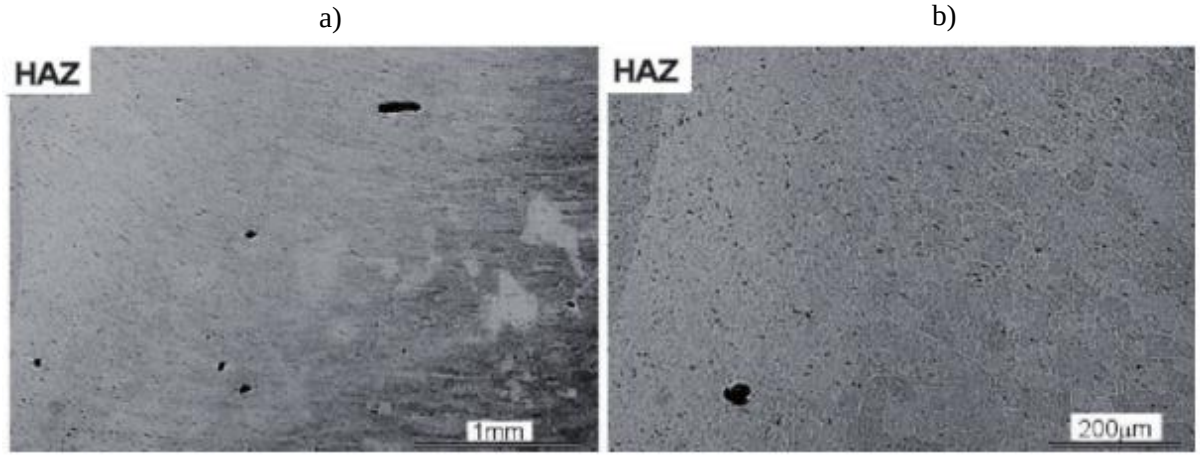

c) d)

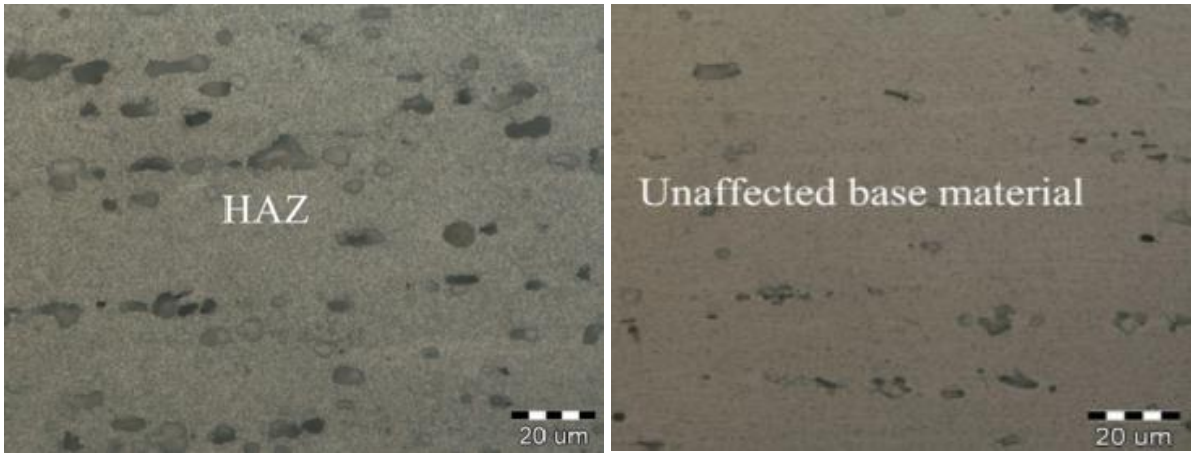

Figure 2.18 - Microstructure of Friction Stir Welded AA6082-T6 Heat Affected Zones

The HAZ retains roughly the same grain structure with the parent material as it does not undergo any mechanically induced plastic deformation. The HAZ may be exposed to aging phenomena and in some cases over aging may occur due to excessive heat in this region. A microstructural transformation takes place due to the thermodynamic instabilities of the precipitates [20]. The over aging of the HAZ in FSW AA6061-T6 produces a transformation of the β″ (needle shape) precipitates into β″ (rod shape) precipitates. Figure 2.19 a and b show the difference between the nugget (image a) and the HAZ (image b) with respect to very fine scale precipitation. Fine needles of β″0Mg_{1-7}Si have nucleated on the dispersoids in the HAZ whilst the dispersoids in the nugget are free from precipitates [18].

a) b)

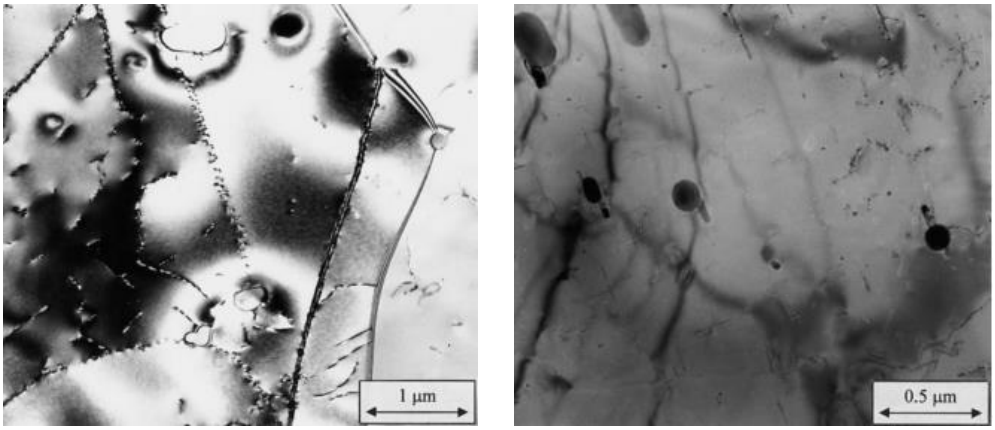

Figure 2.19 – Precipitant Transformation in various Friction Stir Welded Regions

The transformation of the precipitates is one of the main cause of the reduction in mechanical strength of the HAZ as they contribute to fractures such as hardness and grain quality.

2.3.2 Forces Related to Friction Stir Welding

Unlike most other purely thermal welding process, the forces generated during any FSW application are considerably large. This is due to the mechanical stirring and feeding of the tool through the working material. Neglecting to monitor and control these forces can result in poor quality welds and

extreme damage to welding equipment. Figure 2.20 proves a schematic free body diagram of the forces and moment accustom with FSW [21]. The longitudinal force, F_x, is perpendicular to the traversing axis. The transverse force, F_y, is the force acting in the direction of the tool as it feeds along the weld bead. The magnitude of this force can indicate the temperature of the material is as it is this force required to overcome the resistance of the material to the translation of the tool. Commonly known as the normal force, F_Z, it acts along the tool central axis. It is the most important force as it maintains the tool relative to the welding surface. Insufficient force has been shown to result in welding defects such as pin holes and tunnels. The torque applied to the tool, M_Z, was the critical design point used for the design and specification of the tool. This moment needs to be taken into account whilst designing the tool.

Monitoring of these forces during welding should always be done as the respective force and moment profiles are clear indicators weather irregularities occurred during welding. Excessive force will also stress the tool to a greater extent thus increasing tool wear and reducing the repeatability of the welds.

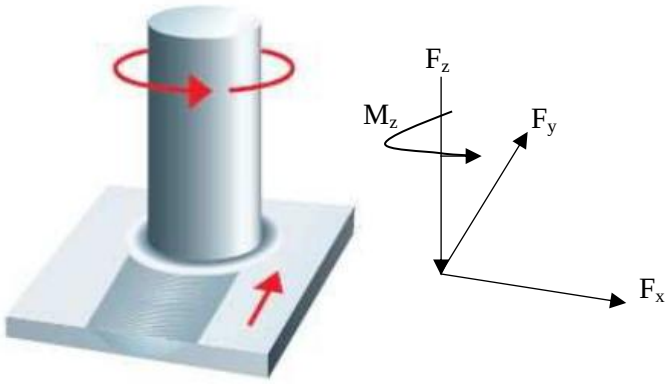

Figure 2.20 - Schematic Layout of Forces Related to Friction Stir Welding

Assessing the normal force and torque while welding shows four distinct events, these relate directly to the four phases discussed in section 2.2.2. Initially, when the pin makes contact with the material the normal force increases rapidly due to the physical drilling of the cold material. The force continues to increase as the pin enters the material. The force then quickly increases to its maximum value as the shoulder makes contact with the surface. At the start of the dwell period the force begins to steadily reduce as temperature build up occurs yielding the material easier. Depending on the selected welding parameters the normal force should achieve a steady state within a few millimetres of the weld. The force will remain fairly constant until reaching the end of the weld, at which point the forces return to zero as the tool is retracted. Figure 2.21 shows an example of how much greater the normal force is compared to the welding (transverse) force during FSW, the regions previously explained can be clearly be seen [22].

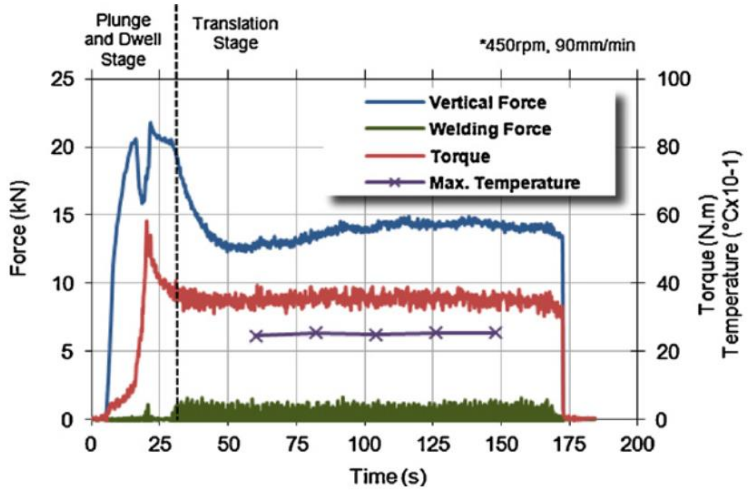

Figure 2.21 - Examples of Normal Force Monitoring during Friction Stir Welding

Figure 2.22 shows the effects of varying the feed rate during FSW [23]. It is evident when comparing like combinations of welds that the greater the feed rate the higher the normal forces. This is accredited to the fact that as the weld speed increases the temperature of the forthcoming material is much lower thus a higher force is required to yield the material.

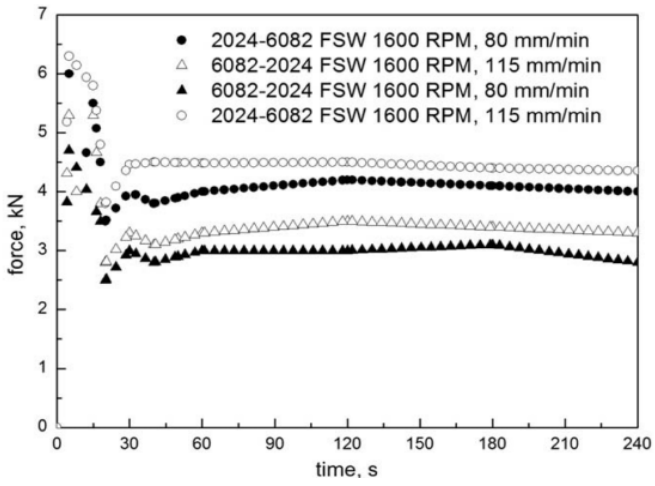

Figure 2.22 - Normal Force Variations due to Different Welding Parameters

It should be noted that in both examples of normal forces the magnitude is of the kN range. This shows that the process of FSW is related to extremely high forces which need to be controlled and monitored.

2.3.3 Thermal Effect and Temperature Generation during Friction Stir Welding

The temperature generated during FSW attributed to by the interaction between the rotating tool and working material. The temperature distribution of the welded and surrounding area greatly influences the overall mechanical properties and character of the joint [11].

Many attempts have been made by researchers to accurately measure and simulate the thermal process of FSW. Common methods employed is the use of multiple embedded thermocouples placed along the welding material, these thermocouples need to be placed sufficiently close to the edge of the weld to accurately record the temperature. Once the feed stage has begun, a number of thermocouples can be placed across the recently welded material in order to obtain a temperature map across welded material. Alternatively, estimations of the temperature can be made through analysis of the post weld microstructure. A secondary method of temperature capture is through the use of an infrared thermal camera which records their infrared signature of the weld thus leading to the determination of the temperature of the welded component.

The temperature generated is heavily influenced by the size and shape of the welding tool, the welding parameters (spindle speed, feed rate and plunge depth) and the material being welded. Table 2.4 lists the maximum temperatures generated in various aluminium alloys due to various welding tool geometries and welding parameters. The maximum temperatures for all welding combinations were all well below the individual material's melting temperatures.

Table 2.4 - Maximum Measured Temperatures from various Friction Stir Welding Applications

Alloy	Tool Geometry [mm]		Welding Parameters				Measured
	Shoulder Diameter	Pin Diameter	Spindle Speed [RPM]	Feed Rate [mm/min]	Welding Rate [rev/mm]	Normal Force [kN]	Measured Max Temp. [°C]
AA7108-T79 [24]	15	5	1500	300	5.00	7	375
			1500	480	3.13	7	290
			1500	720	2.08	7	250
AA6061-T6 [25]	24	19	344	132	2.61	13	425
AA6061-T651[26]	25.4	10	390	144	2.71	22	466
AA6082-T6 [24]	15	5	1500	300	5.00	7	321
			1500	480	3.13	7	275
			1500	720	2.08	7	250
			180	51	3.53	20	355
			180	78	2.31	25	350
			180	102	1.76	28	320
AA7050-T7451 [27]	20.4	7.2	360	102	3.53	24	400
			540	150	3.60	34	390
			810	228	3.55	39	430
AA7050-T7451 [28]	19	6.4	490	84	5.83	20	220
			700	60	11.67	13	260
			700	114	6.14	16	220
			700	156	4.49	18	210

Of particular interest are the measured maximum temperatures of the FSW of 6 mm thick AA6082-T6 aluminium. For clarity, the data has been plotted in Figure 2.23 As expected an increase in welding rate results in an increase in the maximum temperature generated in the weld [29]. The normal welding force has been indicated next each data point. For the constant force of 7kN and spindle speed of 1500 RPM, there was a fairly linear increase temperature with increasing welding rate whilst for varying force and much lower spindle speed the near linear trend was no longer observed. This may be attributed to the varying normal force. Although it would be assumed that a higher RPM would result in a greater temperature the welds conducted under greater force but lower welding parameters which equated to similar welding rates produced the higher maximum temperatures. What should be noted is that the slower speed welds were done at welding force 286%, 357% and 400% higher than those of the higher welding parameter.

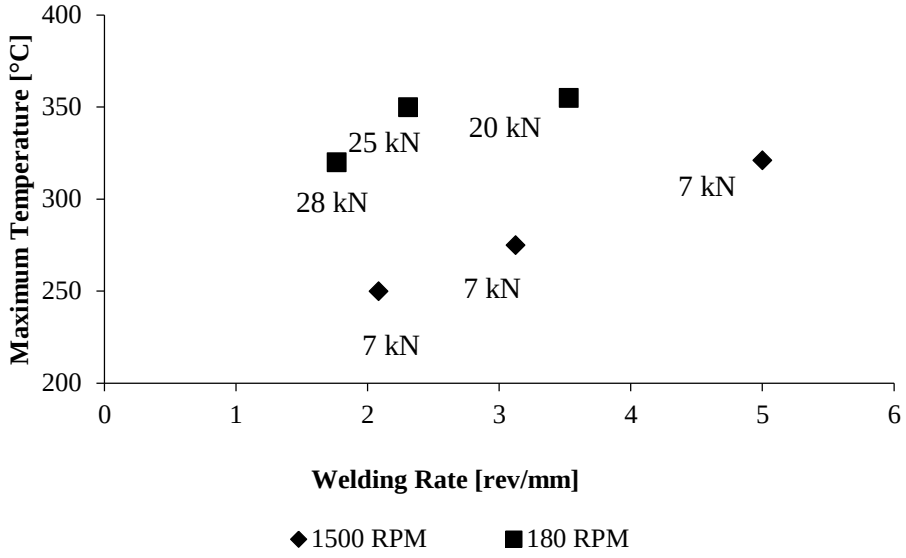

Figure 2.23 - Maximum Measured Temperatures which occurred during the Friction Stir Welding of AA6082-T6

From Table 2.4 and Figure 2.23, it can be concluded that increasing welding rate results in a higher temperature. Thus, an increase in tool rotational speed for a fix feed rate would produce a higher peak temperature. Varying welding force affects the linearity of the increase in maximum recorded temperature. It is expected that the higher the normal welding force the higher the temperature, this fact was confirmed by Figure C.3 in Appendix C.2 [30]. The effects of tool geometry and alloy could not be concluded fully, but intuitively one would expect that the greater the surface area of the tool the more frictional heat that would be generated. These assumptions were confirmed by Figure 2.24 which shows the effect of increasing tool rotational speed for a fixed feed rate [31]. It is clear that the peak temperature increases with increasing spindle speed. The highest temperatures were measured at the centre of the weld, with a steady decrease being observed moving away from the centre. This data was produced at a fixed feed rate of 120 mm/min. It can be seen that at the weld centre that the difference between 300 and 650 RPM was roughly 40°C whilst the difference between 650 and 1000

RPM was only 20°C. This suggests that the rate of temperature increase is lower for higher tool rotational speeds. It has been confirmed that for a given tool geometry the maximum temperature is strongly influenced by the tool rotational speed whilst the rate at which the heating of the weld occurs is a function of the feed rate [32].

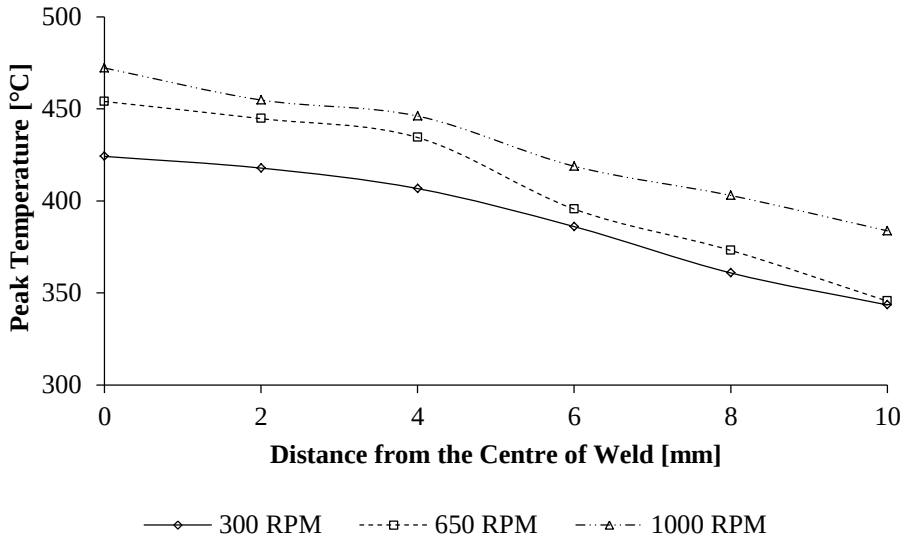

Figure 2.24 – Effect of Tool Rotational Speed on Peak Temperature as a function from the Weld Centre Line for AA6061-T6

A recent study was conducted in order to gain a greater understanding of the temperatures through the thickness a FSW joint. The study was conducted using a number of embedded thermocouples in 6.35 mm thick AA7075-T651. In this experiment, the peak temperature distribution adjustment to the stirred zone was achieved. Figure 2.25 shows the variation in peak temperatures through the welded sample [11]. Two extremely important observations can be made about this temperature distribution:

1. The maximum temperatures were recorded at locations close to the stirred zone.
2. The upper surface was the highest temperature, with a steady decrease in temperature through the thickness of the weld.

Although the temperature does get fairly high it should never surpass the melting temperature of the material.

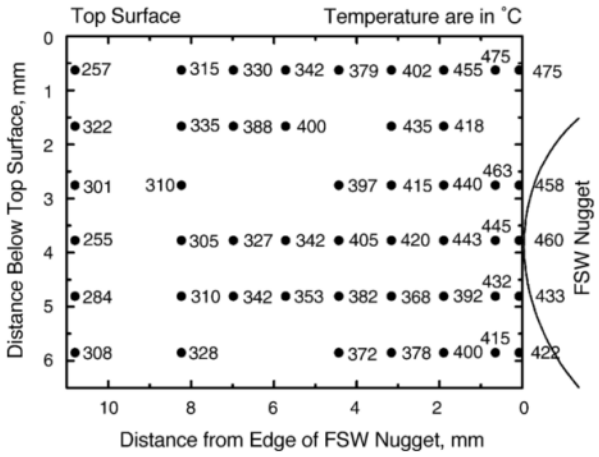

Figure 2.25 - Peak Temperature Distribution in Friction Stir Welded AA7075-T651

A similar attempt to obtain the temperature distribution through the welded was attempted in 6.4 mm AA6061-T6. The various thermocouples across the welding area were embedded at three depths through the thickness (1.59, 3.18and 4.76 mm). Figure 2.26 shows the variation in temperature across the welded [31]. Thermocouples which were placed on the opposite side of the weld showed no difference in temperature from the side of the weld shown below. The approximate symmetry in the temperature distribution across the weld was not observed by all researcher as it has been noted that there have been cases were slightly higher temperatures on the advancing side of the joint where the tangential velocity vector direction was the same as the forward velocity vector [33]. The peak temperature was found to occur in the region close to the centre of the weld and the temperature steadily decreased moving further outwards from the centre. The decrease in temperature through the thickness can again be seen here as the thermocouples which were closest to the top surface of the weld recorded the highest temperatures. This result was obtained with a tool rotation of 400 RPM and feed rate of 122 mm/min. The change in temperature through the thickness and up to 4 mm from the centre of the line was fairly small, indicating that the temperature distribution throughout the stirred zone was relatively uniform.

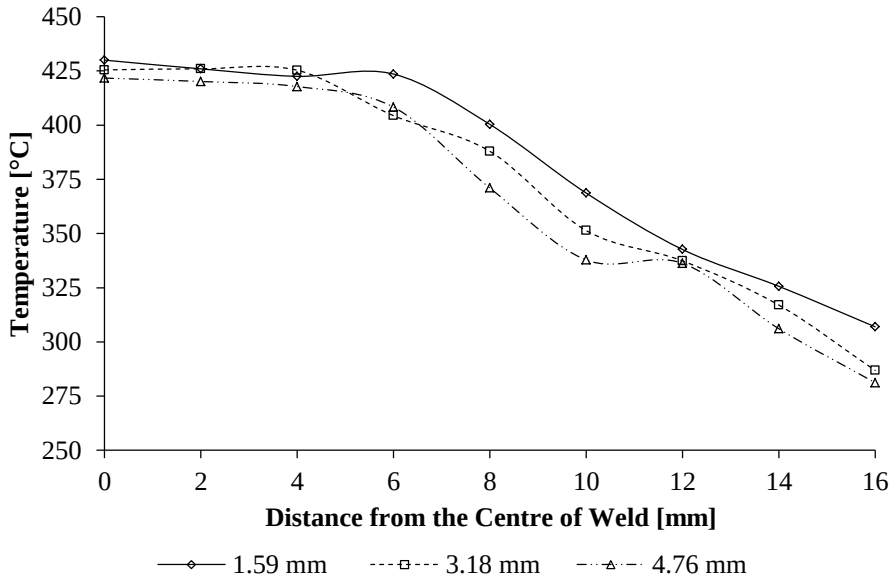

Figure 2.26 – Variation in Peak Temperature with Distance from the Weld Centre at various Depths in Friction Stir Welded AA6061-T6

Figure 2.27 shows the typical temperature history different positions along the weld [31]. It can be seen that during the plunge stage of the process a sharp increase in temperature occurs. The maximum temperature is achieved during the dwell stage, followed by a decrease in temperature upon the material plasticising. The temperature at each measurement position tended towards a fairly constant value once the feed stage begins. The temperature tended to steadily decrease during the feeding process of the weld.

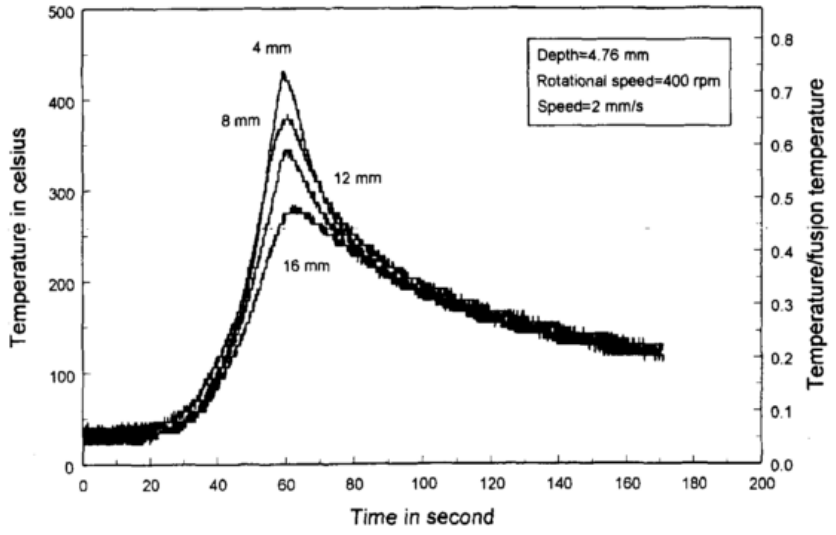

Figure 2.27 - Temperature History during the Full Friction Stir Welding Process

It is evident that the effect of temperature generation during the welding process is affected by the tool geometry and welding parameters. The quality and strength of the joint is directly influenced by the temperature as research has shown that unacceptable tensile strength are achieved if the tool-work

piece interface temperature is not high enough. These welds were found to fail in the nugget zone rather than the HAZ. Similarly, welds with shoulder temperatures above the solidus temperature results in a degradation of the weld quality [34].

2.3.4 Welding Defects

Inherent with all welding methods is the possibility of defect formation during the joining procedure. A defect is characterised as microstructural or geometric abnormity which adversely affects the performance of the joint [35]. Known causes of defects in FSW are related to process temperatures, material flow, welding parameters and tool design. The three main categories that define FSW defects can be broken down into the effects of the combination of feed rate and RPM. Cold processing defects are formed due to insufficient temperature during the weld. The inverse holds true for hot processing defects in which an excessive amount of heat causes defects to be formed. The third know defect cause is known as geometry related defects, in which poor and insufficient penetration of the tool occurs at the root of the weld. The Figure 2.28 shows the general trend of how defects are related to RPM and feed rate [35].

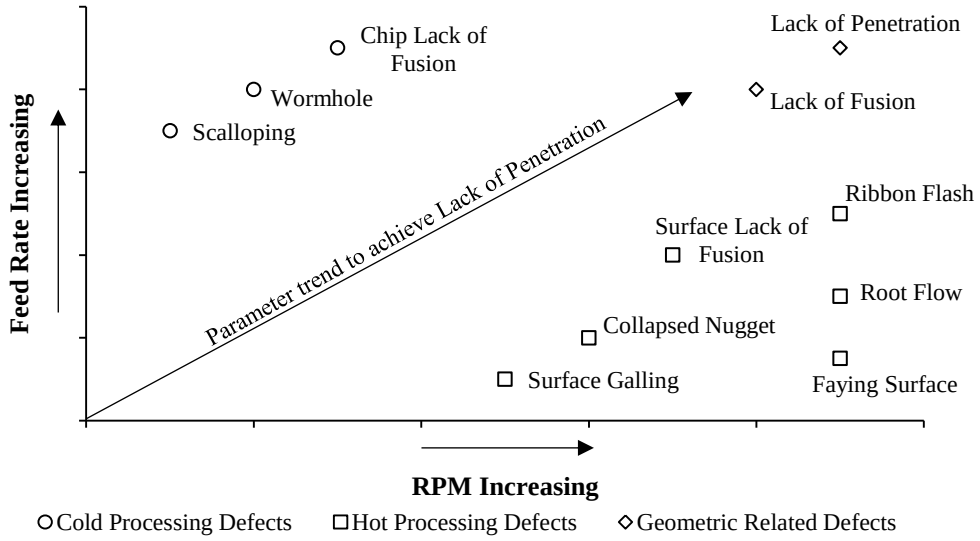

Figure 2.28 - Effects of Welding Parameters on the Type of Defect Formation

As indicated by the figure above high feed rates and RPM result in the best possibility of the formation of joints with Lack of Penetration (LOP). It is obvious that the flaws result due to insufficient pore and stirring of the material under these higher parameters. It was shown by [36] that if the welding rate is too fast then there is insufficient time for the weld to be filled leading to the formation of defects within the weld.

2.3.4.1 Scalloping

Scalloping can be defined as a series of small voids which are located on the advancing side interleaving the stir zone along the weld. This defect is caused due to insufficient temperature of the weld, not enough forging pressure created from the welding tool and a low welding pitch. Extensive scalloping will have a negative effect on the mechanical properties of the weld. Figure 2.29 shows the interlayer voids formed by this type of scalloping defect [35]. This cold process defect can be corrected by increasing the welding rate.

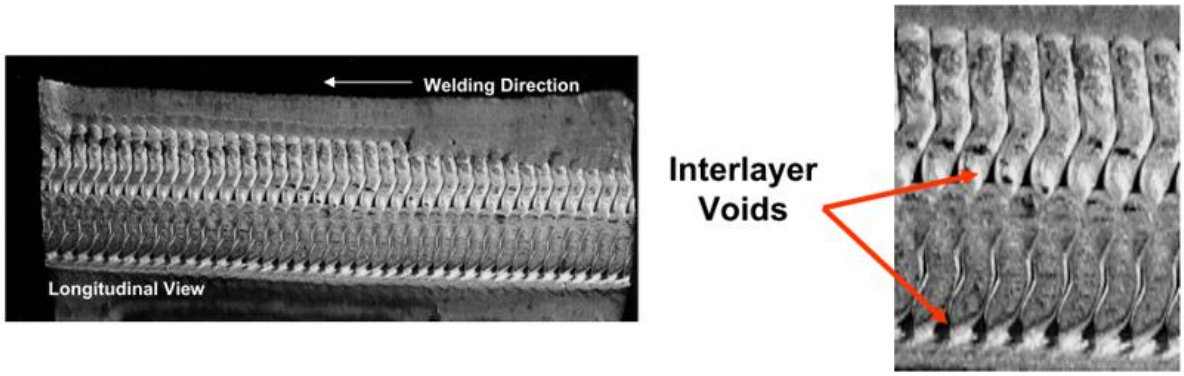

Figure 2.29 - Example of Extreme Scalloping

2.3.4.2 Wormholes and Voids

A wormhole is a tunnel like defect which is formed due to inadequately consolidated and forged material. The tunnel defect will typically be found on the advancing side and runs in the longitudinal direction [37]. The defect is caused by insufficient material flow in either the region where the pin and shoulder flow regions intersect or near the root. This lack of material flow can be corrected by better selection of the feed rate and RPM of the tool which will increase the welding temperature making it easier to manipulate the material. Severe worm holes will considerably reduce the mechanical properties of the weld. Figure 2.30 provides an example of the presence of a wormhole in the advancing section of the FSW sample [35].

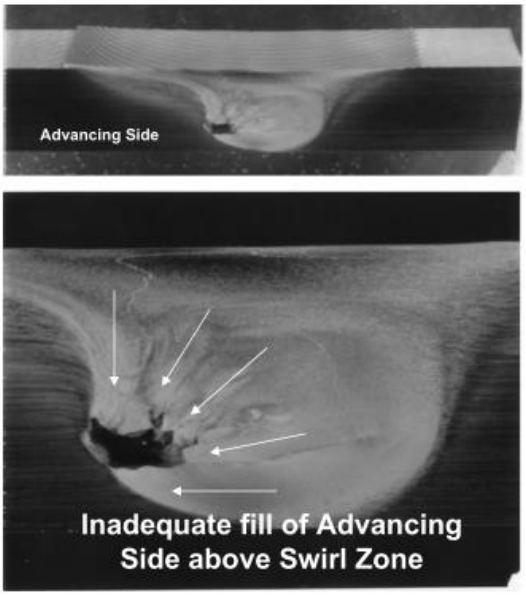

Figure 2.30 - Wormhole Formation due to Inadequate Filling of Material

Internal voids are exactly like a wormhole defect without propagating along the bead of the weld. A void is formed due to insufficient downward pressure of the tool, insufficient clamping pressure or too large a feed used in the welding process. Figure 2.31 shows examples of the presence of voids within FSW [21], [38].

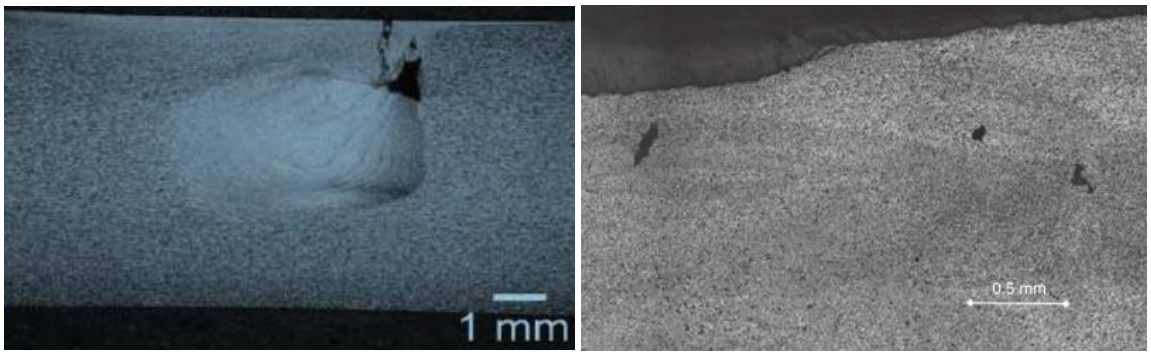

Figure 2.31 - Example of Voids formed in Friction Stir Welds

2.3.4.3 Chip Lack of Fusion

This defect is a type of void which is formed by small shards of metal that were sheared off the parent material. These shards maintain their form and are placed into regions of the welds forming discontinuities within the joint. They are caused by insufficient heating which causes shearing and cutting of the parent material. This defect most commonly occurs with excessively cold defects. The chips cause a reduction in the mechanical properties of the weld due to the formation of discontinuities in the joint. Figure 2.32 provides an example of this form of defect [35].

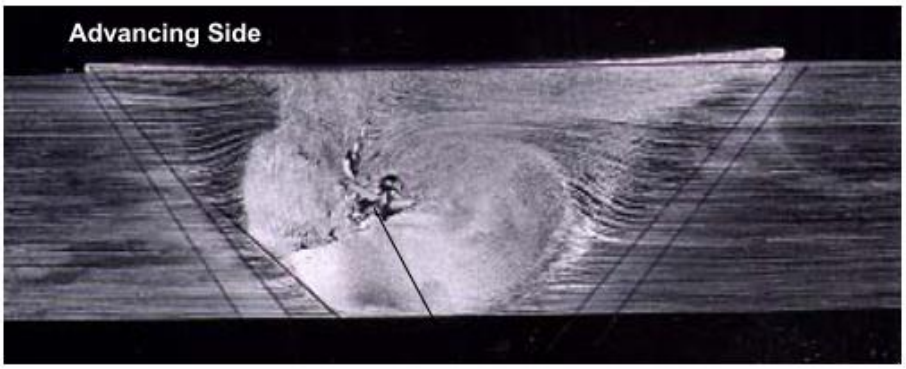

Figure 2.32 - Example of Chip Lack of Fill in Friction Stir Welded Joints

2.3.4.4 Surface Galling

Surface galling is the tearing of the metal on the top surface of the weld beneath the pin. The defect occurs at the crown surface of the weld. It is caused by excessively hot welds which are related to parameters which give high welding rates. Severe surface galling produces a negative effect on the mechanical properties of the weld. Figure 2.33 provides an example of surface galling [35].

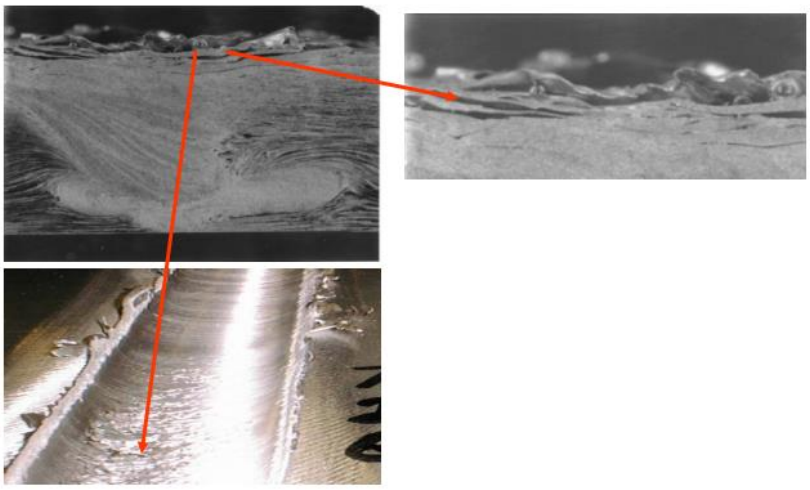

Figure 2.33 - Example of Surface Galling caused by Tearing of Joint during Friction Stir Welding

2.3.4.5 Nugget Collapse

This defect occurs due to improper formation of the dynamically recrystallized zone. It is caused by excessive flow arm formation and material flow from the advancing side into the nugget area. This defect is typical of an excessively hot weld, related to a high welding rate. The collapse will negatively affect the mechanical properties and the structure of the weld. Figure 2.34 shows an example of nugget collapse, an excess flow of material can clearly be seen from the left hand side (advancing) of the weld [35].

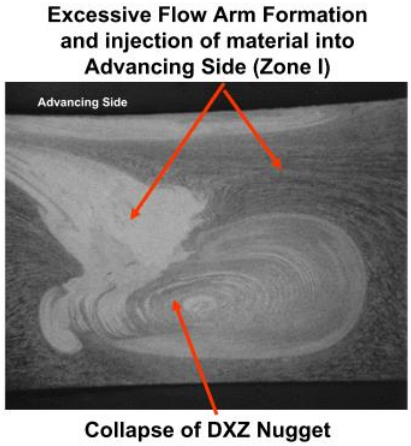

Figure 2.34 - Example of Nugget Collapse of a Friction Stir Welded Joint

2.3.4.6 Surface Lack of Fusion

Surface lack of fusion is a crown surface void which is formed on the advancing side of the weld. It is caused due to insufficient flow arm formation across the crown surface of the weld. The defect is caused by insufficient downward pressure or clamping pressure as the plates move apart. In the cases of an extreme amount of surface lack of fusion the mechanical properties of the joint can be greatly reduced. Figure 2.35 provides an example of insufficient completion of the welding surface, which occurs on the advancing side of the weld [39].

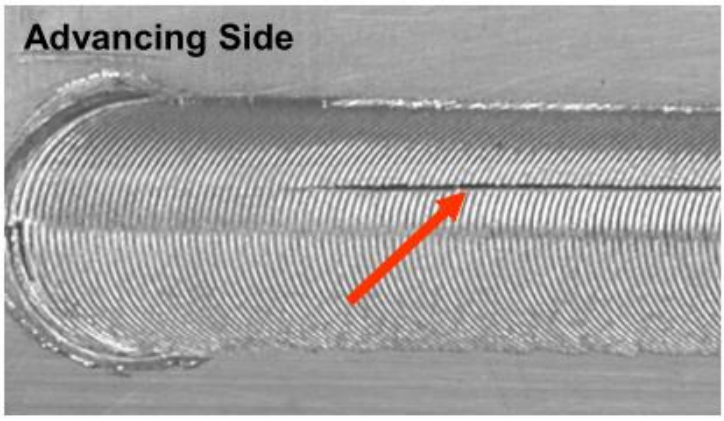

Figure 2.35 – Example of Surface Lack of Fusion Occurring in Friction Stir Welds

2.3.4.7 Faying Surface

This flaw is a layer or line of discontinuous second phase particles or oxides located within the weld. Causes of this defect are due to the original surface not being broken up, excessively hot welds caused by a high welding rate and improper seam tracking during welding. Excessive amounts of this defect occurring may cause a detrimental effect on the weld. Figure 2.36 shows a clear example of surface faying occurring between the layers of the nugget and TMAZ [35].

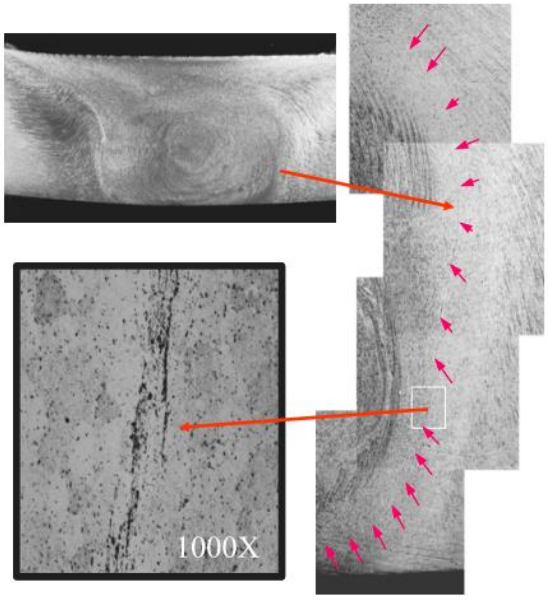

Figure 2.36 - Example of Surface Faying in Friction Stir Welded Joints

2.3.4.8 Ribbon Flash

Ribbon flash is a type of exterior to the weld defect in which excessive amounts of material are expelled on the crown surface. As the tool moves along the weld, a corrugated or ribbon-like string of material is left along the side of the weld. Typically occurring only on the retreating side but extreme cases have shown the ribbon formation occurring on both advancing and retreating sides. It is caused by excessive forging load or plunge depth, a variation in thickness of the welding sheets and excessively hot weld. The extreme reduction in thickness of the joint has an effect on the mechanical properties. The fatigue life is affected as large stress concentration factor is formed at the edge of the tool.

Figure 2.37 - Example of Excessive Ribbon Flash Formation during Friction Stir Welding

2.3.4.9 Root Flaws

This defect is an exterior defect occurring on the root surface of the weld. Chevron shaped flow patterns are visible along the root of the weld. It is caused by excessive material flow within the nugget and the HAZ below the nugget, incorrect pin design, either too long or incorrect pin tip radius and excessively high welding temperatures.

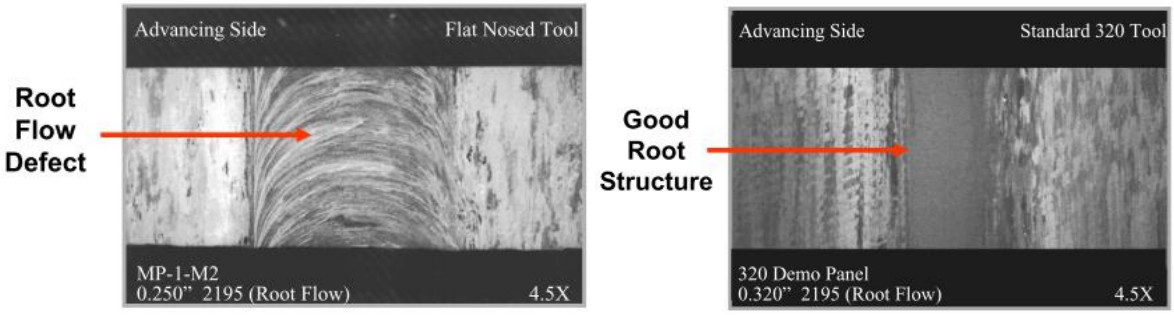

Figure 2.38 - Example of Root defect compared to that of Good Friction Stir Welded Root Structure

Accustom to FSW using the backing bar method is for the root surface to have defects such as scratches and striation which are found on the backing plate. An imprint of the backing bar is produced on the root so to speak. Figure 2.39 provides an example of the imprint effect of the backing surface as one can see the scratches created from the backing plate [40].

Figure 2.39 - Example of Imprint of Backing Plate on Friction Stir Welding Root Surface

2.3.4.10 Lack of Fusion and Joint Line Remnants

This root defect occurs due to remnants of the original faying surface on the root surface below the nugget. This layer of oxide comes from the two sheets that are to be joined. It is caused due to improper alignment of the welding seam, insufficient machining of the parent material and the surfaces of butting plates not properly held causing one portion of the weld joint not to be fused to the adjacent portion of the weld. Excessive lack of fusion will have a detrimental effect on the mechanical properties of the weld as a crack is formed in the weld. Figure 2.40 provides a clear example of the lack of fusion in Friction Stir Welding, were the oxide layer occurs below the nugget and terminates at the root [35].

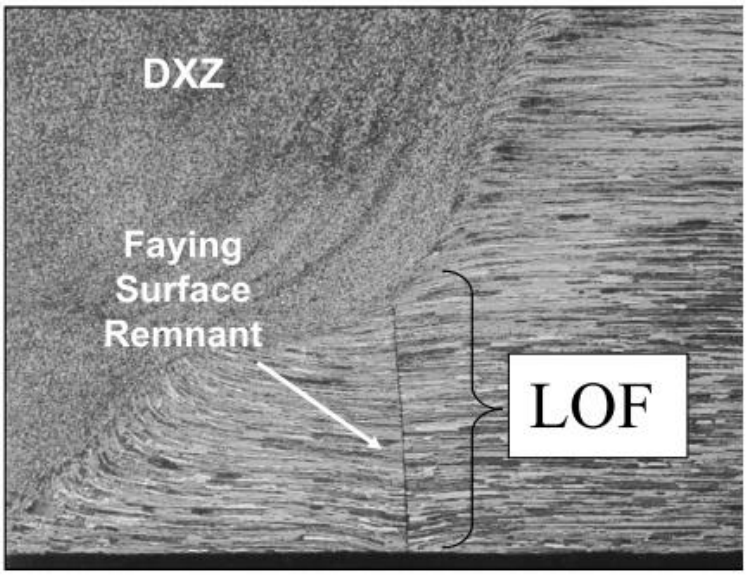

Figure 2.40 - Example of Lack of Fusion / Joint Line Remnants

2.3.4.11 Lack of Penetration

As previously shown welding parameters have a great influence on the quality of the weld. In combination, factors such as tool design, welding forces and position of the pin's axis can influence a verity of interconnected properties such as tensile strength, fatigue life, hardness and microstructure formation. Poor welding parameter selection, incorrect tool design, tool wear or parent material sheet inconstancies can inadvertently result in the creation of a welding defect known as Lack of Penetration (LOP). LOP has also been referred to as a kissing bond in literature. This defect causes a region in which the two sheets are not connected. The defect is formed when there is insufficient forging force which leaves the original parent sheets un-welded, producing a finite gap between the adjacent plates. Occurring at the root of the weld, LOP is seen as a crack initiation site which can significantly influence the fatigue behaviour of the joint [41]. Research has shown that the fatigue life of 4 mm thick AA2024-T3 welds containing LOP was 33 to 80 times shorter than that of flaw free welds machined under the same parameters [42]. Figure 2.41 shows an example of a FSW joint that has the presence of LOP in a butt weld performed on AA2024 [41].

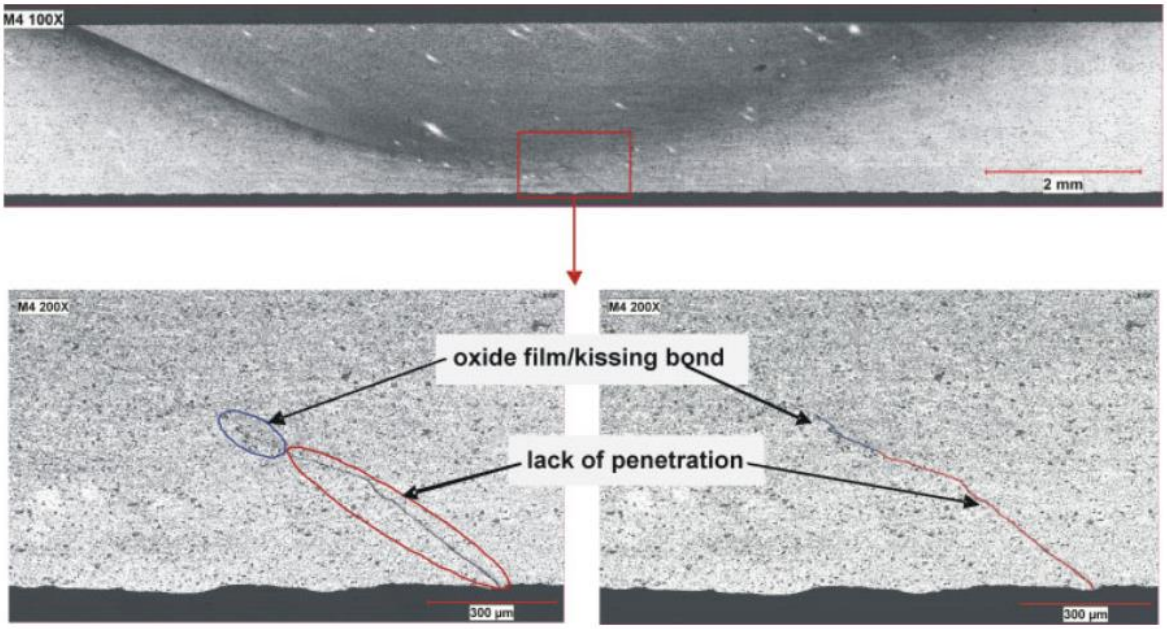

Figure 2.41 - Example of the Presence of Lack of Penetration

In single-sided welding, the tool pin will generally penetrate up to 90–95% of the plate thickness. The suggested tolerance of ±0.2 mm from the end of the pin to end of the plate thickness must be maintained to avoid defect formation [43]. Care must be taken to ensure that the distance between the pin and backing bar is not made to smaller resulting in contact between the two objects. Figure 2.42 provides a schematic breakdown of the penetration of the welding tool and the position of LOP.

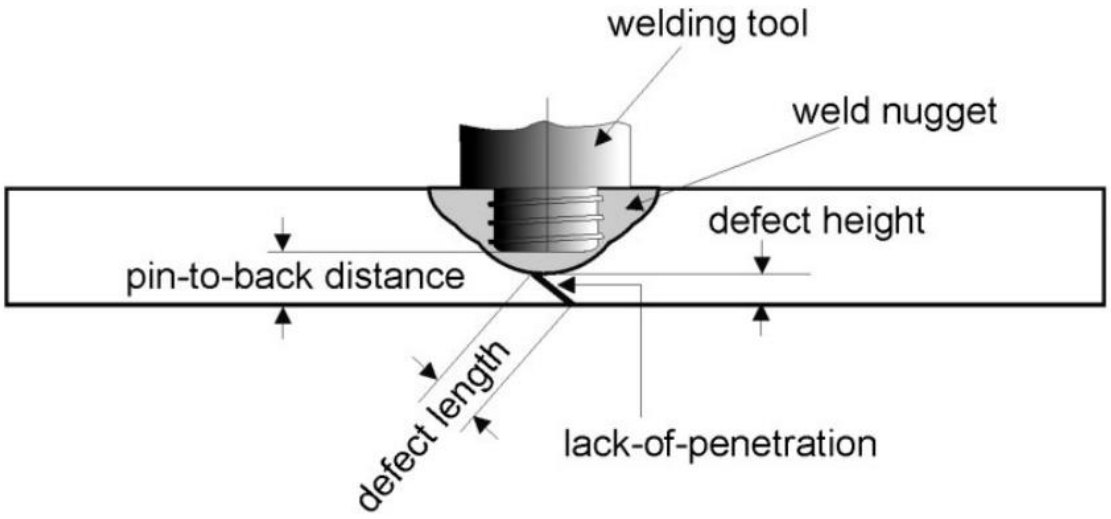

Figure 2.42 - Schematic Diagram representing the Penetration of the Pin and the Formation of LOP during Friction Stir Welding

As with all the welding defects previously discussed, the presence of the defect negatively affects the quality of the weld. The presence of a crack, regardless of the size, will reduce the mechanical properties of the material in which the crack is present [44]. Figure 2.43 indicates the detrimental

effects of increasing size of LOP on the tensile strength of FSW 2xxx series Aluminium [45]. This trend of decreasing strength is to be expected as the crack depth increases because of the reduced amount of thickness of the joint which is of a good quality. Contributing to this reduction would be the geometry of the crack tip of the LOP.

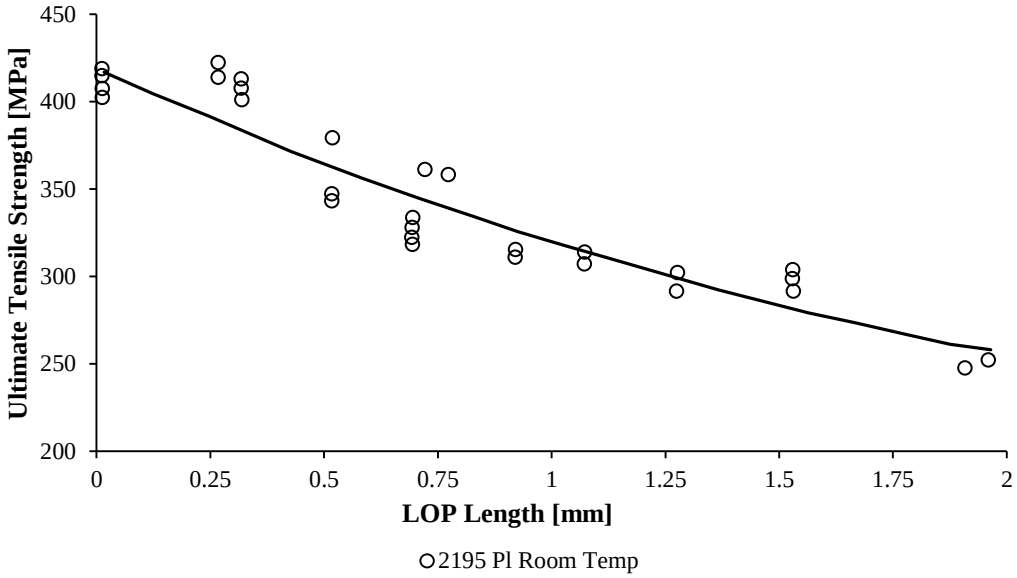

Figure 2.43 - Effect of Lack of Penetration on Tensile Strength

Researchers have shown that it is possible to easily introduce controlled amounts of LOP into FSW joints used controlled pin penetration whilst welding to achieve controlled introduction of LOP [41] . The welding parameters were fixed whilst a retractable pin varied its penetration depth linearly as a function of the tools transverse position along the length of the weld. The variation of the pin depth produced a decreasing depth of LOP defect. Figure 2.44 provides a schematic of the variation in pin penetration with varying weld position. Various Non-destructive and destructive methods were employed in order to determine the effects of the changing pin penetration depth on the size of the LOP [41].

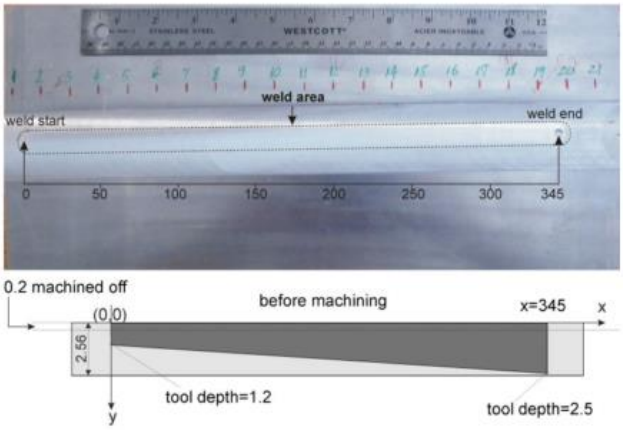

Figure 2.44 - Schematic Diagram of the Pin Penetration Depth Variation with Welding Position

Figure 2.45 shows the variety of different non-destructive methods employed by Mandache to track the presence of LOP along the length of the weld [41]. Image A was produced using conventional eddy current methods. The LOP is represented as the change in colour from left to right in the upper image of A. The presence of LOP can be seen to approximately 165 mm from the start of the weld. The upper and lower image of A and B are of a continuous scan along the length of the weld. Image B was produced with a pulsed eddy current using a square wave form. This technique shows the defect boundaries in a greater detail rather than the actual defect. These methods indicated LOP up to 160 mm from the start of the weld. Image C was produced using liquid penetrant techniques the downfall of this method is that the defect must be open to the surface of the weld. These techniques showed LOP defects clearly occurring from the start of the weld to approximately 110 mm. This matched well with image A [41].

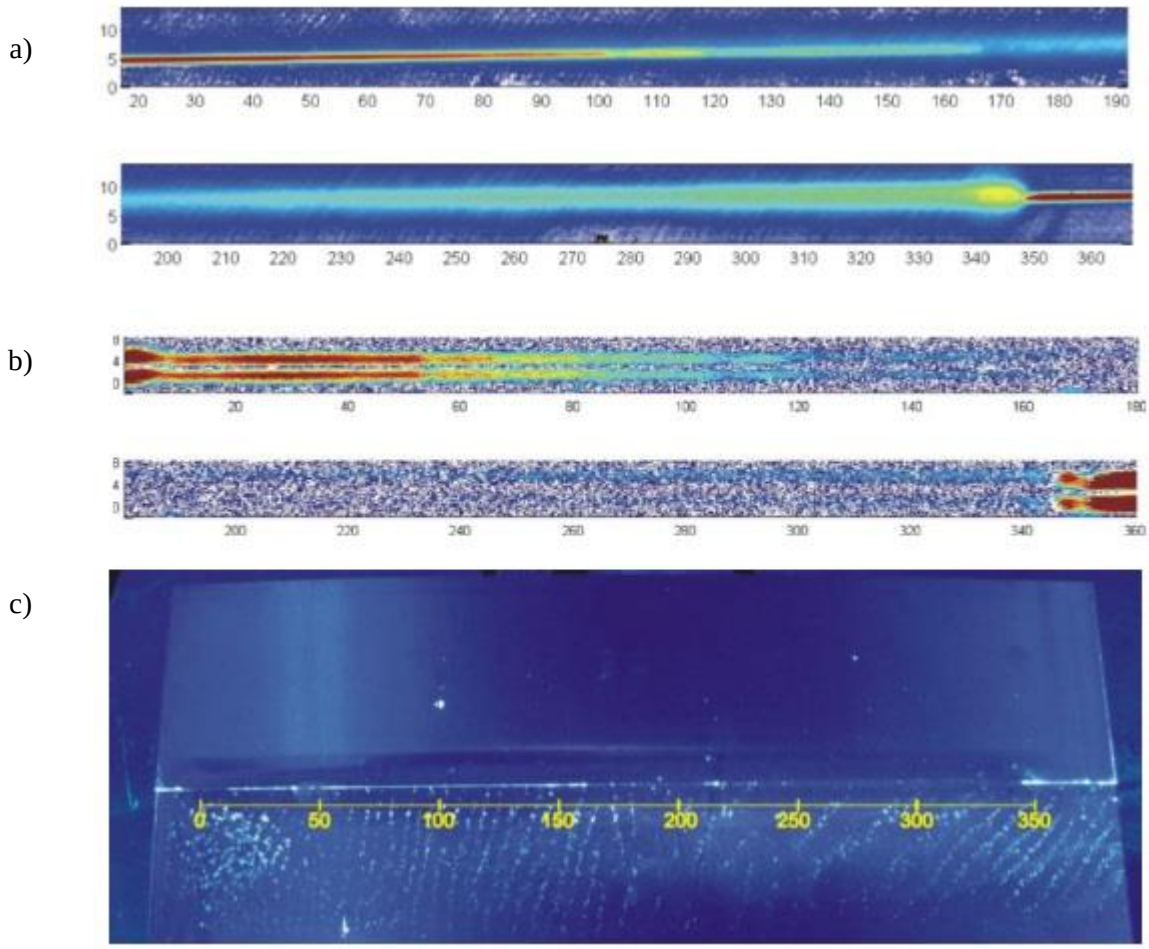

Figure 2.45 - Non-Destructive Methods indicating Lack of Penetration

Destructive tests were completed to verify the results presented above. Metallographic examinations at 13 locations along the length of the weld indicated the presence of LOP from the start of the weld to approximately 150 mm. Kissing bonds were also noted at this point. This type of defect was found to propagate from the tip of the crack of LOP and along the nugget boundary. The orientation of the

crack formed through LOP was noted to be inclined at an angle of approximately 20° to the vertical and increased to 59° at 150 mm along the weld. The inclination of LOP can be seen in Figure 2.41. Three-point bending tests were performed, it was concluded that the bending samples broke when LOP defects were present and that cracks formed in the samples which had kissing bonds present. Figure 2.46 shows the results of the destructive three-point bending test which indicates the presence of the two defects discussed [41].

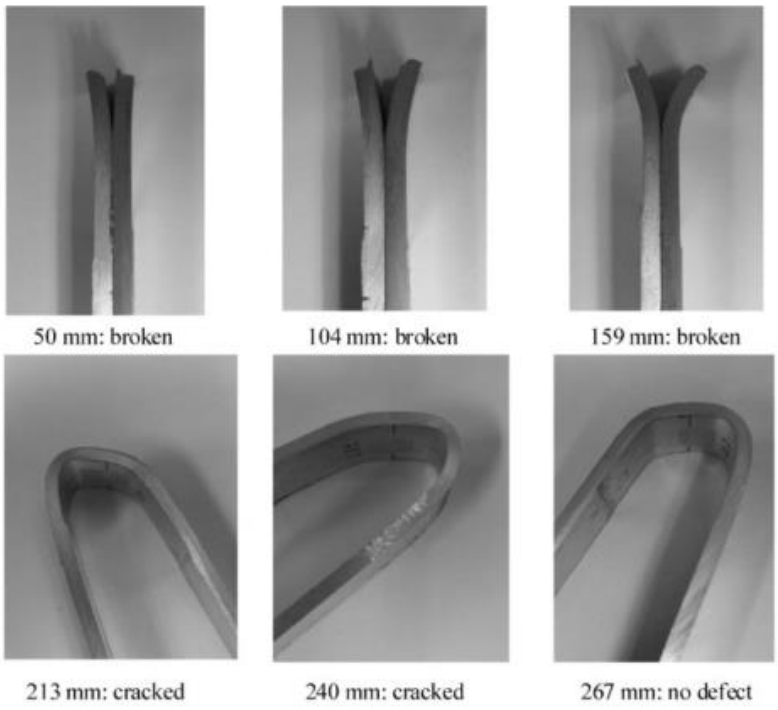

Figure 2.46 - Three Point Bending Tests Indicating the Presence of Lack of Penetration and Kissing Bonds

Figure 2.47 shows the variation in the size of the defects with the relative position of the welding pin [41]. The maximum vertical size of the LOP achieved was approximately 0.95 mm, which is a fairly substantial crack within the joint.

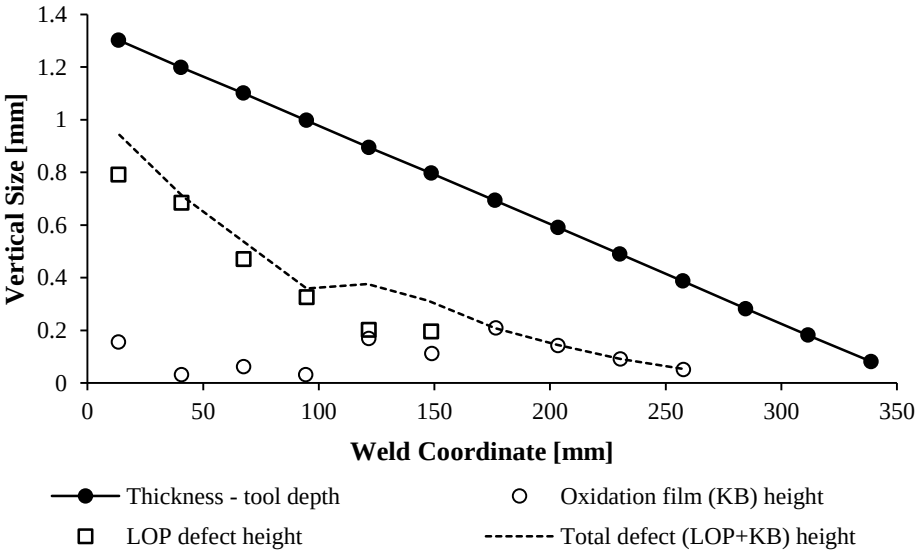

Figure 2.47 – Vertical Size of Defects formed along Weld Length

From the figures, the detrimental effects that LOP can have on the FSW joint can clearly be seen. If the welding position of the tool is not correctly controlled a crack can be formed through as much as 40% through the thickness of the weld.

2.3.5 Effects of Process Parameters on the Performance of Friction Stir Welded Joints

Various researchers have experimented with a wide combination of welding parameters, tool configurations, clamping/support systems and materials in the attempt to produce a predictable process and efficient bond. Relevant cases of the performance of previous FSW experiments completed by other researchers on the same material (AA6082-T6) will be considered in this section. The parameters selected to be investigated are thought to be a fair representation of the parameters used in industry. The influences of thickness, variations in sample sizes and welding set up between different sources will be neglected in an attempt to understand the trends of the parameters and the effects of such parameters on the resulting mechanical properties of the respective joints.

2.3.5.1 Joint Hardness Performance

The hardness profile of a typical AA6082-T6 FSW joints varies from region to region within the weld. As expected the HAZ and welding nugget may have a decrease in hardness of up to 15–20% and 5-10% from the base material. General trends have shown softening on either side of the welding nugget. Figure 2.48 shows the typical across profile hardness of two separately investigated AA6082-T6 welds. Each hardness profile was produced by [16],[18] using the Vickers microhardness measurement method but with difference indentation forces. As shown, there is considerable softening in the regions on either side of the welding nugget.

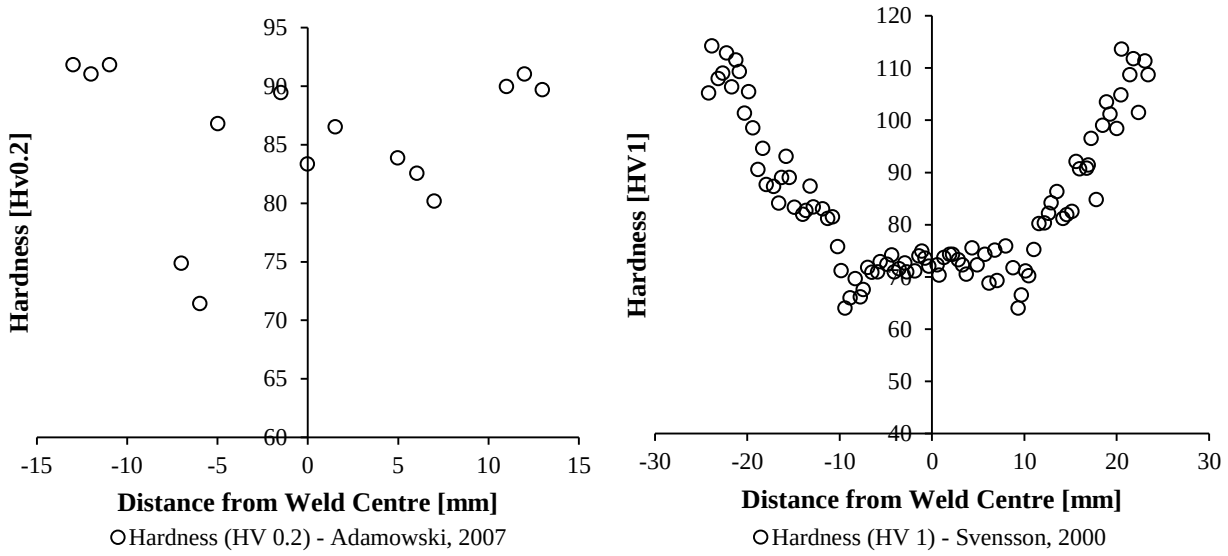

Figure 2.48 - Hardness Profile of Typical AA6082-T6 Joints

The "W-shaped" hardness profile is consistent with what is expected for a precipitation hardening alloy. The thermal effects of the FSW process cause the lower hardness values thus it is as expected that the TMAZ is the region of lowest hardness. The lower temperatures in the HAZ causes greater initial precipitation hardening of the base material thus it would retain a similar hardness value to that of the base material. Fractures of the joints in fatigue and tensile testing have been found to occur within and close to the HAZ, the region corresponding to the lowest hardness.

2.3.5.2 Joint Tensile Performance

From the experimental results of [16], [46] a decrease in the tensile strength of the welded component compared to the parent material was apparent. Reference [46] reported a reduction of 16 to 21.5% in tensile strength across a variety of joints compared to that of the unwelded base material. The expected cause of the reduction in strength is due to the absence of the β''- Mg_5Si_6 which is present in the base material but is easily dissolved during the welding process due to temperatures that are higher than 200 to 250 °C [18]. It was concluded that the tensile strength of the joint is directly proportional the welding speed and feed rate. Research has shown that the strength of the joint improves with increasing tool rotation and feed rate to the point at which the strength decrease due to the parameters causing a coarse grain structure to be formed in the welding region [46].

Figure 2.49 shows the results of the tensile strength of AA6082-T2 FSW joints obtained by other researchers. Neglecting the effects caused by varying welding tools, material thickness and other welding parameters, the figure shows that for constant RPM the joint strength increases with increasing feed rate. Data for 710 RPM was obtained from reference [16] and 880, 1230 and 1700 RPM from reference [47] .

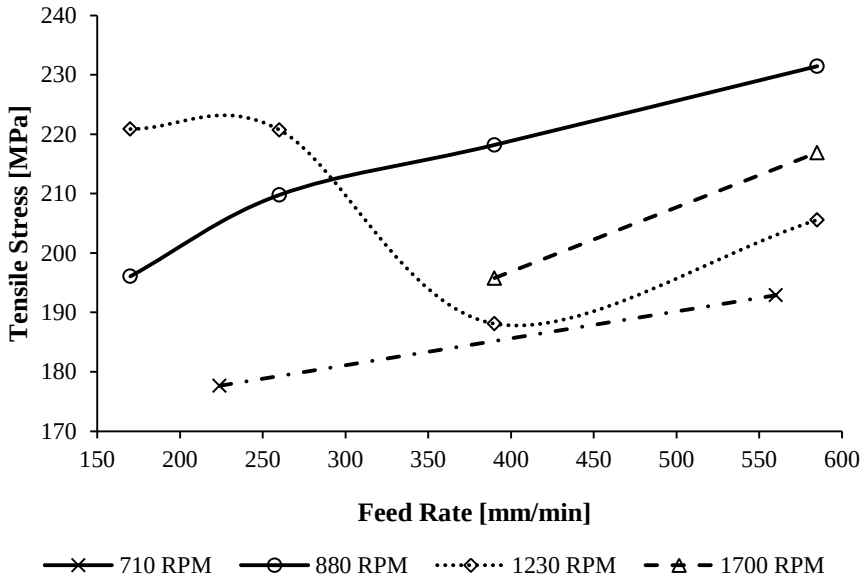

Figure 2.49- Tensile Results for Varying Parameters

The fracture was found [48] to occur in the outer edges of the tool shoulder on the top surface of the weld. The failure surface was inclined towards the centre of the welding through the thickness of the plate. Although it was displaced away from the weld axis, the fracture surface was closest to the weld axis at the root side of the weld. It was concluded that the failure line was related to the positions of lowest hardness within the weld, the heat affected zone.

2.3.5.3 Joint Bending Strength

Three-point bending test can be completed in order to test the mechanical resistance of any sample. This form of testing allows for the immediate identification of near surface flaws due to the sensitivity of the test.

Experimental results of bending tests conducted on the AA6082-T6 base material as well as FSW samples. The results of these tests are shown in Figure 2.50 [49].

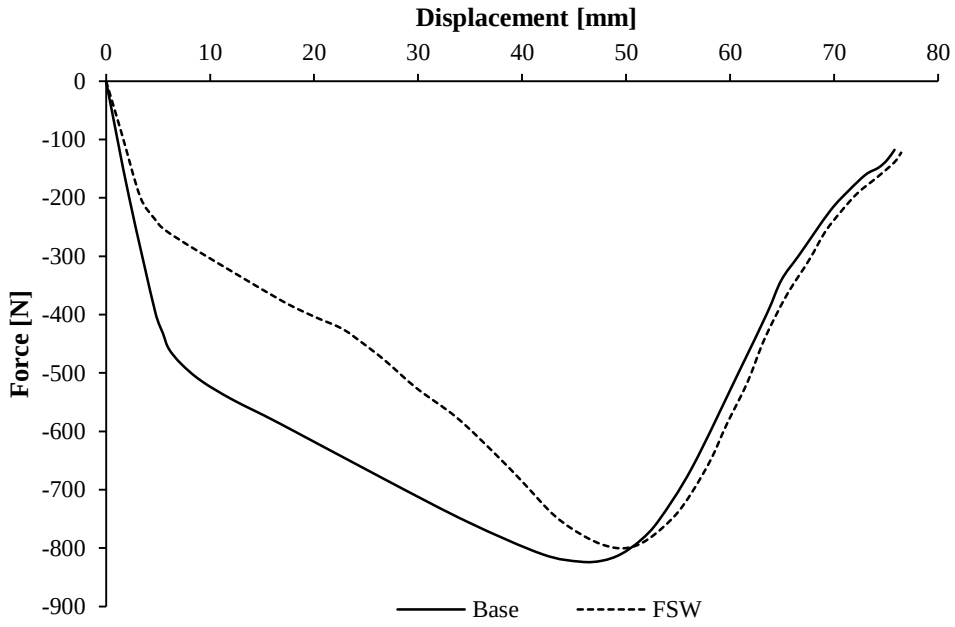

Figure 2.50 - Three Point Bending Results of Base Material and Friction Stir Welded Components

It can be seen in the Figure 2.50 that both the base material and FSW sample indicate regions of linear displacement during the lower loading scale. The linear region of the FSW sample ended at a lower force to that of the base material sample, this was due to various effects of the FSW process on the joint.

2.3.5.4 Joint Residual Stress Performance

The residual stress state of an FSW joint is directly linked to the fatigue resistance of the component. The presence of high tensile residual stress can negatively affect the mechanical properties, most, in particular, the fatigue properties. Measurement of the residual stress after FSW results in a roughly M-shaped profile, with the maximum tensile stress occurring just after the edge of the welding shoulder whilst compressive stress were found further away from the weld line [50]. Figure 2.51 shows an example of the longitudinal (along the weld) and transverse (across the weld) residual stress profile. This portion of the measured joint was manufactured at steady state welding conditions, the measurement was done using neutron diffraction. The weld was produced on 3 mm thick AA6082-T6 Aluminium with the welding parameters of 200 mm/min at 560 RPM [51].

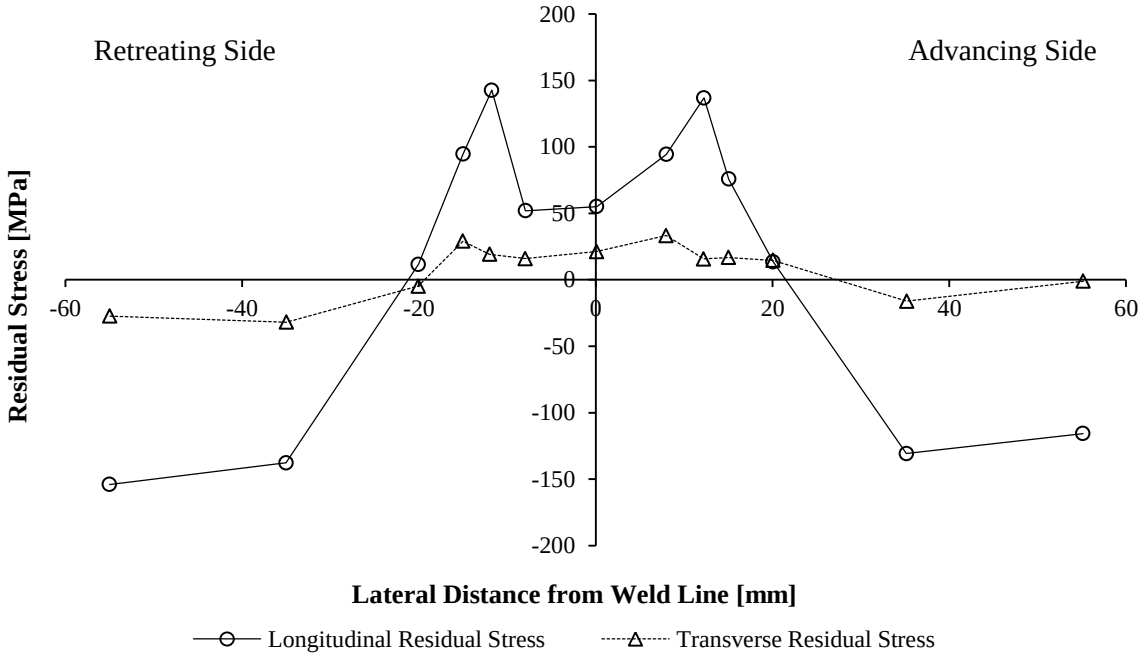

Figure 2.51 - Across Weld Residual Stress Profile

It can be noted that the stress profile in the longitudinal direction is slightly asymmetric about the centre of the joint line, this is purely due to the asymmetric nature of the resulting FSW joint microstructure. A shoulder of 18 mm was used to manufacture the joint in which the measurements were obtaining for Figure 2.51. The peak tensile stress was found to occur on both sides of the weld within the HAZ. The nugget and TMAZ have consistently been found to be in tension but this region of the weld is not the highest stressed zones as confirmed by the figure and similar measurements taken in AA2024 Aluminium welded under similar conditions [50]. The peak tensile is roughly three times that of the stress within the nugget and TMAZ. It is suspected that this is due to the dissolution of the hardening precipitates, as described in section 2.3.5.2. The dissolution results in the reduction in the local yield strength thus limiting the build-up of residual stress. The edge of the shoulder is also the transition between the TMAZ and HAZ a region which has a change in grain and material orientation. This figure indicates that it would be expected that the failure of the joint would almost always occur within the weld as the residual stress after the HAZ tends towards becoming extremely compressive just like the remainder of the unaffected base material.

2.3.5.5 Joint Fatigue Performance

The joints manufactured for this research are intended to one day fully in the aviation industry, an industry where all components are exposed to a loading case in which cyclic loads work towards weakening the joint resulting in failure of that component. It has been shown that FSW fatigue strength far surpasses the fatigue performance of other conventional joining methods such as TIG and MIG welding for the same material. Figure 2.52 below shows the variation fatigue strength of

AA6082-T6 4 mm thick samples which had been FSW at low speeds, 700 mm/min and 2200 RPM, and high speed, 1400 mm/min and 2500 RPM [52].

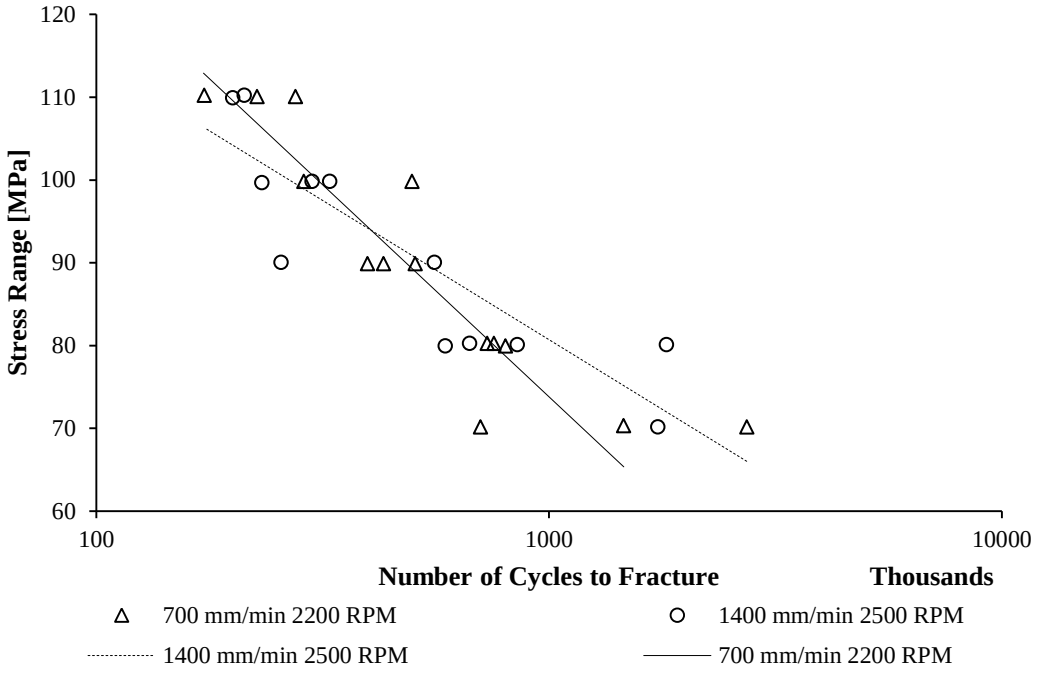

Figure 2.52 - Influence of Friction Stir Welding Parameters on the Fatigue Life

It should be seen from the data presented that there is very little difference in fatigue performance of components that were welded using a low and high speed parameter settings. Each set of components showed equivalent endurances allowing for the assumption that fatigue life is fairly independent of feed rates. This is assumed as the lower feed rate is half of that of the higher feed rate and the rpm settings are fairly similar.

For the data provided in Figure 2.52, the components fractured within the weld with no preference shown to either the advancing or trailing side. In another case of FSW AA6082-T6, researchers found that fracture occurred on the welding line and on the edge of the HAZ [53]. Thus, it is assumed that for this material fracture will all most always occur within the weld.

2.4 Laser Shock Peening

Laser Shock Peening (LSP) is an innovative post manufacturing materials process used to introduce favourable residual stress within a component. Making use of the same ideology of conventional shot peening, LSP is used to impart Compressive Residual Stress (CRS) into and to control the stress profile in the specific area of a component. The ability to introducing large CRS at higher penetration depths will increase the component's resistance to surface-related failures. LSP has been shown to drastically improve the natural fatigue life and corrosion resistance of a metallic component [54]. LSP is a far more favourable process to that of conventional shot peening as the through thickness stress profile can be altered much greater in magnitude and component thickness. LSP has been used to successfully treat a variety of materials such as cast iron, Aluminium alloys and titanium alloys. The process has been used extensively in the aerospace industry with the treatment of compressor blades and rotor components [55]. Figure 2.53 shows an example of the treatment of compressor blade.

Figure 2.53 - Treatment of Compressor Blades Using Laser Shock Peening

LSP makes use of a high energy pulse laser to produce a pressure wave that cold works the material. The pressure wave is commonly known as a shock wave, which is created by the laser striking the surface of the component which is almost instantaneously vapourised into extremely high temperatures and causes the formation of high pressure plasma by ionisation. The plasma continues to absorb the energy of the laser causing the creation of a rapidly expanding plasma bubble. The bubble grows to a point where cavitation occurs, the collapse of the bubble cause the shock wave. The interaction of the propagating wave and the material yields and plastically deforms the surface. This develops favourable residual stresses through the introduction of uniaxial dynamic strains near that

area of treatment. By firing the laser pulse in a predetermined pattern a layer of favourable residual stress can be developed in the component. Figure 2.54.a illustrates the interaction of the laser with the impact plane of a sample which is placed into a tensile state upon discontinuing the laser pulse. Figure 2.54.b illustrates a biaxial compressive residual stress field in the regions besides and below the impact zone [56].

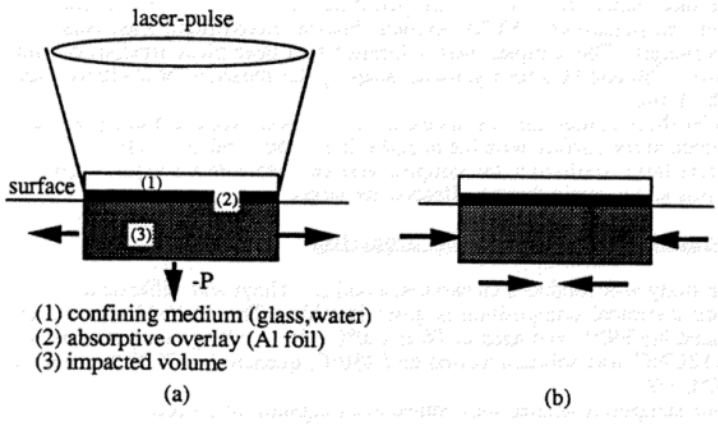

Figure 2.54 - Mechanism of Generation of Residual Stresses through Laser Shock Peening

Direct ablation is the instant when the plasma interacts with the surface of the material which does not have a coating. Peening can also be completed in the confined mode, also known as confined ablation, were an opaque coating and a transparent material is applied to the surface of the material. The thermal effects on the target are mitigated because of the opaque confinement (water) layer. The instant of peening with a coating, known as LSPC, the energy of the laser is in the region of 100 J with a pulse length of 6 to 25 ns. Processing without a coating, known as LSPwC, the energy of the laser is in the range of a few Joules at most and a very short pulse length. In both cases plasma pressure can reach in excess of tenths of a GPa. Research has shown that the higher the pressure pulse the greater the enhanced outcome of CRS. Figure 2.55 indicates a schematic configuration of laser shock peening without an opaque coating.

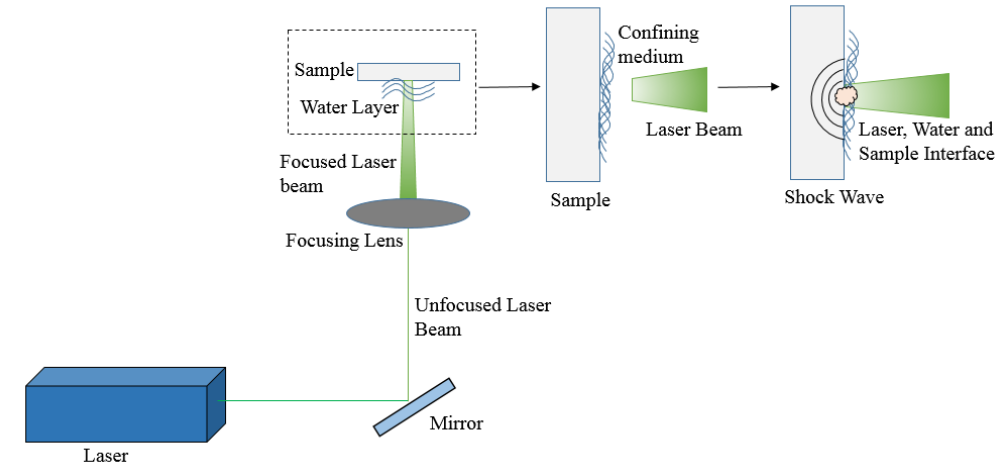

Figure 2.55 - Laser Shock Peening Process

The effects of LSP has been shown to penetrate up to the millimetre range through the thickness of a component [57]. The precision of the laser processing allows for the treatment of critical areas without influencing the remainder of the sample. LSP can be used to resist high and low cycle fatigue, stress corrosion, crack initiation and growth [58]. It has been reported that LSP produces up to 70% more CRS at the surface of a component compared to that of standard shot peening, Figure 2.56 indicates the variation in compressive stress for Ti-6Al-4V components that were treated using shot and shock peening [59].

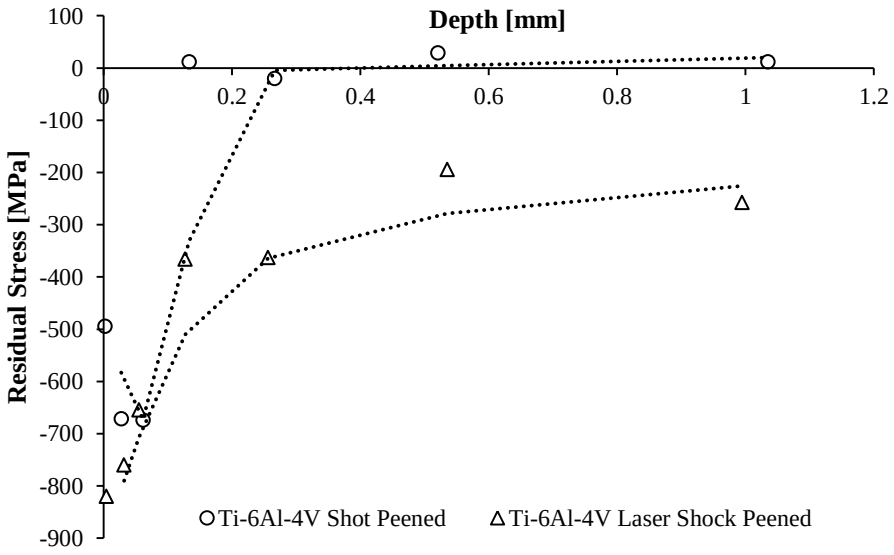

Figure 2.56 - Variation in Residual Stress for Shot and Shock Peening

2.4.1 Laser Shock Peening Process Parameters

A Neodymium-Doped Yttrium Aluminium Garnet (Nd:YAG) laser is most suited for this application as it is capable of operating at the required wavelength as well as operating in the continuous or pulsing modes. The power output of this laser is of the order of a few Watts but due to the short pulse

durations and focusing of the beam to a relatively small beam diameter high power intensities can be achieved in order to cold work metallic components. A near infrared wavelength of 1064 nm is the most commonly used wavelength for LSP. This is due to the modest absorption rate in a water overlay, the highest dielectric breakdown threshold and satisfactory interaction with the surface of the material [55].

The LSP process parameters define the characterisation of the shock wave, pulse pressure and the mechanical performance of the treated component. Emphasis must be placed on a number of key parameters which need to be assessed individually.

2.4.1.1 Laser Power Density

The Laser Power Density/ Intensity was the amount of power per unit area produced by the pulse. Measured in GigaWatts per square centimetre (GW/cm^2) and is calculated according to equation 2.2.

$$\boldsymbol{I_o}\left(\frac{\boldsymbol{GW}}{\boldsymbol{cm^2}}\right) = \frac{\boldsymbol{400 \cdot E_{beam\ energy}(mJ)}}{\boldsymbol{\pi \cdot \tau(ns) \cdot d_{spot}{}^2(cm)}} \tag{2.2}$$

2.4.1.2 Frequency or Repetition rate

It is the rate at which laser pulses are fired. Measured in Hertz (Hz) and is given by equation 2.3.

$$\boldsymbol{f} = \frac{\boldsymbol{1}}{\boldsymbol{T}} \tag{2.3}$$

2.4.1.3 Pulse energy

It is the amount of energy that a single laser pulse achieves. It was measured in Joules (J).

2.4.1.4 Fluency

Is the energy intensity on an irradiated area. It is measured in Joules per square centimetre (J/cm^2) and is given by equation 2.4.

$$F = \frac{E_{pulse}}{A_{spot}} \tag{2.4}$$

2.4.1.5 Beam size and shape

The characteristics of the beam are determined by its physical size and shape. Common beam shapes used in industry and research are typically square or circular. The shape of the beam is determined by the design and optics of the laser. There are methods in which a circular beam can be shaped into a square beam, and vice versa, but this falls out of the scope of this research. The resulting characteristics of the laser impact are directly related to the geometry of the beam.

A negative characteristic of laser shock peening is the occurrence of a region of no induced residual stress at the centre of the impact; this is mostly impacts circular spot profiles, such as the Gaussian

profile. Figure 2.57 illustrates a dark region which represents the focalisation effects in the centre of the circular impact. This region of the impact has minimal to no effect on the residual stress of the interacting material [56]. The ‘dead spot’ can be mitigated by introducing further impacts slightly adjacent to the focussed region thus imparting the required stress through repeated laser impacts. This fact has been proven as the inhomogeneity of the laser impacts are removed by using a higher overlapping strategies, a minimum of 66% spot overlap has been suggested for circular beam shapes to mitigate these effects [60].

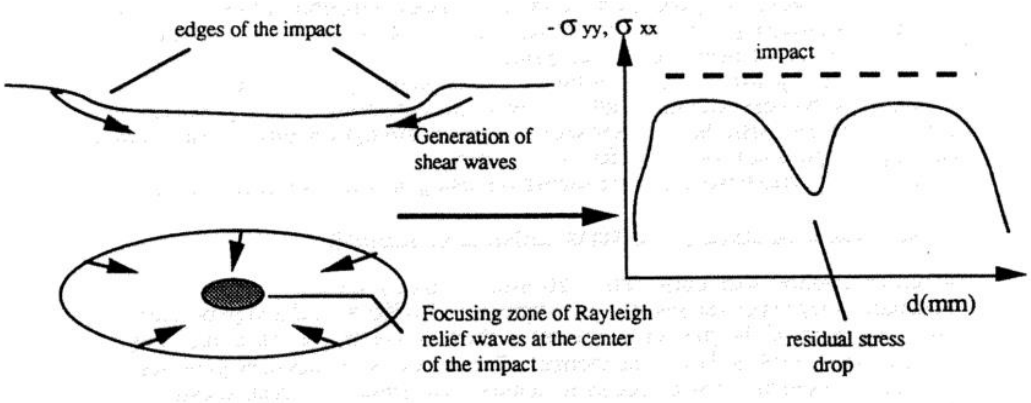

Figure 2.57 - Heterogeneities at the Centre of a Circular Laser Impact Profile

The beam size is dependent on the position of the lens and the component relevant to one another. The spot size of the focused beam is dependent on the focal length properties of the lens as the beam converges and diverges during propagation. The size of the beam is generally measured in millimetres (mm).

2.4.1.6 Laser wavelength

A laser wavelength can be defined as the distance in which the pulse repeats itself and is measured in nanometres (nm). For typical LSP processing, a common wavelength of 1064 nm has been used considerably in industry and research environments. A closer look at the effects of the wavelength on the LSP process shows a considerable dependence between the wavelength and the peak pressure. Figure 2.58 shows the effects of the wavelength of a 1064 nm and it fundamental harmonics on the peak pressures [61]. All measurements were taken in confined water. It can clearly be seen that a lower wavelength produces a higher peak pressure but the boundary of the dielectric breakdown is considerably sooner than that of the 1064 nm threshold. This saturation pressure shows that once reached the increase of power intensity will have no further effect.

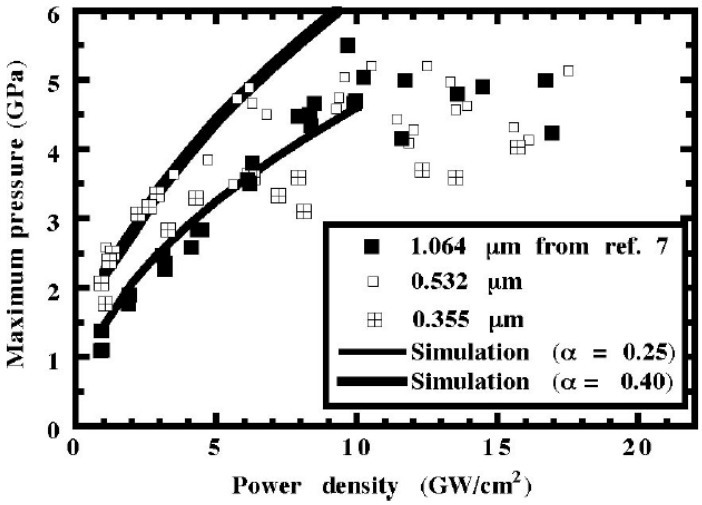

Figure 2.58 - Maximum Pressure generated at varying Power Intensities at different Laser Wavelengths in a water confined

2.4.1.7 Pulse width

The rise of the energy intensity for the duration of a single laser shot. It is described as the Full Width at Half Maximum (FWHM). Figure 2.59 shows an example of a Gaussian pulse and the characterisation of the FWHM. The pulse width is measured in nanoseconds (ns) [62].

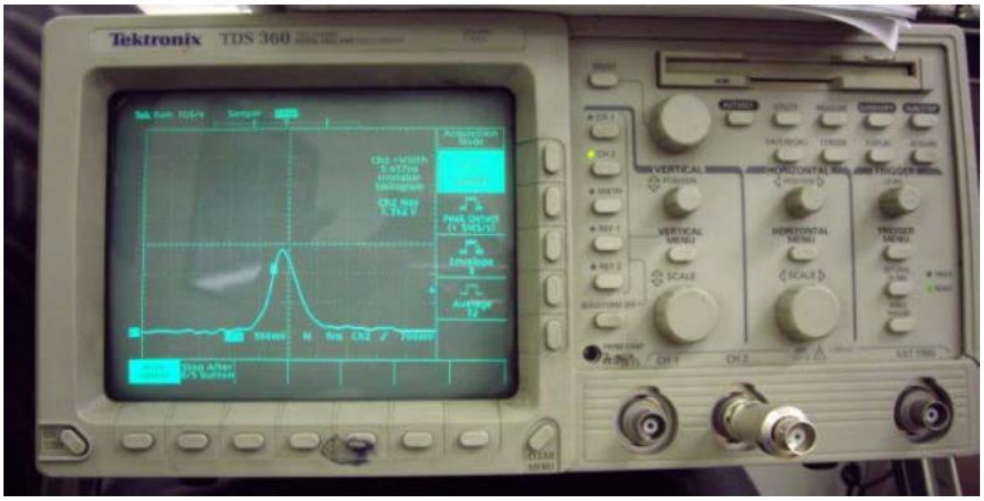

Figure 2.59 - Characterisation of Full Width at Half Maximum on a Gaussian Profile

2.4.2 Laser Beam Profiles

A beam profile refers to the characterization of a spatial profile of an optical emission (in this case a laser beam). The emitted beam profile from a solid state laser can be defined by a variety of different profiles such as Gaussian, Super-Gaussian and a Top-hat/square beam. Typically produced by passing a Gaussian beam through a diffractive optical element, the Top Hot profile is the most commonly used profiles in industry due to their uniform spatial intensity distribution. This feature of the beam gives it the ability to attain extremely uniform surface treatments. Due to the circular nature of a

Gaussian profile, it will display a centralised peak intensity area or simply put as a ‘hot-spot’. It is the easiest to attempt to replicate and removes the need for expensive beam homogenization. Figure 2.60 provides examples of beam profiles used by other LSP researchers [63].

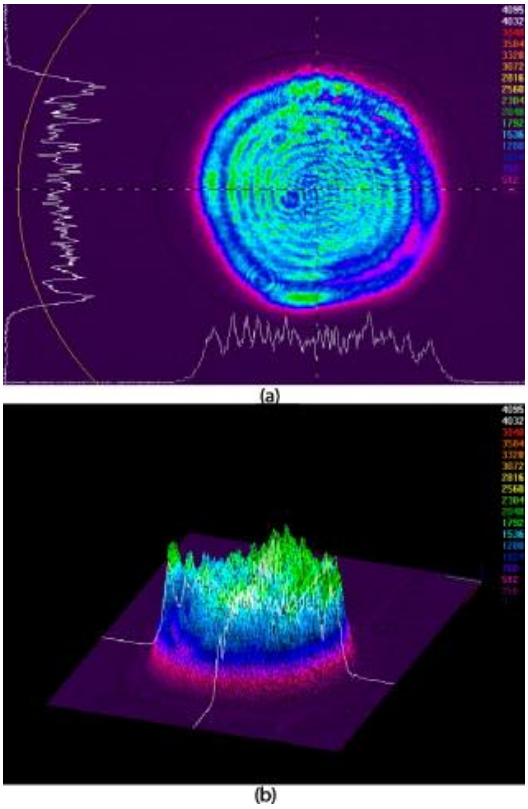

Figure 2.60 - Examples of Beam Profiles used in other Laser Shock Peening Research

2.4.3 Coverage, Overlay Rate and Number of Impacts

The nature of LSP is to use multiple sequential laser shots to effectively cover a required surface area of the component. Typically, a standard beam spot size is of few millimetres thus a single shot would not be able to fully treat most aircraft sized components. By increasing the number of overlapping spots the penetration depth and magnitude of the introduced residual stress is far greater. Figure 2.61 shows this fact that deeper residual stresses can be achieved with a greater number of laser shocks [64].

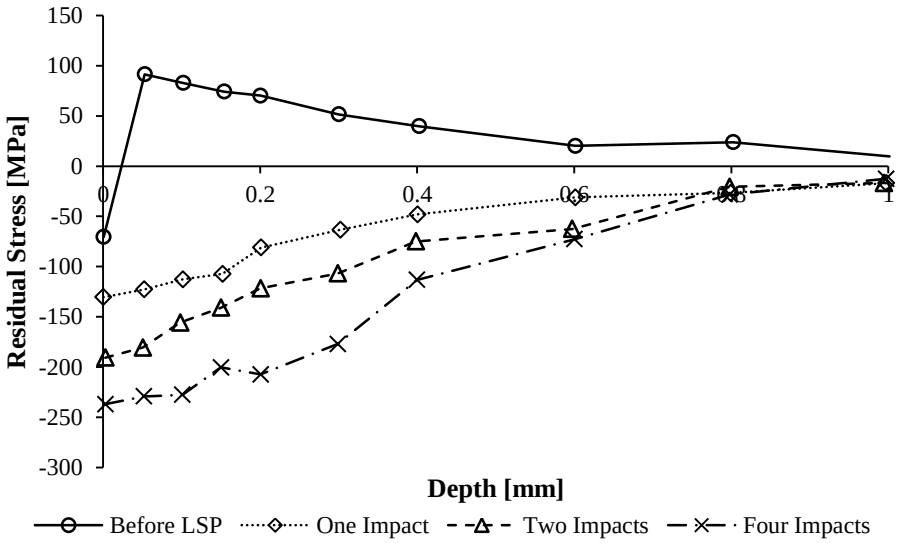

Figure 2.61 – Residual Stress variation with Depth after different Laser Shots on AZ31B Mg Alloy

Different users of LSP have developed multiple overlap strategies to obtain the desired effects of introducing compressive residual stress. The overlapping rate is a parameter which relates the processing coverage and the interaction/overlap of two adjacent laser spots. By increasing the overlapping rate, defined according to equation 2.5, a defined area will be exposed to far greater laser exposure. Figure 2.62 shows the overlap of adjacent laser spots for a single line of processing [65].

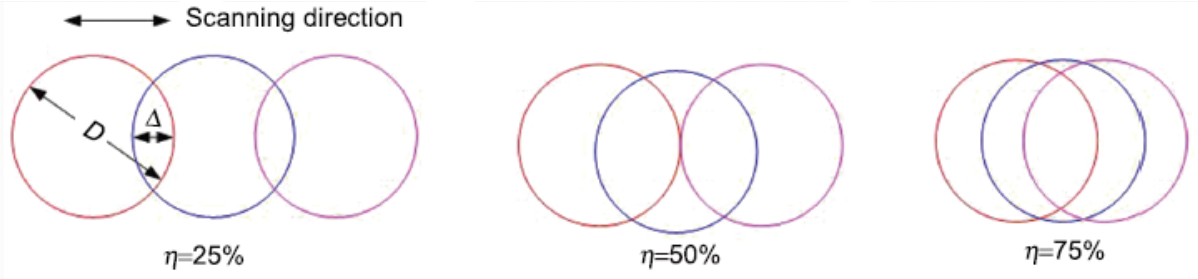

Figure 2.62 - Laser Spot Overlap Strategies

$$\eta = \frac{\Delta}{D} \tag{2.5}$$

The laser processing strategies have been found to be influenced by whether a protective coating is used or not. When larger, more powerful lasers (up to 100 J) are used a very low overlap is employed. This is done in order to prevent extensive damage to the surface of the component.

2.4.4 Laser Shock Peening Coordinate System

The movement of the component during conventional Laser Shock Peening has been typically defined by two naturally perpendicular directions, these being the scanning and stepping direction respectively. Figure 2.63 shows the processing directions of various other LSP operators, it can be seen that the processed area is treated in singular strips and upon reaching the edge of the defined area

the component steps in the y direction [66], [67]. The x-axis is classified as a horizontal movement whilst the y-axis produces a vertical moment of the sample. To maintain uniformity with current standards this reference system has been adopted throughout this research.

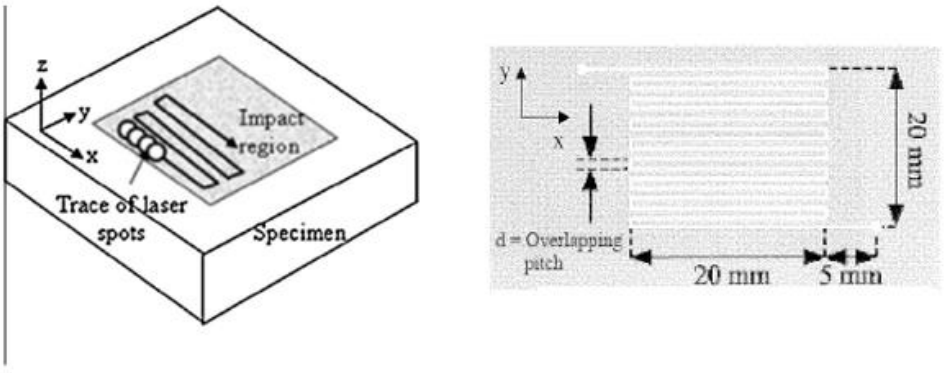

Figure 2.63 – Laser Shock Peening Reference System

The movement of the component in this 'zigzag' pattern produces a very distinct overlapping pattern. This relates back to section 2.4.3 to the overlap strategies in which the coverage is defined by the percentage of each laser spot that overlaps the previous set of laser impacts. Figure 2.64 shows a schematic and real example of the 'zigzag' peening strategy. This method is well suited to LSP as it is easy to translate the sample in the required directions as well as the overlap can be easily controlled by monitoring and fixing the movements of the sample in the respective directions.

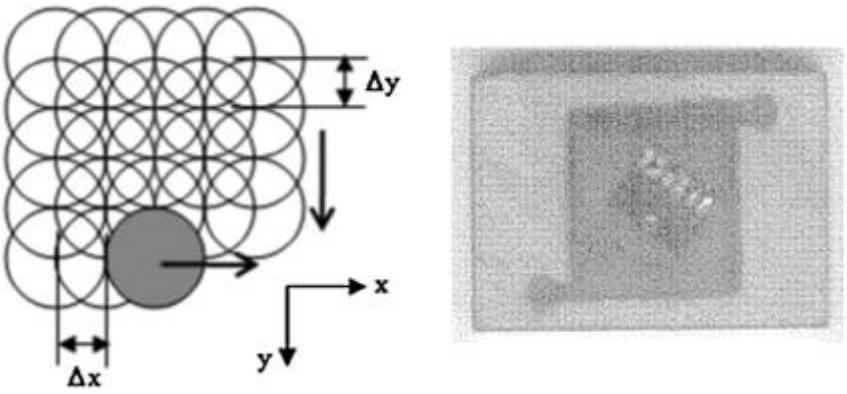

Figure 2.64 - Examples of 'Zigzag' Laser Shock Peening Processing Strategies

2.4.5 Juxapositioning and Proximity of Sequential Laser Pulses

Although very little work has been done in this field, Juxtapositioning refers to the effect of the proximity of sequential laser pulses. Strain hardening of the material and the existence of a residual stress field within the component affects interaction of the laser impact and the respective material. Figure 2.65 depicts three square laser impacts, spot 1 is a pre-existing impact which residual stress profile was measured before and after the addition of spots 2 and 3.

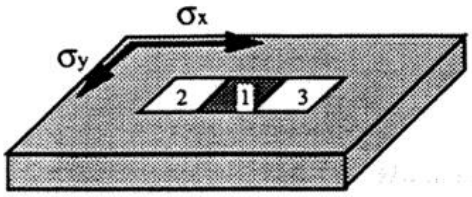

Figure 2.65 - Sequential Juxtapositioning of Square Laser Impacts

Figure 2.66 shows the results of the residual stress field at spot 1 before and after the additional flanking spots. It can be clearly be seen that sequential laser impacts increase the compressive residual stress of adjacent treated positions [56].

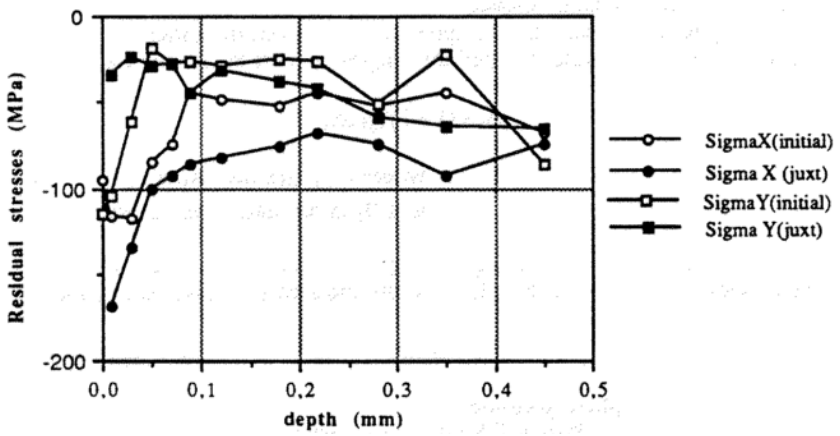

Figure 2.66 - Juxtapositioning Effects on Residual Stress Profiles of Laser Shock Peening treated AS12UNG-1 Aluminium

Comparing the juxtaposition stress measurements, it should be noted that σ_x is fairly more compressive through the thickness to that of σ_y. Figure 2.66 illustrates that the measurements are taken with reference to different perpendicular axis similar to that of the stepping and scanning directions. This result indicates that an anisotropic residual stress field was introduced with reference to the component movement axis. It has been shown that stress improvement is dependent on the laser processing pattern [68]. Figure 2.67 illustrates an example of how the residual stress varies due to the direction of the peening process [68].

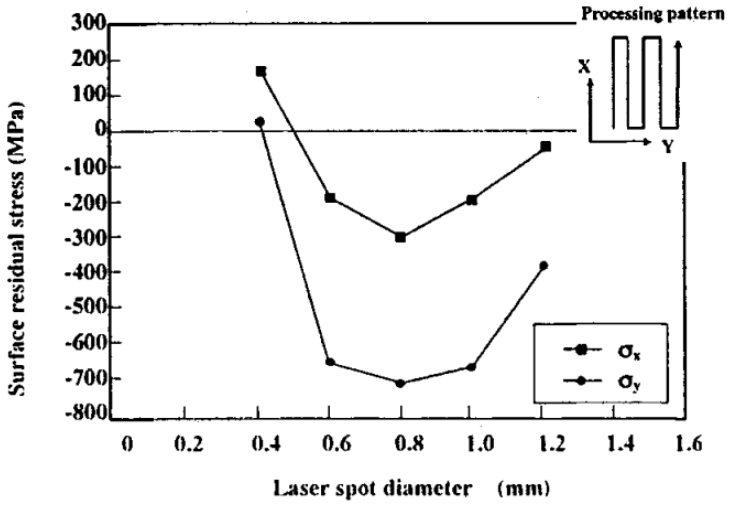

Figure 2.67 - Anisotropic Residual Stress Field

2.4.6 Laser Shock Peening Process Breakdown

During any high power laser application, one must be cautious of the generation of absorbing plasma. This plasma is created during the transmission of a powerful focused laser beam through a clear medium such as air or water. At the irradiance threshold, the transparent material has a sudden rise in absorption coefficient which creates a defocusing absorption plasma [69]. The occurrence of this phenomena is known as Laser Induced Breakdown (LIB) [70]. The mechanism of the formation of the plasma is out of the scope of this research, but a clear indication of the occurrence of LIB is a bright flash along the path of the laser. Figure 2.68 provides an example of LIB during an LSP procedures [71].

Figure 2.68 – Laser Shock Peening example of Laser Induced Breakdown

Formation of plasma due to LIB is ideally the fundamental mechanism of LSP but the formation of the plasma is required to occur at the target surface and not along the path of the laser. In the event that breakdown occurs either in the air or water a phenomena known as Plasma Shielding occurs.

Plasma Shielding is the formation of a plasma which absorbs either a portion or the full amount of the laser transmission energy thus a notable reduction in delivered energy to the target occurs. The absorption plasma will continue to grow because of the high temperature and pressure sustained by the propagating laser beam [72]. As the plasma absorbs the energy a Laser Absorption Wave (LAW) is formed which travels along the laser line of sight back towards the source of the energy. By increasing beam energy the power intensity is increased which creates a much larger plasma length on formation. Figure 2.69.a and b, clearly indicate how the length of the plasma is significantly affected by increasing energy [73]. Higher energy resulted in larger plasma lengths. This threshold effects can clearly be seen in Figure 2.58 in section 2.4.1.6 were after surpassing the dielectric breakdown threshold power intensity there is no further increase in peak pressure. It can be concluded that power intensity and the quality of the transmission medium was critical to successful LSP processing and needed to be controlled and monitored during completion of this research.

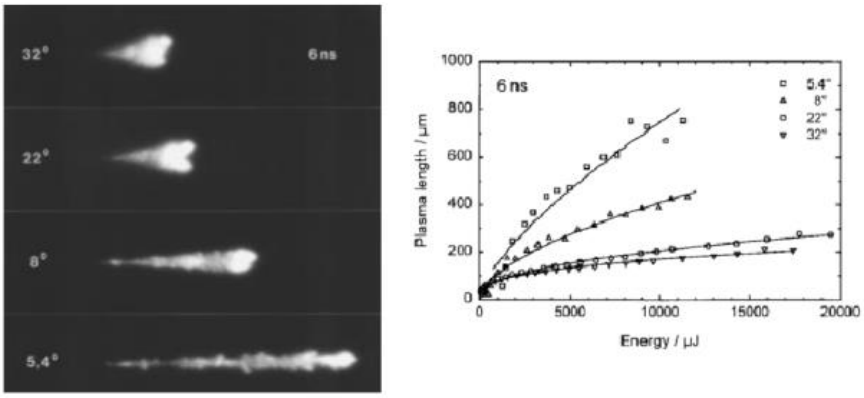

Figure 2.69 – a) Plasma Length with varying Focusing Angles b) Plasma Length as a function of Laser Energy

2.4.6.1 Laser Induced Breakdown of Air

For the purpose of this research, it is impractical to expect that a viable industrial LSP process could be completed in the environment of a perfect vacuum or optimum clean room conditions as most aircraft components are of a considerable size and are manufactured on a moving assembly line. With this in mind, one needs to be aware that all further LSP research was conducted with the laser passing through ambient conditions within the LSP facility.

To obtain the large power intensities accustom with LSP the laser beam has to be focused to the particular spot size. At the irradiance threshold, a plasma spark is formed and is heated to a point where it becomes opaque to the laser. During the plasma expansion, nearby air is heated due to UV emissions from the hot plasma. This continued growth of the plasma continues whilst the laser pulse is maintained. Figure 2.70 indicates the growth of the plasma, the newly formed plasma will actively increase the amount of screening of the laser radiation to the desired target [72].

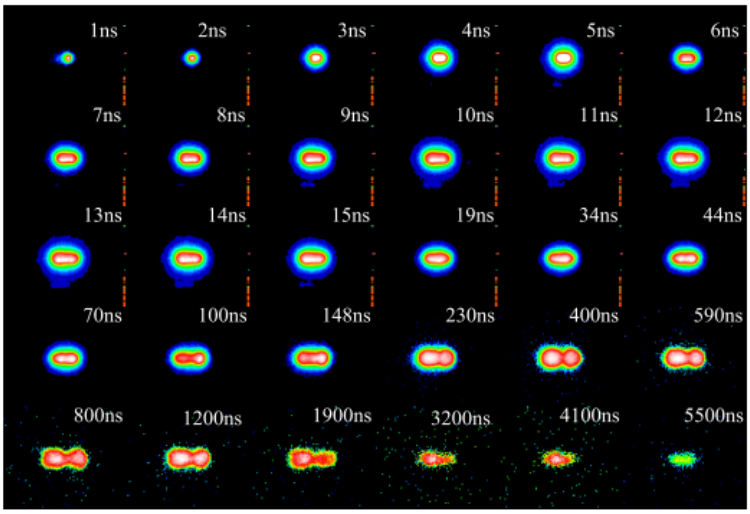

Figure 2.70 - Plasma Formation during a Laser Pulse

An increase in the focal length has been found to cause a shift of the plasma flash in the direction towards the laser. Figure 2.71 provides a schematic showing the plasma flashes, in air, for various energies created at the focal volume. It has been found that by progressively increasing the intensity energy causes a backwards shift of the flash away from the focal spot [72]. This needs to be considered in the setup and selection of lenses used in any LSP apparatus.

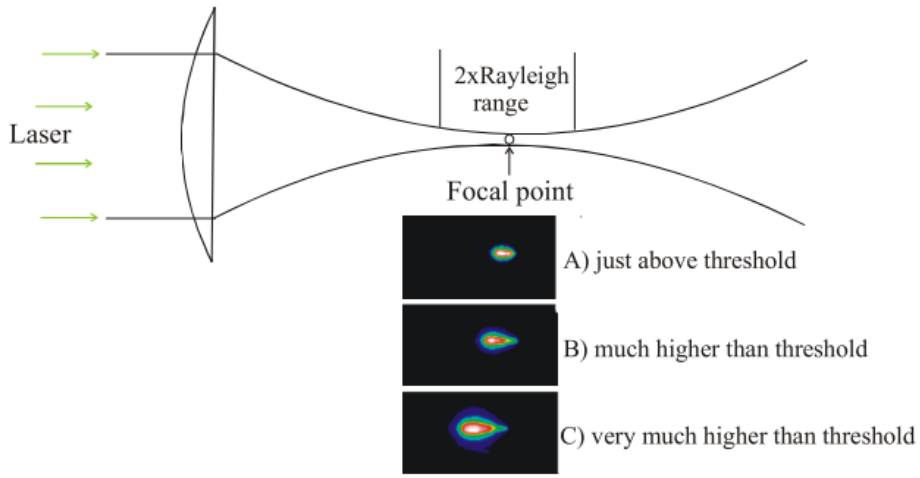

Figure 2.71 - Schematic indicating the effects of Increasing Power Intensity and Focal Length

The success of any LSP process is hinged on the level of quality at which the system is being operated in. Special attention must be given to the selection of lenses and the energy ranges which are used to prevent the formation of LIB.

2.5 Effects of Laser Shock Peening on the Mechanical Properties of Processed Material

Many researchers have shown that LSP is a viable option to improve the fatigue properties of a component of various metallic compositions. In this case, peening of Aluminium alloys will be investigated to find the similarities of the effects of LSP on the base material of AA6082-T6.

2.5.1 Effect of Laser Shock Peening on Hardness of the Material

Shock hardening of the material in the areas where there is direct interaction with the shock wave occurs due to the plastic deformation. Shock hardening effects are a common occurrence for both shot peening as well as LSP. Figure 2.72 indicates the variation in hardness of the material with increasing depth and varying LSP parameters [74].

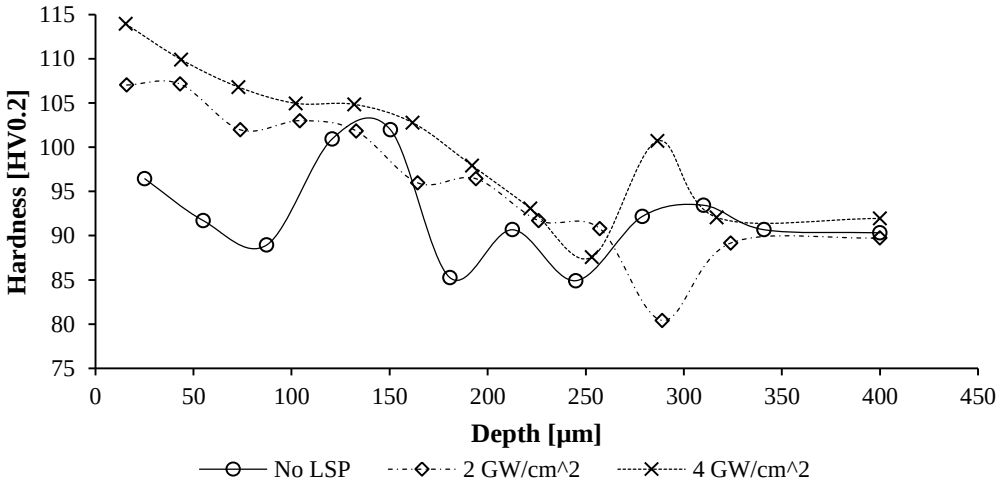

Figure 2.72 - Hardness Variation with Varying LSP Parameters

Figure 2.72 shows that with increasing power intensity material closest to the target surface is strain hardened to a much higher extent. In this case, the changing power densities from 2 to 4 GW/cm^2 had a 16.3% and a 23.9% increase in hardness over the base material near the surface.

2.5.2 Effect of Laser Shock Peening on Residual Stress Profile

During the LSP process, a near perfect uniaxial compression plane which is parallel to the surface is created. This compression plane interacts with the surrounding area and a compressive stress field is generated, while leaving the underlying material in a tensile state [55]. During the propagation of the shock wave through the material, plastic deformation occurs to a depth at which point the peak stress will no longer exceed the Hugoniot Elastic Limit (HEL), defined by equation 2.6.

$$HEL = \frac{(1-v)\sigma_y{}^{dyn}}{(1-2v)} \tag{2.6}$$

Strain hardening and compressive residual stresses result when the dynamic stress of the shock wave is greater than the dynamic yield strength of the peening component, this causes a plastic deformation within the material. The affected depth is a function of the peak dynamic stress as the deformation continues until this stress falls below the dynamic yield strength. Thus, the plastic deformation depends purely on the HEL number, Table 2.5 summarizes the suitable HEL number range for LSP.

Table 2.5 - Hugoniot Elastic Limit Range

HEL Range	Effect
0 – 1 HEL	Peak dynamic stress is below HEL no plastic deformation.
1 – 2 HEL	Plastic strain occurs but with purely elastic reverse strain.
2 and above HEL	Elastic strain gets saturated and the plastic strain fully occurs.

The residual stress profile of AA6082-T6 components which had undergone LSP treatment were measured using X-ray diffraction methods. Three measurement angles provide a clear indication of the through-thickness stress profile of three types of Aluminium component which had undergone no peening, LSP at 2 GW/cm^2 and LSP at 4 GW/cm^2. Figure 2.73 shows the measured through-thickness residual stress [74].

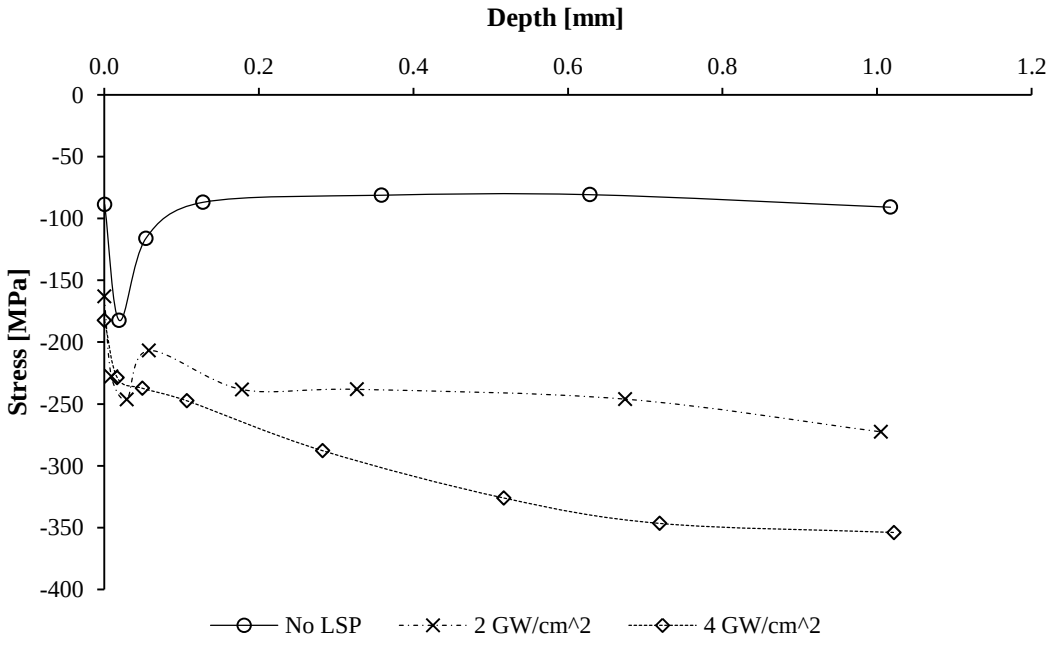

Figure 2.73 - Residual Stress Measurement at Φ=90

From the figure, it can be seen that the higher power intensities produced the highest compressive residual stresses. LSP generates large compressive stress at the surface compared to that of the untreated material. There seems to be minimal difference in the magnitude of the introduced CRS within the first 0.05 mm produced by the two sets of LSP parameters. The turning point of maximum

CRS has been shown to be an LSP process norm were beyond a particular thickness a rapid increase in residual stress occurs. The true effects of LSP can be seen mainly within approximately the first 0.1 mm of the processed component. The through-thickness residual stress was shown to increase through the thickness of the part.

2.5.3 Effect of Laser Shock Peening on the Fatigue Life of a Material

It has been shown countless times that LSP improves the fatigue life of the component being treated. The improvement is due to the compressive residual stresses as well as the enhanced surface quality which delays the onset of fatigue cracking and failure. No data could be found on AA6082-T6 thus for the demonstration that LSP is capable of increasing the fatigue life of Aluminium alloys results from equivalent fatigue test carried out on AA7075-T7351 will be presented. Figure 2.74 shows the S-N curves for untreated, shot peened and laser peened AA7075-T7351 [75].

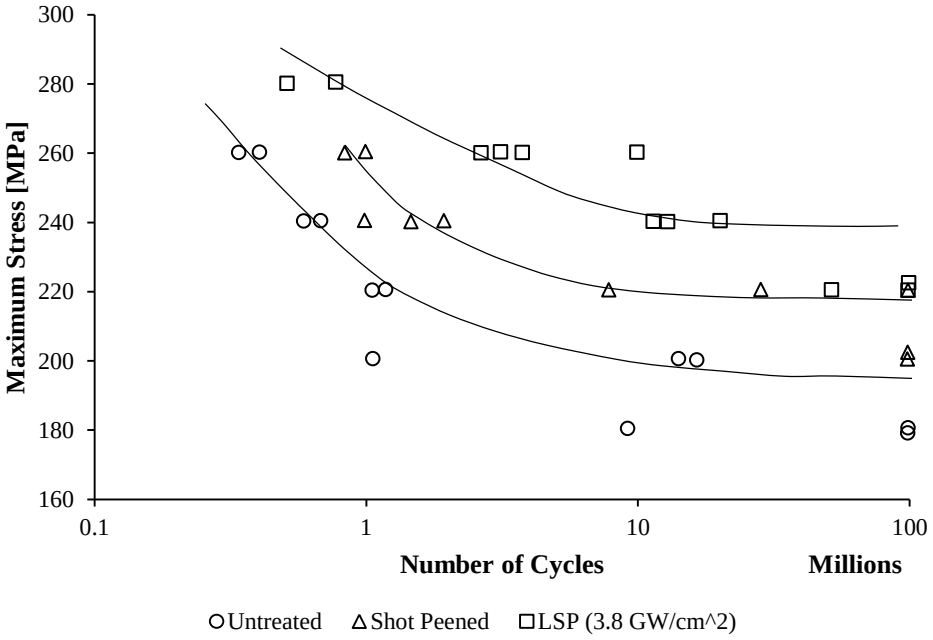

Figure 2.74 - S-N Curve for Untreated, Shot Peened and Laser Shot Peening

From the figure, it can be clearly seen that LSP improves the fatigue life of the component at any stress intensity compared to that of shot peening and the base material. This is purely due to the deeper compressive stress field induced by the LSP process.

LSP has been used to successfully arrest crack or delay the onset of crack initiation, cracking and failure of the component. Figure 2.75 shows the difference in crack initiation, cracking and failure for AA7075-T7351 components that has an applied stress of 260 MPa. A notching process was used to localise any crack initiation to the notch root [75].

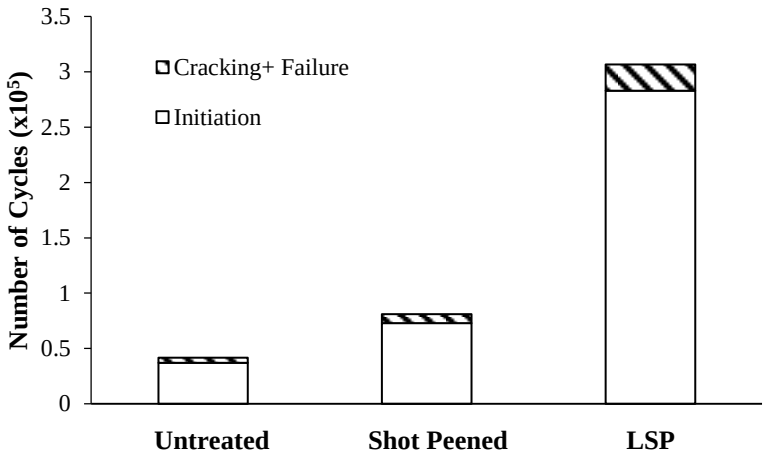

Figure 2.75 - Crack Initiation, Growth and Failure of AA7075-T7351

The figure shows that LSP increases the number of cycles to initiate a crack increased by up to three times to that of the untreated components. Figure 2.76 show the measured crack growth for AA2024-T3 Aluminium components of the base material and exposed to LSP treatments [54].

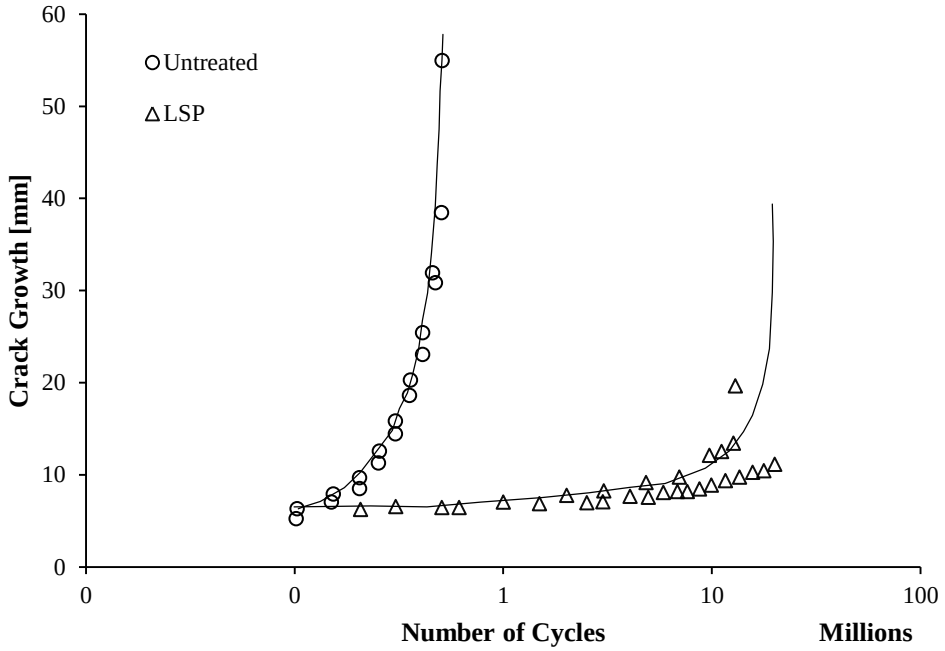

Figure 2.76 – Number of Cycles for a Crack to Propagate

It can be seen that the rate of crack growth is slowed compared to that of an untreated sample. Figure 2.74 to Figure 2.76 show that LSP treatment of Aluminium alloys will increase the fatigue life. The results of these figures indicate that laser peened components which have pre-cracks, potentially such as in the case of components with LOP, fatigue life of the specimen can be improved. The addition of LSP, in theory, will be able to better the fatigue life of the untreated base material and dependent on the crack properties the fatigue properties of defective components.

2.6 Friction Stir Welding and Laser Shock Peening

In the previous sections above FSW and LSP have been investigated in isolation, now that the effects of each process are better understood an attempt should be made to investigate the dynamics of the two processes in combination with one another.

The effects of LSP on FSW joints were investigated with the focus mainly on 2xxx, 6xxx and 7xxx series Aluminium alloys. As there is no published data on the material of interest, AA6082-T6, this section will cover previous work completed on other Aluminium alloys. Table 2.6 lists the FSW and LSP parameters used to manufacture the test samples for the cases that will be investigated within this section.

Table 2.6 – Friction Stir Welding and Laser Shock Peening Parameters used to Manufacture Test Samples

Case	Researcher	Material	FSW Parameters	LSP Parameters
1	Sano (2011) [76]	AA6061-T6 3 mm thick	RPM: 1400 Feed rate: 41mm/min	Peened on both crown and root sides without coating. Power density: 2 GW/cm^2 Energy: 60 mJ
2	Hatamleh (2008) [77]	AA2195 12.5mm thick	RPM: 300 Feed rate: 150 mm/min	Power density: 5GW/cm^2 Square spot size
3	Lordachescu (2011) [78]	AA2024-T351 4 mm thick	RPM: 1000 Feed rate: 300 mm/min Through thickness welding	Power density: 11.5 – 15 GW/cm^2 Energy: 2.8J

2.6.1 Effects of the Combined Processes on the Hardness of the Joint

Experimental research has shown that the reduction in the fatigue life or strength of FSW joints was due to the softening of the material and the introduction of tensile residual stresses caused by the welding process. Restoring the component to the original standard can be completed some form of surface treatment technique which aims to attempt to work harden the material and induce compressive residual stresses. Alternatively, some form of heat treatment process can be done to remove the thermal effects of the joining process but in some cases such as large aircraft components, this is not feasible.

AA2024-T351 Aluminium was welded and peened under the conditions listed in Table 2.6. These components showed an increase in hardness between samples which had just been FSW and those

which were FSW+LSP. Figure 2.77 shows the substantial increase in hardness for the combination of processes [78].

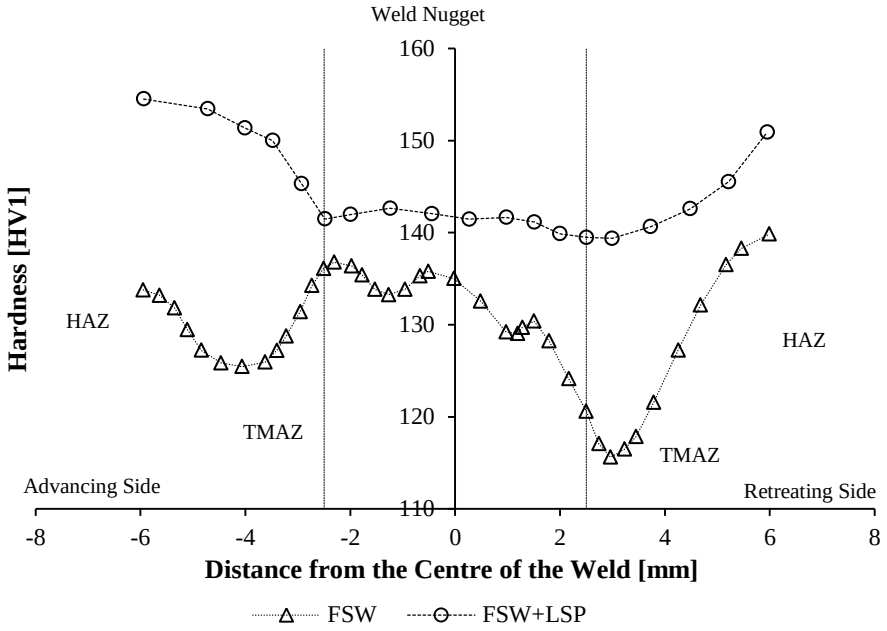

Figure 2.77 - Hardness Profile of Friction Stir Welds with Laser Shock Peening AA2024-T351 Aluminium

Besides increasing the hardness in every region of the FSW, LSP nearly fully reverse the effects of the softening of the TMAZ. LSP tends to induce somewhat linear increase in hardness between the TMAZ and the HAZ whilst keeping the hardness of the nugget nearly constant.

2.6.2 Effects of the Combined Processes on the Stress and Strain of the Joint

The processing of AA2024-T351 using the parameters listed in case 3, Table 2.6, provide data on the effects of the combination of FSW + LSP on the stress and strain properties of the alloy. Figure 2.78 shows the difference in the stress-strain curve for a verity of process combinations [78].

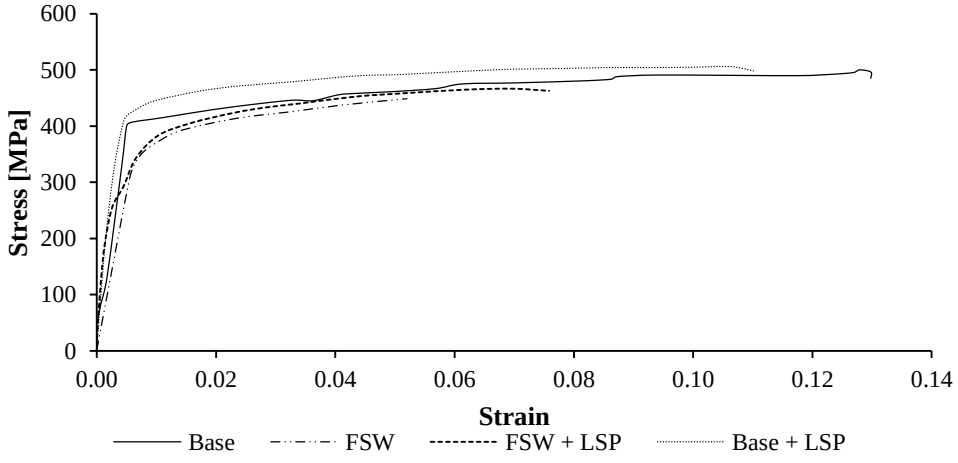

Figure 2.78 - Stress-Strain Curve of Varies Combinations of Friction Stir Welding with Laser Shock Peening on AA2024-T351

For this case, the failure of the different welded combinations of joints all occurred in/at the TMAZ. As this is not AA AA6082-T6 Aluminium it may be likely that the point of failure would not be the same as in this case but potentially similar. The point of failure did occur in the region of the lowest hardness. The figure shows that LSP delays the point of failure of the component by positively affecting the ductility of the welded joint. LSP is capable of increasing the tensile loading capability of the joint considerably.

2.6.3 Effects of the Combined Processes on the Residual Stress Profile of the Joint

From measuring the across weld residual stress profiles of AA6061-T6 it can be seen that the FSW process courses a variation in residual stress states from tensile to compressive areas on the both the crown and root surfaces of the material. The residual stress measurements of the samples manufactured according to the parameters in case 1 listed in Table 2.6, were taken at multiple points across the joint for FSW and FSW+LSP using X-ray diffraction methods. Figure 2.79 shows the results obtained from the measurements on the crown and root sides respectively [76].

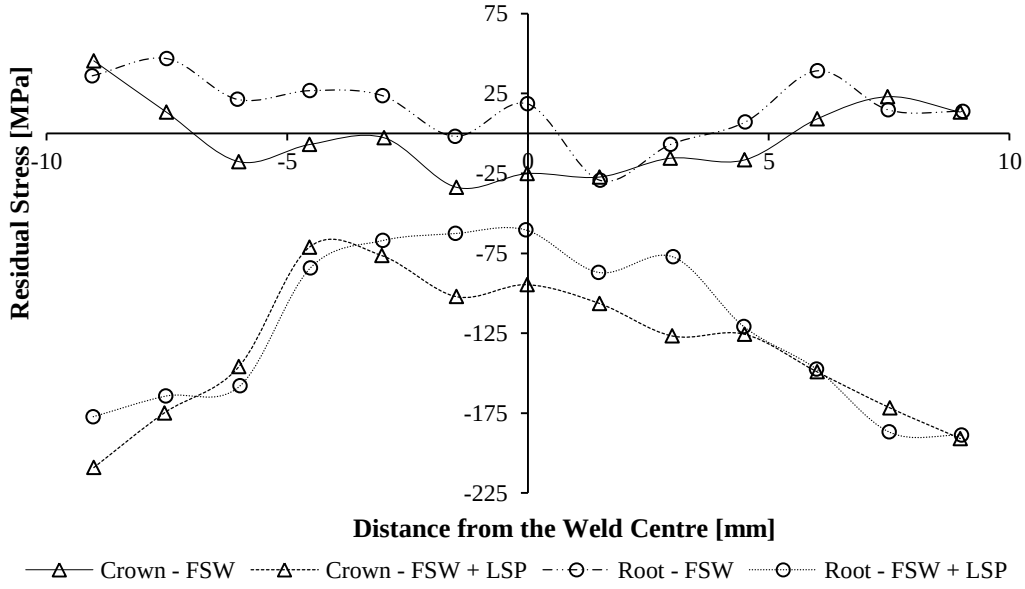

Figure 2.79 - Residual Stress Profile on the Crown and Root side in Combination with LSP

The results of the unpeened surfaces show the variation of tensile and compressive stresses induced within the material during the welding process. The root is fairly in a tensile stress state, which is not conducive to high cycle fatigue life. The crown and root surfaces were peened at different coverage's in order to obtain a flat surface specimen. The variation in peening parameters resulted in both components surfaces being sent into fully compressive stress states. It can be seen that the effects of the LSP on the different regions of a standard FSW varies from zone to zone. As the HAZ is the closest to the base material it is expected that the residual stress within this zone would tend to be in the range of that of the base material treated with the same LSP process. The figure clearly shows that LSP significantly induces compressive residual stresses within a FSW joint.

2.6.4 Effects of the Combined Processes on the Fatigue of the Joint

The fatigue life of the combination of processes was investigated through pure bending fatigue tests conducted on the material described in case 1, listed in Table 2.6 above. Four combinations were tested, with the constant bending strain amplitude load applied perpendicular to the weld line. The results of the S-N curves are shown in Figure 2.80 [76].

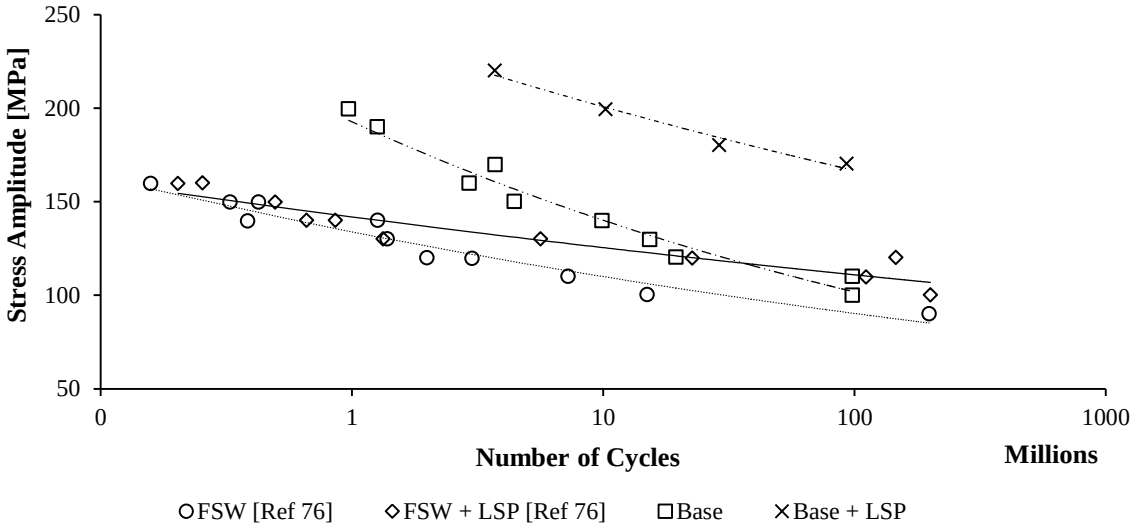

Figure 2.80 - S-N Curve of AA6061-T6 for Different Process Combinations

This result confirms that addition of LSP to FSW joints will increase the fatigue life by some amount. Figure 2.80 shows that LSP had its least effect on the FSW joints when higher stress was applied as there is only a slight increase in fatigue life of the LSP samples. This is accredited to the fact that the applied load is introducing a stress which is almost equivalent to the CRS created during peening. The benefits of LSP are greater noted at the high cycle fatigue ranges were the difference in cycles to failure between the FSW and FSW+LSP are much greater

2.7 Multi-Objective Design and Parameter Optimisation Techniques

Computational optimisation of any process can be complicated and tedious thus using sophisticated software packages such as modeFRONTIER allows for quick and easy optimisation of most engineering systems. Developed by Esteco, this software allows for a multidisciplinary approach to the optimisation of processes and determination of multiple perspective design dependents on a number of user-defined inputs, outputs and objectives. Using the multitude of built in functions such as the Design of Experiments (DOE), scheduler nodes and Response Surface Methodology (RSM) applications one is capable of producing optimisation algorithms, graphical representation and statistical analysis of results that will suit the user's requirements. ModeFRONTIER can be used to optimise processes in the attempt to achieve a system state that is known as Pareto Frontier. Pareto frontier or efficiency, named after the Italian Economist Vilfredo Pareto who used the concept of a state of allocation of resources in the best possible manner. The best possible Pareto efficiency is

achieved when the situation of a single party cannot be improved without negatively affecting the situation of another party [79].

2.7.1 Design of Experiments

Design of Experiments is a methodology which maximises the information gained from experimental results. By varying one input and keeping all others constant one is able to determine the effects of the varying parameter on the system at large and the results. Carrying out the physical experimentation of every particular parameter combination is not only time consuming and near impossible but can be taxing on experimental resources. DOE allows for the elimination of redundant tests, observations and reduces the time and resources required to carry out full optimisation of a process by extracting the most amount of information from a few number of tests and results.

The DOE's are used to complete the following applications:

- To create sampling for process parameter sensitivity.
- To create data points to assess the robustness and reliability of the process.
- To generate approximate points to produce response surface approximations.
- To provide optimisation algorithms and potential combinations of designs.

To complete the above points a hypothetical design space, which is a multidimensional space where all combination of parameters can be represented. Space filling techniques are used to fill this space according to the nature of intended optimisation. Some of the most commonly used space filling techniques used within modeFRONTIER are discussed in Table 2.7 [80].

Table 2.7 – Design Space Filling Techniques

Technique	**Description**
DOE Sequence	User defined inputs of the initial designs.
Uniform Latin Hypercube	Random numbers are generated which conform to a uniform distribution. Points are uniformly distributed over a set variable range as the statistical distribution is split into a number of intervals with the same probability with random values selected within each interval.
Incremental Space Filling	The algorithm takes into account existing experimental trials and generates points within the design space which are uniformly distributed.
Random	Random points are generated on the basis of the theory of random number generation and spread uniformly within the design space.
Sobol	Mimicking the random algorithm, this technique is a deterministic algorithm which achieves uniform sampling with reduced clustering of random sampling.

2.7.2 Optimisation Schedulers

The function of the scheduler is to use the number of designs produced in the DOE function and converge on an optimised design which is dependent on a number of user defined objectives and statistical multi-objective algorithms. This function is required to be paired with the DOE function in modeFRONTIER. The variety of scheduler nodes which are available in modeFRONTIER are described in Table 2.8 [80].

Table 2.8 - Optimisation Algorithms for Schedulers

Algorithm	Description
Simplex	Based on a single-objective algorithm, it is applicable to discrete values as multiples of a base value assigned to each parameter. This sequential algorithm has the tendency to converge fairly slowly.
B-BFGS	The Bounded Broyden-Fanno-Fletcher-Goldfarb-Shanno gradient algorithm requires that all variable be continuous. Each entry in the DOE table is used as a sequence of initial points for different local optimisation problems.
Levenberg-Marquardt	This algorithm is a well-suited method for finding the minimum of a sum of squares of nonlinear functions. This trust-region method combines effectively two different algorithms: the Gauss-Newton algorithm and the steepest descend method.
MOGA-II	This scheduler is an efficient multi-objective algorithm which is capable of preserving the solution without reaching premature convergence. It does not require many user-provided inputs and provides a robust and efficient optimiser.
ARMOGA	Based on the MOGA algorithm, this Adaptive Range Multi-Objective Genetic Algorithm (ARMOGA) is well suited for converging on the best solutions in a very large design space. Requiring a larger number of user-defined inputs this scheduler is far more complicated than the MOGA-II algorithm.

2.7.3 Response Surface Methodology

Response Surface Methodology (RSM) is a statistical method which explores the relationships between a number of independent variables (inputs) and the corresponding response variable (output). It is extremely useful in the optimisation of a particular output. RSM allow for the analysis of the effect of two input variables on a single output to be investigated at the same time.

ModeFRONTIER has a number of available RSM algorithms built into the programme. A number of these are outlined in Table 2.9 [80].

Table 2.9 - Response Surface Methodologies

Response Surface Methodology	Description
Shepard & K-Nearest	Extremely good interpolating method used for large databases. Does not work well when applied to small databases.
Kriging	Suitable for small databases this interpolation method is highly dependent on the noise parameters.
Anisotropic Kriging	It is a refined version of the Kriging model that allows for the control of the relative importance between input variables.
Gaussian Process	A regression based model which is specified by the parameterized mean and covariance functions. Best suited for non-polynomial responses, the numbers of requested designs are dependent on the number of input variables.
Radial Basis Functions	These functions are multivariate scattered data interpolates who's values are dependent on the distance from the origin.
Neural Networks	Models generic non-linear relationships between inputs and output. It attempts to solve problems in a similar method to that of a human brain.
Evolutionary Design	Uses genetic programming methodology for symbolic regression.

2.7.4 Practical Example of the Usefulness of Response Surface Methodology in the Optimisation of Friction Stir Welding Parameters

Al-Jarrah made use of RSM techniques in the process of optimising the independently controlled parameters of FSW to achieve the best yield strength of the joints. Process parameters such as RPM, feed rate, sheet thickness and shoulder diameter were varied at five levels, with four independent variables producing thirty one experiments [1]. Figure 2.81 provides the surface plots which relate two inputs to an output thus allowing for one to identify the effects of each parameter [1]. Focusing on Figure 2.81.a, one can see that a maximum rotational speed combined with the maximum feed rate produces the joint with the best yield strength of the joint. The ease of being able to note the effects of the combination of parameters on the outcomes as shown is the main reason for the use of this technique.

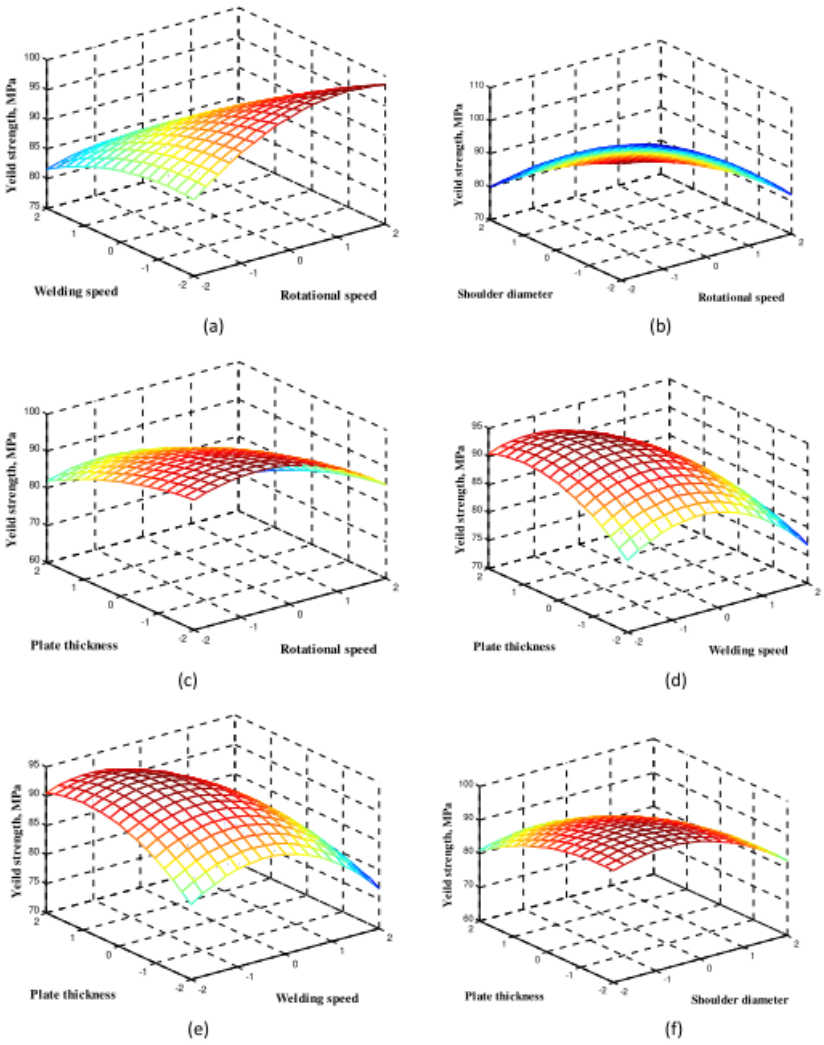

Figure 2.81 - Response Surface Methodology Optimisation of Friction Stir Welding Parameters

Assessment of the remaining RSM's one should note that different maximum or minimum combinations of RPM and feed rates should be selected for achieving a variety of different output goals. Great care should be taken when selecting the parameters for FSW as the parameters should aim to achieve the best joint performance for a specific outcome or application.

2.8 Fracture and Fatigue Mechanics

Due to the nature of this research some background in the field of fatigue and fracture mechanics was investigated.

2.8.1 Fracture Mechanics

The application of a sufficient tensile load to Aluminium sample would result in ductile failure of the part. The common transgranular failure would be expected from the failed component. Ductile failure encompasses the nucleation, growth and formation of micro-voids. The voids cause separation of the

material at grain boundaries. Eventually, these areas do not have enough material to support the applied load and the component fails.

The meaning of flaws has already been discussed, but for this research LOPS was assumed to resemble micro-cracks such as the ones referred to in literature. A method to assess the effects of the LOP on the strength of the joint is to calculate the fracture toughness of the weld. This is defined as the measure of the ability of a material which contains a flaw to withstand an applied load [81]. The fracture toughness (K_c) is the stress intensity factor (K) required for a crack to propagate. The stress intensity factor is calculated according to equation 2.7. The geometry factor and load case match the crack formed from LOP perfectly. From the static loading, the effects of the LOP can be investigated. Figure 2.82 shows a schematic of the fracture toughness sample.

$$K = f\sigma\sqrt{\pi a} \tag{2.7}$$

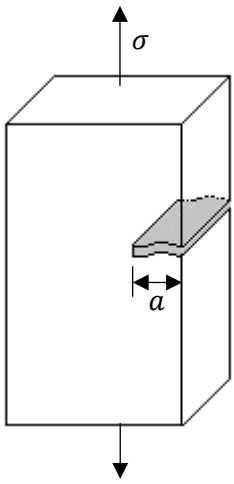

$f = 1.12$ for a small single-edge notch

Figure 2.82 – Schematic drawing of the Fracture Toughness Sample

This stress intensity factor is a good measure of the stress at the crack tip as it propagates. The rate at which the crack grows per cycle can be represented by the stress intensity factor. By plotting the rate of the crack growth against the crack size we are able to show the effects of increase the stress intensity results in a faster crack growth. Figure 2.83.a provides an example of the crack growth curves typically used in fracture mechanics. The slope of the crack growth curves results in the growth of the crack per cycle. Figure 2.83.b provides an example of the rate of growth per cycle [82].

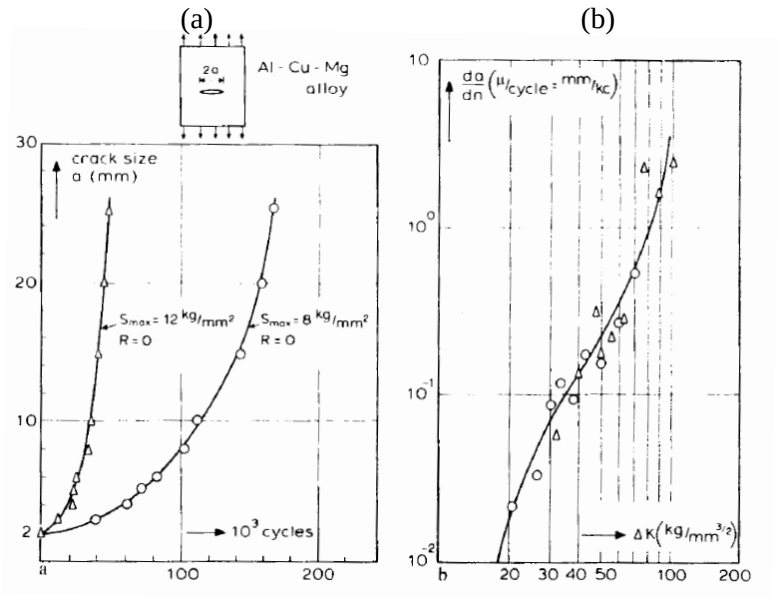

Figure 2.83 – Fatigue Crack Propagation a) Crack Growth Curves b) Crack Propagation Rates

The fracture surface of a statically loaded ductile material leads to a very specific fracture surface. The two effects that dominate the formation of the fracture surface is the creation of micro-voids and deformations due to slip. A flat faced region is present as this is the area where the flaw first nucleates, followed by a small shear lip. Closer inspection of the fracture surface reveals a dimpled surface. Each dimple is a trace of the microvoids formed during fracture. The dynamic fracture or better known as fatigue failure will now be discussed.

2.8.2 Fatigue Damage Mechanism

Components which are designed for most engineering applications are exposed to a variety of complex, fluctuating and repeated stress. The failure of a component which is subjected to repeat loading and unloading is known as fatigue or failure due to cyclic loading. Over an extended period of time and cycling of these loads, the component tends become weaker and weaker until failure occurs. Fatigue failures have been shown to begin at a crack nucleation sites, manufacturing faults and material defects. Under the cyclic loads, these defects tend to propagate and grow in size. In the vicinity of highly stressed regions new cracks and defects tend to form due to the fatigue process. The total life of a fatigue component can be broken down into three major stages. These stages of fatigue failure are outlined as followed [83]:

1. **Crack Initiation:** The type of material has a direct influencing on the type of the crack initiation process followed by the component. Due to the discrepancy in materials this stage is broken into two broad sections:
    a. **Ductile Material:** The ability of ductile materials to locally yield at the stress concentration site allows the material distort and create slip or shear bands. As the load continues to cycle additional bands are formed and cracks are formed. The

growths of the cracks are progressive processes. Examples of ductile materials are Aluminium and steel.

b. **Brittle Material:** As brittle materials do not have the same ability to yield like their ductile components, cracks are formed far easier. Generally, brittle materials skip this stage of crack initiation and proceed directly to crack propagation at sites were pre-existing defects are present. Examples of brittle materials are cast iron and glass.

The nucleation sites are typically at or near to the surface of the material. Surface defects such scratches, pits and sharp corners act as stress concentration factures amplifying the local stress which is typically highest at the surface of the material [81].

2. **Crack Propagation:** Every time the applied load becomes tensile a stress concentration is formed at the pre-existing crack, which was either formed during manufacturing of the component or during the crack initiation stage, resulting in small amounts of crack growth after each application of the load. Crack growth is caused purely by tensile stress that cycle below and above the yield strength of the material. The crack will always grow along planes normal to the maximum tensile stress. As the crack becomes larger so does the stress concentration induced by it. This implies that the rate of crack growth increases with time. A growing crack will cause a progressive decrease in residual strength of a structure, to the point where the structure can no longer carry the applied load. The crack will continue to grow under the applied load until the part fails.
3. **Fracture due to unstable crack growth:** After sufficient time and tensile load cycles the cracks will grow to a length which will cause complete and sudden failure of the component. Ideally, failure occurs when there is insufficient remaining material to carry the applied load. Figure 2.84 shows two examples of ductile fatigue failure under high and lower applied stresses [84]. It can be noted that higher loading causes a smaller crack initiation area with a rapid fracture surface, whilst the opposite is observed in lower applied stressed components. The larger crack initiation surface in the lower loaded component is due to the greater amount of cycles required for the crack to grow as the material has more time to locally yield around the crack tip. Typically the surface at the origin of the failure is fairly smooth and tends to become rougher as the original crack size increases. Beach is the term that defines the "clamshell marks" which are formed in the propagation stage. These marks are formed during intermittent or changing loads during service of the component. The striations, present in Figure 2.84.b, indicate the growth of the crack tip after each cycle.

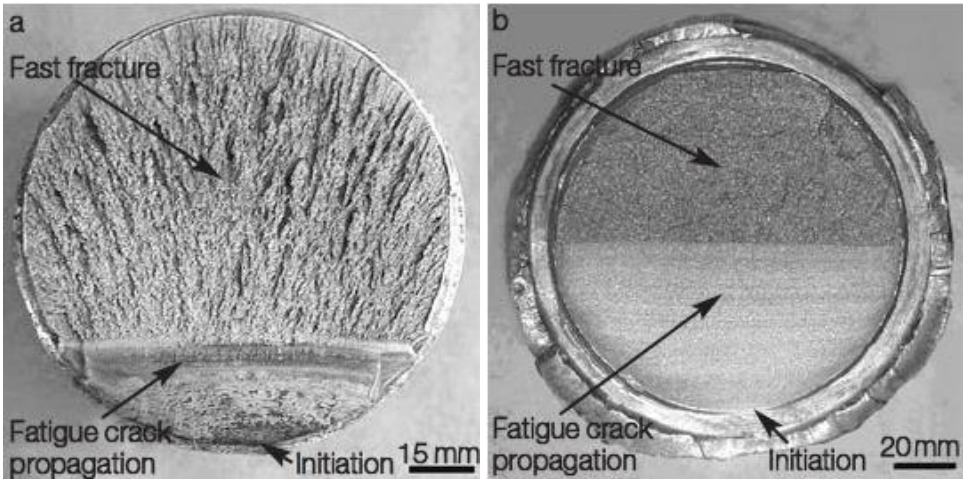

Figure 2.84 - Fatigue Fracture Surface of Components under a) High Applied Loads and b) Low Applied Loads

2.8.3 Fatigue Analysis

A common sample may see a variety of fluctuating fatigue stress cycles during its service life. In some cases either the compressive load may be larger than that of the tensile and vice versa. Fully reversed cyclic loading is the category name given to the load case in which the maximum tensile stress is equal to the maximum compressive load. Figure 2.85 provides an example of this type of fatigue loading.

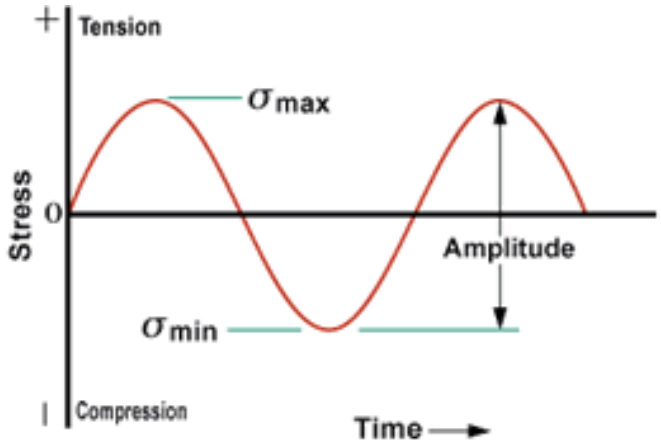

Figure 2.85 - Fully Reversed Cyclic Loading

The difference between the maximum and minimum stress is defined as the stress range, it is defined according to equation 2.8.

$$\sigma_r = \sigma_{max} - \sigma_{min} \tag{2.8}$$

The stress amplitude is the half distance between the maximum and minimum stress, it is calculated according to equation 2.9.

$$\sigma_a = \frac{\sigma_r}{2} = \frac{\sigma_{max} - \sigma_{min}}{2} \quad (2.9)$$

The mean stress is the average between the maximum and minimum stress, it is defined according to equation 2.10.

$$\sigma_m = \frac{\sigma_{max} - \sigma_{min}}{2} \quad (2.10)$$

Two useful ratios are commonly used to describe cyclic loading which is the stress ratio (R) and amplitude ratio (A), each defined according to equations 2.11 and 2.12 respectively.

$$R = \frac{\sigma_{min}}{\sigma_{max}} \quad (2.11)$$

$$A = \frac{\sigma_a}{\sigma_m} = \frac{1-R}{1+R} \quad (2.12)$$

Fatigue samples tested under fully reversed alternating loads leads to the formation of the S-N curve, examples of these have been shown in Figure 2.2, Figure 2.52 and Figure 2.80. Classified under the Stress Life Fatigue Method, this extremely important graph maps the relationship between a materials number of cycles to failure versus the applied stress amplitude. This method of analysing a component is known to mainly associate with high load repetitions, typically over 10^4 cycles and it is assumed that there are no initial defects or flaws within the component. This approach is commonly known as High Cycle Fatigue (HCF). The loading cycle loading stress is generally lower than that of the yield strength of the material [85]. Materials such as steel are known to have a fatigue life or endurance limit which is a stress level which is low enough that the load can alternate indefinitely without the failure of the component. Unfortunately, Aluminium does not possess this characteristic but are represented as a continuously decreasing log line.

2.9 Residual Stress X-ray Diffraction Measurements

X-ray crystallography is a method to determine the atomic structure of crystalline materials with small grain sizes. The crystal structure causes the incident X-ray beam to diffract into a number of specific directions, hence the name X-ray Diffraction (XRD). By measuring the strain in a crystal lattice and using the elastic constants the resulting residual stress can be calculated. The elastic constants are assumed to be a linear elastic distortion of the appropriate crystal lattice plane. The penetrative ability of the X-rays is dependent on the strength/energy of the beamline as well as the material of the sample being measured. With the appropriate parameters this technique can be used to measure the residual stress up to several millimetres into the sample. The beneficial aspect of this technique is that it is non-destructive but is limited to crystalline materials ideally with small grain sizes.

2.9.1 Fundamental Theory of X-ray Diffraction

The principle of X-ray diffraction is based on the Bragg's Law. This law defines the condition necessary for two reflected X-rays to interact in a constructive manner. The law states that the two reflected beams, from different plans within the material, will only interact constructively when the beams are in phase with one another only when the path difference is equal to a whole number of wavelengths. This concept of how X-rays interact constructively was shown in Figure 2.86 [86].

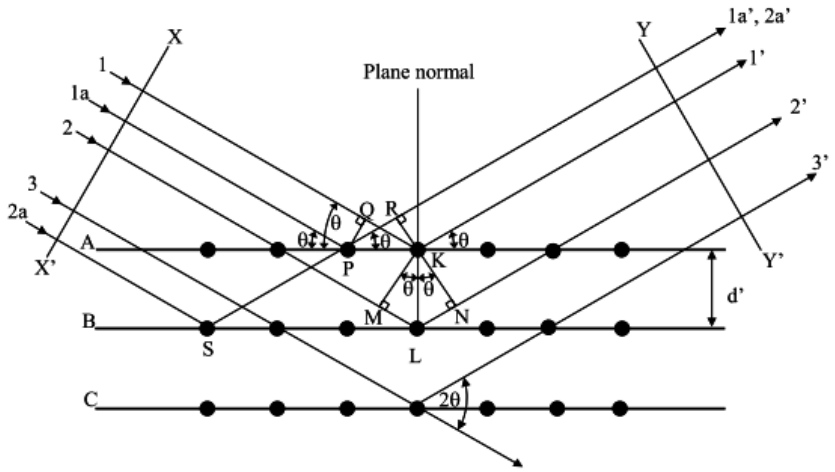

Figure 2.86 – Diffraction of X-rays by a Crystal Lattice

This theory can be represented in an equation, the derivation is well known and falls out of the scope of this research thus it has been simply presented as equation 2.13.This equation indicates the nature of the interference of the X-rays and the inter-planar spacing and the wavelength of the incident X-ray radiation.

$$n\lambda = 2d' \sin\theta \tag{2.13}$$

Using the theory above and an X-ray diffractometer one can simply perform strain measurements on metallic materials. When the X-rays are exposed to the crystal lattice of the sample it will produce diffraction patterns. Setting the diffractometer to scan through an arc around the sample, diffraction peaks can be identified and thus used to calculate the residual stress. When a component or material is acted on by some form of strain, the crystal lattice deforms (typically elongates and contracts) which changes the inter-planar spacing {hkl} lattice planes. The deformation causes a change in the d value, in equation 2.29, this shifts the diffraction pattern. Recording the shift allows for the measurement of the strain within the material. If the unstrained inter-planar spacing d_0 is known, by measuring the peak positions at values of 2θ and solving Bragg's equation for d_n, the strain can be calculated according to equation 2.14.

$$\varepsilon_Z = \frac{d_n - d_0}{d_0} \tag{2.14}$$

This shows that the strain within the surface can be measured and then compared to an unstrained sample thus an accurate measurement of the unstrained material is required. By tilting the specimen in the diffractometer through angles of ψ the planes can be measured, the ψ angle was shown in Figure 2.87 [86]. This schematic illustrates how a plane can be rotated to a specific angle in order to satisfy Bragg's Law.

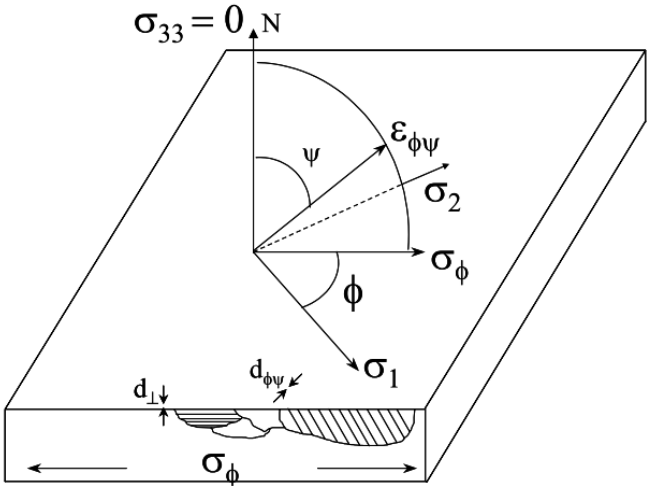

Figure 2.87 - Schematic of the Diffraction Planes and relevant angles associated in the measurement of the Strain

Equation 2.14 can now be written so that any object can be measured by tilting the surface until Bragg's law is satisfied. Combining equation 2.30 with Hooke's Law and knowing that any strain in a particular direction can be written in terms of the Poisson's ratio and the known strain, equation 2.15 can be derived.

$$\theta_{\phi} = \frac{E}{(1+\nu)\sin^2\psi}\left(\frac{d_{\psi}-d_n}{d_n}\right) \tag{2.15}$$

This $\sin^2\psi$ method is the most common XRD method. The 2-theta peak positions are measured and plotted as shown in Figure 2.88 [86].

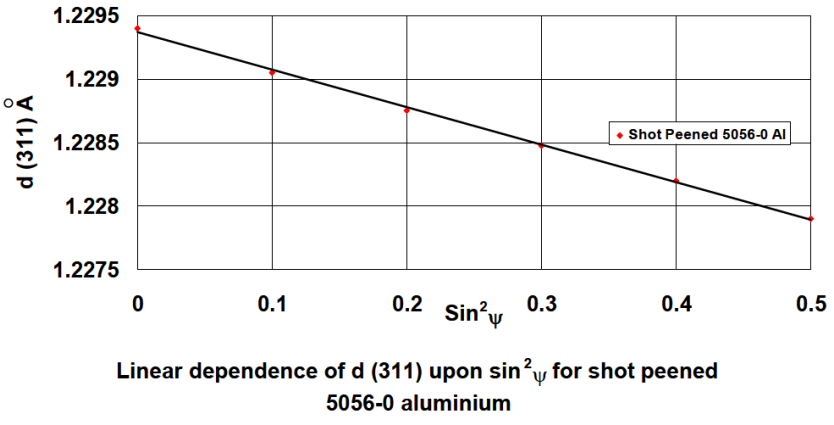

Figure 2.88 – X-ray Measured Inter-Planar Spacing versus $\sin^2\psi$ plot

Calculating the gradient of the line and knowing the material properties of the component one is capable of calculating the stress. It should be noted that this method assumes that a zero stress at $d=d_n$, where d is the intercept on the y-axis when $\sin^2\psi$ is equal to zero. The final stress can then be calculated according to equation 2.16.

$$\theta_\phi = \left(\frac{E_{youngs}}{1+v}\right) m \tag{2.16}$$

2.9.2 Elettra Synchrotron

Located on the outskirts of Trieste, Italy, this source of high powered light radiation is a specialised research facility which provides a number of researchers, from all over the world, the possibility to perform high quality materials characterisation experiments. A synchrotron is a circular electron accelerator which uses extremely powerful magnetic fields to maintain the particles on a closed path. As the electrons pass through these various magnetic fields, extremely bright and high energy light is produced. By channelling specific wavelengths of light off the main beam, a number of experimental workstations can be set up to conduct a diverse number of experiments. Figure 2.89 shows the various beamlines available at Elettra [87].

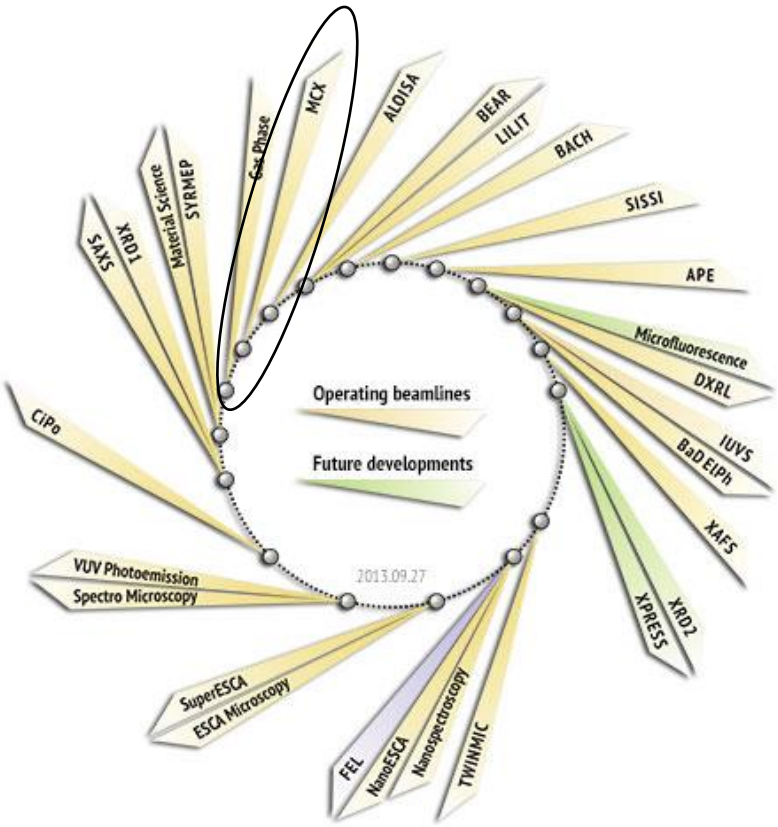

Figure 2.89 - Elettra Beamline Schematic

As indicated in the schematic, the Materials Characterisation by X-ray (MCX) diffraction beamline is of particular interest to this research. The beamline has the capabilities of performing a range of non-

single crystal diffraction experiments such as residual stress measurements in crystalline materials. Elettra has implemented the Chi Method of measuring residual stress. In this technique the sample is placed in an Eulerian cradle which allows for the sample to be rotated about the ψ and Φ axis. Figure 2.90 illustrates an example of the relative angles associated to the ψ method.

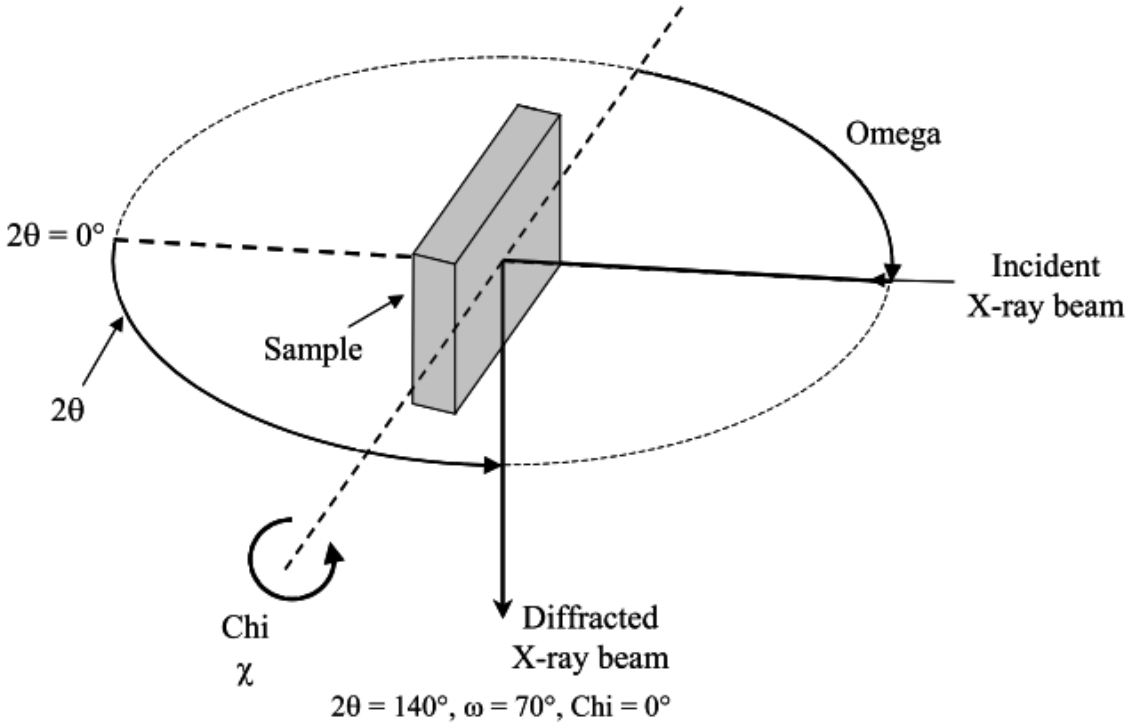

Figure 2.90 – Schematic of ψ Method of Residual Stress Measurement

By implementing the methods discussed previously in this section the deformed crystal structure can be measured by scanning over a region of particular interest. This beamline has the ability to operate at a number of energy levels from a few eV to as much as 20 keV. It has been shown that the X-rays have a penetration depth of as much as 145 μm at an energy of 20 keV when interacting with Aluminium alloys [21]. Although this depth is but a fraction of the sheet thickness this technique allows for the accurate evaluation of the stress distribution within the region where the effects of LOP would be most prominent. This non-destructive method allows for further testing to be performed on the exact sample were the residual stress profile is known.

3 Objectives

The objectives outlined within this section are the intended research goals that will be achieved in the completion of this research. Primary and secondary objects have been listed below. The secondary objects are accomplished through the work that is conducted in the completion of either of the primary objectives.

- Development of a FSW tool which would be capable of manufacturing joints of a high industrial standard. The tool must be designed to obtain high standard FSW in the selected Aluminium alloy and thickness of plate used.
- An investigation into a suitable FSW operational parameter window, with experimental assessment of the influence of the FSW parameter combinations on the quality of the joints: welding forces, thermal effects, microstructure, external quality of the joint and static strength of the joint.
- Optimisation of the FSW process through the application of a multi-objective optimisation process to fully investigate the FSW parameter window, develop the ability to predict a number of experimental outcomes based on the results achieved and the selection of the most suitable parameters to obtain the best FSW joints with this Aluminium alloy and manufacturing set up.
- Define a robust FSW procedure for introducing controlled and constant LOP defects in FSW joints.
- Characterise the effects of the LOP defects on the mechanical properties of the optimised FSW joints.
- An investigation into a suitable LSP operational parameter window, with an experimental assessment of the influence of the LSP parameter combinations on base AA6082-T6 Aluminium and FSW AA6082-T6.
- Optimisation of the LSP process through the application of a multi-objective optimisation process to fully investigate the LSP parameter window, develop the ability to predict a number of experimental outcomes based on the results achieved and the selection of the most suitable parameters to obtain the best LSP parameters to achieve the most suitable results.
- Combining the most suitable parameters of the FSW and LSP process to investigate the effects of combining the process on the joints residual stress and dynamic load capacity.
- Comparative evaluation of the fatigue performance of FSW (LOP) and FSW (LOP) with LSP.
- Provide greater understanding in the ability of LSP to recover the effects of welding defects within the FSW joints.

4 Research Approach

A research and project plan was developed in accordance with the expectations of the project sponsors and academic supervision. A number of milestones were set out in order to give the research direction and form of timeline which was required to be followed. Figure 4.1 provides a breakdown of each of the key objectives and areas which formed the total cycle of this research. Each area was explained to provide more information in the area.

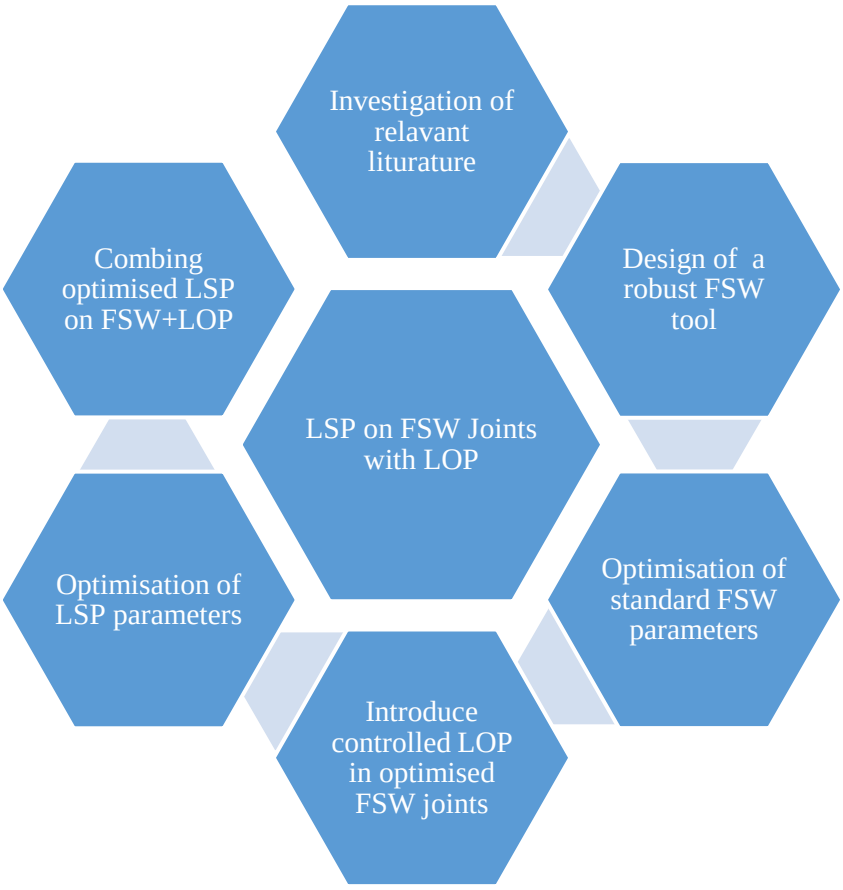

Figure 4.1 – Research Project Outline and Methodology

The following areas were required to be completed in order for the completion of this research. The following provides a detailed breakdown how the methods and tasks required to be completed to achieve each item in Figure 4.1:

1. **Investigation of relevant literature:** Research and analysis into previous works completed in the field of FSW, parameters and methods of introducing LOP in a FSW joint and the field of LSP was completed. Once a greater understand of three aspects of this research was gained better selection of process parameters and understanding of the dynamics of each process in isolation and combined was achieved leading to the best form of processing possible. The

outcome of this aspect of the research has been presented in the literature survey, section 0 of this report.

2. **Design of a robust FSW tool:** FSW of AA6082-T6 3mm thick sheet had never been completed at the University of the Witwatersrand. For this completely new welding tools had to be developed in order to be able to successfully weld the material. Using suggested tool geometry from literature and experimental optimisation a final tool configuration was achieved. The process followed has been described in the experimental setup, section 5.
3. **Optimisation of standard FSW parameters:** Upon finalising the design and set up of the welding tool, parameter optimisation of the FSW process was completed. In an industrial welding process, the best possible welds are required to be achieved. As this research was broadly based for an industrial application of manufacturing of aircraft the wide parameter window had to be identified. The initial window was selected according to literature and the capabilities of the welding machine (specific RPM setting which was dependent on the gearing of the CNC machine). Design of Experiments was used in the optimisation of the parameters to identify the best possible welding parameters. A number of experimental results such as tensile strength, bending strength, machine loads and joint material thickness were related to the various welding parameter combinations. The decision to first obtain the best, defect free joint was made to show that this facility had the capacities of creating sound welds before purposely introducing defect as this method closely represented what an industrial process would hope to achieve. The outcomes of this section have been presented in section 6.1.
4. **Introduce controlled LOP in optimised FSW joints:** Using the previously optimised FSW parameters and the techniques identified from literature LOP defects were introduced into FSW samples. The optimised welding parameters were used to simulate the process in an industrial application as it is highly unlikely that welding would ever be completed at anything other than the optimum welding tool and set of parameters. Using irregular thickness of welding sheets to attempt to introduce LOP is not a feasible method as generally base material sheet undergo strict quality control before being used in the manufacture of any metallic object. A feasible method identified from literature to introducing these defects would be to offset the welding tool whilst welding as slight misalignments in welding sheets and tool can easily occur in a welding process due to insufficient clamping, human error, wear on the tool and manufacturing environment changes such as thermal effects of ambient conditions. The detail of this area was presented in section 7.
5. **Optimisation of LSP parameters:** As with the FSW process the LSP parameters were instigated in isolation. Being able to understand the dynamics of the LSP in isolation was vital in understanding and predicting how the process would affect the FSW joints. Optimisation of the LSP process was conducted by varying power intensity and coverage

areas. With each parameter combination, a number of experimental results were achieved which were then used in optimisation of the LSP process. The details this area was presented in section 6.2.

6. **Combining optimised LSP with FSW+LOP:** Once the three aspects of this research were mastered it was possible to successfully combine then in a repeatable manner which could be useful for various industrial applications. The desired outcome of this section was to attempt to demonstrate that LSP could be used to improve FSW as well as attempt to correct for the presence of a welding defect such as LOP. This section has been described in section 8.

5 Experimental Facility

This section covers the major aspects of the apparatuses used in the manufacture of all test samples.

5.1 Friction Stir Welding Equipment

The following provides information on the major equipment used in the manufacture of FSW samples. All equipment within this section can be located in the North West Engineering Laboratory at the University of the Witwatersrand.

5.1.1 Maho MH-C 700 CNC Retrofitted Friction Stir Welding Machine

The MAHO MH-C 700 is an electrically driven horizontal vertical tool room milling machine. Implanting a displacement controlled methodology the CNC has a positioning resolution of 0.01 mm in all three axes. Figure 5.1 shows the main features of the machine used to complete all friction stir welds used for this research.

Figure 5.1- Layout of Maho MH-C 700

Table A.2 in Appendix A.2 lists the detailed specifications of the MAHO MH-C 700.

5.1.2 Clamping and Backing Plate

Securing of the sheets to the backing bar is achieved by six taper end clamps and two 25 x 10 mm steel extrusions. Once the plates have been aligned with the traversing direction of the spindle of the CNC, a steel extrusion is placed on top of the plates. Three taper end clamps are used per sheet. Each of the clamps was supported by stepping blocks and was bolted down securing the extrusion and

ensuring that the plates do not move during welding. Figure 5.2 provides an example of the clamping system.

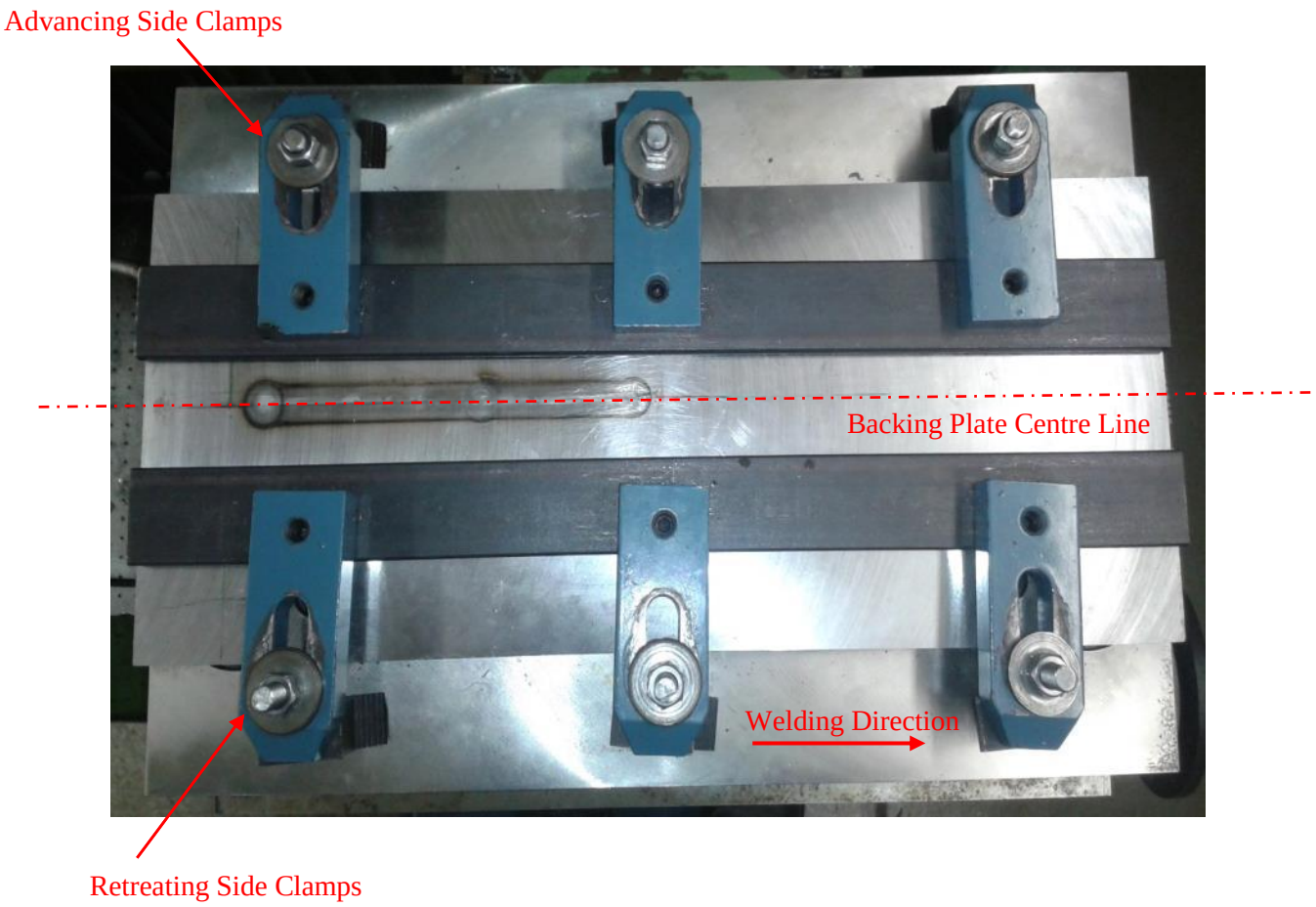

Figure 5.2 - Schematic Example of Clamping System

The steel backing plate, designed by Correia [21], was intended to provide the levelest surface as possible. The backing plate is designed to bolt directly to the CNC table bed. The backing plate was designed to accommodate a work piece area of 254 x 600 mm.

5.1.3 Kistler Piezoelectric Sensors

The Kistler Piezoelectric Sensors are used to monitor and capture the applied forces in each of the principle axes as well as the moments created during the welding process. The Kistler is made up of a multicomponent force link set type: 9366CC0.5, the detailed specifications can be found in Table A.4 in Appendix A.3 [88]. Each one of the four force links is connected to a summing box. The summing box is connected to an amplifier which passes the increased signal to a Data Acquisition (DAQ) to capture the data. The measuring range of the unit is -25 kN to +25 kN. Figure 5.3 shows the Kistler multicomponent force link unit. The force directions shown in the figure is according to the layout specified by the manufacturer.

Figure 5.3- Kistler Multicomponent Force Link Unit

For the unit to be successfully implemented into this testing apparatus the force links had to be mounted to a mild steel base plate, with a stainless steel plate on top. The backing plate is attached directly to the force link set up, as shown in Figure 5.4.

Figure 5.4 - Force Link Integrated into FSW Machine

During the welding, this dynamometer can be used to record the force in the transverse direction to the tool translation (F_x), the force in the welding direction (F_y) and in the normal direction (vertical direction) to the backing bar (F_z). These forces are combined with the placement of the sensor to determine the three principle moments. The moment which occurs about the Z-axis can be considered as the applied torque.

5.1.4 FLIR T640 Thermal Imaging Camera

The FLIR thermal camera is used to monitor and measure the temperature of the welding material during the process. It allows for easy and accurate measurements of the temperature of the welding tool, support systems and welding material. The camera requires a direct line of sight of the object in question to measure its temperature. The camera allows for three different temperature ranges these

being -40 to +150 °C, +100 to +650 °C and +300 to +2000 °C. Table A.5 in Appendix A.5 lists the specifications of the FLIR camera. Figure 5.5 shows the infrared camera used for the measurement of the thermal data [89].

Figure 5.5 - FLIR T640 Thermal Camera

5.2 Friction Stir Welding Tool Design

The most important aspect of the FSW process, the welding pin and shoulder combination has the greatest influence on the resulting performance and structure of the welded joint. Commonly made of two different materials the pin and shoulder are required to withstand all process loads these being either mechanical or thermal loading [13]. Due to all the factors of the welding process the material being considered for the manufacture of the pin and shoulders should have the following attributes:

- Good wear resistance.
- High temperature strength and temper resistance.
- Extremely tough.
- Dimensional stability.

It has been shown that tool steel is suitable for applications in which Aluminium is the welded base material. Hot-worked tool steel is an extremely popular material being used by a number of researchers for the manufacture of their welding tools. This is because tool steel is easily available, heat treatable, machinability, high thermal fatigue and wear resistance. For this reason, AISI H13 hot-worked tool steel was selected for the shoulder base material. This grade of steel is commonly used in FSW Aluminium alloys [13].

In the pursuit of Airbus continuing to make advancements in the field of FSW they have concluded that MP-159 tool steel has been found to produce the most successful results in the trials conducted by them. This material is more than capable of withstanding the extreme bending moments and shearing loads caused by the welding process. For this reason, this material was used in the manufacture of the welding pin used in this research.

5.2.1 Experimental Trial Design of Shoulder of Friction Stir Welding Tool

AA6082-T6 had never been FSW at Wits before thus very little was known about the weld ability of the 3 mm thick material. For this reason, it was decided that the tool would be designed intuitively and experimentally. A key element to the design of the tool was the prolongation of the CNC machine. As expected, larger shoulder diameters produce high loadings on the motors of the machine. Three welding tool trials were conducted each with a different tool combination.

5.2.1.1 Trail 1 – Rudimentary Welding Tool

The basic welding tool was a single piece machined AISI H13 hot-worked tool steel component. This tool was designed by Prof. Polese to weld 1.6 mm Aluminium plates in the standard method. The tool had a pin diameter of 5 mm, pin length of 1.5 mm and a shoulder diameter of 20 mm. The decision was taken to extend the pin length to 2.8 mm by skimming down the shoulder until the required pin length. To improve material flow around the pin, three facets were machined into the tool. Figure 5.6 shows the pin and shoulder profile along with the general shape of the tool. To create the facets on the pin an A-shape profile had to be machined into the shoulder by consequence.

Figure 5.6 - Single Piece Friction Stir Welding Tool

The tool geometry summary has been listed in Table 5.1.

Table 5.1 - Single Piece Friction Stir Welding Tool Geometry Summary

Characteristic of Tool	Value
Pin diameter	5 mm
Pin length	2.8 mm
Pin profile	3 Face facetted
Shoulder outer diameter	20 mm
Shoulder profile	Flat with angled scribing
Shoulder to Pin Ratio	4:1

To investigate how this tool would compare against results obtained from literature a set of tensile samples were welded to so that the quality of the process could be assessed. Table 5.2 lists the parameters selected and the average tensile strength of the joints manufactured using this rudimentary tool [90]. Calculation of experimental uncertainty has been shown in Appendix F.

Table 5.2 - Parameter Set and Tensile Strength of Initial Friction Stir Welding Trial

RPM	Feed [mm/min]	Ultimate Tensile Strength [MPa]	Uncertainty [MPa]
630	50	186.86	6.22
630	100	202.50	6.36
630	250	220.23	6.53
1000	50	63.97	5.44
1000	100	110.96	5.66
1000	250	163.80	6.03
15000	50	28.15	5.36
15000	100	Weld stuck to backing bar	0
15000	250	Weld stuck to backing bar	0

Comparing these results to literature shows that similar trends of increasing feed rate improve the tensile strength of the joint but the experimental results were considerably less than that of other researchers. Figure 5.7 shows the comparison of the obtained results to literature. At all welding parameter combinations, this tool produced welds which were below that of other researchers. The same trends were observed in that increasing feed rate produced a stronger joint. This is due to superior material flow. Experimental data has been indicated by solid joining lines whilst literature results are represented by dashed lines.

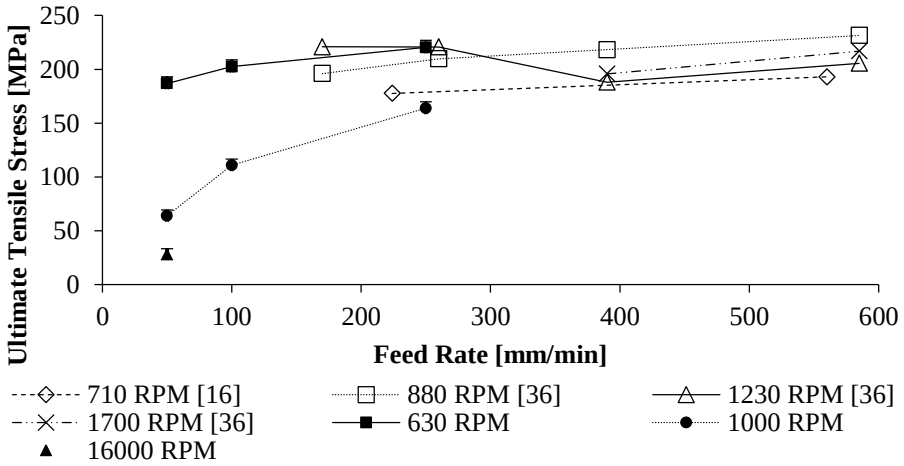

Figure 5.7 - Comparison of Tensile Strength of Experimental of Rudimental Welding Tool to Literature

The results presented in Figure 5.7 show that the rudimental tool is not sufficient for the production of sound FSW joints thus a superior tool is required.

5.2.1.2 Trial 2 – Facetted Pin and Spiralled Shoulder Combination Welding Tool

The tool was designed according to the recommendations of the Airbus-NAC project framework, with the initial design being credited to Correia. Tool aspects such as shoulder outer diameter, pin diameter and pin length were specified by this framework. The tool was designed to the specifications listed in Table 5.3.

Table 5.3 – Spiralled Pin and Shoulder Combination Friction Stir Welding Tool Geometry Summary

Characteristic of Tool	Value
Pin diameter	5mm with a constant taper to 4 mm at the tip
Pin length	2 mm from shoulder to pin end
Pin profile	3 Face facetted
Shoulder outer diameter	30 mm
Shoulder profile	Flat with clockwise + anti-clockwise spiral
Shoulder to Pin Ratio	6:1

Due to the inability of the MAHO MH-C 700 CNC machine being unable to perform any tool tilting during the welding process, the shoulder had to be spiralled. The welding tool was designed with a flat spiral shoulder according to the recommendations of [11] and [13].

In order to manufacture the shoulder, a coordinate system of points was required to be derived in order to CNC mill the feature into the shoulder. It was decided that smooth, uniform scrolls, extending from the centre of the shoulder out to the edge in a clockwise and anticlockwise directions would tend to draw material towards the pin. To achieve this a logarithmic spiral was selected, the equations used to derive the points are shown below [21].

The equation of a logarithmic spiral is given by equation 5.1 [91]:

$$r = Ae^{B\theta} \tag{5.1}$$

The logarithmic spiral can be represented in Cartesian coordinates by the following equations:

$$x = r\cos\theta \tag{5.2}$$

$$y = r\sin\theta \tag{5.3}$$

Thus, the spiral points can be produced by combining the above equations:

$$x = Ae^{B\theta} \cos\theta \tag{5.4}$$

$$y = Ae^{B\theta} \sin\theta \tag{5.5}$$

Assigning the values of *A = 15* (half the shoulder diameter), *B = 0* and varying θ from 0° to 360° in increments of 10° a range of coordinates were obtained. Figure 5.8 shows the coordinate points of the two spirals with the shoulder and pin diameters represented as well.

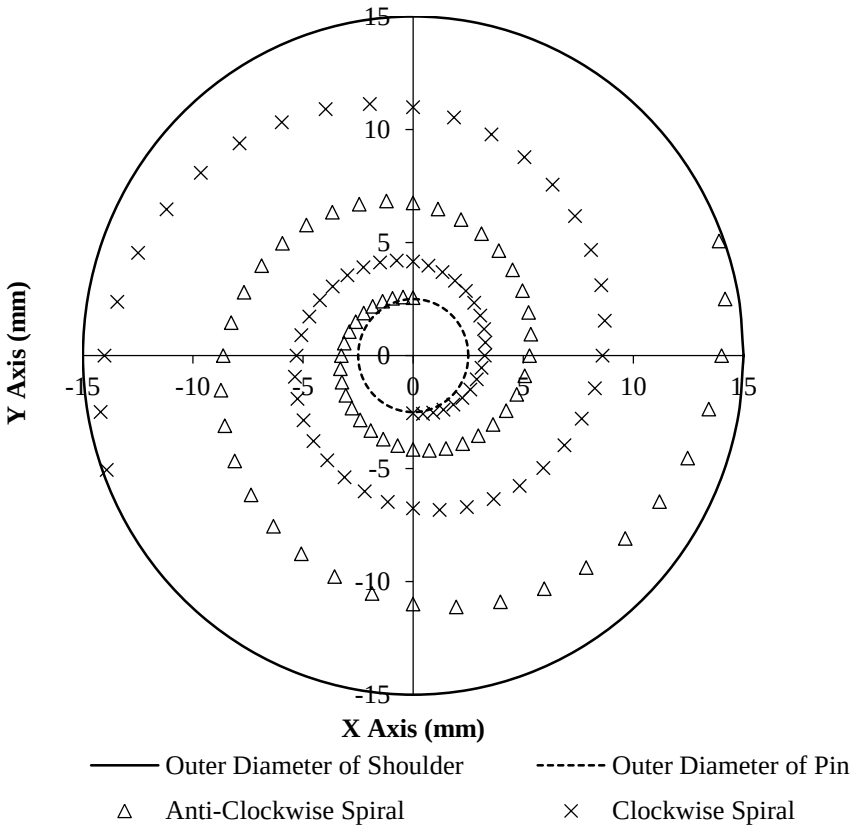

Figure 5.8 - Plotted Representation of Spiralled Shoulder

Each spiral was machined with a width and depth of 0.4 mm. The shoulder and pin combination can be seen in Figure 5.9.

Figure 5.9 – Facetted Pin and Spiralled Shoulder Combination Friction Stir Welding Tool

5.2.1.3 Trial 3 – Facetted Pin and Reduced Diameter Spiralled Shoulder Combination Welding Tool

During welding trail 2, using the facetted pin with a 30 mm diameter spiralled shoulder extremely large welding forces were recorded. The MAHO MH-C 700 CNC machine reached its maximum current draw and motor loading. It was expected that if further welding trials had been completed using this 30 mm diameter shoulder the CNC would experience mechanical failure. Figure 5.10 shows the maximum normal forces produced during welding with the two variations in tools described above. Although the welding parameters were not the same there is a clear shift in forces when looking at welds produced with an RPM of 1000. These high forces coupled with the high motor loading were linked directly to the size of the tool and with little influence by the parameters used during welding.

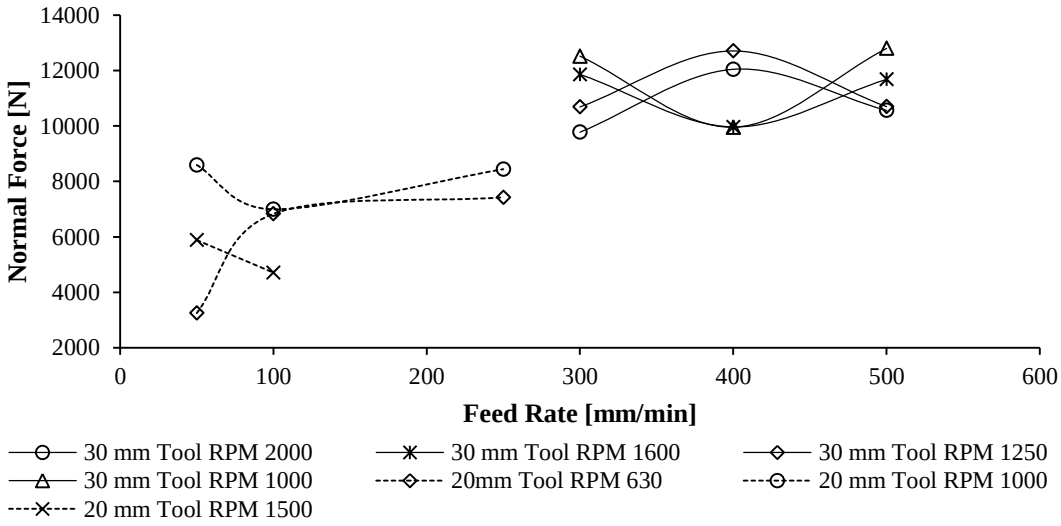

Figure 5.10 - Welding Forces Experience during Friction Stir Welding Trials

To avoid the high motor loading the 30 mm spiralled shoulder was reduced to an outer diameter of 20 mm. It was expected that a smaller shoulder would exert the lower force on the welding machine whilst still being able to produce acceptable FSW.

Improved material flow was seen with the spiralled reduced diameter shoulder over the single piece welding tool. Due to the improvements in reducing the welding forces and better material movement, the final tool design as described in Table 5.4 was used in the completion of the remainder of welded samples described in this research. Figure 5.11 shows the facetted pin and 20 mm diameter spiralled shoulder combination welding tool, used from here on out.

Table 5.4 - Finalised Friction Stir Welding Tool Geometry Summary

Characteristic of Tool	Value
Pin diameter	5mm with a constant taper to 4 mm at the tip
Pin length	2 mm from shoulder to pin end
Pin profile	3 Face facetted
Shoulder outer diameter	20 mm
Shoulder profile	Flat with clockwise + anti-clockwise spiral
Pin to Shoulder ratio	4:1

Figure 5.11 - Facetted Pin and Reduced Diameter Spiralled Shoulder Combination Friction Stir Welding Tool

5.2.2 Pin Design

A tapered cylindrical, three facetted pin was designed and manufactured to be used in combination with the tool shoulders described in sections 5.2.1.3. The tri-flat pin was designed with a diameter of 5

mm tapering to 4 mm, this tapered, small diameter reduced the traverse forces experienced by the pin. The profiling of the pin was selected in an attempt to increase the surface area of the pin in frictional contact with the material being stirred. This profile provides significant stirring effects and disperses residual oxides in the weld [21].

The pin was manufactured from MP-159 tool steel, this was suggested by the Airbus project supervisor. In order for the pin to be at the required strength for welding, it had to be heat treated according to a fairly complicated heat treatment cycle. The heat treatment was generously completed by Pierre Rossouw at The Centre of Scientific and Industrial Research (CSIR). Engineering drawing B1 and B2 of the pin and shoulder respectively can be found in Appendix B – Engineering Drawings.

5.3 Laser Shock Peening Equipment

The following section provides information on the major equipment used in the LSP treatment of all samples within this research. All equipment within this section can be located at The National Laser Centre (NLC) of the Centre of Scientific and Industrial Research.

5.3.1 Quanta Ray Pro-270 Nd:Yag Laser

The Pro-270 Nd:Yag laser is a pulse, oscillator/amplifier system which has a beam locking assembly. The dual pump chamber assembly allows for higher energies to be achieved [92]. The full assembly of the laser system used in this research comprises of the Pro-270 laser, the Pro-series power supply and analogue controller. Figure 5.12 provides the setup of the laser system used. Appendix A.2 contains Table A.3 which lists the detailed specifications of the laser.

Figure 5.12 – Quanta Ray Pro- 270 Nd:Yag Laser

5.3.2 Coherent Field Max II – Top Laser Power/Energy Meter

The Field Max II Laser Power Energy Meter was used to measure and analyse the laser power and energy whilst setting up and during continuous testing. The meter was connected to the J-10GE-LE Energy Max sensor, in which the laser was directly fired into the germanium photodiode, instantly providing a reading of the beams wavelength, power and energy. The full specifications of this meter and sensor have been placed in Appendix A.5 and A.6 in Table A.6 and Table A.7. Figure 5.13 shows the diode and meter as used in the LSP set up.

Figure 5.13 - Coherent Field Max II - Top Laser Power/Energy Meter

5.3.3 OPHIR Photonics Spiricon Silicon CCD Camera

The Spiricon SP620U 190 – 1100 nm USB Silicon CCD camera is a high resolution beam profiler. By firing a single shot of the laser through MD filters and then into camera one is able to capture the spatial intensity of the laser leading to the determination of the quality, intensity and dimension of the beam. Figure 5.14 shows the CCD camera as used to gain the measurement of the beam size and profile [93].

Figure 5.14 – OPHIR Photonics Spiricon Silicon CCD Camera

Beam analysis was completed using BeamGage which is a PC based laser analysing program. This program is used to represent the beam profile in both 2D and 3D, calculate the diameter of the beam and to determine the specific beam type (Gaussian or top hat). Figure 5.15 provides an example of the type of analysis achievable using this setup. Image A is the 2D display of the power intensity and geometry of the beam profile. Image B is the Beam display in 3D which allows the user to determine the type of beam captured. The software calculates the beam diameter according to the ISO D4 Sigma method which calculates the second moment diameter for a circular beam.

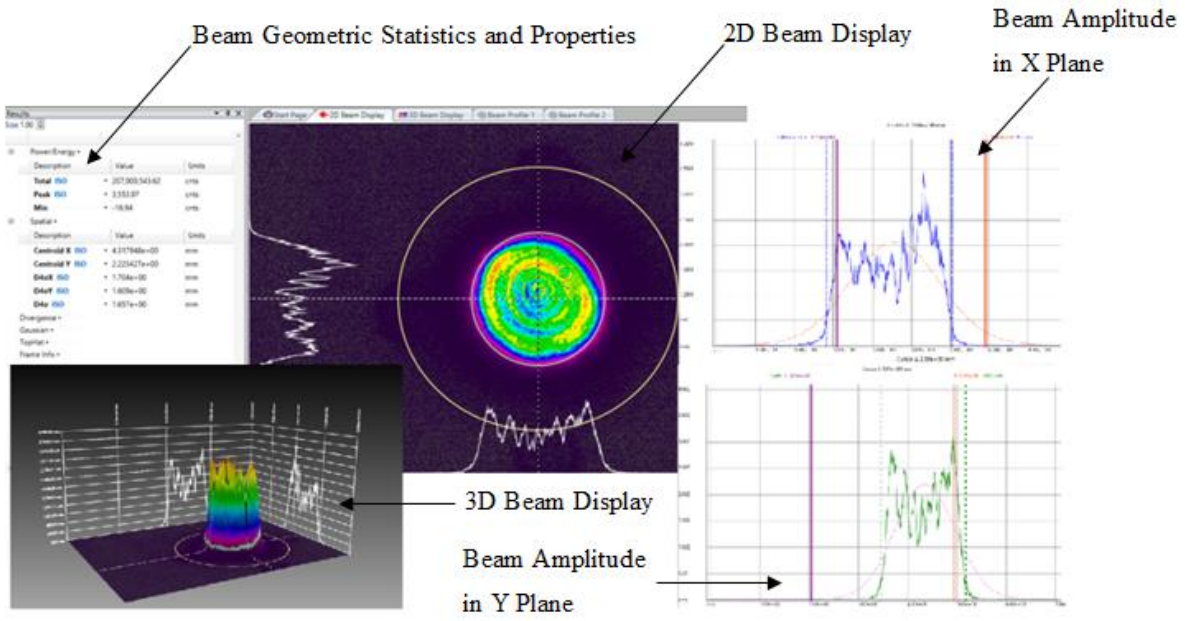

Figure 5.15 - Example of the Type of Analysis Achieved with BeamGage

5.3.4 X-Y Automated Position Controller, Water System and Air Knife

The X-Y position controller is a two axis automated support apparatus to which all samples are mounted to during processing. The mounting stage is controlled by two stepper motors which are linked to a standard CNC machining code. The CNC program allows the user to directly input the number of steps and the speed at which the stage must move, these two inputs are calculated using the equations 5.6 and 5.7.

$$x_{steps} = \frac{10}{\sqrt{S}} \tag{5.6}$$

$$v_{steps} = x_{steps} \times 600 \tag{5.7}$$

Table 5.5 lists the steps and speeds used for the respective samples manufactured under the various coverage's used throughout the LSP testing. The values listed were fed indirectly to the CNC program.

Table 5.5 - Steps and Speeds for Respective Coverage's Used

Coverage [spots/cm^2]	Steps [mm/spot]	Speed (mm/min)
50	1.414	848.528
100	1.000	600.000
250	0.632	379.473
500	0.447	268.328
1000	0.316	189.737
2000	0.224	134.164

The distilled water layer required to pass over the sample whilst peening was applied by a laminar flow nozzle. The stream of water is applied directly to the surface of the sample. A layer of laminar water of a few millimetres thick flows over the sample. Monitoring and determining the effects of the water layer thickness, water temperature, quality and type fall out of the scope of this research, reference should be made to the work completed by Glaser [62]. Figure 5.16 provides a closer view of the nozzle system.

Figure 5.16 - Close View of Water Nozzle Applicator

A recirculation pump which was contained within a water sump, pumps the distilled water through the system at a set flow rate. The flow rate of the water stream was controlled by setting the valve to a point which leads to an appropriate flow rate. The adjustability of the nozzle allowed for laminar flow to be maintained over the full sample whilst peening. The water flows off the sample into the Perspex collector and back into the sump. Figure 5.17 provides a schematic layout of the water delivery system.

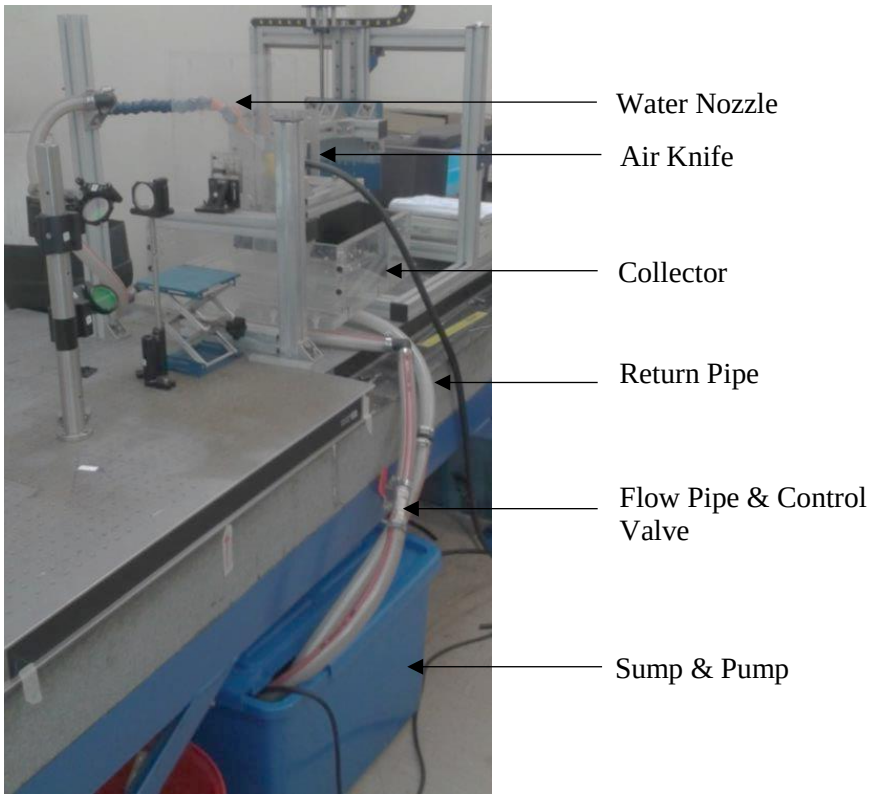

Figure 5.17 - Schematic Layout of Water Applicator System

Continuous modifications to the LSP set up occurred during the course of this research. Initially, a rudimentary air knife was used to prevent splashes of water, which occurred from the laser processing, interfering with the beam and from collecting on the optics. This knife was manufactured by squashing the end of a brass tube to form an air nozzle which was connected to a ±6 bar air pressure line. The nozzle was then bolted to a piece of plastic which had a hole in which that laser beam passed freely through, this configuration can be seen in Figure 5.18.

Figure 5.18 - Rudimentary Air Knife

To improve the application of the required high pressure air jet a WindJet AA727 nozzle was used to manufacture a more effective knife. This type of nozzle provided an efficient, controlled and uniform spray distribution in a flat fan pattern. Figure 5.19 shows the design of the nozzle and how it was added to remaining LSP apparatus.

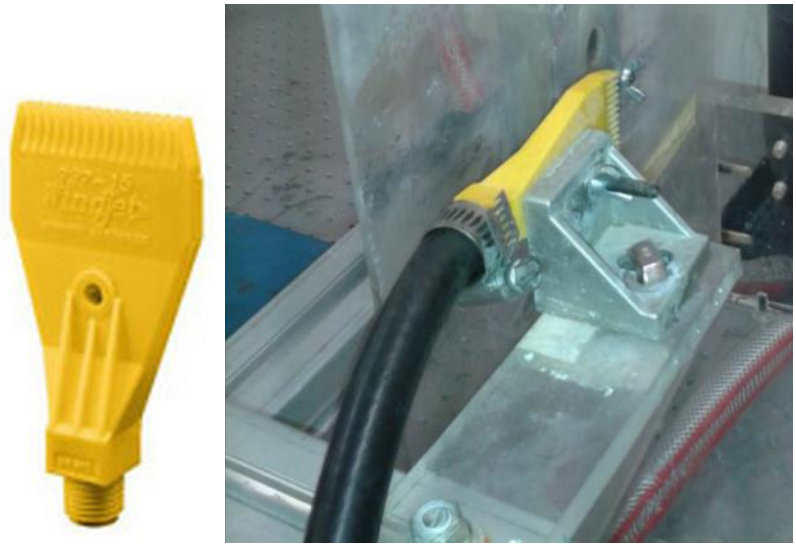

Figure 5.19- WindJet AA727 Nozzle and Integration into Laser Shock Peening Apparatus

The reasoning behind this alteration was due to the distortion of the beam profile as the beam passed through the rudimentary knife. The distortion can be seen in Figure 5.20 were the profile in image A shows a wave pattern caused by the air knife influencing the profile whilst image B to shows no sign of air influence on the profile of the beam as it is passing through the new commercial knife. Image C shows the profile with no air on. It can be concluded by examining images B and C that the air knife has no effect on the beam profile which is what is required of high quality LSP processing.

Image A

Image B

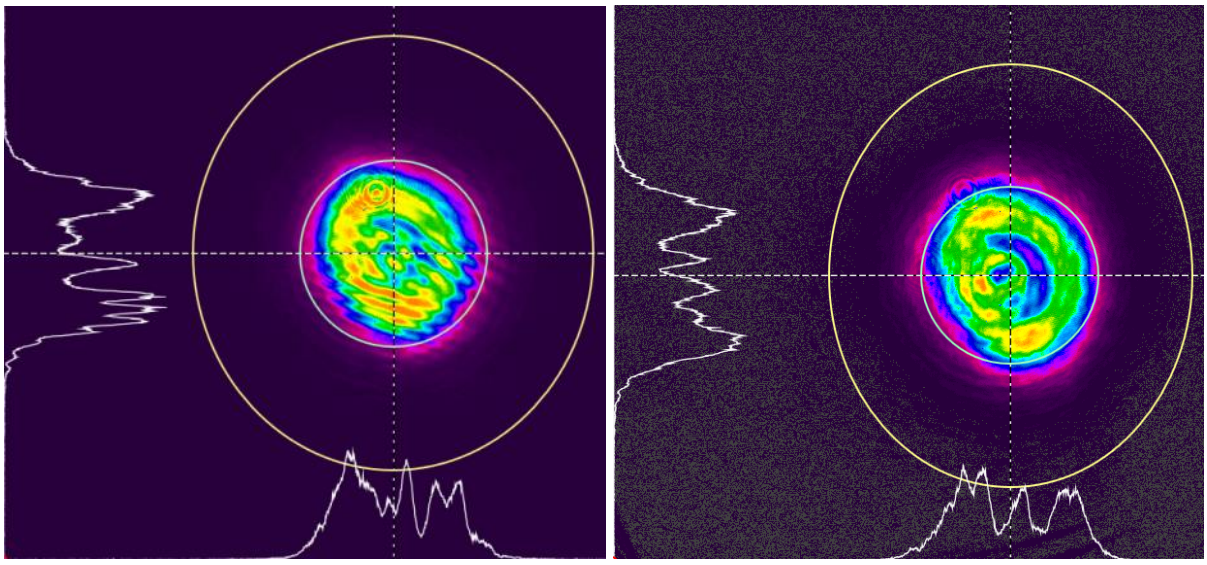

Image C

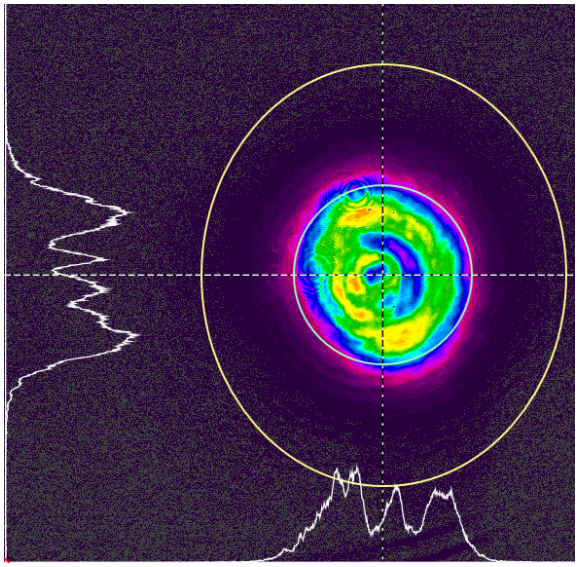

Figure 5.20 - Beam Profiles once passed through two types of Air Knives

To show that the modifications to the apparatus did not have a major effect on the end processing results Almen strips were manufactured with same laser properties and coverage to determine the deflection of the strip with the two different air knives described above. The uncertainty of the measurement was taken as ±0.005 mm as this was half of the smallest increment that could be measured by the dial gauge. Figure 5.21 shows the maximum deflections of the strips manufactured with varying air knives and the following laser parameters:

- Power Intensity: 2 GW/cm^2
- Spot Size: 1.5 mm

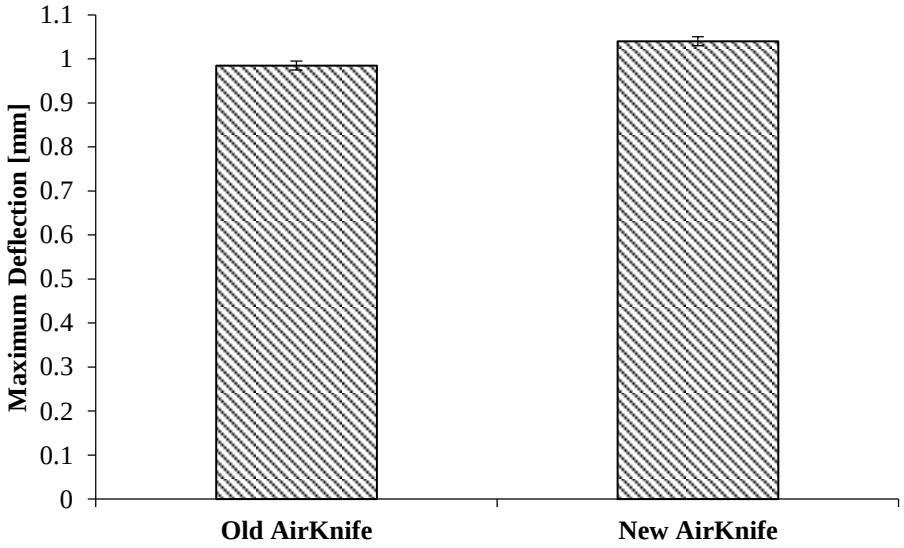

Figure 5.21 – Almen Strip Testing with Varying Designs of Air Knives

A maximum deflection for the old and new airknife was 0.98 mm and 1.06 mm, this was a percentage difference of 5.3%. As this deviation was not substantially large it can be stated that the new air knife did not drastically affect the results. The variation in laser energy per pulse was more likely the cause of the discrepancy.

5.4 General Testing Equipment

The following section provides information on the major equipment used in the preparation and testing of the variety of samples manufactured in this research.

5.4.1 Mounting

A variety of samples were sectioned to be cold mounted in Clarocit powder (methyl methacrylate) resin and Clarocit solution. The solutions are mixed in a 2:1 ratio of powder to resin by weight. The specimens were sectioned to fit within a 30 mm diameter mounting cup. Support clips were put on each side of the samples. Figure 5.22 shows an example of samples which have been mounted and need to undergo surface preparation.

Figure 5.22 - Cold Mounted Samples

5.4.2 Surface Grinding

Grinding and polishing of the mounted samples was completed using the Struers Labopol-21 surface grinding and polishing machine. This equipment is located in the North West Engineering building at the University of the Witwatersrand. This machine makes use of two rotating surfaces which has either grinding or polishing discs attached to prepare the surface of the mounted sample. Figure 5.23 provides the schematic of the LaboPol-21 machine, this machine has a fixed rotation of 250 rpm.

Figure 5.23 - Stuers Labopol-21 Surface Grinding and Polishing Machine

Table 5.6 lists the procedure followed in surface preparation for the Aluminium samples.

Table 5.6 - Outline of Surface Grinding and Polishing of Aluminium Samples

Step	Stage 1 Grinding	Stage 2 Grinding	Stage 3 Grinding	Stage 1 Polishing	Initial Polishing	Final Polishing
Surface	SiC-Paper 320#	SiC-Paper 500#	SiC-Paper 1000#	MD-Largo	MD-Mol	MD-Chem
Suspension	-	-	-	DiaPro Allegro/Largo (9µm)	DiaProMol (3µm)	OP-S (0.5 µm)
Speed [rpm]	250	250	250	250	250	250
Lubricant	Water	Water	Water	-	-	-
Force	120 N	120 N	120 N	150 N	150 N	100 N
Time	1 min	1 min	1 min	5 min	4 min	1-2 min

After undergoing this process a near mirror finish should be achieved in the mounted samples.

5.4.3 Chemical Etching

Two reagents were used to chemically reveal the microstructure of the AA6082-T6 joints. By applying these chemicals directly to the surface of the sample one is capable of revealing the grain structure and the size of the various regions of the welds. The sample preparation was completed in accordance with ASTM E407 standards. The reagents used have been listed below:

- 50/50 mixture of the following two compounds:

- Compound 1: 19 parts deionised water (H_2O) 1 part Hydrofluoric Acid (HF)
- Compound 2: 18 parts deionised water (H_2O) 2 parts Sulphuric Acid (H_2SO_4)

5.4.4 Microstructural Characterisation

The Nikon Stereoscopic Microscope SMZ1500 was used to view the microstructure of the etched samples, to view the welding tool at high magnifications and take high magnification images. This equipment is located in t-he North West Engineering building at the University of the Witwatersrand. The microscope has a magnification range from times 3.75 to times 540 with a zoom of times 15. A Motic Moticam 2500 camera was used to record the images. Figure 5.24 shows the microscope and camera in the state which was used for this research.

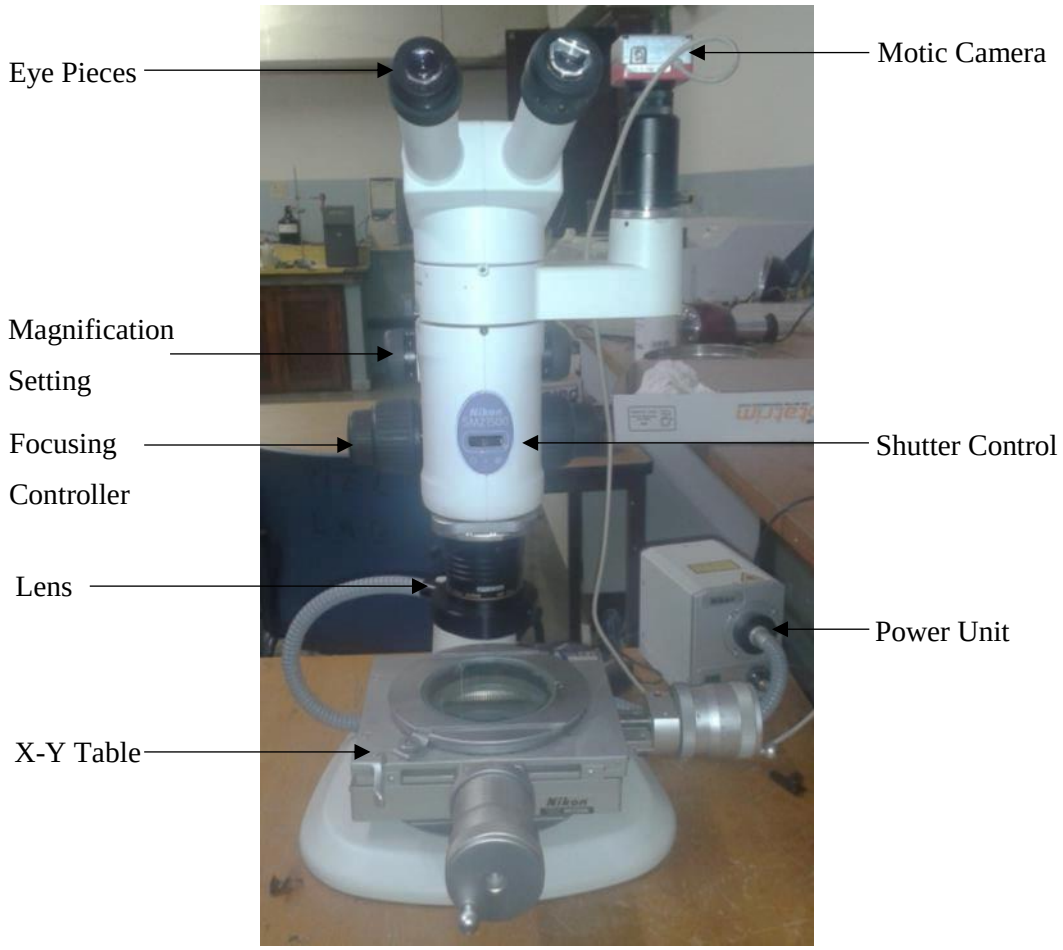

Figure 5.24 - Nikon SMZ1500 Stereoscopic Microscope and Motic Camera

Additionally, a Leica DFC 490C light microscope using polarized light was used to show the etched microstructure. Capable of time 500 magnifications this microscope was used to measure the relative regions of the joints. Figure 5.25 shows the microscope used.

Figure 5.25 - Leica DFC 490C Light Microscope

5.4.5 Micro-Hardness Test

Micro-hardness testing was completed on the Matsuzawa Seiki CO. Vickers micro-hardness tester. This equipment is located in the National Laser Centre at the CSIR. The tests were conducted according to ASTM E384 with a load of 100 gf held for a dwell time of 10 seconds. Figure 5.26 shows the hardness tester used for these measurements.

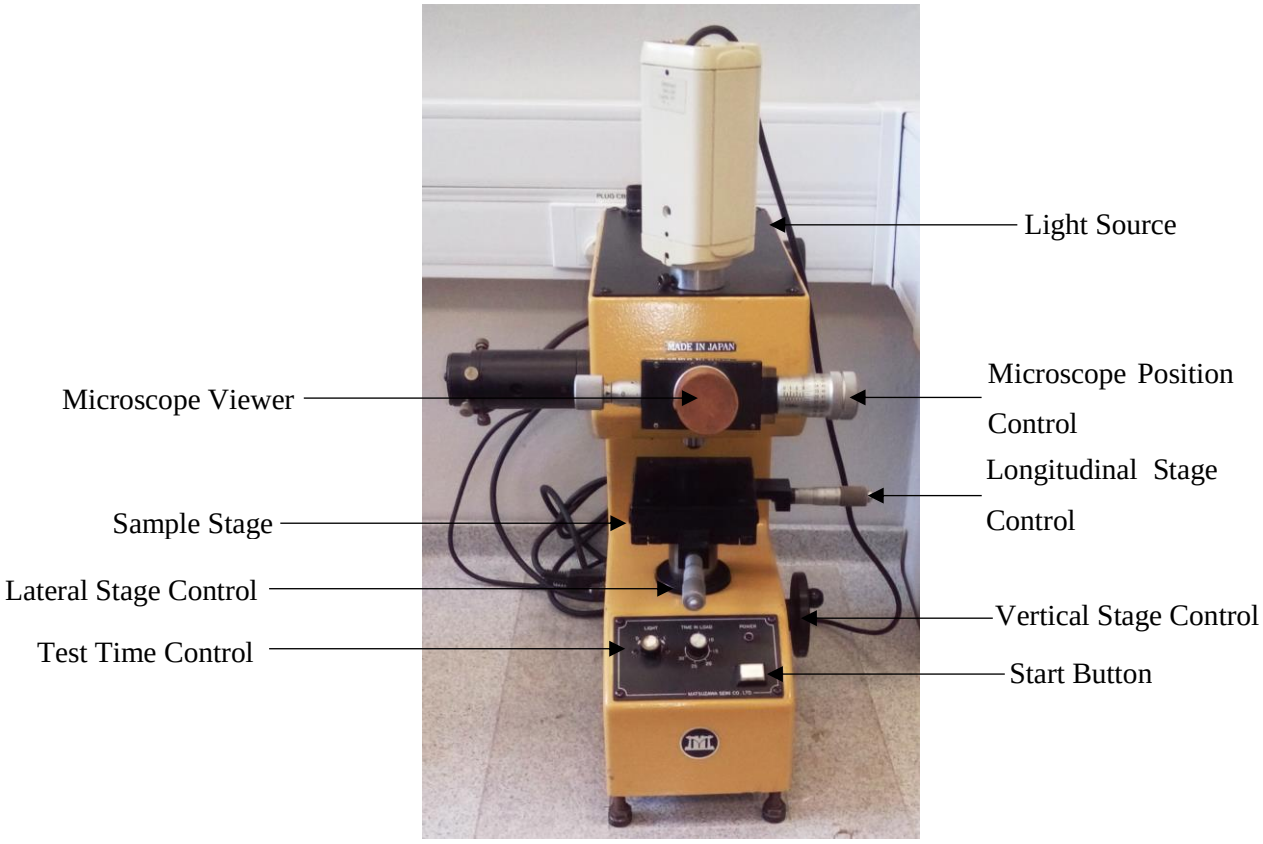

Figure 5.26 - Matsuzawa Seiki CO. Vickers Micro-Hardness Tester

Each of the diagonals of the diamond indentations was measured, an example of the measurements is shown in Figure 5.27.

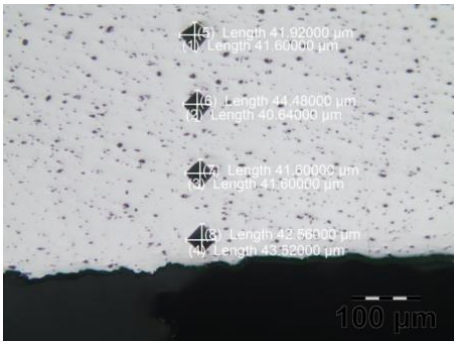

Figure 5.27 - Example of Measurements of Micro-Hardness Diamond Indentation Diagonals

The hardness was calculated using the equation 5.8.

$$HV = \frac{1854\, F_{indentation}}{L_{diagonal1} \times L_{diagonal2}} \tag{5.8}$$

5.4.5.1 Micro-Hardness Sample Calculation

Using the measurements of the diagonals at the first point nearest the crown surface in Figure 5.27 the micro-hardness was calculated as followed.

$$HV = \frac{1854\, F_{indentation}}{L_{diagonal1} \times L_{diagonal2}}$$

$$HV = \frac{1854\ (100)}{42.56 \times 43.52}$$

$$HV = 100.10$$

5.4.6 Scanning Electron Microscopy

The fracture surfaces of various samples were examined using the Zeiss LEO 1525 Field Emission Gun Scanning Electron Microscope. This equipment is located in the Richard Ward building at the University of the Witwatersrand. The secondary electron mode was used to record images of the topography of the fracture surfaces. Figure 5.28 shows the scanning electron microscope used in this research.

Figure 5.28 - Zeiss LEO 1525 Field Emission Gun Scanning Electron Microscope

5.4.7 Static Tensile and Three Point Bending Testing

All static and bending tests were performed on the Shimadzu AG-IC series Ag-20kN/50kNICD electric universal tensile tester. This equipment is located in the North West Engineering building at the University of the Witwatersrand. The attached load cell had a capacity loading of 20 kN with an accuracy of ±1%. The cross head speed ranged between 0.5 and 500 mm/min. Trapezium 2 software was used as the controller software for the running of the machine. Figure 5.29 shows the Shimadzu set up for a tensile test.

Figure 5.29 - Shimadzu AG-IC series Ag-20kN/50kNICD Electric Universal Tensile Tester

By replacing the tensile grips with the appropriate equipment a three-point bending tests can be completed. This form of testing is one of the most popular destructive welded joint tests used in industry as it easily indicates the presence of weld defects. Figure 5.30 provides the schematic of the equipment used in the running of these tests.

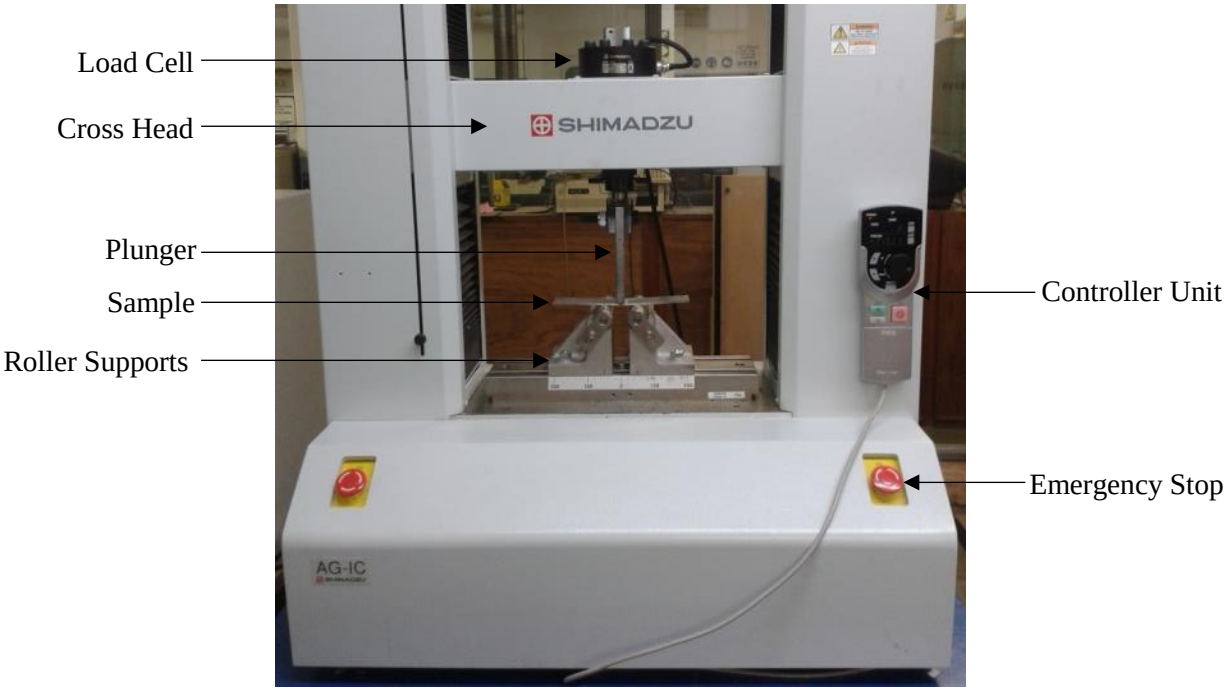

Figure 5.30 – Shimadzu set up for Three Point Bending Tests

The samples tested in these two manners were manufactured out of single sheet welds. A welded plate of approximately 240 mm in length produced three tensile specimens and two three-point bending specimens. Figure 5.31 provides the layout of samples locations along a welded sheet. All tensile and bending samples location were taken in an alternating position. A minimum of 5 mm had to be left on each edge of the samples to allow for suitable CNC milling of the samples.

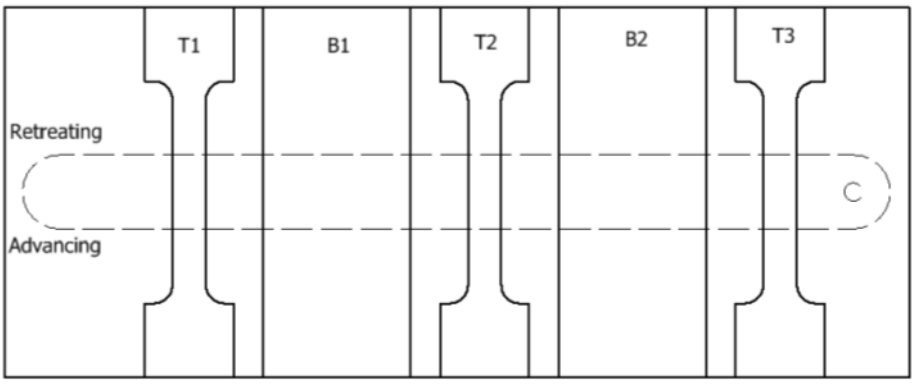

Figure 5.31 - Schematic of Sample Layout for Tensile and Bending Tests

Tensile specimens were load axially to the point of failure. Data logged by the Shimadzu gave applied force and stroke of the cross head of the testing machine. From this information the engineering stress and strain were calculated, these have been given in equation 5.9 and 5.10.

$$\sigma_{engineering} = \frac{F_{applied}}{A_0} \tag{5.9}$$

$$\varepsilon_{engineering} = \frac{\Delta L}{L_0} \tag{5.10}$$

Using these two equations at each interval of recorded data leads to the possibility of creating a standard stress-strain curve. From the curve one is capable of obtaining the Ultimate Tensile Strength (UTS), yield strength and Young's Modulus. Figure 5.32 shows an example of the stress strain curves produced for the base material used in this research.

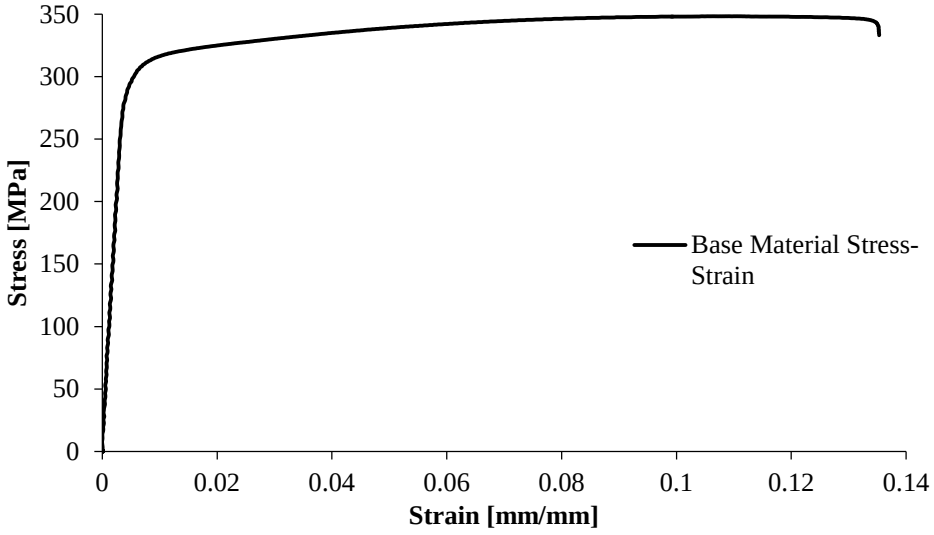

Figure 5.32 - Experimental Stress Strain Curve of Aluminium AA AA6082-T6

The UTS of the tensile samples was calculated according to equation 5.11. It was assumed that area of the sample remained constant at force above the yield strength, this is not true but allowed for easy computation.

$$\sigma_{UTS} = \frac{F_{\max applied}}{A_0} \tag{5.11}$$

The yield strength of the samples was calculated using the 0.2% offset strain method. A linear line is fitted with an equal gradient of that of the linear section of the experimental stress strain curve. The curve is then offset by 0.2% on the x-axis. Figure 5.33 provides an example of the yield strength calculation of the base material. From this experiment, the yield strength of the base material was found to be 301 MPa.

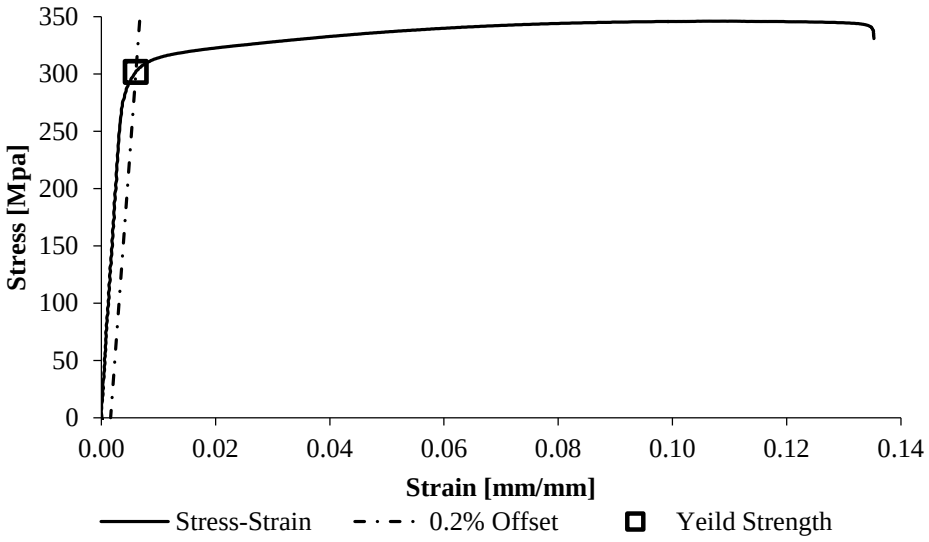

Figure 5.33 - 0.2% Yield Strength Calculation

5.4.7.1 Tensile Stress Sample Calculation

This section provides the opportunity to complete a full sample calculation of the tensile stress measurement, demonstrating the technique followed throughout to obtain the remaining results which will be demonstrated in the coming sections. This sample calculation has been completed using the data provided in Figure 5.32.

The gauge area of the reduced section of the tensile sample was calculated accordingly.

$$A_{tensile} = T \times L$$

$$A_{tensile} = 3 \times 12.5$$

$$A_{tensile} = 37.5\ mm^2$$

This data will be used in the provided sample calculations. Poission's effects were neglected during the calculations of the tensile stress within the sample. All tensile tests were run at a crosshead speed of 10 mm/min.

The following calculations selected to point out of the linear region of the stress-strain curve. The corresponding output data from the Shimadzu during a standard tensile test for two specific positions in has been listed in Table 5.7.

Table 5.7 - Output Data for a Single Point from a Tensile Test

Location in test	Force (N)	Stroke (mm)
Linear region	5600	1.933
Maximum applied force	13 229.38	11.425

The stress within the tensile sample at that exact point was calculated according to equation 5.9.

$$\sigma_{engineering} = \frac{F_{applied}}{A_0}$$

$$\sigma_{engineering} = \frac{5600}{(3 \times 12.5)}$$

$$\sigma_{engineering} = 149.33\ MPa$$

The gauge length was set to be 75 mm. Using equation 5.10 the strain in the component was calculated.

$$\varepsilon_{engineering} = \frac{\Delta L}{L_0}$$

$$\varepsilon_{engineering} = \frac{((1.933 + 75) - 75)}{75}$$

$$\varepsilon_{engineering} = 0.02577\ mm/mm$$

The ultimate tensile strength of the sample was calculated at the application of the maximum force. Using this data listed in Table 5.7 the maximum tensile strength was calculated using equation 5.11.

$$\sigma_{UTS} = \frac{F_{\max applied}}{A_0}$$

$$\sigma_{UTS} = \frac{13229.38}{(3 \times 12.5)}$$

$$\sigma_{UTS} = 352.783\ MPa$$

The 0.2% offset method was used to obtain the yield strength of the component. A line with an equal gradient to the linear section of the stress-strain curve was produced. The intercept of the 0.2% line and the actual stress-strain curve resulted in the yield strength. This was done purely graphically thus no sample calculations can be provided. For the example being used in this section, the 0.2% yield strength was determined to be 303 MPa.

5.4.8 Residual Stress Measurements

The residual stress analysis performed in this research was conducted at the facilities at Elettra Synchrotron, described in section 2.9.2. The measurements were conducted on the Materials Characterisation by X-rays diffraction (MCX). Energy levels of the beamline varied between 10 to 18 keV. The size of the beam at the sample was approximately 10 by 1 mm^2 to 0.3 by 0.3 mm^2, with a photon flux of 10^{11} photons per second.

The welded samples were held on an extremely sophisticated Eulerian cradle. The Huber goniometer provides a 2-theta precision greater than 0.0001°. The sample holder was capable of supporting sample sizes of up to 250 by 150 mm with a 1 micron position resolution in all three principle axis. The maximum sample weight of 5 kg can be supported. Figure 5.34 shows the general arrangement of the beamline equipment.

Figure 5.34 - Diffractometer of the Materials Characterisation by X-ray Work Station at Elettra

The items shown in Figure 5.34 are all housed in the experimental hutch of the beamline. Controlled access to the hutch is required as it is imperative to ensure that no person can be close to the beam exit during operation. A key control/shut off system has been employed at the facility to ensure that no operator may be exposed to harmful X-rays. The system is controlled externally at the controller station situated outside of the hutch. The Portable Instrument Control Interpreter (PINCER) controller system software was used to operate and set the measurements.

The procedure and technique used to measure the residual stress in a component was developed by the Elettra MCX beamline staff, Dr Lausi and Dr Plaiser. These members of staff were responsible for the readiness of the MCX station for residual stress measurements and for the changing of energy.

The controlling software records the intensity counts per second at the corresponding 2θ position. By measuring the intensities through a sweep of angles one is capable of determining the peak location, denoted by X_c, defines the angle at which the diffraction peak occurs. There is a wide range of methods for determining the peaks but previous research has shown that the most suited mathematic function for this purpose is the Lorentzian function. Figure 5.35 provides an example of the running plot which is produced during the measure of the residual stress at a single point, the data presented in

the figure corresponds to the residual stress measurement of sample 5mm from the centre of the weld on the advancing side with a beam energy of 15keV in the Φ=0 direction.

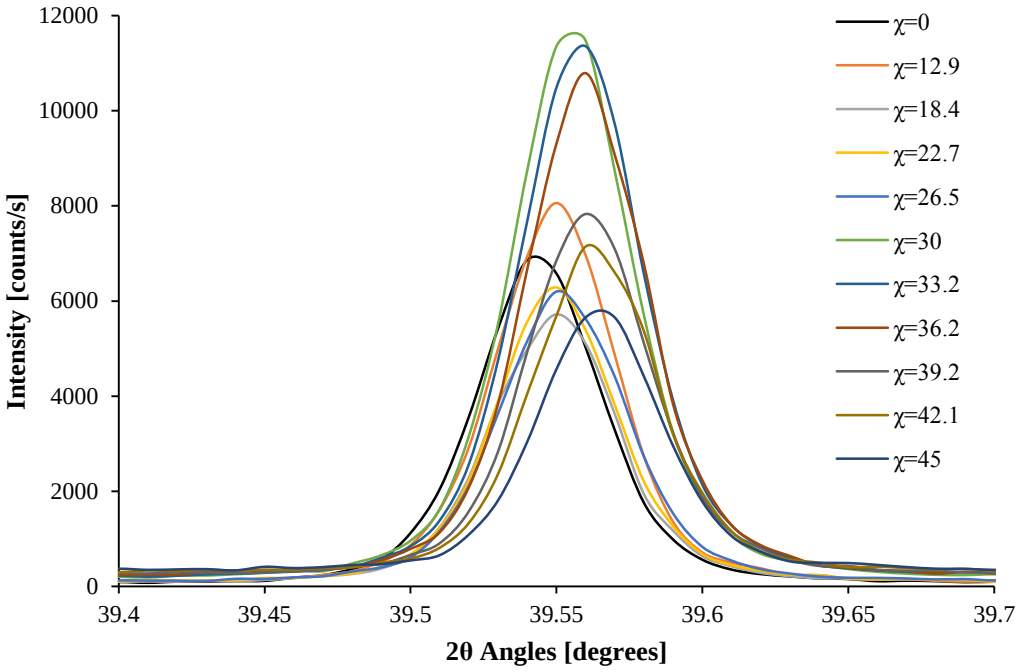

Figure 5.35 - Lorentzian Peak fitting to the Data obtained in Single Run

The location of the peak needs to be resolved extremely accurately as the peak shifts occur over a very small range, as shown in the Figure 5.35. Previous researchers at the University of the Witwatersrand have compared multiple methods in the determination of residual stress from the peak shifts of the XRD data. The preferred method is based on the error in the locations of the diffraction peaks (X_{ce}) [86]. The Lorentz fitting function has been found to produce the least amount of error when applying the X_{ce} method. The calculation entails the resolving of the peak locations plotted in Figure 5.35. The error in peak position and the coefficient of determination (R^2) is determined using an advanced statistical processing program known as OriginPro 8.5. Inter planar spacing (d) can then be determined according to equation 2.13. The equation has now been presented in the rearranged format needed in equation 5.12.

$$d_{hkl} = \frac{n\lambda}{2\sin\theta} \tag{5.12}$$

Where the wavelength is calculated using the energy level of the beam and Plank's law. In equation 5.13 Plank's constant (h) and the speed of light (c) carry their usual values.

$$\lambda = \frac{hc}{E} \tag{5.13}$$

Plotting the inter planar spacing against the $\sin^2(\psi)$, as shown in Figure 2.88, allows for the slope of the linear line of best fit to be determined, the slope is represented as m. Using this result and equation 2.16 the residual stress can be determined. Equation 2.16 has been repeated below for completeness shake.

$$\sigma_{\phi} = \left(\frac{E_{young's}}{1+\nu}\right) m \tag{2.16}$$

5.4.8.1 Residual Stress Sample Calculation

This section provides the opportunity to complete a full sample calculation of the residual stress measurement, demonstrating the technique followed throughout to obtain the remaining results which will be demonstrated in the coming sections.

The sample calculation will be conducted for the data represented in Figure 5.35 corresponding to the residual stress measurement of sample 5mm from the centre of the weld on the advancing side with a beam energy of 15keV in the Φ=0 direction. The wavelength was calculated according to the energy of the beam, 1keV is equivalent to $1.60217657 \times 10^{-16}$ Joules.

$$\lambda = \frac{hc}{E}$$

$$\lambda = \frac{6.0626896 \times 10^{-34} \cdot 299792458}{15 \cdot 1.60217657 \times 10^{-16}}$$

$$\lambda = 0.826561 \times 10^{-10}\, m$$

Table 5.8 lists the calculated data from the Lorentz function produced from OriginPro at the various χ angles.

Columns 2 to 4 are outputs of OriginPro. Column 5 is determined by inputting the χ angle into the $\sin^2(\chi)$ equation. Inter planar spacing for a χ angle of 0° has been completed as a sample calculation.

$$d_{hkl} = \frac{n\lambda}{2\sin\theta}$$

$$d_{hkl} = \frac{1 \cdot 0.826561}{2\sin(19.772)}$$

$$d_{hkl} = 1.2217 \times 10^{-10} \mu m$$

Table 5.8 - Computed Data for a Single Residual Stress Measurement

χ angle [Degrees]	Peak position [Degrees]	Error of peak fit	R^2 of fit	$Sin^2(\chi)$ [Degrees]	Inter planner Spacing [µm]
0.000	19.772	1.53E-04	0.9881	0.000	1.2217
12.921	19.775	1.55E-04	0.9872	0.050	1.2215
18.435	19.775	1.75E-04	0.9849	0.100	1.2216
22.786	19.775	1.47E-04	0.9886	0.150	1.2216
26.565	19.776	1.68E-04	0.9865	0.200	1.2215
30.000	19.778	1.40E-04	0.9895	0.250	1.2214
33.211	19.779	1.55E-04	0.9879	0.300	1.2213
36.271	19.780	1.54E-04	0.9877	0.350	1.2212
39.232	19.780	1.59E-04	0.9874	0.400	1.2212
42.130	19.782	1.65E-04	0.9863	0.450	1.2211
45.000	19.782	1.59E-04	0.9871	0.500	1.2211
47.870	19.783	1.56E-04	0.9876	0.550	1.2211

Completing this procedure for all twelve points one was able to produce Figure 5.36.

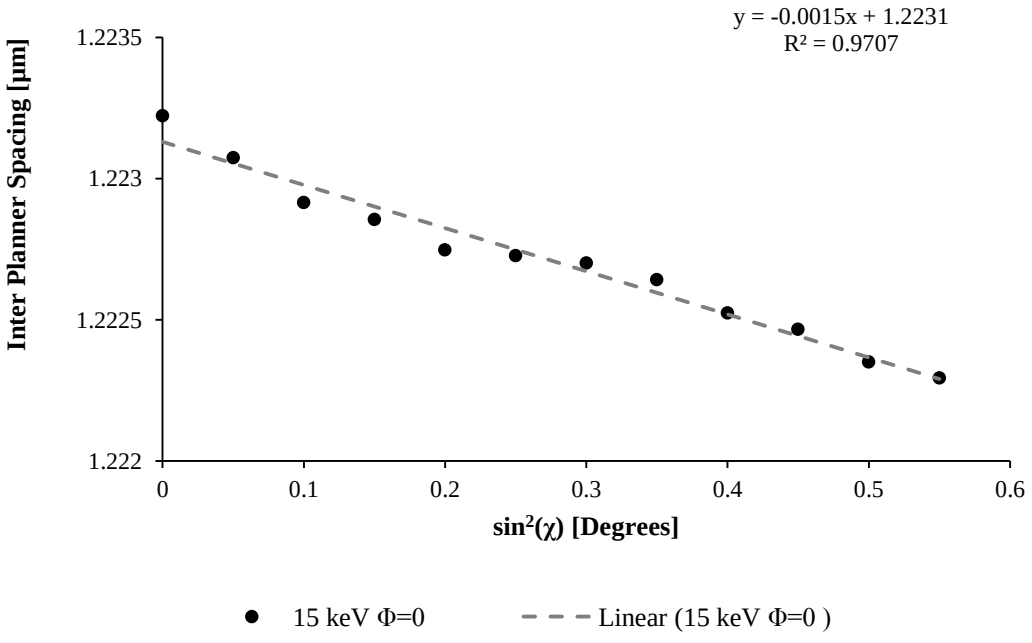

Figure 5.36 – Inter Planar Spacing vs $sin^2(\chi)$ Sample Calculation

Feeding in the last two columns of data listed in Table 5.8 into OriginPro provides the following data listed in Table 5.9.

Table 5.9 - Slope and Slope Error of Inter Planar Spacing Plot

	From Origin (Slope)	From Origin (Slope Error)
Parameter A	1.22168	1.95E-05
Parameter B	-1.15E-03	6.00E-05

Using the outputted slope of the linear line and equation 2.16 the residual stress can be determined.

$$\sigma_{\phi} = \left(\frac{E_{youngs}}{1+v}\right) m$$

$$\sigma_{\phi} = \left(\frac{70}{1+0.33}\right) \cdot -1.15 \times 10^{-3}$$

$$\sigma_{\phi} = -60.526\ MPa$$

The error in the reading was calculated using the error in the slope, as shown below.

$$\sigma_{\phi error} = \left(\frac{E_{youngs}}{1+v}\right) m$$

$$\sigma_{\phi error} = \left(\frac{70}{1+0.33}\right) \cdot 6 \times 10^{-5}$$

$$\sigma_{\phi error} = 3.158\ MPa$$

The calculated error was assumed to be the error bounds both above and below the calculated residual stress.

5.4.9 Bending Fatigue Testing

Possibly the most vital of tests performed in this research, the bending fatigue testing was performed using an Avery Type 7303 bending fatigue apparatus. This equipment is located in the North West Engineering building at the University of the Witwatersrand. The device has the capability to apply a dynamic load range of up to 28.25 Nm at a load cycle frequency of 1420 cycles per minutes. Figure 5.37 provides an example of the fatigue apparatus.

Figure 5.37 – Avery Type 7303 Bending Fatigue Apparatus

The ends of a bending fatigue dog bone sample were clamped to a fixed measuring arm and driving arm respectively. The driving arm was connected double eccentric motor. The eccentric motor assembly provides the oscillatory motion which applies the bending moment/load to the sample. The applied load can be adjusted through the setting of the double eccentric to a desired throw off the driving arm. The motor is mounted to a vertical slide which is used to set the stress ratio of the applied stress. The samples were mounted on its central axis to ensure equal distribution of the loads meeting the requirement of a fully reversed fatigue stress test. To align the centre of the sample with the centre of the machine, spacing pads are used to adjust the height of the component when it is clamped to the two arms. To ensure repeatable clamping the bolts were tightened to 10 Nm, using a small torque wrench. A dynamometer spring was mounted beneath the measuring arm which measures the displacement of the sample per rotation of the motor. The deflections are represented by two dial gauges which then can be used to determine the stress within the component.

This out-dated technique was replaced by the ability of more advanced load-sensing capabilities. A data acquisition system (DAQ) was used in conjunction with a special calibration bending fatigue sample. This calibration sample has a strain gauge mounted on the upper and lower surface of the specimen. A National Instruments SCXI-1314 Universal Strain Terminal Block was used with a National Instruments SCXI-1520 module to connect the strain gauge in a Wheatstone bridge configuration. This set up allows for the determination of the strains and subsequent stress imposed on the sample by the apparatus. Figure 5.38 provides an example of the various components used in the calibration of the bending fatigue apparatus.

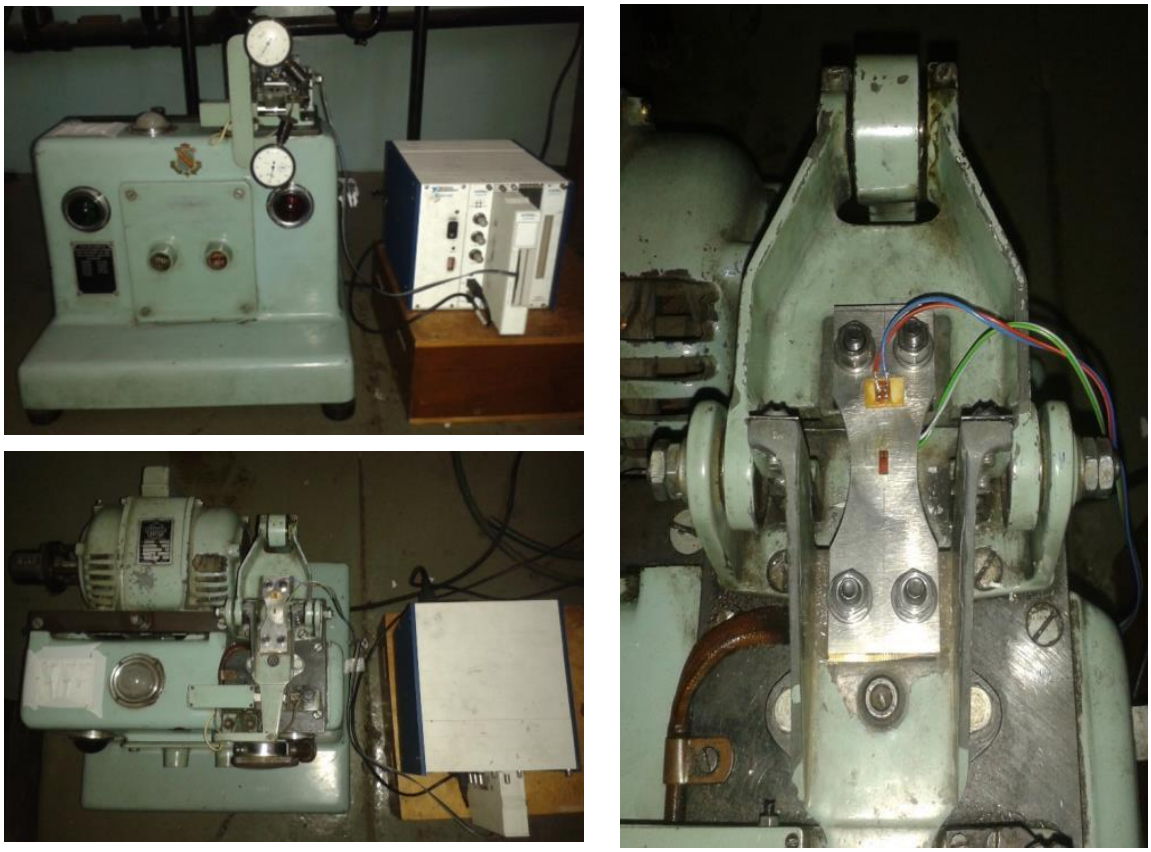

Figure 5.38 - Calibration Equipment of the Fatigue Testing Apparatus

As previously described, the applied load can be altered through the adjustment of the double eccentric. Figure 5.39 shows the layout of the double eccentric and the motor height adjustment screw. The height of the motor is altered by adjusting the screw, by raising the motor the stress is increased and lowering the motor reduces the stress applied to the component. Fine adjustments of the screw are needed to balance the maximum and minimum applied forces.

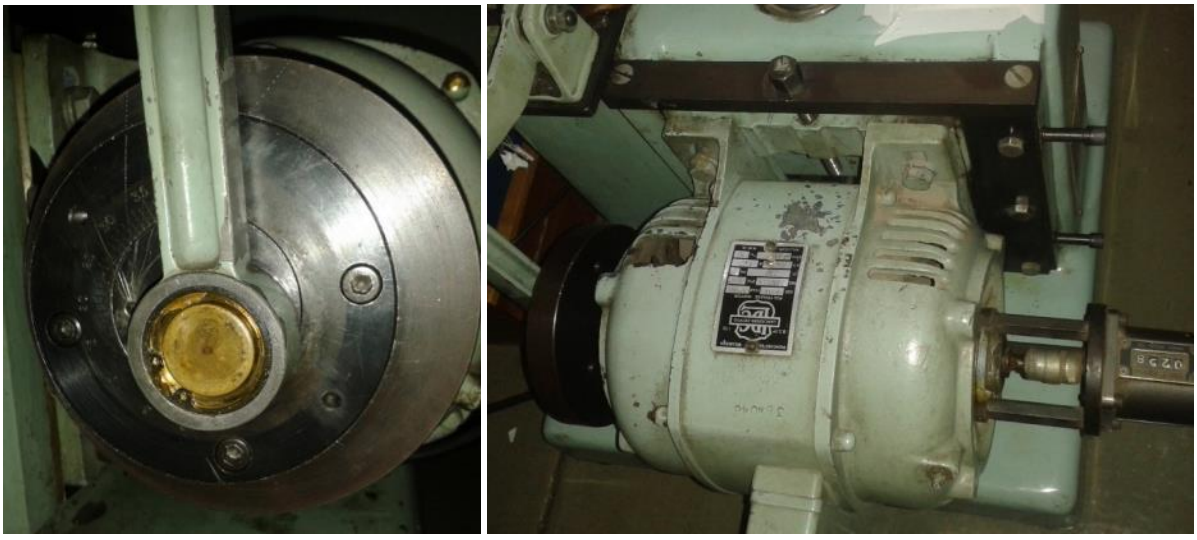

Figure 5.39 - Double Eccentric and Motor Height Adjustment Screw of the Fatigue Testing Machine

The calibration sample outputs the measured strain thus the stress within the component can be calculated using Young's modulus of the material. Equation 5.14 relates the measured strains to the strains under the assumption that calibration sample is perfectly elastic.

$$\sigma_{bending} = E_{young's} \times \varepsilon_{measured} \tag{5.14}$$

With the calibration secured to both arms and a specific eccentric position selected, the stress level can be determined by cranking the eccentric by hand and recording the strain readings for a few rotations of the motor. One should avoid turning on the motor when the calibration sample is in place as this will overload and damage the strain gauges causing inaccuracies. Plotting the output of the measured strains against the measuring time allows for the stress ratio to be determined. Figure 5.40 provides an example of the calculated stress from the measured strains at an eccentric setting of 11, which correlates to an applied stress which ranges between 160-170 MPa. This data was from the testing of the base material. This motor height has been adjusted to gain a stress ratio close to -1, fully reversed. The stress ratio is calculated according to equation 2.11.

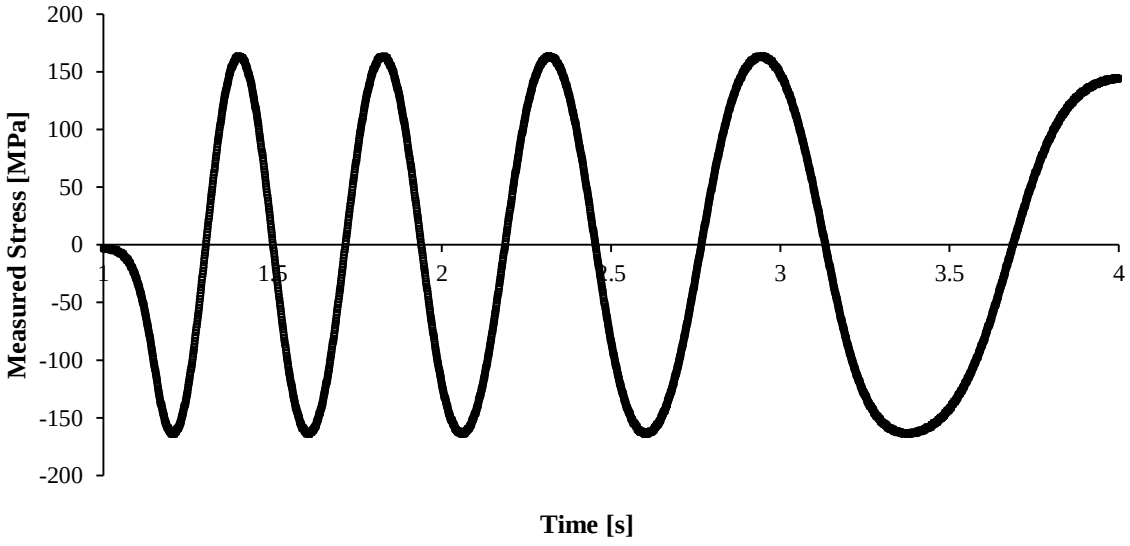

Figure 5.40 - Motor Height Stress Ratio Adjustment

With each new calibration sample, an eccentric setting load correlation curve is required to be determined. For each deviation on the eccentric the load is balanced to ensure that it is fully reversed. The motor is rotated and the strains recorded for that setting. Figure 5.41 provides the load correlation for the various eccentric settings. The stress range is the change in stress from the maximum to minimum recorded strain. The calibration sample must never be run at a setting which applies a load which is higher than the yield strength of the material and the strain gauge. This will cause damage to the calibration samples and result in errors in the readings of the other tests performed after using this calibration sample.

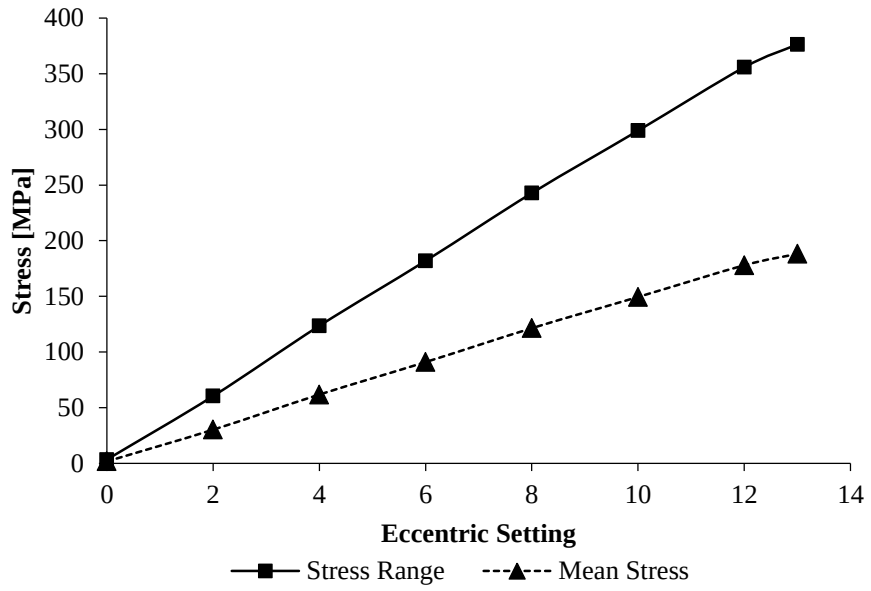

Figure 5.41 - Load Correlation for various Eccentric Settings for a 3mm AA AA6082-T6 Sample

Once the stress levels have been calibrated within an acceptable range, all securing bolts must be tightened and the calibration sample replaced with the actual test sample. Care must be taken to not adjust or alter any of the settings on the machine once it has been calibrated for that specific test. Before starting a test the sample must be checked to ensure that the centre of the sample is aligned with that of the machine.

As the sample is aligned with the machine's central line of force application one is capable of determining the stress at any point through the centre of the test sample. Figure 5.42 provides a schematic of the possible applied loads as the motor rotates. During the upward rotation, the upper surface of the test sample is placed into compression whilst the lower surface is placed into tension. If a crack is present on the lower surface it is at this point when the applied load is most detrimental.

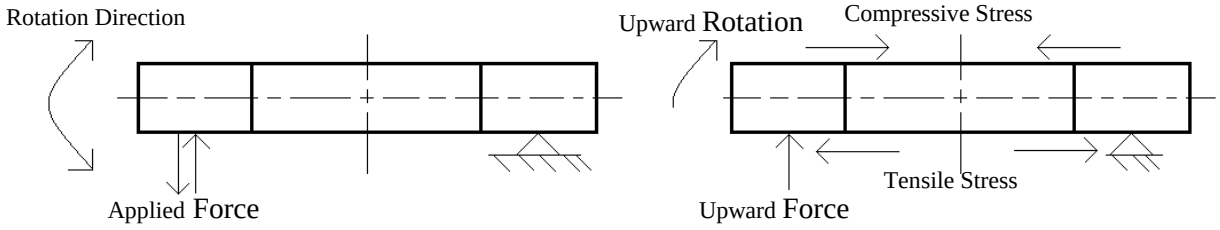

Figure 5.42 - Schematic of the Bending Force Applied to a Test Sample

Figure 5.43 shows a schematic of the bending stress distribution through the centre of the component during the application of the bending load. Assuming that the sample material is perfectly isotropic the stress distribution grows linearly from the centre out towards the surface of the test sample, where the stress was measured. With this assumption, the stress at any point through the thickness can be determined.

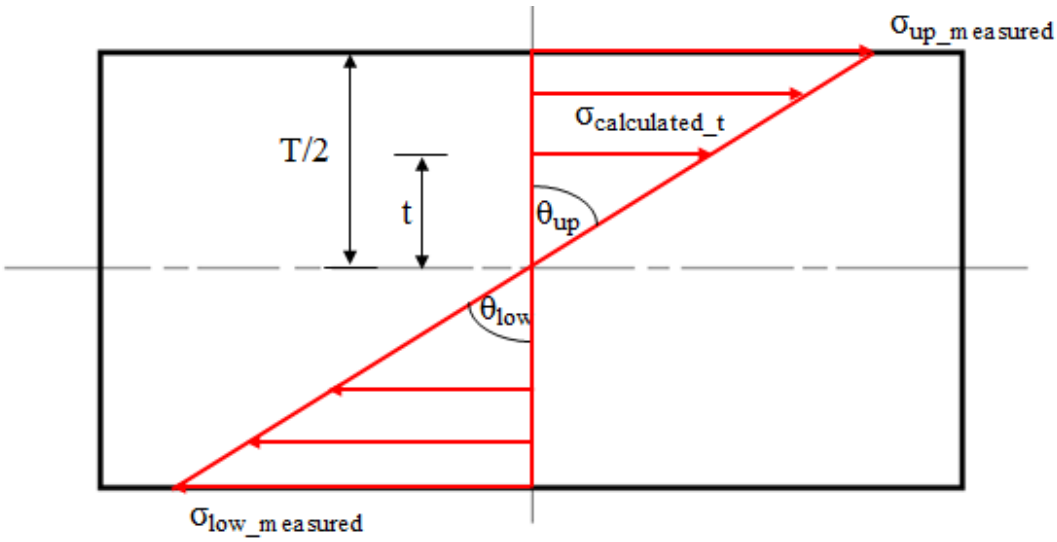

Figure 5.43 - Schematic of the Bending Stress through the Thickness of the Test Sample

The angle formed between the vertical centre line and the stress distribution can be calculated with the use of simple geometry.

$$\theta_{up} = \tan^{-1}\left(\frac{\sigma_{up\_measured}}{T/2}\right) \tag{5.15}$$

The same can be applied to the minimum force thus determining the lower angle. Once these angles have been determined the stress at any point through the thickness can be found by the following equation.

$$\sigma_{calculated\_up} = t \times \tan\theta_{up} \tag{5.16}$$

This model can be used to compensate for any variations in thickness differences between the calibration sample and actual test samples. As long as the central line of the test and calibration samples align with that of the machine this assumption is valid.

A digital camera, which is linked to a computer, was used to track the time for which the fatigue sample runs. The camera takes a still shot of the top of the sample every minute. Knowing when the test is started and using the first image after a crack appears in the image, Figure 5.44 shows the first and final image of the test sample run for the base material set on an eccentric of 11. An equation which relates the number of cycles to failure can be derived using the time stamps of the images and fact that the motor runs at 1420 rpm resulting in equation 5.17. The fatigue test was started as soon as the first image was produced. The images were taken ever sixty second and with this one cannot be exactly sure of the precious time, down to the seconds, of failure of the test sample as failure occurred during the time lapse between recorded images. At minimum the error in cycles to failure was 1420 cycles.

Figure 5.44 - First and Final Image of Fatigue Test Sample

$$n = (t_{end} - t_{start}) \times 1420 \tag{5.17}$$

After each test, the stress level of the machine needs to be checked to identify if the machine had changed its stress level by working the securing bolts loose through vibration. If the stress setting was not close enough to be considered a fully reversible test within some limit the test needs to be repeated.

5.4.9.1 Bending Fatigue Sample Calculations

This section provides the opportunity to complete full sample calculation involved in the bending fatigue stress measurements of the various samples, demonstrating the technique followed throughout to obtain the remaining results which will be provided in the coming sections.

All calculations have been performed for the fatigue test completed on the base material sample which data was presented in Figure 5.40. The maximum and minimum recorded strains from Figure 5.40 are used to calculate the corresponding stresses according to equation 5.14. For this sample calculation, the maximum and minimum measured strains were 0.002332 mm/mm and -0.00232mm/mm respectively.

$$\sigma_{max\ bending} = E_{young's} \times \varepsilon_{max\ measured}$$

$$\sigma_{max\ bending} = 70000 \times 0.002332$$

$$\sigma_{max\ bending} = 163.24\ MPa$$

$$\sigma_{min\ bending} = E_{young's} \times \varepsilon_{min\ measured}$$

$$\sigma_{min\ bending} = 70000 \times -0.00232$$

$$\sigma_{min\ bending} = -162.40\ MPa$$

The stress ratio was calculated using equation 2.11.

$$R = \frac{\sigma_{min}}{\sigma_{max}}$$

$$R = \frac{-162.40}{163.24}$$

$$R = \text{-0.99485}$$

The stress range and mean stress were calculated according to equations 2.8 and 2.11.

$$\sigma_r = \sigma_{max} - \sigma_{min}$$

$$\sigma_r = 163.24 - (-162.40)$$

$$\sigma_r = 325.64MPa$$

$$\sigma_m = \frac{\sigma_{max} - \sigma_{min}}{2}$$

$$\sigma_m = \frac{163.24 - (-162.40)}{2}$$

$$\sigma_m = 162.82\ MPa$$

Figure 5.44 provides the amount of time that the sample ran for before a catastrophic fracture was detected. This sample ran for a total of two hours and ten minutes. The number of cycles to failure calculated using equation 5.17.

$$n = (t_{end} - t_{start}) \times 1420$$

$$n = 130 \times 1420$$

$$n = 184\ 600\ cycles$$

At this point, the stress settings were rechecked to ensure that the apparatus had not altered its settings. The same procedure was followed. The results of the recheck have been listed in Table 5.10.

Table 5.10 - Recheck of Stress Settings Post Fatigue Test

Measurement / Calculation	Value	Percentage difference to start value
Maximum Strain	0.00236 mm/mm	1.2% increase
Minimum Strain	-0.00233 mm/mm	0.43% increase
Maximum Stress	165.34 MPa	1.29% increase
Minimum Stress	-163.1 MPa	0.43% increase
Stress Ratio	-0.9864	0.849% reduction (further away -1 is worse)
Stress Range	328.44 MPa	0.8598% increase
Mean Stress	164.22	0.8598% increase
Acceptable test	Yes, all % differences are within acceptable limits.	

6 Investigation and Optimisation of Process Parameters

This section will cover the investigations into the effects of varying process parameters on the FSW and LSP processes with the aim to achieve a greater understanding of each of the process as well as the set of parameters which can be used to create the best possible outcome. Each process was treated in isolation for this section.

6.1 Friction Stir Welding Optimisation

This solid state process formed the cornerstone of this research in that without it no further progression could occur. The working material of 3 mm thick AA6082-T6 had not been used for any welding activates at the University of the Witwatersrand. According to previous experience of FSW of thin Aluminium sheets and literature selection of the tool rotation and feed rate are the two main welding parameters that require careful selection in order to achieve an optimum joint. In this investigation of suitable welding parameters, a number of the lesser important welding parameters were fixed in order to narrow down the number of combination of welding parameters. By reducing the number of levels of process parameters, the study was able to focus on expanding the number of combinations of key parameters such as tool rotation and feed rate.

6.1.1 Selection of the Fixed Friction Stir Welding Parameters

The plunge rate had to be selected so that the welding pin was not loaded to a point which would cause failure or extreme amounts of wear of the tool. From previous experimentation, the plunge was specified as 5 mm/min. During the plunge stage, the axial force was monitored; the resulting effects of the plunge rate in combination with the various tool rotations were explored in 6.1.3.

The length of time for the initial dwell period was by far the most important of fixed parameters at this stage of the weld allows for the development of the thermal fields for preheating the material and of the welding tool. Numerous of researchers specified that a suitable range for the length of the dwell stage should vary between 5 to 20 seconds [22]. This is dependent on the rotation of the tool and the material thickness. Combining results of literature and previous welding experiments at this facility a 10 second initial dwell period was selected. These allowed for suitable thermal build up to occur at both the higher and lower ranges of tool rotations investigated.

The end dwell period was selected based on previous experimentation. The length of time which would not allow sufficient build-up of temperature to in some way cause the welded sheets to stick to the backing plate. The end dwell has no effect on the weld, it was to allow for the tool to build up sufficient heat for an easy retraction of the tool from the welding plates. The welding tool was allowed to dwell for a total of 2.5 seconds upon reaching the desired length of weld.

The retraction rate of the welding tool once the end dwell phase had been completed was specified as 20 mm/min. This fairly fast rate was selected as a quick and clean retraction of the tool from the weld. Table 6.1 provides a list of the fixed parameters which were maintained during this research.

Table 6.1 - Summary of Fixed Friction Stir Welding Parameters

Phase of Weld Parameter	Fixed Value
Plunge Rate	5 mm/min
Initial Dwell Period	10 seconds
End Dwell Period	2.5 seconds
Retraction Rate	90 mm/min

For this research, the key stage of the FSW process was the actual feeding of the tool as LOP only occurs during this stage. Leading on from this an expansive investigation of the effects of tool rotation and feed rate was completed.

6.1.2 Friction Stir Welding Variable Parameter Window

Figure 5.7 formed the foundation for the selection of the initial welding parameter window which was investigated. Research showed that majority of researchers who had previously FSW this material selected tool rotations and feed rates ranging from 700 – 2000 RPM and 150 – 600 mm/min. The decision was taken to select a similar welding window, within the operational capabilities of the FSW machines, as the researched work would allow for a standard to judge the effectiveness of this facilities ability to produces comparable welds.

The fixed gearing of the welding machine constrained the selection of the tool rotational speed. Table A.1 in Appendix A.1 provides the possible rotations of the spindle. The Maho CNC machine had the functionality to select any feed rate and thus the combination of this welding parameter was selected from the previously used values of other researchers. The welding rate has been shown to the most influential parameter when FSW [53]. A sweep of welding rates was achieved by having multiple levels of rotational speeds and selecting a minimal number of feed rate levels. An unlimited number of feed rates could have been selected but by only selecting three different factorial levels an orthogonal experimental array could be determined. Reference to Figure 5.7 again showed that researchers clustered the used feed rates between 150 to 600 mm/min thus the varied feed rates used was 200, 400 and 600 mm/min. An attempt to match the rotational speeds used in literature was made but due to the limitations of the CNC a fixed number of rotational speeds had to be used. The lowest and highest rpm used in literature was 710 and 1700 rpm thus a lower and upper bounds of rpm selected for this optimisation of welding parameters was 630 and 1600 rpm. Figure 6.1 provides the initial welding parameter window used in order to optimise the FSW process.

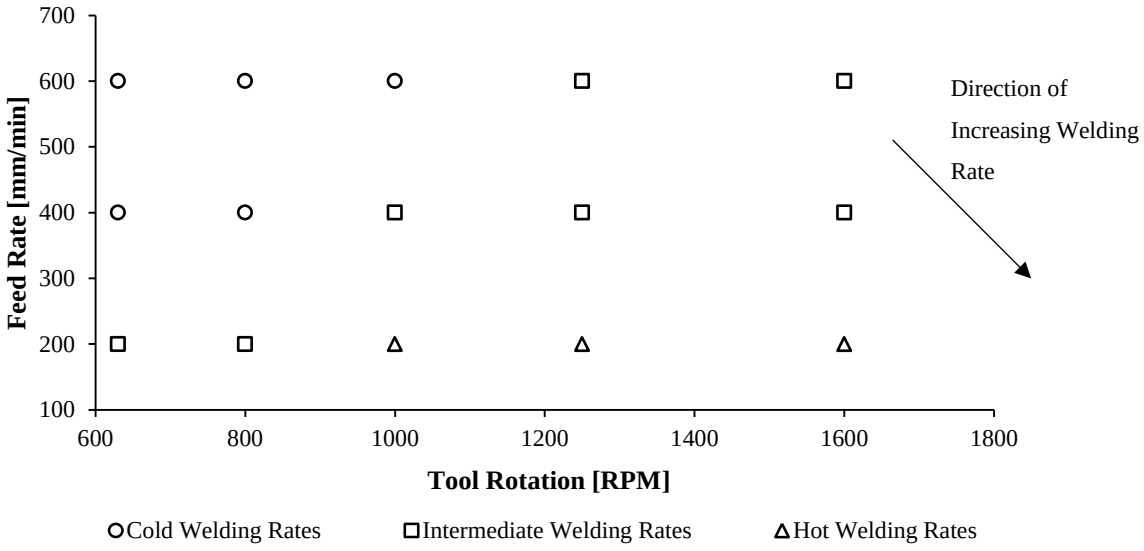

Figure 6.1 - Friction Stir Welding Parameter Combinations

Table 6.2 provides the parameter combinations used to suitably investigate the possible parameters and their effects on a variety of mechanical and joint structural properties. Each of the welds was made on individual 250 mm long sheets which allowed for FSW to be made roughly 220 mm long (distance from plunge position to retraction location).

Table 6.2 - Friction Stir Welding Instigation of Window of Parameters

Parameter Name	Tool Rotation [rpm]	Feed Rate [mm/min]	Welding Rate [rev/min]
S1	630	200	3.15
S2	630	400	1.58
S3	630	600	1.05
S4	800	200	4.00
S5	800	400	2.00
S6	800	600	1.33
S7	1000	200	5.00
S8	1000	400	2.50
S9	1000	600	1.67
S10	1250	200	6.25
S11	1250	400	3.13
S12	1250	600	2.08
S13	1600	200	8.00
S14	1600	400	4.00
S15	1600	600	2.67

Using standard Design of Experiment techniques, these combinations of parameters were used in the optimisation of the FSW process. The effects of these combinations had on the formation of the joint, the welding process and the overall mechanical properties were investigated and used in the multi-objective optimisation to find the best possible set of welding parameters.

6.1.3 Influence of Friction Stir Welding Parameters on Process Forces and Moments

Whilst welding each the various combinations, the welding forces and moments in each principle direction were recorded with the use of the Kistler Piezoelectric Dynamometer. The forces of interest were the perpendicular to the translation of the tool, in-plane with the tools translation and normal to the tools translation. The torque applied to the tool about the Z axis was the only the moment which needed to be considered as the remaining directions did not provide any tangible information. Figure 6.2 shows the various force-time plots recorded in the three principle directions for the first set of welding parameters, 630 RPM and 200 mm/min feed rate. Figure 6.3 shows the recordings of the three principle moments for the same set of welding parameters. The uncertainty in each measurement of the force was specified as approximately 7.8 N in F_x and F_y and 3.8 N in F_z.

a)

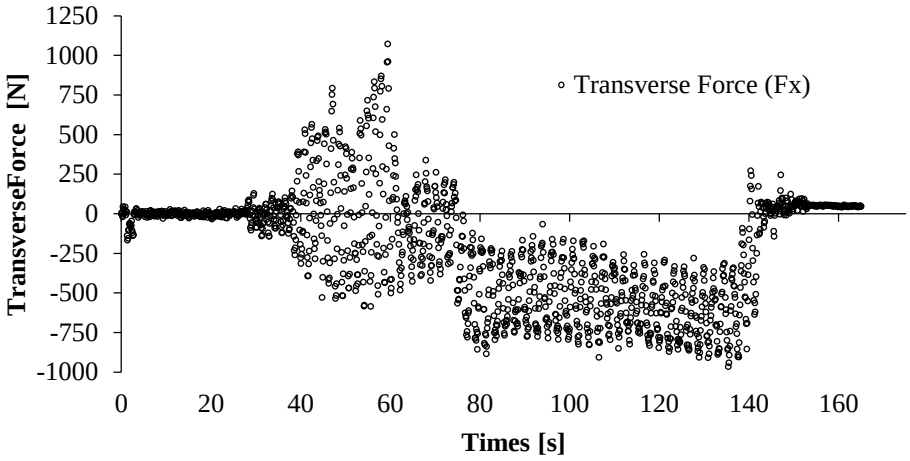

b)

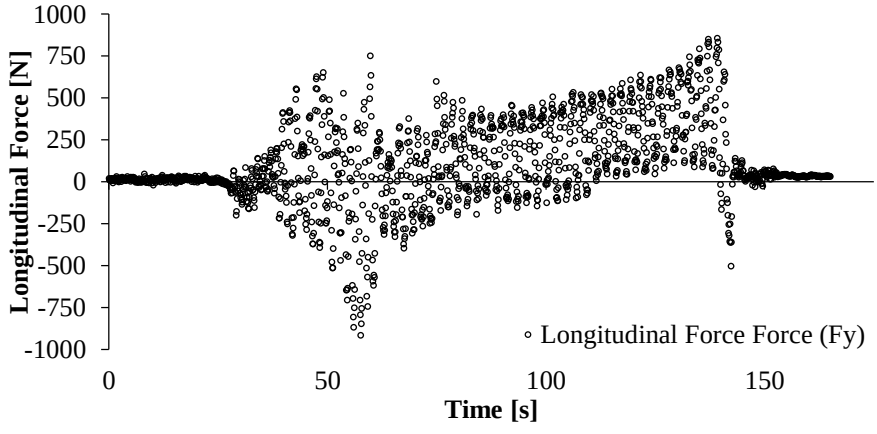

c)

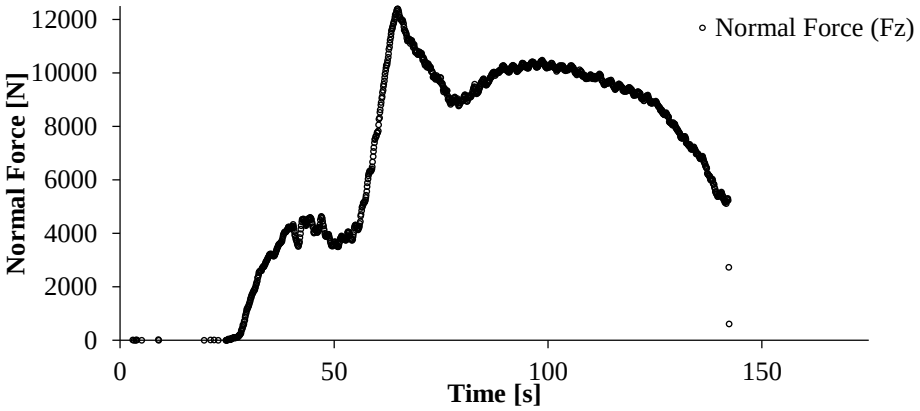

Figure 6.2 - Recorded Forces during Friction Stir Welding a) F_x b) F_y c) F_z

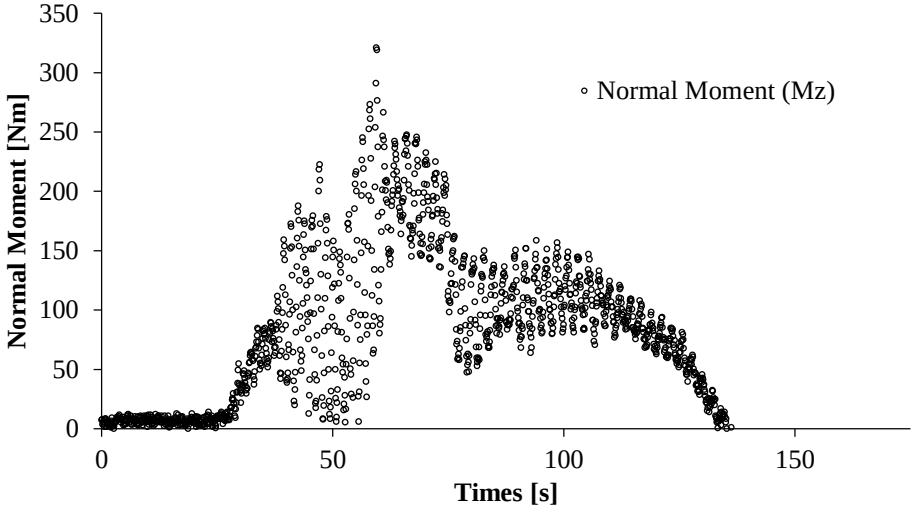

Figure 6.3 - Recorded Torque during Friction Stir Welding

The force and moment profiles showed very distinctive key stages of the welding process which needed to be investigated. All parameter sets exhibited the trend of clear transitions in forces and moments which corresponded to each distinctive stage of the welding process. The parameter set of 1600 RPM and 200 mm/min feed rate has been provided with the occurrence of the transition of each stage. Figure 6.4 provides the force distribution in the longitudinal direction. The forces were fairly symmetrical in the initial stages. This corresponds to the plunge and dwell phase where the tool is not translating along the weld. The highest loads are experienced during this stage due the interaction of the tool and the cold material. The loads as the pin technically drilled into the material are fairly constant as the tool plunges. Upon the shoulder making contact the greater surface of the sheets a fairly rapid decrease in tool loads occur. This is attributed to the softening of the material due to the higher temperatures caused by the frictional heat of the tool. The translation of the tool causes a shift of the values to be more negative. The negative direction correlates to the retreating side of the weld. The potential cause of this shift may be due to the material flow and depositing of material towards

the retreating side as the tool rotates. The flash formation is always greatest on the retreating side which can lead to the assumption that with higher rates of material flow in that region of the weld a high force is required in control the dynamics of the material flow. Further investigations are required to confirm this fact.

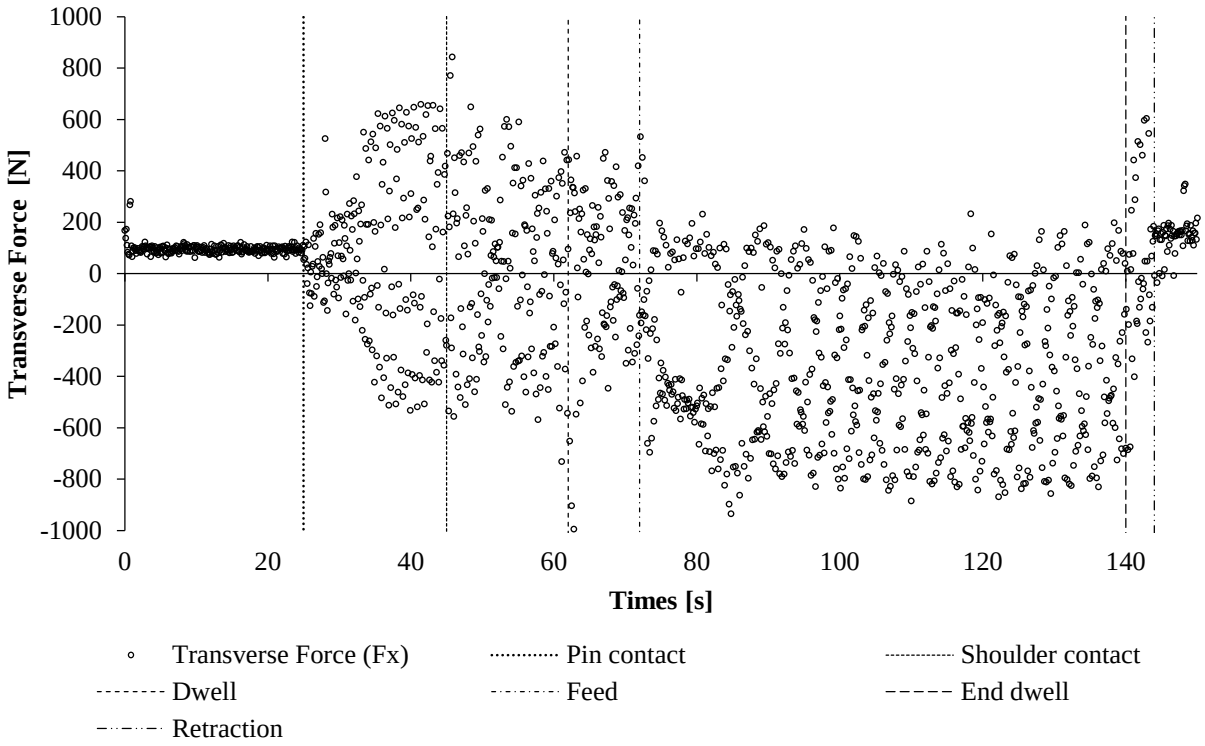

Figure 6.4 - Stages of Friction Stir Welding Process on Transverse Force

Figure 6.5 shows the recorded forces in the longitudinal direction. Again the forces are fairly symmetrical whilst the tool is not traversing along the joint line. The symmetry of the longitudinal and traversing forces during the stationary phases of the weld is to be expected. During this stationary phase, the directions and magnitudes should be equal as the tool is hypothetically applying the same force in both directions as it rotates. The feed phase produces forces of relatively equal magnitude to that previously found in the transverse direction. The positive inclination was due to the applied load being in the positive direction of that axis. It makes sense that a similar magnitude of force would be experienced in this direction to that of the previous as this is the welding force which is accustomed to overcoming the material. Researchers have shown that in some cases there are discrepancies between the magnitudes of the forces in the longitudinal and transverse directions, this may be accredited to the use of a tilted tool during welding.

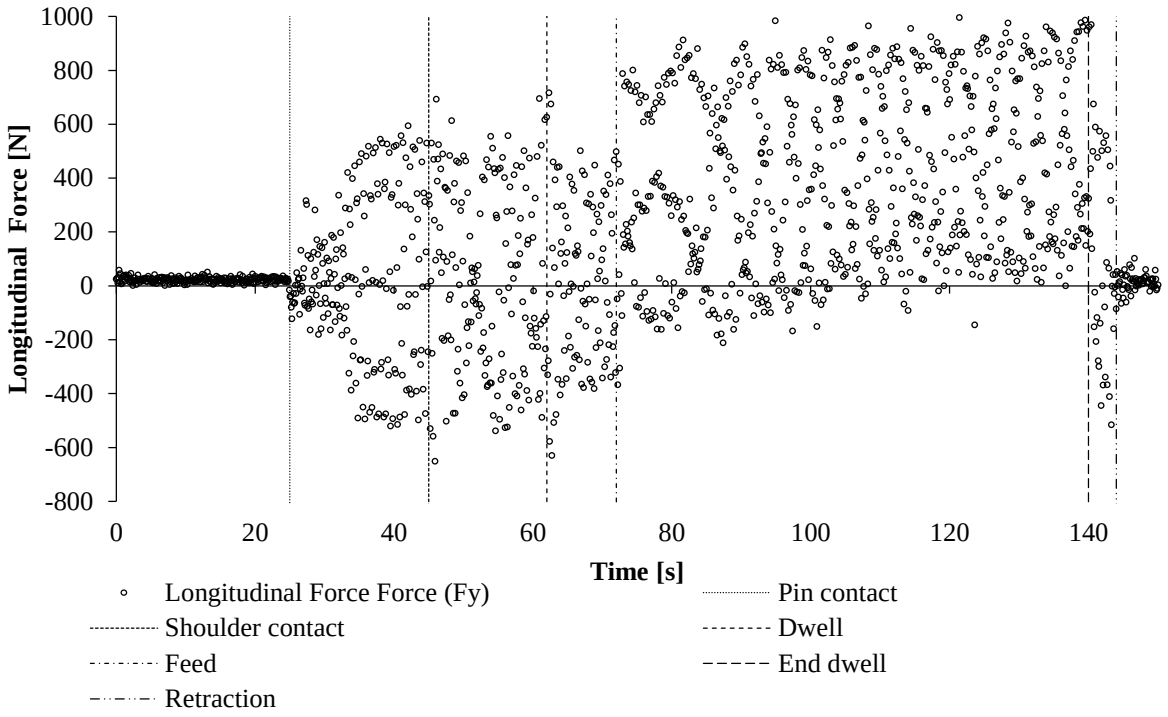

Figure 6.5- Stages of Friction Stir Welding Process on Longitudinal Force

Figure 6.6 provides the normal force profile during this welding process. A sharp increase in force occurs when the pin first comes into contact with the material. The force in this region peaks and then begins to decrease, this is due to the fact that once a sufficient amount of the length of the pin makes contact with the material a rapid increase in temperature occurs and the material around the pin becomes sufficiently soft reducing the amount of force acting upon the pin during the plunge. The forces level off which leads to the theory that this alloy of Aluminium may have a critical temperature which once achieved results in an extreme reduction in the yield strength. Once the tool is plunged sufficiently that the shoulder comes into contact with the material a rapid increase in the normal force occurs. The occurrence of these two peaks during the plunge stage was observed by [22] and can be seen in Figure 2.21. A turning point is achieved again showing a sharp decrease in the load on the tool during the plunge. The theory of a critical temperature is again suggested for this occurrence. At the start of the dwell stage, the material begins to heat and worked to a greater extent this is shown in the even great reduction in the amount of force required during the dwell stage. A sharp increase in force occurs once the tool begins to feed. The increase in the force is due to the fact that initially the tool encounters fairly hot material which had been heated during the dwell stage, as the tool moves further and further way from the location of the dwell the material becomes colder and thus higher loads are required to heat and stir the material. There is a region of the feed stage in which a near steady state is approximately achieved. This fact is extremely promising in that it promotes the fact that the FSW completed was of a good quality and repeatable.

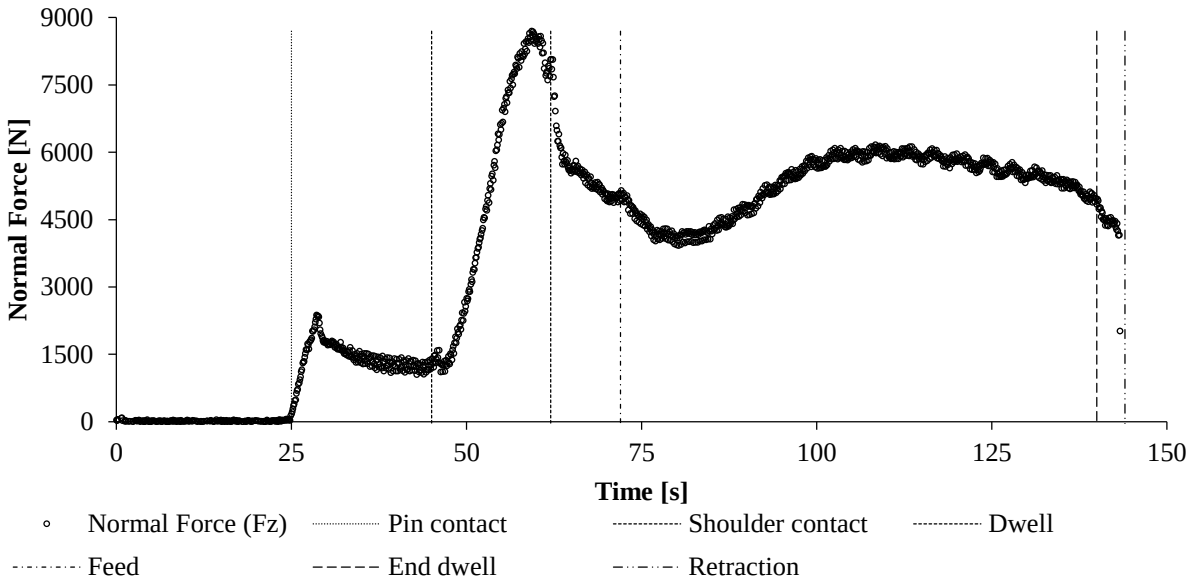

Figure 6.6 - Stages of Friction Stir Welding Process on Normal Force

The general trends observed in the normal force distributions roughly replicate that of the profile produced in Figure 2.21. The forces are extremely high thus at a first glance the FSW process was comparable to other welding institutions. The inability of being able to verify the magnitude of the force in the published data was due to welds not being completed at that tool rotation and due to the fact that the tool design significantly affects the force generation during welding. The fact that the normal forces generated at all stages during the experimental welding was below the published example can potentially lead to the confirmation that a lower tool rotation results in higher machining loads throughout the welding process.

The distinction in between each stage of the welding process was evidentially clear on the recording of torque applied to the tool during the welding process. Figure 6.7 clearly shows that the average torque applied to the tool increased during the initial plunge stages of the weld. The reduction of the torque during the dwell was attributed due to the effects of the material softening and the reduction in the normal force during this stage. The torque profile was found to replicate that of the normal force due to obvious reasons. The slight increase in torque due to the progression of the tool along the weld was due to the tool coming into contact with the colder material. From the figure, it was evident that the torque tends towards a constant steady state but took a reasonable length of weld for this state to be achieved.

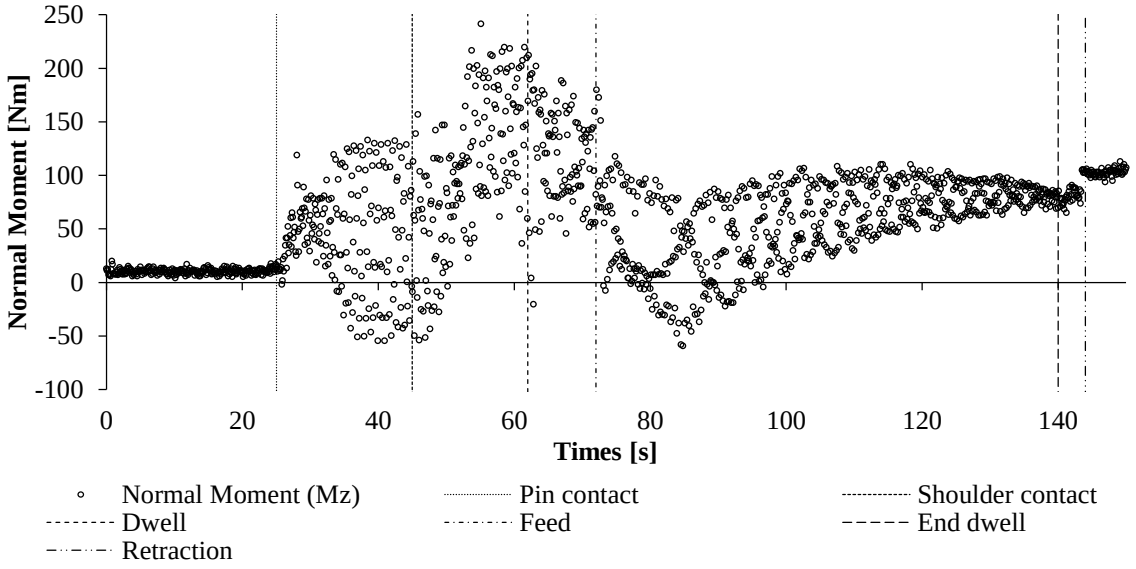

Figure 6.7 - Stages of Friction Stir Welding Process on the Moment about the Z-Axis

Error bars have purposefully been neglected from all force plots due to the sheer number of point's. The presence of error bars would only reduce the clarity of the figures. The dynamometer had a measuring force range in the X and Y directions of -25 kN to 25 kN with a sensitivity of 0.01 N and -25 to 60 kN with a sensitivity of 0.01 N in the Z direction.

Table 6.3 lists the maximum and average recorded forces which occurred in the vertical direction (F_z) during the various trials. The Normal force was selected to be presented as it is the most important of the three forces. In most of the cases, the maximum force occurred during the plunge stage once the shoulder of the tool had been in contact with the working material.

Table 6.3 - Maximum and Average Force during Feed Stage in the Vertical Direction

RPM		**630**		**800**		**1000**		**1250**		**1600**	
Forces [N]		**Max Overall**	**Ave. Feed**	**Max Overall**	**Ave. Feed**	**Max Overall**	**Ave. Feed**	**Max Overall**	**Ave. Feed**	**Max Overall**	**Ave. Feed**
Feed Rate [mm/min]	**200**	14589.8	12666.5	14727.8	11815.0	12266.8	9362.4	11171.9	7458.5	9950.0	7156.1
	400	16623.5	14918.4	16363.5	14886.1	15003.7	13255.6	12189.9	10978.5	10043.9	8866.6
	600	18142.1	16414.1	18043.2	15939.4	17502.4	15134.0	15318.6	13348.6	13503.4	11053.6

Figure 6.8 showed that by increasing the spindle speed, a reduction or shift in the magnitudes of the forces can be achieved. The effect of increase feed rate resulted in higher loads being produced during welding, this was confirmed by published data and trends in Figure 2.22. The observed increase in loads was due to the temperature effects related to the lower welding rates (increase in feed rate) in that the welding tool acts upon much cooler material for a much shorter period of time. The uncertainty range was too small to be clearly seen in the figure.

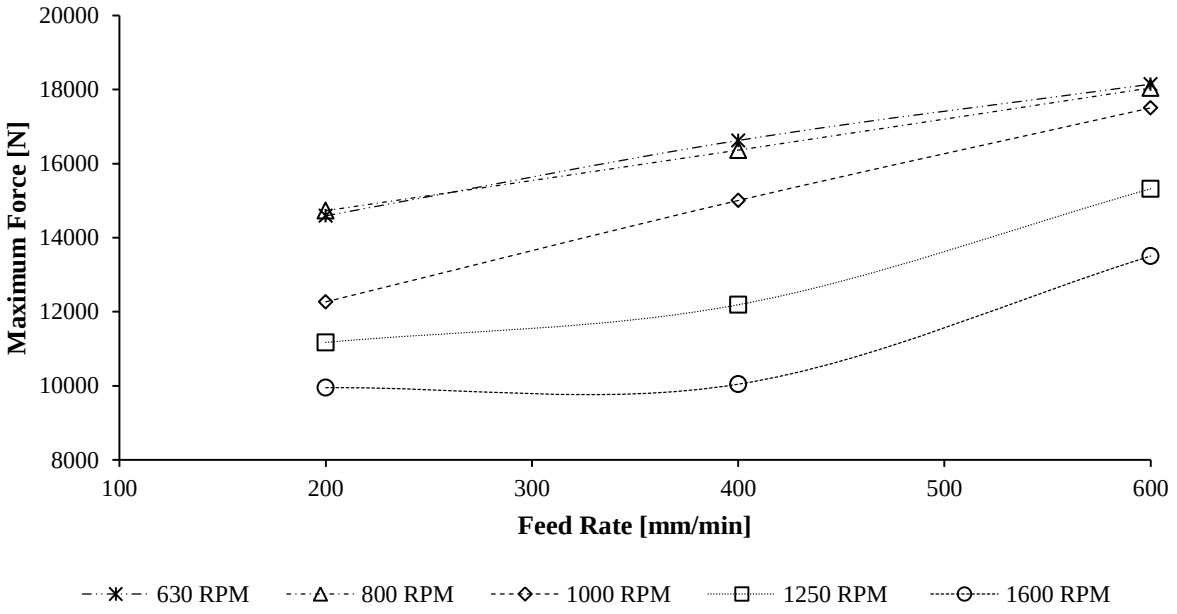

Figure 6.8 - Maximum Normal Force during Friction Stir Welding of Parameter Combinations

Figure 6.9 showed that an increase in feed rate reduced the averaged normal force during the feed stage of the weld. The shifts between lines of constant spindle speed were again apparent. It can be concluded that higher welding rates reduce the load on the tool and welding machine.

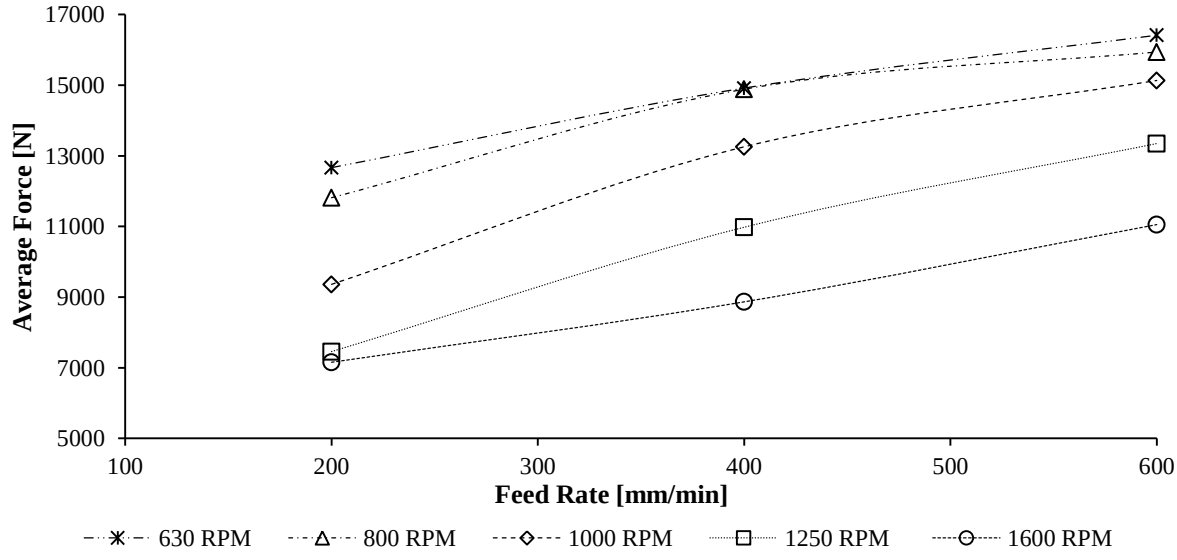

Figure 6.9 – Average Normal Force during Feed Stage of Friction Stir Welding of Parameter Combinations.

Appendix C.1 contains further analysis of the maximum vertical forces which occurred during the plunge stage of each welding combination. This analysis confirmed that an increase in spindle speed resulted in lower processing forces.

An analysis of the resulting torque acting on the tool was conducted to determine whether similar trends would be observed. Figure 6.10 and Figure 6.11 shows the distribution of maximum torque which occurred during the feed stage and over the complete welding process. From the figure, it was not possible to clearly see a variation in the magnitude of the torque as with the plot of the maximum force. It is unclear as to why spindle speeds of 800 and 1250 RPM at a feed rate of 200 mm/min produced some of the lowest magnitudes. What is evident from this figure is that increasing feed rate resulted in higher magnitudes of applied torque.

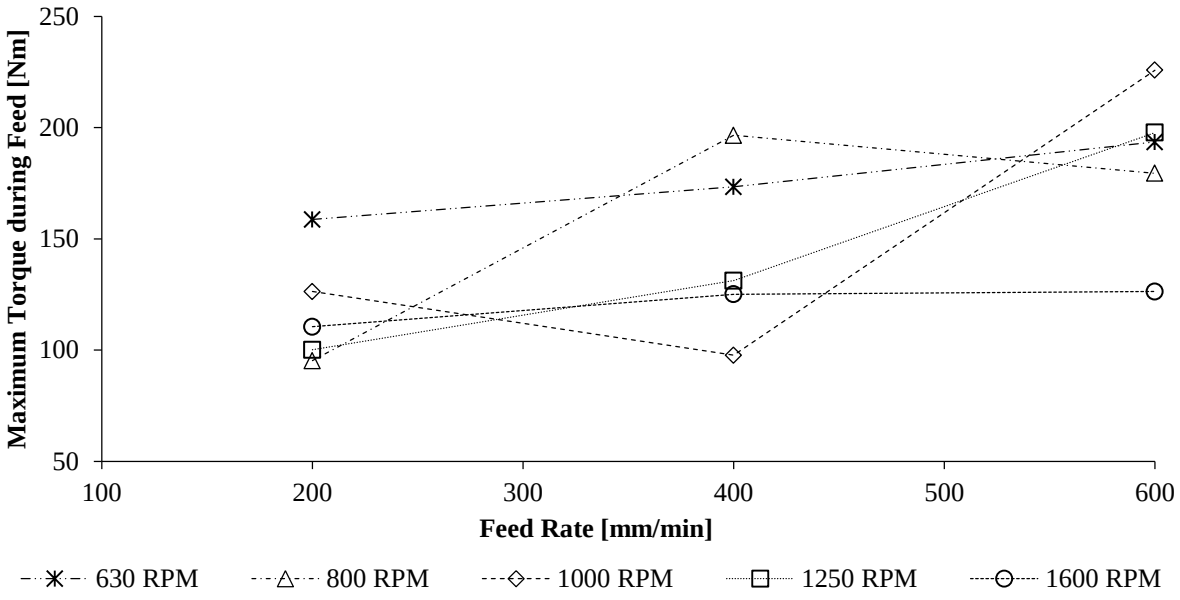

Figure 6.10 - Maximum Torque Recording During Feed Stage of Friction Stir Welds

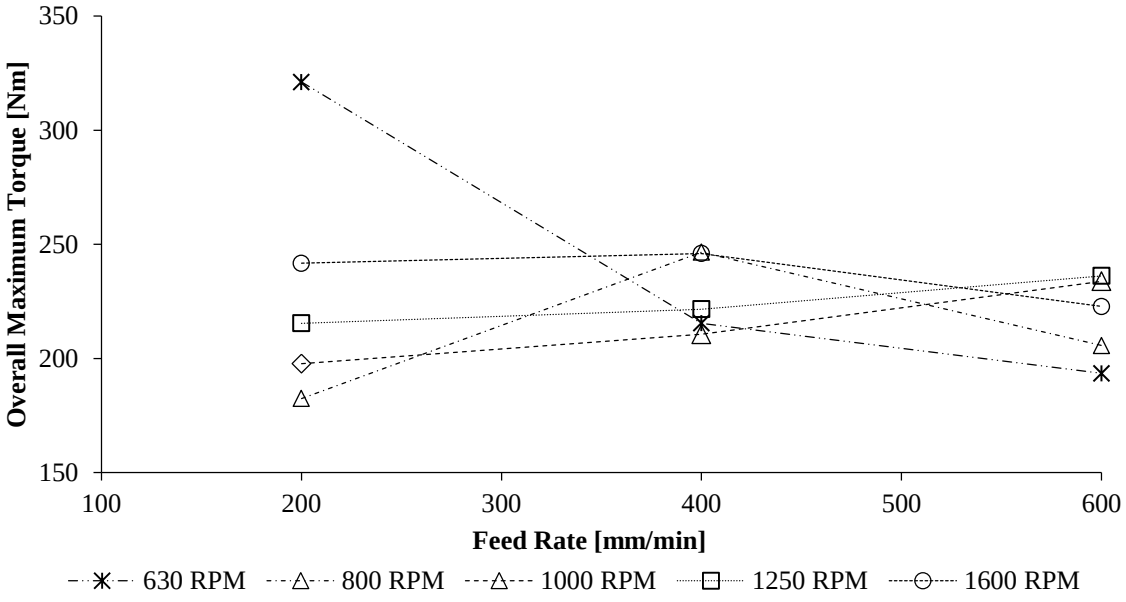

Figure 6.11 - Maximum Torque Recorded During Full Friction Stir Welding Process

The data for all forces and moments recorded during welding have been placed in the attached digital Appendix.

6.1.3.1 Conclusion

From the results presented in this section the following can be concluded:

1. Each stage of the FSW process can be clearly indicated on the normal force profile.
2. Typically the highest normal force occurred during the plunge and dwell stage where the shoulder had made contact with the work material but had not built up sufficient heat to plasticise the material.
3. A clear reduction of welding force was noted at the start of each feed stage due to the thermal softening of material during the dwell stage. Upon the tool encountering colder material which was further away from the dwell position, an increase in normal force occurs.
4. An increase in feed rate results in an increase in the maximum normal force required to perform the weld.
5. An increase in tool rotational speed results in an overall lowering of the normal force required to weld for the same feed rate.
6. Although not fully conclusive, an increase in feed rate results in an increase in maximum torque applied to the tool.

6.1.4 Variation of Thermal Effect caused by varying Friction Stir Welding Parameters

The thermal and material flow dynamics associated with FSW is two of the most vital aspects associated with this process. The successfulness of the joint is completely dependent on of how these aspects are achieved with varying welding parameters. Material flow during welding is effected directly by the thermal effects produced by the welding tool. The change in temperature during each weld was recorded using a thermal imaging camera described in section 5.1.4. Figure 6.12 shows the change in temperature during the course of welding at 1600 RPM and 200 mm/min, captured using two different measurement ranges. Column (a) represents images taken during a recording in the 0°C to 660°C whilst column (b) was recording using a temperature range of 100°C to 3000°C. The welds were recorded using these two ranges to achieve an accurate representation of the temperature during the various stages of Friction Stir Welding undertaken at various welding parameters. If the temperature of the object being observed fell outside of the indicated range then the logged temperature was replaced by the minimum or maximum possible value for that measurement range. The lower measuring ranges did allow for much higher resolution of footage to be captured, as seen in Figure 6.12. Stated in Table 2.2 the melting temperature of AA AA6082-T6 Aluminium was 555°C. The mechanics behind FSW is not to physically melt the material thus temperatures which exceeded the published melting temperature of the material were assumed to be attributed to the temperature build up in the welding tool as no signs of melting was evident on any of the welded samples.

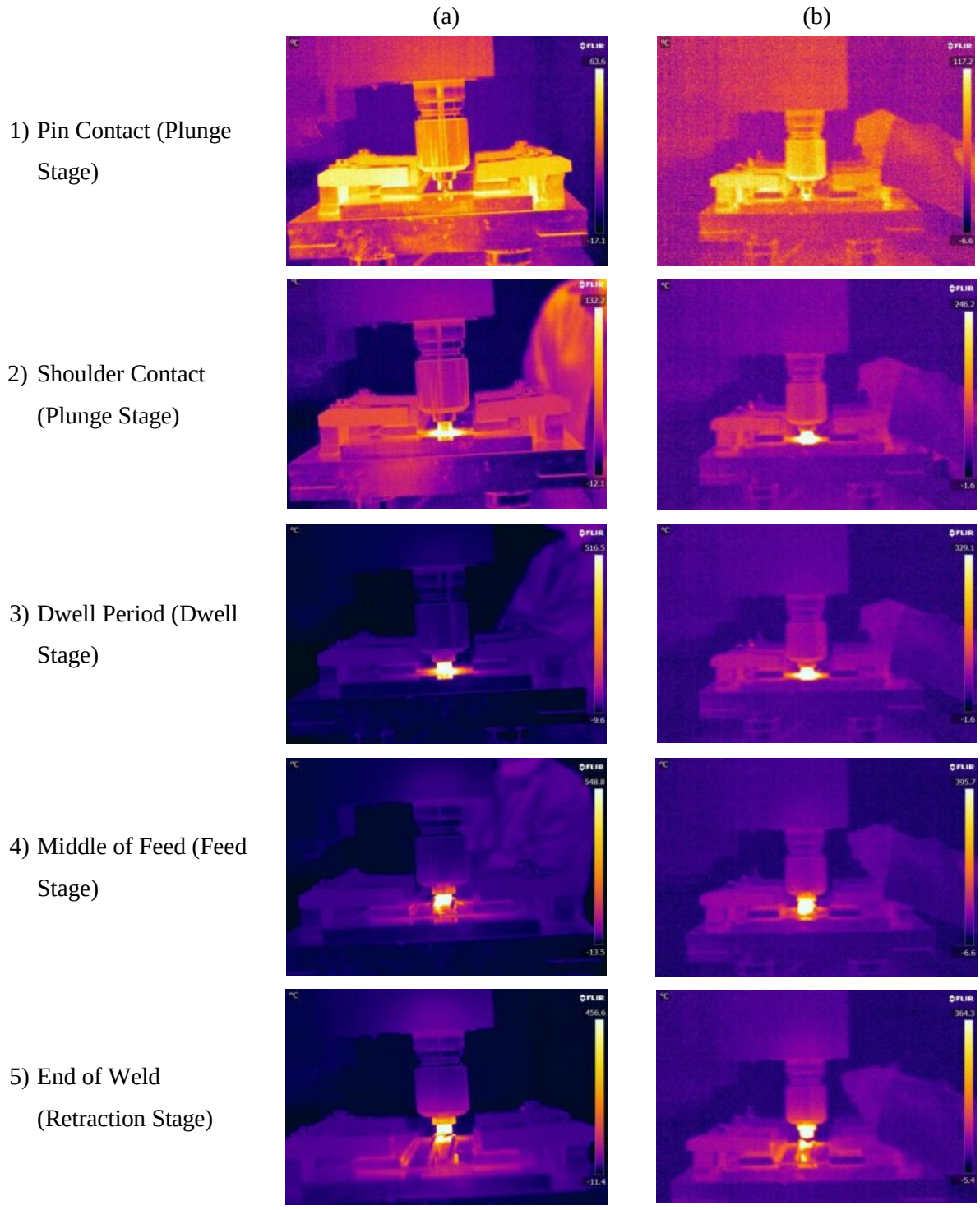

Figure 6.12 - Thermal Imaging of the Welding Process at Two Measurement Ranges

The parameters which were used in the calibration of the recordings were listed in Table 6.4. Varying these values did influence the measured temperature data. The emissivity was the greatest contribute to the correctness of the temperature data. It was recommended by the manufacturer of the thermal camera that during recording the emissivity should be set to as high as possible and then corrected during the post processing of the footage. An emissivity of 0.82 was used during recording. The emissivity value for commercial sheet Aluminium was stated as 0.09 [89]. The value used for this

case was determined to be 0.11. The atmospheric temperatures were measured to be 20°C and assumed that the temperature in the room remained approximately constant. The reflective and extended optics temperature was assumed to be at the same temperature as the room in which the welding was completed. The distance between the camera lenses and the welding tool was set to be 1m.

Table 6.4- Thermal Imaging Recorded Parameters

Parameters	Values
Emissivity	0.11
Reflective Temperature	20 °C
Distance	1.0 m
Atmospheric Temperature	20 °C
Extended Optics Temperature	20 °C
External Optics Transmission	1.00
Relative Humidity	50.00%

6.1.4.1 Temperature Measurements across the Welded Area

To obtain a temperature map across the welded samples during the feed stage of the weld, a number of probes were placed in strategic positions across the welding area. These probes recorded the temperature at those positions during the footage. Initial a total of eight single point probes were placed on each weld, as shown in Figure 6.13.

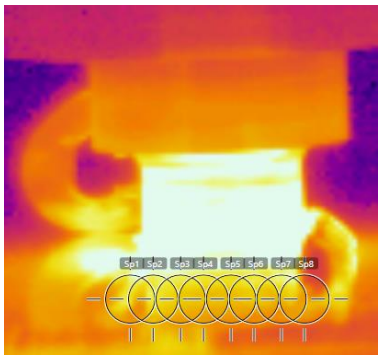

Figure 6.13 – Initial Probe Positions for Thermal Mapping of the Weld

The data obtained from this setup was found to not have suitable repeatability, resolution and nor could the probes be placed in the approximately same positions between different videos. For this reason, an alternative probe placement strategy was used. Three lines of single point probes with line tracking probes overlaid. The three lines were set to achieve the following:

Line 1: To attempt to measure the tool – welding material interface during feed stage.

Line 2: To attempt to measure the temperature of welded material which had just been welded and the presence of the extremely hot weld would not influence the measurement.

Line 3: To attempt to measure the temperature of material which was unaffected by the welding tool. Comparisons between line 2 and 3 would provide an indication of the cooling rate of the welds.

Figure 6.14 shows the placement of the probes and overlaying probes. The placement was whilst at an x5 magnification. The description of each line has been broken down into step form in the figure.

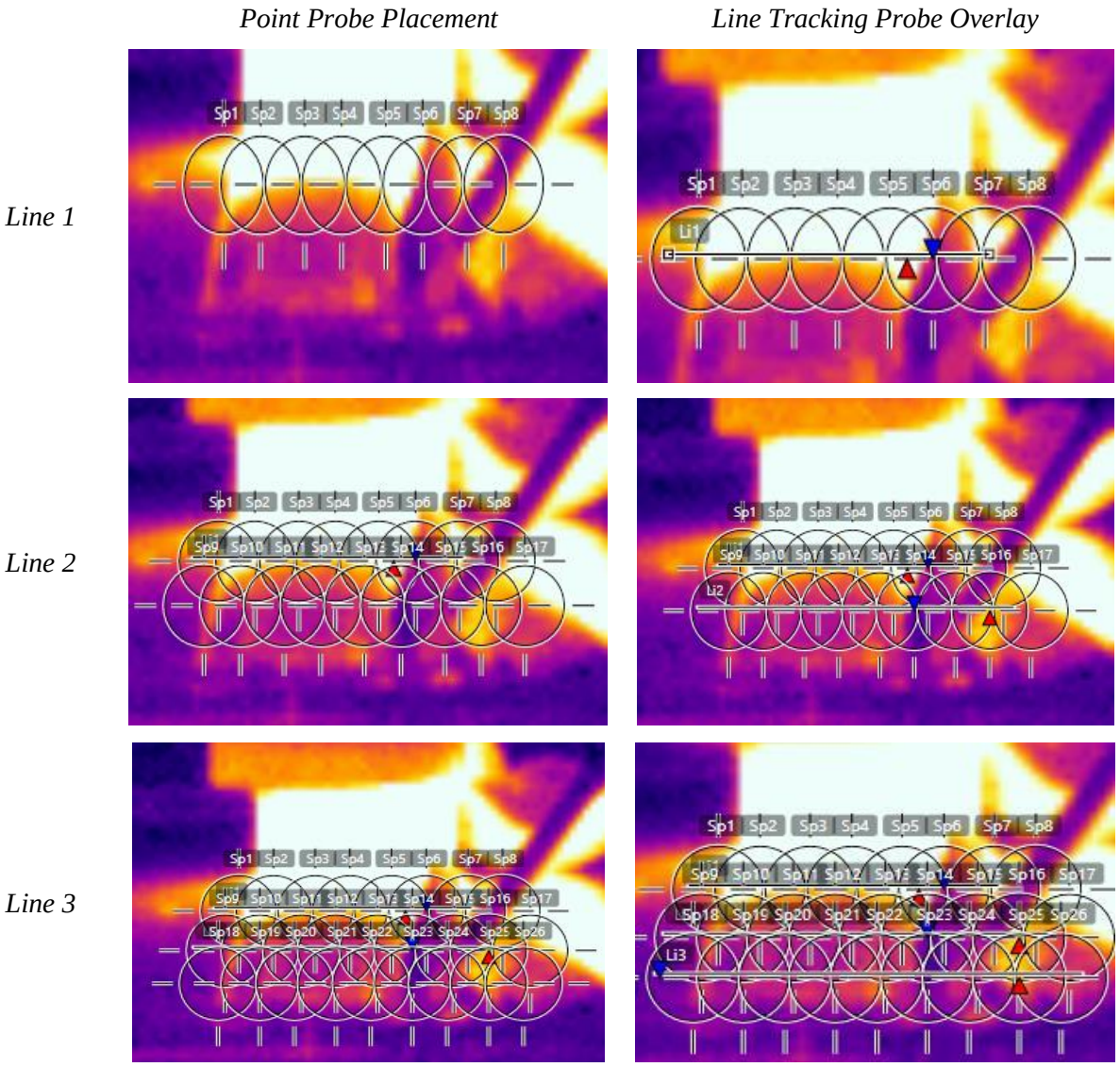

Figure 6.14 - Final Temperature Probe Measurement Positions

Table 6.5 lists the intended/approximated positions of the probes relative to the centre of the weld. The region in which the probes occur has also been indicated. Roughly three probes were placed per side of the weld to measure the surface temperature of the recently welded material. An extra two probes were placed on the retreating side in order to determine the temperature of the forming flash.

Table 6.5 - Approximate Positions of Thermal Probes

	Line 1	Line 2	Line 3	
Probe Number	**Approximate Position of Probe [mm]**	**Approximate Position of Probe [mm]**	**Approximate Position of Probe [mm]**	**Region of Weld**
1	12	10	10	Advancing
2	10	6.67	6.67	Advancing
3	5	3.34	3.34	Advancing
4	0	0	0	Centre of weld
5	-5	-3.34	-3.34	Retreating
6	-10	-6.67	-6.67	Retreating
7	-12	-10	-10	Retreating
8	-14	-13.34	-13.34	Retreating
9	No probe	-15	-15	Retreating

Figure 6.15 shows the output figure obtained from FLIR Tools. The software plots the temperature history of each probe along the length of the footage. Using this output data, it was possible to break up the data into the various regions of the weld.

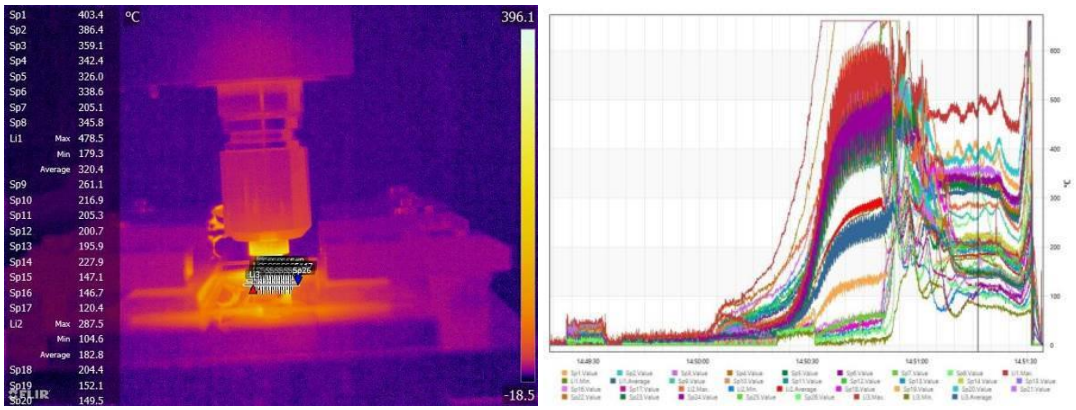

Figure 6.15 – Results of each Temperature Probe

Figure 6.16 shows the temperature history of the central probe in line 2 for both measurement ranges of a 630 RPM and 200 mm/min feed. The various effects of each stage of FSW process can be seen and have been indicated in the figure. During the pin plunge the temperature drops slightly, this drop in temperature was more apparent during the initial dwell period where the temperature drops from 600°C to approximately 350°C, this was attributed to the material being measured becoming plasticised due to the temperature and rotational effects of the tool. This occurrence of material

plasticisation has been noted by multiple researchers in this field [94]. At a number of probes, the temperature during the plunge and dwell stage fell outside of the measurement range for the camera. The temperatures during the feed stage fell roughly into the 100 to 450 °C range. The figure shows the temperature history of probes positioned in roughly the same position.

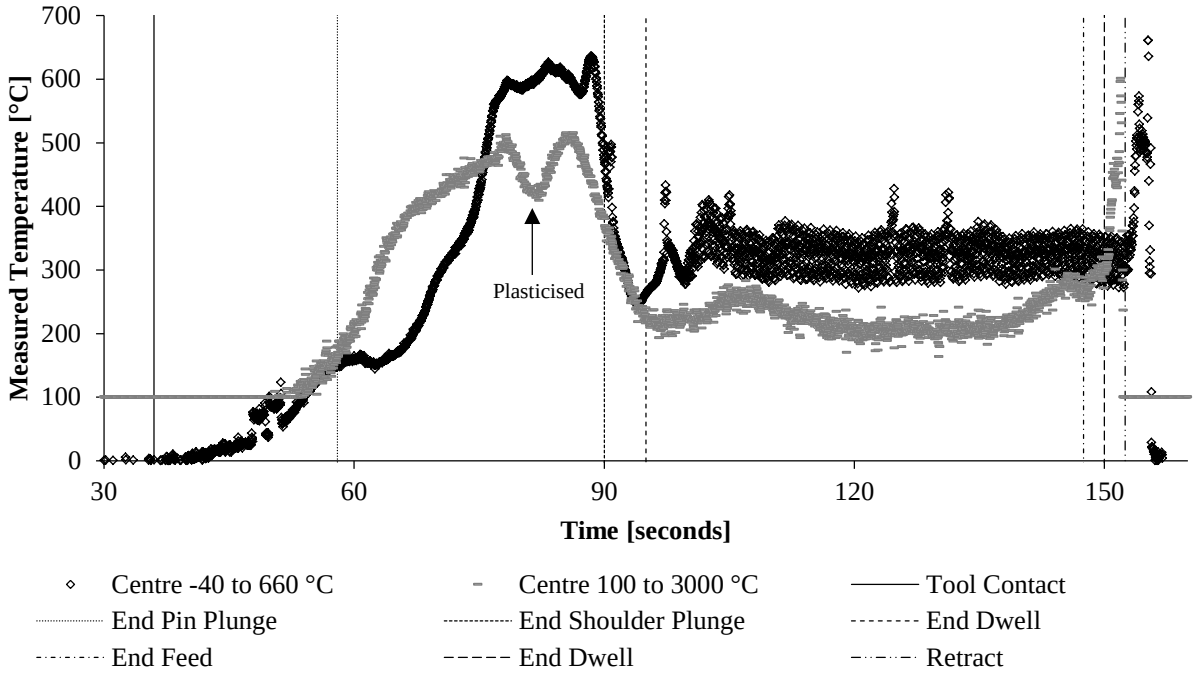

Figure 6.16 - Temperature History at Centre Probe indicating Various Stages of Friction Stir Welding Process

A Matlab script was written in order to batch process a large amount of data produced from the numerous probes used. A copy of the code can be found in the digital Appendix.

The temperature during the feeding stage of the weld was the most important sector. The rough start and end of the feed stage of the weld had to be determined initially before the batch processing could begin. To be as accurate as possible the central probes for each line was plotted in FLIR Tools. By visually matching the start and end of the feed stages in the video to those positions in plotted figures, one can identify the same positions along the figures which had been plotted in Matlab. Figure 6.17 shows the process of identifying the start of feed stage in various processing software packages. This partitioning was completed for each line of probes and every weld. The first line of images identifies the start whilst the second line of images is the classification the end of the feed stage. The third line was the partitioning of the line probe which overlaid the spot probes.

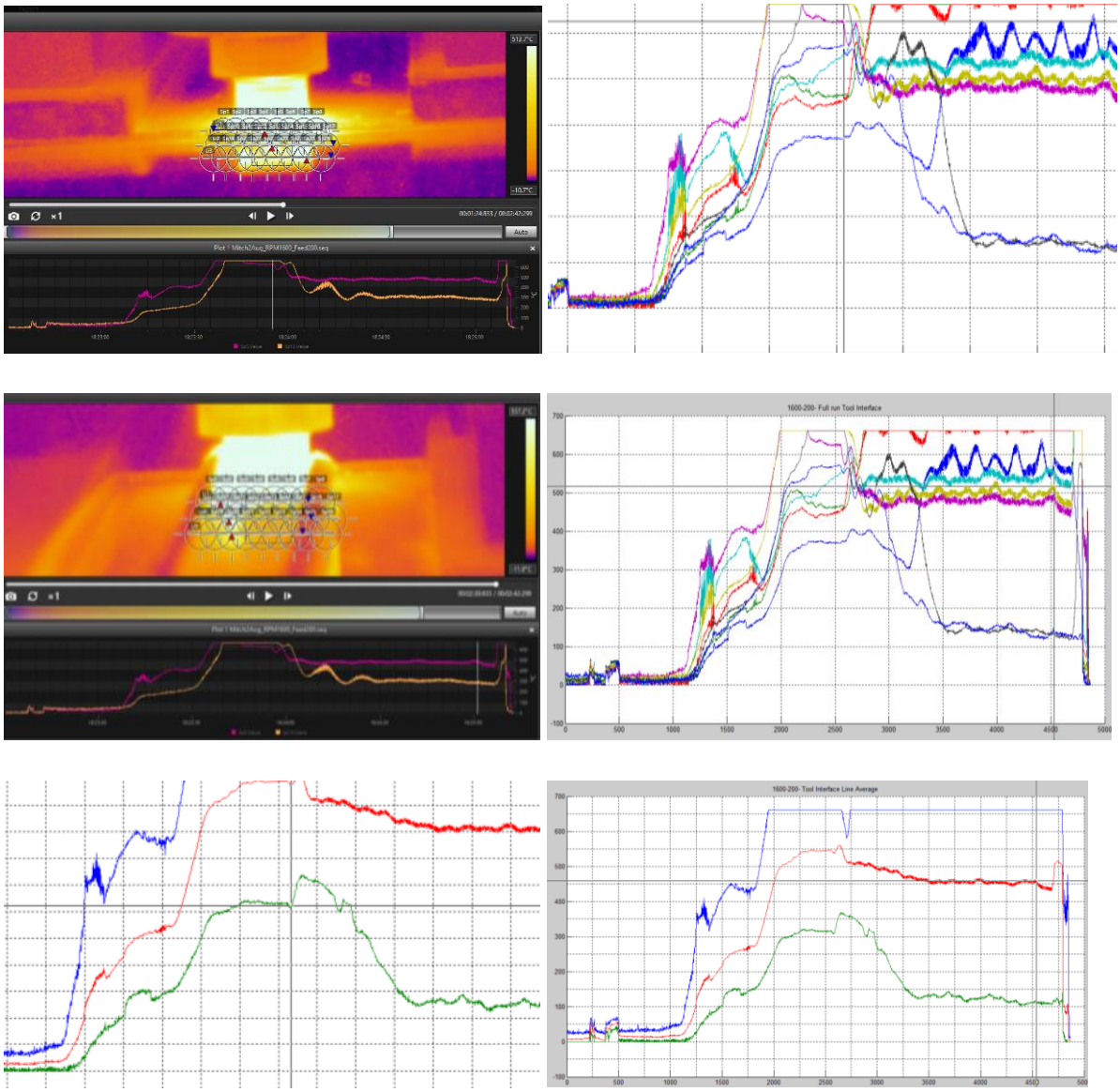

Figure 6.17 – Partitioning of Thermal Data for each Recorded Friction Stir Weld

Using the partitioned data, the code would then search for the highest temperature overall, the highest during the feed stage and would calculate the average temperature during the feed. The average overall temperature for the welding parameter combination was determined by combining the average temperatures at probe positions 5, 0 and -5 mm. These probes were selected as they are just outside of the pin region / nugget region which according to Figure 2.24 were the hottest portion of the weld. Using the temperature history of each probe a thermal surface across the weld against time was produced for each weld.

6.1.4.2 Processed Thermal Data

The various welding parameters sets were processed according to the outlined procedure above. Figure C.4 in Appendix C.2 shows the probe positions, the temperature history of each probe, the

temperature surface over the length of the weld and the temperature surface during the feed stage for the various welding parameter combinations that were investigated.

A close assessment of the temperature profiles shows that each weld had a region in which the temperature tended towards a steady state temperature or a more stable temperature. A study was conducted to determine if there was a large influence in the average temperature if the initial unsteady region was accounted for in the calculation of the average feeding temperature. The average temperature for the two measuring ranges was conducted for two cases. Figure 6.18 provides an example of the regions described:

1. Purely steady state region
2. Full feed, including the portion of the profile from the start of the feed region

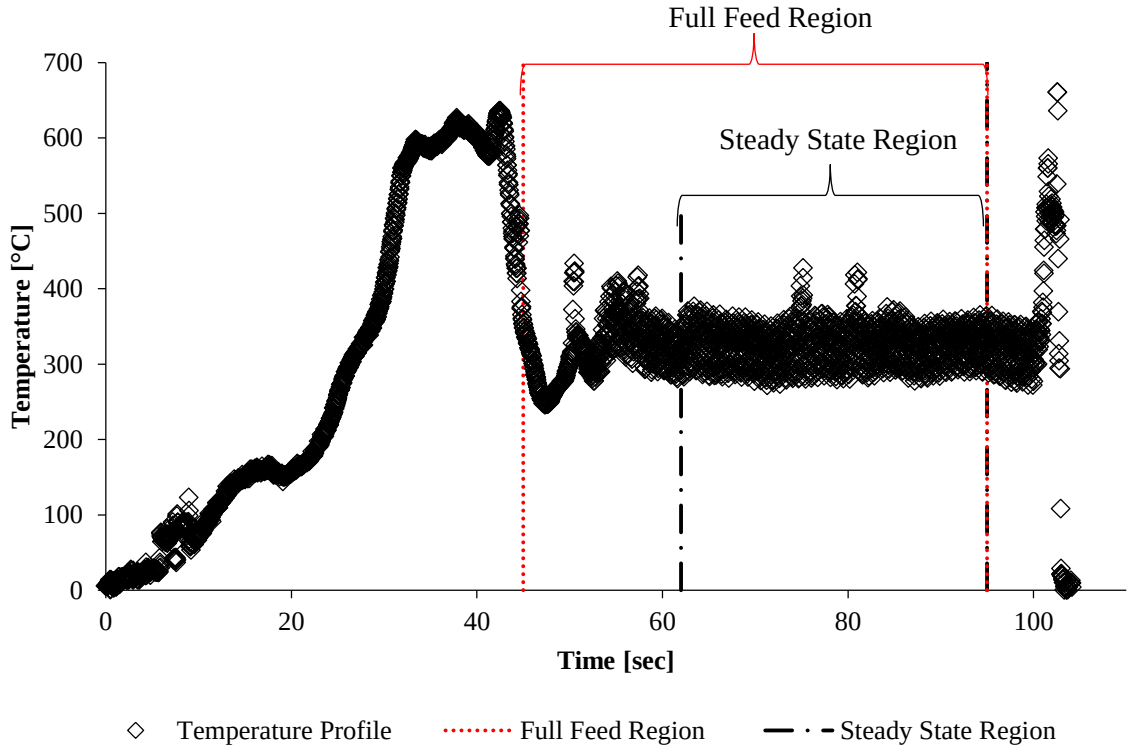

Figure 6.18 - Steady State and Full Feed Regions used in Temperature Calculations

Table 6.6 lists the calculated temperatures for both measuring ranges, along with the difference in temperature and percentage difference between measuring cases in which the data was taken. It can be seen in the majority of parameter combinations, the percentage differences were fairly small. There are some outlying cases were the percentage differences are greater than 5%. The reason for these welds having large variations was due to the step change in temperature between the two regions. The rapid change in temperature causes a significant shift in the average temperatures calculated in the regions. An example of this was shown for the worst case of 14.04% (Measuring range 100 to 3000°C, 1000 RPM- 400 mm/min), see Figure 6.19.

Table 6.6 - Percentage Difference between Thermal Measuring Ranges

Percentage Difference								
Welding Parameters	**0 to 660 °C**				**100 to 3000 °C**			
	Steady State [°C]	**Full Feed [°C]**	**Difference [°C]**	**%**	**Steady State [°C]**	**Full Feed [°C]**	**Difference [°C]**	**%**
630RPM-200mm/min	478.30	482.01	3.72	0.78	435.09	436.80	1.70	0.39
630RPM-400mm/min	337.73	367.07	29.35	**8.69**	354.04	372.56	18.51	**5.23**
630RPM-600mm/min	399.24	429.90	30.66	**7.68**	312.51	324.79	12.28	3.93
800RPM-200mm/min	472.86	476.14	3.28	0.69	460.99	456.71	-4.28	-0.93
800RPM-400mm/min	527.30	529.32	2.03	0.38	274.44	287.89	13.44	4.90
800RPM-600mm/min	427.57	436.39	8.82	2.06	375.35	408.52	33.17	**8.84**
1000RPM-200mm/min	448.37	458.33	9.96	2.22	296.78	300.93	4.15	1.40
1000RPM-400mm/min	443.66	464.70	21.03	4.74	315.10	359.34	44.24	**14.04**
1000RPM-600mm/min	524.80	533.39	8.59	1.64	383.96	393.02	9.06	2.36
1250RPM-200mm/min	475.58	492.84	17.26	3.63	369.04	363.24	-5.80	-1.57
1250RPM-400mm/min	551.58	552.59	1.01	0.18	518.21	520.73	2.51	0.48
1250RPM-600mm/min	522.54	544.74	22.19	4.25	447.03	470.29	23.26	**5.20**
1600RPM-200mm/min	558.11	557.61	-0.49	-0.09	480.51	481.13	0.61	0.13
1600RPM-400mm/min	495.07	499.76	4.69	0.95	494.03	501.34	7.31	1.48
1600RPM-600mm/min	585.70	590.35	4.65	0.79	433.74	462.45	28.72	**6.62**

The welds which had high percentage differences were all welds manufactured with the medium to high feed rates (400 – 600 mm/min). The weld length was approximately 230 mm which results in a feed time of 69 seconds (200 mm/min), 34.5 seconds (400 mm/min) and 23 seconds (600 mm/min). As the welding time was significantly shorter for the fast welds it was extremely difficult to achieve a steady state period in the length of the weld. This may have had a negative effect on the quality of the joints and the repeatability of the welds at the higher feed rates.

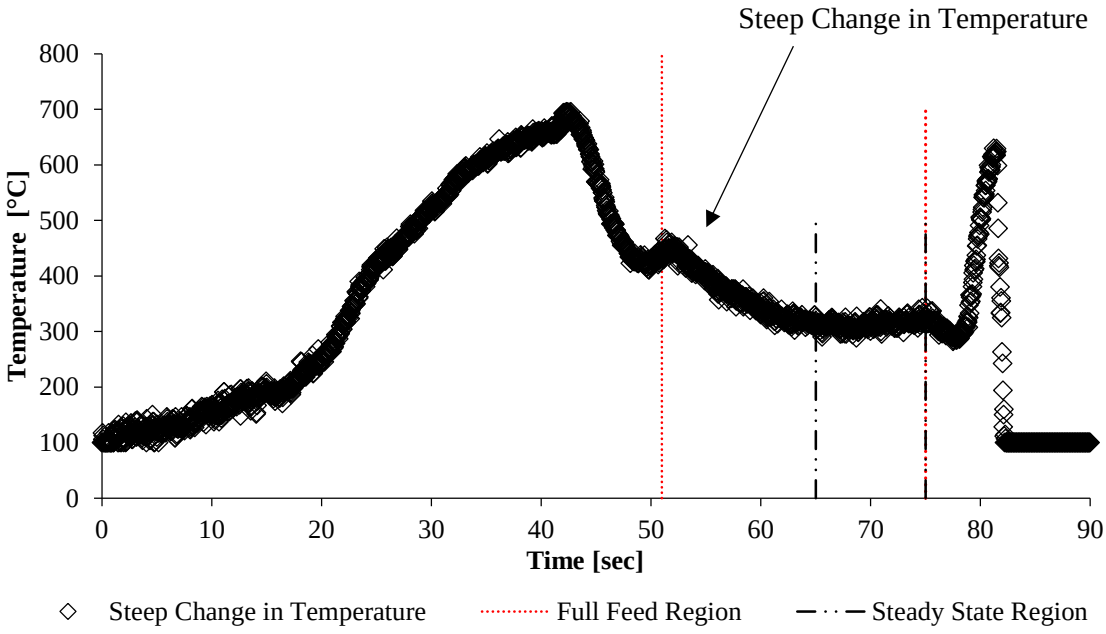

Figure 6.19 - Steep Temperature Change between Full Feed and Steady State Regions

From the data above it was concluded that in general using the average temperature of the steady state weld region was a fair representation of the dynamics of the temperature occurring in the joints during welding. Only two combinations in the 0 to 660-degree measuring regions had welds which exceeded the 5% mark and four cases in the 100 to 3000-degree region. In addition, the first 10 to 30 mm of the weld was also discarded as this region was considered a region of unsteady welding.

Figure 6.20 shows the steady state average temperatures of each parameter set during the feeding stage of the welds. The figure provides the average measured temperature of the three central probes for both measuring ranges as well as the FLIR average line temperature which took into account the fully welded area. This resulted in the value being cooler towards the shoulder edges of the joint. It can be seen that the average temperatures tended to increase with increasing spindle speed, which was to be expected as the higher RPM resulted in more tool to material interaction. There was not a clear indication as to the effect of increasing feed rate besides the fact that generally a feed rate of 200 mm/min resulted in the highest average temperature during the feed. Intuitively, a lower feed rate would result in a higher temperature as confirmed by Figure 2.23. The indication of this fact was not seen in the majority of the results were shown. The reason for this was unclear and it was anticipated

that there were inconstancies in the technique or the equipment used. Alternative methods were not used to verify the data thus further work will need to be conducted to validate this data.

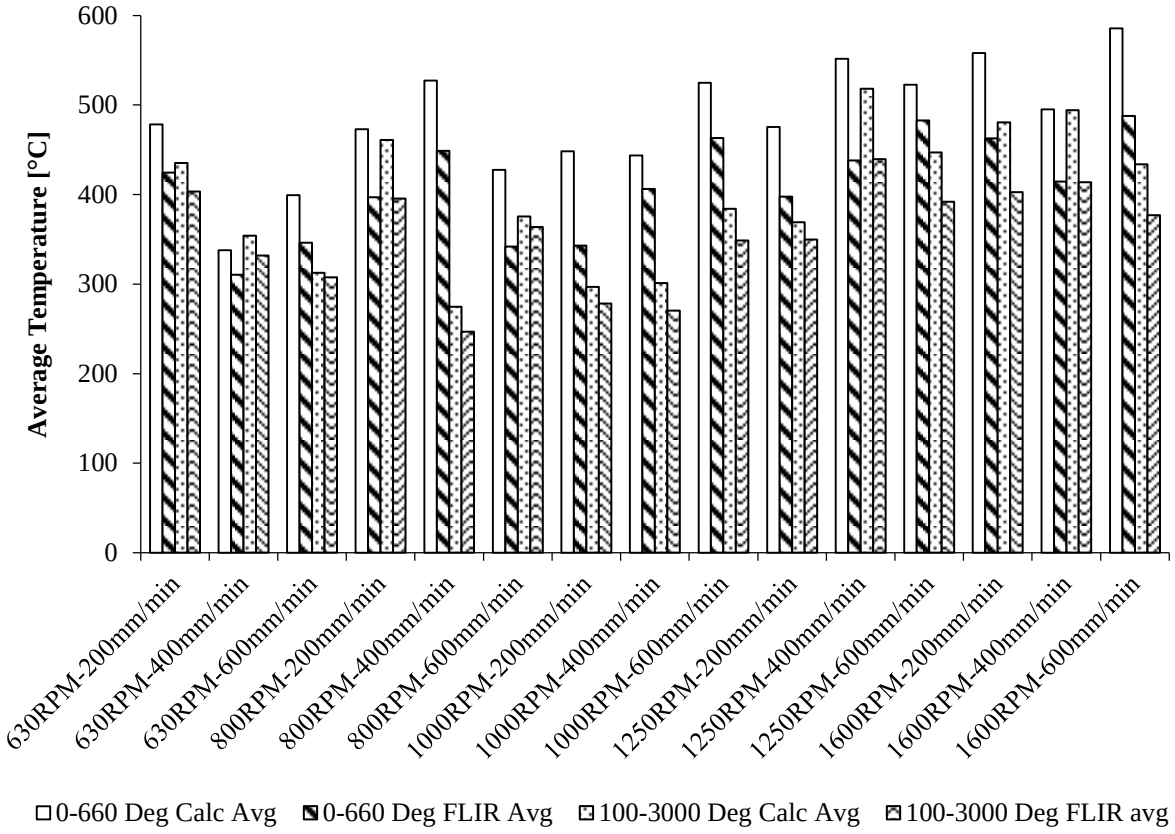

Figure 6.20 - Average Temperature across Thermal Probes and FLIR Average Line Function

The specified melting temperature of the base material was indicated as 555°C. Some of the welds exceeded the melting temperature of the melting temperature of the material. This was not desirable as the point of this welding technique is not to melt the material rather just soften the material. It has been reported that an optimum temperature for FSW was in the region of 80% of the melting temperature. Figure 6.21 provides the percentage of the melting temperature of the average temperature. The calculated averages of the higher welding spindle speeds showed very high percentages. Six welding combinations exceeded 90% of melting temperature with two of the welds manufactured at 1600 RPM being higher than the melting temperature. This was enforced with the large flash formation and the plates sticking to the backing bar in a number of positions along the weld. If one considers the FLIR averages in both ranges these values typically range in the 70 to 90% of the melting temperature range which was desired for successful welding.

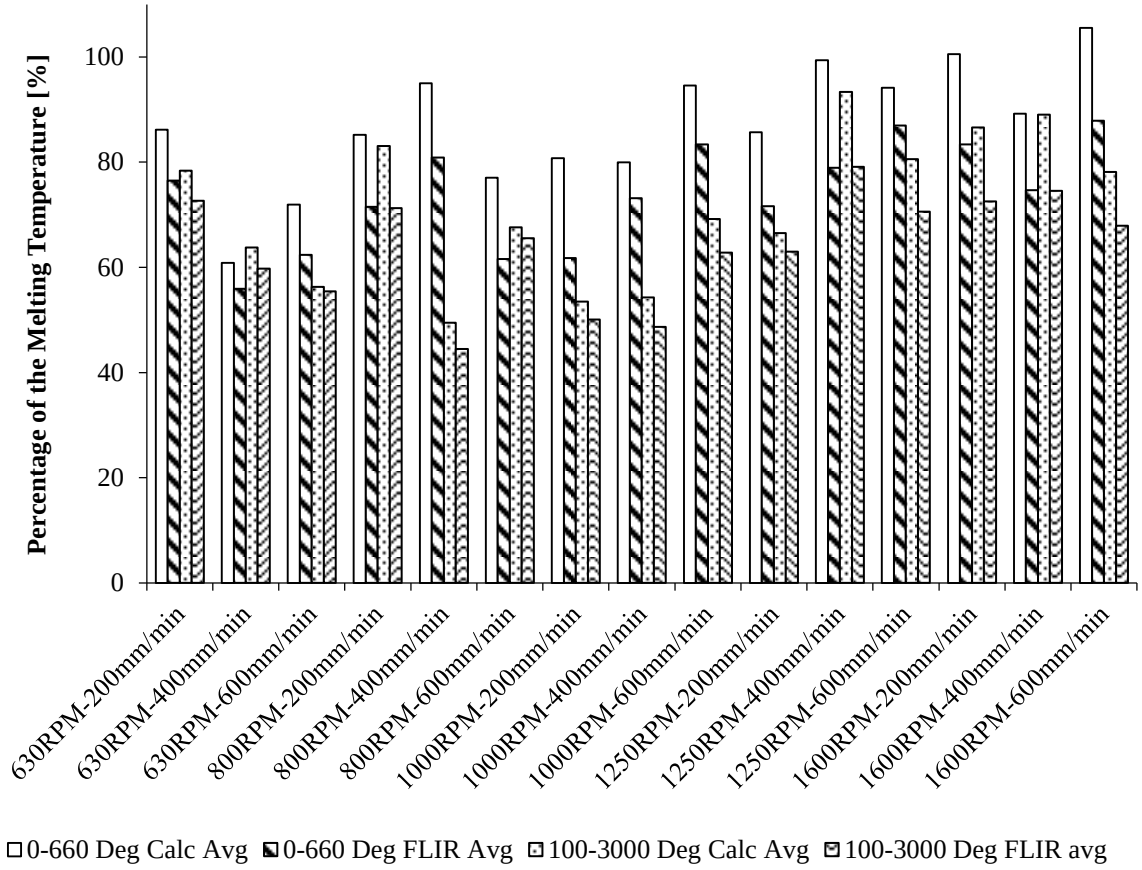

Figure 6.21 - Percentage of Melting Temperature of Base Material

Researchers have shown that the centre of the weld tends to be the hottest region of the weld with the joint cooling towards the edges of the joint. The average temperature per probe across the welds showed that this technique of measuring the temperature with a thermal imaging camera shows that the advancing and central regions are the hottest portions of the joint. The retreating portion of the joint typically followed the trends of the published data shown in Figure 2.24 were the temperature decreased moving away from the centre of the weld. Figure 6.22 illustrates the across weld average temperature distribution for the probes placed at the tool and material interface (plots on the left hand side of the figure) and probes placed along the next line (plots on the right hand side), shown in Figure 6.14. The 0 to 660 °C measuring range was selected to be presented as the range encompasses all temperatures expected within the feed stage of the process.

630 RPM all feed rates

(Tool & Material Interface)

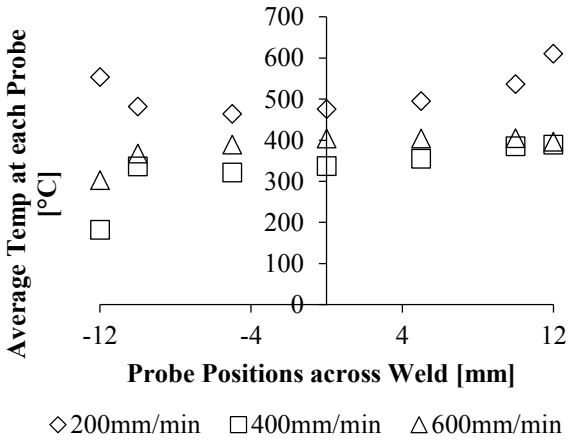

(Next Line of Probes)

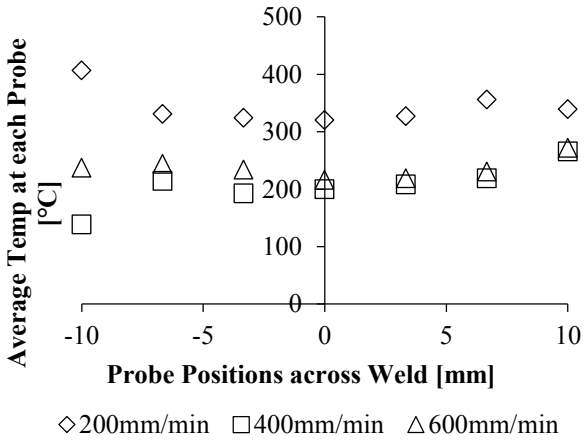

800 RPM all feed rates

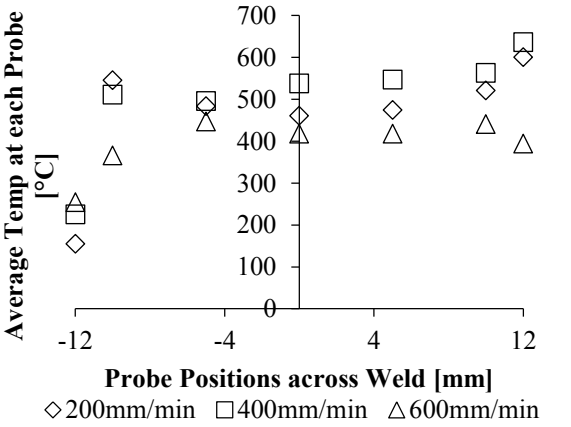

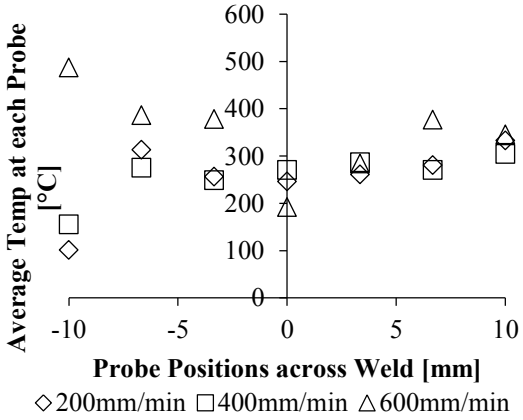

1000 RPM all feed rates

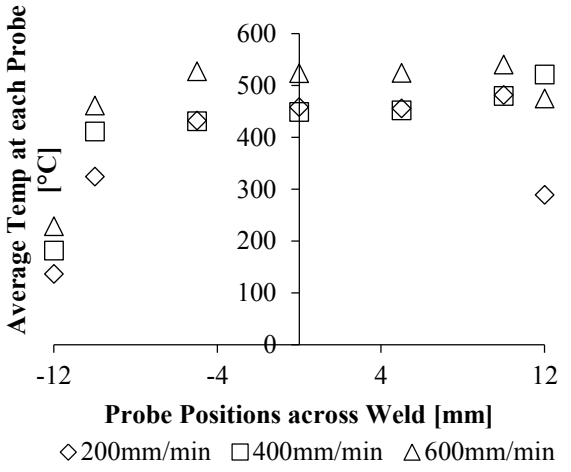

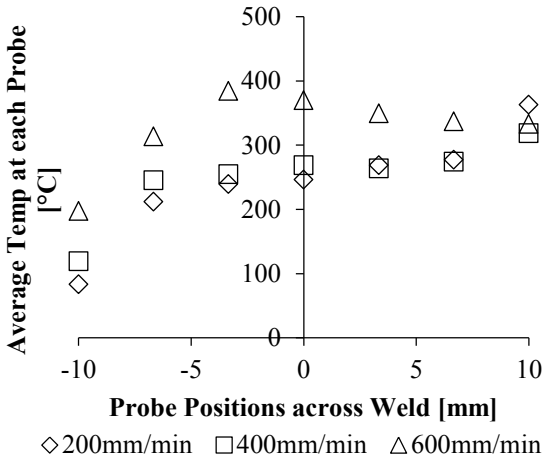

1250 RPM all feed rates

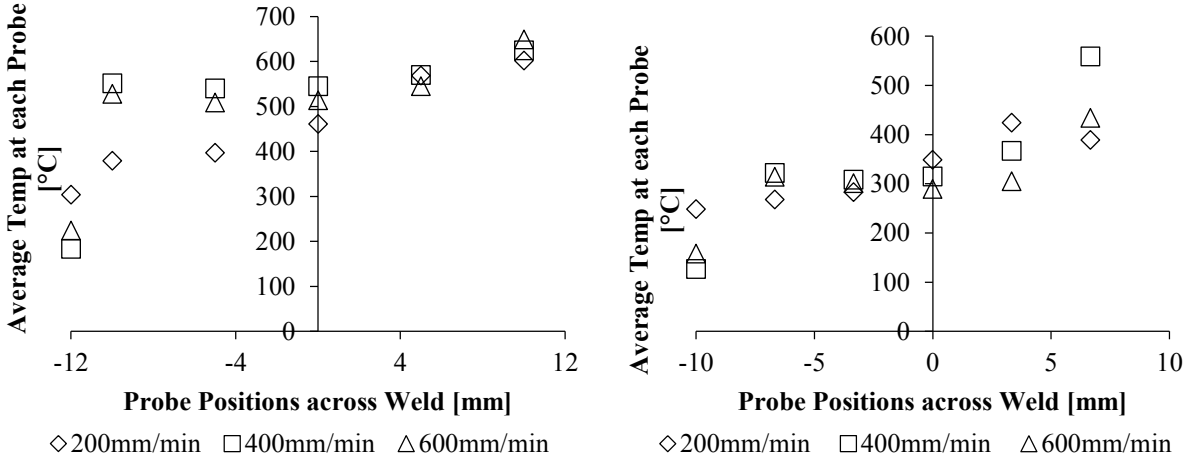

1600 RPM all feed rates

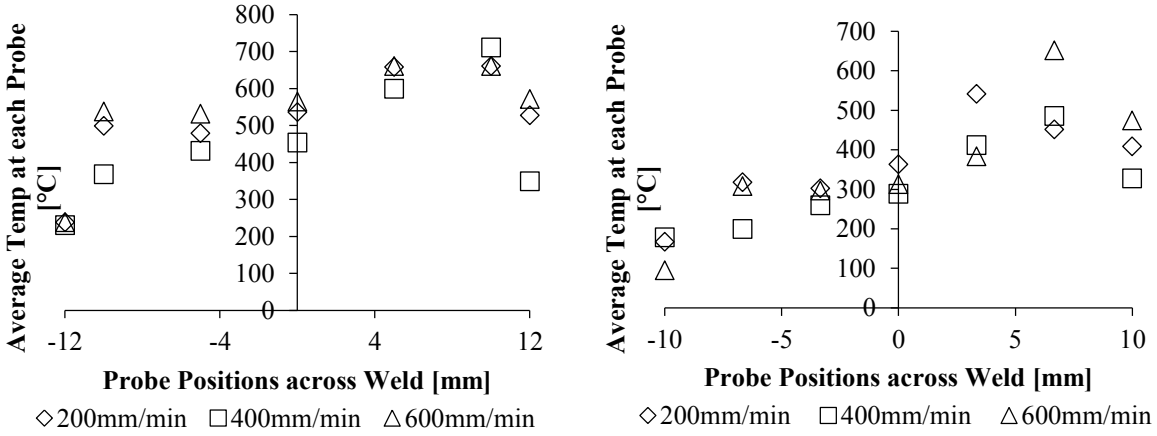

Figure 6.22 – Average Temperature Distribution across the First and second line of Probes for the 0 to 660 Degree Measuring Range

All weld parameter combinations which had a feed rate of 200 mm/min have been overlaid with the data presented in Figure 2.23 to allow for the comparison of the trends. The presented data was produced at a number of spindle speeds with a feed rate of 120 mm/min in the working material of AA AA6061-T6 [31]. The temperature probes within 5 mm of the centre of the weld tended to correlate very well with the data present by Tang [31].

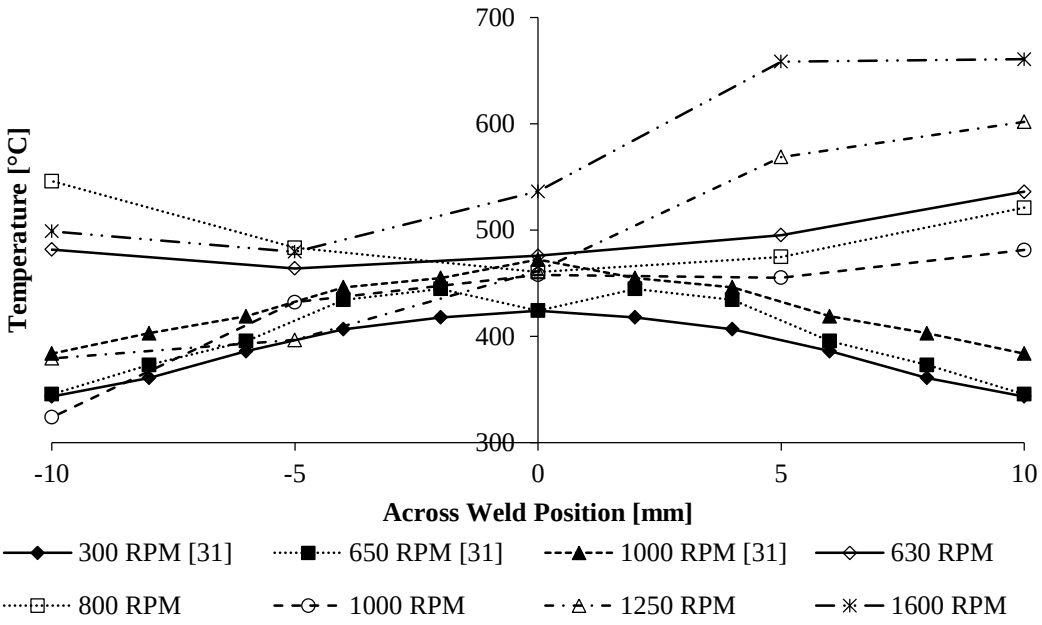

Figure 6.23 - Comparison of Temperature Distributions of AA AA6061-T6 at Similar Feed Rates

Tang stated that the maximum temperature values at each probe were equal on both sides of the weld. They did not state exactly the position in the thickness direction were the values were measured but the welding force was controlled. Unlike Tang the symmetrical temperature profile on both sides of the welds were not symmetrical as it would be expected. The differences in welding material may have been a factor but both materials are 6xxx series Aluminium thus variations in the material may not be a large effecting factor. Other potential discrepancies in the symmetry of the profiles may have been due to two possible reasons:

1. The force was not kept constant during welding and thus, there could have been variations in the force with the rotation of the tool. Reference to Figure 6.2.A and B shows a cyclic change of the lateral and longitudinal forces during the feeding stage. This implies that different regions of the weld may have been under different magnitudes of force.
2. In some cases, unequal material cooling rates across the joint may have caused a variation in the temperature measurements at the respective probes. Figure 6.24 illustrates the concept of the unequal or unequal temperature recognition of the thermal camera by showing a number of snapshots of two welds created under different spindle speeds and presented in Figure 6.23. The first set of images was of the weld parameter combination of 1000 RPM and 200 mm/min, it was clear that there were no distinguishable hot zones which trailed the tool during welding. The second set of images was of the welding combination 1600 RPM and 200 mm/min, a very clear region on the advancing side of the weld of higher temperature was evident along the weld. The position of the red arrow of the FLIR line tool remained on the advancing side of the joint for both cases which correlate to the data presented about.

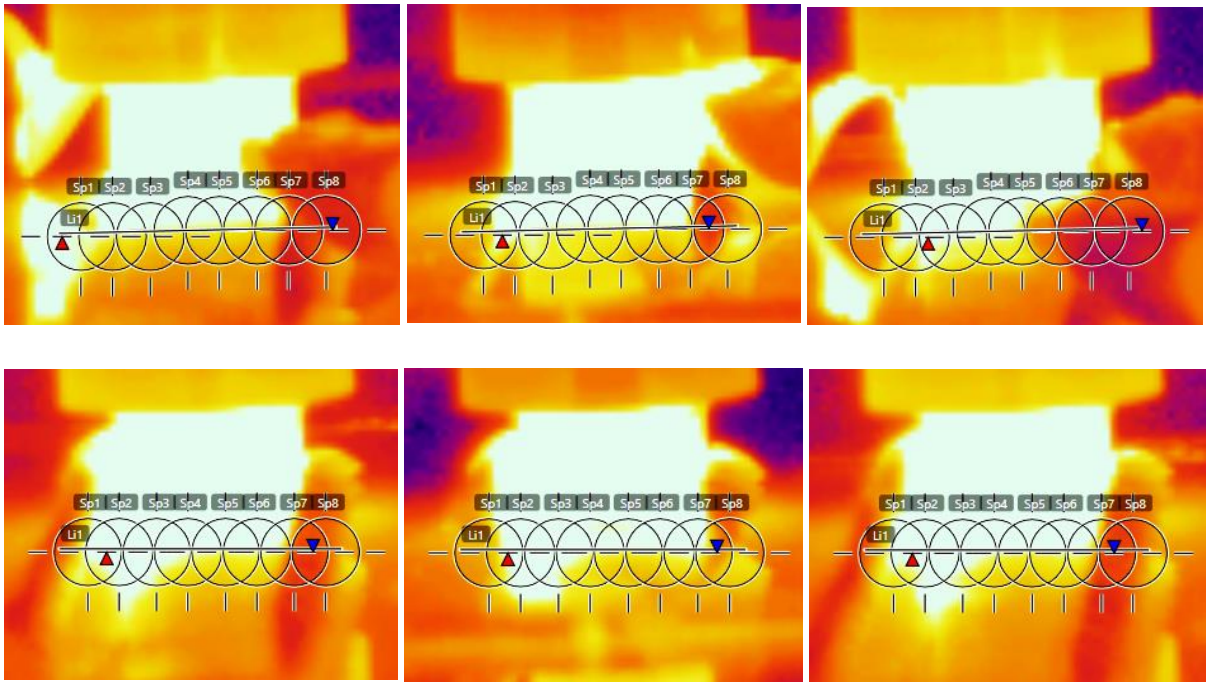

Figure 6.24 - Unequal Cooling across the Joint during the Welding Process

Using the measured temperature data at the approximate locations of the probes and the welding time, thermal temperature history maps were created to show an overall temperature mapping during welding. These plots were found to be a necessity as previous data provided an overall averaged value of the temperature at the individual probes. Figure 6.25 illustrates the full thermal map of the welds manufactured at a 1250 RPM and varying feeds (200 mm/min, 400 mm/min and 600 mm/min). From the surfaces, it was evident that highest temperatures occurred during the initial and end dwell periods, as expected. The temperature during the feed stage of the process tended to be fairly constant throughout the full length of welding.

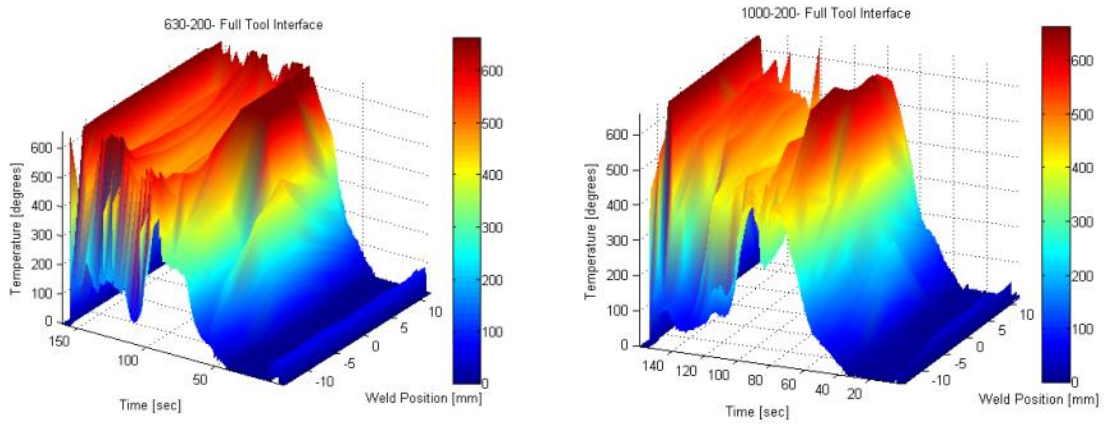

Figure 6.25 - Thermal Map for Full Welding Process for Selected Parameter Combinations

All welding parameter combinations achieved very high temperatures, often exceeding the melting temperature of the working material, which was not desirable but allowed for the tool to build up

sufficient thermal loading as not to cause damage to the tool. The feeding portion of the process was of most concern as the occurrence of unsteady temperature may have led to unsteady welding which would negatively affect the assumption of assuming exact/near the similar joint structure, mechanical properties and defect formation over the full length of the joint for a constant set of parameters. Figure 6.26 provides the 3D surface plots of the thermal variation during the numerous welds.

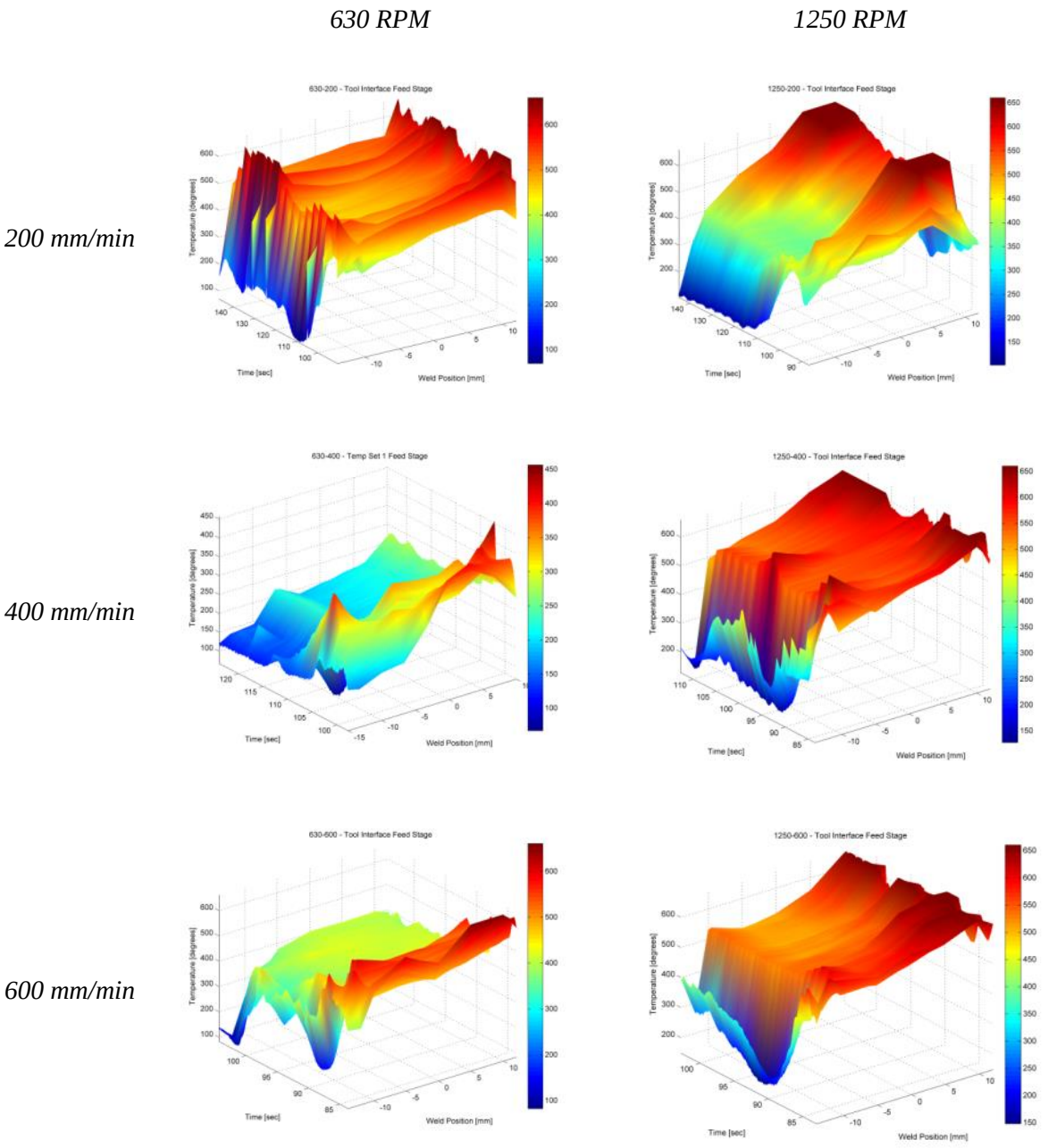

Figure 6.26 – 3D Temperature Maps during Feed Stage of Friction Stir Welding with select parameter combinations

Figure 2.23 showed how constant controlled normal forging force leads to an approximately linear increase in temperature with increasing welding rate for constant spindle speed. The figure also showed that lower welding rates resulted in higher forging forces in uncontrolled normal force FSW but still maintain the increasing temperature with welding rate. The uncontrolled force FSW did not

exhibit the same linear increase but rather a trend of a plateau or small increase in temperature with increasing feed rate. All experimental spindle speeds average weld temperatures have been plotted to show that the average welding force increases with welding rate, the average force for the 630 and 1600 rpm welds have been indicated as the parameters are closest to the published data. The lower rotational speeds showed signs of increasing temperature with increasing welding rates whilst the higher speeds tended to exhibit similar plateaued/constant temperature for increasing welding rates. The variation in the magnitude of the welding forces was expected to be caused by a difference in the size and geometric profile of the welding tools.

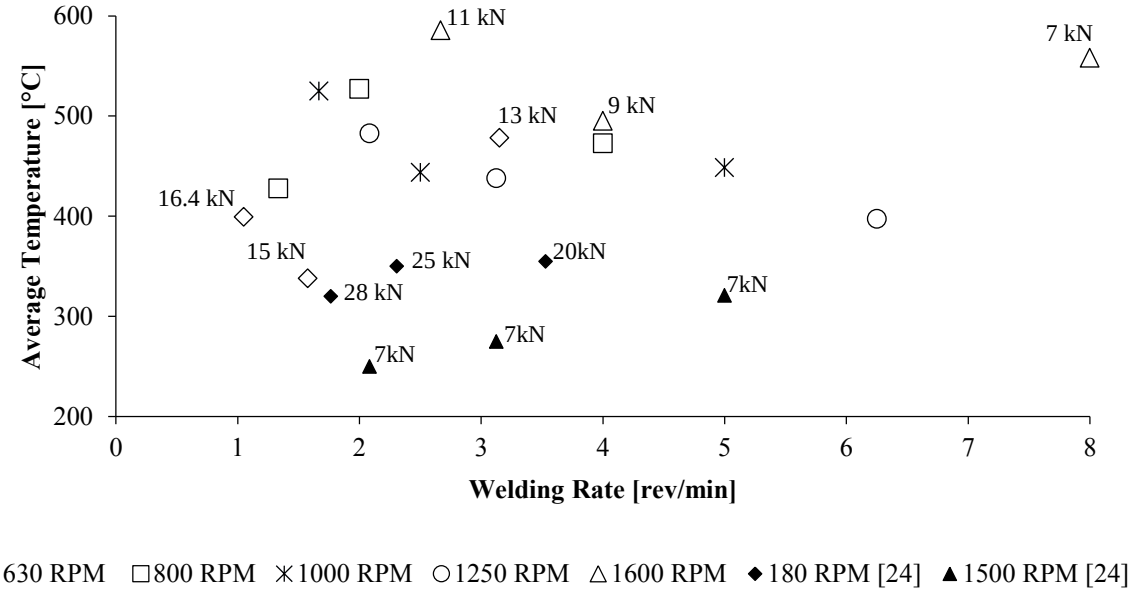

Figure 6.27 - Average Forging Force and Welding Temperature Distribution

It has been shown that FSW parameters, tool design, welding temperature and forging force are directly linked to one another. Figure 6.28 illustrates a number of weld parameter combinations normal force and temperature profiles (central thermal probe) during the joining process. In all cases, the rate of increase in temperature was extremely similar to the rate of increase in force. Local maximums in the thermal profiles lead to a local decline in the force, which was to be expected as the higher temperature lowered the yield strength of the material. These figures showed that monitoring of either force or temperature could be used as a reflection of what may be occurring in either of these parameters. What must be noted was the fact that although the temperature during the feed stage ranged from 500 to 600 °C for all presented profiles the magnitude of the force varied considerably. This implies that the temperature needs to be considered across the entire joint.

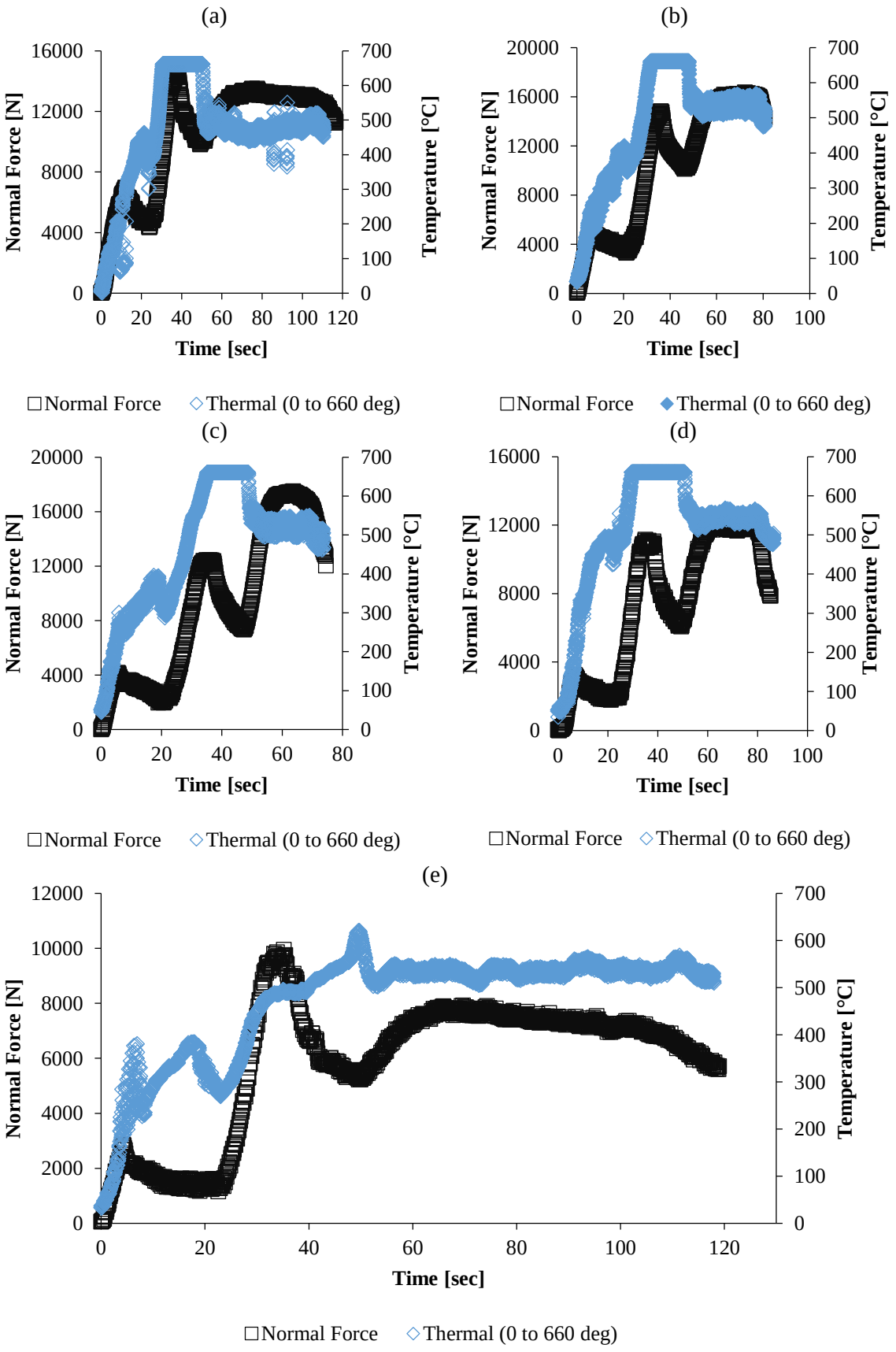

Figure 6.28 – Normal Force and Central Temperature Profiles a) 630 rpm – 200 mm/min, b) 800 rpm – 400 mm/min, c) 1000 rpm – 600 mm/min, d) 1250 rpm -400 mm/min, e) 1600 rpm – 200 mm/min

Figure 6.29 provides the relationship of the welding rate, welding temperature, average and maximum forging force. The plotting technique required that the forging force was placed as an output of the welding rate and the temperature and thus has specified the colour distribution of the figures according to the highest magnitude of the force. In both cases and as illustrated previously, the highest welding forces, lowest temperatures were achieved during the lowest welding rates.

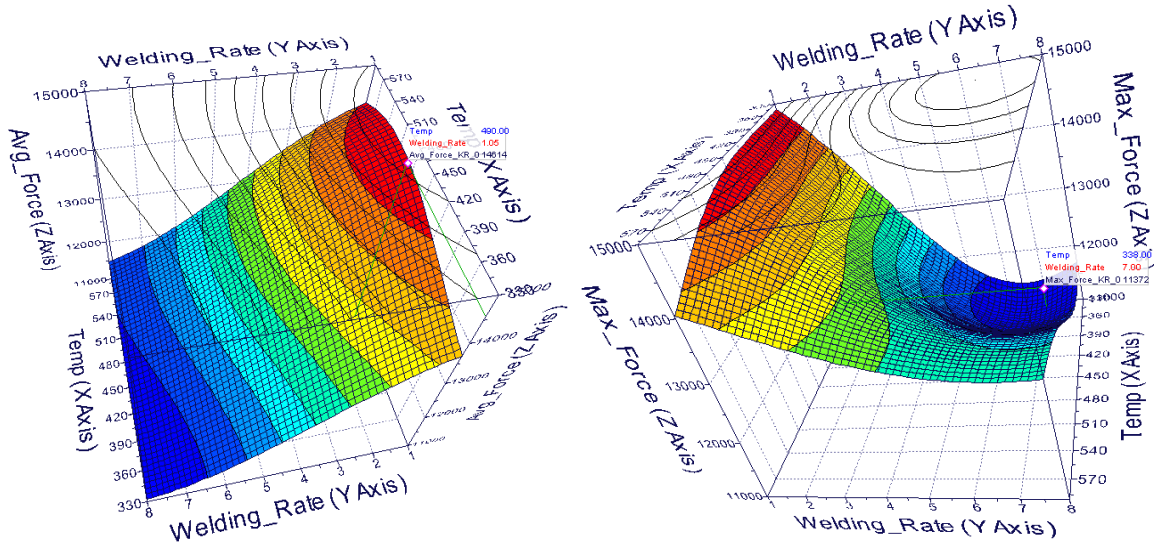

Figure 6.29 – Variation of Welding Force due to Thermal and Welding Rate variations a) Average Forging Force b) Maximum Forging Force

6.1.4.3 Conclusion

From the results presented in this section the following can be concluded:

1. A secondary method of measuring temperature needs to be used to validate thermal readings obtained using a thermal camera.
2. Lower feed rates allowed for much longer welding time which allowed for a steady state welding conditions to be achieved faster and create more length of weld under these conditions.
3. There was a good correlation between the temperature measured in the central region of the joint and that of published work.
4. The parameter and tool combinations resulted in welding temperatures which ranged in the region of 60 to 100 percent of the melting temperature of the working material.
5. This technique did not indicate a linear increase in temperature due to feed rate but overall an increase in spindle speed resulted in an increase in welding temperature.
6. There was an extremely good correlation between the force and temperature distributions. In that, the plots matched one another almost perfectly.
7. An increase in welding rate typically resulted in an increase in temperature and a reduction in force.

6.1.5 Friction Stir Welding Defect formation due Process Parameter Combinations

It is well established that numerous defects are formed during FSW with changing parameters, this was discussed in section 2.3.4. The heat generation and forging force are the dominate factors in the formation of these defects. The forging force and welding temperature have been shown to be directly linked to the selection of the parameters. A number of undesirable defects were observed on closer inspection of the macro and micro structure of the joints created with varying welding parameters.

6.1.5.1 Large amount of Flash Formation

Ribbon flash formation has been shown in research to be a defect which is formed due to the high tool rotational speeds and moderate feeds. This combination of parameters leads to a higher welding rating with high welding temperatures being associated with the weld. These high temperatures thermally soften the working material sufficiently that it makes material movement extremely easy thus fair amounts of material is expelled from the side of the tool in a ribbon-styled fashion during welding. This material, unfortunately, is removed from the thickness of the joint which does reduce the strength of the joint due to the reduced thickness of the weld. Table 6.7 shows an overview of each full length of the weld and a closer view of the end portion of the various welds.

Table 6.7 – Flash Formation due to Friction Stir Welding Parameter Variations

Parameters	Images
Spindle Speed: **630 RPM** Feed Rate: **200 mm/min** Welding Rate: **3.15 rev/mm** **Note:** Constant flash formation on the retreating side of the weld.	
Spindle Speed: **630 RPM** Feed Rate: **400 mm/min** Welding Rate: **1.575 rev/mm** **Note:** Fair amount of flash formation within the first half length of weld then reduced to the minimum amount on retreating side.	
Spindle Speed: **630 RPM** Feed Rate: **600 mm/min** Welding Rate: **1.05 rev/mm** **Note:** Fair amount of flash formation within the quarter length of weld then reduced to the minimum amount on retreating side.	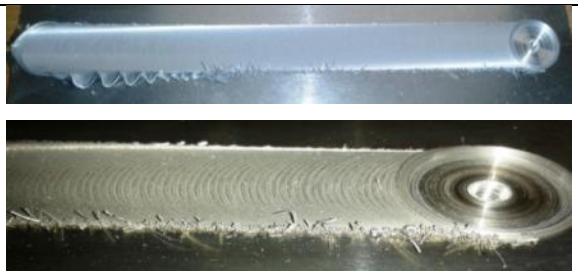

Spindle Speed: **800 RPM** Feed Rate: **200 mm/min** Welding Rate: **4.00 rev/mm** **Note:** Constant flash formation on the retreating side of the weld.	 
Spindle Speed: **800 RPM** Feed Rate: **400 mm/min** Welding Rate: **2.00 rev/mm** **Note:** Constant flash formation on the retreating side of the weld. Tended to reduces slightly over the length of weld.	 
Spindle Speed: **800 RPM** Feed Rate: **600 mm/min** Welding Rate: **1.33 rev/mm** **Note:** Fair amount of flash formation within the quarter length of weld then reduced to the minimum amount on retreating side.	 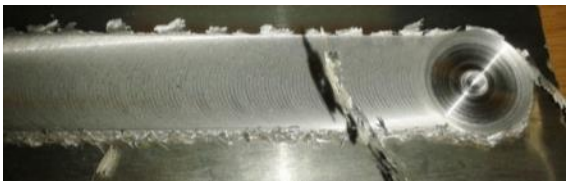
Spindle Speed: **1000 RPM** Feed Rate: **200 mm/min** Welding Rate: **5.00 rev/mm** **Note:** Constant flash formation on the retreating side of the weld.	 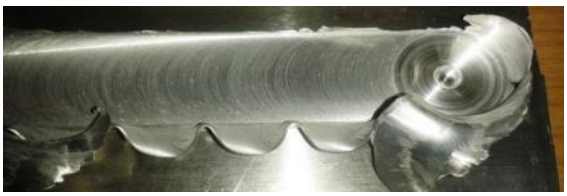
Spindle Speed: **1000 RPM** Feed Rate: **400 mm/min** Welding Rate: **2.50 rev/mm** **Note:** Constant flash formation on the retreating side of the weld.	 
Spindle Speed: **1000 RPM** Feed Rate: **600 mm/min** Welding Rate: **1.67 rev/mm** **Note:** Fair amount of flash formation within the quarter length of weld then reduced to the minimum amount on the retreating side.	 

Spindle Speed: **1250 RPM** Feed Rate: **200 mm/min** Welding Rate: **6.25 rev/mm** **Note:** Constant flash formation on both sides of the weld.	 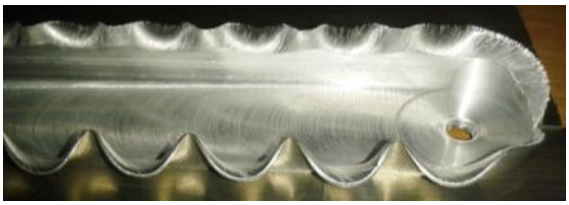
Spindle Speed: **1250 RPM** Feed Rate: **400 mm/min** Welding Rate: **3.125 rev/mm** **Note:** Constant flash formation on the retreating side of the weld.	 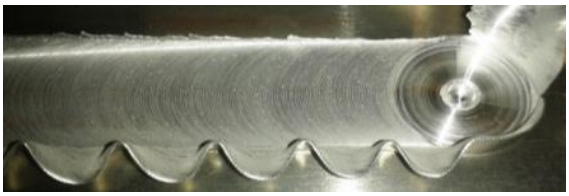
Spindle Speed: **1250 RPM** Feed Rate: **600 mm/min** Welding Rate: **2.08 rev/mm** **Note:** Constant flash formation on the retreating side of the weld. Flash formed on advancing side within the first quarter of the weld length.	 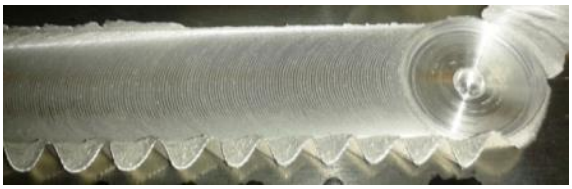
Spindle Speed: **1600 RPM** Feed Rate: **200 mm/min** Welding Rate: **8.00 rev/mm** **Note:** Constant flash formation on both sides of the weld.	 
Spindle Speed: **1600 RPM** Feed Rate: **400 mm/min** Welding Rate: **4.00 rev/mm** **Note:** Constant flash formation on both sides of the weld.	 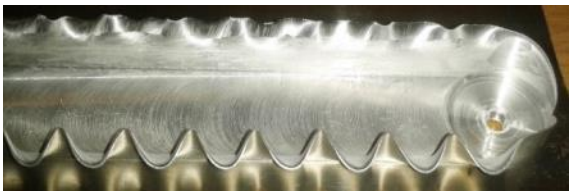
Spindle Speed: **1600 RPM** Feed Rate: **600 mm/min** Welding Rate: **2.67 rev/mm** **Note:** Constant flash formation on both sides of the weld.	 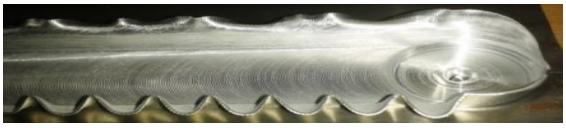

Vilaça suggested three ranges of welding rate magnitudes which roughly correlated to the temperature of the joints [10] the ranges are as following:

WPR < 2 – Cold temperature weld

WRP 2 to 4 – Intermediate temperature weld

WPR > 4 – Hot temperature weld

The formation of the flash correlated well to the three ranges in that all welds manufactured under a welding rate of 2 revs/mm did not produce constant flash which implies a cooler weld. Welding rates between 2 and 5 rev/mm produced fairly constant flash on the retreating side of the weld, this correlated well with an intermediate temperature range. Likewise, all welds, including the outlying weld of 1600 rpm -600 mm/min, manufactured with welding rates exceeding 5 revs/mm resulted in flash forming on both sides of the welds, indicating higher hot welding temperatures. Table 6.8 summarizes the data present in the figure as different welding rates resulted in varying amounts of the flash formation. The limit of 4 rev/mm needed to be increased to 5 revs/mm.

Table 6.8 - Correlations between Welding Temperatures, Welding Rate and Flash Formation

Condition	WPR Range	Flash Formation
Cold	<2	Inconsistent amounts of flash formations along the joint. Tends to reduce along the weld. All flash deposited on the retreating side of joint.
Intermediate	2 - 5	Constant flash formation along the full length of the joint on the retreating side of the weld.
Hot	>5	Constant formation along both sides of the joint.

6.1.5.2 Microstructure of the Friction Stir Welded Joints

As discussed in section 2.3.4, a number of internal defects can form due to the variation in the FSW parameter combination. Figure 6.30 provides the etched microstructure of the investigated FSW parameters. The advancing side of the joints have all been placed on the left hand side of the images. Due to the length of the joints, the images had to be taken in a number of segments and spliced together to form a complete image of the microstructures. The etchant used did not fully reveal the complete microstructure in all the images. In most cases, the typical FSW microstructure of the nugget, TMAZ and HAZ zones were distinguishable. The nugget regions were made up of the typically onion rings structure, seen by many researchers. An asymmetric flow arm originating from the advancing side of the weld could generally be seen in all the images. The revealed nugget region tended to be positioned closer to the advancing side of the joint for all welding parameter

combinations. The TMAZ on the retreating side of the joints tended to be slightly larger than those on the advancing side. The black spots on a number of the images are not wormholes or internal voids but rather dust that had collected and could not be removed without damaging the surface of the sample. All parameter combinations produced joints which did not have internal defects such as worm holes and voids. Further investigation would be required to confirm this but the 630 RPM 200 mm/min joint indicated signs of nugget collapse or improper formation of the stirring region, this was seen in the slightly lighter region were the TMAZ tended to encroach on the region of the joint were the nugget should have formed. The images indicate that the hotter welds or lower welding rates tended to create joints with a greater formation of the respective regions of the FSW joint and larger more defined TMAZ and smaller nugget regions.

630 RPM 200 mm/min

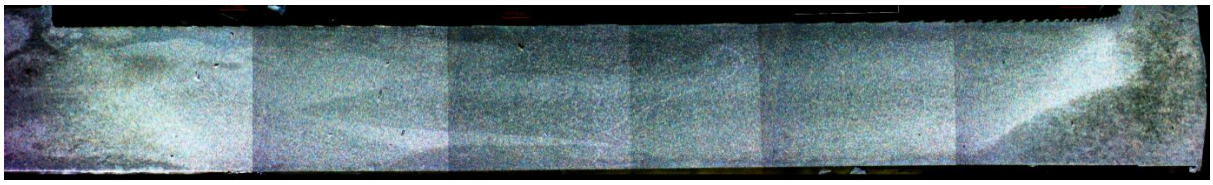

630 RPM 400mm/min

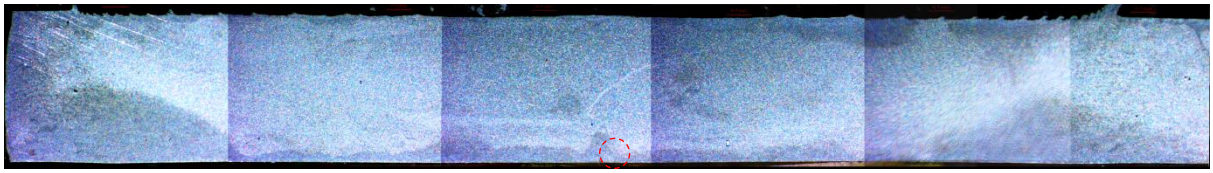

630 RPM 600 mm/min

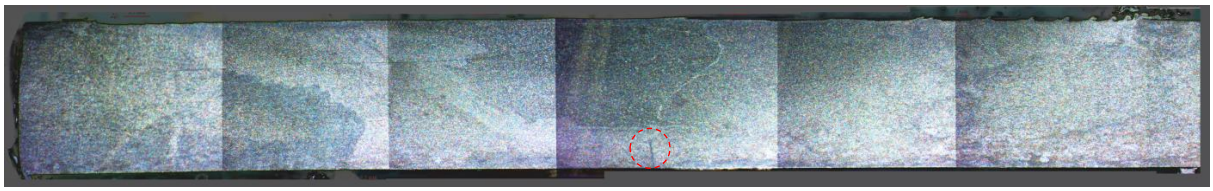

800 RPM 200 mm/min

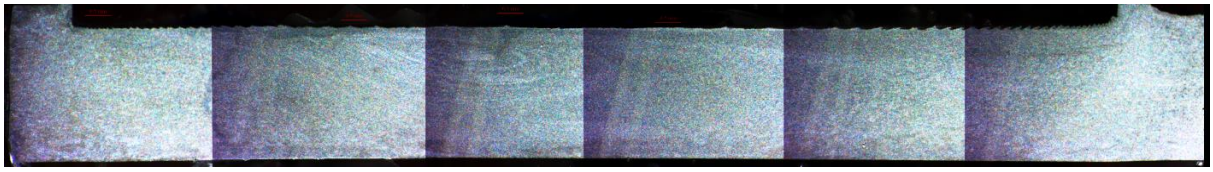

800 RPM 400 mm/min

800 RPM 600 mm/min

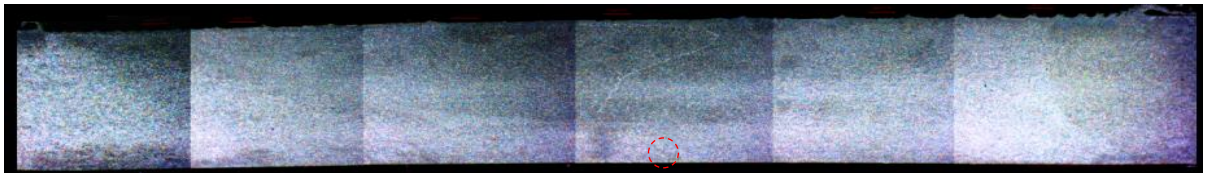

1000 RPM 200 mm/min

1000 RPM 400 mm/min

1000 RPM 600 mm/min

1250 RPM 200 mm/min

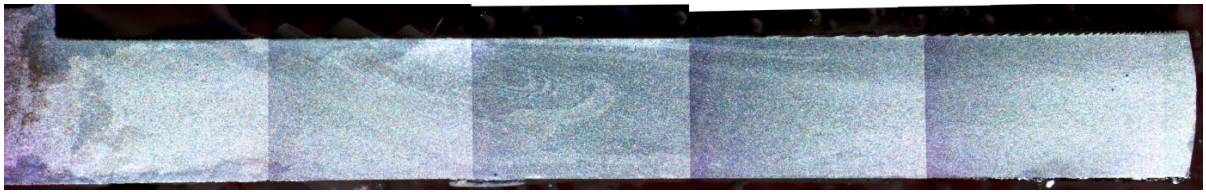

1250 RPM 400 mm/min

1250 RPM 600 mm/min

1600 RPM 200 mm/min

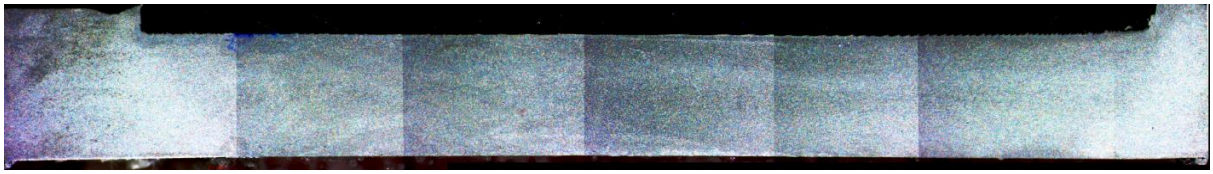

1600 RPM 400 mm/min

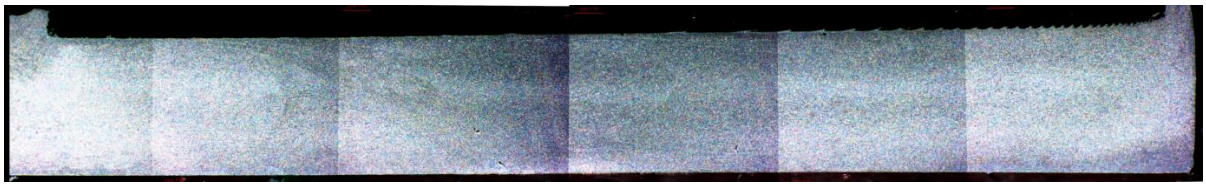

1600 RPM 600 mm/min

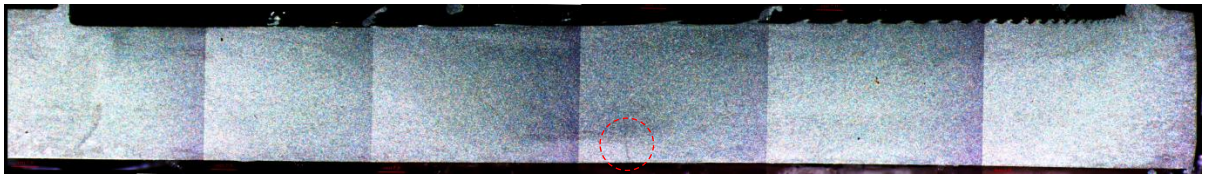

Figure 6.30 - Microstructure of Friction Stir Welded Joints manufactured with numerous Parameter Combinations

The only internal defect that was seen within the joints was the formation of Lack of Penetration (LOP) or Kiss bonds originating from the root surface of the joints. These defects can be clearly seen within the dotted circles of 630 RPM - 600mm/min, 1000 RPM – 400 mm/min, 1250 RPM – 600 mm/min and 1600 RPM – 600 mm/min joints. On average, the joints manufactured with a feed rate of 200 mm/min were the only joints that were free of all defects including LOP and kiss bonds. The worst cases of the defect presented itself as fully formed crack like defect which originated at the root surface and proceeded through the lower band of the TMAZ (the region below the nugget) to the start of the nugget zone. Figure 6.31 provides a number of examples of the LOP defects which formed in the joints. The approximate length in which the LOP defects stretch from the root surface has been listed alongside the image titles. The depth in which the defects affected the joints ranged from approximately 275 to 607 µm. The defects followed the typical behaviour of LOP in that the initial inclination of the crack was towards the advancing side of the weld.

630 RPM – 400 mm/min (LOP depth 369.53µm)

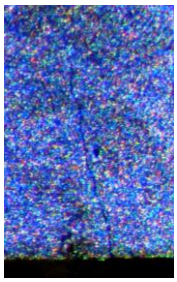

630 RPM – 600 mm/min (LOP depth 369.53µm)

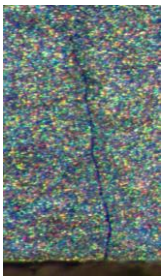

800 RPM – 600 mm/min (LOP depth 606.74µm)

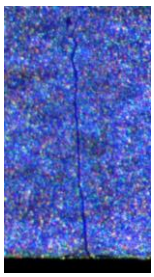

1000 RPM – 400 mm/min (LOP depth 363.86µm)

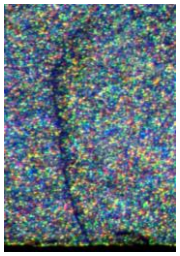

1000 RPM – 600 mm/min (LOP depth 308.28µm)

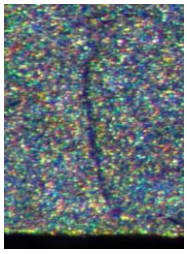

1250 RPM – 400 mm/min (LOP depth 351.10µm)

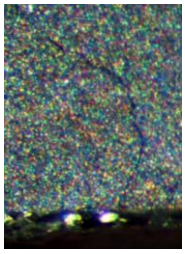

1250 RPM – 600 mm/min (LOP depth 274.96µm)

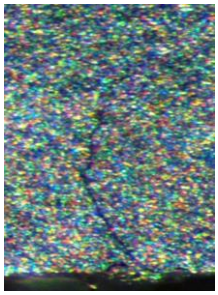

1600 RPM – 600 mm/min (LOP depth 397.13µm)

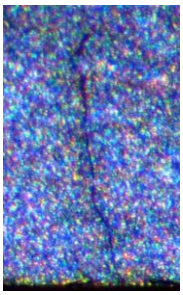

Figure 6.31 - Examples of Lack of Penetration defects in Friction Stir Welding Joints with various Parameter Combinations

From the figures within this section, it was clear that a wide range of welding parameters caused the formation of a LOP defect from the root surface. As the depth of the joint in which the defect affects varies, it can be stated that the geometry, inclination and size of the defect was linked to both the tool position as well as the welding parameters used in the manufacture of the joint. A low feed rate was shown to produce non-defective joints.

6.1.5.3 Parameter Effects on Friction Stir Welded Joint Thickness

The welding rate or parameter combinations of feed rate and tool rotation have been shown to produce various effect associated with the generation of thermal effects, material flow and defect formations. The strength of any FSW joint is related to the efficiency of the stir and the thickness of the joint. Typically a thicker joint has the ability to carry higher loads as long as there are not secondary effects such as defects or poor stirring effect related to that joint. A case may be put

forward that although an FSW joint may only have a reduction in thickness of a less than 5% from the base material insufficient stirring has occurred thus the joint would most likely fail under the application of load well before the expected value. Sections 6.1.5.3 and 6.1.6 aim to provide a clear conclusion to the effects of reduction of the welded joint thickness and the quality of the stir to the joints ability to sustain the application of loads.

Table 6.9 lists the measured averaged weld thickness of joints manufactured with various parameter combinations. A total of three measurements were taken across the three tensile samples. An average out of the three per tensile was obtained. For each parameter combination, a total of three tensile samples were manufactured thus the averages listed in the table is the overall average of the average thickness per sample. The base material was measured for each sample and using the averaged thickness of the joint the percentage reduction was calculated according to equation 6.1.

$$\%\, Reduction = \frac{T_{average\ weld}}{T_{base}} \times 100 \tag{6.1}$$

Table 6.9 - Average Friction Stir Welded Joint Thickness and Percentage Reduction of the Joint from the 3 mm Base Material

RPM	Feed	Ave. Weld Thickness [mm]	% Reduction from base Material
630	**200**	2.67	12.79
	400	2.78	7.81
	600	2.85	3.63
800	**200**	2.70	10.22
	400	2.76	8.40
	600	2.83	6.00
1000	**200**	2.43	19.29
	400	2.61	11.46
	600	2.85	5.44
1250	**200**	2.28	23.24
	400	2.45	17.66
	600	2.60	12.15
1600	**200**	2.24	25.77
	400	2.32	21.93
	600	2.49	16.02

Figure 6.32 shows the variation of average joint thickness and the percentage thickness due to welding rate. It is clear that an increase in welding rate reduces the thickness of the welded section of

the joint. This was visually enforced by a large amount of flash which formed during the welding of the joints with the higher welding rates. Associated to the joint thickness, the percentage reduction in the thickness of the joint was seen to increase with increasing welding rate.

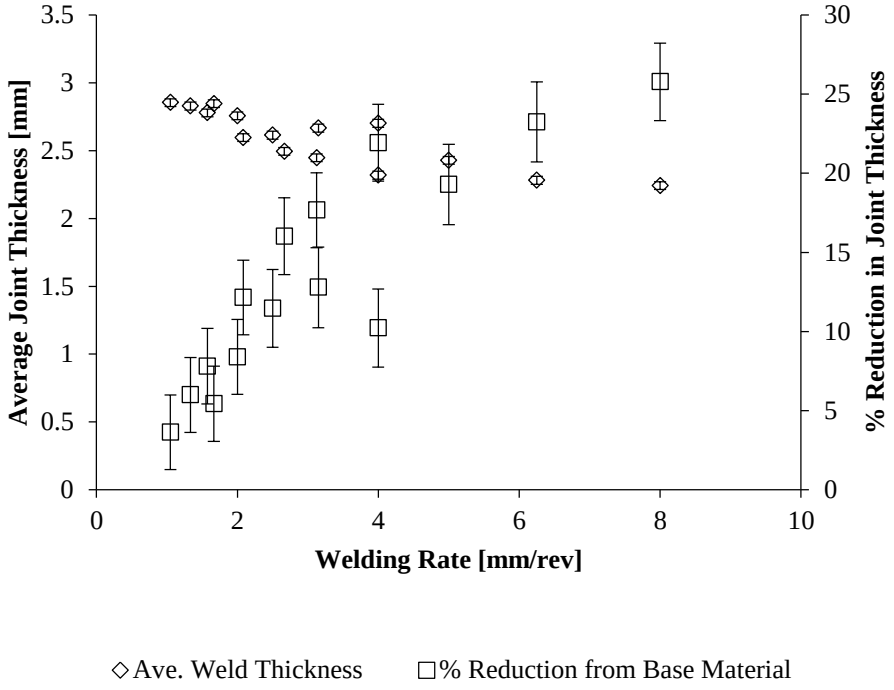

Figure 6.32 - Average Friction Stir Weld Thickness and Percentage Reduction variation with Welding Rate

Measurements of the thickness of the welded section showed a trend that the thickness varied across the joint with the retreating side being the thickest section of the weld. Figure 6.33 shows how the thickness varies across the section of the welds for a number of tool rotations. It can be seen that for all cases the retreating side was generally thicker than that of the advancing side of the weld. In a number of cases the centre section was the thinnest portion of the weld. The uncertainty in the thickness measurement was taken as ±0.05 mm but has been left off for clarity of the figure.

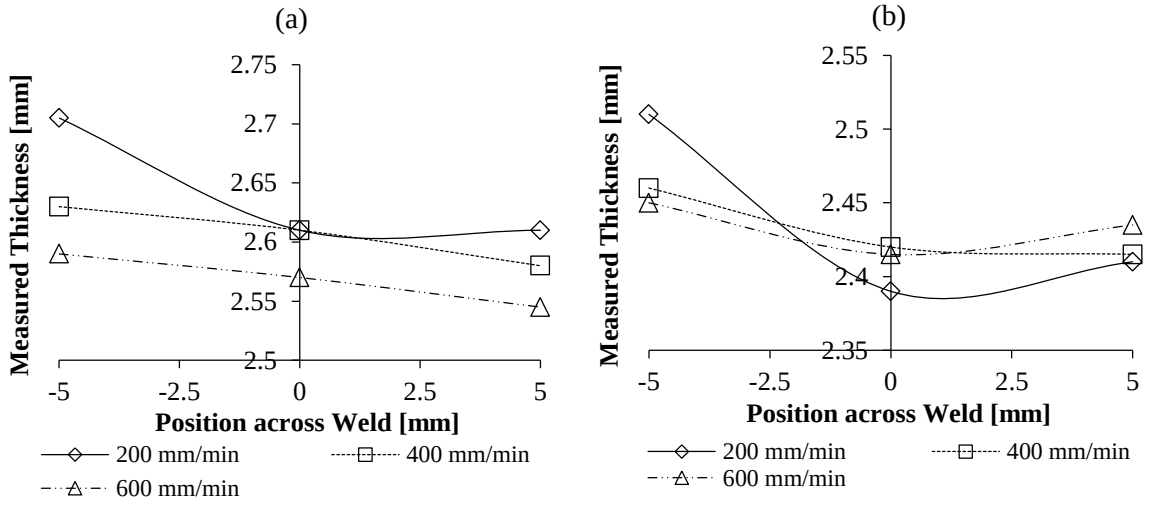

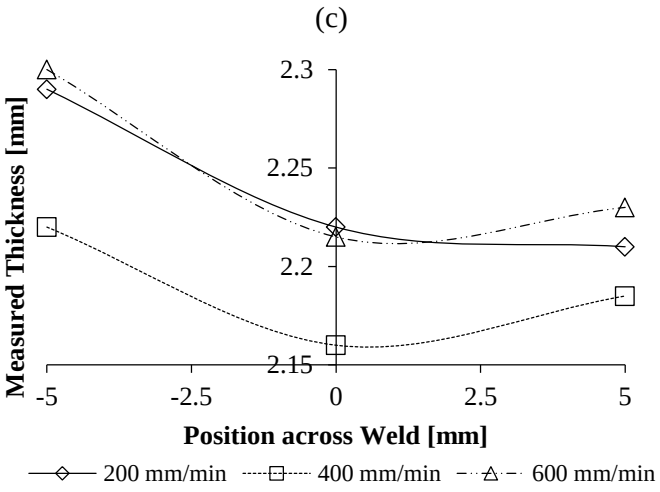

Figure 6.33 - Variation in Joint Thickness across the Welded Area for a number of Spindle Speeds a) 630 RPM b) 1000RPM c) 1600 RPM

Figure 6.34 shows the variation in thickness across for different feed rates. It can be seen that an increase in feed rate results in a notable reduction in joint thickness with a tool rotational speed of 1600 RPM being the thinnest joint across all feed rates. The uncertainty in the thickness measurement was taken as ±0.05 mm but has been left off for clarity of the figure.

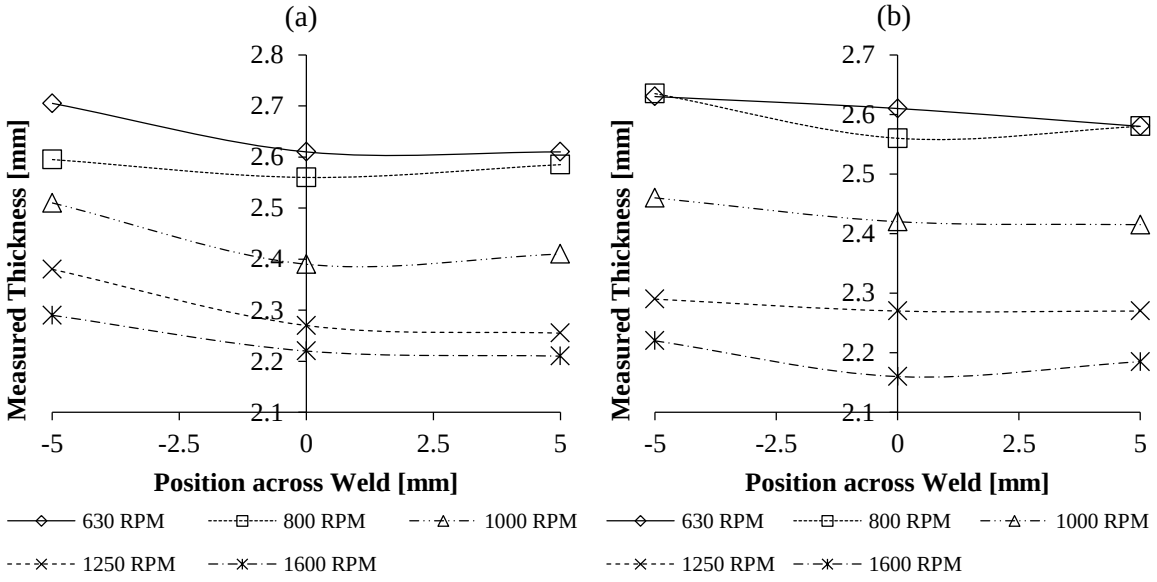

(c)

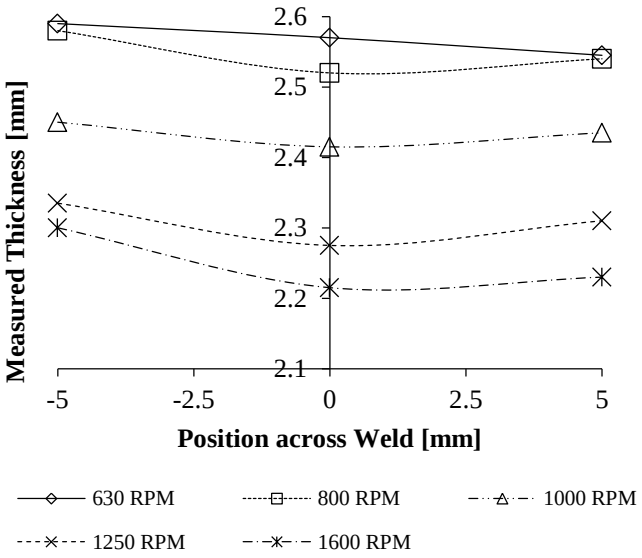

Figure 6.34 - Variation of Thickness across the Weld with constant feed rate a) 200 mm/min b) 400 mm/min c) 600 mm/min

6.1.5.3.1 Conclusion

From the results presented in this section the following can be concluded:

1. An increase in welding rate results in the thinnest joint.
2. An increase in welding rate maximises the percentage reduction of the joint relative to the base material.
3. The joint thickness varied across the cross section, with the retreating portion being the thickest throughout all welding parameter combinations.
4. An increase in tool rotational speed results in a reduction in the thickness of the joint due to the large flash formation.

6.1.6 Influence of varying parameters on the Static Strength of Friction Stir Welded Joints

Within this section, the influence of the various parameters on the static strength of the joints was investigated. The joints were tested according to standard tensile and three-point bending guidelines set out in their various internationally recognised ASTM standards.

6.1.6.1 Tensile Testing of Friction Stir Welded Joints

All tensile samples were manufactured and tested according to the ASTM E8 standard, which provides the outline for specification of the sample dimension and procedure for performing the test. The tensile coupon engineering drawing has been shown in Figure B.3 in Appendix B.

Figure 6.35 provides an example of the calculated engineering stress and strain of the tensile tests conducted according to ASTM standards for the samples manufactured using a tool rotation of 630

RPM and multiple feed rates. The Shimadzu records the applied force and stroke of the cross head. Using this data in combination with equations 5.1 to 5.3, the engineering stress and strain was achieved.

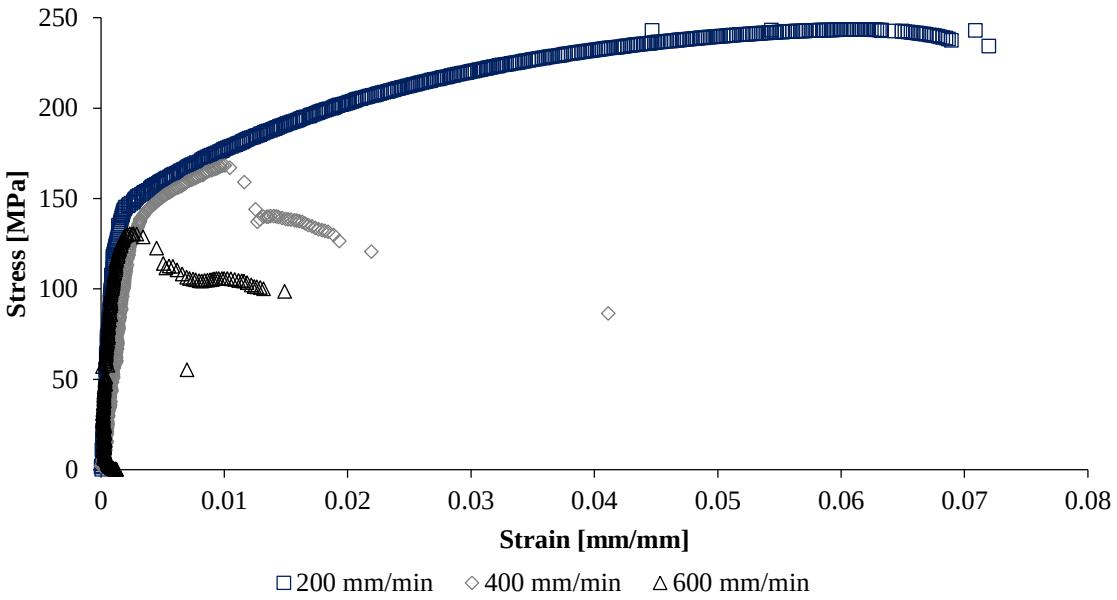

Figure 6.35 – Stress-Strain of Joints Manufactured at a Tool Rotational Speed of 630 RPM with various Feed Rates

Figure 6.36 demonstrates the 0.2% method employed to calculate the yield strength of each of the tested samples. The engineering stress and strain were firstly plotted, followed by calculating the gradient of the linear elastic region. Creating a straight line with the same gradient previous calculated and an x-intercept of 0.2% strain, an interception point where the stress-strain curve crosses the straight line can be found. This intersection point or better-known yield point has been indicated by the large dot in the figure below. It is evident that the slower feed rate produced a better quality joint as a higher axial load was sustained by the three joints. The remaining tool rotations engineering stress-strain curves have been placed in Figure C.5 in Appendix C.3.

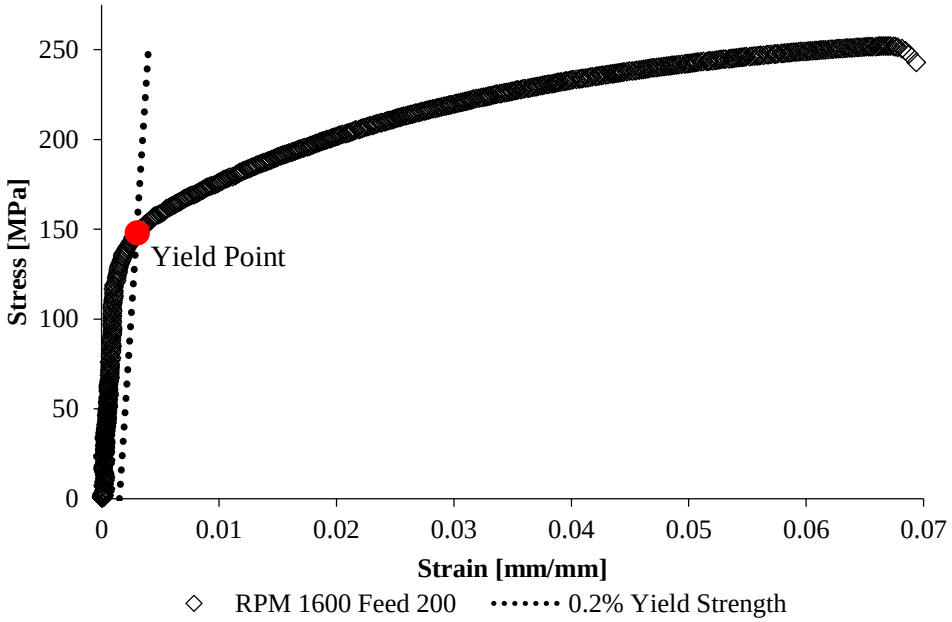

Figure 6.36- Example of the method used to calculate the Yield Strength of Friction Stir Welded Joint

Table 6.10 lists the key outcomes of the tensile tests. Each result was calculated as the average of three tensile samples.

Table 6.10 - Data Corresponding for Various Outcomes Related to Tensile Tests

RPM	Feed	Ultimate Force [N]	Yield Strength [MPa]	Ultimate Stress [MPa]	Yield Efficiency [%]	Ultimate Efficiency [%]
630	**200**	8272.05	154.73	248.28	50.95	71.17
	400	6814.28	151.24	196.21	49.80	56.25
	600	5990.66	117.43	167.94	38.66	48.14
800	**200**	7833.30	147.69	231.99	48.63	66.50
	400	7500.85	143.11	217.73	47.12	62.42
	600	6529.96	141.38	184.70	46.55	52.95
1000	**200**	6579.50	143.70	216.76	47.31	62.14
	400	8235.18	143.70	252.02	47.31	72.25
	600	7532.21	144.92	211.71	47.71	60.69
1250	**200**	7066.56	149.79	247.77	49.32	71.03
	400	7688.81	151.20	251.32	49.78	72.05
	600	7755.42	149.81	239.01	49.32	68.52
1600	**200**	7139.89	150.62	254.81	49.59	73.05
	400	6392.82	143.19	220.56	47.14	63.23
	600	7147.38	143.87	229.25	47.37	65.72

Tool rotational speeds of 630, 800 and 1600 RPM all produced the strongest joints at a feed rate of 200 mm/min whilst 1000 and 1250 RPM strongest joints were produced at 400 mm/min. This can clearly be seen in Figure 6.37. An increase in feed rate resulted in a substantial decrease in the strength of the joints. Error bars have been left off the figure to provide clarity amongst the data, all uncertainty for the ultimate tensile strength has been listed in Table F.1 in Appendix F.

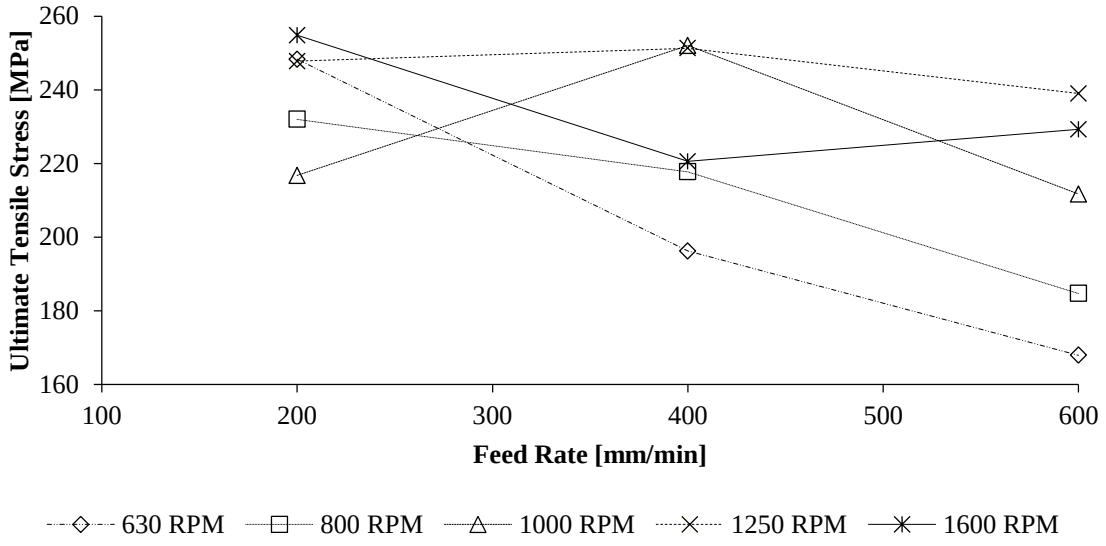

Figure 6.37 - Ultimate Tensile Strength of Tensile Joints distributed according to Spindle Speed and Feed Rate

The weld parameter combination of 1600 RPM and 200 mm/min was found to produce on average the strongest joint with the axial load applied.

Figure 6.38 shows the variation of maximum forces carried by the various joints manufactured with different welding rates. It is evident that lower welding rates had the ability to carry a greater load to those of higher rates. The variation in average welded joint thickness has been included in this figure. The purpose of this was to show in combination with Figure 6.39 that although the joints manufactured at a lower rate could carry higher loads they did not sustain the same amount of axial stress which was introduced into the joints. The joint manufactured with a welding rate of 8 had the lowest thickness thus joint area but was capable of sustaining a reasonable amount of force. This indicates that this welding parameter combination resulted in the most efficient stir as it had the capabilities to sustain the higher level of stress.

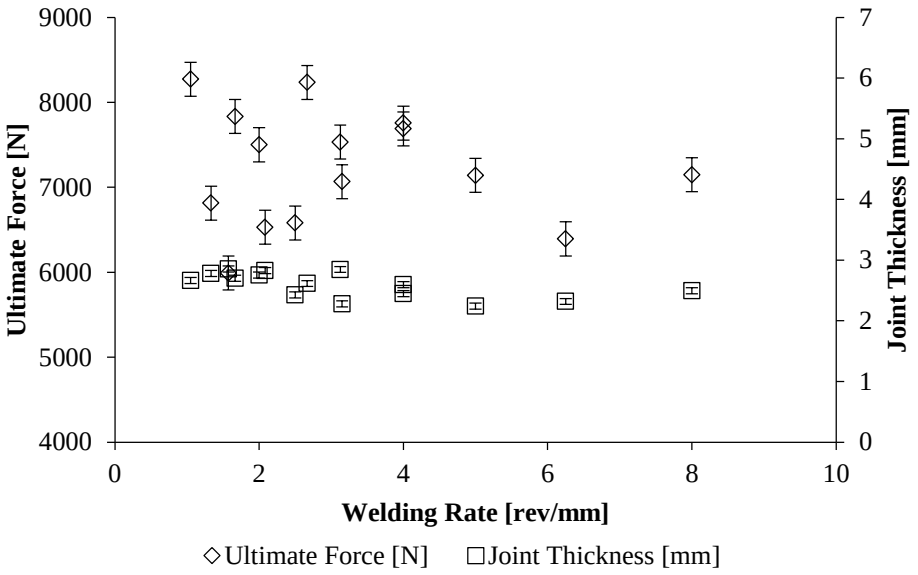

Figure 6.38- Distribution of Averaged Ultimate Force and Joint Thickness relative to the Welding Rate

Figure 6.39 provides an indication of the variation of the maximum stress sustain in the various joints manufactured with different welding rates. The yield strength of each joint presented to the group in the region of 150 MPa.

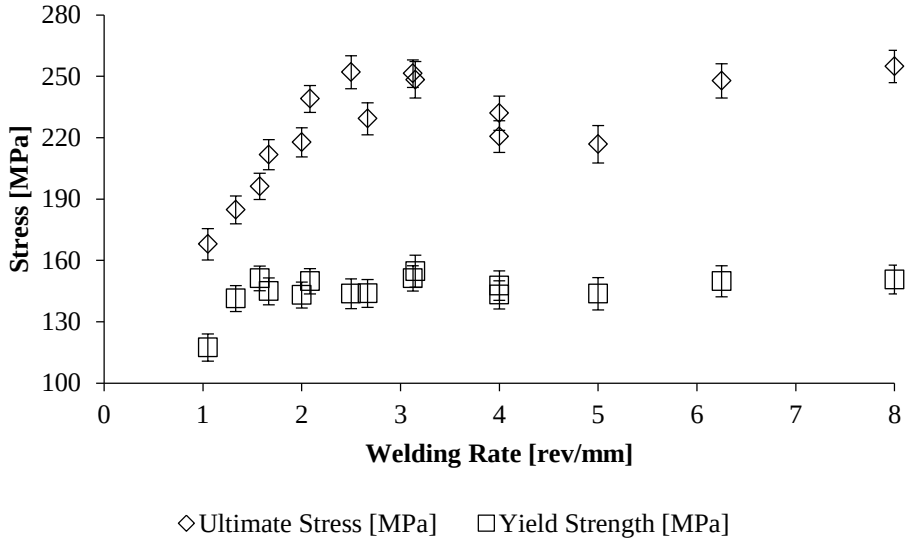

Figure 6.39- Distribution of Ultimate Strength and Yield Strength relative to the Welding Rate

The weld efficiencies at yield and ultimate were calculated by determining the percentage each result for the various welds compared to the base material. Figure 6.40 provides a comparison of the ultimate tensile strength weld efficiency. It is clear from the figure that welds manufactured with a feed rate of 200 mm/min had on majority the highest efficiencies. The highest efficiency overall was the produced with a welding parameter combination of 1600 RPM and 200 mm/min. The efficiencies

were in the range of those achieved by other researchers which obtained maximum efficiencies in the range of 70 to 80% [21].

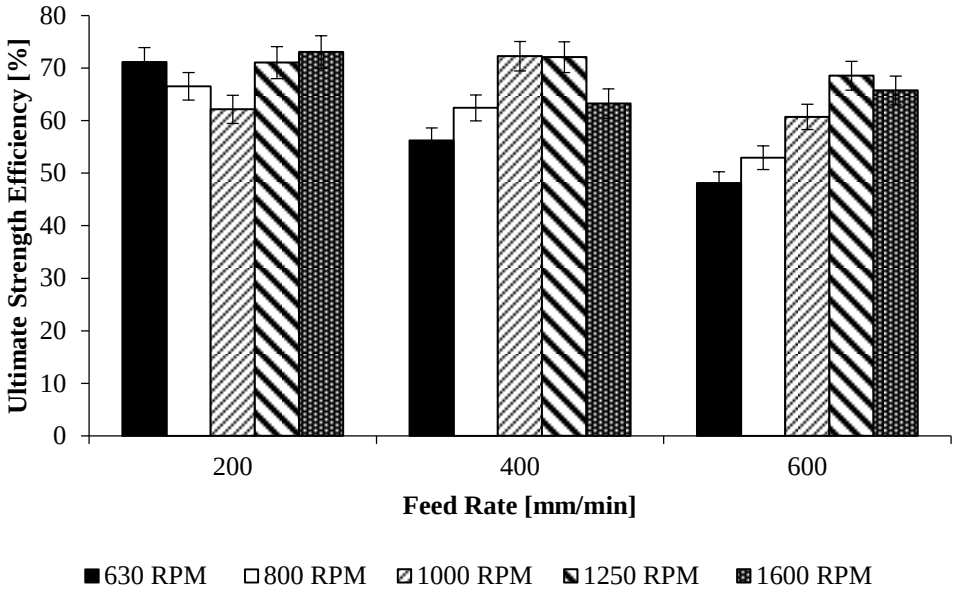

Figure 6.40 - Ultimate Tensile Strength Weld Efficiency

From the figure the joint efficiency of 1600 RPM and 200 mm/min was evident and at this point, it was a strong candidate for the optimum parameters.

6.1.6.2 Failure Position of Friction Stir Welded Tensile Joints

The fracture locations for the tensile coupons occurred in two different regions of the welded zone. All samples failed in the welded area. The two locations in which failure occurred was in roughly in the centre of the welded area, the Nugget Zone and at approximately the shoulder boundary of the Heat Affected Zone (HAZ) and the base material, on the advancing side of the weld. Figure 6.41 indicates these locations along the joints.

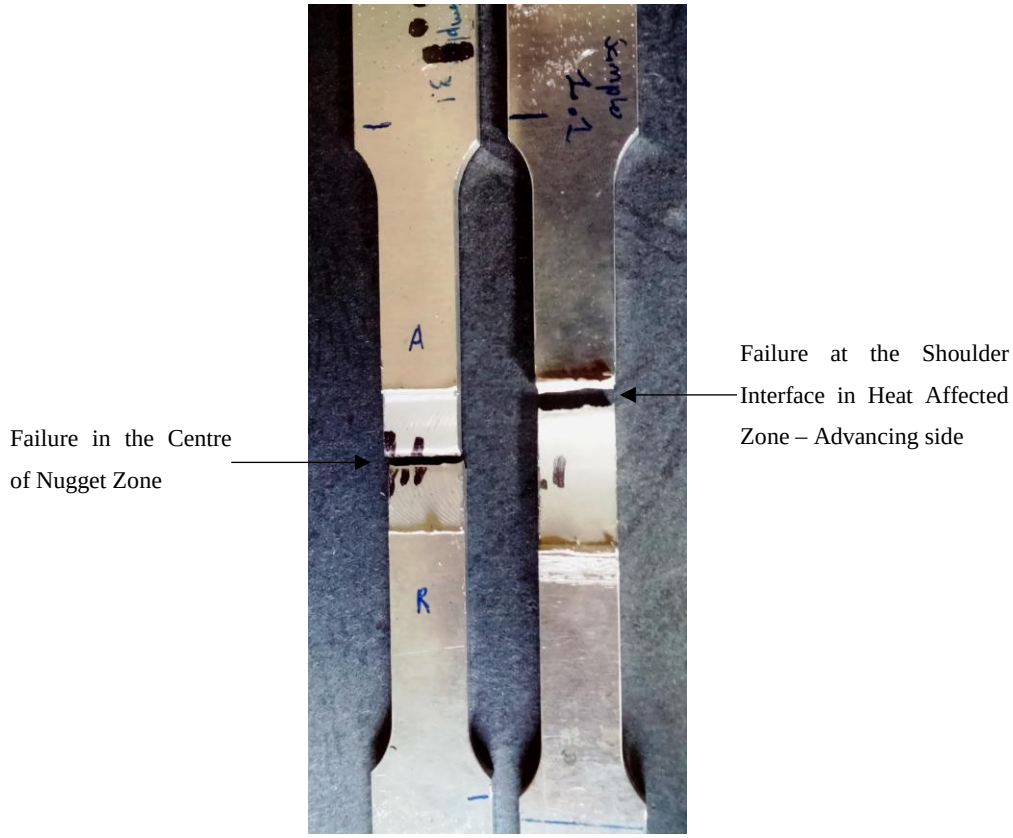

Figure 6.41 - Failure Positions Encountered During Tensile Testing

Figure 6.42 provides the failure locations for the tensile coupons welded under varying parameters. It was evident that all coupons manufactured with a feed rate of 200 mm/min failed in the region close to shoulder boundary in the HAZ on the advancing side. Failure of tensile samples on the advancing side rather than the retreating was observed by a number of researchers such as Adamowski [16], Cirello [53] and Liu [95]. This failure location correlated to the joints which were in the majority the strongest joints. The welds manufactured with 1000 and 1250 RPM spindle speed and 400 mm/min feed rate consistently failed at this location as well. Possible reasons for this failure were:

1. Figure 2.48, shows a typical across the FSW joint in AA6082-T6 Aluminium. It could be seen that the welding process significantly affect the hardness of the joint by reducing the level of hardness from the base material. It was been identified that in the case of defect free joints the failure position is defined by the hardness profile of the joint [95].
2. The intensive stirring actions within the nugget and TMAZ influences the hardness more than the thermal effects would alter the HAZ. This caused a variation the in the hardness profile across the joint. The hardness variation was due to the grain refinement within the highly stirred zones [16].
3. The results present within this section and those of other researchers confirm the fact that during the application of a tensile force, a stress-strain concentration takes place in the region of the lowest strength within the joint. Due to this build up, the joint fractures at its weakest

point. The constant failure within the advancing side of the joints indicates that the advancing side of the joint was weaker than that of the retreating side. This implies that material flow during welding can to hold influence on the mechanical properties of the joint [53].

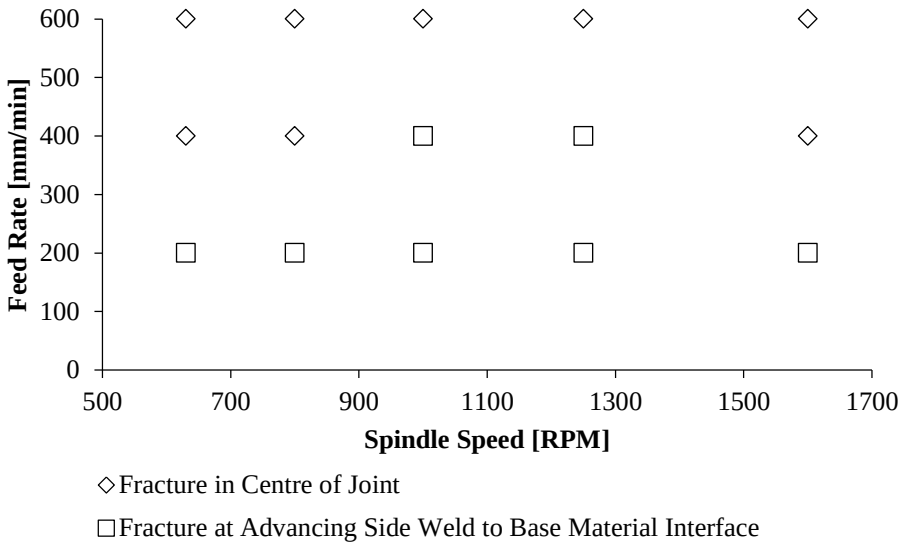

Figure 6.42- Failure Locations of Tensile Samples for Various Friction Stir Welding Parameter Combinations

The remaining welding parameters combinations failed within the nugget zone of the weld. Failure within this region was attributed to the possibility of the presences of a crack or weld defect on the root surface of the weld.

6.1.6.3 Comparison of Other Friction Stir Welding Published Results

Figure 6.43 has been provided to indicate or to benchmark the manufactured joints to weld strengths of other researchers. It can be seen that the majority welds that were manufactured for this research outperformed those of other researchers who used the same welding material of 3 mm thick AA AA6082-T6.

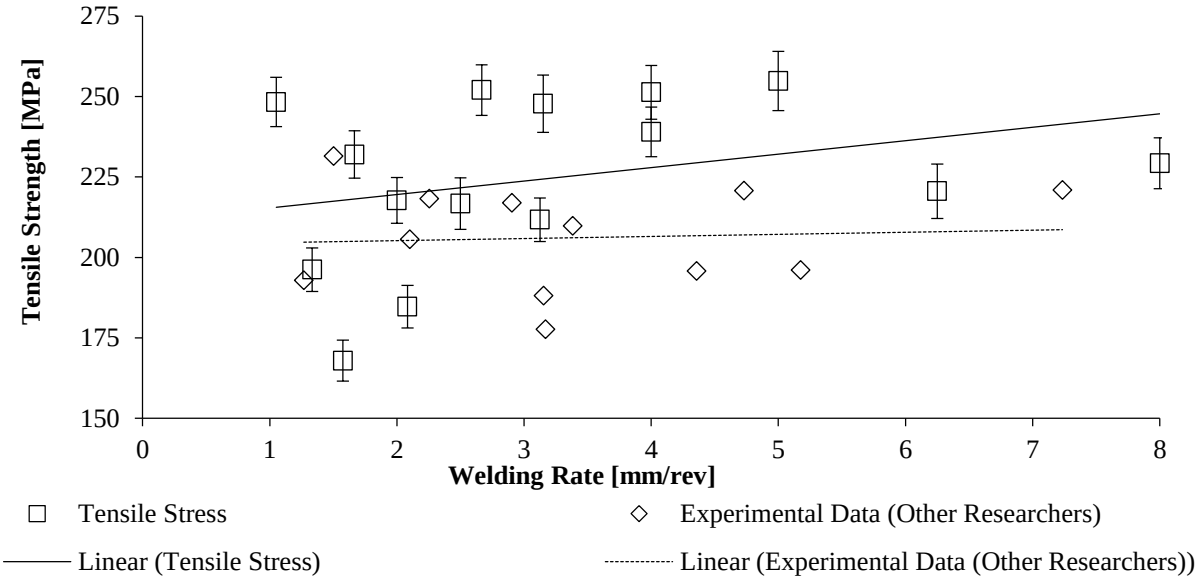

Figure 6.43- Comparison of Ultimate Tensile Strength to Published Results

It is noted that tool geometry and secondary welding parameters such as plunge depth and dwell time would also influence the results. By simply comparing the tool rotation and feed rate a novel benchmarking exercise can be completed, it shows that high-quality joints can be manufactured. These experimental joints can compete with industry developed FSW processes and thus are suitable to perform further research on these manufactured joints.

6.1.6.4 Ductility of Friction Stir Welded Joints Manufactured with Varying Parameters

The ductility of the welded joints was investigated by performing standard three-point bending tests according to section 5.4.7. The sample dimensions have been shown in Figure B.4 in Appendix B. During each test the root surface of the coupon was placed in tension by the plunger in order to establish whether the weld would exhibit signs of root defects such as lack of penetration or kiss bonds. The greater the angle in which the coupon bends around the plunger with the least amount of growth of a crack at the root surfaces the better. The bending force diagrams for each sample can be found in Appendix C.4.2.

Figure 6.44 provides an example of the measured output of bending force and plunger position during a standard three-point bending test of the first set of welds. Two samples for each weld parameter combination were used in the calculation of the averaged maximum bending force which the coupons could withstand before failure. The remaining bending-displacement plots have been placed in Figure C.6 in Appendix C. 3.2.

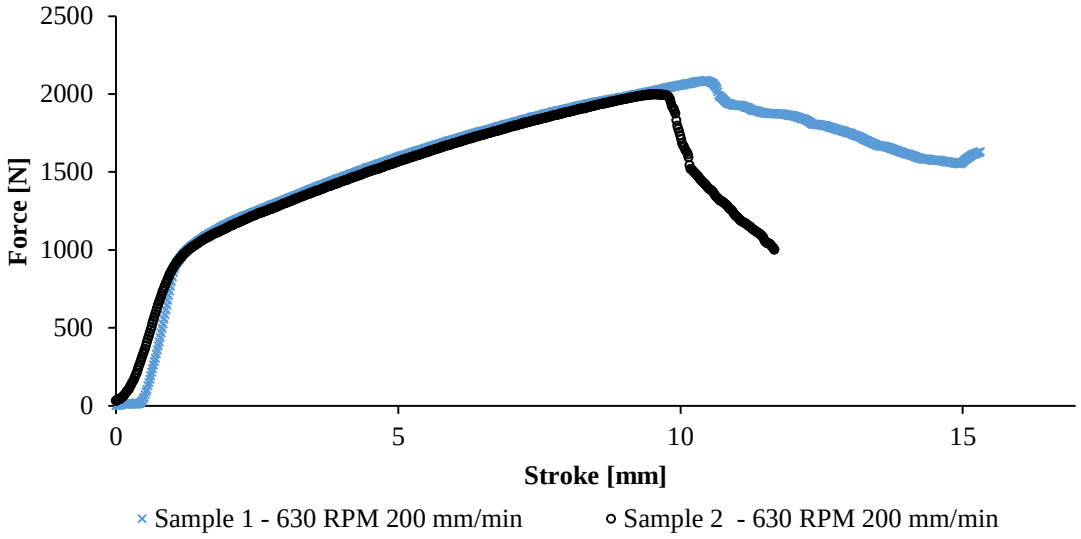

Figure 6.44 – Measured Output of Bending Force with Plunger Stroke for Three Point Bending Tests

Figure 6.45 provides an example of the bent samples at each weld parameter combination. For the majority of the samples, there was an extremely good correlation between the maximum force, bend angle and fracture/defect development. From the figure, it is clear that the higher spindle speed and lower feed rate produced the most ductile joint with no signs of defect developing on the root surface bend.

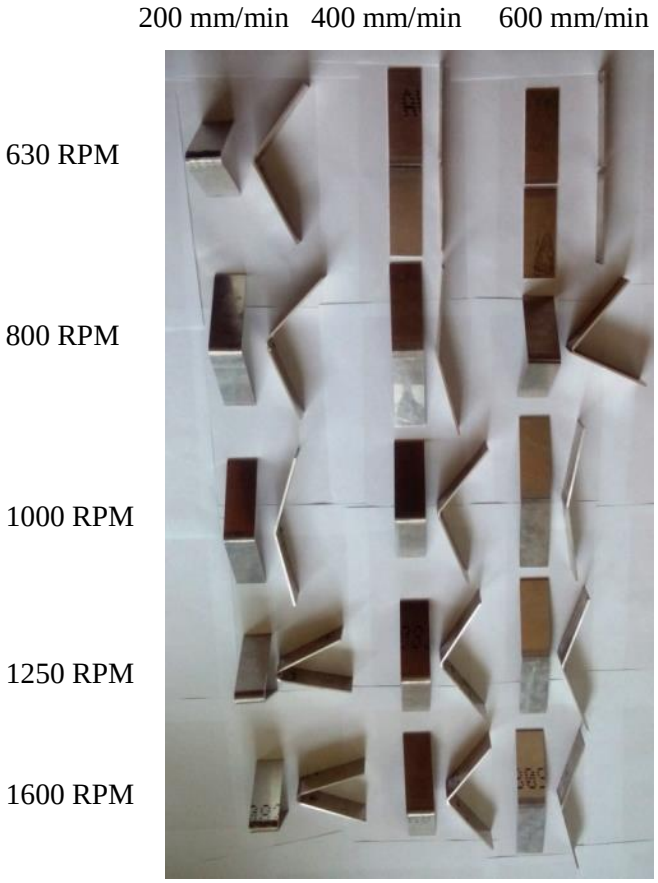

Figure 6.45 - Sample of the Various Three Point Bent Samples across the Welding Parameter Window

Table 6.11 lists the results of the test of each weld combination. The maximum force and the bend angle were averaged over the two samples. The remark refers to the type of defect or fracture which occurred at the centre of the root face after the tests.

Table 6.11- Data Corresponding for Various Outcomes Related to Three Point Bending Tests

RPM	Feed	Average Maximum Bending Force [N]	Average Bend Angle at end of Test [°]	Remark on Fracture/Defect Formation
630	200	2041.56	98.5	Large crack
630	400	1186.88	-	Full fracture into two halves
630	600	1315.94	108.5	Extreme crack/close to full fracture
800	200	2112.50	72.25	Large crack
800	400	1555.00	21.75	Slight crack
800	600	1191.56	108	Large crack
1000	200	1586.25	50.75	Extreme crack
1000	400	2130.00	70.25	Slight crack
1000	600	1530.00	18	Slight crack
1250	200	1820.94	135.75	No signs of damage
1250	400	1970.63	71.25	Slight crack
1250	600	1711.88	32.75	Slight crack
1600	200	1695.63	139	No signs of damage
1600	400	1843.44	74.5	Slight crack
1600	600	1516.25	28.5	Slight crack

Figure 6.46 provides the distribution of the maximum bending force for the different spindle speed and feed rates. It can be seen that all welds manufactured with a feed rate 600 mm/min resulted in the majority of the welds which could carry the lowest maximum bending force before fracturing. The possible reason behind this may be due to the insufficient stirring of the material and penetration of the tool thus the root surface of the weld quickly fractures or begins to open as the plunger forces the bend. The welds of 1000 RPM, 400 mm/min and 800 RPM, 200 mm/min carried the highest loads. Although these samples could carry the highest loads, large defects/cracks were produced during the tests as the root surface was bent. Both samples managed a bend angle in the region of 70° before the test ended. The fact that a crack occurred indicates that welds were not fully free of defects and although they carried the highest loads they cannot be considered a good weld from a quality point of view. Figure 6.48 shows a closer view of the extent of the defects or cracks which formed during the testing of the highest load carrying samples. From the figure it was evident that two trends could be noted, the ultimate force all feed rate - spindle speed combinations below 1000 RPM tended to reduce

with increasing feed rate. Secondly, all tool rotations higher than 1000 RPM showed that a feed rate of 400 mm/min produced the strongest joint. The possible reasoning for these two trends may be due to the following:

1) Trend 1 – a feed rate of 200 mm/min produced a joint with minimal defects on the root surface. Due to the lower tool rotational speed, the joints were substantially thicker than those of the higher tool speeds.
2) Trend 2 – Samples manufactured at 200 mm/min and +1000 RPM were some of the lowest loading carrying joints due to the substantial reduction in joint thickness due to the formation of flash during welding. These joints were still fairly efficiently mixed as almost no defects were noted within these joints. Samples manufactured at 400 mm/min were the thickest joints but also fairly effectively mixed joints. If bending load carrying capability was the most important aspect in parameter selection then this feed rate would be the optimum value. Joints manufactured at 600 mm/min were the worst as they were not effectively stirred during the welding process. This was evident by the fracture surface of the joint post testing. The uncertainty in the measurement of the ultimate force was ±1% of 20 kN, this was specified by the load cell used during the experiment. Error bars have been left off for clarity.

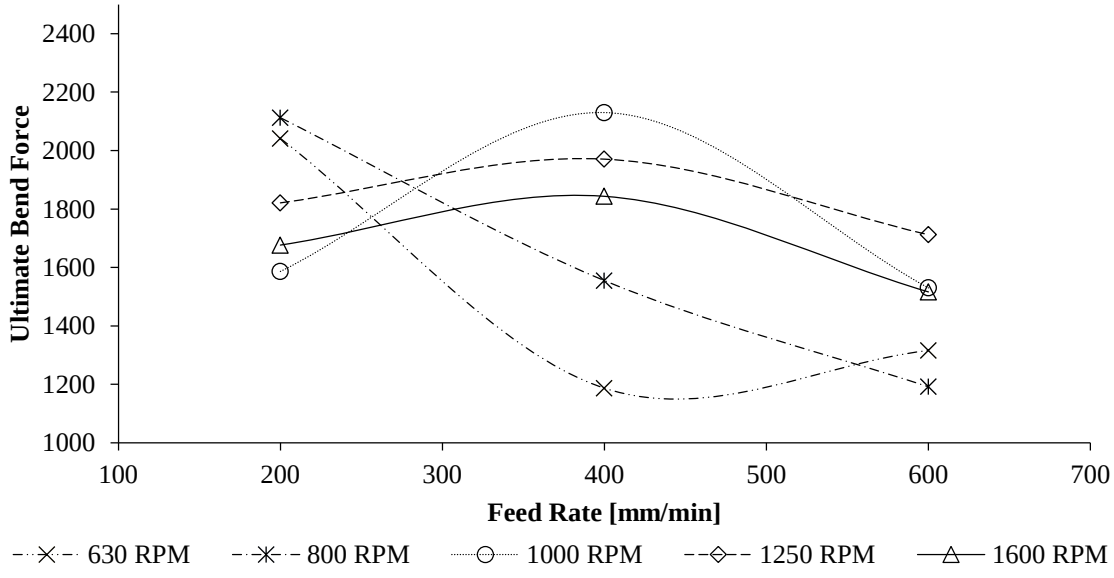

Figure 6.46 - Ultimate Bend Force distributed according to Spindle Speed and Feed Rate

Although load carrying capability was of high importance when selecting parameters for FSW the quality of the joint must also be considered. The latter portion of this research required a parameter set that did not result in defective joints, for this reason, greater emphasis must be placed on the ductility and fracture surface.

The bend angle refers to the change of angle from a flat plate coupon to the angle at which the sample was left at the end of the test. Figure 6.47 provides the distribution of the averaged bend angle between the two bending samples. A feed rate of 200 mm/min resulted in the most ductile welds as the bend angles for these samples across the various tool rotational speeds were highest. Visual inspection of these joints, see Figure 6.48, also showed their superior ductility to it counterparts, The slow feed rate produced the hottest welds thus more efficient stirring could be achieved due to the softer material and the tool was capable of penetrating the material more effectively. All samples besides 1600 RPM - 200 mm/min and 1250 RPM - 200 mm/min showed signs of damage and cracks propagating from the root surface during the bending tests. As no cracks or damage was evident on these samples they were considered the best welds from a ductility standpoint and were strong candidates to be used as the selected welds for the latter parts of this research. During the introduction of the controlled lack of penetration a perfect joint, defect free weld must be used as then it can be concluded that presence of the LOP would not be due to the selection of the tool rotational speed or feed rate. The uncertainty of the measured angles was ±0.5°.

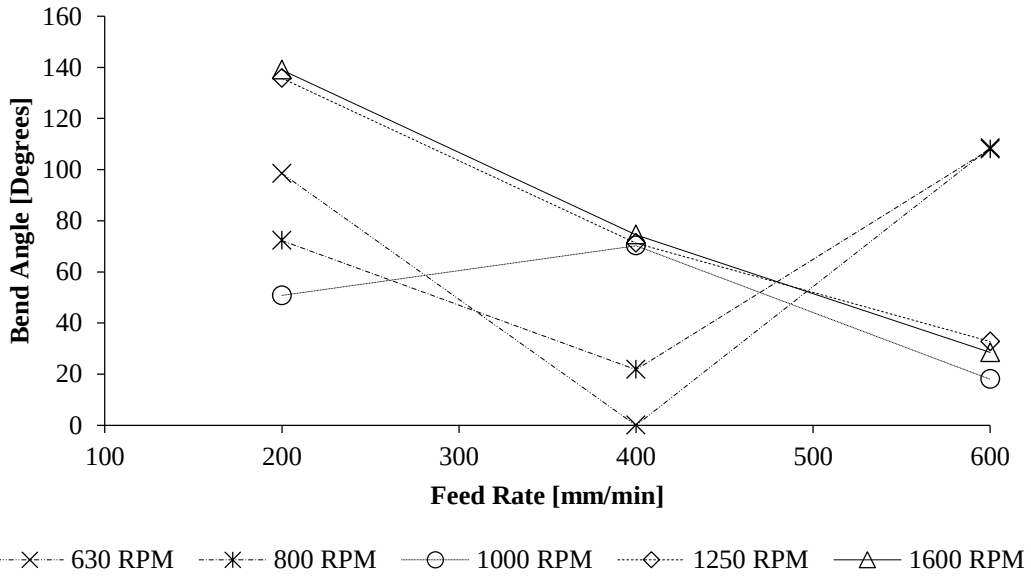

Figure 6.47 - Average Bend Angle distribution according to Spindle Speed and Feed Rate

Figure 6.48 provides an example of the type of fracture or defect which formed during the three-point bending tests.

630 RPM – 200 mm/min - Large crack

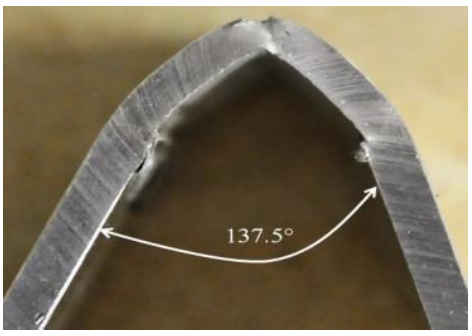

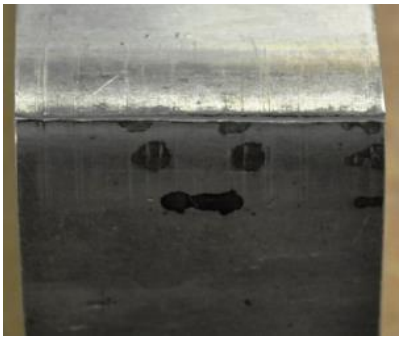

630 RPM – 400 mm/min - Full fracture

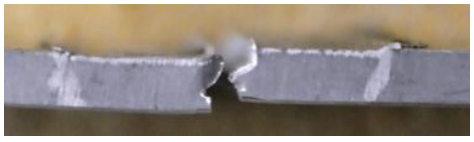

630 RPM – 600 mm/min - Full fracture

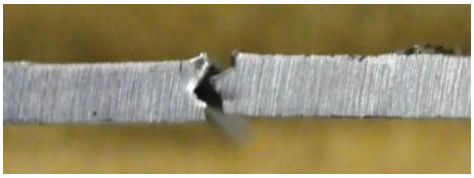

800 RPM – 200 mm/min - Large crack

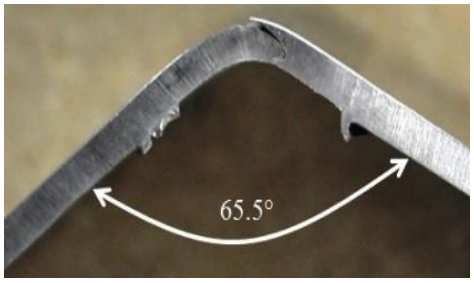

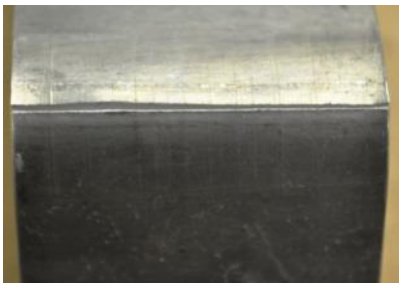

800 RPM – 400 mm/min - Slight crack

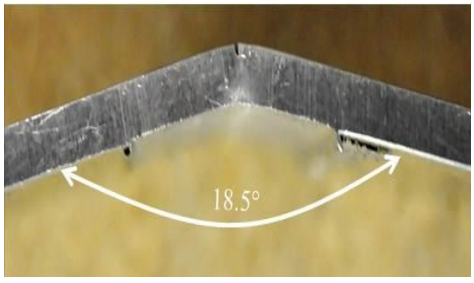

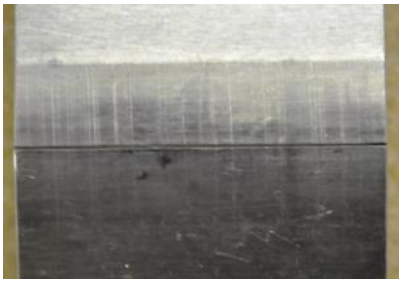

800 RPM – 600 mm/min - Large crack

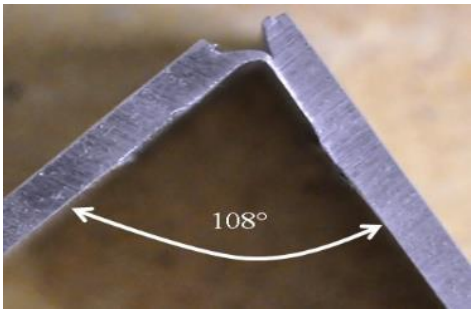

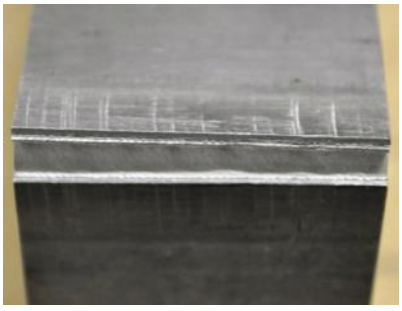

1000 RPM – 200 mm/min - Extreme crack

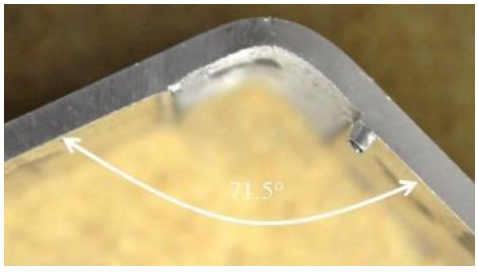

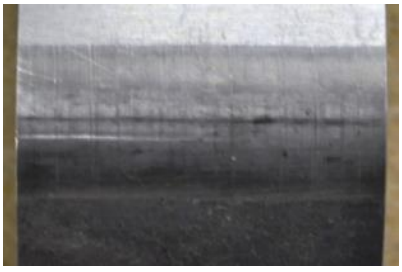

1000 RPM – 400 mm/min - Slight crack

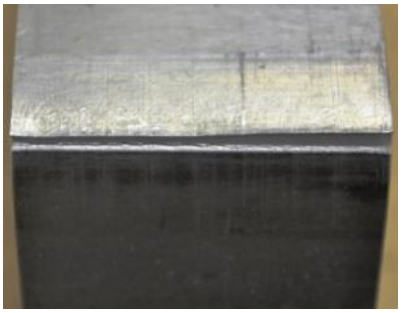

1000 RPM – 600 mm/min - Slight crack

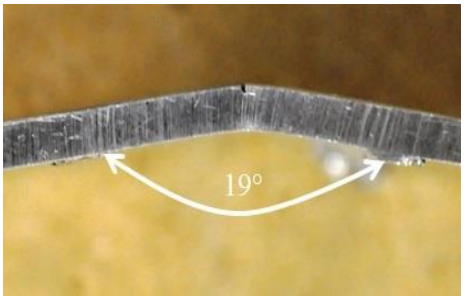

1250 RPM – 200 mm/min - No signs of damage

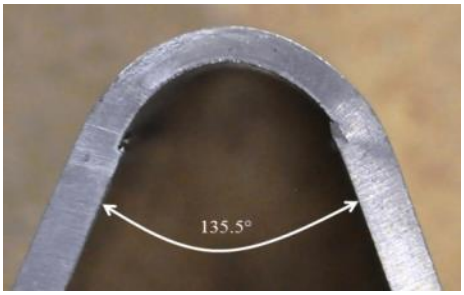

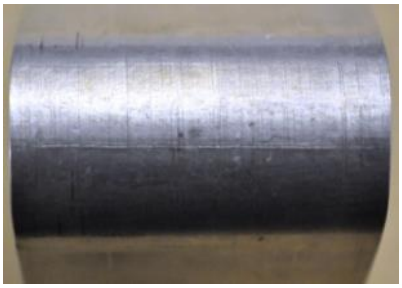

1250 RPM – 400 mm/min - Slight crack

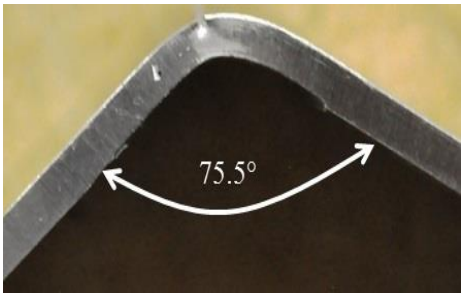

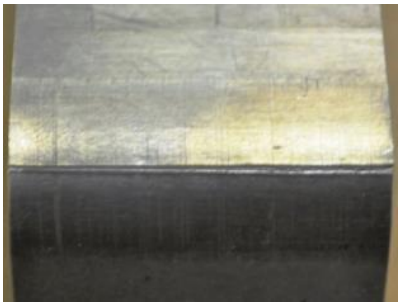

1250 RPM – 600 mm/min - Slight crack

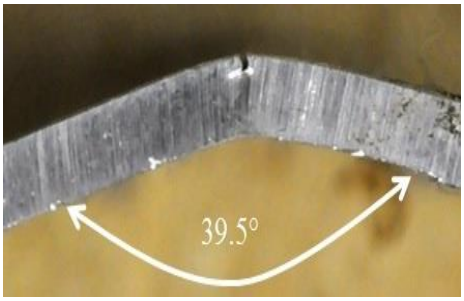

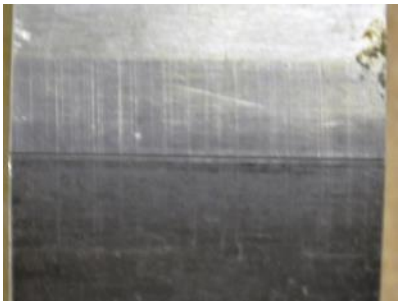

1600 RPM – 200 mm/min - No signs of damage

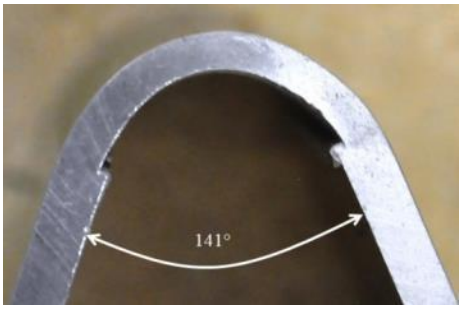

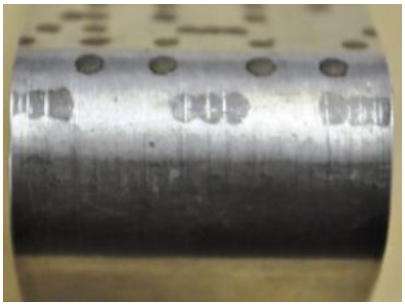

1600 RPM – 400 mm/min - Slight crack

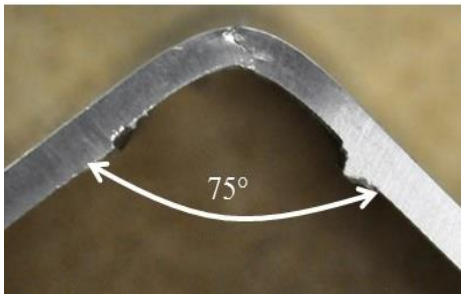

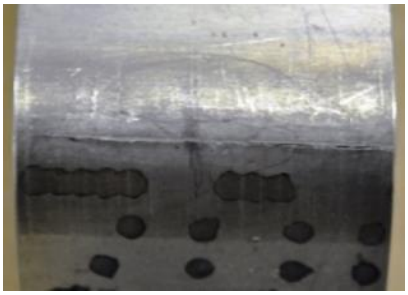

1600 RPM – 600 mm/min - Slight crack

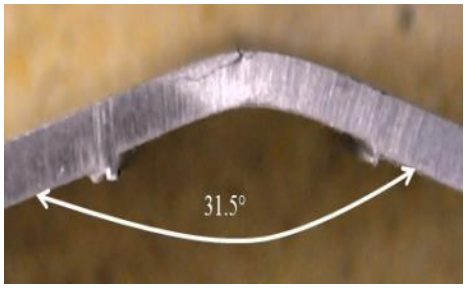

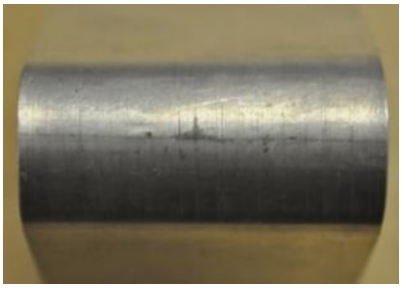

Figure 6.48 - Example of Fracture/ Defect Formed during Bending Test

Figure 6.49 provides the distribution of maximum bending force with welding rate. It can be seen from the figure that lower welding rates resulted in welds which were not able to sustain high bending loads. The distribution of bend angle shows a general tendency for the welds to become more ductile with greater welding rates. This could be attributed to the fact that higher temperatures are occurring and more efficient stirring of material was being achieved thus no defects or lack of penetration of the tool occurred. The trends seen in this figure were similar to those seen in Figure 6.38, in that welds manufactured with a welding rate in the range of two to four produced welds which were capable of carrying high loads. It must be reiterated at this point that a perfect weld, a weld which was free from defects was required to be obtained before continuing on with the next stage of introducing controlled lack of penetration.

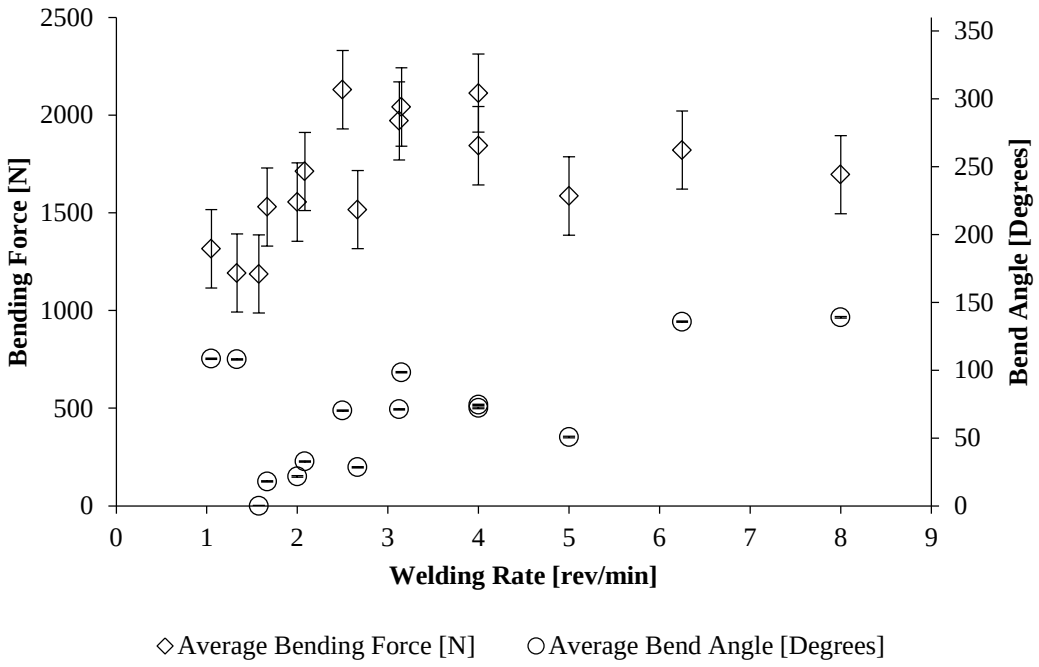

Figure 6.49 - Distribution of Bending Force and Bend Angle with Welding Rate

6.1.6.4.1 Conclusion

It is anticipated that the most ductile welds did not carry the highest loads purely due to these welds being on average the thinnest joints.

From the results presented in this section the following can be concluded:

1. Higher feed rates result in the poorest bending force carrying capability.
2. Welds which carried the highest loads were not the most ductile out of the welds investigated.
3. An increase in welding rate produces an increase in the ductility of the welded joints.
4. The welding combination of 1600 RPM and 200 mm/min produced the most ductile weld, which was still capable of sustaining significantly high loads without showing signs of any form of damage after undergoing a full bend test.

6.1.7 Multi-Objective Optimisation of the Friction Stir Welding Process

Using the discrete values of the investigated FSW parameter window, previously discussed in the earlier parts of this chapter, a multi-objective optimisation exercise was conducted with the aims of confirming the relationships noted previously, to determine the expected values of welding parameters which fall between the investigated parameters and to attempt to identify the most optimal welding parameters. modeFRONTIER 4.3.1 was used for the optimisation process. The software package and methodology behind its functions has been outlined in section 2.7.

6.1.7.1 modeFRONTIER Methodology

The modeFRONTIER optimisation was a multi-step process which required a number of steps to be completed in a very specific order. This section was completed to outline the steps required.

1) The experimental inputs (spindle speed and feed rate) and outputs (results from experiments) needed to be entered into the creation of the Work Tables Tool in the Design Space.
2) Use the Response Surface Methodology (RSM) functions to create the initial response surfaces for the inputted experimental data. A number of fitting algorithms needed to be tested to identify the best functions which fit the data with the least amount of errors.
3) Using the trained algorithms from step 3, a project workflow needed to be designed which will explore the various set input parameters which then aim to predict the outputs.
4) The optimal parameters can then be obtained.

6.1.7.2 Algorithm Development for Optimisation of Friction Stir Welding Process

This section was set out to describe, in detail, the initial development and training of the algorithms to the experimental inputs and eventual outcomes.

The Friction Stir Welding parameter window investigated focused on the tool rotation and feed rate. Table 6.12 lists the various inputs and outputs which were used in the optimisation of the FSW process.

Table 6.12 - Work Table Inputs and Outputs for Friction Stir Welding Optimisation

Inputs	Outputs
Spindle Speed [RPM]	Average Welding Force during Feed [N]
Feed Rate [mm/min]	Average Temperature during Feed [°C]
	Average Joint Thickness [mm]
	Ultimate Tensile Force [N]
	Ultimate Tensile Strength [MPa]
	Joint Efficiency [%]
	Tensile Fracture Location
	Maximum Bending Force [N]
	Bend Angle [°]

The failure location of the tensile samples was initially not numerically represented as a value that could be placed into modeFRONTIER as it was a failure in a specific region of the joint. By placing numeric values to the failure positions of the tensile samples, the optimisation can attempt to predict how the FSW joints would fail. Tensile samples which failed in the heat affected zone on the

advancing side of the weld were set as failure position 1 whilst failure along the centre line was given a failure position 2.

The work table was developed by inputting all relative output data for each known weld parameter according to the listed items in Table 6.12.

Using the Response Surface Methodology [RSM] tool in modeFRONTIER, the surface algorithm relating each input to the respective output was developed. This was done so that the mathematical relationship between the inputs and the outputs could be obtained and used during the design of the optimisation workflow. An RMS function was required for every single output. Parameter screening was completed to identify the relative strengths of the input variables and their influence on the outcome of the various outputs. The performance indices were calculated by means of Smoothing Spline ANOVA algorithm. Figure 6.50 illustrates an example of the results of the screening process, taken directly from the modeFRONTIER optimisation.

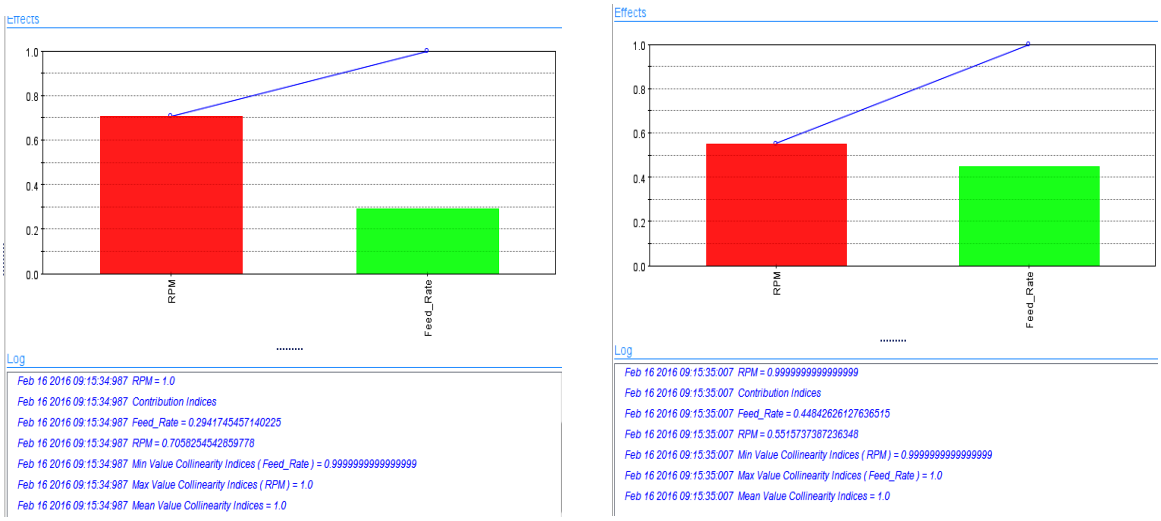

(a) Average Joint Thickness (b) Average Welding Force during Feed

Figure 6.50 - Example of the Screening Results for a number of Friction Stir Welding Outputs

Table 6.13 lists the performance indices and the relative contributions that each input parameter had on the outcome of the numerous results. The feed rate was the dominant input for six out of the nine categories. This table indicates that the selection and control of both parameters are vital in obtaining high-quality friction stir welded joints.

Table 6.13 - Relative Strength of Input Variables of Friction Stir Welding

	Relative Strength of Input [%]		Dominate Input
Output	**Spindle Speed [RPM]**	**Feed Rate [mm/min]**	
Average Welding Force during Feed [N]	55.16	44.84	Spindle Speed
Average Temperature during Feed [°C]	99.77	0.23	Spindle Speed
Average Joint Thickness [mm]	70.58	29.42	Spindle Speed
Ultimate Tensile Force [N]	6.32	93.68	Feed Rate
Ultimate Tensile Strength [MPa]	46.85	53.15	Feed Rate
Joint Efficiency [%]	46.48	53.52	Feed Rate
Tensile Fracture Location	6.33	93.67	Feed Rate
Maximum Bending Force [N]	14.57	85.43	Feed Rate
Bend Angle [°]	11.65	88.35	Feed Rate

In the creation of the various RSM, a training technique needed to be selected. modeFRONTIER allows for the selection of a number of functions but not all functions are as well suited to this small scale data set. The most applicable functions which were used were: Kriging, Anisotropic Kriging and Radial Based Functions. Only a single RSM per output can be used in the optimisation process thus each function has to be evaluated against themselves to determine which was best. This was done by assessing their residual charts, an example of the charts for the maximum welding force was shown in Figure 6.51.

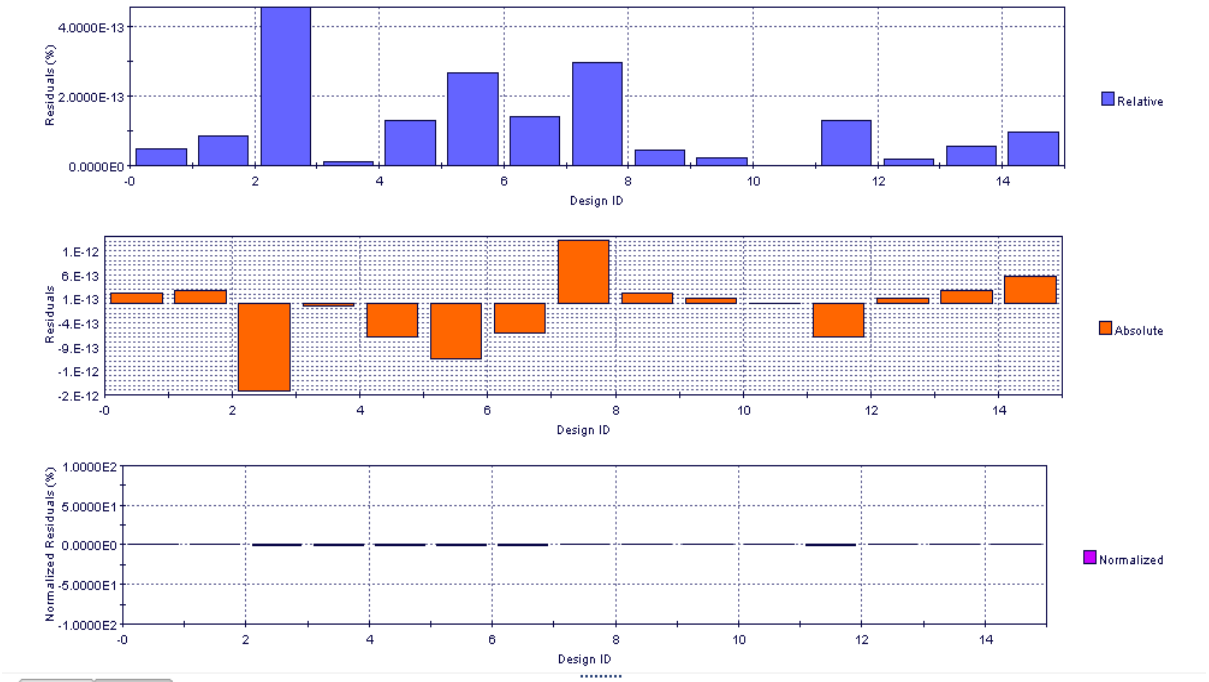

Summary | Residuals

Max Abs. Error	2.E-12	Max Rel. Error	5.E-13	Max Norm. Error	3.E-13
Mean Abs. Error	5.E-13	Mean Rel. Error	1.E-13	Mean Norm. Error	9.E-14
Regression	1.E0	Error Mean	-1.E-13		

Figure 6.51 - Residual Charts for Response Surface Methodology Algorithms for Friction Stir Welding Optimisation

For each function a number of regression parameters were calculated, these were listed in the summary table in Figure 6.51. Table 6.14 lists the regression data for all of the outputs used in the multi-objective optimisation. The best algorithms for each output were selected through an iterative process in which the functions are compared to one another against a number of criteria. These criteria, listed in order of importance, have been listed below:

1) Regression Parameter must be equal to one this indicates a perfect fit of the algorithm to the data. If a value of one was not achieved the function would be automatically excluded.
2) The two functions which have the lowest maximum and mean absolute error processed as the top two functions.
3) The best function out of the two was determined by selecting the function with the lowest error mean.

Table 6.14 - Response Surface Methodology Algorithm Regression Data for Friction Stir Welding Outputs

Output	Average Weld Force [N]	Average Temp Feed [°C]	Average Thickness [mm]	Ultimate Tensile Force [N]	Ultimate Tensile Strength [MPa]
Best Suited Algorithm	Kriging	Kriging	Kriging	Kriging	Anisotropic Kriging
Max Absolute Error	7.00E-12	2.00E-12	9.00E-16	3.00E-12	3.00E-14
Mean Absolute Error	4.00E-12	5.00E-13	2.00E-16	1.00E-12	1.00E-14
Regression	1	1	1	1	1
Max Relative Error	8.00E-14	5.00E-13	3.00E-14	4.00E-14	2.00E-14
Mean Relative Error	3.00E-14	1.00E-13	8.00E-15	1.00E-14	5.00E-15
Error Mean	5.00E-13	-1.00E-13	3.00E-17	-3.00E-13	-8.00E-15
Max Normal Error	4.00E-14	3.00E-13	3.00E-14	3.00E-14	1.00E-14
Mean Normal Error	2.00E-14	9.00E-14	7.00E-15	1.00E-14	4.00E-15

Output	Joint Efficiency [%]	Tensile Fracture	Max Bend Force [N]	Bend Angle [°]
Best Suited Algorithm	Anisotropic Kriging	Kriging	Kriging	Kriging
Max Absolute Error	1.00E-14	3.00E-15	3.00E-12	3.00E-13
Mean Absolute Error	5.00E-15	8.00E-16	6.00E-13	1.00E-13
Regression	1	1	1	1
Max Relative Error	3.00E-14	1.00E-13	1.00E-13	1.00E-12
Mean Relative Error	8.00E-15	5.00E-14	3.00E-14	3.00E-13
Error Mean	5.00E-16	5.00E-16	3.00E-13	-3.00E-14
Max Normal Error	2.00E-14	1.00E-13	1.00E-13	2.00E-13
Mean Normal Error	7.00E-15	4.00E-14	3.00E-14	9.00E-14

The trained algorithms were used to relate the two inputs to any single output. Figure 6.52 illustrates the 3D RSM plots for the various trained algorithms.

Joint Efficiency *Maximum Bend Force*

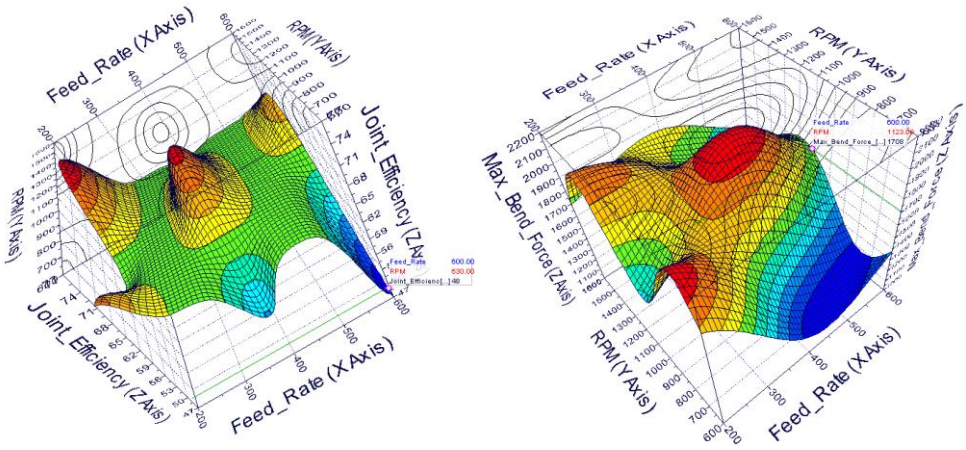

Maximum Bend Angle

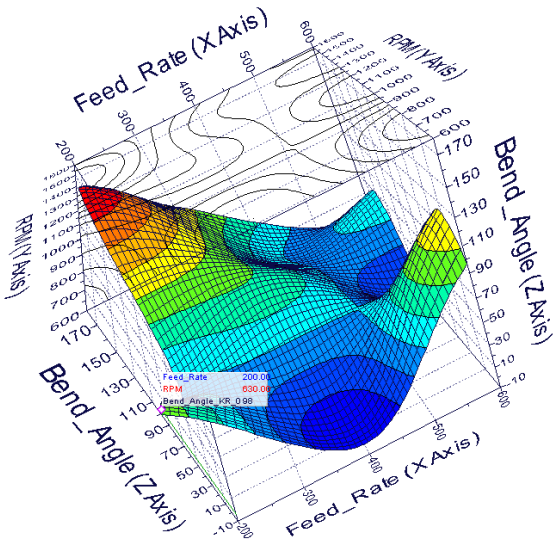

Average Welding Force

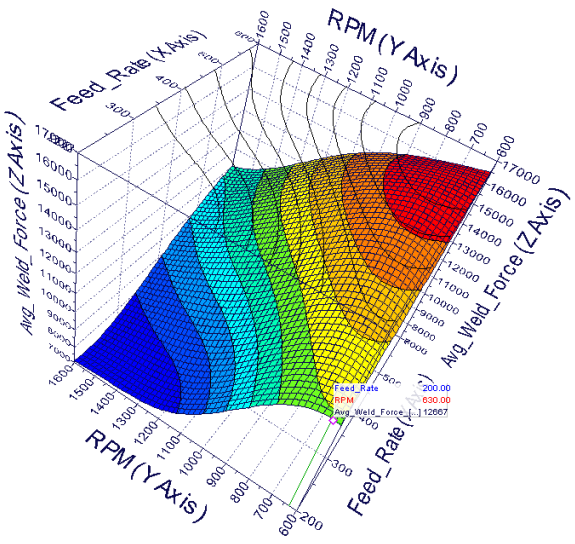

Average Joint Thickness

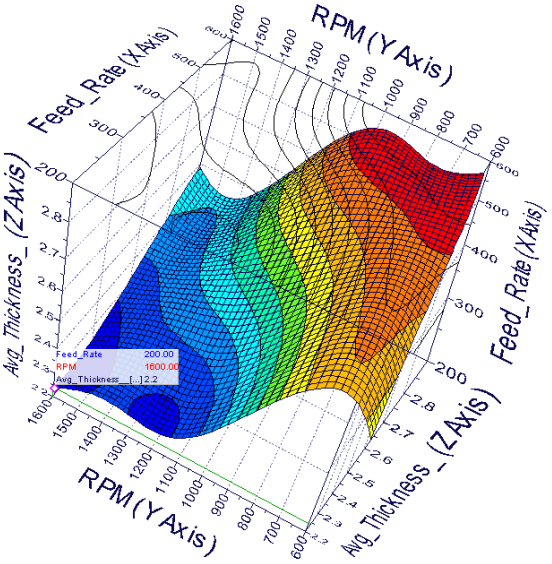

Ultimate Tensile Strength

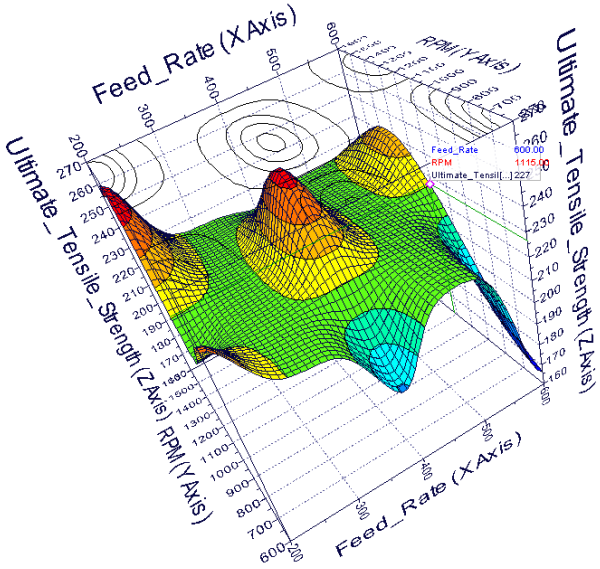

Ultimate Tensile Force *Tensile Fracture Position*

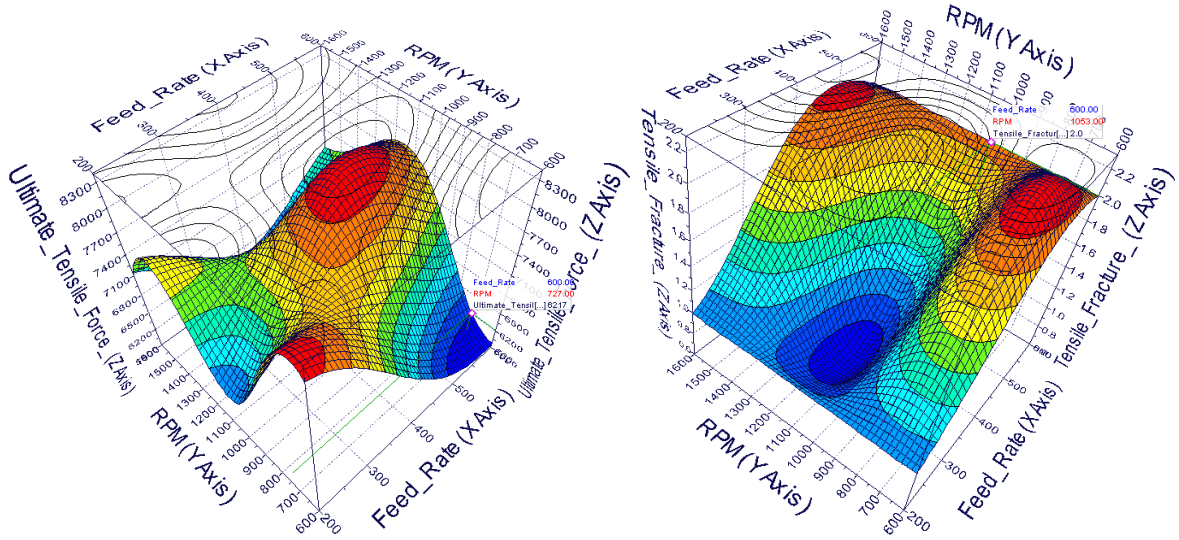

Average Temperature during Feed Stage

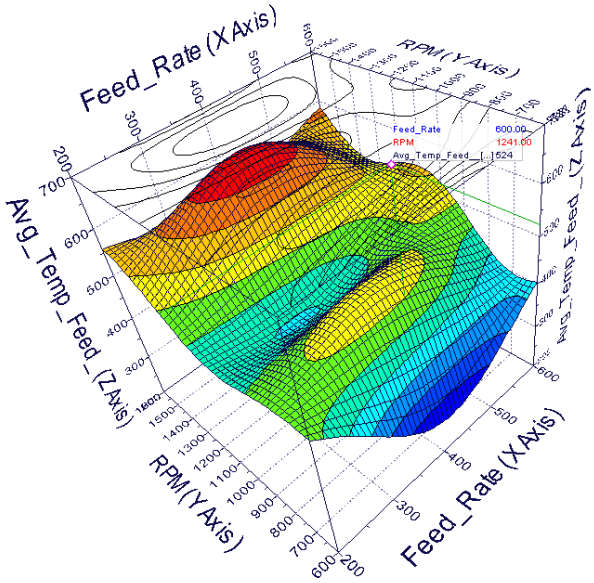

Figure 6.52 - Response Surface Methodology Plots Relating Friction Stir Welding Parameters to the Process Outputs

6.1.7.3 Optimisation of Friction Stir Welding Parameter Workflow Design

The workflow, as the name suggests was a setup of interlinking nodes/elements which work together to select input parameters and predict the output dependent on the RSM functions previously created. Figure 6.53 provides an example of the workflow used to optimise the FSW parameters.

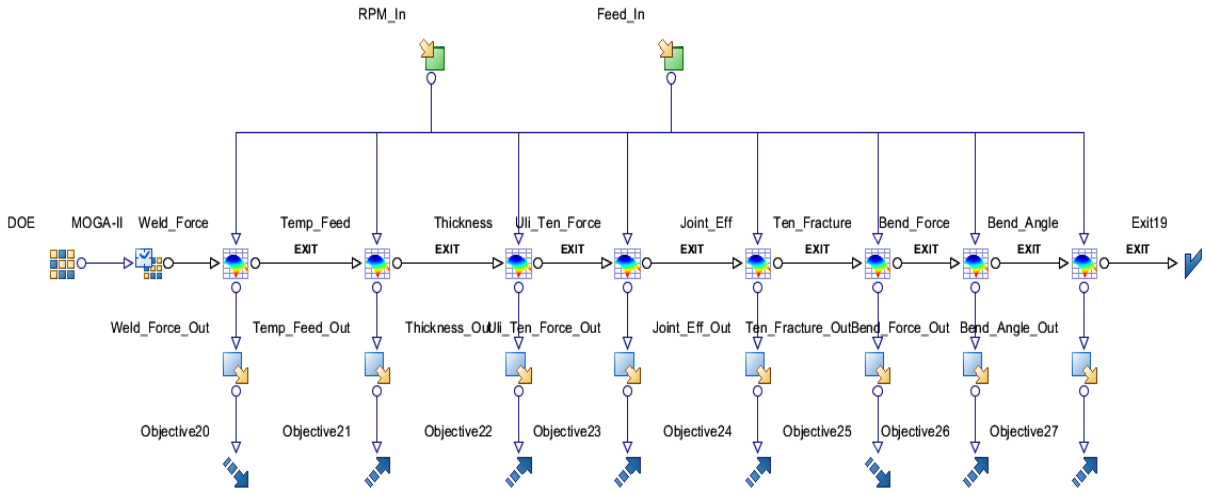

Figure 6.53 - Example of modeFRONTIER Workflow to Optimise the Friction Stir Welding Parameters

Each node in the chain has the following function:

1) **Input Nodes –** The two input nodes, Tool Rotation [RPM] and Feed Rate [mm/min] were varied to select values between predetermined boundaries. These inputs feed into each one of the RSM nodes. The parameters needed to be set to resemble the values used in the physical experimentation thus were extended slightly beyond the tested parameters. Table 6.15 lists the upper and lower bounds and ranges for which each input was varied.

Table 6.15 - Input Boundaries for Friction Stir Welding Input Nodes

Parameter	Unit	Lower Bound	Upper Bound	Range
Tool Rotation	RPM	600	1650	1050
Feed Rate	mm/min	150	650	500

2) **Output and Objective Nodes –** Each of the RSM functions was required to be associated with a specific output node and optimisation objective. This objective was either to maximise or to minimise the values. Table 6.16 lists each of the output functions and their related optimisation function.

Table 6.16 - Optimisation Objective for Output Functions for Friction Stir Welding Process

Outputs	Optimisation Objective	Reason for Objective Selection
Average Welding Force during Feed [N]	Minimise	Reduces load on tool and welding machine.
Average Temperature during Feed [°C]	Maximise	Optimum non-defective welding was achieved when higher temperatures were produced. Published works have shown that optimum welding temperatures range at 75 to 80% of the melting temperature of the working material.
Joint Efficiency [%]	Maximise	The joint efficiency relates the strength of the weld to the base material. Ideally, one would aim to have a 100% efficiency of the welded joint.
Average Joint Thickness [mm]	Maximise	Thicker joints correlate to minimal loss of material due to the flash formation as well as thicker joints ideally have a higher load carrying capability.
Ultimate Tensile Force [N]	Maximise	The higher strength of the joint was preferable for load carrying capability.
Ultimate Tensile Strength [MPa]	Maximise	The higher strength of the joint was preferable for load carrying capability.
Tensile Fracture Location	Minimise	According to allocation joints which failed in the centre was due to poor stirring and this position was assigned a value one.
Maximum Bending Force [N]	Maximise	The higher strength of the joint was preferable for load carrying capability.
Bend Angle [°]	Maximise	The larger the angle the more ductile the joint.
Fracture and Defect Formation	Minimise	According to allocation a joint which showed no signs of damage after the bending test was assigned a value of zero.

3) **Response Surface Methodology Nodes –** These nodes were set to be the most appropriate RSM functions for each output as listed in Table 6.14. Each design was passed through the

RSM functions thus using the trained algorithm this functioned attempted to predict its relative value. They had to be linked to one another with each input flowing into the node and one output with objected attached.

4) **Design of Experiments (DOE) Node –** This node allowed for the selection of the design space fuller. A Sobol sequence was the most suitable and a set of 500 designs were generated based on the boundaries of the input variables.
5) **Scheduler Node –** The Multi-Objective Algorithm II (MOGA-II) optimiser was selected out of all scheduler functions due to its ability to achieve fast convergence and its robust efficiency. For each of the designs from the DOE node, 100 generations were created. This gave a total of 50 000 different designs.

6.1.7.4 Results of Optimisation of the Friction Stir Welding Process

The optimum FSW parameters to be used in the later portions of this research were identified by using the post-processing technique of defining all the simulated designs on a parallel chart, as illustrated in Figure 6.54. The figure shows the link between each input and the expected outcome of numerous combinations of tested designs.

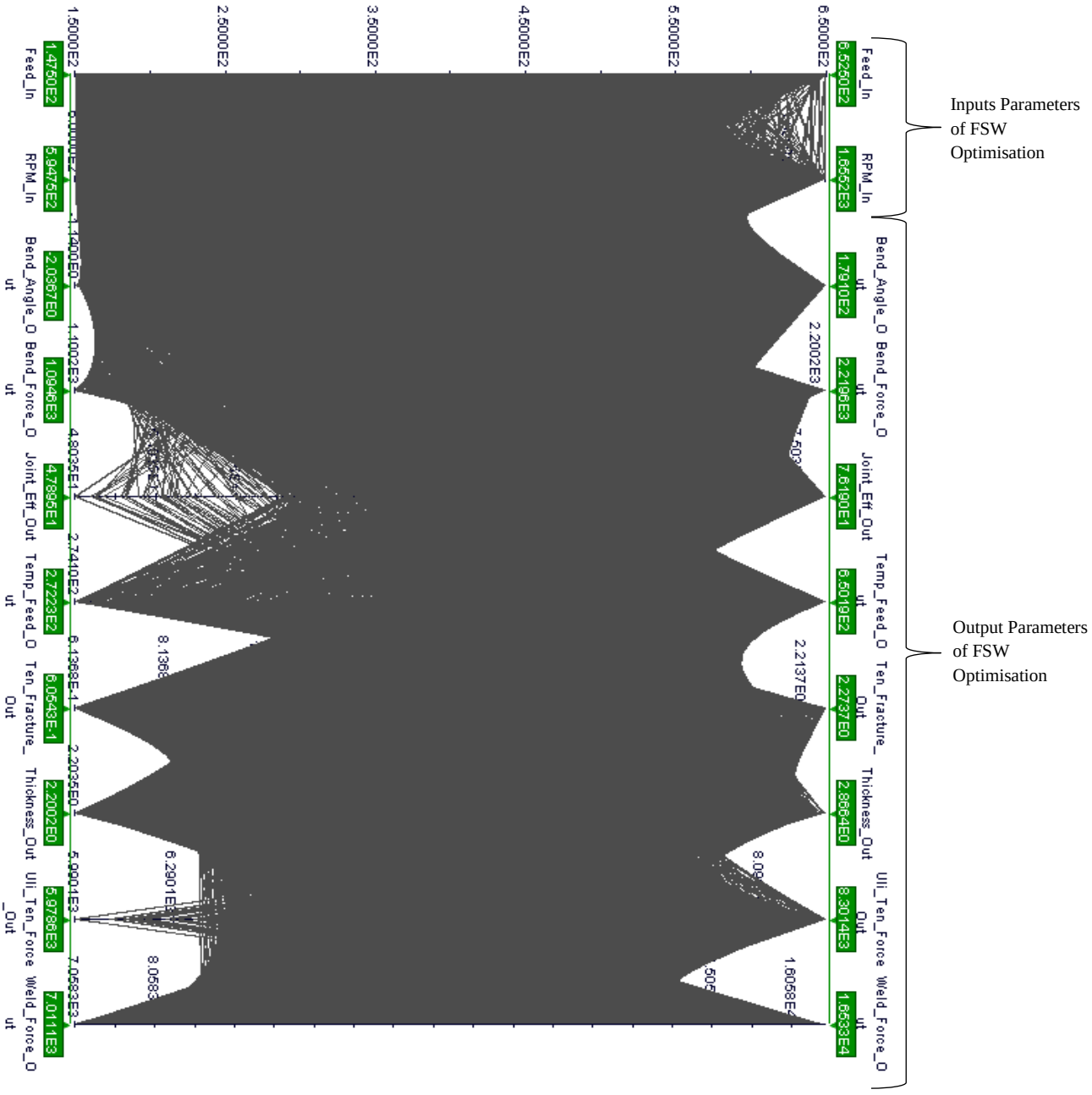

Figure 6.54 - Friction Stir Welding Optimisation Parallel Axis Chart Indicating all Designs

Axes of the chart can be manipulated in order to exclude numerous designs depending on a number of criteria. The reasoning behind the optimisation of the parallel axis chart was completed according to the listed criteria. Figure 6.55 shows the optimised parallel axes chart. The boundaries of Figure 6.54 of each output have been manipulated to:

- Reduced tensile fracture slider to be close to a value of approximately 1.2 as this predicts a joint which would not fail under a tensile force due to the presence of a defect in the centre of the joint.
- Maximise the bend angle as this would predict a non-defective joint.
- Maximise the tensile and bending force to obtain the strongest joint.

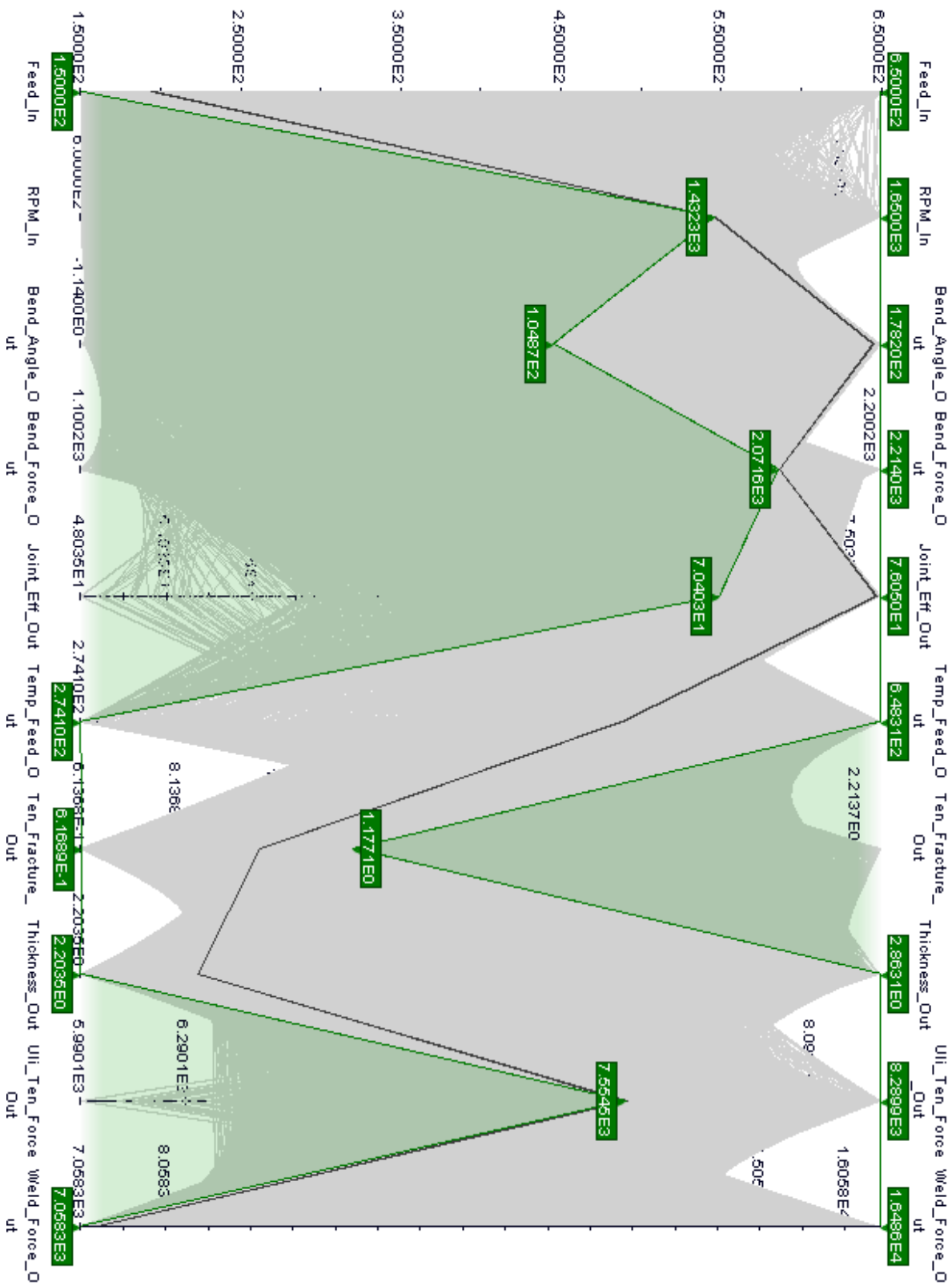

Figure 6.55 –Friction Stir Welding Optimised Parallel Chart according to stated Criteria

The adjustments of the sliders lead to the ability to select a design which would ideally be the most suited optimised set of inputs to the process. Two designs fell within the constraints of the

optimisation and were considered the most optimal set of parameters. Figure 6.56 shows the output of the design parameters.

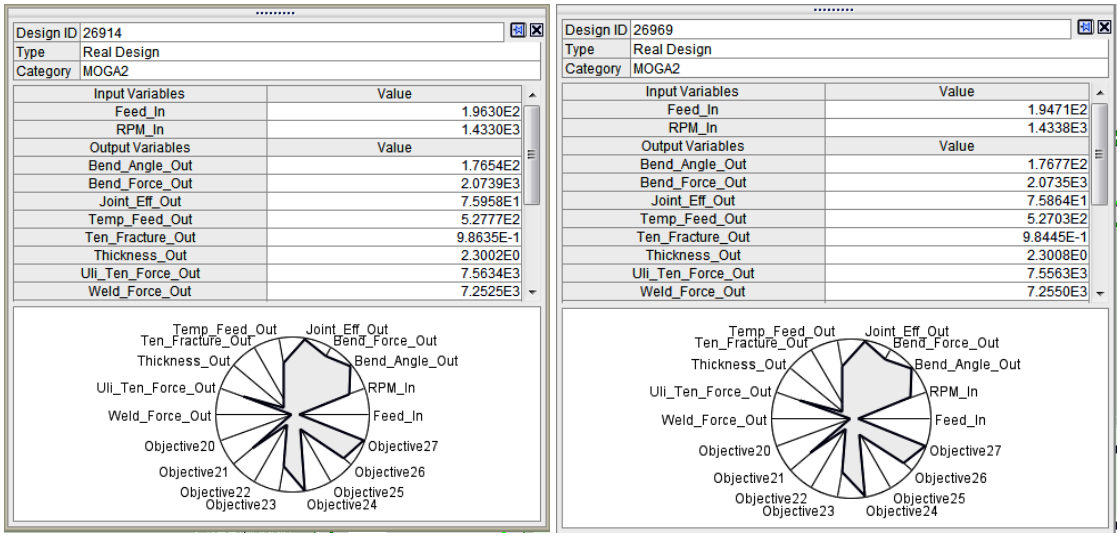

Design ID	26914
Type	Real Design
Category	MOGA2

Input Variables	Value
Feed_In	1.9630E2
RPM_In	1.4330E3
Output Variables	**Value**
Bend_Angle_Out	1.7654E2
Bend_Force_Out	2.0739E3
Joint_Eff_Out	7.5958E1
Temp_Feed_Out	5.2777E2
Ten_Fracture_Out	9.8635E-1
Thickness_Out	2.3002E0
Uli_Ten_Force_Out	7.5634E3
Weld_Force_Out	7.2525E3

Design ID	26969
Type	Real Design
Category	MOGA2

Input Variables	Value
Feed_In	1.9471E2
RPM_In	1.4338E3
Output Variables	**Value**
Bend_Angle_Out	1.7677E2
Bend_Force_Out	2.0735E3
Joint_Eff_Out	7.5864E1
Temp_Feed_Out	5.2703E2
Ten_Fracture_Out	9.8445E-1
Thickness_Out	2.3008E0
Uli_Ten_Force_Out	7.5563E3
Weld_Force_Out	7.2550E3

Figure 6.56 - Optimum Friction Stir Welding Parameters indicated by modeFRONTIER

The inputs indicated by these two design cases can be considered the most optimum set of parameters as they were estimated to produce the best set of outcomes according to the criteria stated earlier. Combination of the two designs predicts welding parameters of the following:

- Tool rotation speed: 1433RPM
- Feed rate: ±196 mm/min
- Resulting welding rate: 7.3 revs/mm

Unfortunately, due to the fixed gearing of the FSW machine, the indicated rotational speed could not be achieved. The closest speeds to the optimum value were 1250 RPM or 1600 RPM. The higher, 1600 RPM speed was selected for further use due to it being slightly closer to the optimum value than the 1250 RPM speed. Added to this, the welds manufactured at 1600 RPM, in most experimental outcomes, outperformed the 1250 RPM samples. A feed rate of 200 mm/min was selected as the parameters for the further part of this research due to the fact that the optimum feed rate was significantly close to 200 mm/min. Extensive experimental research had already been conducted at this feed rate already. Reducing the feed rate from 200 mm/min to 196 mm/min would also increase the welding rate from 8 revs/mm to 8.16 rev/mm, this was undesirable as the welding rate would be moving away from the optimum value. In summary, the final parameters which were used from here on out regarding Friction Stir Welding were:

- Tool Rotation: 1600 RPM
- Feed rate: 200 mm/min
- Welding rate: 8.00 mm/min

6.2 Laser Shock Peening Optimisation

Due to the sheer nature of LSP, one cannot simply optimise the process like it was done with the FSW part of this research. LSP is a multi-factor process which requires each level to be investigated before the most optimum process parameters can be selected. Factors such as air breakdown, which cannot be easily quantified make the optimisation process a twofold process. When determining the most opportune process parameters one should look at both the quantifiable and qualitative effects of the laser parameters. Figure 6.57 identifies the four most key and relevant aspects to the laser process. The four core areas indicated in the figure outline the general areas which were investigated in this optimisation process.

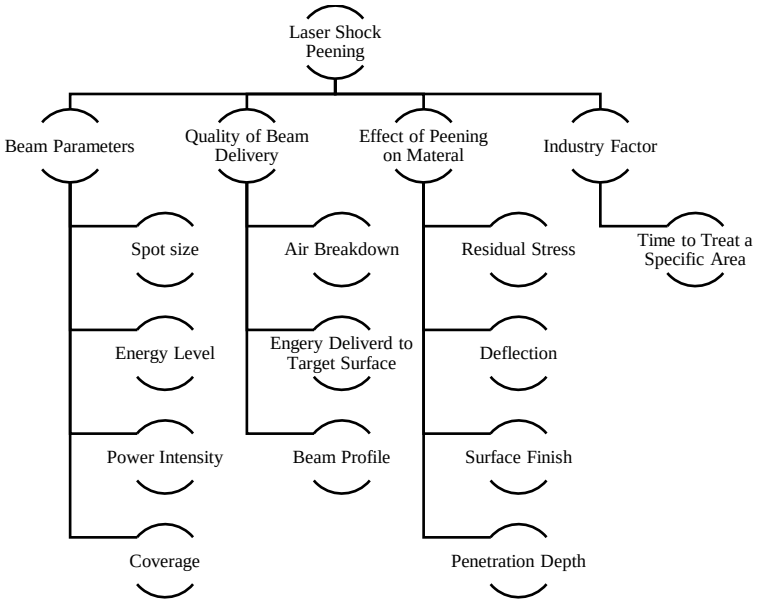

Figure 6.57 – Important Factors of Laser Shock Peening

Each of the factors will most likely influence other factors, which make up other key groups. These links have not been shown as at this stage the effects cannot be conclusively determined.

6.2.1 Beam Parameters

The four subfactors which have been identified to be the most influential will be discussed. The beam parameters have the largest effect on all the other aspects of the peening process and can be attributed to the final result of the effects of the process.

6.2.1.1 Spot Size of the Beam, Energy Level and Power Intensity

These three factors have been grouped into a single section as they are all related to one another through equation 2.2.

$$I_o = \frac{400 \cdot E_{\text{beam energy}}}{\pi \cdot \tau \cdot {d_{\text{spot}}}^2}$$

The spot size of the laser which interacts with the target was shown to significantly affect the mechanical results of the processed samples at the surface due to the surface release waves and at a depth due to attenuation effects. For this reason variation of the power intensity was achieved by varying the energy of the beam. The energy of the beam was also the easiest to vary as this was done by optimising the amplifier and oscillator voltages on the laser. The laser which was used was rated to be capable of outputting a maximum energy of 1.7J but it was strongly suggested by the National Laser Centre (NLC) to operate below 1J as this will improve the spatial intensity of the beam profile and will prolong the life of the laser and consumables associated with the set up. In addition, if the power intensity was altered by changing spot size than the coverage factor would be varied and thus little consistency between processed samples could be achieved.

In order to determine the diameter of the spot the redefined approach was used. This method requires a lens performance test in that the laser is set to a stable energy and at no time can the lens be moved, all measurements of the laser profile and spot size were completed at various distances from the lens. The spot profile and size was recorded with the use of the NLC's CCD camera. Figure 6.58 provides the results of this lens performance test. The spot sizes were determined at three different energy levels. For the tests to be successful a linear trend must be achieved by the predictions of the geometric optic. From previous work completed by Glaser [62], a spot diameter of 1.5 mm was suggested to be used for this processing as it provided a suitable coverage factor, as well as stable power intensities, could be achieved at these energies. The experimental uncertainty error bars have been neglected as the error in distance from the lens was specified as ±0.5 mm and the spot diameter as ±0.05 mm.

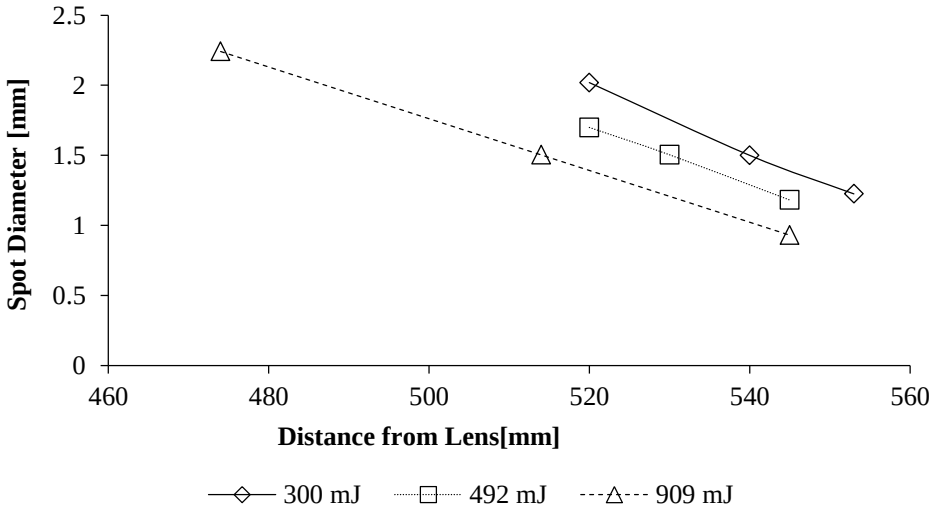

Figure 6.58 - Lens Performance Evaluation

Beam diameter and energy level of the beam directly influences the power intensity. As discussed in section 5.3.2 the laser spot size at the point of contact with the target surface is calculated according to

the ISO D4 Sigma method which calculates the second-moment diameter for a circular beam. This method calculates the diameter in the x or y directions according to four times the standard deviation of the marginal distribution.

The energy level of the laser was varied by optimising the amplification and oscillation through setting these factors on the controller unit of the laser. The energy was varied from 100 to 900 mJ to obtain the desired power intensity. Due to the setup of the laser one has to be mindful of the drop in energy of the beam as it propagates from the laser exit to the lens for this reason the energy had to be measured just after the lens and the assumption that the loss in energy of the focused beam is negligible during the propagation from the lens to the target surface.

The power intensity of the laser was varied from 1 to 6 GW/cm^2. This range was what was possible to achieve at a spot diameter of 1.5 mm and the energy output range of the laser. To achieve a lower intensity would have resulted in setting the laser amplification and oscillation to an extremely unstable energy level. Literature has also shown that a power intensity of above 0.5 to 1 GW/cm^2 is required to achieve the desired peening effects. Increasing the energy to achieve an intensity which was greater than 6 GW/cm^2 resulted in large amounts of air breakdown which negatively affected the repeatability and quality of processing and placed a large amount of strain on the extremely delicate laser. Figure 6.59 shows the initial operational window identified for further processing and how the energy affects the outputted power intensity.

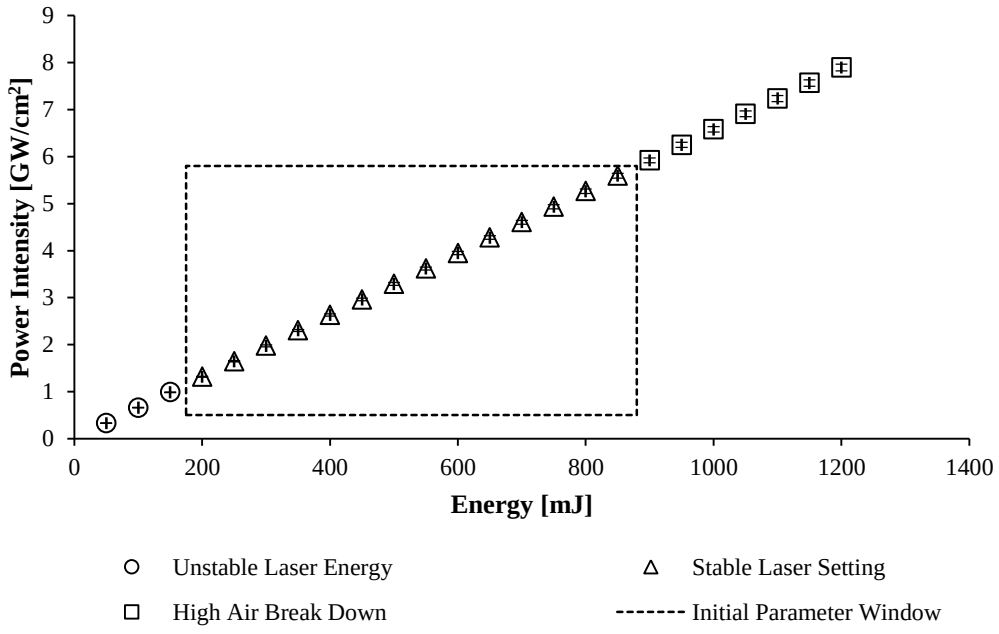

Figure 6.59 - Power Intensity Operational Window for Current Set Up for LSP

Table 6.17 lists the parameters which were required to achieve the desired power intensities whilst maintaining a spot diameter of 1.5 mm.

Table 6.17 - Laser Set Up for Achieving Various Power Intensities for a Spot Diameter of 1.5 mm

Energy output [mJ]	Power Intensity [GW/cm^2]	Spot Diameter [mm]	Distance from Lens [mm]
150	0.987	1.5	520
550	3.619	1.5	536
765	5.034	1.5	523

6.2.2 Quality of Beam Delivery

The laser parameter window was identified as discussed above, it was required that the quality of the laser beam be investigated within this desired window. This was required in order to have confidence in the quality of processing being completed.

6.2.2.1 Air Breakdown

Air breakdown is the formation of absorption plasma as the high powered laser beam propagates through a clear medium; this has been discussed in section 2.4.6. As the power intensity increases with increasing laser energy, the threshold of air is approached resulting in a so to speak explosion of air along the propagation of the laser. The occurrence of the blocking plasma flash, seen in the figures below as bright flashes of light, causes a reduction in beam energy, profile distortion and poor processing, it should try to be avoided as much as possible. It is very difficult to quantify the drop in energy or the change in profile directly caused by the phenomena thus a qualitative investigation can only be considered with this section. Figure 6.60 was provided through initial investigations into the effects of varying laser parameters on the quality of LSP, conducted by Glaser [62]. The power intensity was varied in 1 GW/cm^2 intervals from 1 to 10 GW/cm^2. Figure 6.60 illustrates substantial plasma flashes at the target surface which is to be expected due to the interaction with the water confinement layer. Three images were randomly selected during the operation of the laser at various power intensities.

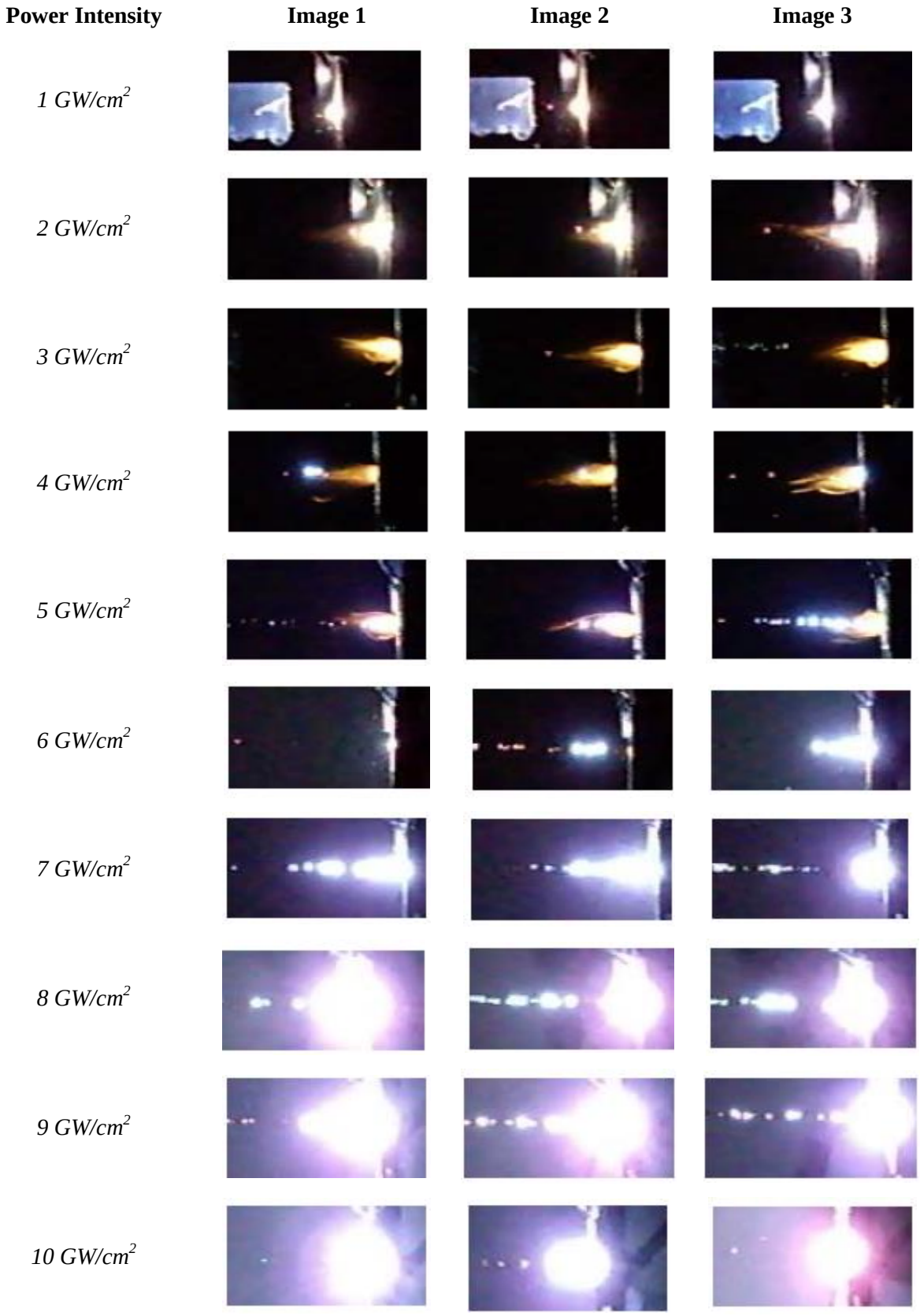

Figure 6.60 - Air Breakdown with Varying Power Intensity

Avoiding the occurrence of plasma flashes in the regions preceding the surface target was of vital importance in the selection of the best process parameters. From a power intensity of 7GW/cm^2

extensive plasma flashes occurred. These power intensities were unacceptable and all processing was avoided. This qualitative study confirmed the initial selection of the processing window. It was noted during processing that at the higher energies required to achieve the power intensities the laser energy became far more unstable and fluctuated significantly to that of the lower power intensities.

6.2.2.2 Beam Profile at Investigated Power Intensities

The beam profile was recorded by firing a single shot into the CCD camera. Surpassing the energy threshold of the camera would result in permanent damage to the equipment thus to avoid these ND filters were used to filter the beams whilst maintain the geometric properties and profile of the beam.

From the initial literature investigation, a Gaussian beam profile was preferred for this application but due to the laser forming part of the Rental Pool equipment at the NLC, it had been set up to be a versatile laser catering to a number of different experimental needs. Due to this, the manufacturers specification of a pure Gaussian beam could not be fully achieved. Figure 6.61 provides examples of the beam profiles at the fixed spot diameter of 1.5 mm for a number power intensities investigated.

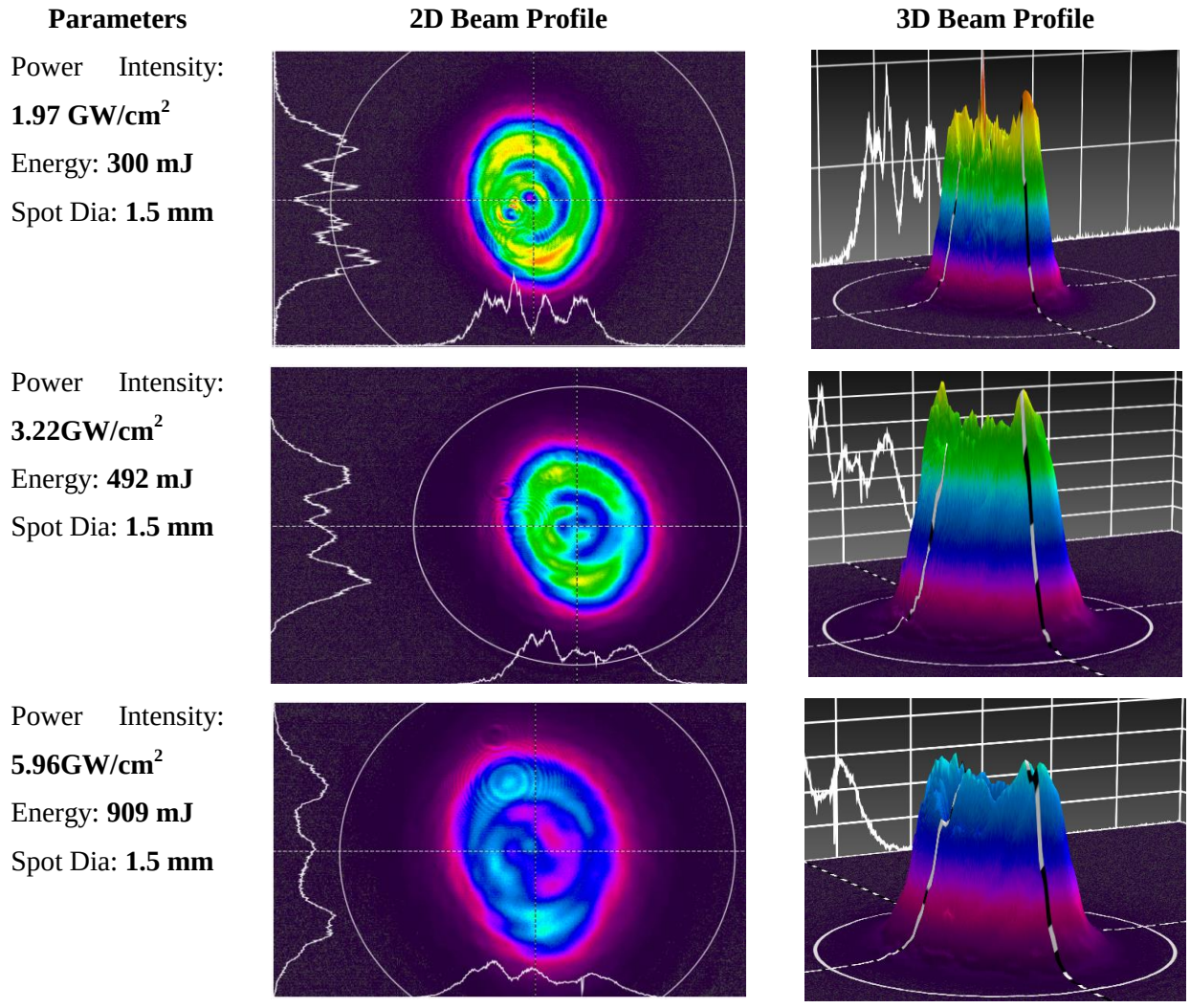

Figure 6.61- Characterisation of the Beam Profiles

As seen in the figures the profiles achieved were not completely Gaussian but resembled more of a Top-Hat beam profile. This combination of the two is known as a Super-Gaussian beam profile. The variation in colours through the peaks was directly affected and controlled by the number of ND filters used to control the intensity of the beam. In the 2D profiles, it can be seen that the profiles exhibited a slightly oval shape rather than a perfect circle which is associated with a pure Gaussian beam profile. In the profiles a set of concentric rings were observed in the profiles, this was due to damage to the laser pump rods and could not be altered or corrected as these items are the source of the laser. The size, shape and profile of the beams were fairly consistent across the spread of power intensities.

6.2.2.3 Overlap and Coverage of Laser Spots

As the spot size was fixed the only variable parameters were the power intensity and the coverage of laser spots. A number of laser pulses in a given area were controlled by varying the coverage. By changing the amount of laser impacts per square centimetre one could begin to control the overlapping area of adjacent pulses, deflection of the material, the depth and distribution of residual stress and the time taken to treat a required area. The coverage was initially varied from a minimum of 50 spots/cm^2 up to a maximum of 2000 spots/cm^2. This initial identification of the coverage parameters was selected from assessments of literature and mainly on the previous experience of fellow users of this laser system.

A standard cross and step LSP strategy were employed in the processing the area of the treated samples. This strategy has been commonly used by most LSP facilities across the globe. Section 5.3.1 outlines the operation of the automated table which the samples were all mounted to during the peening process. Figure 6.62 shows the peening strategy used throughout this research. Each circle in this image is representative of a single laser pulse striking the target surface. Dependent on the coverage required a number of these pulses overlap one another. This overlap can be defined as the coverage factor. The coverage factor was calculated according to equation 6.2. This factor relates the number of pulses in a given area to the area of a single laser pulse, which is dependent on the size of the spot. The amount of overlapping area of the adjacent pulses can influence the resulting residual stress within the component as a higher overlap increases the attenuation energy exposed on a position on the treated component.

$$C_v = N_p \times A_p \tag{6.2}$$

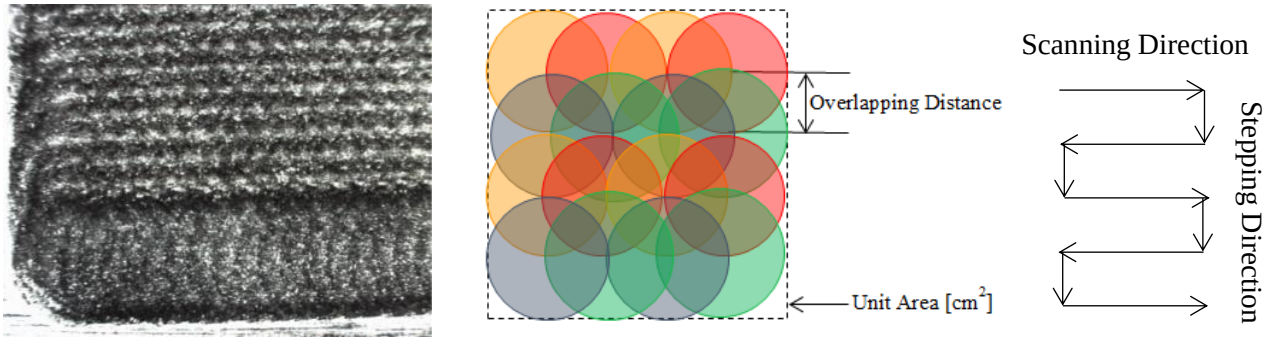

Figure 6.62 - Laser Shock Peening Strategy and Overlap of Pulses on a Target Area

The initial LSP parameter window was specified according to those listed in Table 6.18.

Table 6.18 - Initial Parameter Window for Laser Shock Peening Optimisation

	Coverage [spots/cm^2]					
Power Intensity [GW/cm^2]	**50**	**100**	**250**	**500**	**1000**	**2000**
1	Samp 1	Samp 2	Samp 3	Samp 4	Samp 5	Samp 6
2	Samp 7	Samp 8	Samp 9	Samp 10	Samp 11	Samp 12
3.5	Samp 13	Samp 14	Samp 15	Samp 16	Samp 17	Samp 18
5	Samp 19	Samp 20	Samp 21	Samp 22	Samp 23	Samp 24

6.2.3 Effect of Peening on Material

To investigate how these parameter combinations influenced the material a number of exponential tests were performed on the base material as well as Friction Stir Welded samples.

6.2.3.1 Deflection, Distortion and Intensity of the Laser Peening Process

To identify how the material was influenced by the various combinations of coverage and power intensity the technique of Almen strips were used. Almen strips are used extensively in the investigation of Shot Peening parameters, as the test quantifies the shot intensity of the process. Standard sized coupons of a particular material are used for these tests. As an investigation into the effect of LSP parameters on the base material was required, samples of standard Almen strip geometry was machined out of the base material, the size of the Almen strips used can be seen in Figure B.6 in Appendix B. The strips are processed completely on a single surface. Almen strips are a current form of quality control technique used by commercial providers of LSP. Previous studies have shown that the deflection of the Almen strips may be used as an effective indication of the generation of compressive residual stress in the strips. This provides an efficient technique to investigate the intensity of the various combinations of the laser and process parameters. Figure 6.63 shows a set of Almen strips and how they have deflected after been treated with respective parameters.

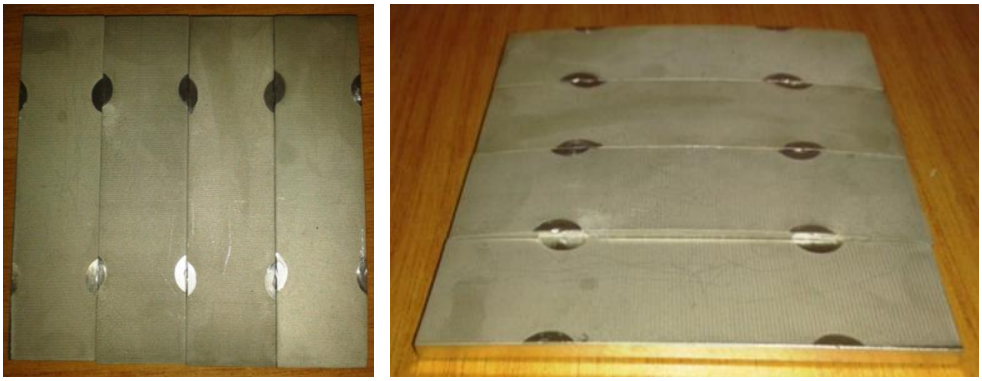

Figure 6.63 -Almen Strip Samples

Figure 6.64 shows the results of the processed AA6082-T6 Almen strips. The samples were treated according to the parameter combinations listed in Table 6.18. This figure resembles a typical Almen curve associated to Shot Peening. The saturation point associated with Shot Peening is known as the first point when the exposure time of a stream of shots was doubled at which the arc height increases by less than 10%. Apply the same logic for LSP, it can be said that the sample was saturated when there was less than a 10% increase in arc height when the coverage is doubled. It can be clearly seen that surpassing coverage's of 1000 spots/cm^2 resulted in less than a 10% increase in arc height. For this reason, the maximum coverage of any area was set to no more than 1000 spots/cm^2.

The most apparent characteristic of the results in Figure 6.64, was the differences in deflections of the samples processed at 1 GW/cm^2 compared to the others. There was a fairly close grouping of the remaining samples at different power intensities. Typically, the greater the intensity the higher the arc deflection which suggests according to previous work by members of the Wits Laser Shock Peening Group a greater influence of the LSP process on the residual stress within the component [96]. The uncertainty in the deflection was specified as ±0.005 mm for each measurement completed with a dial gauge. The error bars have been left off as the uncertainty range was too small to clearly be seen in the figure.

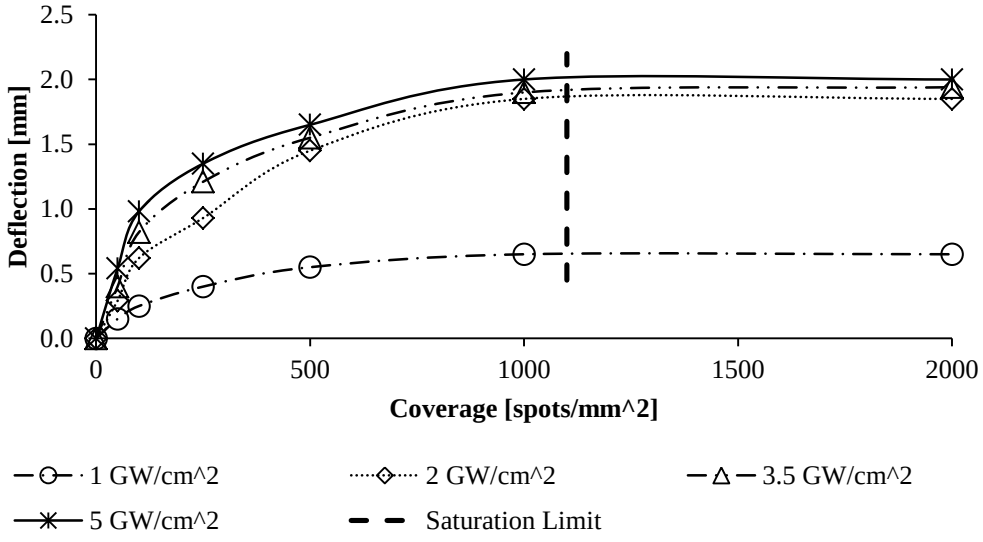

Figure 6.64 - Almen Strip Measured Deflections

The difference between the higher intensity lines tended to become smaller and smaller. This suggests that as the intensity increase the power intensity saturation point was being the approach. This refers to the limit were increasing power intensity results in no change in the mechanical property of the treated sample. For all sets of samples (samples processed with common power intensity) a rapid increase in arc height was noted at the lower coverage's, all sets follow the same trend. The effect on increase intensity tended to increase the arc heights for the same coverage.

6.2.3.1.1 Conclusions

From the results presented in this section the following can be concluded:

1. 1000 spots/cm^2 was the limit to the applied coverage, as not further increase in coverage resulted in a substantial increase in arc height.
2. Previous work has shown that the arc height can be used as an indication of the residual stress introduced into the component.
3. An increase in power intensity results in an increase in arc height for the same coverage.
4. The figure suggests that there exists a limit of power intensity in which an increase in power intensity will not affect the mechanical properties in any way.
5. A power intensity of 1GW/cm^2 has very little effect on the coupons thus suggesting that little amount of compressive stress was generated in the component.

6.2.4 Surface Roughness Variations Due to Laser Shock Peening Parameters

Many factors such as residual stress, component geometry and surface quality can be linked to the fatigue performance of most engineering components. A major contributor to the surface quality would be the post peened components surface roughness. Processing of a component with Laser Shock Peening without a coat results in an ablated layer being created as the laser interacts with the

target surface. Figure 6.65 shows two examples of different samples being processed with LSP without a coating. A large orange-yellow spark was ejected from the target surface, this was found to be the emissions of the ablated layer of the processed material [97].

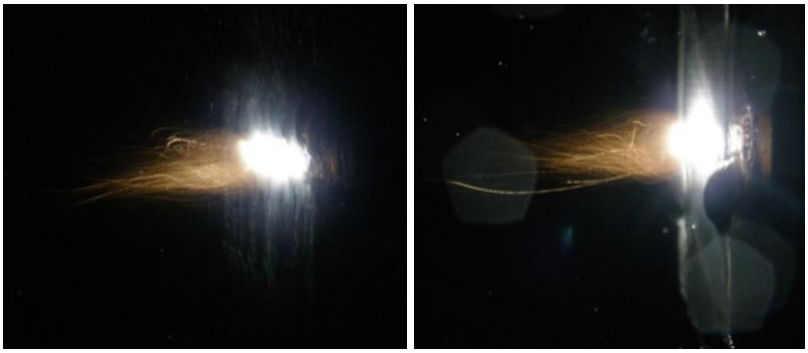

Figure 6.65 - Ablation of the Target Surface during Laser Shock Peening without a Protective Coating

LSP without coating results in a new surface layer being formed one which was substantially different to the base material layer. It has been found that the interaction of the laser with the target surface both ablates and melts the surface to form a dimpled, re-melted surface [98]. All processed surfaces, no matter the coverage and intensity, resulted in a clouded layer which can be seen in Figure 6.66.

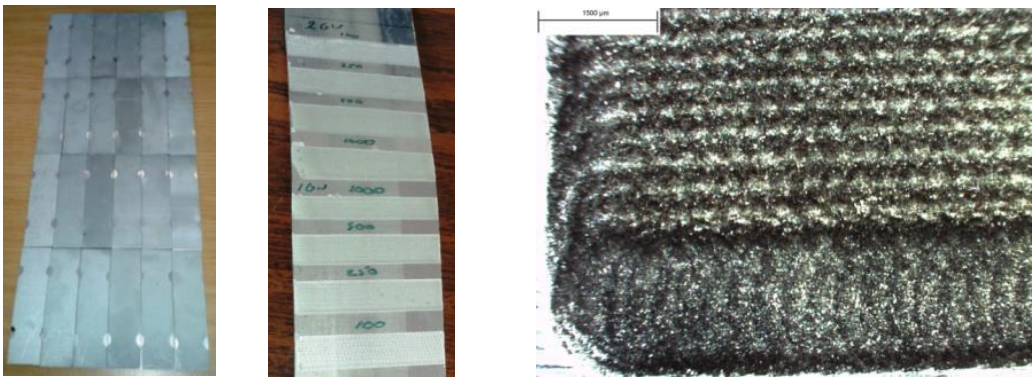

a) Processing on the Base Material, AA AA6082-T6

b) Processing on the Friction Stir Welded Surface

c) Microscopic view of the Laser Peened Surface

Figure 6.66 - Laser Shock Peened resulting Surface due to Melting and Ablation of the Target Surface

The post peened surface without a protective covering would result in a change in surface roughness compared to that of the base material. This change in surface roughness from that of the parent material needs to be characterised in terms of varying power intensity and coverage. Although the fatigue life may be improved through the introduction of compressive residual stress a poor surface finish and roughness is known to cause detrimental effects on the life of the component. Combining LSP on FSW results in a combined increase in surface roughness, it must be said that the overall roughness was based on the initial roughness of the surface to which LSP was applied [98]. The surface roughness of the base material+LSP and FSW+LSP were measured using a Bondetec BR-

3932 portable surface roughness tester, these tests were completed by Rahim. Multiple laser parameter combinations were applied to the base material and the root surface of an FSW joint. The parent material and the peened surface of the FSW joint had an average measured roughness of 0.29 µm and 0.45 µm. Figure 6.67 and Figure 6.68 shows the general trends of the surface roughness increasing with increasing coverage [99]. This trend may be attributed to the fact with increasing coverage results in a greater amount of laser impacts which are introduced on the surface. During the re-solidification of the melted layer a number of microcracks may have formed. Add to this LSPwC creates cavities in the surface. The highest power intensity was shown, in both cases, to result in the highest surface roughness. It would be intuitive to assume that the surface roughness would increase with power intensity for equivalent coverage due to the fact that higher peak pressures would cause the formation of a deeper/larger cavity on the external peened surface. Under this rationale, it was unclear as to why the data set of 3.5 GW/cm^2 to exhibit a surface roughness that was typically lower than all other laser parameter combinations. The uncertainty in each measurement was specified as ±0.005µm. Error bars have not been shown due to the size of the error range not showing clearly in the figures below.

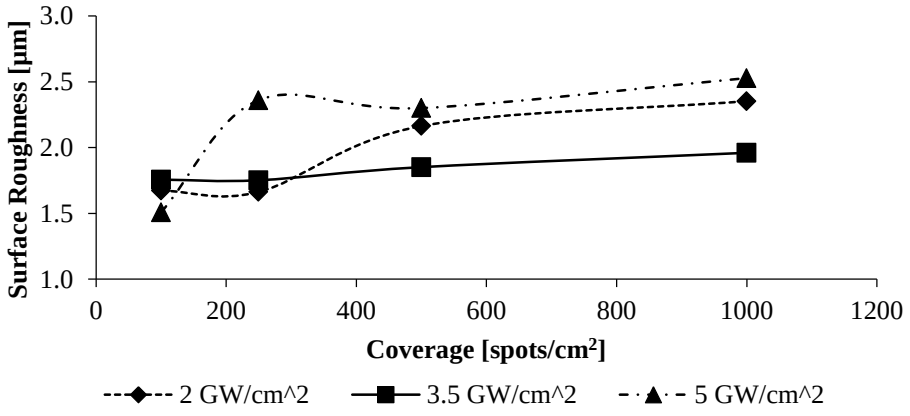

Figure 6.67 - Variation of Surface Roughness due to Varying Laser Shock Peening Power Intensity and Coverage on Base material

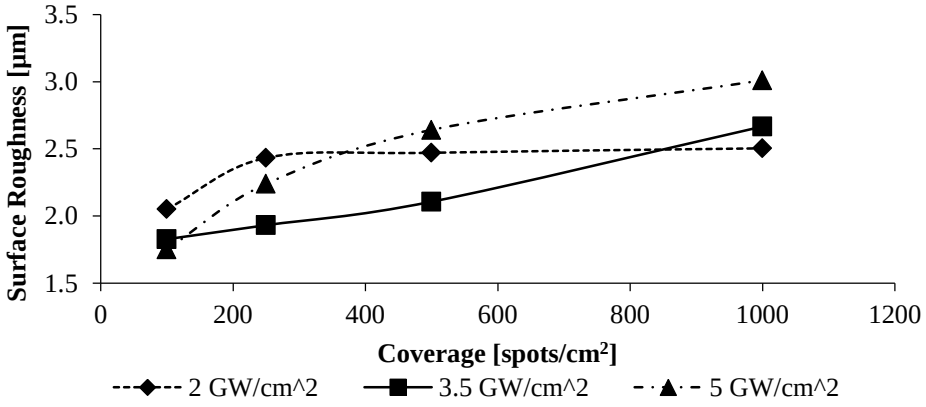

Figure 6.68- Variation of Surface Roughness due to Varying Laser Shock Peening Power Intensity and Coverage on Friction Stir Welded

It can be seen in Figure 6.69 that surface roughness of the FSW+LSP samples were on average higher than the equivalent Base+LSP, this trend follows that seen in literature.

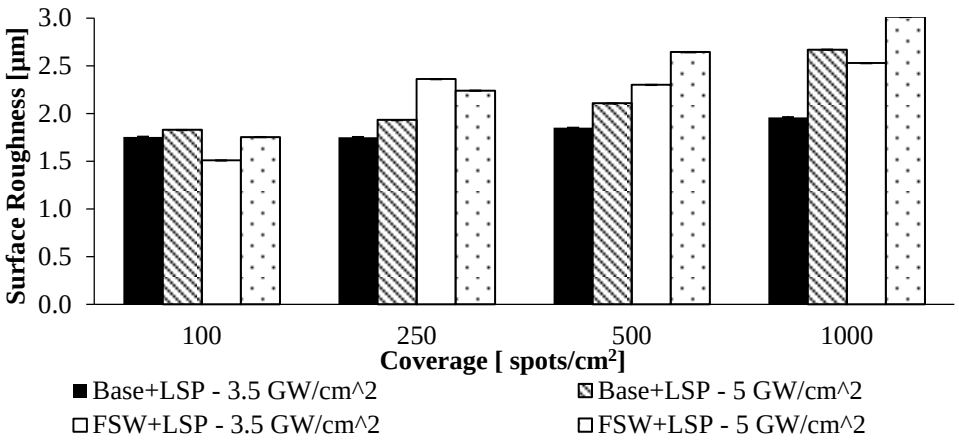

Figure 6.69 – Distribution of Surface Roughness on different Laser Peeing Material

Due to the 2GW/cm^2 data set not following similar trends to that of the remaining datasets one cannot without a shadow of a doubt conclude that increasing power intensity increases the surface roughness. It can be concluded that in an increase in coverage results in a higher surface roughness. Due to limitations in the use of the equipment these results could not be confirmed or repeated.

6.2.4.1 Conclusion

From the results presented in this section the following can be concluded:

1. Not all the laser power intensities displayed the trend of increasing surface roughness with constant coverage. This could not be conclusively confirmed but higher power intensity resulted in the highest surface roughness. This may have been due to the higher peak pressures of the laser pulse ablating a greater amount of the surface resulting in deep cavities forming on the surface.
2. In general, the trend of increasing surface roughness due to increasing coverage was shown throughout all data sets.
3. The initial surface roughness of the sample in which LSPwC was applied. The greater the initial surface roughness the greatly the final roughness of the peened samples.

6.2.5 Penetration Depth of the Effects of Laser Shock Peening

Literature states that the Laser Shock Peening process is capable of strain hardening a treated component up to a few millimetres from the surface. The strain hardening of the surface is one of the fundamental dynamics in which the LSP improves the fatigue life of the samples [54]. The peak pressure generated through the variation of power intensity and the coverage would strain harden the

material differently for each set of parameter combinations. For this reason, a study of the penetrative effect of LSP on the material was required.

The goal of this research was to investigate the possibility of using LSP to improve FSW joints which contained lack of penetration defects within the joint. LOP can be modelled as a crack which has partially propagated through the thickness of the joint. The size and inclination of the crack were determined by the severity of the offset of the welding tool. These LOP cracks should behave as all crack do under cycling load in that, during the application of a tensile load the crack opens at the tip and propagates further along the joint until the joint fails under the load. In order for LSP to be an effective means to retardation or hindrance to the propagation of the defect, substantial compressive residual stress would need to be introduced to completely surround the crack with compressive stress. This would work towards attempting to preserve the defect and to maintain its current geometric size. A schematic demonstration was shown in Figure 6.70, in that the crack/defect is surrounded by tensile residual stress throughout the thickness of an untreated FSW sample. By peening the root surface, the surface from which the defect initiates, compressive residual stresses can be generated by the crack. The depth of the affected area, as indicated, is a function of the LSP parameters.

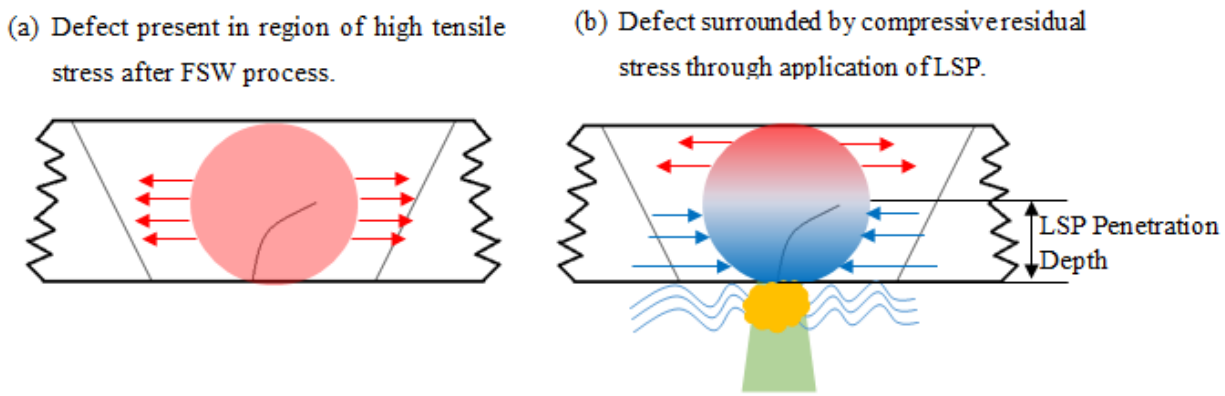

Figure 6.70 - Schematic of Laser Shock Peening surrounding the Welding Defect

The LSP processing is known to strain harden the parent material as the shock wave propagates through it. By measuring the hardness at multiple locations through the thickness of the peened joint the through thickness hardness profile can be obtained. The depth at which the hardness returns to the original value of the unpeened sample can be considered the location in which the LSP no longer affects the material. For this to be a valued experiment it was conducted on an FSW sample as the combination of the two processes was the final goal. It was uncertain whether the combination of FSW and LSP may influence the results, this added to the reason why the tests were performed the FSW samples rather than LSP base material. Various peening parameter combinations were applied to a Friction Stir Weld completed at 1000 RPM and 400 mm/min.

Figure 6.71 - Laser Shock Peened Strips of Varying Parameters on 1000 RPM and 400 mm/min

Vickers microhardness testing was used with a 100g applied load, diamond indenter and a load time of 10 seconds being used to measure the hardness. The indentations were made every 100 µm, beginning at the root surface through to the crown of the weld. The indentations were also made along the centre line of the joint. Figure 6.72 provides an example of the indentations made through the thickness of the joint. An example of Lack of Penetration can be seen just to the left of the set of indentations in the largest image in the figure. The Laser Shock Peened surface has been indicated, the peening parameters for the displayed sample was 2 GW/cm^2 and 500 spots/cm^2. This sample was selected purely for the quality of the image and the clarity of the LOP. By counting the number of indentation, the length of the crack can be roughly estimated to be as much as 600 µm long. This shows the requirements of finding parameters which are able of affecting the welded material well passed 600 µm.

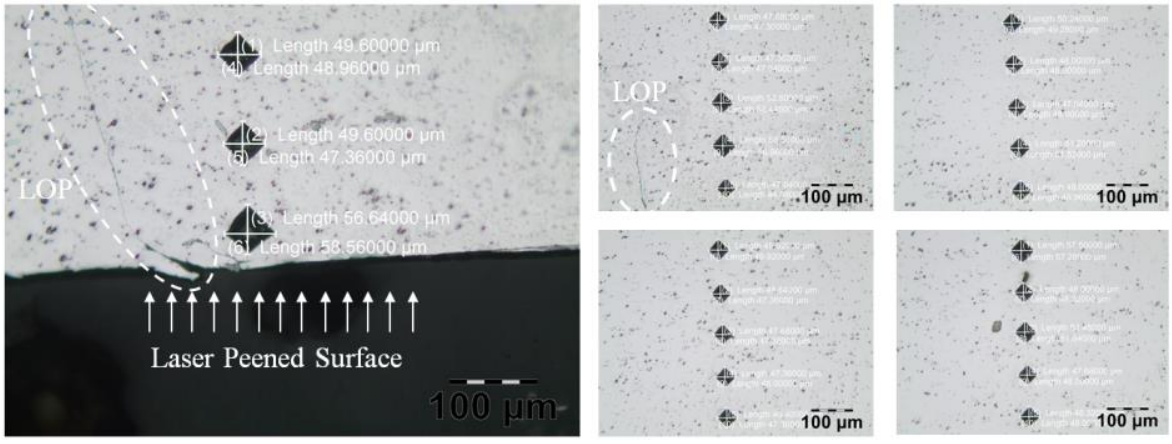

Figure 6.72 - Example of the Indentations made through the Thickness with the Presence of Lack of Penetration

Table 6.19 lists all the most important results from the various micro-hardness tests performed on the various laser shock peened samples. Due to the amount of data the table has been cut over three layers. The uncertainty range associated with the hardness measurements was calculated to vary from 0.28 to 0.58 $HV_{0.3}$. The uncertainty has been listed in Table F.2 in Appendix F. Due to a large number of data points, the error bars have been left off in the interest of clarity of the figures.

Table 6.19 –Important Results from Micro-Hardness Tests Performed on various Laser Shock Peened Samples

Power Intensity [GW/cm^2]	**1 GW/cm^2**				**2 GW/cm^2**			
Coverage [Spots/cm^2]	**Maximum Hardness [HV 0.3]**	**Average Hardness [HV 0.3]**	**% Increase from FSW**	**Penetration Depth [mm]**	**Maximum Hardness [HV 0.3]**	**Average Hardness [HV 0.3]**	**% Increase from FSW**	**Penetration Depth [mm]**
100	86.71	77.90	-0.71	100.00	98.62	83.31	12.93	600.00
250	94.40	83.33	8.09	500.00	102.36	86.22	17.21	800.00
500	96.47	85.79	10.46	900.00	85.53	76.76	-2.06	900.00
1000	95.83	83.58	9.73	900.00	102.36	88.66	17.21	1100.00

Power Intensity [GW/cm^2]	**3.5 GW/cm^2**				**5 GW/cm^2**			
Coverage [Spots/cm^2]	**Maximum Hardness [$HV_{0.3}$]**	**Average Hardness [$HV_{0.3}$]**	**% Increase from FSW**	**Penetration Depth [mm]**	**Maximum Hardness [$HV_{0.3}$]**	**Average Hardness [$HV_{0.3}$]**	**% Increase from FSW**	**Penetration Depth [mm]**
100	100.85	88.27	15.49	1500.00	97.89	85.57	12.09	1200.00
250	107.13	88.75	22.67	1600.00	106.33	89.90	21.75	1600.00
500	107.96	88.65	23.63	1600.00	107.13	91.35	22.67	1600.00
1000	106.33	89.90	21.75	1700.00	112.43	92.76	28.74	1600.00

Base Friction Stir Weld	
Maximum Hardness [$HV_{0.3}$]	**Average Hardness [$HV_{0.3}$]**
87.33	79.29

Figure 6.73 provides an example of the results of the microhardness profiles the base FSW and joints which were processed with a power intensity of 5 GW/cm^2 and different amounts of coverage. The triangular black data points indicate the hardness of the un-peened FSW welded joint. It can be seen that this profile shows very little variations through the thickness besides for a number of points in the latter region (last 500 μm) of the joint. All LSP processed samples exhibited significant increases in near-surface hardness compared to that of the base FSW. For samples displayed in this figure, the hardness tends to become linear after 1000 μm, a fact which corresponds with the theory of LSP affecting material up to 1 mm in depth [57]. It was found that a reduction in power intensity reduced the penetrative effects of the strain hardening of the process. The hardness profiles for the remaining

power intensities have been placed in Figure C.7 to Figure C.9 in Appendix C.4. A 1000 spot/cm^2 was found to be the hardest nearest the peened surface which was to be expected as this was the highest energy per area peening parameter combination. The near surface hardness for each parameter combination decreased as the coverage decreased again this was to be expected as the strain hardening would be intuitively less due to the lowering of the number of impacts of the laser. The trend of decreasing near surface hardness with decreasing coverage was exhibited by all power intensity combinations. Similar trends were observed by other LSP groups [58].

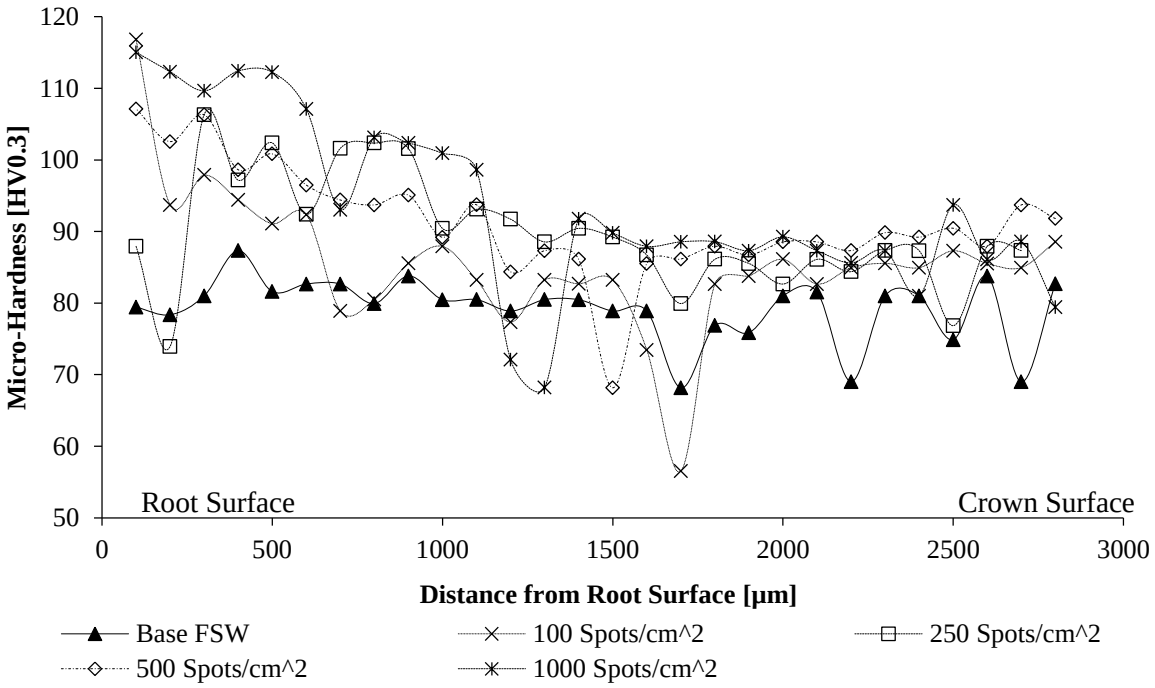

Figure 6.73 - Micro-Hardness through the thickness of the Friction Stir Welded Joint which had been Laser Shock Peened at a Power Intensity of 5 GW/cm^2

In a number of indentations nearest the root and crown surfaces tended to have the highest error as the diamond shape indentation created by the indentor become distorted as there was insufficient material surrounding the indentation to resist the deformation, defect or crack may have influenced the result as seen in Figure 6.74. The first measurement for the sample of 3.5GW/cm^2 and 500 spots/cm^2 not symmetrical. This inevitably affected the reading of the hardness at that position, this point had a hardness of 55.9 whilst the indentation 100 µm away had a hardness of 78.9, a percentage difference of as much as 29.2%.

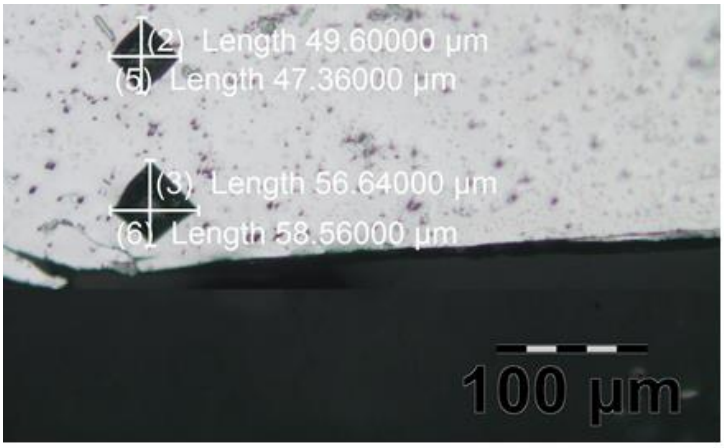

Figure 6.74 - Error Induced in Micro-Hardness Measurement due to Uneven Deformation of Indentation

Figure 6.75 shows the distribution of the maximum recorded hardness values for each peening parameter set. The maximum base FSW has been plotted as a straight line to benchmark the peened samples against. All parameter combinations flow similar trend of increasing strain hardening with increasing coverage. Coverage of 250 spots/cm^2 appeared to be the minimum amount of laser pulses to achieve a substantial effect. Besides for the 5 GW/cm^2 distributions, there was very little variation in maximum hardness. All hardness values displayed were taken within the first 200 µm from the root surface. LSP increased the maximum surface hardness by as much as 28.74% (5 GW/cm^2 and 1000 spots/cm^2), with the lowest notable increase being 8.09% for peening parameters of 1 GW/cm and 250 spots/cm^2. Parameter combination of 1 GW/cm^2 and 100 spots/cm^2 increased the hardness by less than 1% and thus was eliminated as the parameter set had no substantial effect on the welded material. The uncertainty of the measured hardness presented in the figure below fell in the uncertainty range listed in Table F.2. The error bars have been left off in the interest of clarity of the figure.

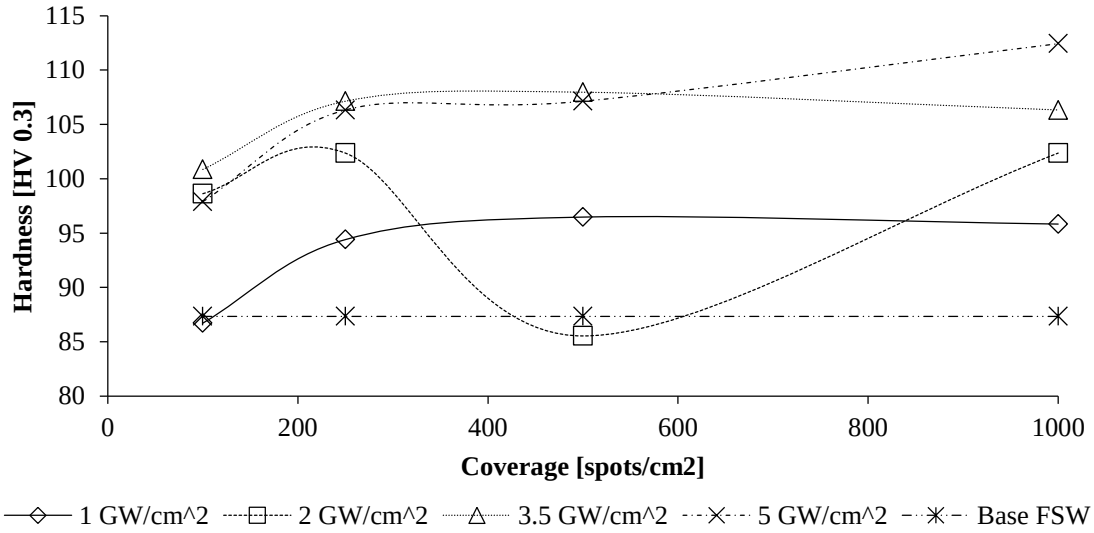

Figure 6.75 – Distribution of Maximum Hardness Induced by Laser Shock Peening

Figure 6.76 shows the approximate penetration depths of the notable effects of the LSP process at various parameter combinations. This was an approximated value as it was only accurate to the nearest 100 µm. The penetrative effects of the process increased with increasing coverage. This was due to the higher induced plastic [98]. The uncertainty associated with the penetration depth of the effects of LSP was taken as ±100µm due to this being the indentation interval.

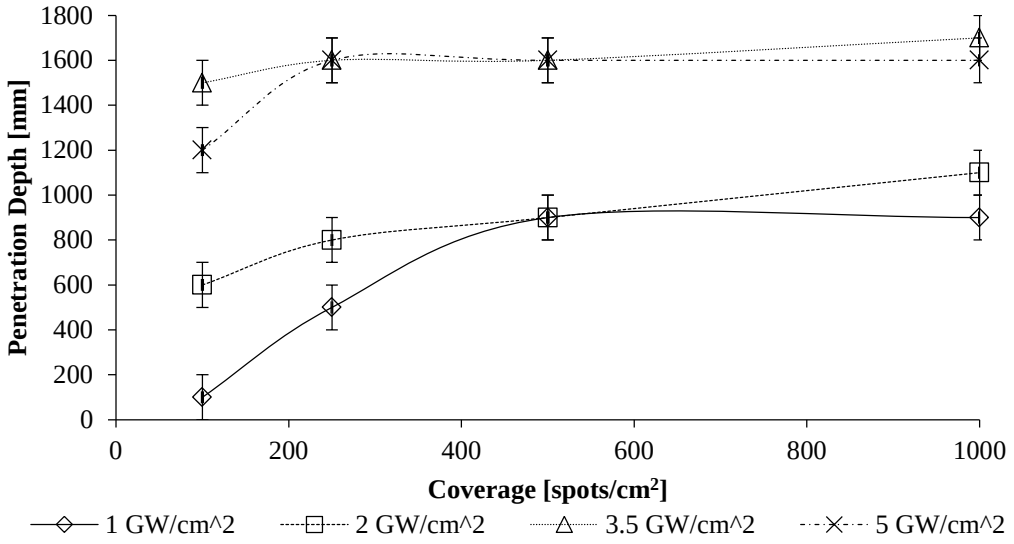

Figure 6.76 - Approximate Penetration Depths of Laser Shock Peening Parameter Combinations

The decrease in hardness from the peened surface has been attributed to the possible presence of tensile residual stresses insert [100]. A number of researchers have associated the increase in the hardness due to LSP causing multiplication of dislocations within the material [101]. The trends in Figure 6.75 were observed by others [102], in which the hardness values reached a limit and no appreciable increase was noted. It is suspected, yet not confirmed that an increase power intensity which increases the peak pressure of the wave increases the dislocation density within the processed area. As with the arc height of the Almen strips, it is suspected that a threshold to the hardness for a given peak pressure is achieved and thus no further increases in hardness are achieved. Further studies need to be conducted into proving this claim.

6.2.5.1 Conclusions

From the results presented in this section the following can be concluded:

1. All Laser Shock Peening parameter combinations investigated was able to strain harden the peened material in some fashion.
2. The increase in near surface hardness was attributed to the multiplication of dislocations introduced through the peening process.

3. The expectation of Laser Shock Peening increasing the hardness in regions near the peened surface and slowly returning to the hardness of the parent material was maintain even though the parent material was Friction Stir Welded AA6082-T6. This indicates that LSP was a well-suited process to be paired with FSW.
4. Higher power intensities and coverage increased the penetrative effects of the LSP process. Strain hardening depths of as much as 1700 μm were achieved. This was more than 50% of the way through the welded material.
5. A minimum of 250 spots/cm^2 was required to obtain a notable increase in hardness of the FSW joint.
6. It is suggested that this material has a threshold which cannot be surpassed for a given peak pressure of the beam. This is suggested due to the fact that on Figure 6.75 and Figure 6.76 displayed regions of extremely little change or no change in hardness with increasing pulse coverage.
7. The literature stated that the increase in hardness in the region of the peened area was due to the introduction of dislocations and compressive residual stresses. The tendency of the hardness to return to the parent material was due to this region progressively increasing in tensile residual stress. These claims have not been verified in this study.

6.2.6 Effect of Laser Peening Parameters on the Fatigue Life of the Base Material

Many researchers have shown the Laser Shock Peening was able to significantly improve the fatigue life of the treated components. The introduction of compressive residual stress through LSP is credited with the improvement. In the Wits LSP Group, very little was known regarding how the various LSP parameters influenced the fatigue life of the 3mm AA6082-T6 Aluminium base material. A fatigue study was completed in which untreated base material was tested in order to obtain its S-N curve. Three samples per stress amplitude with a fully revered test (R=-1) strategy employed, Appendix D, shows the experimental data plotted against that of published data in order to benchmark the results of the test as well as the material [6].

To ascertain the effect of varying laser peening parameters on the fatigue life of the base coupons a number of bending fatigue samples were treated at the four levels of power intensity investigated. The coupons were initially machined from the base material with the rolling direction of the material was parallel to the longest length of the coupon. It was suggested by a colleague in the Wits LSP group that the peening area should surpass the reduced area of the coupon on both sides. This was suggested as previous work showed the peening a small region in the reduced section placed high tensile stresses at the location where the largest width meets the reduced section. The standard fatigue samples and peened area have been shown in Figure 6.77. The peened area was shown as the grey area of the component, an example of the extent of the laser impulses has been shown as the multiple overlapping black circles on the left-hand side of the peened area.

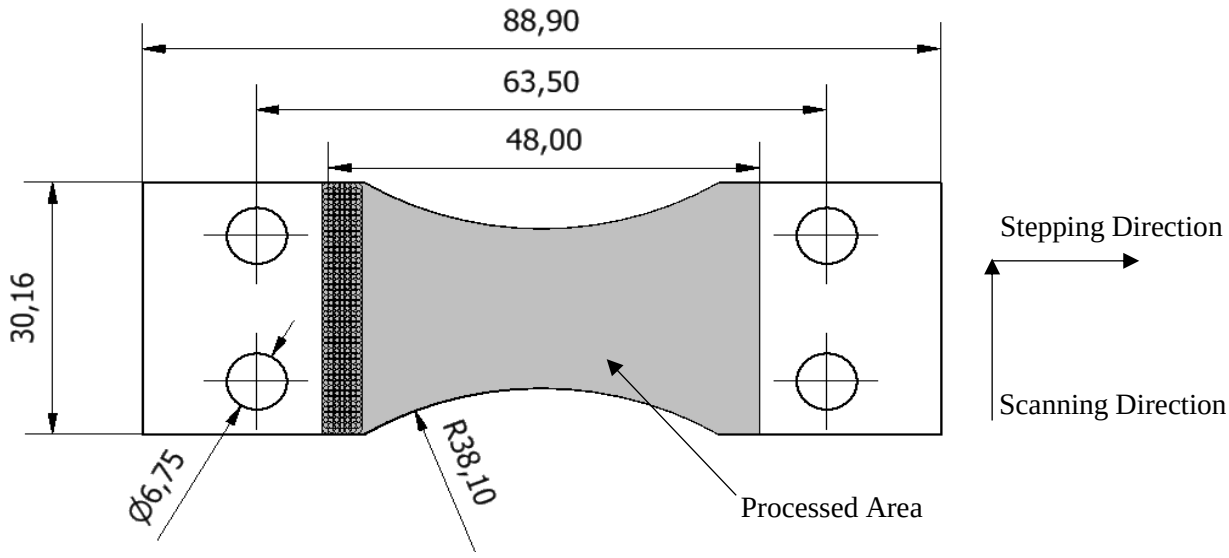

Figure 6.77 - Bending Fatigue Coupons with Laser Shock Peened Area Indicated

The base material coupons were attached to a steel backing plate by the bolt holes during the peening process. It was initially intended for the samples to be treated with varying power intensities and coverage but during the processing of first samples which were peened at 3.5GW/cm^2 and 100 spots/cm^2, the peened surface began to deflect away from the backing plate. This caused the bending coupon to become bowed thus it could not be used as a viable sample. The approach adopted by Toshiba Corporation (a world leader in Laser Shock Peening applications, research and development) had to be used in order to achieve a flat sample. This method involves treating the front and back surfaces of the coupon with different overlaps and layers to gain a flat sample. The combination of the number of layers and overlap was achieved iteratively. A layer of 500 spots/cm^2 was first applied to the front surface, followed by a 250 spots/cm^2 layer on the back surface and finally two layers of 50 spots/cm^2 on the front surface. This fact that the peening process induced substantial deflection of the bending coupon was taken into account for the latter FSW+LSP and FSW+LOP+LSP samples. As it was not easy to vary the combination of peening as it may introduce uncertainty thus all samples were treated with the same combination, with the results providing more information into the effect of the power intensity of the fatigue lives of the coupons rather than combination effect of the power intensity and coverage. Figure 6.78 provides an example of the top surface of the fatigue samples. It can be seen that the intensity and detail of the dimples (the locations were the laser pulse has stuck the material) increase with increasing power intensity.

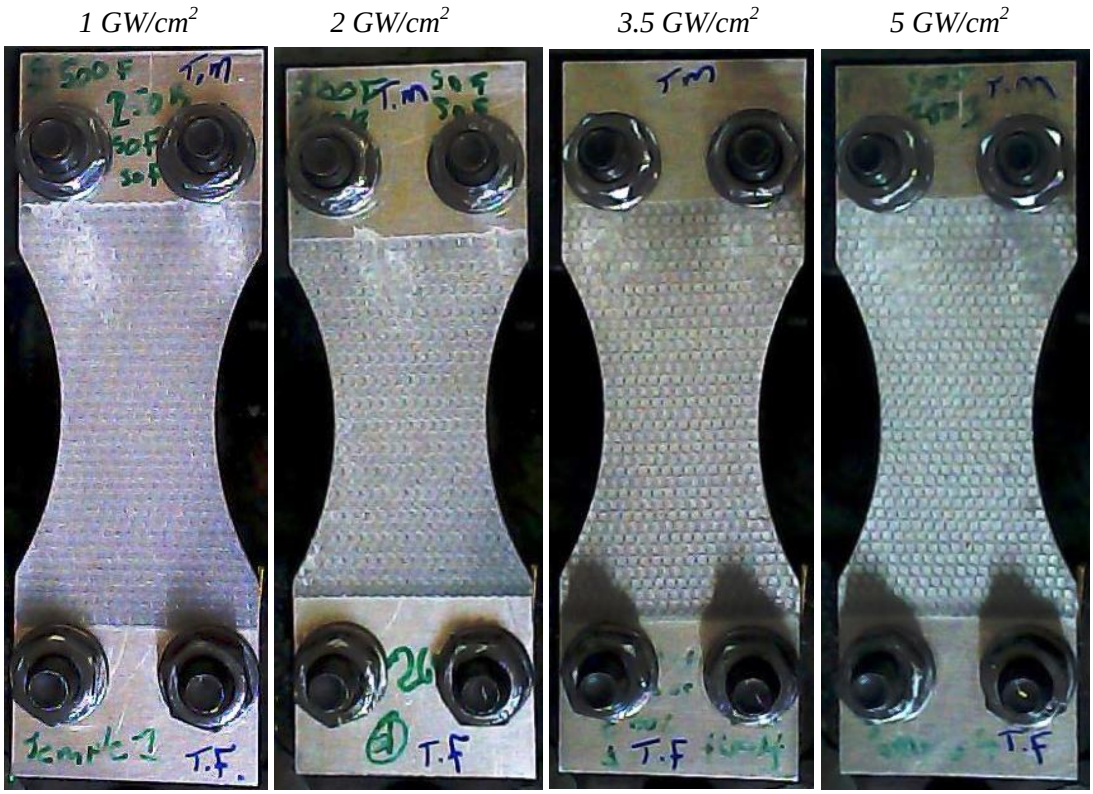

Figure 6.78 - Example of each sample Laser shock Peened at Different Power Intensities

Table 6.20 lists the setup parameters for each of the base material with LSP applied. The data was listed in the order in which the tests were run. It can be seen that the stress settings were listed for the measured stress pre-test and post-test. The bending fatigue machine did not provide the ability to ascertain the stress amplitude during the test thus it had to be checked after the test to ensure that the stress amplitude had not substantially drifted from the pre-test calibration. For the majority of the tests, there was a fairly good correlation in the setup pre and post testing. The final stress after the test can be considered as the error limits in the experiment as the stress intensity would have varied between those values. A table of the average number of stress amplitude and number of cycles has also been provided below the main table. On average the tests were fully reversed with all samples having an average stress ratio of -1.

Table 6.20 – Set up Parameters and Recorded Data for Laser Shock Peening on Base material at different Process Parameters

Power Intensity [GW/cm^2]	Sample Name	Pre Max Stress [MPa]	Pre Min Stress [MPa]	Stress Amp [MPa]	R	Calc. no. cycles	Post. Max Stress [MPa]	Post Min Stress [MPa]	Post R
5 GW/cm^2	Base+LSP_5_1	165.13	-164.22	164.68	-1.01	932940	169.33	-163.66	-1.03
	Base+LSP_5_2	166.53	-165.48	166.01	-1.01	1222620	171.22	-159.53	-1.07
	Base+LSP_5_3	165.20	-164.99	165.10	-1.00	938620	162.19	-167.16	-0.97
3.5 GW/cm^2	Base+LSP_3.5_1	165.41	-164.01	164.71	-1.01	1018140	162.68	-169.26	-0.96
	Base+LSP_3.5_2	166.32	-165.76	166.04	-1.00	1640100	173.32	-158.76	-1.09
	Base+LSP_3.5_3	165.83	-164.92	165.38	-1.01	1364620	164.01	-165.69	-0.99
2 GW/cm^2	Base+LSP_2_1	164.78	-164.99	164.89	-1.00	1422840	160.65	-169.89	-0.95
	Base+LSP_2_2	165.27	-165.41	165.34	-1.00	1989420	-	-	-1.01
	Base+LSP_2_3	166.67	-165.13	165.90	-1.01	1475380	165.90	-167.30	-0.99
1 GW/cm^2	Base+LSP_1_1	165.90	-166.60	166.25	-1.00	416060.	169.47	-163.52	-1.04
	Base+LSP_1_2	166.60	-165.90	166.25	-1.00	323760	169.47	-164.50	-1.03
	Base+LSP_1_3	167.16	-166.04	166.60	-1.01	264120	160.02	-172.27	-0.93

Power Intensity [GW/cm^2]	Ave Stress Amplitude [MPa]	Ave R	Ave Cycles
5 GW/cm^2	165.26	-1.00	1031393
3.5 GW/cm^2	165.38	-1.01	1340953
2 GW/cm^2	165.38	-1.00	1629213
1 GW/cm^2	166.37	-1.00	334646

Figure 6.79 provides the results of the substantial base material treatment and the results of the multiple LSP samples. It can be seen that LSP, no matter which power intensity improves the fatigue life of the parent material. A Stress amplitude range of 160 to 170 MPa was select to for these tests. The reasons for this was that it was feared that running at the higher stresses would damage the calibration sample over time with the requirement of having to check the stress level before and after every test and the drift in stress amplitude at stress levels higher than 170 tended to drift substantially during the tests. As with all experiments preceding these fatigue tests, the samples manufactured at 1 GW/cm^2 performed very similarly to the parent material. Some increase has been noted but the full advantages of the LSP process were not achieved. The fatigue test data for the base material illustrated in Figure 6.79 has been listed in Table D.2 in Appendix D.

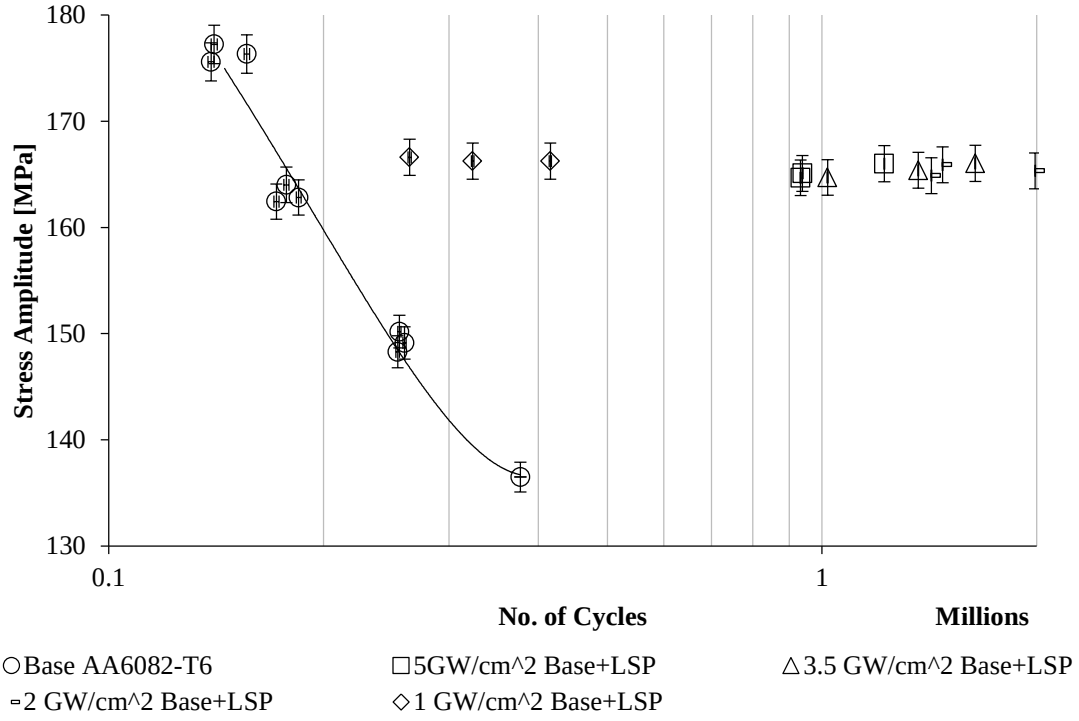

Figure 6.79- S-N Curve of Base Material and Base Material Laser Shock Peened Samples with varying Power Intensity

5 GW/cm^2 resulted in the lowest fatigue life at of the three remaining power intensities. There may be two possible reasons for why the 5 GW/cm^2 samples performed the worst:

1) During the peening process, signs of air breakdown had occurred. This may have resulted in a less efficient peening process which thus would not have introduced enough compressive residual stress compared to the other intensities.
2) The combination peening may have also relocated tensile residual stress into a critical depth or position in the component. When the load was applied the fatigue life would be worsened.
3) The surface finish of the 5GW/cm^2 tended to be rougher than those peened at lower power intensity. The higher peak pressure of the pulse ablated the surface, leaving a deep dimple on the surface, this was seen in Figure 6.66, Figure 6.68 and Figure 6.78. The increases surface roughness due to LSP may have increased the rate at which the samples failed. This would be due to the higher roughness causing an earlier nucleation of the cracks which would eventually cause failure.

The fracture surfaces of all fatigue samples shown in Figure 6.80. The surfaces all indicated crack initiation from the edges of the samples. This was confirmed by the surface fretting which in majority occurred close to the edges of the samples. The final failure occurred within the central region as the surfaces indicated general quick overload failure.

The black regions in the fracture surfaces in Figure 6.80 were regions in which fretting occurred due to fatigue machine failing to stop operation. The across weld fracture pattern of the base and Base+LSP samples were similar in that both sets of samples failed in roughly a straight line (2 and 3.5 GW/cm^2) and in a jagged step (1 and 5 GW/cm^2). The fracture surfaces of the base material fatigue coupons, tested at various stress amplitudes, have been shown in Figure D.3 in Appendix D. This showed that the failure pattern was not dependent on the final surface quality imposed by the large number of dimples created during the LSPwC. The base material fracture positions have been shown in Figure D.3, in Appendix D.

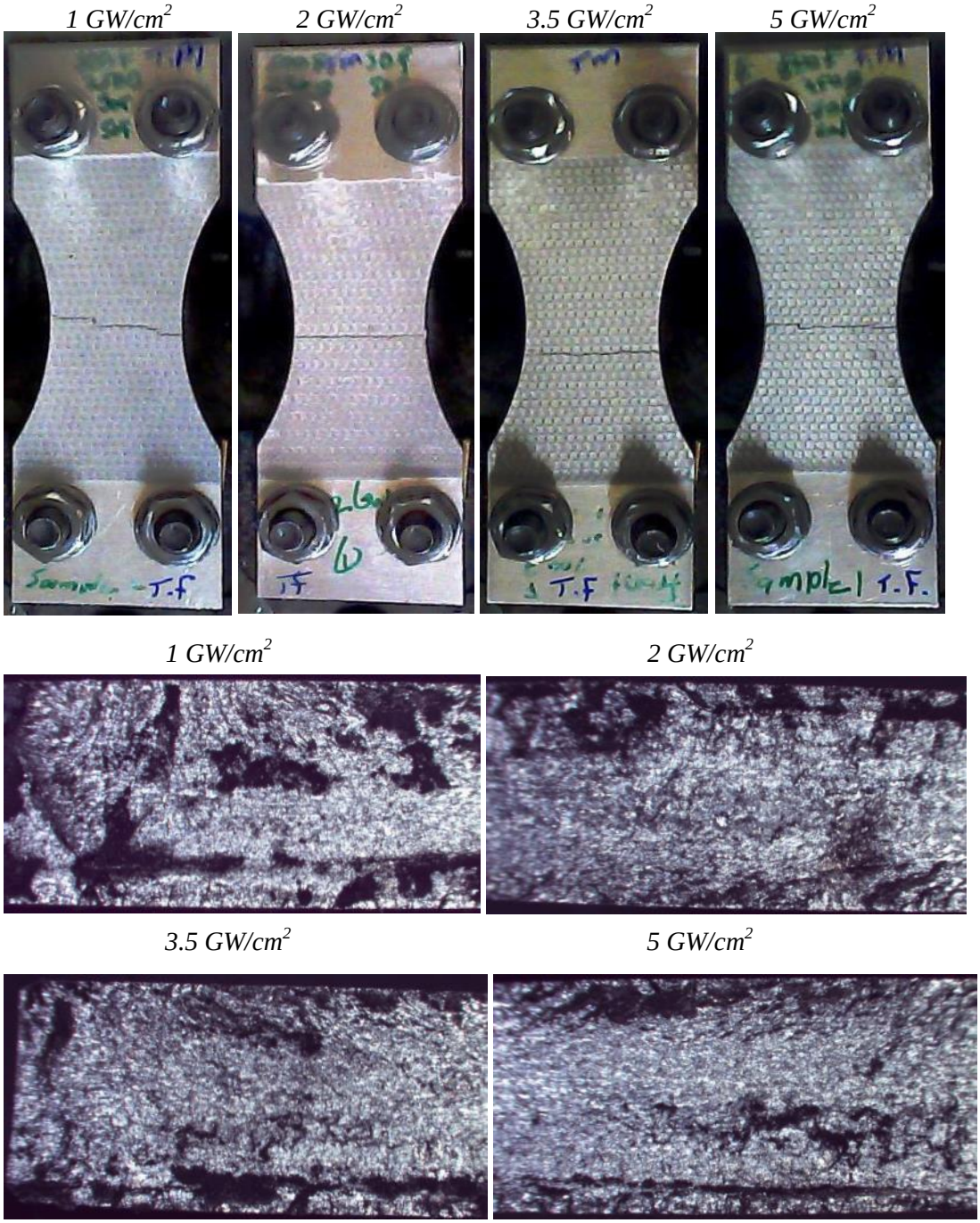

Figure 6.80 - Fracture Position and Surface of the Laser Shock Peened Base Material

Figure 6.81 illustrates the fracture path through the base AA6082-T6 components that had been LSP with various power intensities. The lower surfaces showed substantial damage which correlated to the fracture beginning at the low surface of the components.

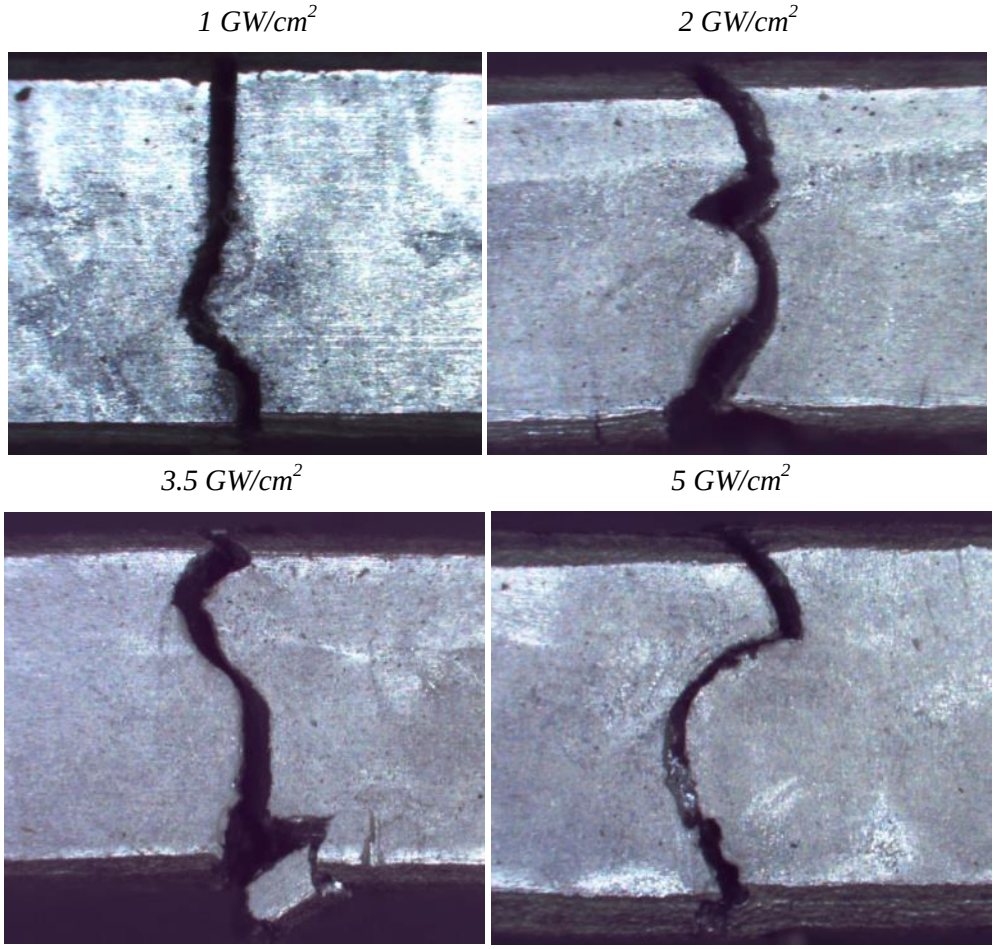

Figure 6.81 - Fracture Path through Base Samples Treated with Laser Shock Peeing

Samples processed at a power intensity of 2 GW/cm^2 gave the overall best average number of cycles. Figure 6.79 showed that the samples manufactured at a power intensity of 3.5 GW/cm^2 in majority performed roughly equally to that of the majority of the 2 GW/cm^2 samples. Figure 6.82 provides the comparison of an average number of cycles to failure of the peened samples. It again can be seen that a power intensity of 1 GW/cm^2 provided a small increase but the full effects of peening were not achieve as an increase in life compared to the base material of 1.88 times was achieved to that of 8.14 or 7.53 achieved with LSP at power intensities of 2 and 3.5 GW/cm^2. The uncertainty in the number of cycles to failure was specified as ±1420 cycles as this was the number of cycles between images.

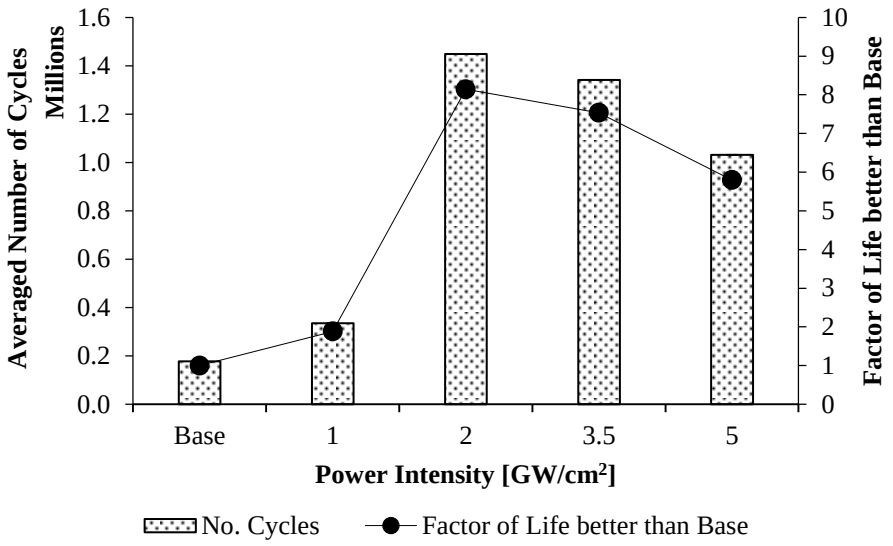

Figure 6.82 - Average Number of Cycles per Power Intensity and Factor of Cycles greater than the Base Material

This showed that LSP can sustainably improve the fatigue life of the base material through introducing deep compressive residual stresses.

6.2.6.1 Conclusions

From the results presented in this section the following can be concluded:

1) Samples processed with power intensities of 2 to 3.5 GW/cm^2 gave the best increase in fatigue life.
2) It is suspected that the surface finished created by the peening process may have influenced the failure rate of the samples.
3) An improvement of as much as eight times the base material life can be achieved through Laser Shock Peening.
4) The samples all failed from the outer edges inward. This showed the importance of introducing deep compressive stress within the near surface region to prevent quick initiation of fatigue cracks.

6.2.7 Multi-Objective Optimisation of the Laser Shock Peening Process

The optimisation of the Laser Shock Peening process was performed similarly to that of the Friction Stir Welding process, outlined in section 6.1.7. Due to the extreme similarities this section was set out to provide a brief overview of the setup of the optimisation and focuses on the results of the process.

The point of this exercise was to fully investigate the design space to ensure the correct selection of parameters and provide context for the selection of the LSP parameters used in the later sections of this report.

6.2.7.1 Algorithm Development and Training for Optimisation of Laser Shock Peening Process

The Laser Shock Peening parameter window investigated focused on two variables these being power intensity and coverage. Due to the poor experimental performance of all samples peened at 1 GW/cm^2 it was excluded from this analysis. The extreme boundaries of the coverage settings of 50 and 2000 spots/cm^2 have also been neglected to the minimal effects the 50 spots/cm^2 and the surpassing of the approximate saturation point of 1000 spots/cm^2 would not be beneficial to the investigation. Table 6.21 lists the various inputs and outputs which were used in the optimisation of the LSP process.

Table 6.21 - Work Table Inputs and Outputs for Laser Shock Peening Optimisation

Inputs	Outputs
Power Intensity [GW/cm^2]	Deflection and distortion [mm]
Coverage [spots/cm^2]	Surface roughness [µm]
	Maximum strain hardening [HV0.3]
	Penetration depth of LSP effects[µm]
	Fatigue life of LSP base material [number of cycles]
	Air breakdown

In an attempt to introduce a consideration to the quality of the process to the optimisation process, a numerical value was given to classifying the amount of air breakdown or growth of the plasma cloud growth. This was a fictitious value that was developed by the author on the basis of Figure 6.60. It was noted during experimental peening that an increase in the coverage resulted in an increase in the plasma growth due to the increased amount of water splashing. An equation was developed in order to obtain a fictitious value which has no real world significance but can be used in the optimisation simulation. Table 6.22 lists the value of each processing parameter combination.

$$Air\ Break\ Down = Power\ Intersity + \frac{Coverage\ used}{Max\ Coverage\ Investigated} \tag{6.3}$$

Where:

Max Coverage Investigated = 2000 spots/cm^2

Parameter screening was completed to identify the relative strengths of the input variables and their influence on the outcome of the various outputs. The performance indices were calculated by means of Smoothing Spline ANOVA algorithm. Table 6.23 lists the performance indices and the relative contributions that each input parameter had on the outcome of the numerous results. Power intensity was the dominate factor in the Fatigue category due to the fact that for all coverage in a single power intensity were given the same fatigue life value thus this was not a conclusive outcome.

Table 6.22 - Calculated Values of Factor representing magnitude of Air Breakdown

Coverage [spots/cm^2]	Power Intensity [GW/cm^2]		
	2	**3.5**	**5**
100	2.005	3.505	5.005
250	2.125	3.625	5.125
500	2.25	3.75	5.25
1000	2.5	4	5.5

Table 6.23 - Relative Strength of Input Variables of Laser Shock Peening

	Relative Strength of Input [%]		Dominate Input
Output	**Power Intensity [GW/cm^2]**	**Coverage [spots/cm^2]**	
Deflection [mm]	7.26	92.74	Coverage
Surface roughness [µm]	2.94	97.06	Coverage
Maximum strain hardening [HV0.3]	72.62	27.38	Power Intensity
Penetration depth of LSP effects[µm]	87.25	12.75	Power Intensity
Fatigue life of LSP base material [number of cycles]	100	0	Power Intensity
Air breakdown	97.81	2.19	Power Intensity

The same RSM functions previously used in the FSW optimisation were used in the optimisation of the LSP process. The functions selected for the training of the algorithms were Kriging, Anisotropic Kriging and Radial Based Functions. The same criteria to eliminate the functions per output as in section 6.1.7 were used to select the most suited functions.

Table 6.24 – Most Suited Algorithm Functions per Output for Laser Shock Peening Parameter Optimisation

Output	Air Breakdown [-]	Deflection [mm]	Fatigue [no. of cycles]	Max Hardness [$Hv_{0.3}$]	Penetration Depth [µm]	Surface Roughness [µm]
Best Suited Algorithm	Radial Based Function	Kriging	Radial Based Function	Kriging	Kriging	Kriging
Max Absolute Error	1.00E-14	2.00E-15	7.00E-10	7.00E-14	2.00E-12	2.00E-15
Mean Absolute Error	6.00E-15	1.00E-15	3.00E-10	2.00E-14	9.00E-13	9.00E-16
Regression	1.00	1.00	1.00	1.00	1.00	1.00
Max Relative Error	7.00E-13	2.00E-13	7.00E-14	8.00E-14	3.00E-13	9.00E-14
Mean Relative Error	2.00E-13	1.00E-13	3.00E-14	2.00E-14	8.00E-14	4.00E-14
Error Mean	4.00E-15	4.00E-16	1.00E-10	2.00E-15	-6.00E-13	-7.00E-16
Max Normal Error	2.00E-13	1.00E-13	4.00E-14	6.00E-14	1.00E-13	7.00E-14
Mean Normal Error	1.00E-13	6.00E-14	2.00E-14	2.00E-14	5.00E-14	3.00E-14

The trained algorithms were used to relate the two LSP inputs to one of the outputs. The 3D RSM plots for the outputs have been shown in Figure 6.83.

Deflection of Almen Strips

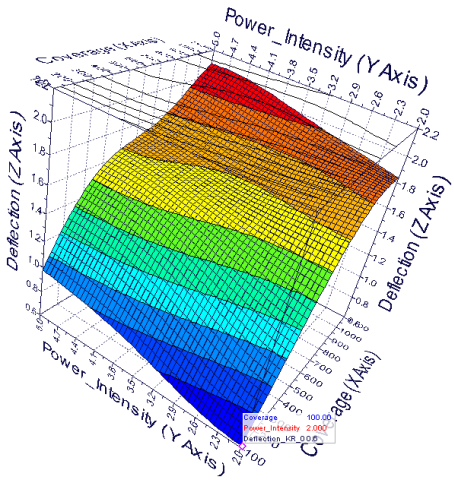

Fatigue Life of Peened Base Material

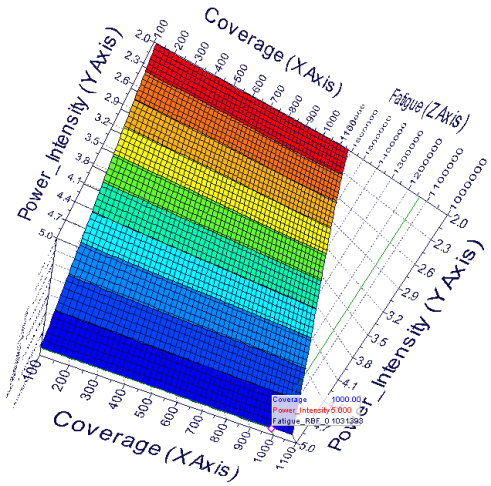

Maximum Strain Hardening at Peened Surface

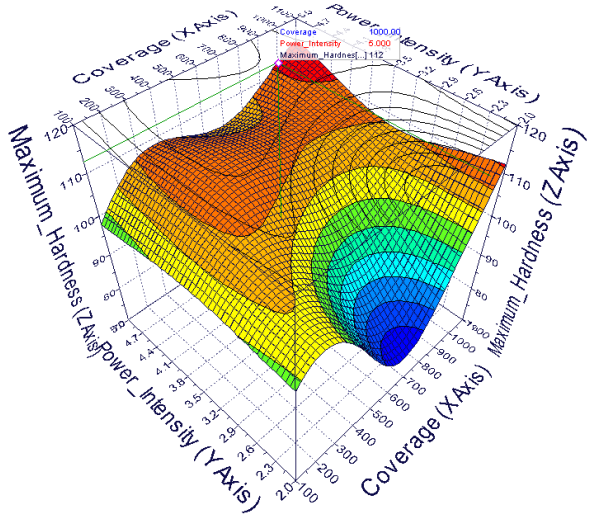

Penetration Depth

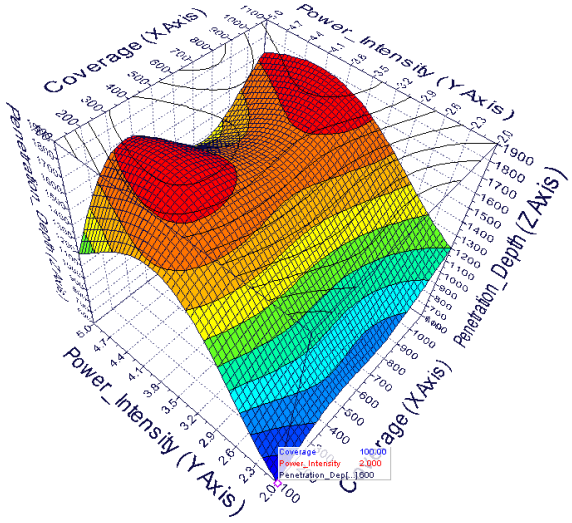

Surface Roughness

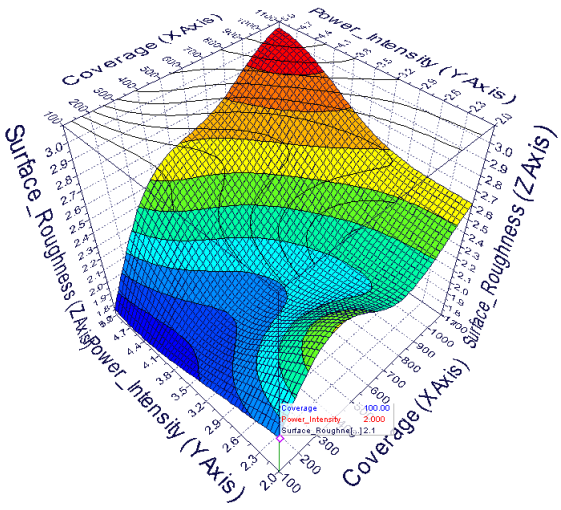

Air Breakdown

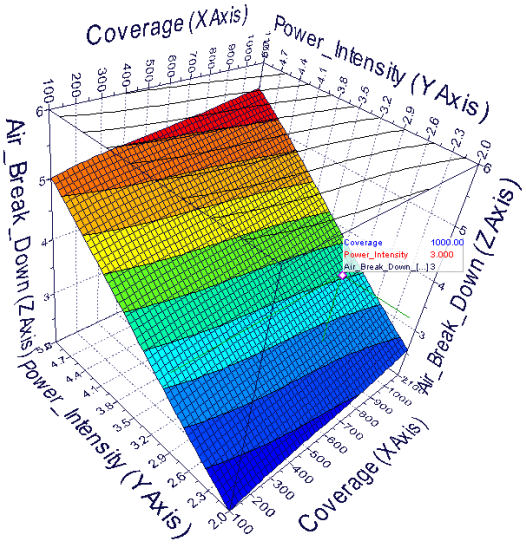

Figure 6.83 - Response Surface Methodology Plots Relating Laser Shock Peening Parameters to the Process Outputs

6.2.7.2 Optimisation of Laser Shock Peening Parameter Workflow Design

The setup of the workflow in modeFRONTIER to complete a multi-dimensioned optimisation a process was extensively outlined in section 6.1.7.3. As the same functions, nodes and methodology were applied within this section a broad outline has been provided. The workflow for the LSP optimisation has been shown in Figure 6.84.

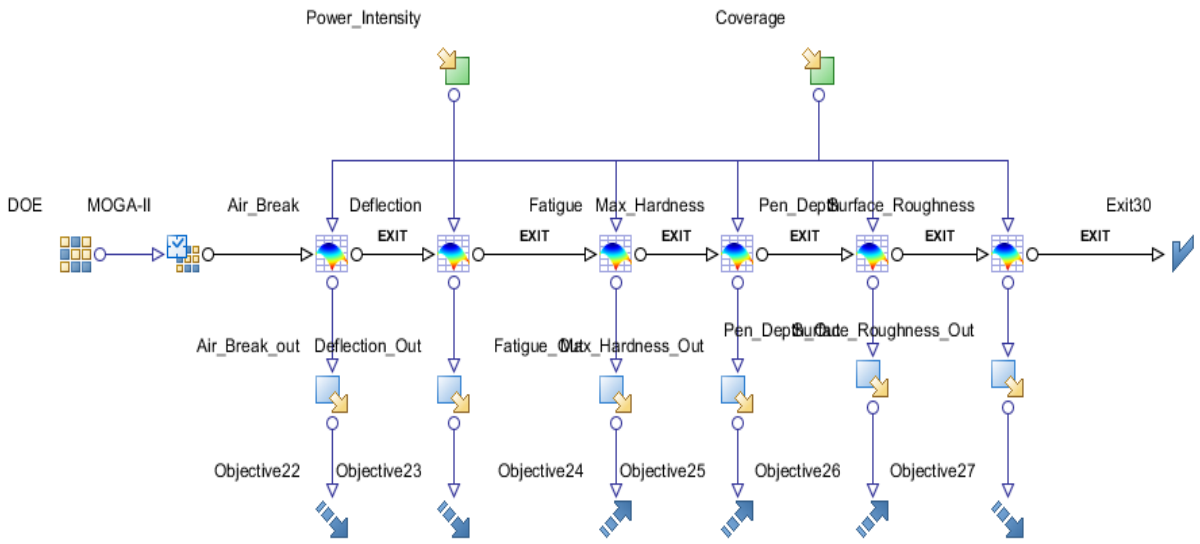

Figure 6.84 - Example of modeFRONTIER Workflow to Optimise the Laser Shock Peening Parameters

The input variables for the LSP optimisation were varied in accordance with the listed values in Table 6.25.

Table 6.25 - Input Boundaries for Friction Stir Welding Input Nodes

Parameter	Unit	Lower Bound	Upper Bound	Range
Power Intensity	GW/cm^2	1.75	5.25	3.5
Coverage	$Spots/cm^2$	50	1650	1650

The output functions were all linked to some optimisation objective which had to be carefully selected. The selected objective and rational behind the selection has been listed in Table 6.26.

The same RSM functions, DOE and Scheduler nodes which were used for the FSW optimisation were selected for the LSP optimisation. The optimisation model was performed using 250 Sobol designs, to fill the design space and 100 optimisation iterations upon these designs using the MOGA-II algorithm.

Table 6.26- Optimisation Objective for Output Functions for Laser Shock Peening Process

Outputs	Optimisation Objective	Reason for Objective Selection
Deflection [mm]	Minimise	Although researchers have shown that there is a proportional link between increasing deflection to increased compressive residual stress but it would be detrimental to aim for high distortion and deflection in high precision parts. Higher deflections may also strain the welded joints.
Surface roughness [µm]	Minimise	By minimising the surface roughness improves the surface finish reducing the effect of the ablation of the surface on the fatigue life of the component. Also reduces the need for further processing of the surface to achieve a better surface finish.
Maximum strain hardening [HV0.3]	Maximise	The harder the surface was an indication of amount of compressive residual stress as well as the depth at which the LSP effects would propagate into the material
Penetration depth of LSP effects[µm]	Maximise	This was required to be as large as possible as for later stages of the research confidence was need to know that the LSP process was surrounding the LOP with compressive residual stress.
Fatigue life of LSP base material [number of cycles]	Maximise	Large increases in fatigue life of the base material were a reflection which translates into a large increase in fatigue life of the welded components.
Air breakdown	Minimise	A Large amount of air breakdown was extremely undesirable as it causes a decrease in the quality of the peening process as well as shielding of the target area from the laser pulse.

6.2.7.3 Results of Optimisation of the Laser Shock Peening Process

The optimum LSP parameters to be used were investigated using the post-processing technique of defining all the simulated designs on a parallel chart. All simulated and real designs are feasible combinations thus need to be considered. Figure 6.85 illustrates a large number of design combinations that were investigated. The figure shows the link between each input and the expected outcome of numerous combinations of tested designs.

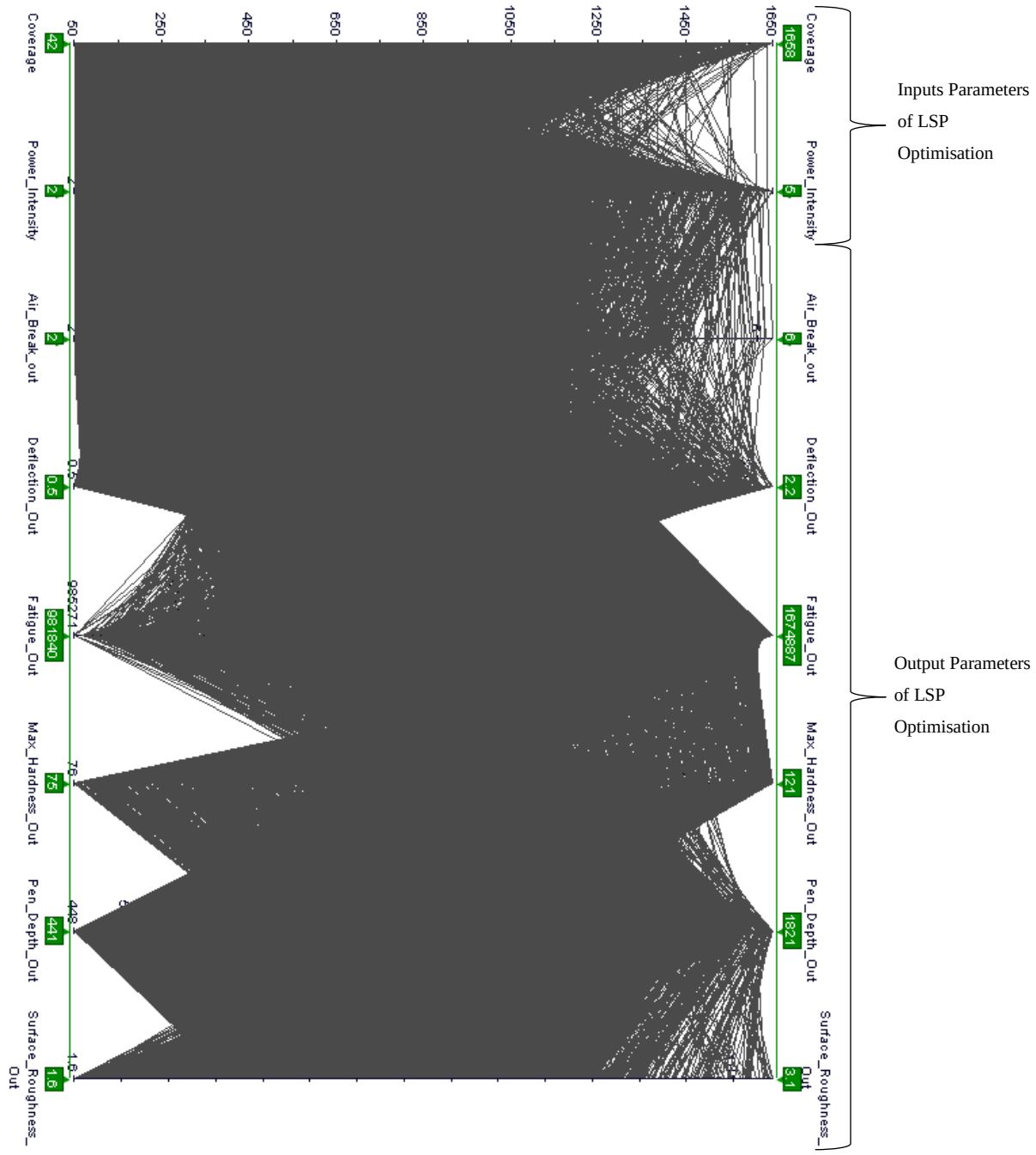

Figure 6.85 - Laser Shock Peening Parallel Chart defining all Iterations of Optimum Parameters

Using the sliders of each axis a number of design iterations can be discarded to narrow down the optimum design based on a number of factors and objectives. In this particular case it was desired to:

- It will be shown in chapter 0 that a number of LOP defects exceeded a 1000 µm in length from the root surface. For this reason, the penetration depth was maximised to exclude all designs in which the penetration depth of the peening process was under 1500 µm.
- The experimental saturation coverage was in the region of 1000 spots/cm^2 thus the coverage was reduced to a maximum value of 1300 spots/cm^2.

- Reduced the air breakdown to improve the quality of the processing. Reduced to a value less than 5.
- Maximise the fatigue life all to achieve the highest life improvement.

By manipulating the sliders a number of iterations of designs were removed. Figure 6.86 shows the reduction of a number of designs with the aim of maximising the fatigue life and penetration depth.

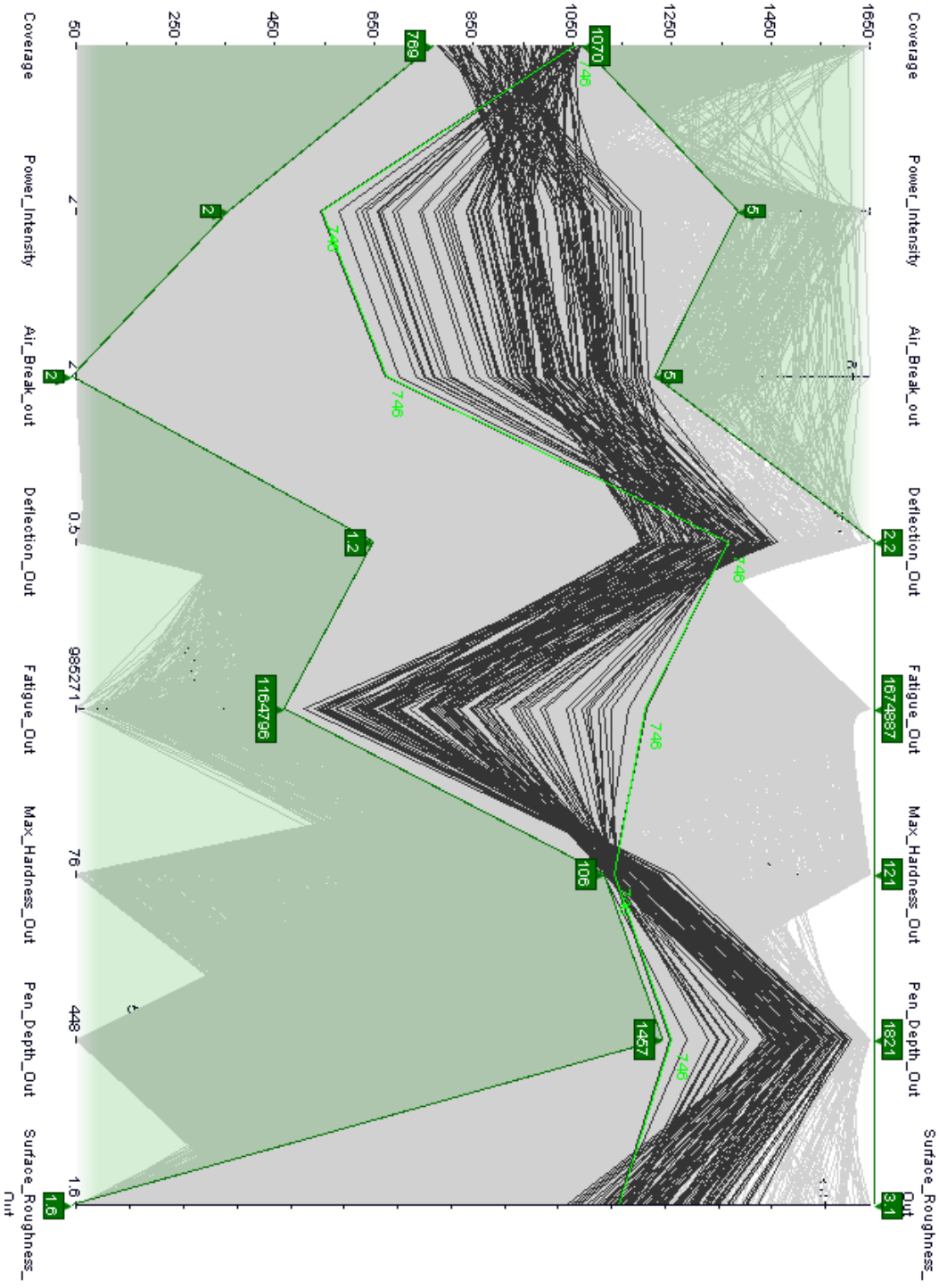

Figure 6.86 - Parallel Chart with Selected Trails Matching an Approximated Optimised Set of Parameters

It was found that from the cluster of design it was not possible to achieve a design which predicted a set of inputs which would result simultaneously in the best fatigue and penetration depth. Three designs were identified for potential solutions to the most suitable optimised set of LSP parameters.

Three design iterations were selected based on which design gave the highest fatigue, maximum penetration depth and a general average between the two major parameters. Table 6.27 list the predicted inputs and outputs of the optimisation process.

Table 6.27 - Resulting Parameter and Outputs from Optimisation Process

	Design Iterations	**#746 - Max. Fatigue**	**#1283 - Max. Penetration Depth**	**#384 – Average Design**
Inputs	Power Intensity	2.835 GW/cm^2	3.986 GW/cm^2	3.333 GW/cm^2
	Coverage	1053 spots/cm^2	1053 spots/cm^2	1067 spots/cm^2
Outputs	Deflection	1.899 mm	2.002 mm	1.948 mm
	Fatigue	1.477x10^6 cycles	1.238x10^6 cycles	1.376 x10^{6}cycles
	Surface Hardness	106.42 Hv	109.24 Hv	106.88 Hv
	Penetration Depth	1.474 mm	1.784 mm	1.667 mm
	Surface Roughness	2.599 µm	2.840 µm	2.676 µm
	Air breakdown	3.341	4.548	3.870

The coverage across all three optimisation designs was found to be 1053 and 1067 spots/cm^2.The final optimised value of the coverage used here on out was set at 1000 spots/cm^2, due to extensive experimental work completed at 1000 spots/cm^2 and that the optimum value was on 67 spots/cm^2 more. From the study of the Almen strips, 50 spots/cm^2 was shown to have a minimal effect on the material. Surpassing 1000 spots/cm^2 would have minimal added effect as the saturation limit of the material would be exceeded. For the application of using LSP on flawed FSW joint, the parameters must be selected to achieve a balance of substantial penetration depth and increase in fatigue life of the component. The variability of the laser energy per pulse was found to be large enough that the operators could not guarantee the exact set value of the power intensity. It was suggested that the power intensity may vary as much as 0.5 GW/cm^2 from the desired value. The most optimum value for the power intensity was found to be 3.33 GW/cm^2 but was set as 3.5 GW/cm^2 due to the variability of the laser and the extensive experimental research conducted at this power intensity. The most optimum parameters and final selected parameters for both processes have been summarised in Table 6.28.

Table 6.28 - Optimised Friction Stir Welding and Laser Shock Peening Parameters

Process	**Friction Stir Welding**		**Process**	**Laser Shock Peening**	
	Optimum value	**Selected values**		**Optimum value**	**Selected values**
Spindle Speed [RPM]	1433	1600	**Power Intensity [GW/cm^2]**	3.333	3.5
Feed Rate [mm/min]	196	200	**Coverage [spots/cm^2]**	1067	1000

7 Characterisation of Lack of Penetration in Friction Stir Welded Joints

Lack of Penetration (LOP) is a Friction Stir Welding defect caused by insufficient penetration of the welding tool. This defect forms from the root surface of the weld and tends towards the advancing side of the joint. Figure 7.1 provides an example of Lack of Penetration within a Friction Stir Welded Joint [41]. The presence of LOP can be identified as a simple crack within the joint. This crack has been found to significantly decrease the strength and mechanical properties of the joint. Factors such as poor tool design, incorrect selection of welding parameters, inconsistencies in welding material thickness and misalignment in the welding tool are just a few of the causes of LOP.

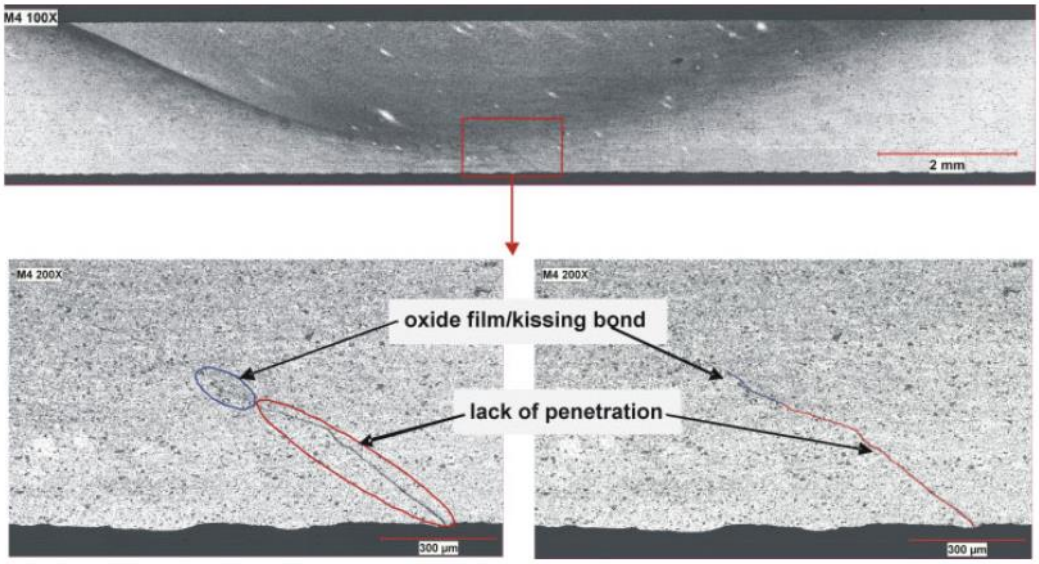

Figure 7.1 - Example of Lack of Penetration in a Friction Stir Welded Joint

This research was completed with the intention that the results may be possibly used in the manufacture of aerospace components. To ensure the relevance and relation of this research to typical ideologies used in an industry, the controlled introduction of LOP into the joints needed to be similar to an event that may occur in an industrial application of FSW. Industrial FSW applications would not select inadequate welding parameters or use unsuitable welding tools thus these techniques could not be used in the introduction of LOP. Strict quality control is typically applied to the selection of material used in the manufacture of aerospace components thus use of substandard welding material could not be investigated as a suitable method of introduction. Possible occurrences in an industrial process, which may lead to the formation of LOP, maybe the slight misalignment of the welding tool or incorrect selection of the plunge depth of the tool due to poor setup conditions. Research has also shown that consistent LOP can be introduced into the joint through the misalignment or variation of

the plunge depth (distance between the backing bar and tool end) of the tool during FSW. For this reason, LOP was attempted to be introduced in a controlled manner through the offsetting of the tool in multiple directions. This section discusses the results of the numerous experimental tests which were done to characterise the effects of the misalignments on the formation of LOP and the effects of LOP on the strength of the joints.

Outlined in section 6.1 was the optimisation of the welding parameters which were selected for this portion of the study. The best tool rotation and feed were required to be determined in order to represent this process as an industrial process. The welding parameters used were 1600 RPM and 200 mm/min. The distance between the backing bar and the end of the tool was set to 0.05 mm during the welds manufactured for the optimisation of the FSW process. This weld formed the benchmark for which the results of this section were compared to. The remaining portion of this chapter was dedicated to determining and characterising the dynamics of the LOP on the joints.

7.1 Offset Coordinate System for Introduction of Lack of Penetration into Friction Stir Welded Joints

The tool offsets were done along the lateral and normal directions (Y and Z axis). All lateral offsets are related to the centre line of the welded joint, with an indication to which region the tool was offset, i.e. advancing, retreating or centre. The normal offsets were referenced from the root surface. The value of the lateral offset indicates the placement of the tool's vertical centre line whilst the normal offsets indicates the position of the tip of the welding tool. Figure 7.1 provides an example of the tool offsets during welding.

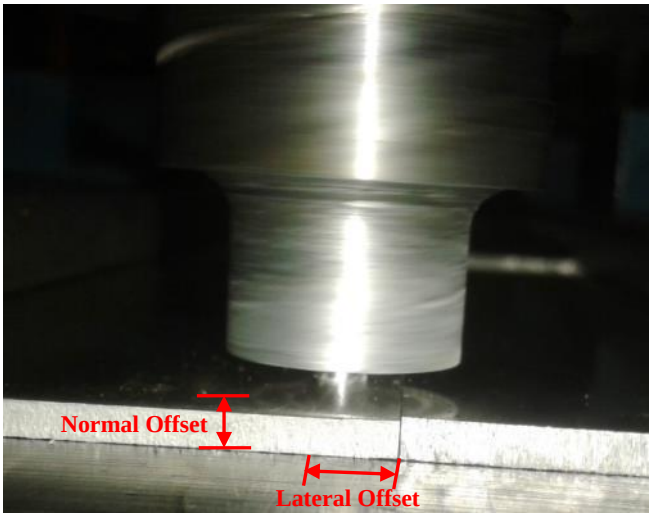

Figure 7.2 - Example of Tool Offset during Friction Stir Welding

Table 7.1 lists the initial set offset combinations investigated. The lateral positions were selected as functions of the pin dimension. For the benchmark weld, the welding pin was located on the centre line thus, 2.5 mm of the pin sat on either side of this joint line. Three lateral positions on the

advancing and retreating sides were selected these being 0.5 mm (20% offset), 1.25 mm (50% offset) and 2.5 mm (100% offset). The plunge depth for the benchmarking weld was placed at 0.05 mm from the root surface. Whilst maintaining the tool on the centre line the plunge depth was increased at 0.1 mm intervals from 0.05 to 0.35 mm. An extreme case was completed to identify the effects of offsets in the lateral and normal directions.

Table 7.1 – Initial Set of Friction Stir Welding Tool Offsets

Sample	Tool Rotation [RPM]	Feed rate [mm/min]	Normal Offset [mm]	Lateral Offset [mm]	Region of Weld
1	1600	200	0.15	0	Centre
2	1600	200	0.25	0	Centre
3	1600	200	0.35	0	Centre
4	1600	200	0.05	1.25	Advancing
5	1600	200	0.05	0.5	Advancing
6	1600	200	0.05	1.25	Retreating
7	1600	200	0.05	0.5	Retreating
8	1600	200	0.35	2.5	Advancing
9	1600	200	0.35	2.5	Retreating
10	1600	200	0.25	0.5	Advancing
11	1600	200	0.25	0.5	Retreating

Throughout this chapter parameter combinations are referred to according to their lateral and normal positions. The key below indicates how the labels should be read. The example was based on sample 1 in Table 7.1.

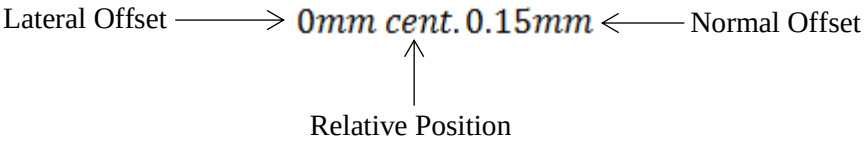

Figure 7.3 provides a schematic representation of the positions of the tool for the various tool offsets. The data point represents the tip of the tool in respect to the cross section of the welded joint.

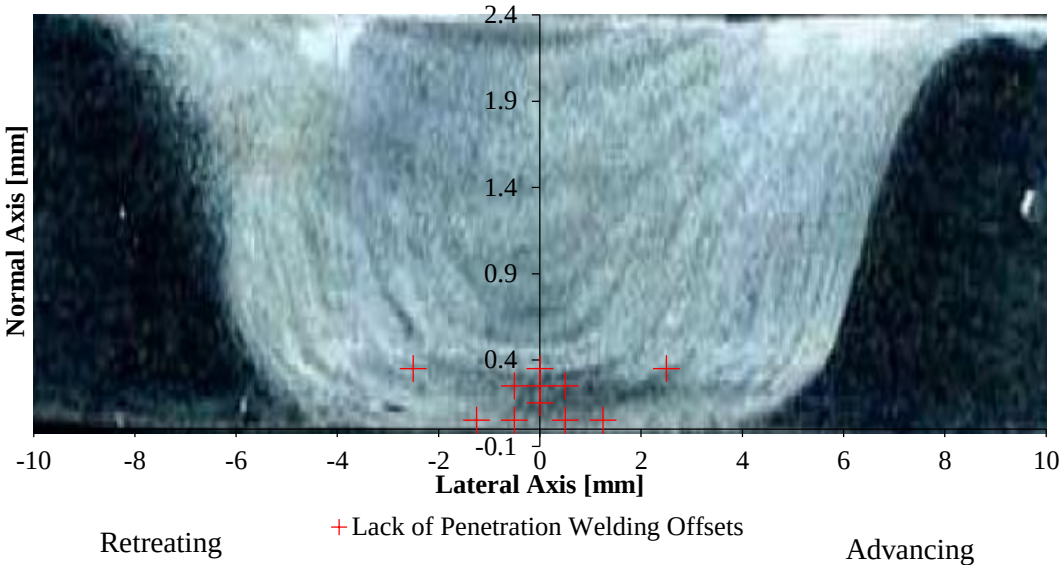

Figure 7.3 - Schematic Representation of Initial Tool Positions

Two batches of tool offsets were conducted due to the initial set not obtaining as favourable results as expected. The initial set was investigated fully in aspects such as welding forces, static strength and fatigue. These tests would allow for the determination of the acceptability of offset method in introducing LOP, the effects of varying sizes of LOP on the joints performance and the consistency of the method to introduce repeatable defects.

7.2 Size and Consistency of Introduced Lack of Penetration

The intentional offsetting of the welding tool was done with the aim of introducing controlled LOP into the joints. A sample of each joint, listed in Table 7.1, was taken and mounted in order to obtain the cross section of the joint. The length from the root surface that the defect extended from was listed in Table 7.2. A number of measurements could not be completed do to the defects not being clearly visible in the joints.

Table 7.2 - Size of Lack of Penetration Introduced due to Intentional Offset of Friction Stir Welding Tool

Normal Offset [mm]	Lateral Offset [mm]	Region of Weld	Depth of LOP [µm]
0.15	0	Centre	0
0.25	0	Centre	175.44
0.35	0	Centre	296.32
0.05	1.25	Advancing	-
0.05	0.5	Advancing	-
0.05	1.25	Retreating	-
0.05	0.5	Retreating	-
0.35	2.5	Advancing	954.5
0.35	2.5	Retreating	916.48
0.25	0.5	Advancing	-
0.25	0.5	Retreating	-

Figure 7.4 shows the measurement of the Lack of Penetration which was introduced into the FSW joints through offsetting the welding tool. It is evident that the length of the defect through the thickness of the weld increased as the tool was moved from the lateral and normal optimum position. The defect was largest at the root surface and tended to a point, similar to the geometric dimensions of a standard crack. Mandache showed the large LOP defects are often accompanied by kiss bonds near to the end of the crack tip, as seen in Figure 2.41[41]. Figure 7.1 indicated an example of this, Figure 7.4 2.5 mm Retreating 0.35 mm displayed the same trend of the formation of a kiss bond. In this case, the height of the affected area has been divided into two lengths these being the length of the LOP and the length of the kiss bond.

0mm Centre 0.35 mm

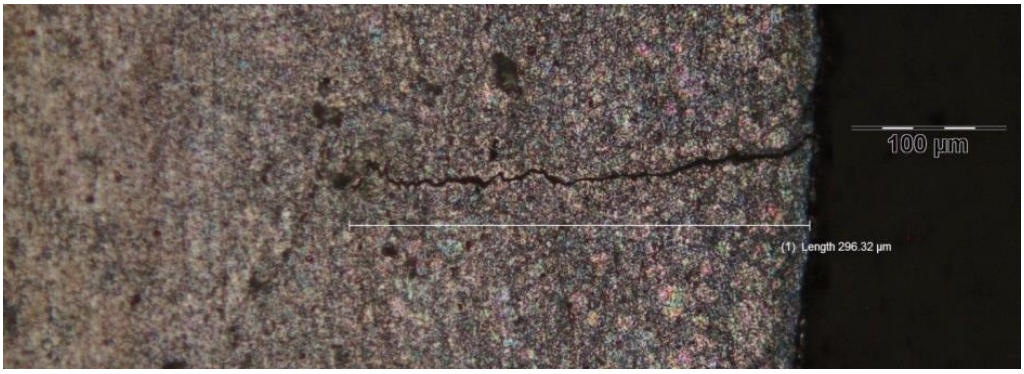

2.5mm Retreating 0.35 mm

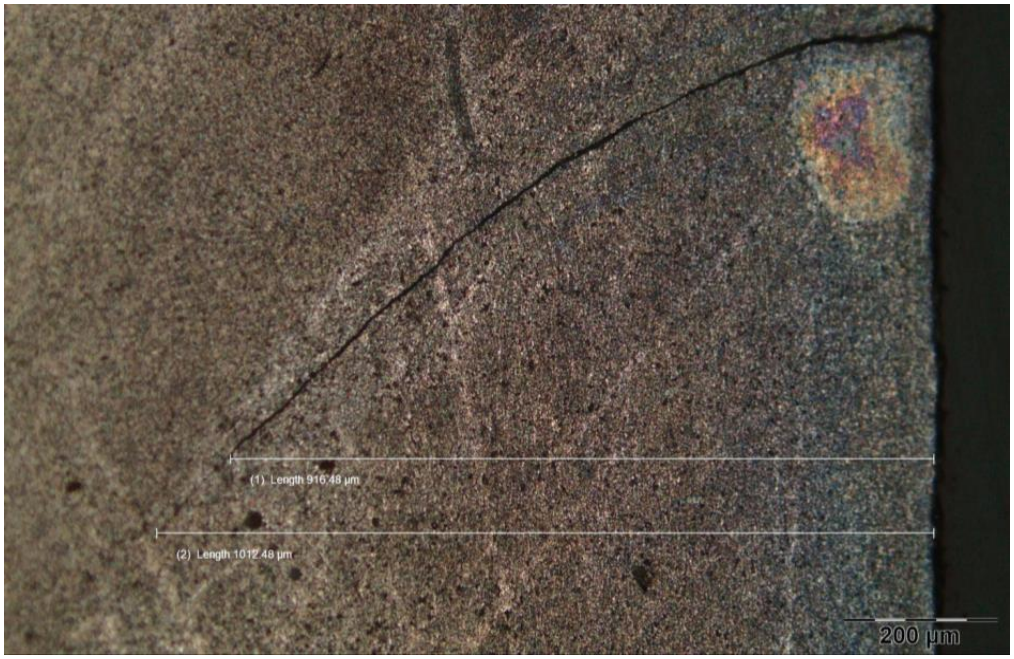

Figure 7.4 - Size of Lack of Penetration within various Offset Tool Friction Stir Welded Joints

A large concern of this method of introducing the LOP was the consistency of the technique over a full-length weld. Multiple test coupons were taken from the length of welds. If the size of the defect varied considerably across the weld length then this would have led to substantial errors and discrepancies between test coupons occurring. To test the consistency of the defects over a long section of the weld, a number of joints were X-rayed using Wits Micro-CT Scanning Unit. This facility allowed for 3D scans of the welds to be achieved, Figure 7.5 provides an example of the CT scan of the welds. This equipment provided a non-destructive technique of obtaining the size and orientation of the internal defects along the length of the welds.

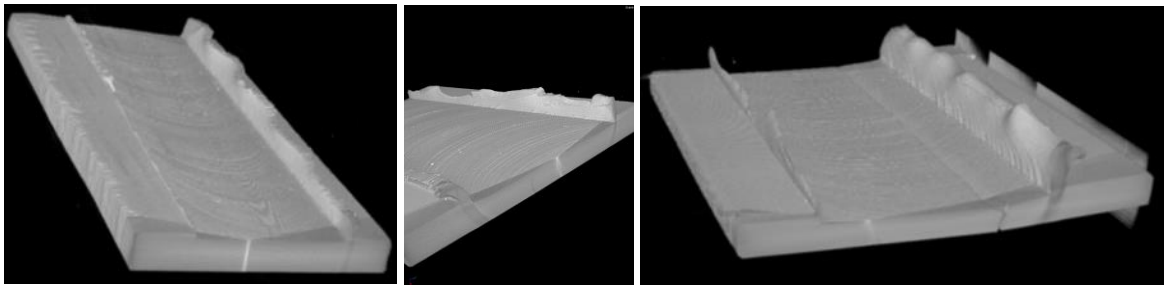

Figure 7.5 - Examples of the 3D Micro-CT Scans of the various Friction Stir Welds

By orienting the scanned welds so that the cross section was visible, the consistency of the defects, which were within the resolution of the scans, can be investigated along the length of the welds. Figure 7.6 provides a number of images of the defects present along the length of welds. These images were selected every 5 mm. It can be seen that there was fairly good consistency between each image in relation to the defects overall size, inclination and position it can be said that this method was appropriate in introducing consistent defects within the joints.

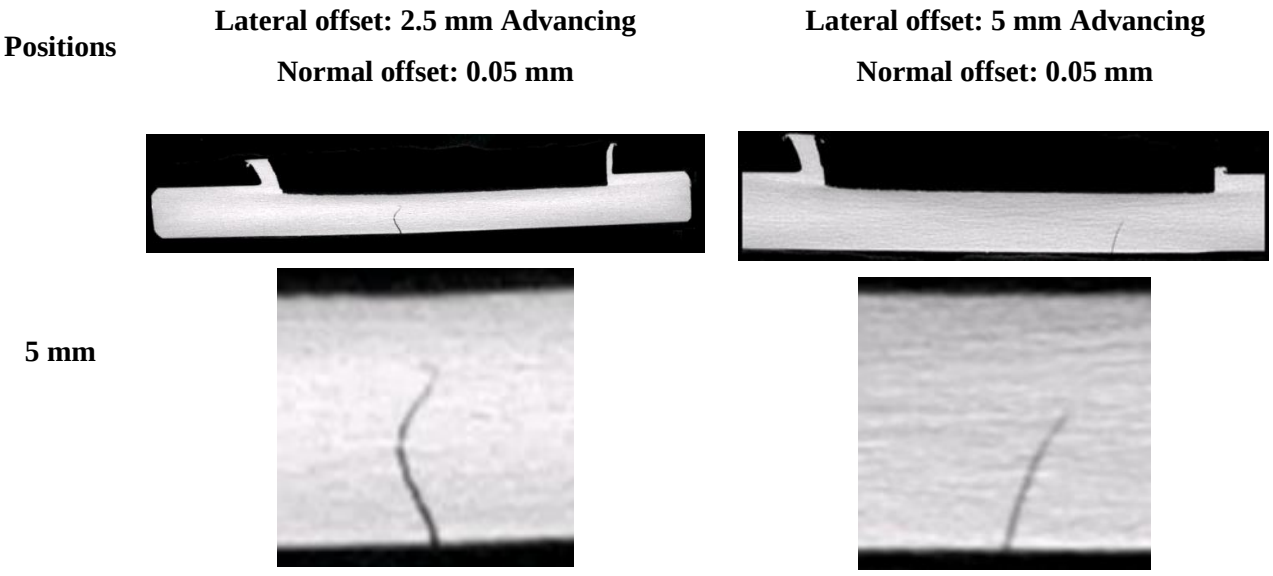

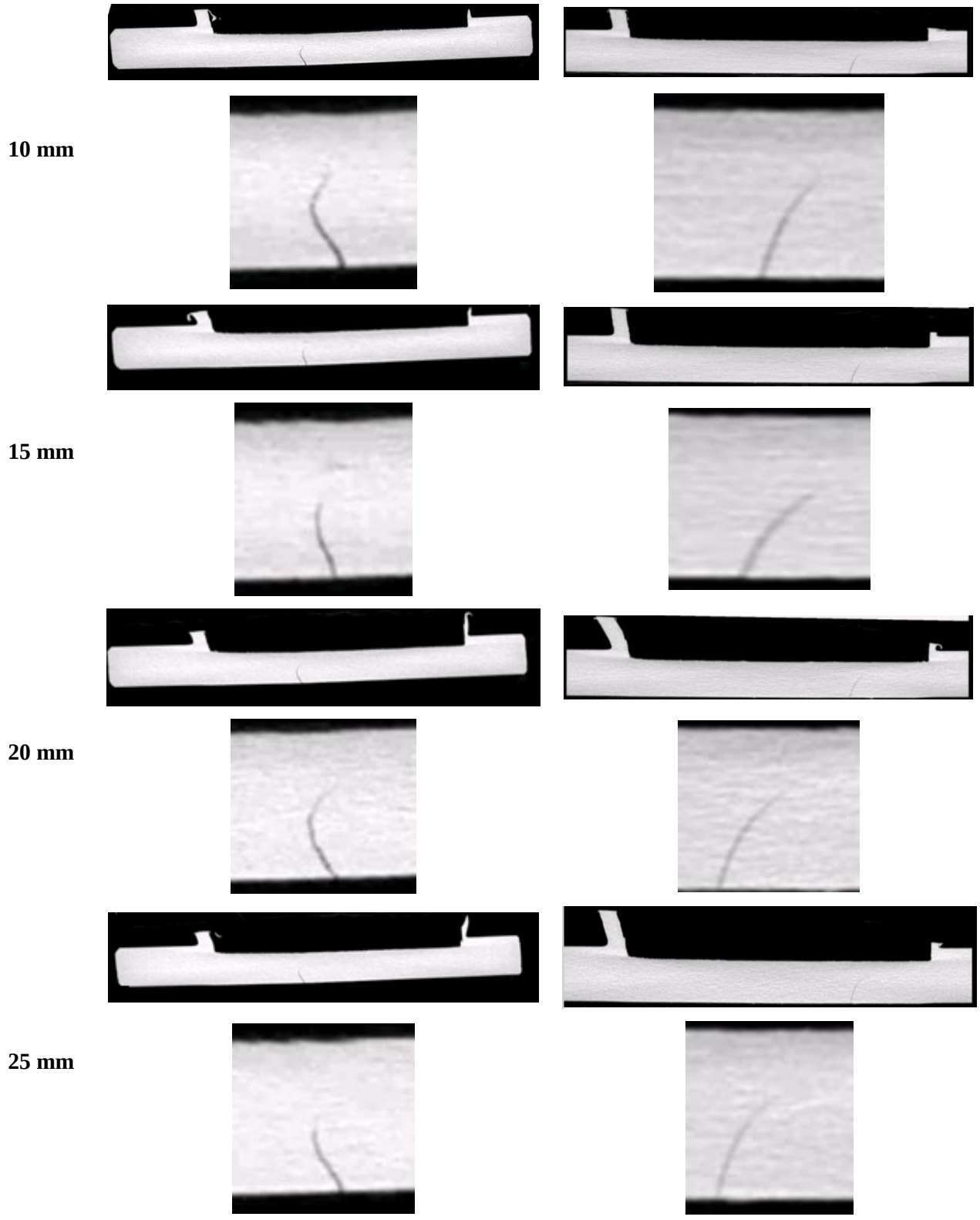

Figure 7.6 - Constancy of Lack of Penetration Defects through the Length of Welds

7.2.1 Conclusion

From the results presented in this section the following can be concluded:

1. Offsetting of the FSW tool may result in the introduction of a welding defect within the joint.

2. The size of the affected thickness through the joint was dependent on the magnitude of the offset tool position from the optimum position.
3. This technique introduced fairly consistent defects in both size and inclination along the length of the weld.

7.3 Effect of Offsets on Welding Force

It is well stated that the formation of LOP can be linked to the parameter selection, tool design and welding tool position [41]. The forging force was directly influenced by those previously mentioned welding characteristics. To better understand the effects of the numerous tool offsets investigated, the welding force at a number of key points were recorded. This was done in an attempt to identify a potential link between the forging force and the formation of the LOP. The same equipment and technique discussed in sections 5.1.3 and 6.1.3 were used to achieve these results. Figure 7.7 provides an overview of the maximum and average forging forces measured in the normal direction during welding with the various tool offsets in the normal and lateral directions. It can be seen that there was very little variation in the measured force for the different offsets. The dominating factor was the tool rotation speed and due to it being fixed at 1600 RPM it was expected that little variation would be observed. The deviation between the maximum and minimum of the average and maximum forging force was 1418 N and 1207 N. This was not as an extreme deviation as observed during the optimisation of the FSW process. The uncertainty in each measurement of the force was specified as 3.8 N in F_z, this was specified by the Kistler specification sheet.

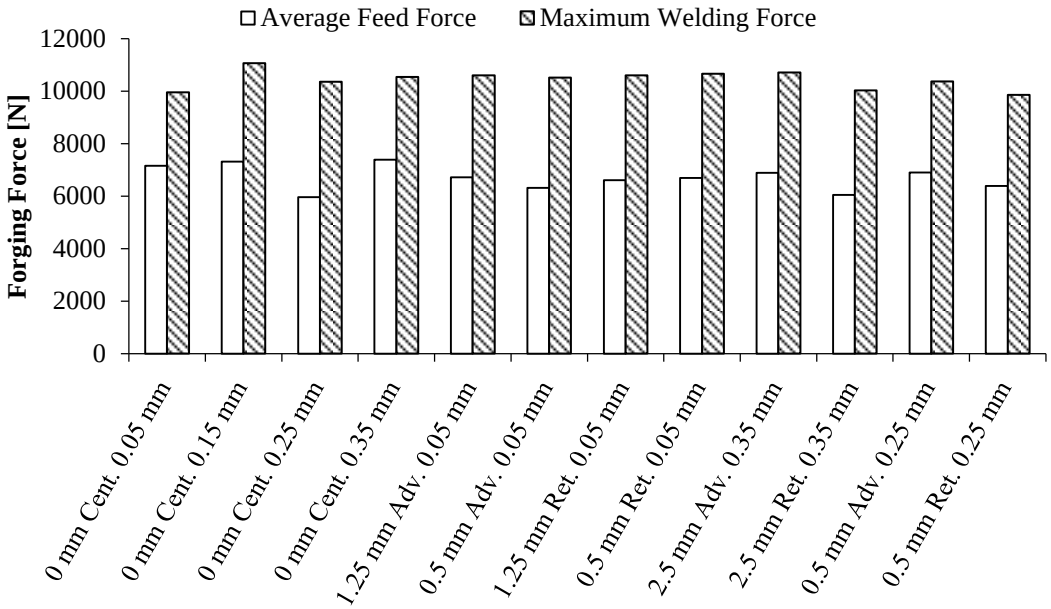

Figure 7.7 - Overview of Maximum and Average Force for all Investigated Offsets

The normal force profiles of the offset welds listed above have been plotted over three individual figures. The purpose of this was to group each type of offset, i.e. an offset only in the normal

direction. Combining all profiles onto a single set of axes would not allow for a clear depiction of the trends. The optimum welding parameters of 1600 RPM and 200 mm/min, from section 6.1 has been plotted on each in order to provide a baseline for which the effects of the offsets can be judged. Figure 7.8 shows the force distribution recorded for vertical tool offsets only. Besides for the 0.25 mm offset, all profiles followed near exact replicas of the optimum weld of 0.05 mm tool position. This implies that a sequential increase in vertical tool positions has little to no noticeable effect on the peak forging and average feeding force. It is anticipated that there is a vertical position in which the force distribution would be affected as the shoulder of the tool would eventually lose contact with the welding material. The deviation of the 0.25 mm profile from the others indicates that something may have occurred during the weld. Nothing out of the ordinary occurred during this weld which can be attributed to this. It was suggested that this deviation may have been caused by variations in the thickness of welding material.

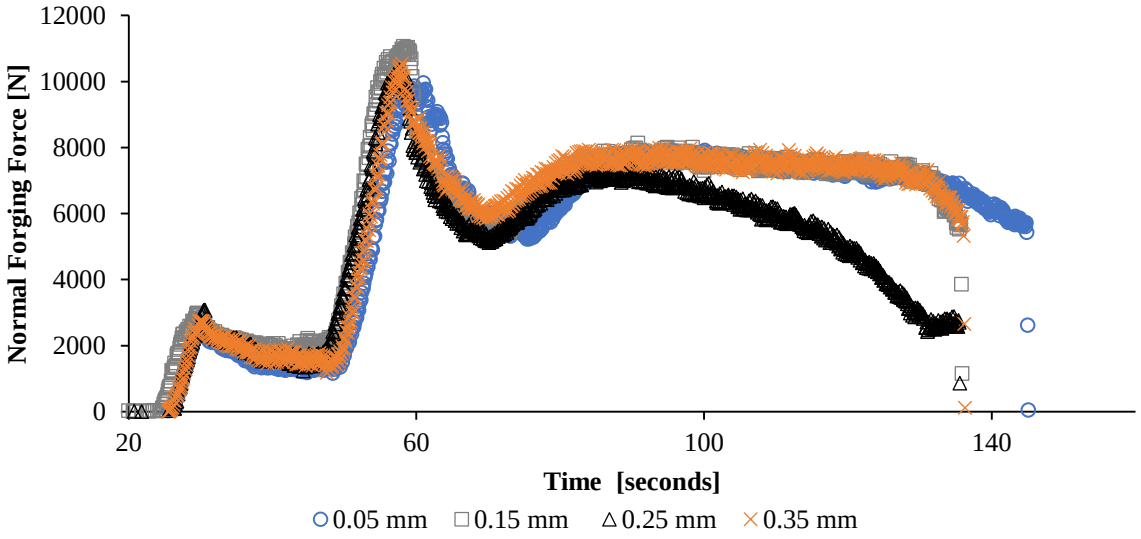

Figure 7.8 - Normal Force Profile for Tool Offsets only in the Normal Direction

Figure 7.9 illustrates the normal force distributions for the horizontal offsets either to the advancing or retreating side of the welding centre line. The baseline of the optimum weld had the lowest peak normal force and the highest forging force during welding. There was very little variation in the profiles due to the various offsets.

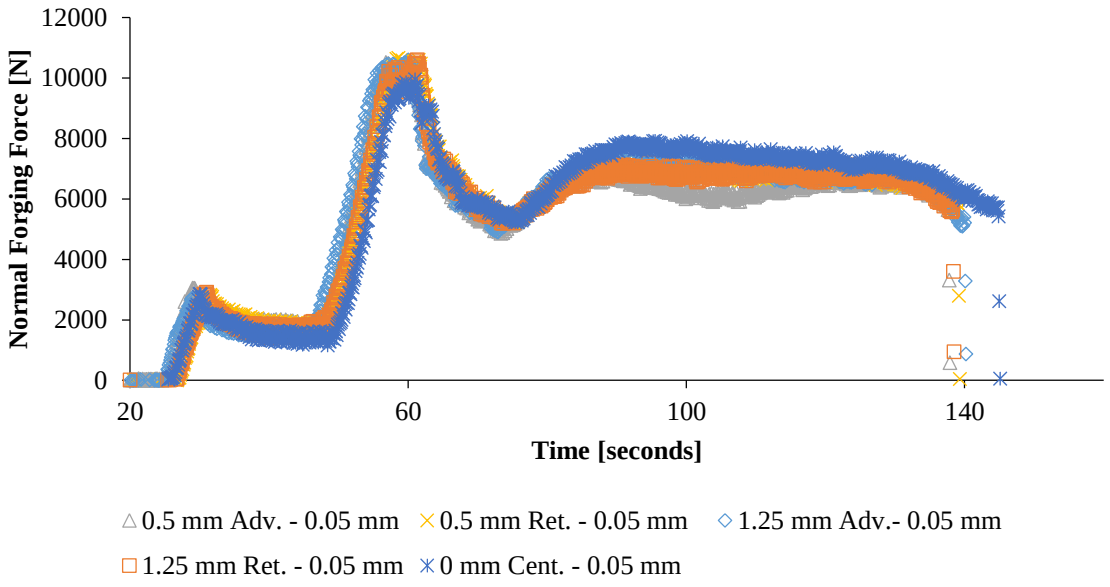

Figure 7.9 - Normal Force Profile for only Lateral Tool Offsets

Figure 7.10 illustrates the similar trends shown in Figure 7.9 that there was very little variation in the force profiles due to the combination of offsets in the vertical and horizontal directions. The optimum welds still had the highest welding force during the feed stage of the process.

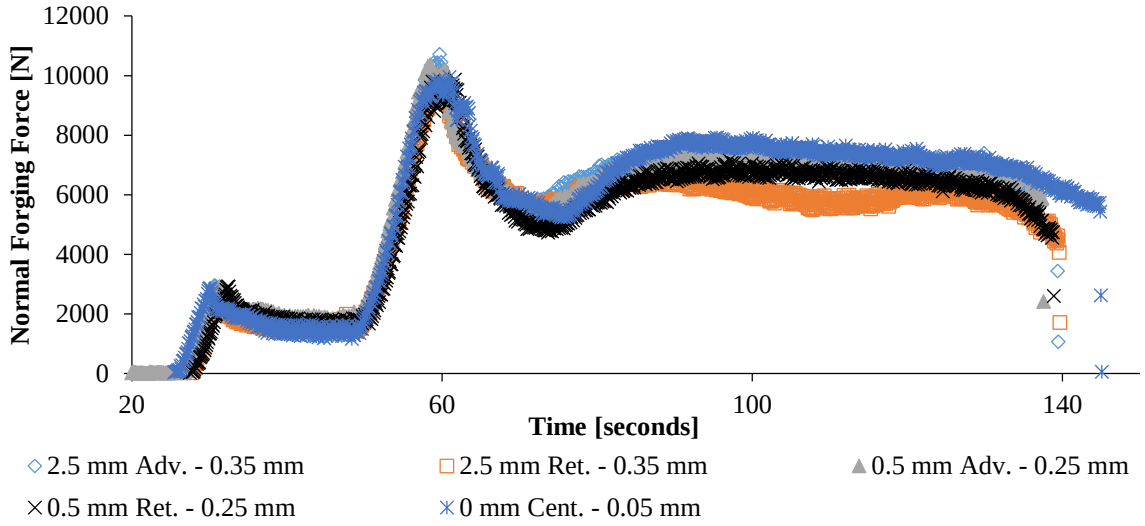

Figure 7.10 - Normal Force Profile for Lateral and Normal Combination Tool Offsets

7.3.1 Conclusion

From the results presented in this section the following can be concluded:

1. The offset of the tool in the two directions has very little to no noticeable effect on the forging force during welding.

2. As shown in section 6.1.4, the magnitude of the maximum force and average welding forging force was a function of the tool rotational speed and the feed rate in which the joint was manufactured.

7.4 Thermal Variations due to Welding Tool Displacement

It was shown in section 6.1.4 that changes in welding parameters resulted in substantial variations in the temperature of the joints. Three tool-off sets were investigated to identify if the offsets would substantially influence the thermal profiles of the joints. Table 7.3 provides the tool locations of the investigated cases. The first set of parameters was set as the optimum welding parameters in order to provide a value as to compare the offsets.

Table 7.3 - Tool Positions for Friction Stir Welded Samples with offset Tool Positions

Spindle Speed [RPM]	Feed Rate [mm/min]	Lateral Offset [mm]	Position of Centre of Line of Tool	Normal Offset [mm]
1600	200	0	Centre	0.05
		0	Centre	0.25
		1.25	Advancing	0.05
		1.25	Retreating	0.05

A measuring range of 100 to 3000 °C was used for the recording of the thermal imaging. The analysis applied to this investigation was exactly the same to that applied in section 6.1.4. A large number of thermal probes were placed across the welded joint in three distinct lines.

Figure 7.11 provides the temperature profile of the central probes at the tool-material interface. Figure a) shows all profiles overlaid to show how there was very little variation in the profiles due to the numerous offsets. Figure b) shows the profiles of the vertical offset compared to that of the most optimum welding case. It can be seen that by offsetting the tool by 0.2 mm in the normal direction a slight decrease in temperature was observed. This correlated well to the lower welding force observed for this welding case. The increase in the temperature at the end of the feed stage was noted due to the probe overlaying a portion of the welding tool thus increasing the measured temperature. Figure c) it can be seen that there was no significant variation in the thermal profiles due to the lateral offsetting of the tool.

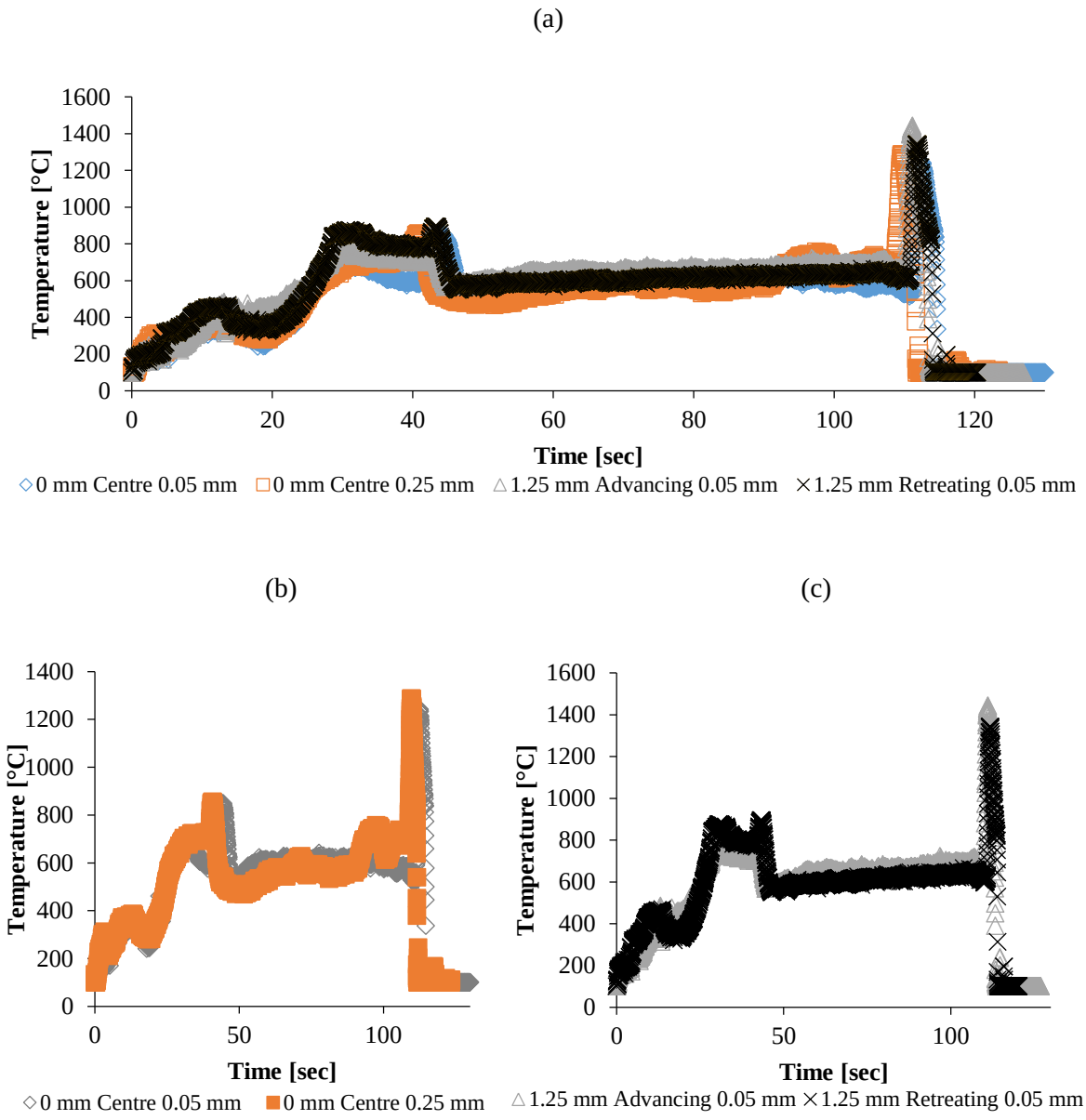

Figure 7.11 - Temperature Profile at Central-Probe for all Lack of Penetration Samples

Figure 7.12 shows the steady state calculated average temperatures for each offset tool position during the feeding stage of the welds. The figure provides the average measured temperature of the three central probes and the FLIR average line temperature function. As previous, the FLIR function predicts a slightly cooler average temperature per weld as it considered a greater distance across the weld. Comparison of the only vertical offset shows a very slight decrease in average temperature. This was accredited to the reduction in forging force due to the welding tool being retracted from the material. The average temperatures of the lateral offset welds were roughly equal to one another with the tool being offset equally on both sides of the weld centre line. This indicated that temperature rise was independent of whether the tool was offset towards either the advancing or retreating side. It may be speculated that alignment of the tool centre line and the plate edges (position were the two sides of the welding plates meet) reduces the difficulty or work required to weld the plates, further

investigation would need to be completed to confirm this fact. Due to the technique of measuring the temperature, an uncertainty analysis could not be completed.

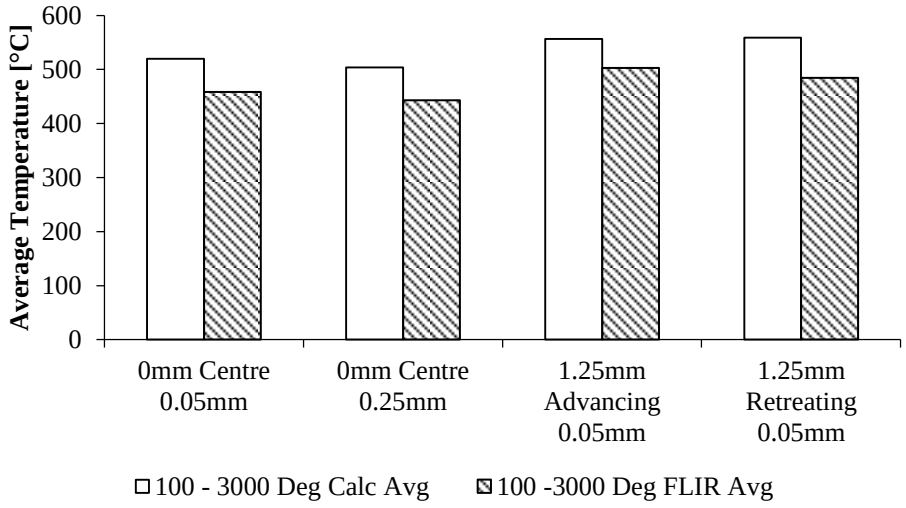

Figure 7.12 - Average Temperature across Thermal Probes for Friction Stir Welding with an Offset Tool

Figure 7.13 shows the average temperature per probe across the welded joints. It was extremely clear that surface temperatures on the advancing side of each weld were the highest, whilst the temperature tended to decrease towards the retreating shoulder's edge. It can be seen again, that the lateral tool offset welds were on average hotter than the baseline weld of 0 mm centre 0.05 mm. The 0.25 mm vertical offset weld was the lowest temperature weld which was to be expected due to the reduced contact of the tool and reduction in forging force. The profiles shown did not match well with literature as the trend of reducing temperatures from the centre out was not seen in these results. This may be attributed to the technique and location through the thickness of the joint in which the temperature measurements were taken in the compared researcher.

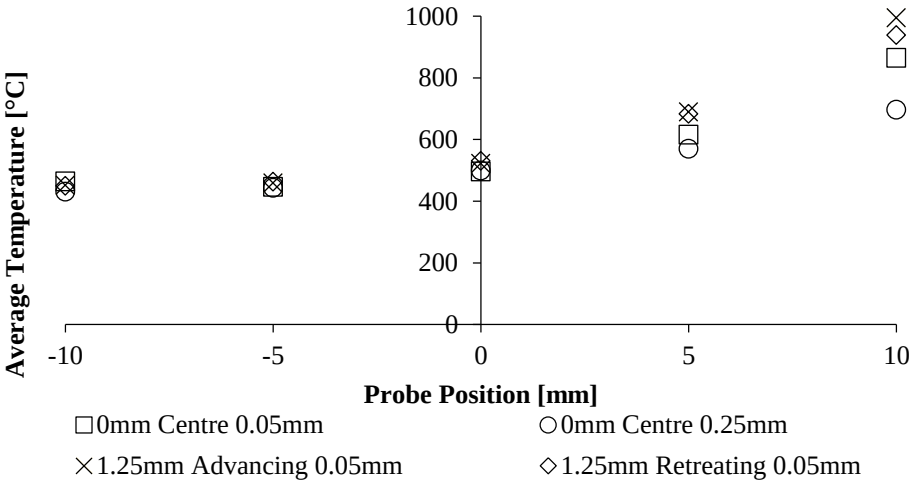

Figure 7.13 - Average Temperature per Probe across the Tool Offset Friction Stir Welded Joints

The overall trend of the advancing side surface being the hottest region was clearly shown in the temperature surface plots presented in Figure 7.14.

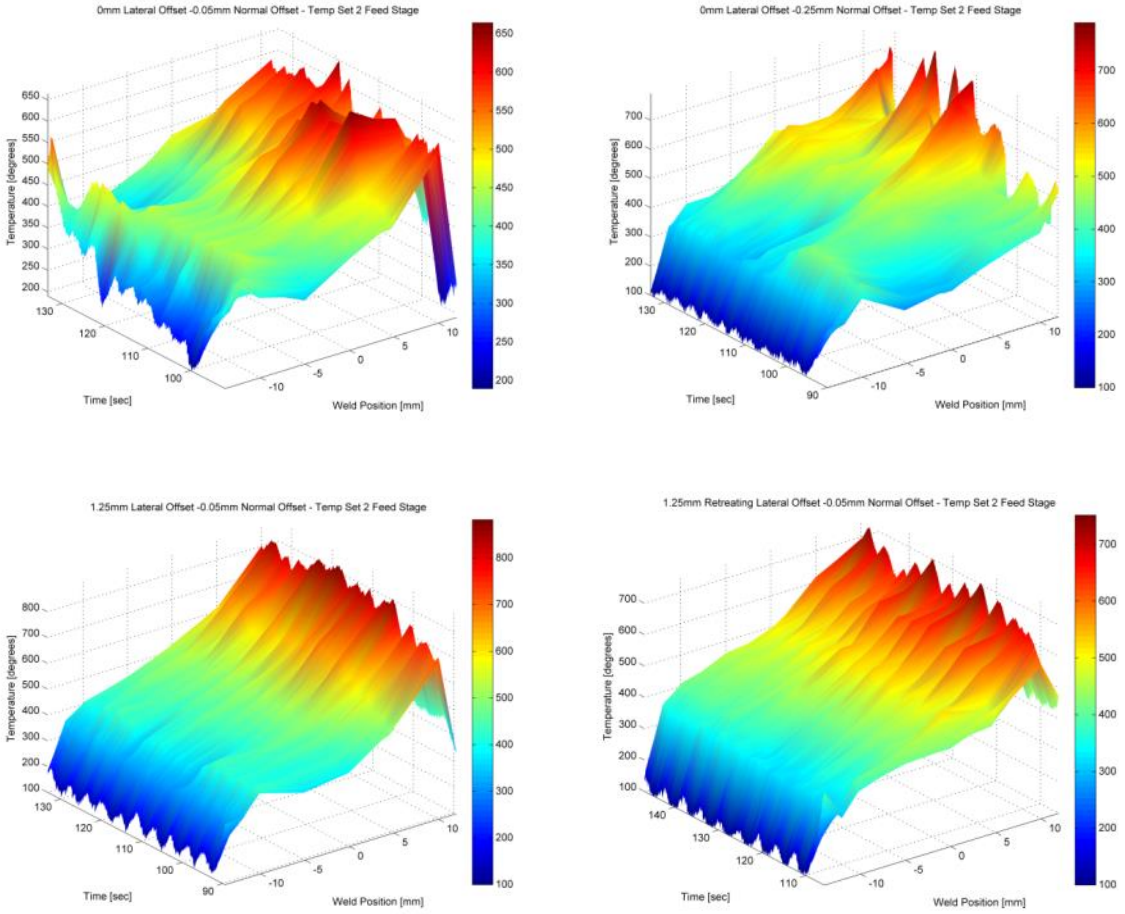

Figure 7.14 - 3D Temperature Maps during Feed Stage of Tool Offset Friction Stir Welding

7.4.1 Conclusion

From the results presented in this section the following can be concluded:

1. Similarly to the force data present above, the tool offsets tended to have very little effect on the magnitude of the average welding temperature.
2. The lateral offsets did, however, show a slight increase in average temperature to joints which had only had normal offsets applied.

7.5 Effect of Offsets on the Thickness of the Joint

Throughout section 6.1.5.3 it was clear that the final joint thickness was a result of the parameter combination which dictated the thermal and forging force generated in manufacturing the weld. Fixing the welding parameters to 1600 RPM and 200 mm/min, now allows for the determination of the effect of the tool misalignment on the final joint thickness.

It was shown in section 7.3 and 7.4 that the vertical offsetting of the welding tool only resulted in an increase in the forging force as well as a reduction in average welding temperature. This trend was noted in the parameter window investigation as the observation of as the forging force reduces the temperature and amount of flash formed increased.

Table C.2 in Appendix C.5 lists all relevant measured thickness of the resulting offset joints. Figure 7.15 shows the final joint thicknesses and percentage reduction from the base material due to the various tool offsets. It was evident that the normal offset was the dominate factor in the resulting thickness as the normal offsets tended to increase in thickness with increasing offset. The lateral offsets had very little variation between offset positions on the advancing and retreating sides of the centre line. Added to that, there was less than a 10% difference in joint thickness between the optimised parameter weld and those which were offset laterally only. This showed that joint thickness could be a possible parameter for monitoring normal tool misalignments. The combination offsets showed that both offsets on the retreating side of the weld were thinner than their advancing offset counterparts. This was not seen in the lateral offset samples thus, it may be vaguely insinuated that combination offsets to the retreating side produced thinner joints. Furthermore extensive testing would need to be completed to verify this fact. The uncertainty associated with the measurement of the joint thickness was specified as ±0.05mm.The calculation of the uncertainty in percentage reduction in joint thickness has been outlined in Appendix F.

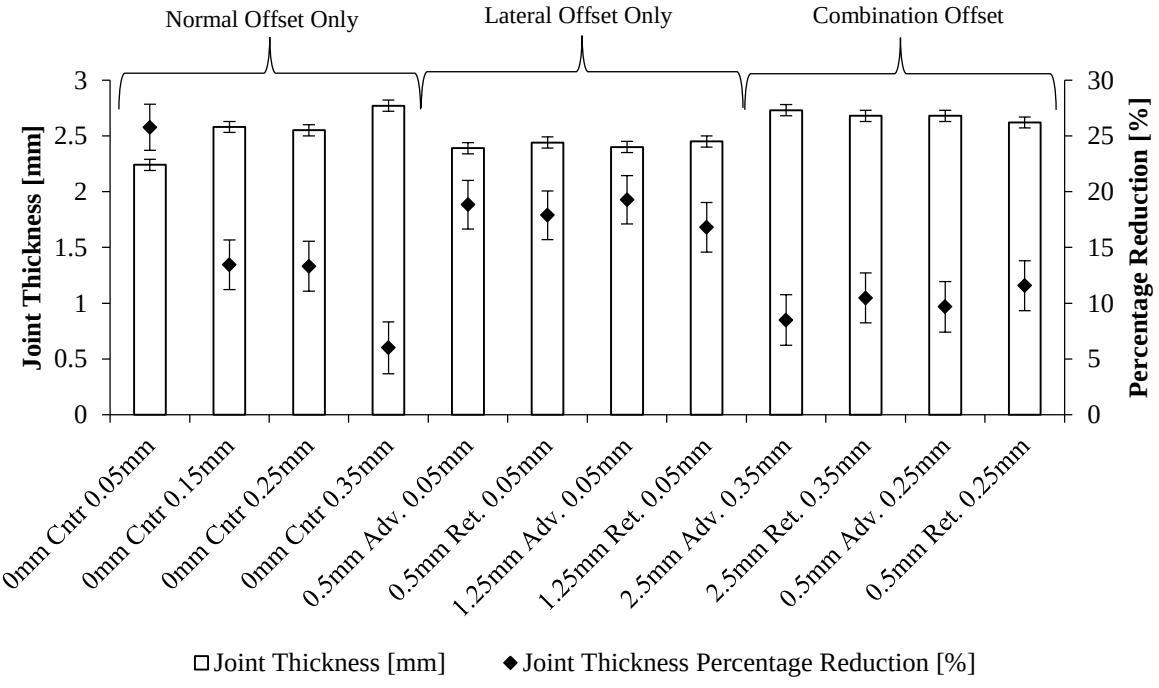

Figure 7.15 - Offset Friction Stir Welded Joint Thickness and Percentage Reduction from the Base Material

7.5.1 Conclusion

From the results presented in this section the following can be concluded:

1. The normal offset was the dominant factor in controlling the final FSW joint thickness.
2. Lateral offsets had minimal effects on the final joint thickness.
3. Combination offsets produced thinner joints when the tool was offset to the retreating side. Further testing must be completed to verify this fact.

7.6 Effect of Offsets and Lack of Penetration on the Strength of Friction Stir Welded Joints

Many engineering disasters have been caused due to a number of defects within materials or joints. No matter how minuscule the defect, its presence can have eventual catastrophic consequences. Section 2.3.4 show how various welding defects can negatively affect FSW joints in numerous ways. Emphases must be placed on Figure 2.43 which showed how increasing the length of the LOP defect reduces the load carrying capability of Aluminium FSW joints. Tensile Testing of Flawed (Lack of Penetration) Friction Stir Welded joints was completed in order to determine the extent of the detrimental effect of the presence of the LOP defects.

7.6.1 Tensile Strength of Flawed Friction Stir Welded Joints

Figure 7.16 illustrates the average ultimate tensile force and strength sustained by the numerous defective joints. It was clear from the figure that various offsets influence the strength capabilities of the numerous joints. As with the previous FSW parameter window investigation, joint thickness had a considerable effect on the tensile force carrying capability of the joint. Added to that a number joints displayed the detrimental effects of the presence of the LOP defects, in that the joints average load carrying capability was extensively compromised by the defect. Samples manufactured with normal only offsets tended to show an increase in the force ultimate force sustained but this was due to the increase in the joint thicknesses. Lateral offsets only showed that samples manufactured with advancing side offsets tended to be weaker than their retreating counterparts. Combination offsets were some of the weakest joints investigated. The joint with the 2.5mm Advancing 0.35 mm offsets was the weakest due to the presence of one of the largest defect within the joint. The uncertainty associated with the ultimate force was specified as ±1% of 20kN as this was the sensitivity of the load cell used in the measurement of the force. The calculated uncertainty for the ultimate tensile stress was covered in Appendix F.

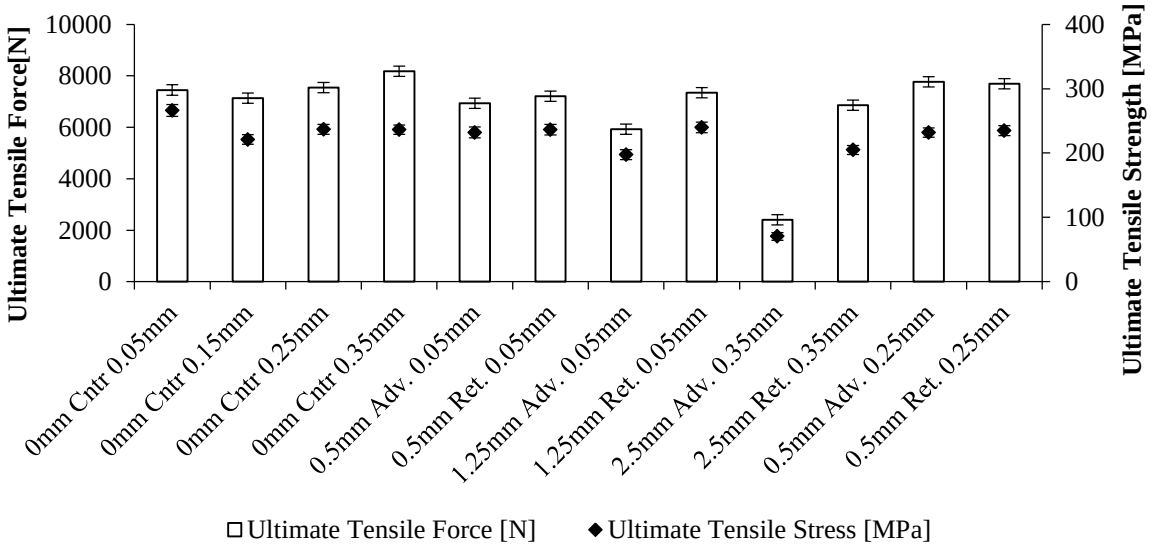

Figure 7.16 – Average Ultimate Tensile Force and Ultimate Stress Maintained by Defective Joints

Figure 7.17 shows the general decrease in the strength of the joints due to the increasing size of the LOP defects. This trend of decreasing strength was expected as the size of the defect grows there would be far less of the unaffected/defect-free joint which could sustain the applied force. The uncertainty associated with the measurement of the LOP was specified as ±0.005µm.

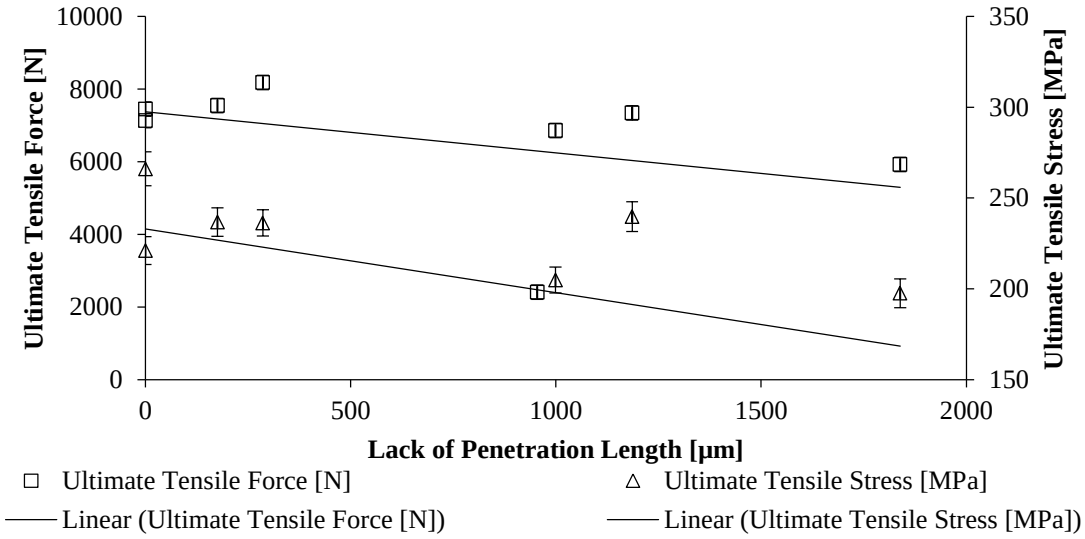

Figure 7.17 - Effect of Lack of Penetration Length on Ultimate Force and Strength

Figure 7.18 illustrates a normalised comparison between experimental results achieved in this study to those obtained by Kinchen. They showed that an increase in LOP size resulted in a near exponential decrease in the strength of the joints under a tensile stress at room temperature [45]. Their FSW was manufactured using 8.128 mm thick AA2195T8M4 Aluminium plate. This plate was 2.7 times thicker than the AA6082-T6 material used in this study, thus for the results to be comparable effectively the datasets have been normalised relative to the maximum stress in each set.

It can be seen in the figure that the trend lines overlap from defect sizes greater than 1mm. The published work tended to show an exponential reduction in strength were as the experimental work was shown in the solid black markers tended to show a far more linear decrease with a number of outlying points. Although the data has been normalised the joint thickness effects are extremely evident in the initial samples with small defects. The main confirmation that was required from this figure was that the experimental samples strength was decreasing with increasing defect size. The calculation related to the uncertainty of the normalised experimental stress has been provided in Appendix F.

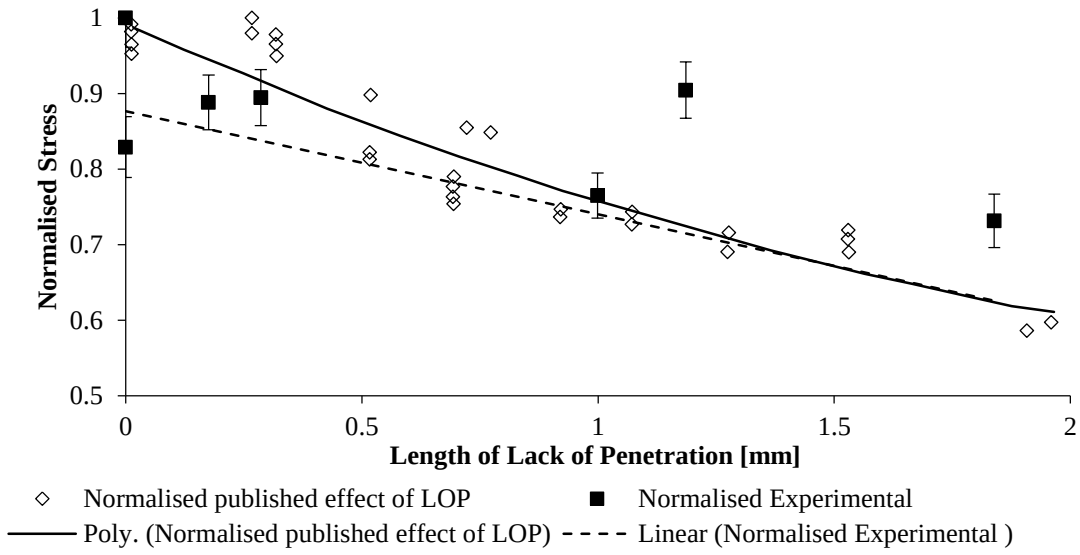

Figure 7.18 - Normalised Comparison to Effect of Length of Lack of Penetration on Joint Load carrying ability

7.6.1.1 Conclusion

From the results presented in this section the following can be concluded:

1. The numerous tool offsets produced joints and LOP defects that showed a significant reduction in joint strength.
2. An increase in defect size resulted in a decrease in joint strength.
3. Normal offset only tended to have an increase in ultimate force sustained as the joints were thicker.
4. Advancing side lateral offsets tended to be the weakest joints in comparison to the other lateral offset only joints.
5. Combination offsets resulted in the weakest joints due to the largest defects forming within the joints.

7.6.2 Fractography Analysis of Flawed Friction Stir Welded Joints

In section 6.1.6.2 the optimum welding parameters of 1600 RPM and 200 mm/min was shown to fail in the region of the advancing shoulder of the joint. The samples consistently failed in that position due to the significant variation in material hardness at the location were the welded material met the unaffected base material. Joints which failed in the centre were said to have failed there due to the ineffective joining of the two plates or due to the presence of some sort of defect which caused the failure. Figure 7.19 shows the failure positions of the various offset tool FSW joints. The axis of the figure provides the normal and lateral positions of the tool. It was evident that although the defects were formed within the joints, not all tool positions failed in the central region. Only five tool positions resulted in failures in the central region. This implies that all through the presence of a LOP defect could be detrimental to the strength of the joint, the most critical or weakest area of a FSW joint was the interface of the HAZ and the base material on the advancing side.

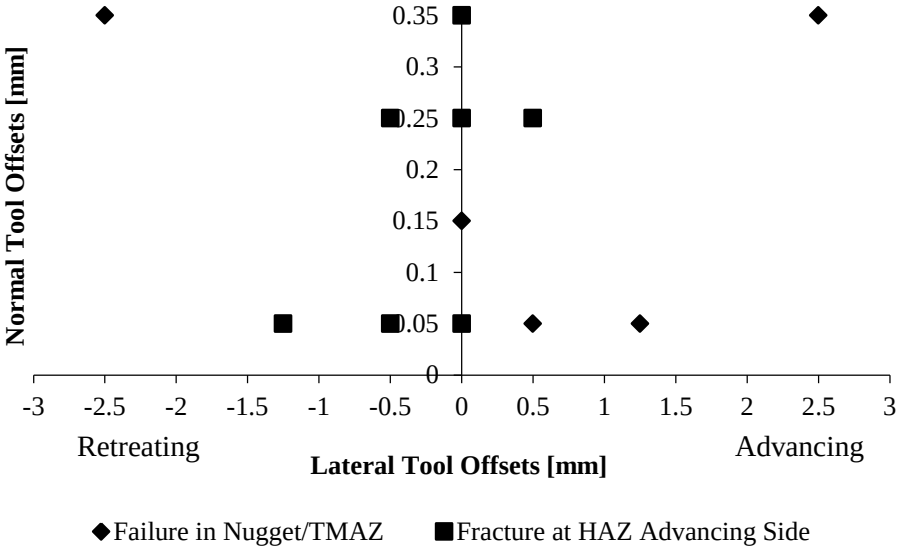

Figure 7.19 – Tensile Failure Positions of Friction Stir Welded Joints manufactured with Numerous Tool Offsets

The fracture surfaces of the two types of failures were examined using a Scanning Electron Microscope. Table 7.4 lists a number of examples of the two types of fracture surfaces which occurred.

Table 7.4 - Scanning Electron Microscope analysis of Tensile Fracture Surfaces

<table>
<tr><td colspan="2">0 mm Centre 0.05 mm (Failed at the Shoulder Edge in HAZ Advancing side)</td></tr>
<tr><td> 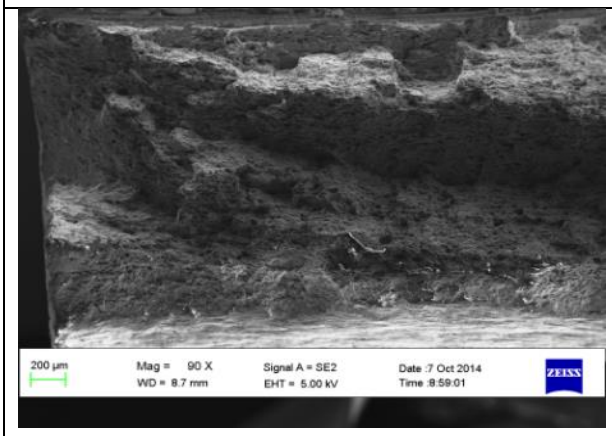
</td><td> 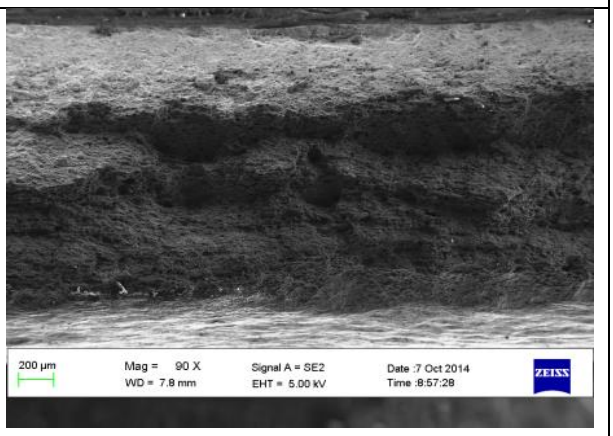
</td></tr>
<tr><td> 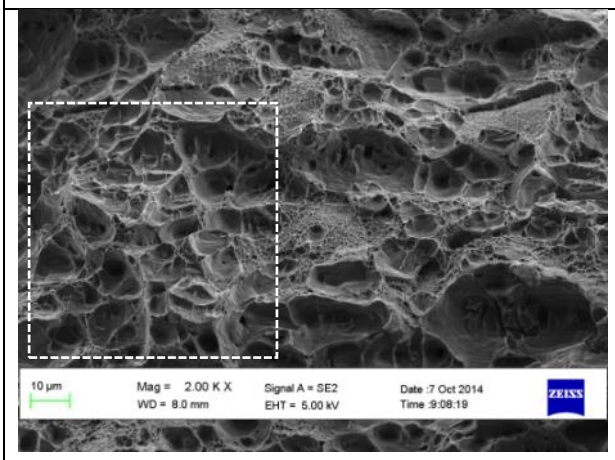
</td><td>The SEM images of the fracture surface of this sample clearly indicate a monotonic overload failure due to the application of the tensile load. The highly dimpled failure has been indicated in the region within the square in the adjacent figure. A dimpled fracture surface resulted which was consistent with a ductile failure. This sample failed at the HAZ shoulder thus no indication of a pre-existing defect will be seen.</td></tr>
<tr><td colspan="2">0 mm Centre 0.35 mm (Failed within Nugget/TMAZ, due to LOP)</td></tr>
<tr><td> 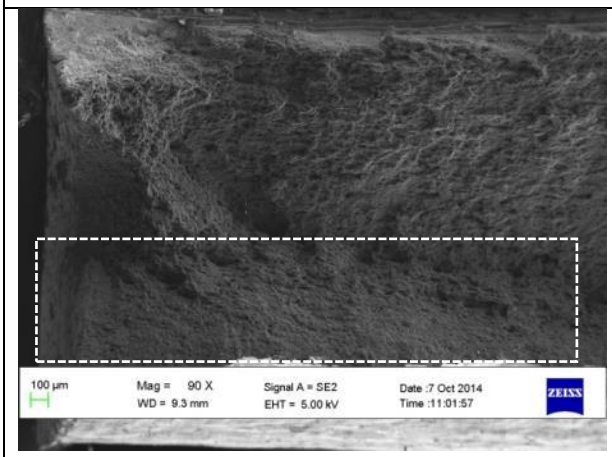
</td><td> 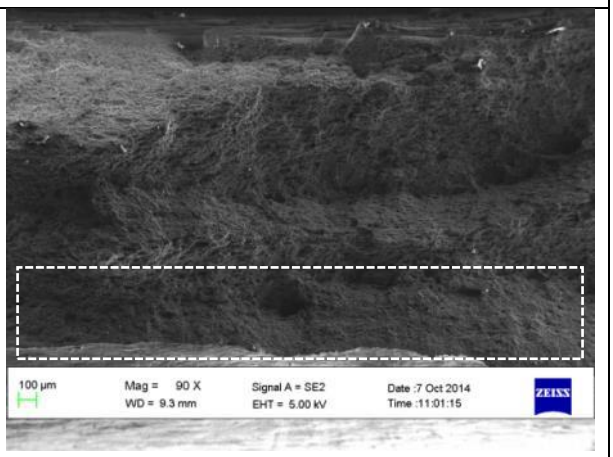
</td></tr>
</table>

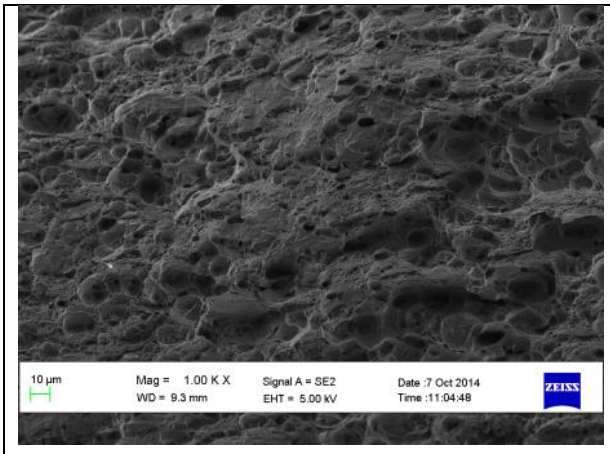

Similar to the fracture surface above, this joint exhibited a monotonic overload fracture. A dimpled fracture surface was seen, indicating a ductile failure. The images show a small smooth region originating from the root surface which was not as jagged as the remaining portion of the joint, this region has been indicated in the square region of the above images. It could be assumed that this region was formed due to the presence of the defect. The defect can be seen in Figure 7.4.

1.25 mm Advancing 0.05 mm (Failed within Nugget/TMAZ, due to LOP)

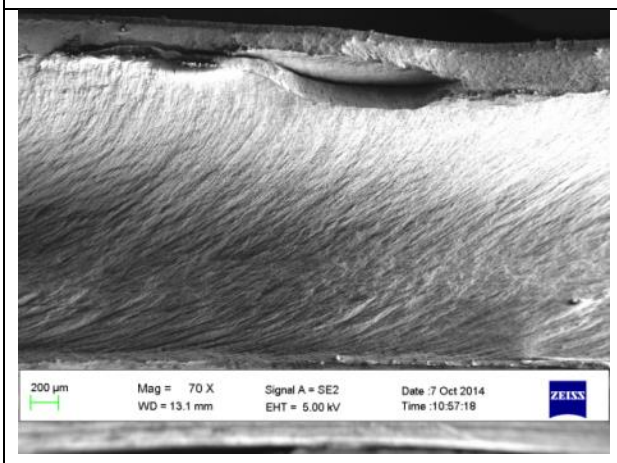

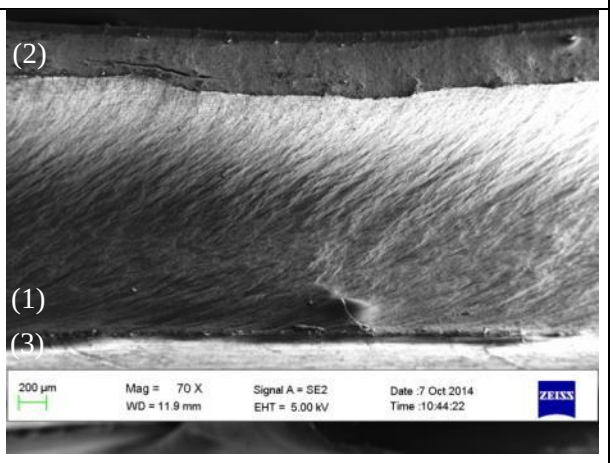

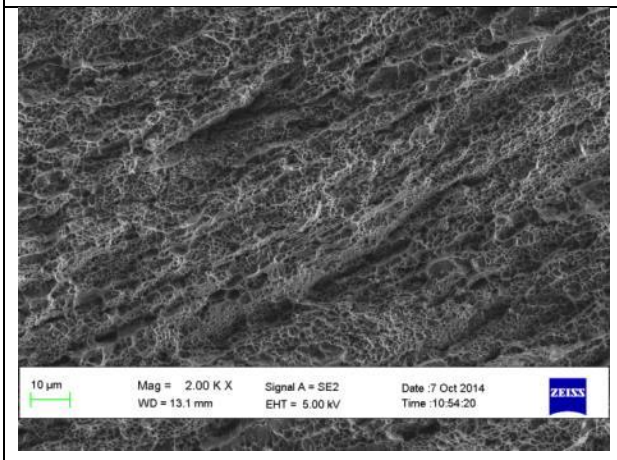

The joint fractured within the nugget/TMAZ region, the final surface did not exhibit the same failure as the joints above.

Dimples were seen on the surface. Three clear regions can be seen in the figures, (1) a large central region which showed a striation like failure which was flanked by (2-3) two monotonic overload failure zones. It was concluded that this central region was the failure of the nugget. Due to the hardness and microstructure variation within this zone compared to the other regions of the joint it would be likely that it would exhibit a different fracture surface. An image of the cross section of the joint has been provided to indicate that the nugget region was surrounded by the TMAZ.

0.5 mm Advancing 0.05 mm (Failed within Nugget/TMAZ, due to LOP)

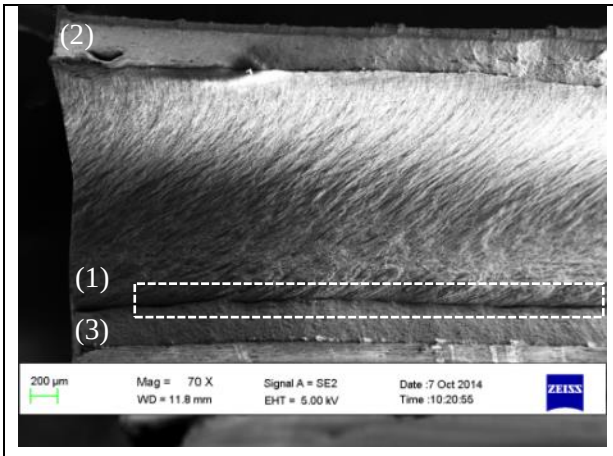

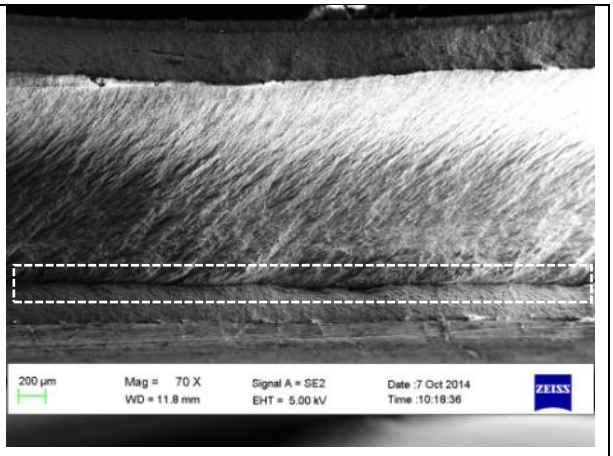

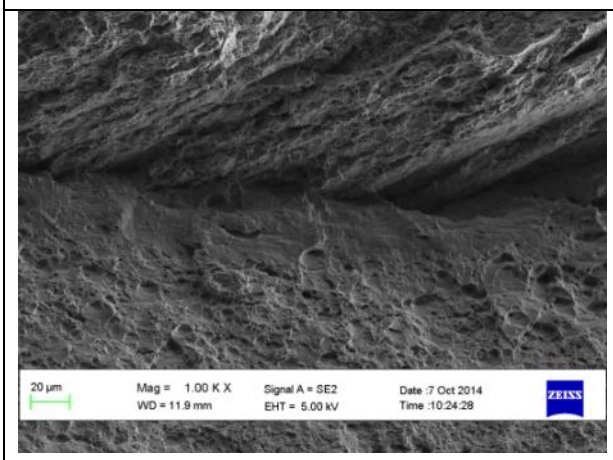

As with the joint which failed within the Nugget zone above, three clear regions of failure were identified, the three regions are indicated as previous. Further magnification of the fracture surface revealed that a dimpled surface resulted in both the lower and upper region of the fracture surface. There was a small region, identified as the darker line region within the square indicator in the initial two images of this set that exhibited brittle like failure. This darker region can be concluded as the transition between the nugget and TMAZ regions.

0.5 mm Retreating 0.05 mm (Failed at the Shoulder Edge in HAZ Advancing side)

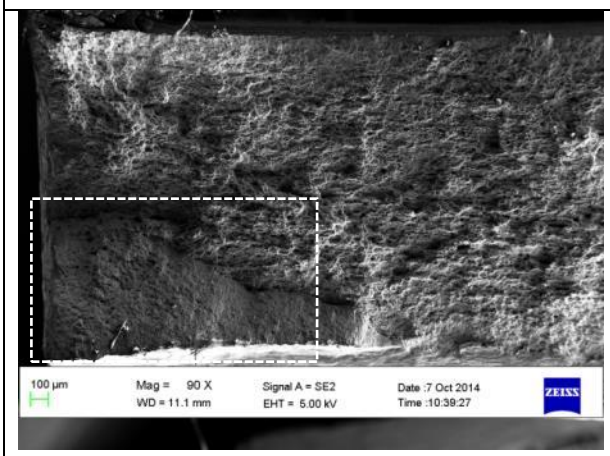

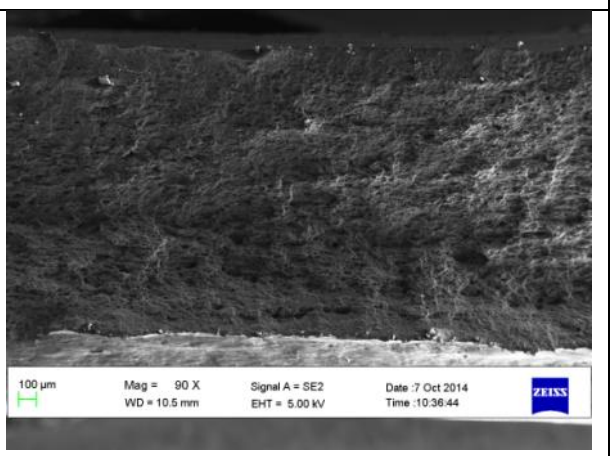

As with the joint which failed in HAZ, clear ductile failure was exhibited. Features on the lower left hand corner which continued as a thin band from the root surface and ran along the joint of the first image in this set of images, indicated in the square region. This showed a region which was different to the remaining upper section of the joint. It was concluded that failure began from this region.

Figure 7.20 shows a series of images taken during the tensile testing of a number FSW joints. The high speed images were taken at a rate of 2000 frames per second. The images all clearly show the ductile failure of the joints at the various failure locations. What can be noted was that the samples that failed within the nugget/TMAZ (failure due to the presence of a LOP defect) all tended to show fast, clean (very little fibrous, shear failure) and straight failure, clearly evident on the 2.5 mm Adv. 0.35 mm joint. The joint which failed in the HAZ showed signs of typical ductile failure, in that microvoids formed followed by final fibrous/shear fracture occurring. Although not completely clear, signs of approximately 45° maximum shear stress regions formed on the edges of the 0.5 mm Ret. 0.05 mm sample. Comparison of the two failure positions clearly indicates the effects of the LOP defects on the mechanical strength as well as the failure of the joints.

0.5 mm Advancing 0.05 mm (Failed within Nugget/TMAZ, due to LOP)

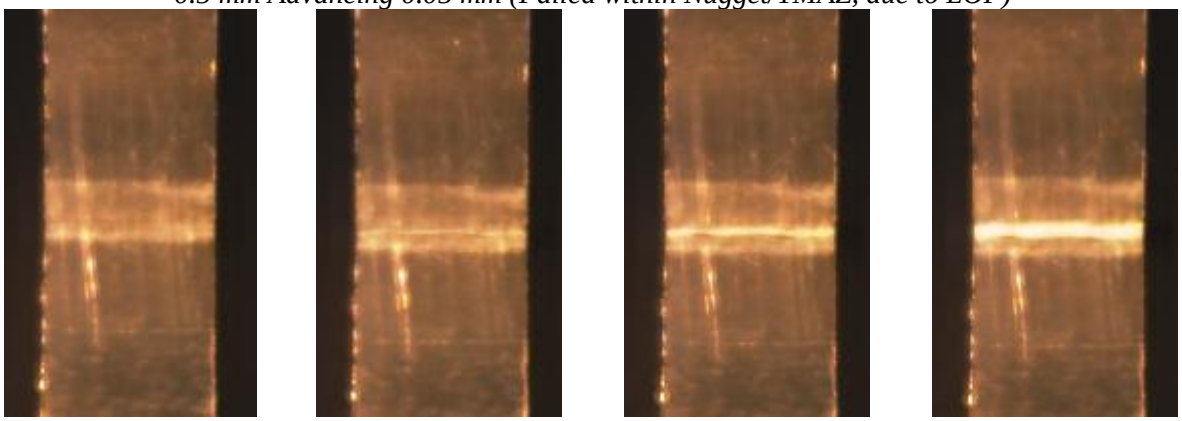

0.5 mm Retreating 0.05 mm (Failed at the Shoulder Edge in HAZ on Advancing side)

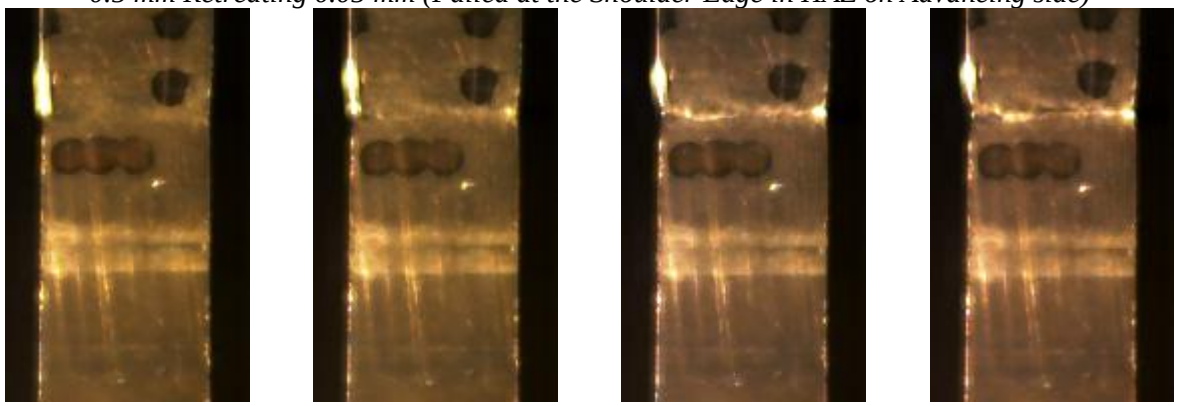

2.5 mm Advancing 0.35 mm (Failed within Nugget/TMAZ, due to LOP)

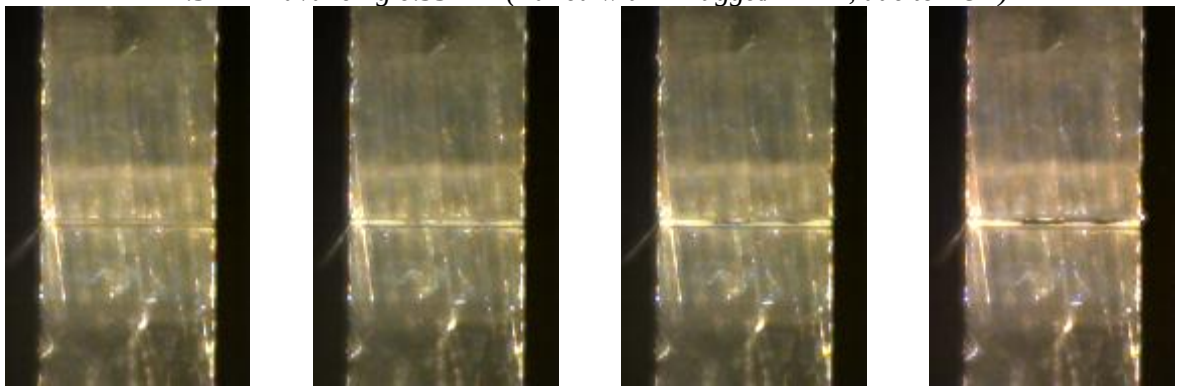

Figure 7.20 - Fracture of Tensile Samples

7.6.2.1 Conclusion

From the results presented in this section the following can be concluded:

1. The presence of a LOP defect within a joint can greatly affect the fracture position of joint under the application of a tensile force.
2. Fracture in the nugget/TMAZ due to a defect results in a distinctive fracture surface compared to that of a failure within the HAZ.
3. All samples failed according to a typical ductile failure mode.
4. In addition to the influence of a LOP defect within a joint, the weakest or most critical region of any FSW joint was the HAZ/base material region as a number of the investigated joints failed in this region rather than in the region of the LOP defect.

7.6.3 Ductility of Flawed Friction Stir Welded Joints

Three points bending of a defective joint is typically one of the most effective destructive methods of identifying the extent of the defect. Section 2.3.4.11, Figure 2.46 showed that samples which fracture completely under this test had prominent LOP defects within the joints. Joints which cracked slightly were ones which displayed signs of kiss bonds within the joints [41].

Figure 7.21 illustrates the average maximum bending force sustained by the FSW joints which were manufactured with a number of tool offsets. It was evident from the figure that not all of the offsets created joints which may have had suitable LOP sizes. Of the various tool offsets combinations, joints manufactured with retreating offsets tended to not show substantial effects of the LOP. The uncertainty associated with the measurement of the ultimate bending force was specified as 200 N. The uncertainty of the measurement of the bend angle was specified as 0.5°.

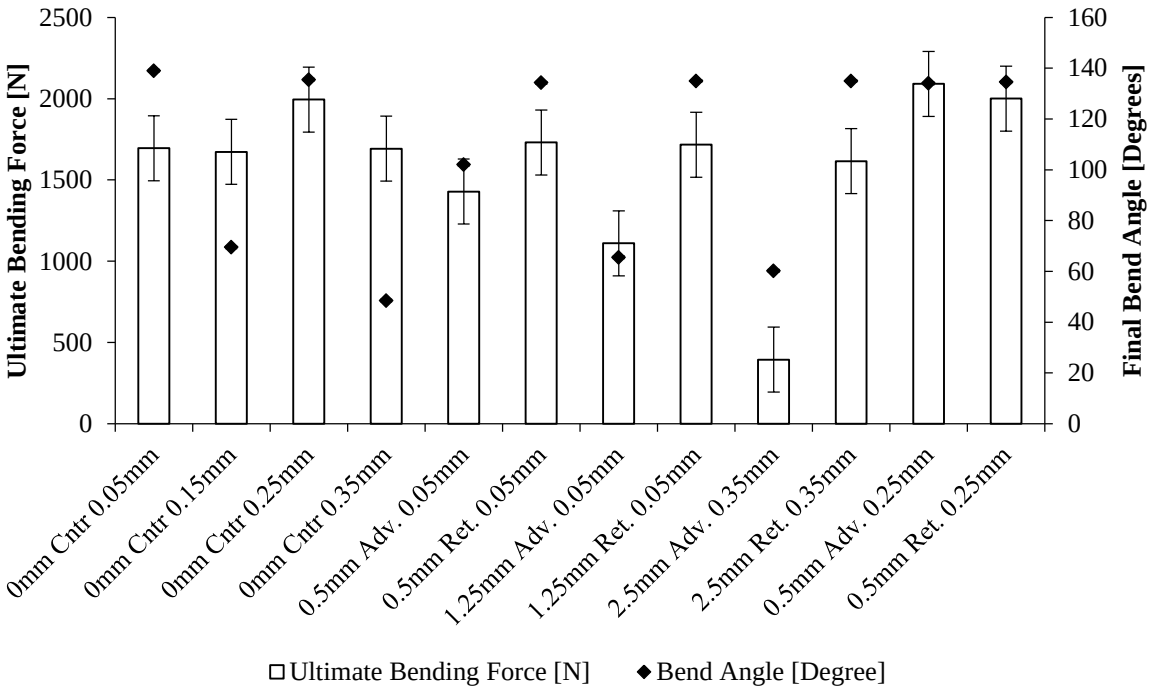

Figure 7.21 - Maximum Bend Force Maintained by Defective Joints

Figure 7.22 shows the side view of the bent samples, with an indication of the bend angle and the root surface of the bent sample. It was clear that a number of the joints produced joints with substantial defects within them, as shown by the root surface of the sample.

0 mm Centre 0.05 mm – No crack or defect

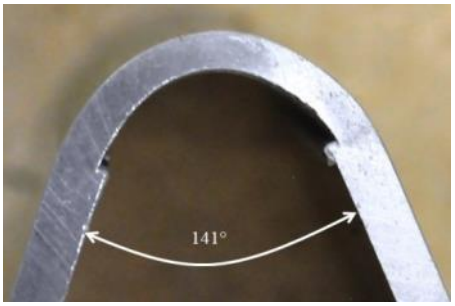

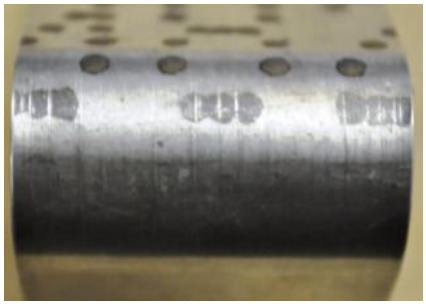

0 mm Centre 0.15 mm – Small crack

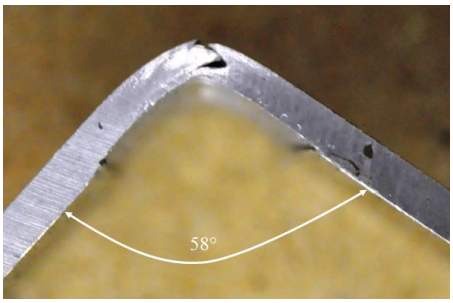

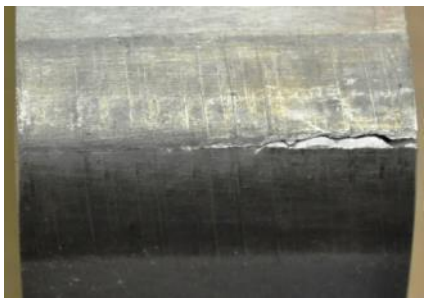

0 mm Centre 0.25 mm – Large crack

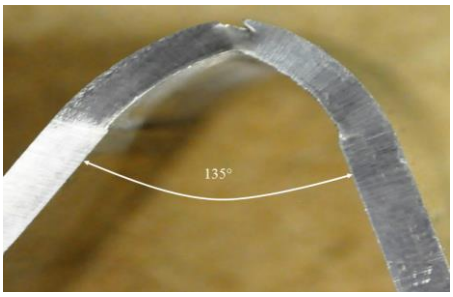

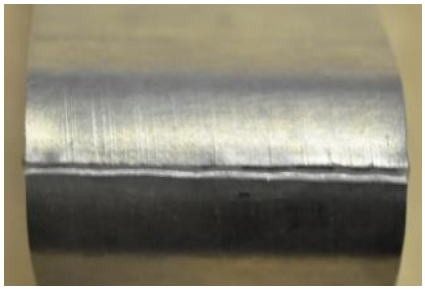

0 mm Centre 0.35 mm – Large crack

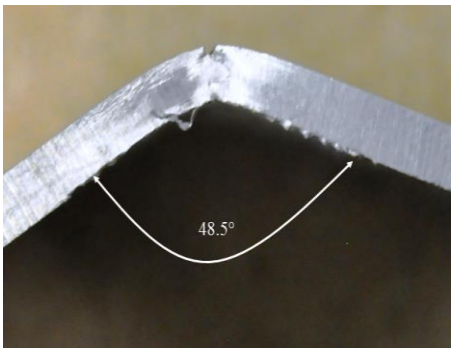

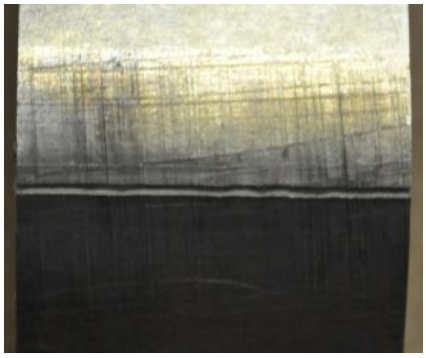

0.5 mm Advancing 0.05 mm – Large crack

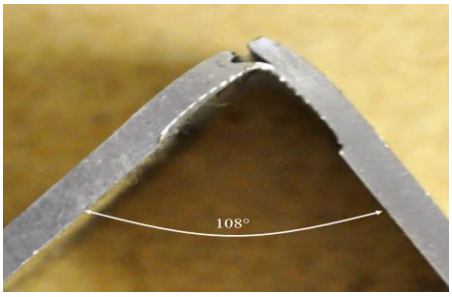

0.5 mm Retreating 0.05 mm – No crack or defect

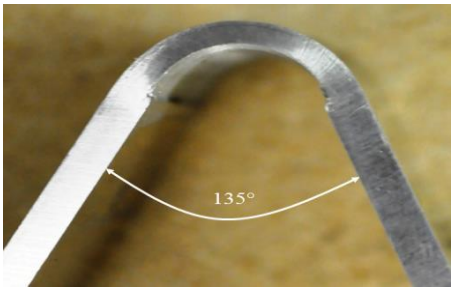

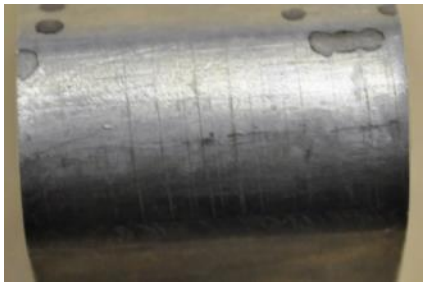

1.25 mm Advancing 0.05 mm – Large crack

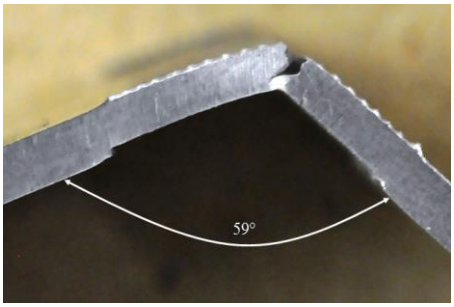

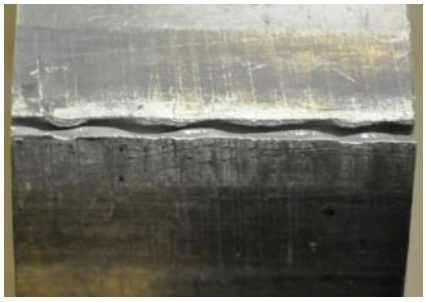

1.25 mm Retreating

0.05 mm – No crack or defect

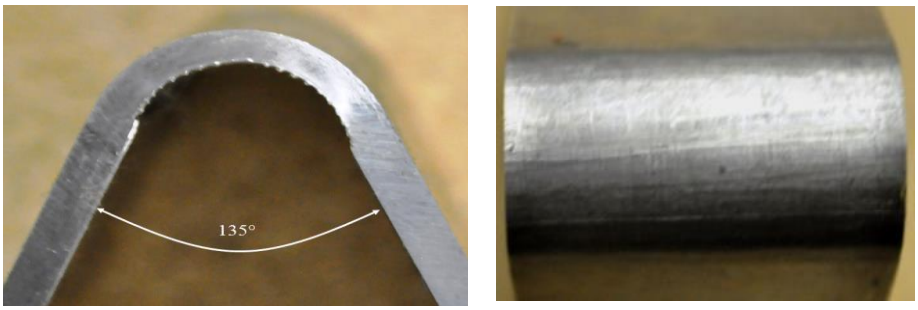

2.5 mm Advancing

0.35 mm – Large crack

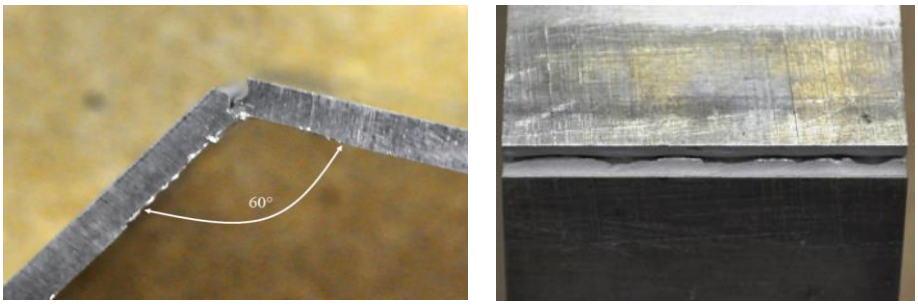

2.5 mm Retreating

0.35 mm – Large crack, one sample full fractured

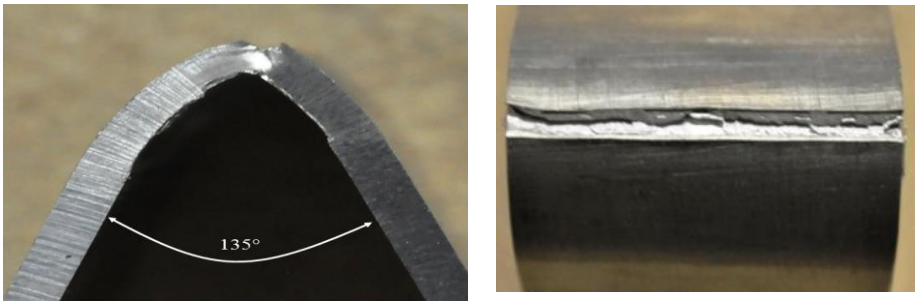

0.5 mm Advancing

0.25 mm – Initial signs of cracking

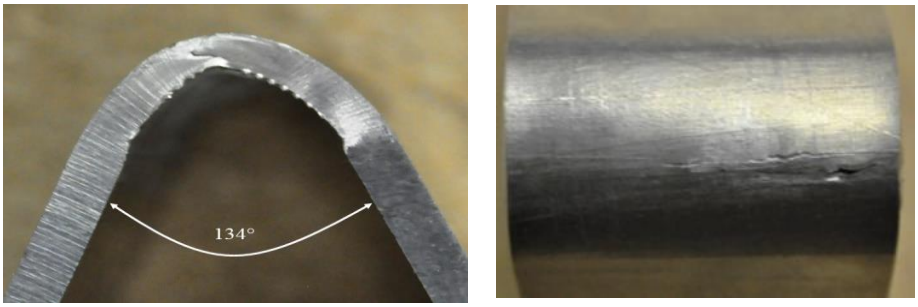

0.5 mm Retreating

0.25 mm – Initial signs of cracking

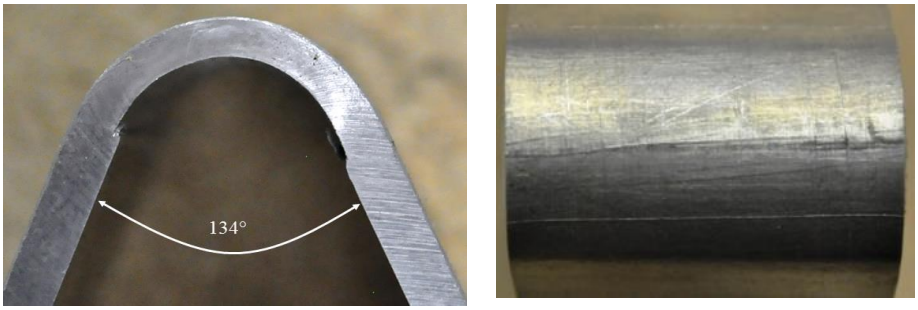

Figure 7.22 - Fracture/ Defect Formed during Bending Test of Defective Friction Stir Welded Joints

7.6.3.1 Conclusions

From the results presented in this section the following can be concluded:

1. The presence of the defect can greatly affect the bending strength of a FSW joint.

2. Three-point bending was a suitable destructive technique in identifying the presence of a defect within the FSW joint.
3. The presence of a LOP defect can greatly affect the ductility of a joint.
4. A variety of the tool offsets resulting in a variation in the ductility of the joint.

7.7 Fatigue Life of Friction Stir Welded Joints with numerous Tool Positions

The application of a cyclic load to any welded component will eventually result in the failure of the joint. The presence of even the smallest inclusion, crack or defect would only add and accelerate the failure of the component. With every completion of the cyclic load, the internal crack or Lack of Penetration tends to gradually propagate until the point that the remaining unaffected thickness can no longer sustain the applied force.

Due to the length of the fatigue tests completed in section 6.2.6, it was decided that a number of FSW tool offsets would be limited. Table 7.5 lists the FSW tool offset positions used in the manufacture of the fatigue samples.

Table 7.5 - Friction Stir Welding Tool Offset for Fatigue Samples

Lateral Position	Lateral Direction	Normal Position
0	Centre	0.05
0	Centre	0.25
1.25	Advancing	0.05
1.25	Retreating	0.05

Fatigue coupons were CNC machined from the welded plates according to the dimensions are shown in Figure B.5 in Appendix B. Figure 7.23 provides an example of the typical manufacture of the coupons from the FSW plates. The figure also provides an example of the coupons.

Figure 7.23 - Manufacture of Bending Fatigue Friction Stir Welded Coupons

Originally, the change in thickness of the base material on the crown surface of the weld was not removed. The reason for this was to avoid introducing or altering the residual stress profile in the coupon due to secondary machining as well as introducing added deformation or damaging the coupons. Two samples from the 0 mm Centre 0.05 mm coupons were tested without the removal of the change in thickness. These samples were run at a stress amplitude of approximately 165 MPa and stress ratio of approximately -1. Both samples failed within 11 and 12 minutes which corresponded to approximately 15620 and 17040 cycles. These samples failed at the edge in which the base material and crown surfaces met on the advancing side of the weld. Figure 7.24 indicates how these joints preformed compared to those of the base material tested at the same stress amplitude. The fatigue lives of the FSW un-skimmed samples were reduced by as much as 90.8% from that of the base material.

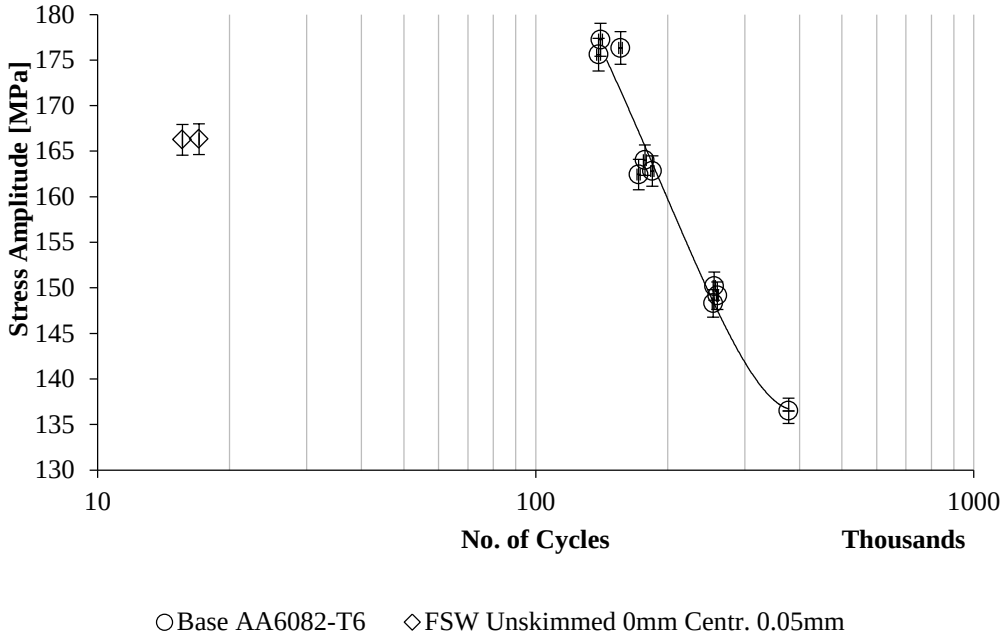

Figure 7.24 – Detrimental Effect of variation in Thickness Caused by Friction Stir Welding Material Lose

Figure 7.25 provides the exact failure position of the un-skimmed samples. Assessment of the fracture surface indicates that due to a fairly granular fracture surface without a clear smooth region it was evident that a failure occurred quickly once the sample began to fracture under the approximately fully reversed bending load. A dark region with black striations moving away from the crown surface can be seen on the fracture surfaces, this indicated that the initiation of the failure may have begun in this region. Due to the nature of reversed bending fatigue loading, fatigue initiation sites would have also occurred from the root surface of the weld, regions of fretting were present near the lower surface of the fatigue coupon. The stress concentration factor which would have occurred due to the variation in thickness and corner radius formed by the tool would have also contributed to the failure of the joint.

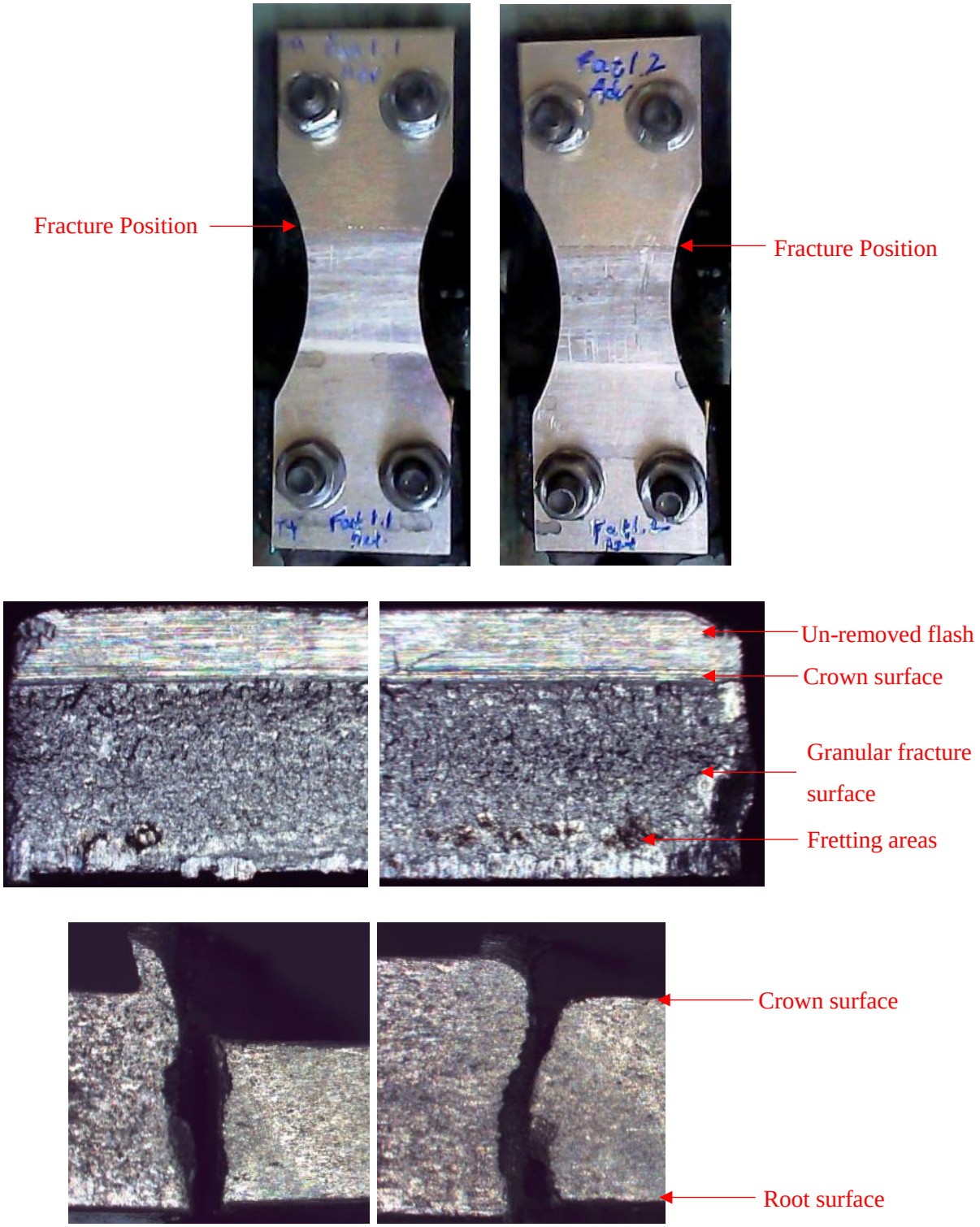

Figure 7.25 - Fracture Position of the Un-skimmed Fatigue Samples

Due to this reason all fatigue samples here on out were skimmed to an approximately constant thickness. The optimum FSW parameter skimmed sample showed an increase in fatigue life from 11.5 minutes to 110 minutes which correlated with an approximate 156200 cycles. The welded samples achieved an 87.77% of the fatigue life of the base material. Figure 7.26 shows the fatigue life of all offset tool FSW coupons which had been skimmed to remove the variation in thickness.

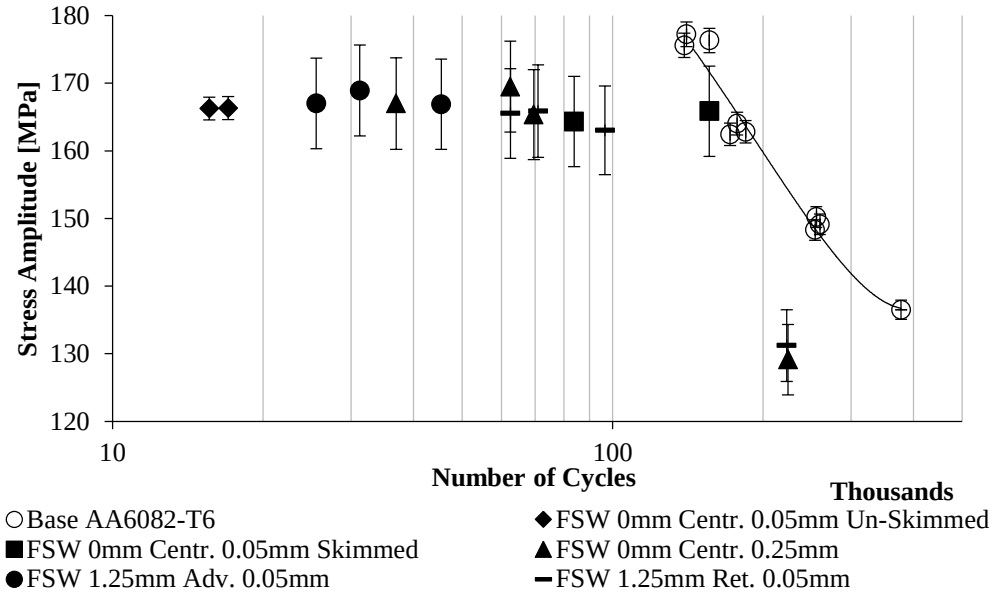

Figure 7.26 - Fatigue Life of Offset Tool Friction Stir Welded Samples with Lack of Penetration

Figure 7.27 and Figure 7.28 provide the average number of cycles for the numerous tool offsets run at stress amplitudes of approximately 130 and 165 MPa. The stress amplitude has been provided as an indication of the applied stress. No data for two sets of samples run at a stress amplitude of 130 MPa were achieved due to an insufficient number of samples. At the time, the 165 MPa samples were deemed to be the most important setting thus required extra samples. The lower stress amplitude showed very little variation in fatigue life between offsets. The two joints run at the lower stress amplitude (0mm Cntr. 0.25mm & 1.25mm Ret. 0.05mm) had less than a 0.7% difference between each joint in the achieved fatigue life. At the higher applied stress, a 36% difference between each joint in the achieved fatigue life was noted. From the figures, it is evident that the combination of the applied stress and the size of the internal defect will affect the fatigue life of the FSW joints.

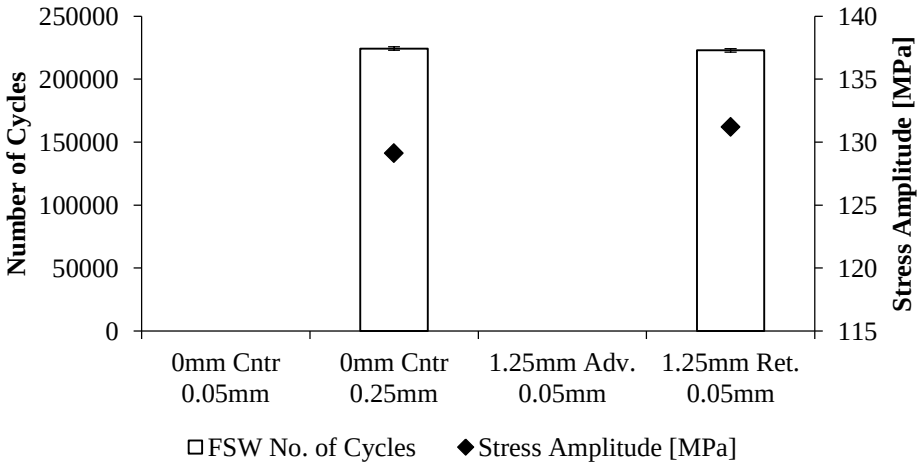

Figure 7.27 - Average Fatigue Life of Offset Tool Friction Stir Welded Samples run at a Stress Amplitude of approximately 130 MPa

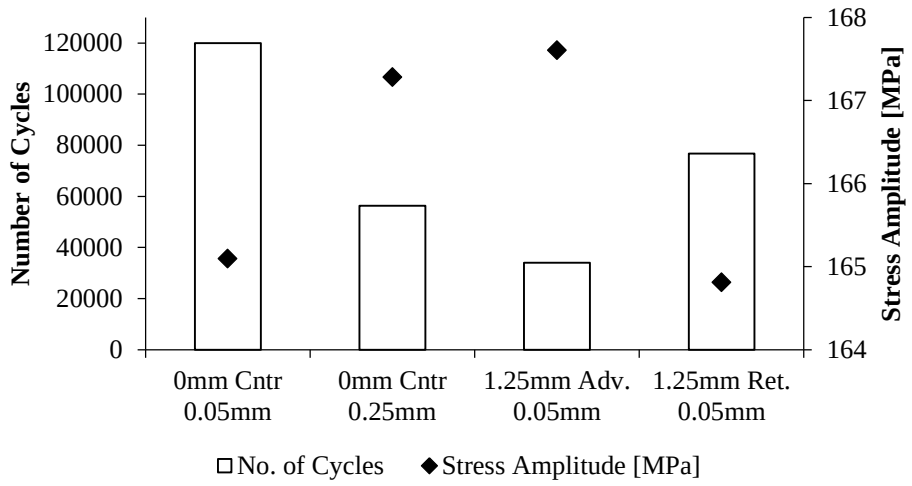

Figure 7.28 - Average Fatigue Life of Offset Tool Friction Stir Welded Samples run at a Stress Amplitude of approximately 165 MPa

Figure 7.29 and Figure 7.30 provides the failure positions of all the skimmed offset tool samples run at approximate stress amplitudes of 130 MPa and 165 MPa. It can be seen that all the samples failed along an approximate line of the pin central pin travel or within the nugget/TMAZ. Failure over the nugget/TMAZ may have been caused due to a discontinuity within the joint. The discontinuity may have been the presence of the LOP within the joints. Once failure initiated from the root surface the cracks proceeded to growth in a far more irregular fashion as shown in a number of fracture surfaces below. The crack tended to follow the geometry of the nugget. Due to the minimal fretting and granular surface in the centre regions of all the fracture surfaces it was evident that fracture occurred from the outer surfaces inwards, with this region failing quickly.

0mm Centre. 0.25mm

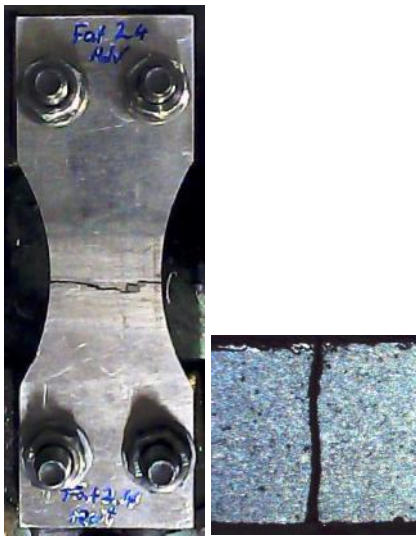

1.25mm Ret. 0.05mm

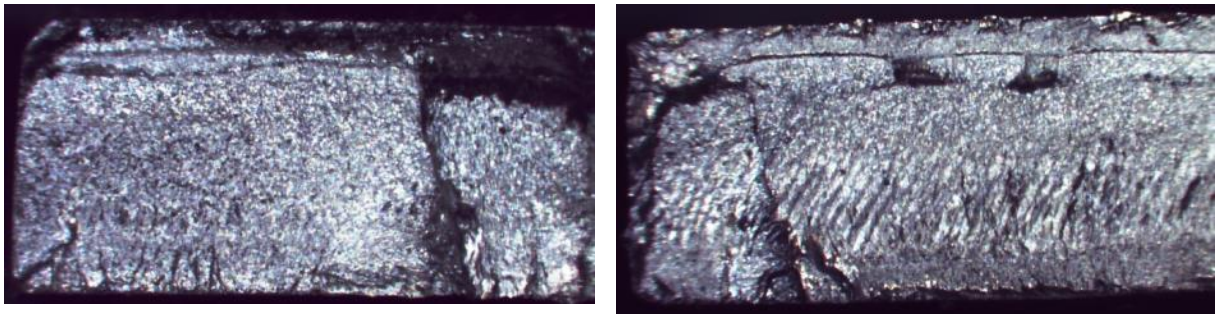

Figure 7.29-Failure Positions of Offset Tool Friction Stir Welded Samples – 130 MPa Stress Amplitude

0mm Centre. 0.05mm 0mm Centre. 0.25mm 1.25mm Adv. 0.05mm 1.25mm Ret. 0.05mm

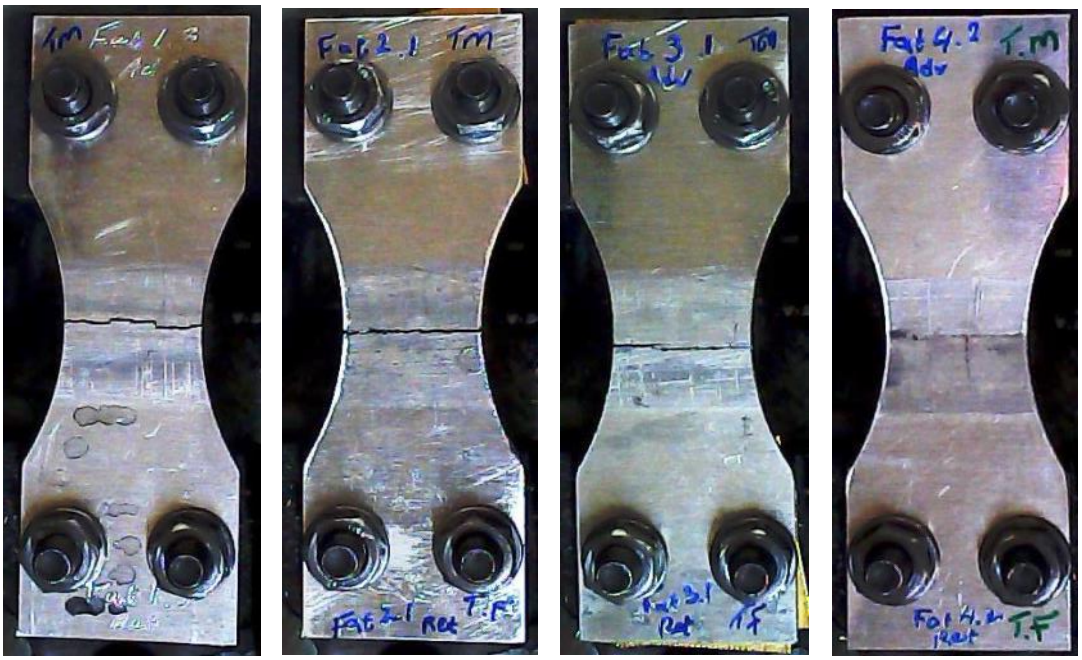

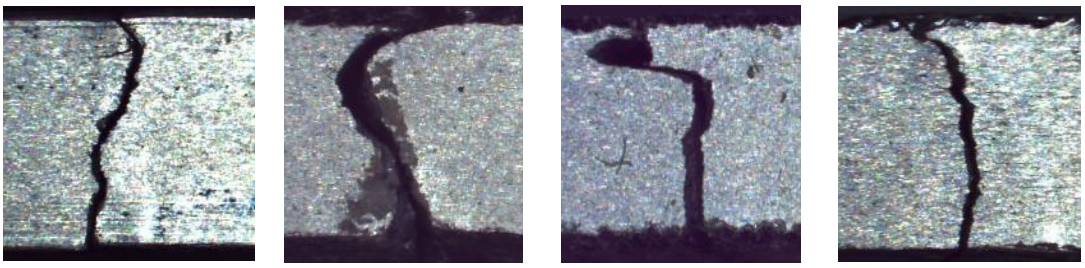

0mm Centre. 0.05mm *0mm Centre. 0.25mm*

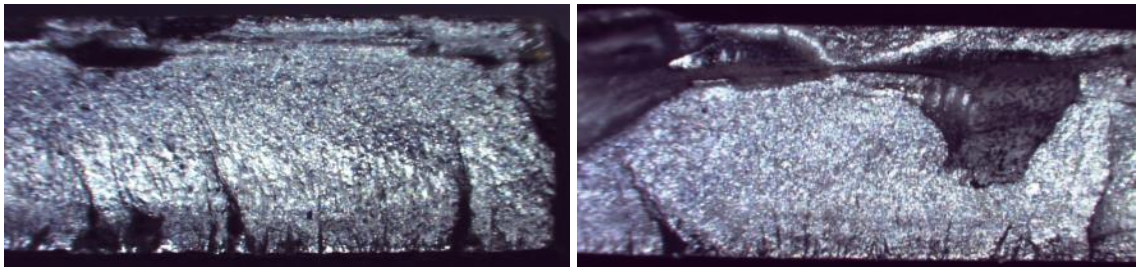

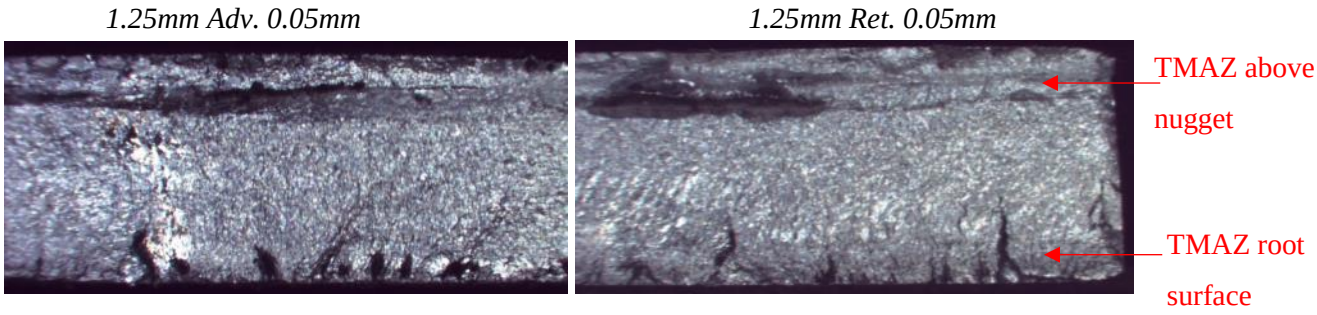

Figure 7.30 - Failure Positions of Offset Tool Friction Stir Welded Samples – 165 MPa Stress Amplitude

Figure 7.31 indicates the percentage of the average fatigue lives relative to the best optimised tool position of 0 mm Centre 0.05 mm. It was clear that the variations in the tool positions resulted in a fair decline in the fatigue life of the components. The 1.25mm Adv. 0.05mm coupons average fatigue life was only 28.4%, whilst the remaining two tool positions achieved 47% and 64% of the best weld.

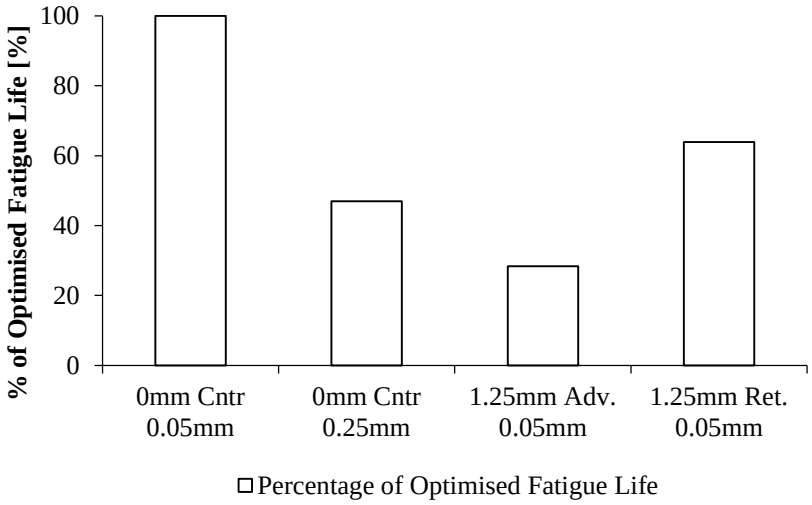

Figure 7.31 - Percentage of Best Optimised Fatigue Life

7.7.1 Comparison of Fatigue Results to Published Results

Figure 7.32 provides a comparison of FSW bending fatigue results obtained from this research to those in published data. From the figure, it was clear that the results are suitable and comparable to those achieved by other researchers. The optimised welded sample performed well in a comparison of the joints manufactured by Sano (1400 RPM 41mm/min) [76] in that at similar stress amplitudes there was a close correlation between the fatigue life of the joints. The flawed joints run at an approximate stress amplitude of 130 MPa, tended to outperform the fatigue life of FSW joints manufactured with spindle speeds in excess of 2000 RPM by Ericsson [52] but were less than those of Sano, this was expected as these joints were fundamentally flawed by the tool offsets. It was anticipated that the optimised FSW samples would perform in the region of those achieved by Sano as the fatigue test parameters (R=-1) and FSW sample parameters (3 mm thick 6-series Aluminium) matched very well to those completed in this study, further testing would be required to validate this.

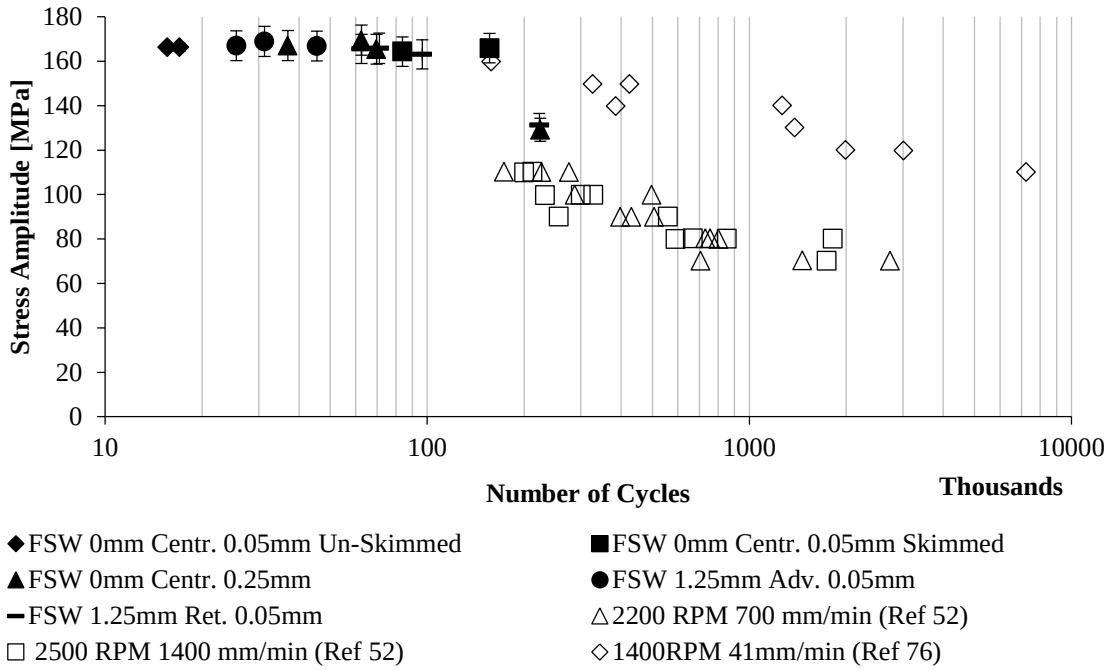

Figure 7.32 - Comparison of Friction Stir Welding Fatigue Results to Published Results

Assuming that variations in tool geometry had little to no effect on the performance of a FSW joint, the close correlation of these results and that the experimental 1600 RPM 200 mm/min was slightly outperformed by the published 1400 RPM 41mm/min parameters indicated that the results of the multi-objective optimisation completed in section 6.1.7 were well suited. The optimisation process predicted the best parameters as1433 RPM and 196 mm/min which matched the published tool rotation speed well. The published work was completed with a tool diameter of 10 mm which was half the size of the tool used for this study. Due to the smaller tool, a lower feed rate would need to be selected to achieve good welds.

7.7.2 Conclusion

From the results presented in this section the following can be concluded:

1. The variation in thickness and stress concentration formed by the flash greatly affected the fatigue life of the FSW coupons. To overcome this, the crown surfaces of the samples were machined to a near constant thickness.
2. The base optimised defect free welding parameters had the highest fatigue life, with this sample achieving a fatigue life which was comparable to those achieved by other researchers.
3. The tool offsets resulted in significant reductions in fatigue life compared to that of the defect free joint.
4. The tool offsets affected the fatigue life through the introduction of a LOP defect within the joints.
5. Failure of the coupons all occurred within the nugget/TMAZ regions of the weld.

8 Influence of Laser Shock Peening on Friction Stir Welded Joints

The aim of this chapter was to investigate the effects of the application of Laser Shock Peening on Friction Stir Welding. The dynamics of each process has shown that the combination of these innovative manufacturing techniques can be extremely prosperous if combined correctly. Secondly and most importantly was the investigation of whether LSP was a suitable technique to reduce or overcome the detrimental effects of LOP in an FSW joint.

8.1 Residual Stress Analysis of Friction Stir Welded Joints and Introduction of Compressive Residual Stress through Laser Shock Peening

Through the thermal and material movements associated with Friction Stir Welding, significant, detrimental tensile residual stresses are introduced into the welded joint. The presence of the tensile stress would only aid the growth of a weld defect, such as LOP. It has become common knowledge that Laser Shock Peening possesses the ability to introduce compressive residual stresses within the near surface region of the target surface. In order to counteract the progressive growth of the defect, LSP can be applied to attempt to surround the defect with compressive residual stress, as illustrated in Figure 6.70. All measurements were taken on the Materials Characterisation by X-rays diffraction (MCX) beamline at Elettra Synchrotron. The residual stress at each measurement position was determined according to the outline of section 5.4.8.

The residual stress, in the near surface region (maximum depth of approximately 120μm from the surface), the analysed samples were manufactured according to the following combinations:

1. Optimum FSW (1600 RPM – 200 mm/min – 0.05 mm plunge) with optimum LSP (3.5GW/cm^2 – 1000 spots/cm^2) with the scanning direction of the laser in the direction of the feeding direction of the weld
2. Optimum FSW only (1600 RPM – 200 mm/min– 0.05 mm plunge)
3. FSW+LOP only (1600 RPM – 200 mm/min– 0.25 mm plunge)
4. FSW+LOP (1600 RPM – 200 mm/min– 0.25 mm plunge)
5. FSW+LOP (1600 RPM – 200 mm/min– 0.25 mm plunge) with optimum LSP (3.5GW/cm^2 – 1000 spots/cm^2) with the scanning direction of the laser in the direction of the feeding direction of the weld

Figure 8.1 illustrates an example of the general layout of the samples which were tested. The residual stress was measured at multiple points across the joints to form a stress profile in the different regions

of the welds. The majority of measurement locations were placed on the advancing side of the weld due to asymmetric nature of the weld.

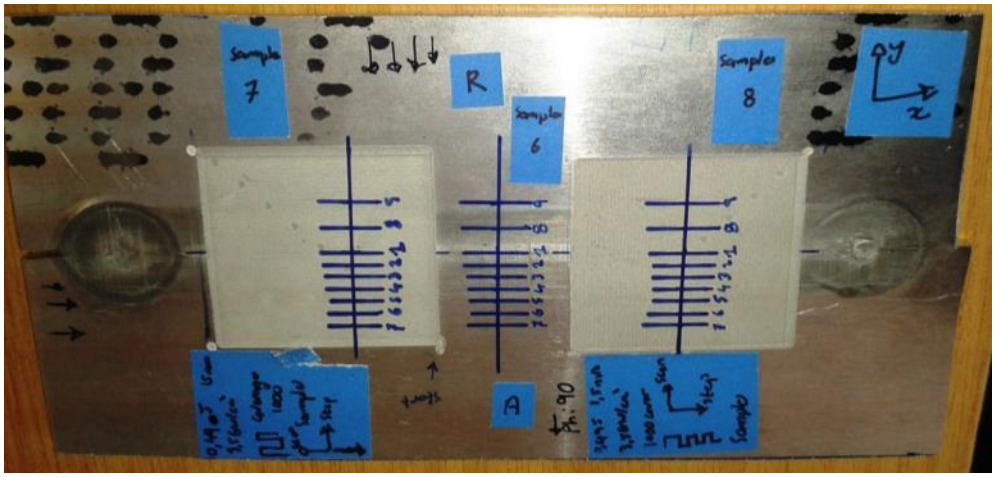

Figure 8.1 - Residual Stress Samples and Measurement Positions across the Friction Stir Welded Joint

A number of these samples were measured at three beamline energies which corresponded to three individual depths through the thickness of the samples, these being 10 KeV (53 µm), 15 KeV (80 µm) and 18 KeV (120 µm). The X-ray measurement directions were the Φ 0° and 90°. Figure 8.2 illustrates the schematic drawing of the measurement directions of the X-rays relative to the FSW and LSP directions.

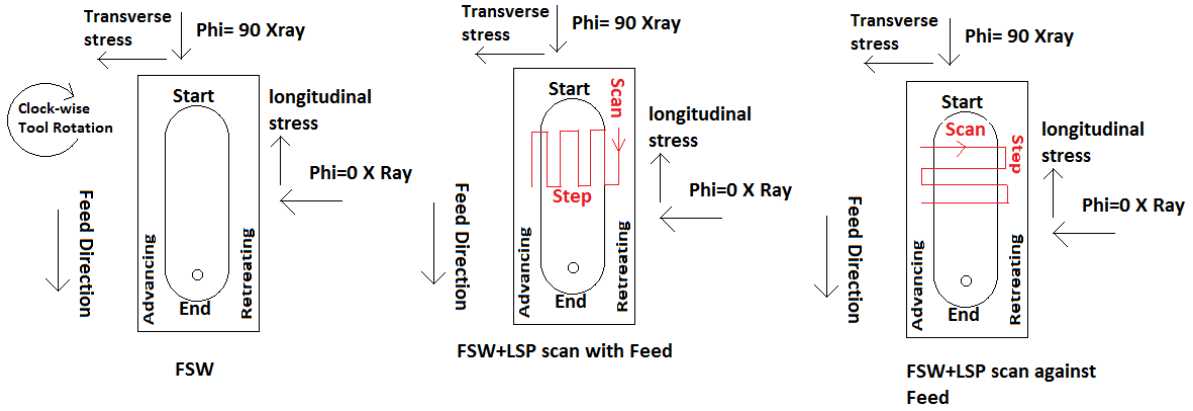

Figure 8.2 - Schematic of X-ray Measurement Directions Relative to the Friction Stir Welding and Laser Shock Peening Directions

Measurement of the residual stress in both directions of the optimum FSW case has been shown in Figure 8.3. It can be seen that stress in the longitudinal directions was the highest compared to the compressive stress of the transverse direction. The pin and shoulder boundaries have been indicated on the figure. The high tensile stresses in the longitudinal direction are significantly large enough to detrimentally affect the joint under any form of applied load. Only one full set of measurement were taken on joint 2. It is clear that the welding process creates a substantially different stress field in the two directions. It is clear from the profiles at the different depths that the welding process leaves the

joint in a state of fairly high tensile residual stress within the near root surface. The highest stress was observed in the central region of the weld and tended to decline towards the shoulder edges of the joint. The point at 15 mm was a reading of the base material in the region of the weld.

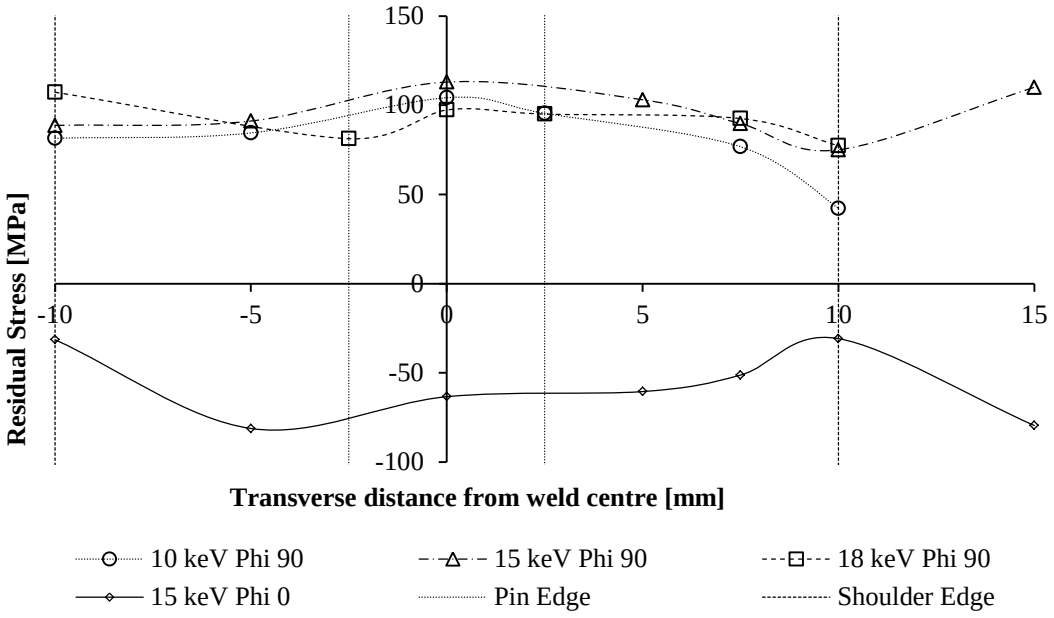

Figure 8.3 - Residual Stress Profile in Φ 0 and 90 directions on Optimum Friction Stir Welded Joint

In order for the LSP to be fully effective in being able to alter the tensile stress shown above, the stepping and scanning directions of the LSP process needed to be oriented correctly, as discussed in section 2.4. Figure 8.4 shows the ability of the LSP process to engineer high compressive stresses in particular directions. Two ranges of compressive residual stresses were introduced in the component with varying the orientation of the peening process, this was seen as in the case where the highest stress was introduced in the Φ 0° direction with LSP stepping in line with the feed direction and alternatively the Φ 90° with the stepping direction across the weld. Using Figure 8.2 and Figure 8.4 it can be seen that the highest stress was in the scanning direction of the LSP process. Thus to introduce the highest stress into the joint in the correct direction all LSP had to have the scanning direction oriented in the direction of the feeding direction.

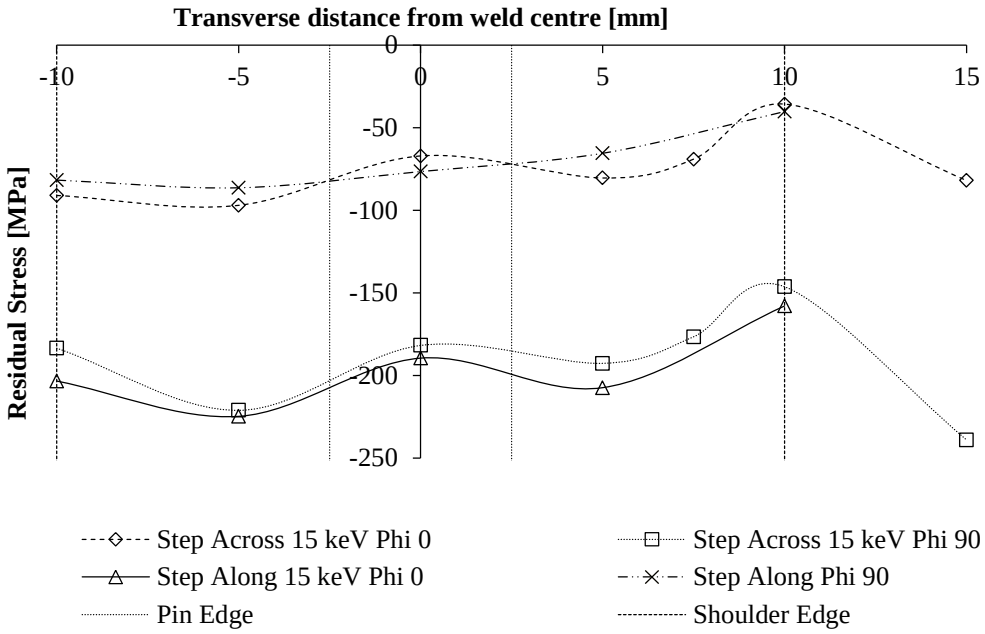

Figure 8.4 - Rotation of the effect of Laser Shock Peening

Figure 8.5 provides the near root surface residual stress profile of a number of welds manufactured with the tool being retracted incrementally per weld. The gap between the optimised weld and backing plate was 0.05 mm whilst the retracted tool positions were at a spacing of 0.15 and 0.25 mm. It can be seen and assumed due to the profiles that the change in tool position tended to cause a reduction in near-surface residual stress when comparing the profiles of the various joints measured with a beam energy of 10 keV. There was not a substantial variation (residual stress varied by ±40 MPa) and not enough samples tested to conclusively conclude that the presence of the defect was the reason for the incremental decrease of tensile residual stress at the centre of the joint within the increasing size of the defect. For the purpose of this study, it was assumed that greater the defect size lower the residual stress would be in the defect surrounding the area. A possible reason for this may be that the defect as a stress relief similar to the idea of the measuring of residual stress through the slitting method. These measurements were taken near the surface of the joint thus in the region where the defect was largest which would also add to the theory that the defect was acting as a stress relief. Unfortunately, due to the limitations of the Synchrotron, residual stress measurements could not be taken in regions near the tip of the defect.

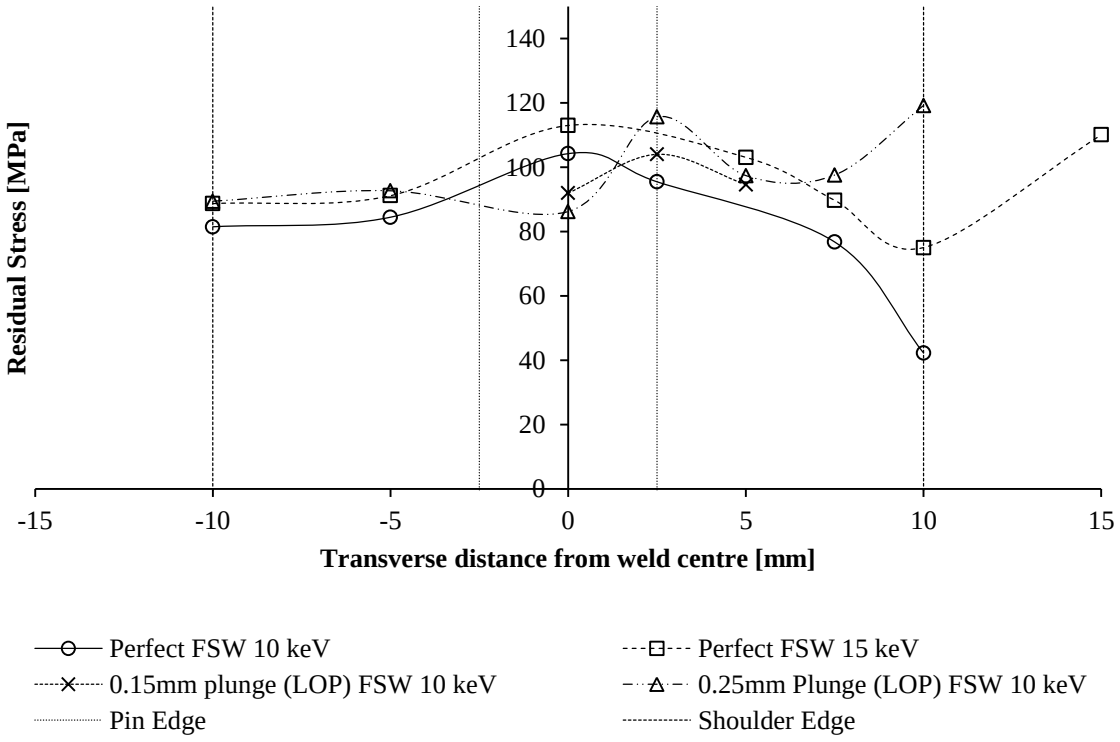

Figure 8.5 - Residual Stress Profile across Weld for increasing Plunge Positions

Figure 8.6 illustrates the residual stress profiles of the optimum FSW joint with and without the application of the optimum LSP processing. It was evident that the FSW process left the joint in a substantial state of high tensile residual stress. The application of the LSP to the FSW joint was able to fully reverse and surpass the tensile residual stress at all three investigated depths. A maximum of -239 MPa was recorded with an average residual stress across the joint at the three depths being -153 MPa, -184 MPa and -188 MPa. This showed that on average the magnitude of the compressive residual stress was increasing with depth, a fact that has been shown in the literature, see section 2.3.5.4 and Figure 2.61.

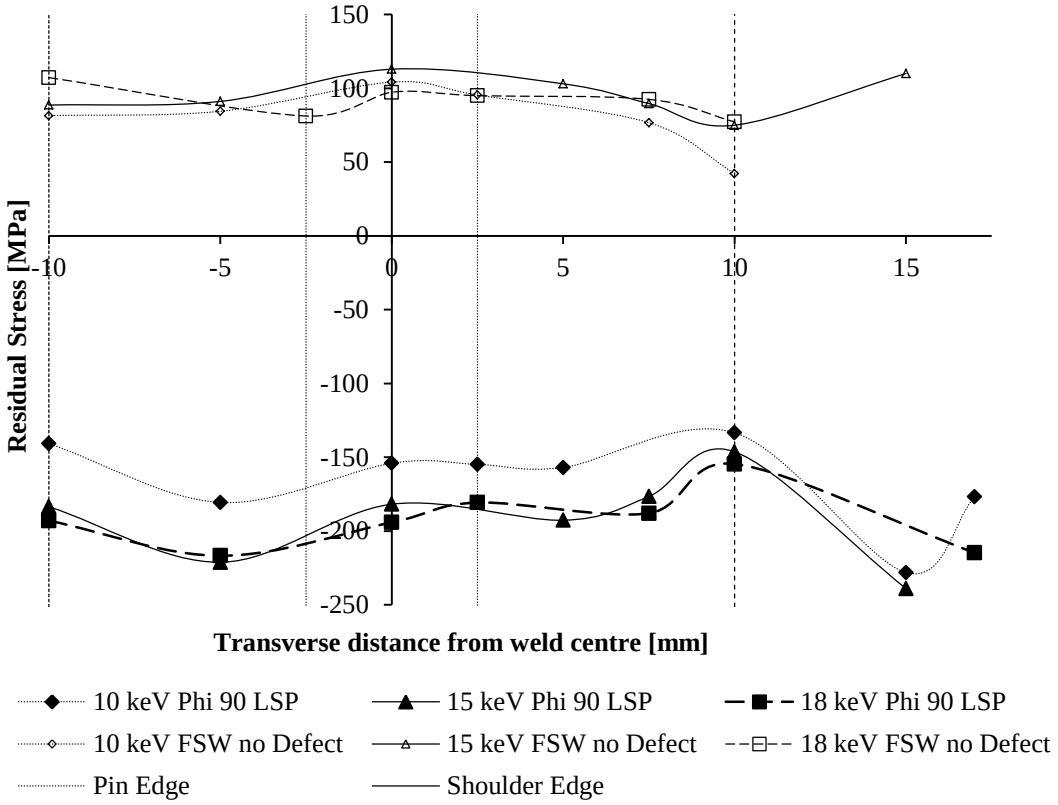

Figure 8.6 – Residual Stress Profiles of the Optimum Friction Stir Welded Joint with and without treatment of Laser Shock Peening

A similar trend of the ability of LSP to fully reverse the magnitude of the near-surface residual stress was shown again in Figure 8.7. The tensile profile of the 0.25 mm tool position joint was shown to be substantially tensile, in the same region as the optimum FSW joint. Post-weld application of LSP again showed that the process was able to significantly introduce significant compressive residual stress into the joint. The average stress across the joint for the purely FSW+LOP joint was in the region of 100 MPa whilst the average for the FSW+LOP+LSP joint was in the region of -146 MPa. It can conclusively state that LSP was an extremely effective method of introducing compressive residual stress into the near surface of the joint whilst shifting the tensile stress from welding to a less critical area.

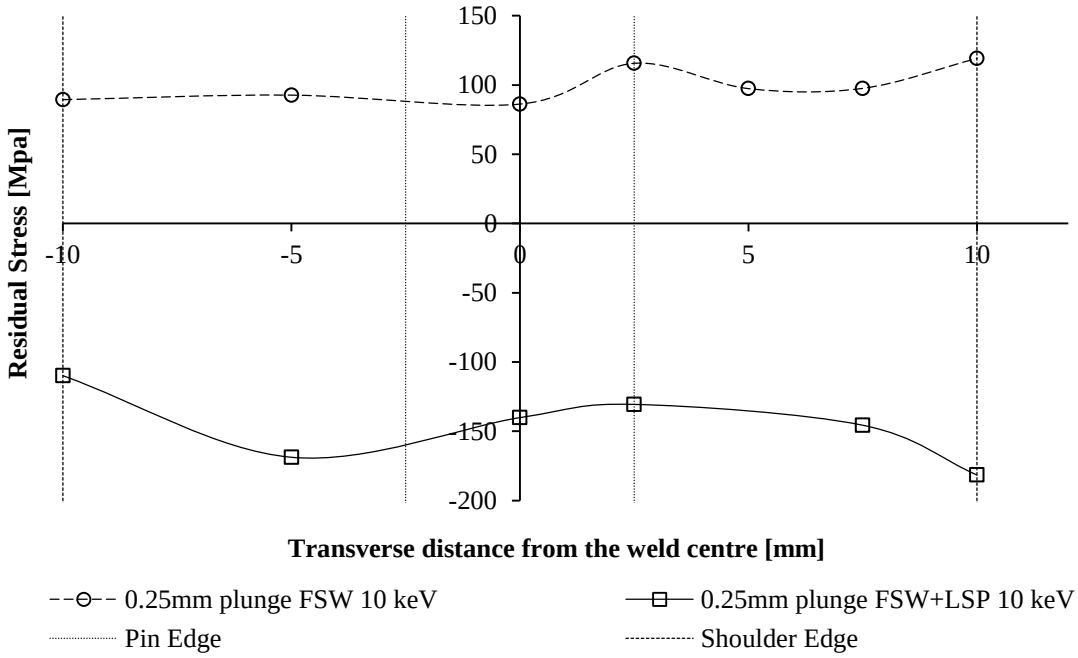

Figure 8.7 - Residual Stress Profiles of the LOP Friction Stir Welded Joint with and without treatment with Laser Shock Peening

Figure 8.8 illustrates the residual stress at the centre measurement location at three depths through the joints of a number of joints. Due to the limitations of the equipment 120 µm from the root surface was the deepest measurement that could be taken through the joints. It was evident that the compressive residual stress was tending to become increasingly more compressive through the thickness which tends to correspond with predictions of the theory. From literature, it was predicted that at a particular depth the residual stress would tend to towards becoming tensile through the remaining thickness of the joint. From these three points, it was evident that these results tend to follow those of literature.

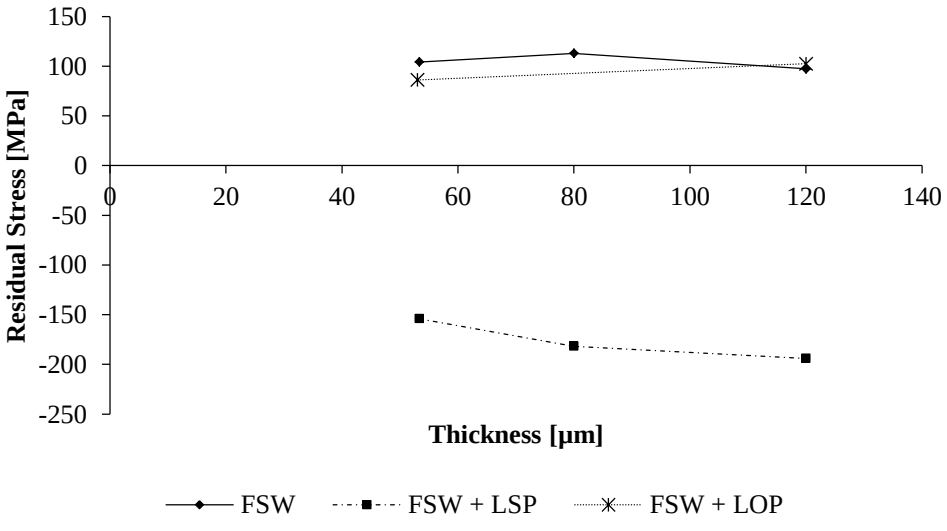

Figure 8.8 – Residual Stress Measured at the Centre Position of the various Joints at Depths through the Thickness

8.1.1 Comparison of Residual Stress Results to Published Data

The following section provides the comparison of the achieve residual stress results achieved in this study to those of published work of Sano [76] and Hatamleh [77].

Figure 8.9 provides the comparison of the near surface residual stress profiles across the various FSW joints measured on the root surfaces. It was clear that the data of Hatamleh matched the best with the results achieved in this research. The data clearly shows and was confirmed by Hatamleh (and multiple other researchers) that the highest tensile residual stresses collected within the nugget/TMAZ region of the joints. The slight asymmetric nature of the residual profile was also confirmed by this published work. It must be noted that the welding tool used by Hatamleh was significantly smaller and the sharp decrease in residual stress was due to the measurement being taken in the unaffected base material.

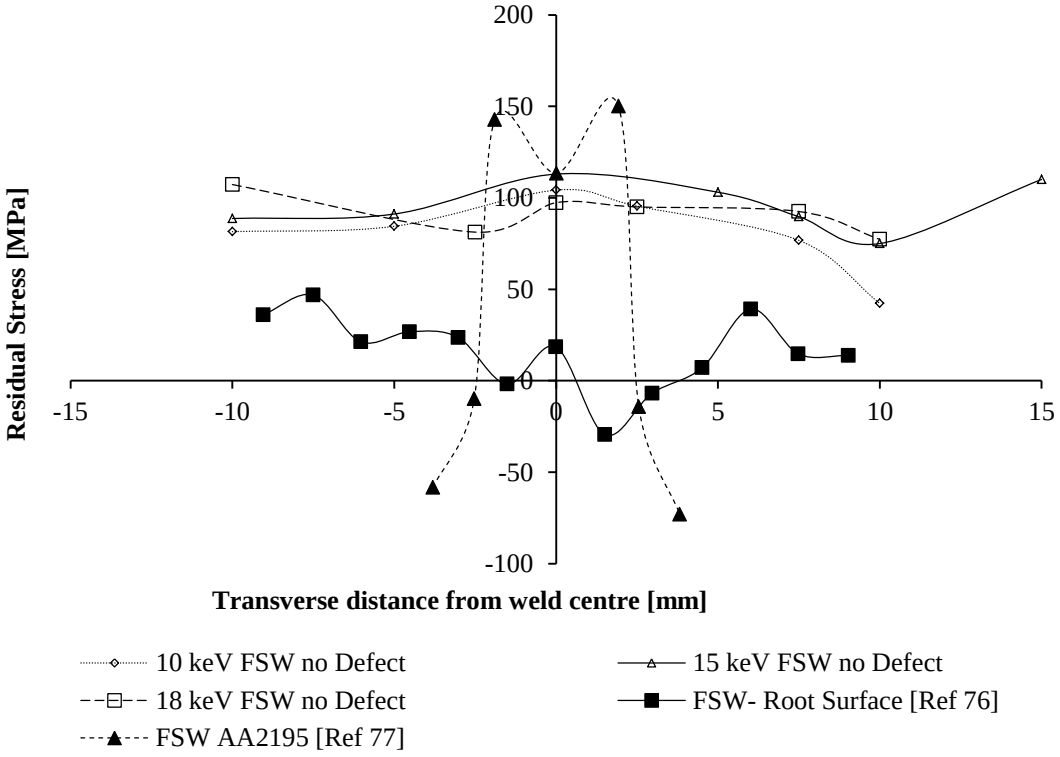

Figure 8.9 - Comparison of across Friction Stir Weld Residual Stress Profile (No Laser Shock Peening)

Figure 8.10 provides the comparison of the near surface residual stress profiles across the various FSW+LSP joints measured on the root surfaces. Like the previous sets of a data, there was a good correlation between the experimental data achieved and the data of Hatamleh in the magnitude of the compressive residual stress introduced into the near surface of the FSW joints due to LSP. The data of Sano confirmed the trend of LSP typically inverting the RS profile of the FSW.

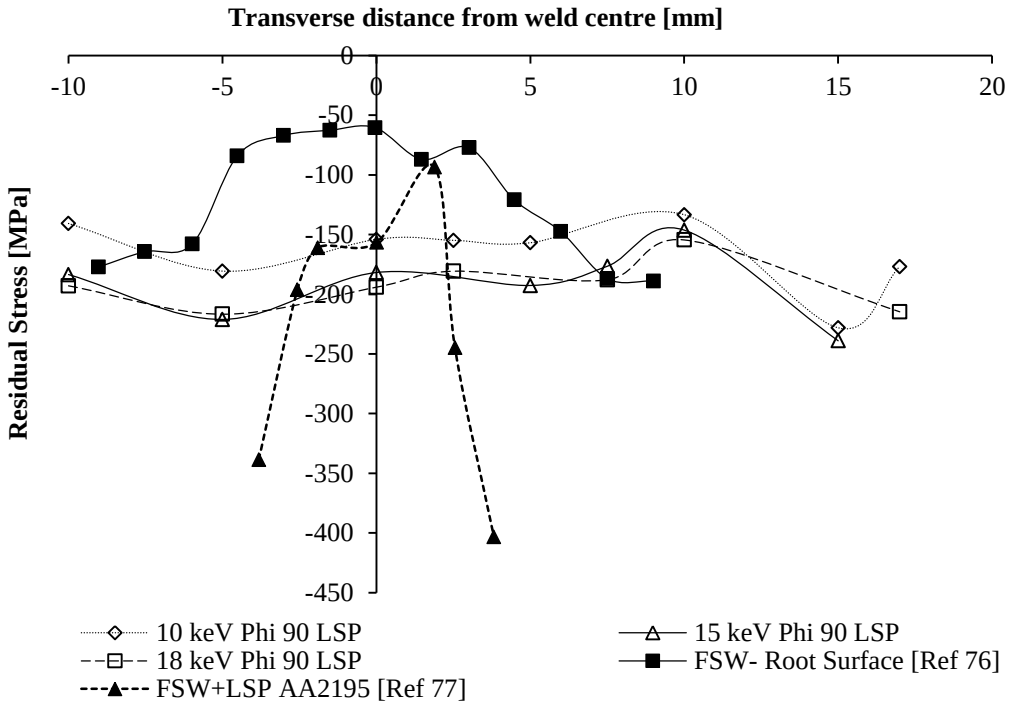

Figure 8.10 - Comparison of across Friction Stir Weld with Laser Shock Peening Residual Stress Profile

8.1.2 Conclusion

From the results presented in this section the following can be concluded:

1. The residual stress profile of the FSW joint varies in the transverse and longitudinal directions. The transverse residual stress profile was compressive whilst the longitudinal residual stress profile was substantially tensile.
2. The tensile residual stress tended to reduce with increasing distance from the weld centre line. An asymmetric RS profile was shown, with the majority of the tensile stress collecting within the nugget/TMAZ of the weld.
3. The presence of a LOP defect has minimal to no effect on the residual stress profile both unpeened and peened samples.
4. Laser Shock Peening was a suitable technique to introduce compressive residual stresses in the near surface area of the weld. It was successful in completely altering the tensile residual stress to a state of complete compressive stress in the near surface.
5. The application of LSP to a FSW joint tended to completely invert the stress distributing in that a region of maximum tensile stress tended to become the region with the largest compressive residual stress.
6. The residuals stress magnitudes and trends correlated with to those of published work.

8.2 Dynamic Influence of Laser Shock Peening on defective and non-defective Friction Stir Welded Joints

Laser Shock Peening is typically known for the processes ability to introduce compressive residual stresses within the near surface of a component in order to improve the dynamic load carrying capacity or fatigue life of the component. The process has been shown to influence number mechanical properties of a component, most notably the hardness of the joint and the residual stress. Mechanical properties such as ultimate tensile stress and ductility are not significantly affected by the processing [103], for this reason, the remainder of this study focused on the dynamic effects of the process on the FSW components.

In order for this research to conform to the intentional industrial application of applying LSP the root surface of a FSW for aviation manufacturing applications, only the root surface was peened. All FSW+LSP fatigue coupons were skimmed to remove the variation in thickness like the fatigue samples shown in section 7.7. As with the Base+LSP fatigue coupons tested in section 6.2.6, the entire reduced area section of the sample was peened to prevent any undue failure due to relocated tensile stress in critical areas in the component.

Figure 8.11.a shows the fatigue life results of the FSW (welding parameters previously presented in section 7.7) coupons which had been LSP with the optimised set of parameters, power intensity of 3.5 GW/cm^2 and coverage of 1000 spots/cm^2, obtained in section 6.2. The FSW results have been included for comparative reasons. It could be seen that the FSW+LSP fatigue samples tested at a stress amplitude in the region of 160 to 170 MPa (low cycle regime), tended to exhibit the same or slightly higher fatigue lives compared to the FSW counterparts. At the lower stress amplitude (high cycle region) the FSW+LSP samples which exhibited no defects in the joint structure showed an improvement of as much as 68% in fatigue life over the FSW samples. This confirmed that LSP can be used on FSW joint to improve the fatigue life of the joints. The 0 mm Centre 0.25 mm joint which had a defect length of approximately 175µm, exhibited approximately 20% increase in fatigue life due to peening. The Figure 8.11.b. has been repeated, with the number of cycles not plotted in the typical log graph fashion. This was done in order to reveal a clearer view of the distribution of the results of the coupons in the high cycle region. Although the stress amplitude varied by ±5 MPa from the desired value of 165 MPa, there were slight local improvements of the peened flawed welds in that two of the three offsets. The consistency and repeatability of the FSW joints was improved through peening as the low cycle fatigue samples tended to have less variation in number of cycles to failure compared to FSW samples. The Error bars have intentionally been left off to prevent a reduction in clarity of the figures.

(a)

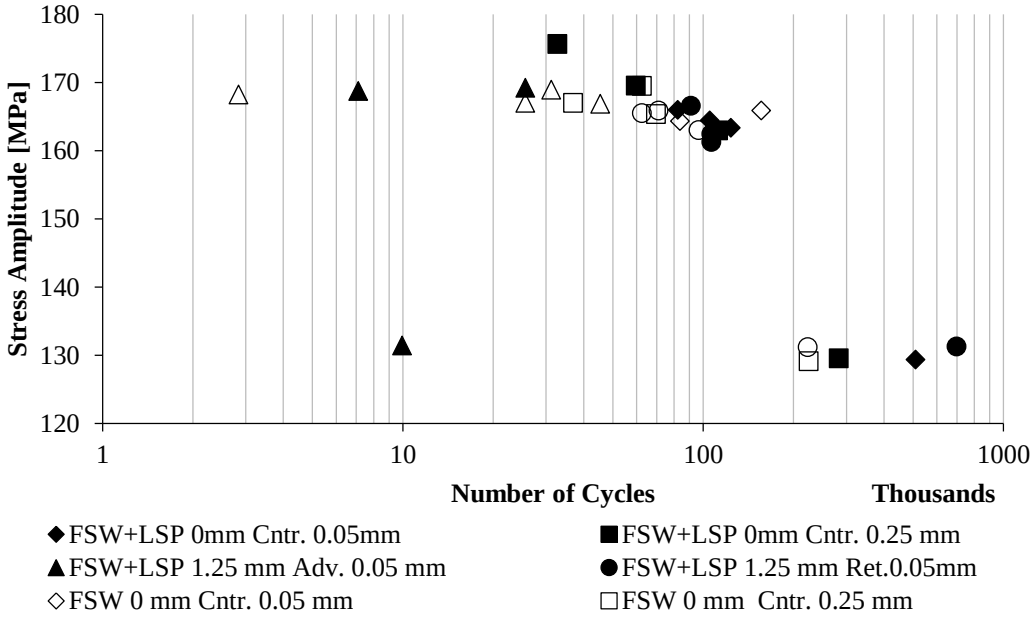

(b)

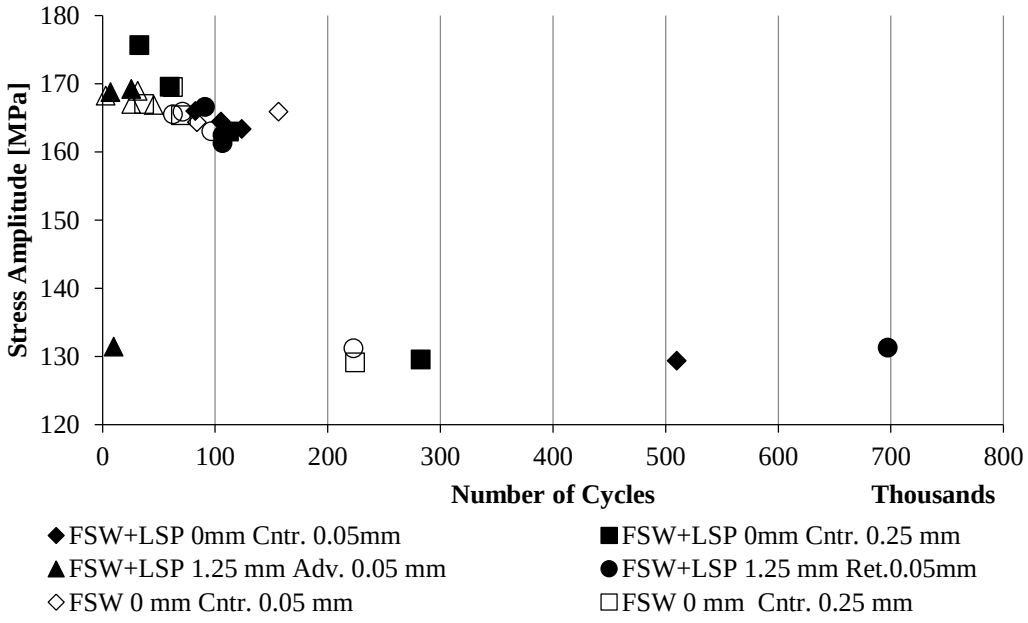

Figure 8.11 - Comparison of Fatigue Life of all Friction Stir Welded Samples which had been treated with Laser Shock Peening

The average fatigue life of the tool positions across the tested coupons have been shown in Figure 8.12 and Figure 8.13. It can be seen that of the available data of the lower stress amplitude, the FSW+LSP samples performed better than the FSW only samples. At the higher stress amplitude, the average improvement was not as noticeable as a number of FSW only samples performed at the same or slightly better than the FSW+LSP samples. This phenomena of LSP+FSW samples performed better at lower applied stress was noted by Sano [76]. It was concluded during the application of the

higher applied stress the compressive residual stress introduced through peening relaxes thus minimising the beneficial effects of LSP on FSW. At the high cycle fatigue, the compressive residual stress introduced through peening was maintained and thus improve the fatigue life of the FSW components. Figure 8.6 showed that the compressive residual stress introduced in the near surface ranged from approximately -130 MPa to -225 MPa across the three measurement depths. During the low cycle fatigue testing the applied stress would have been approximately equal or close to the introduced stress. This showed that LSP tended to become ineffective at the higher applied stresses.

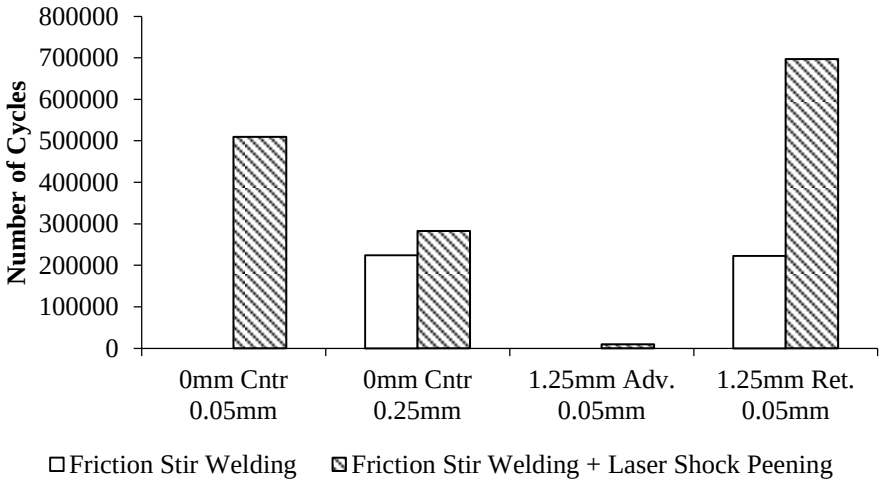

Figure 8.12 - Average Number of Cycles for Friction Stir Welded Samples Treated with Laser Shock Peening run at a Stress Amplitude of approximately 130 MPa

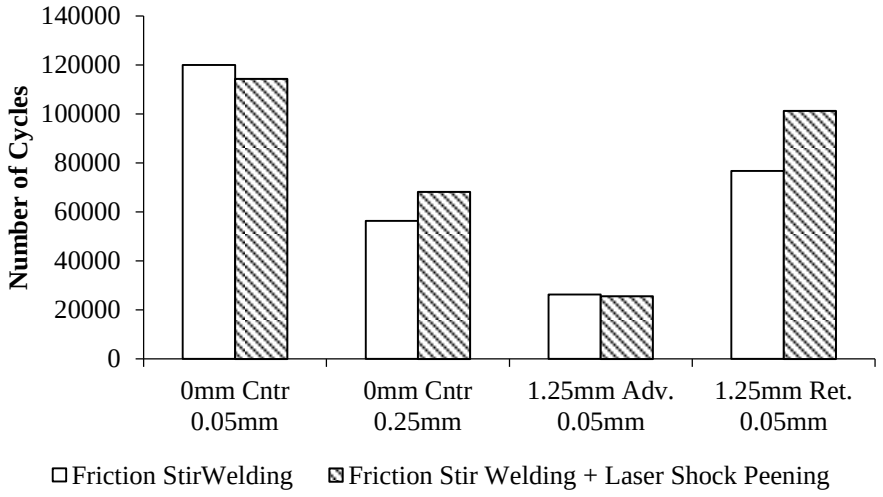

Figure 8.13 - Average Number of Cycles for Friction Stir Welded Samples Treated with Laser Shock Peening run at a Stress Amplitude of approximately 165 MPa

Figure 8.14 illustrates the summary of the low and high cycle fatigue results achieved from all fatigue testing in this research. The Base+LSP did not have the same peening strategy applied to the FSW+LSP thus the 9.5 times improvement of the fatigue life of the base material could not fully be

compared to the other LSP cases but it was anticipated that due to the FSW samples showing an improvement due to the single sided peening that the base material would as well. The defect-free FSW performed 12% lower than the base material in the low cycle regime, was an indication of the quality of the FSW joints which were manufactured. The low cycle fatigue efficiency of the FSW joint was 87.8%, which was better than static joint efficiency. Figure 8.14 showed the effects of the application of LSP to these fatigue coupons. LSP was capable of improving the fatigue life of the defective joint indicating that the introduction of compressive residual stresses in the near surface of the root of the joint was sufficient in slowing the propagation of the defect. During peening the tensile residual stresses are merely shifted to other regions of the joint structures, this was due to maintain stress balance within the joint. It was expected, not confirmed as a through thickness residual stress measurement would be required to confirm, that once the defect did propagate to this region of tensile stress within the most likely the central region of the joint that fast failure would occur.

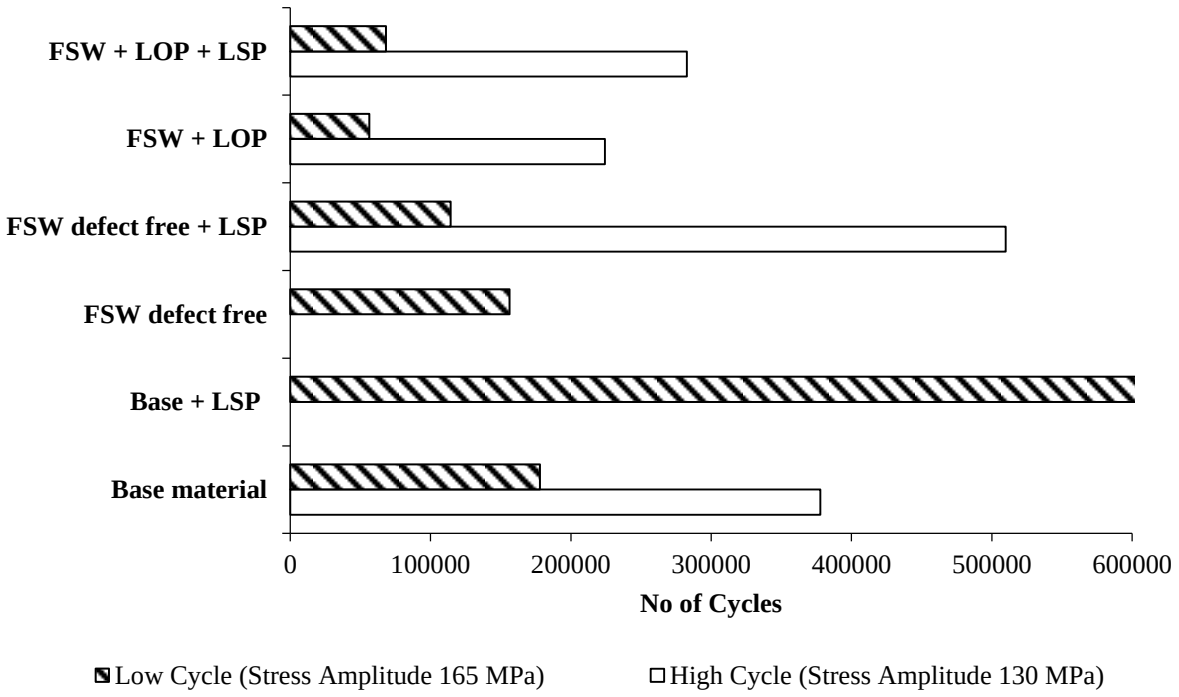

Figure 8.14 – Summary of Fatigue Results across all Combination of Fatigue Samples

Figure 8.15 and Figure 8.16 provide the fracture position, fracture surface and side view of the failure/crack propagation of the FSW and FSW+LSP samples in the low and high cycle fatigue regimes. The tool offsets which were tested both as FSW and FSW+LSP in the high cycle in Figure 8.15, all indicated a relocation of the failure position after the application of LSP. Across all tool positions, the joints failed over the nugget/TMAZ regions. The lower surfaces of the FSW joints all showed significantly more damage/fretting or striations forming in this lower region. These regions indicated that failure of the joint occurred mainly from the lower region. The application of the fully reverse bending stress would also cause failure to begin at the outer edges of the coupon and

propagate towards the centre of the joint, were this central region would fail due to overloading. The application of LSP, indicated a shift in the fracture position of two of the weld cases. These joints failed in the HAZ rather than through the nugget/TMAZ. Sample 0mm Centre 0.25 mm which had a defect size of approximately 175µm was one of the joints which indicated an extension in life due to peening. The fact that this was a defective joint which exhibited an extension of life and did not fail due to the defect showed that LSP did introduce sufficient residual stress to influence the LOP defect at the root surface.

Friction Stir Welding	*Friction Stir Welding + LaserShock Peening*	*Fractography*
0 mm Centre 0.05 mm		
No Sample		*FSW+LSP* 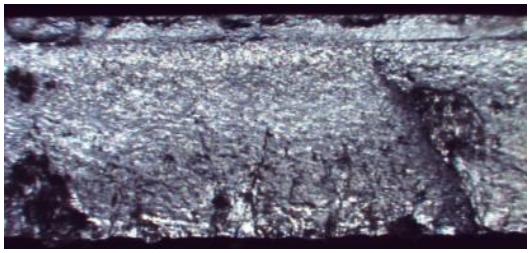 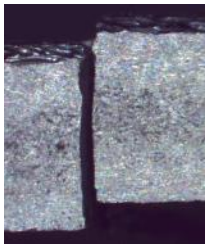
0 mm Centre 0.25 mm		
 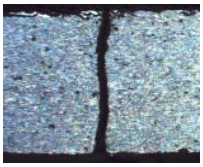	 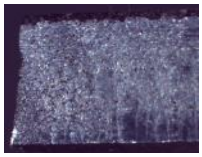	*FSW* 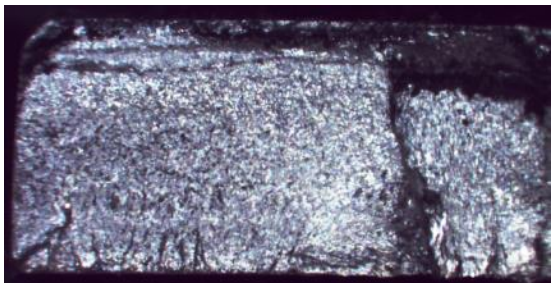 *FSW+LSP* 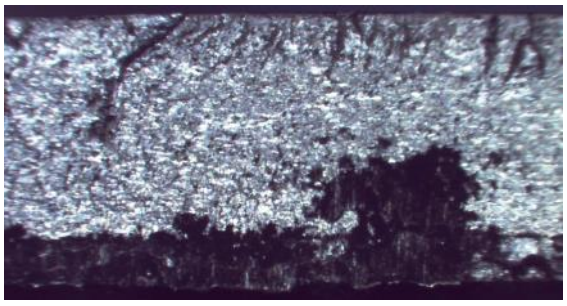

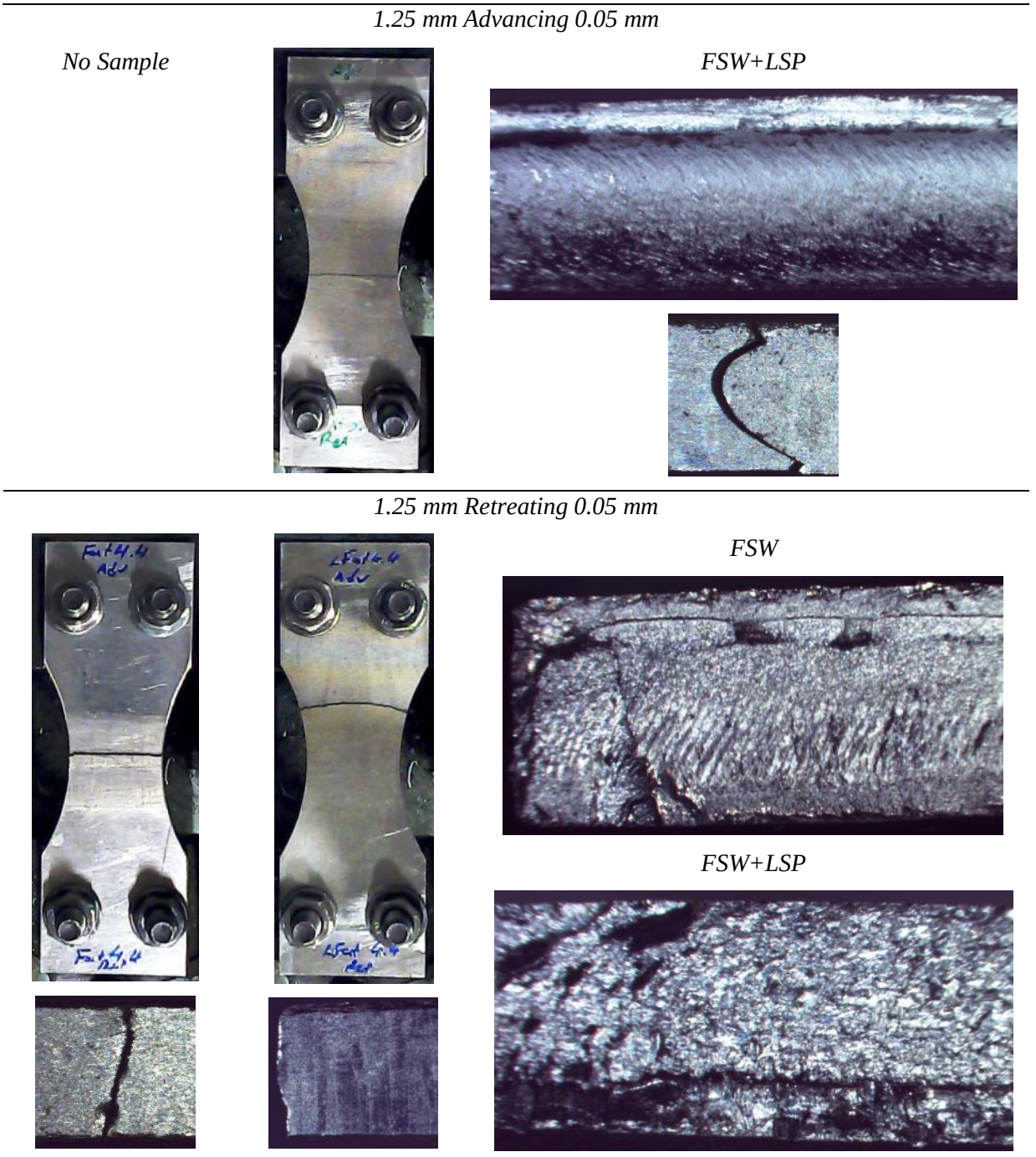

Figure 8.15 - Fracture Position and Surface Comparison for Samples run at a Stress Amplitude of approximately 130 MPa

Figure 8.16 provides the fracture position, surface and propagation of the low cycle fatigue samples. As discussed earlier, due to the application of higher applied stresses the compressive residual stresses introduced through LSP were relaxed and less effective in resisting failure of the coupons. The joints which failed over the nugget/TMAZ all exhibited failure which began at the edges of the coupons and propagated towards the centre of the weld. The propagation path through the samples indicated that failure through the TMAZ followed the direction of a discontinuity such as LOP. Upon the fracture reaching the nugget zone, the fracture path followed the bands which form the onion ring structure of the nugget, this was most evident in the 1.25mm Advancing 0.05mm tool position.

Friction Stir Weld *Friction Stir Welding + Laser Shock Peening* *Fractography*

0 mm Centre 0.05 mm

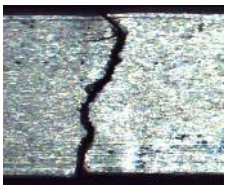

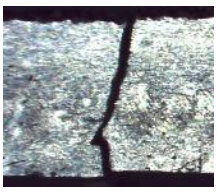

FSW

FSW+LSP

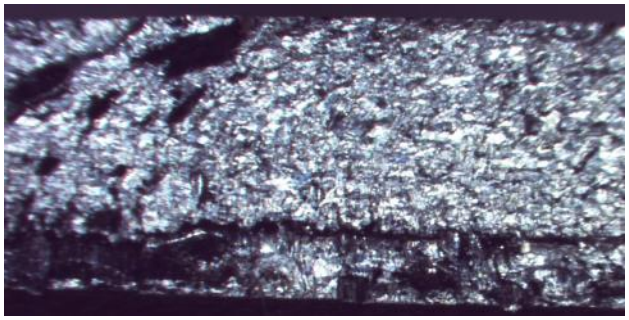

0 mm Centre 0.25 mm

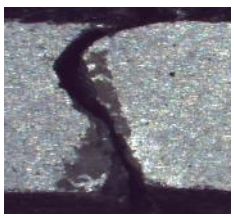

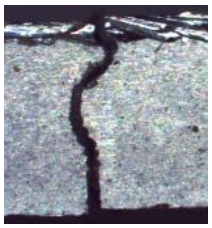

FSW

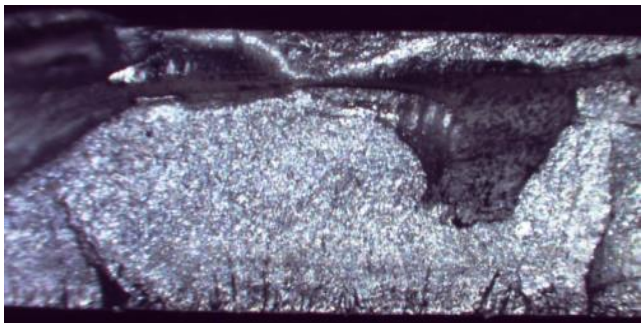

FSW+LSP

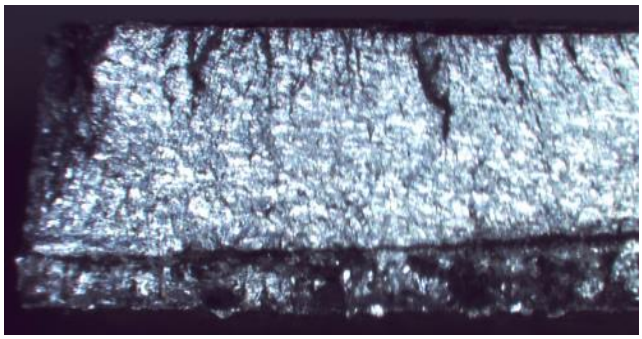

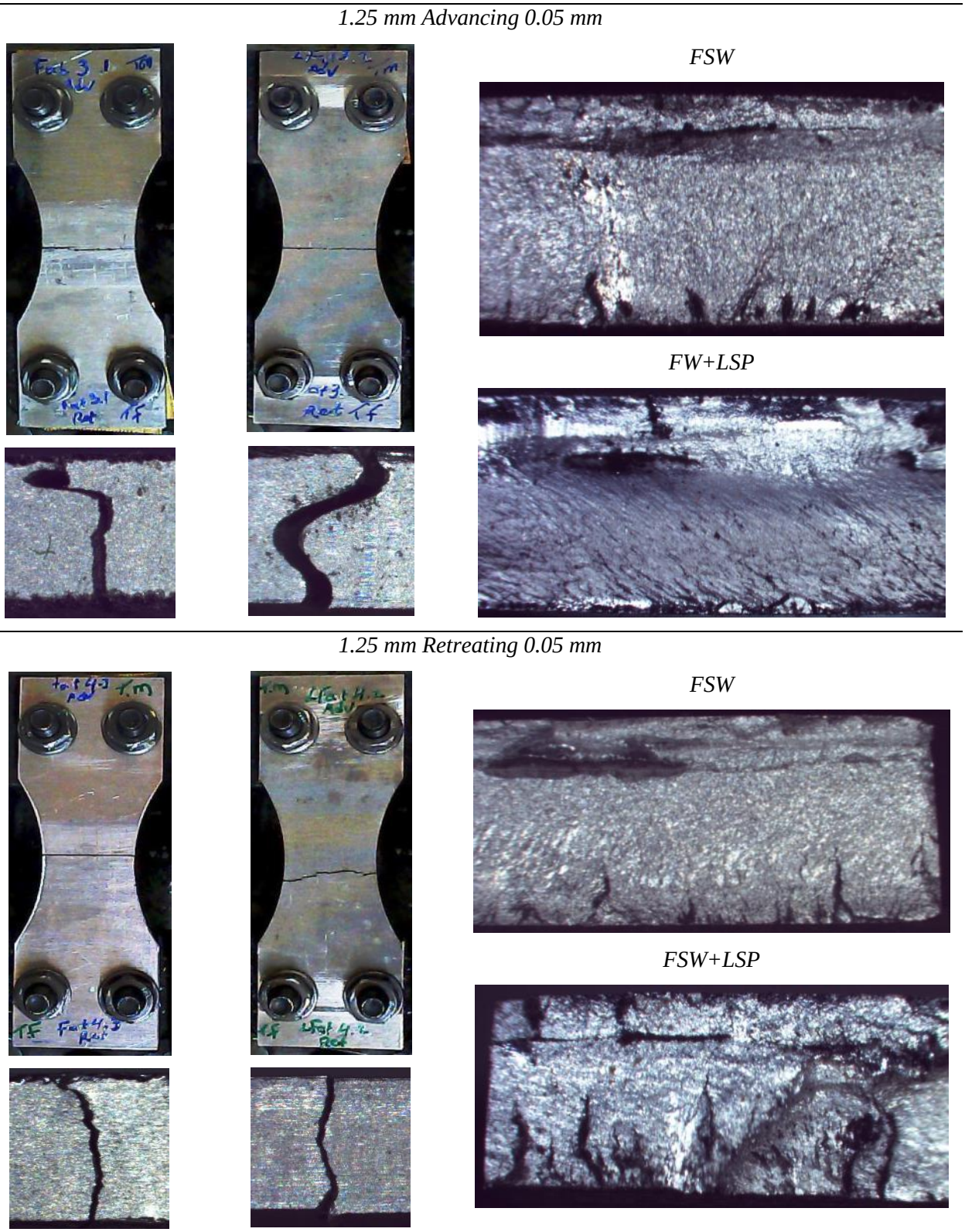

Figure 8.16 - Fracture Position and Surface Comparison for Samples run at a Stress Amplitude of approximately 165 MPa

The lighter granular structure of the central region of the fracture surface of all the samples shown in Figure 8.15 and Figure 8.16 indicated a region of final fast failure due to overloading of the sample. The fracture surfaces all indicated failure from the edges inwards. Figure 8.17 shows a partially

fracture fatigue sample that had been stopped once surface cracks appeared on the component. The joint was still held together by the central region. This confirmed the failure of the FSW and FSW+LSP fatigue samples present in Figure 8.15 and Figure 8.16.

Figure 8.17 - Confirmation of Fracture of Friction Stir Welded Joints under Fatigue Loading

8.2.1 Relocation of Fracture Position

The majority of the unpeened FSW samples tended to failure within the Nugget/TMAZ regions of the joints. The cracks which cause failure originated from the root surface of the component, propagating through the nugget and TMAZ regions of the joint. The fracture path tended to follow the bands which formed the onion ring structure of the nugget. A number of researchers showed a similar failure of the FSW joints due to the collection of tensile residual stress in this region, the geometry of the nugget/TMAZ promoting the fracture in this region and due to discontinuities originating from the root surface of the component [104] [105]. All FSW samples in failed in this mode, with a number of FSW+LSP samples failing at the HAZ on the advancing side of the weld.

After the application of LSP, it was found that every tool position combination except 1.25mm Adv. 0.05mm had, at least, a single fatigue coupon which failed at the HAZ. Both high and low cycle fatigue samples exhibited more samples that failed in the HAZ. Figure 8.18 provides a number of examples of this failure. This indicated that LSP tended relocated fracture position of the fatigue samples. Assessment of Figure 8.6 showed that the region around the HAZ of the FSW+LSP samples tended to have the lowest compressive residual stress across the joint. This showed that the application of LSP introduced and reallocated critical residual stresses within the joint and that the fracture of the component was dependent on the residual stress profile of the component.

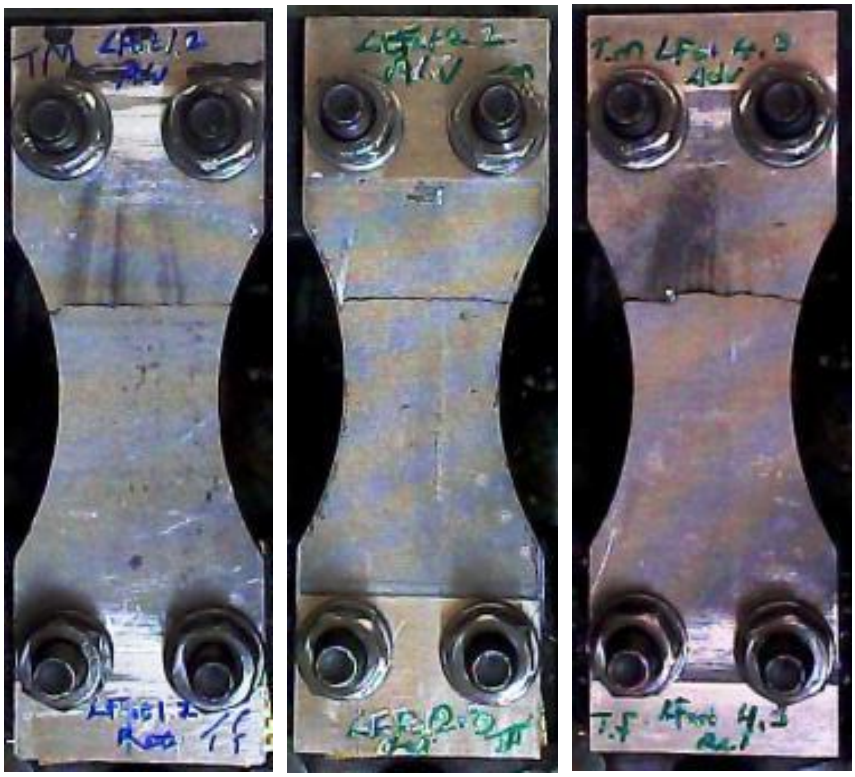

Figure 8.18 – Numerous examples of the variation in Failure Location due to Laser Shock Peening

The FSW+LOP+LSP joints which exhibit an increase in fatigue life whilst fracturing in a region away from the defect showed that LSP had the ability to reduce the effects of the LOP defect within the joint. This can be stated as the LSP joint exceeded the fatigue life of FSW+LOP joint without fracturing at the LOP.

8.2.2 Comparison of Fatigue Results to Published Data

The FSW and FSW+LSP fatigue data has been compared to published data [76]. The experimental fatigue of the FSW and FSW+LSP was comparable to the published results. The influence of the LOP defects are again clearly seen in the reduction of fatigue life of the flawed coupons compared to the results found in literature. The samples which did not exhibit any defect all performed in the region the published work. This again provided a quality assurance of the FSW, LSP process and the actual fatigue testing.

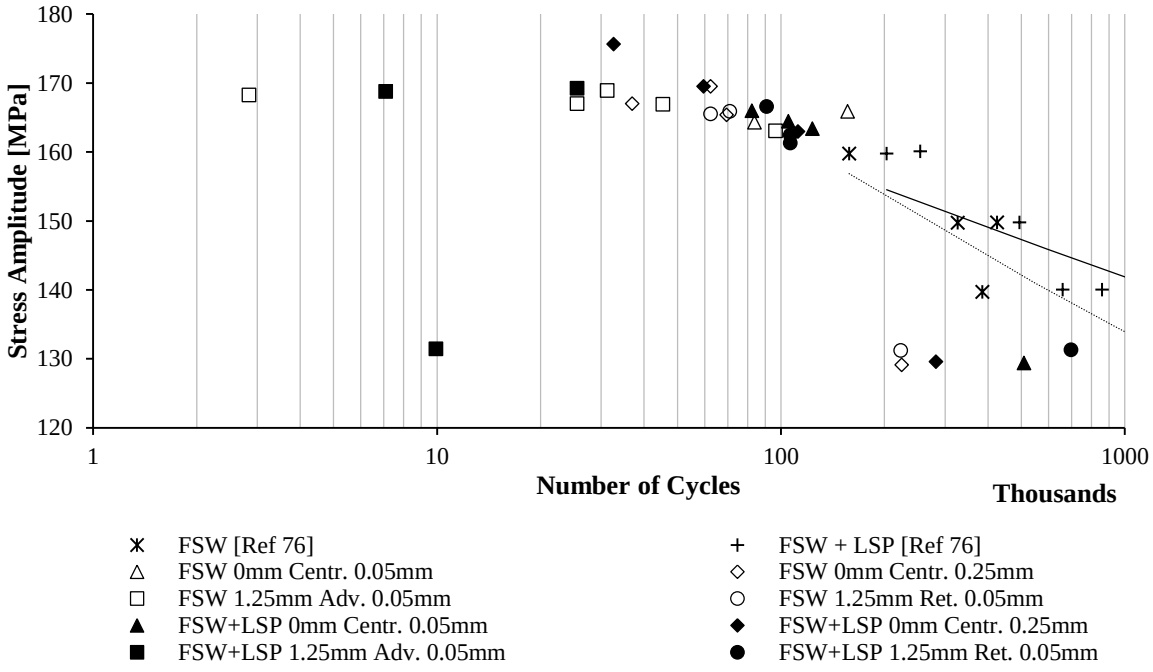

Figure 8.19 - Comparison of Friction Stir Welding Fatigue Result to Published Work

8.2.3 Conclusion

From the results presented in this section the following can be concluded:

1. The effectiveness of LSP and the compressive residual stresses introduced through the process tended to have minimal effect on the FSW joints under the application of the larger applied stress (low cycle fatigue). This was due to the relaxation of the compressive residual stress.
2. LSP showed an improvement in the fatigue life of a coupon which had a defect size of approximately 175 µm. The fatigue life of the flawed FSW sample was improved by as much as 20%.
3. Overall, the application of LSP to the non-defective FSW joints improves the fatigue life by as much as 68%.
4. The FSW+LSP coupons tested in the low cycle fatigue regime exhibited more controlled failure as the samples failed more consistently with less variation in no of cycles to failure.
5. It was anticipated that peening both the root and crown (like done in the Base+LSP) or applying multiple layers of peening to the root surface would introduce higher compressive residual stresses that would be more effective in resisting the applied stresses at the low cycle fatigue as well as improving the ability of the joint to resist the detrimental effects of the LOP in the joint.

9 Discussion

The presentations of the results were stated in the earlier three sections.

During the completion of this research relating to Friction Stir Welding and Laser Shock Peening, it became apparent that the sensitivity and variability in the outcomes were two factors which would influence the success of the implementation of the two innovative techniques. A substantial amount of research was required to be completed in order to fully understand the dynamics of the two processes.

Before viable FSW samples could be manufactured and completed, a FSW tool of a high standard had to be developed. The development of the tool began with the modification to a rudimentary single piece tool which had a three face facet machined into it. The FSW joints manufactured with this tool equalled the performance of the joints found in published research. A number of joints were extremely weak and it was felt that a better tool design would allow for the manufacture of joints which would well surpass those in published works. The three facetted pin and 20mm diameter spiralled should tool was developed by Correia (through his MSc) with modifications in order to reduce the CNC machine loading during welding. The final tool configuration, proved to be a tool configuration which matched and surpassed the quality of welds produced by other researchers across many welding parameter combinations. With confidence, this final tool configuration was used in the completion of the remainder of the research.

The boundaries of the FSW parameters window were selected based on published work and the capabilities of the CNC machined used in the manufacturing of the FSW joints. Tool rotational speed (RPM) and the feed rate (mm/min) were the most vital input parameters that needed to be controlled, as these parameters defined the quality and mechanical properties of the joints. The relationship between the two parameters was defined through the welding rate, which defined the amount of revolutions of the tool to the distance travelled (rev/mm). The consequences of the variation of the input parameters were most noted in the change in frictional heat generated during the welding process. The heat generated during welding defined the majority of outcomes from forging force, joint quality and most mechanical properties. The optimisation of the FSW process for the manufacture of high quality 3mm thick AA6082-T6 joints, illustrated the need for welding at elevated welding rates or higher temperatures. By selecting the best welding parameters of 1600 RPM and 200 mm/min the following was achieved:

- The forging force was reduced to the minimum average amount of 7156 N.
- Sufficient material flow, in turn resulted in a satisfactory internal joint structure that was free of defects and internal discontinuities,

- Joints which performed to industry standards in their general mechanical properties. The joint achieved an ultimate static tensile joint efficiency of as much as 73% to that of the base material. The joints exhibited a high level of ductility without the development of a visible defect.

With all engineering processes, no technique is flawless and FSW was no exception. The combination of the material temperature during welding, the forging force and the material flow resulted in a maximum loss of material of as much as 26%. The very things which made the joint so successful resulted in the formation of the minor defect. Due to the softening of the material during welding, excessive material was lost to the formation of flash on either side of the weld track. This shows the sensitivity and the delicacy of parameter selection which has a knock on effect on all aspects of the welds. A multi-objective optimisation strategy was employed to explore the parameter window at a greater extent, define relationships between multiple inputs and outputs and the selection of the most suited set of parameters. The optimisation predicted a tool rotational speed, feed rate and welding rate of 1433 RPM, 196 mm/min and 7.3 rev/mm. With these optimised parameters, the FSW process would be improved and be more inclined to suit an industrial application of the welding of this Aluminium alloy.

An optimised process has been found to be only as good as the quality of the operator, apparatus (this includes the design of the welding tool and welding support system) and supplied material. Welding tool misalignments, material variations and general wear on the welding apparatus can lead to a number manufacturing anomalies which would most likely result in the formation of a number of defects within the joints. Lack of Penetration, is a root surface defect, formed as a crack which presence within the joint could have detrimental effects on the properties of the FSW joint. Formed at the butting up of the welding plates, this defect is always inclined towards the advancing side of the joints. Through specific welding tool offsets, LOP defects were introduced within the FSW joints manufactured with the closest optimum welding parameters of 1600 RPM, 200 mm/min. The fixed gearing of the FSW CNC machine prevented the welding at the optimum spindle speed of 1433 RPM. Although it was shown that alternative welding parameters caused LOP defects in the joints, section 6.1.5.2, an industrial processes would not implement a manufacturing technique which used the incorrect input parameters thus, a method of introducing the LOP defects whilst maintaining the ‘sweet-spot’ parameters was required. Numerous combinations of normal and lateral tool offsets were found to produce LOP cracks which formed at the root surface and extended at different lengths through the thickness of the joints. The worst resulting offset was found to generate a LOP defect which had an effective length of 954.5 μm, on average this effected 43% of the joints thickness. Each crack was inclined at a slightly different angle but the crack tip and propagation path was generally towards the advancing side of the weld. Non-Destructive Testing showed that the consistency of the defects along the welding track was consistent, with only slight variations in the size and inclination

of the defect. This proved that the technique of offsetting the welding tool in combinations of the normal and lateral positions whilst maintaining welding parameters lead to the formation of stable defects. The tool offsets had minimal effect on the parameter linked outcomes of the welding temperature and forging force. It was shown, that the magnitude of these outputs were based mainly on the selection of the welding parameter (tool rotation and feed rate). The normal position of the tool did have the largest effect on the joint thickness and the loss of material. It was found that increasing the size of the LOP reduced the ultimate static force carrying capabilities of the joints under both tensile and bending applied loads, a reduction in strength in the range of 9% to 27% depending on the length of the defects. The tool offset and LOP defect was also shown to reduce the fatigue life of the components under fully reverse bending by as much as 36% with a defect length of ±175µm. The best welds (non-defective) were found to have mechanical properties comparable to those of other published works. The FSW throughout this research followed the typical behaviour and performance of FSW joints which had been noted in most other published works relating to this research. The notable reduction in strength of the joints, both statically and dynamically, can be attributed directly to the presence of the LOP. As there was slight variations in thermal and forging force profiles of the offset welding to that of the optimal welding parameters, as well as the high standard in which the best parameter welds performed.

It was anticipated that the introduction of compressive residual stresses into the critical or defective areas of the FSW joints would improve or counter the presence of the internal defects. Laser Shock Peening was identified as an innovative post welding process which could be used to introduce these needed residual stresses. LSP by nature was a dynamic and fluid process with the sensitivity of a millimetre variation causing the change in a number of parameters. The Wits LSP Group had limited experience of the application of LSP to the base and FSW AA6082-T6, thus, a full parameter investigation and optimisation was completed in order to understand and identify the optimum implementation parameters of the LSP process, laser power intensity and coverage formed the core of the parameter investigation. A number of notable outcomes were found during the exploration of the LSP parameter combinations:

- The approximate saturation limit of the base material was at 1000 spots/$cm^{2.}$
- The deformation or deflection of the Almen strips was directly related to the increasing power intensity.
- Higher process power reduced the quality and efficiency of the transmitted laser pulse.
- LSPwC created a new ablation layer on the base and the FSW surfaces which were at maximum 10 times and 7 times rougher than the untreated surfaces.
- Although the LSP application strategy was more extensive, a ±9.5 time's increase in the base material fatigue life was achieved through LSP.

The ‘sweet spot’ of LSP parameters was more diverse than that of the FSW optimisation due to the desired outcome or the desired goal that was attempted to be achieved. The predicted optimum LPS parameters for the laser power intensity and coverage were specified as 3.33 GW/cm^2 and 1067 spots/cm^2. It was decided that as the optimum parameters were similar to the test parameter case of 3.5 GW/cm^2 and 1000 spots/cm^2 and were used throughout the remainder of the research.

With a better understanding and the application of the possible optimum parameters, FSW and LSP were combined in the attempt to manufacture a superior joint. The application of LSP to the root surface of the FSW joint introduced significant compressive stresses in the near surface. The average tensile state of the FSW joint was at an average magnitude of 100 MPa whilst after the application of LSP the near surface stress state was completely reversed to an average compressive residual stress of -175 MPa. This influence of the LSP altering the near surface residuals stress profile was in line with published work.

With the confirmation of the altering of the internal residual stress state with LSP, fatigue testing was completed in order to determine the ability of LSP to improve the fatigue life of a FSW joint and to confirm its ability to improve/counteract the presence of a LOP defect in a FSW joint. It was found that the FSW and FSW+LSP joints had comparable fatigue lives to similar Aluminium alloys which had under gone the same manufacturing and testing parameters. The defect free samples exhibited a high and low cycle fatigue lives of ± 156200 cycles (low cycle) for the FSW and ±509780 cycles (high cycle) and ±114310 cycles (low cycle) for the FSW+LPS. It was found that LSP had minimal effect at the lower cycle fatigue regime as the applied stress was similar to that internal compressive stress. The applied stress tended to reduce the internal compressive stress to a magnitude which had no effect on the fatigue strength of the joint. The application of LSP to FSW joints which were tested in the high cycle fatigue regime showed positive signs of fatigue life improvement, with a 68% increase in fatigue (no defect) and 20% increase (with a defect of 175µm. From these results it was indicated that LSP can be used to reduce the detrimental effects of the LOP defect within the FSW joint.

10 Conclusions and Recommendations

Section 3, outlined a number of objectives which formed the framework of this research. The formal conclusion on these objectives has been listed according to the presentation in section 3.

1. Development of a FSW tool capable of manufacturing high quality joints.
    - Through experimental development, the final 20 mm diameter concentric spiralled H13 high speed tool steal shoulder and 5 mm diameter MP-159 tool steel three facet taper pin tool combination was developed.
    - This tool manufactured FSW joints in 3 mm thick AA6082-T6 that surpassed the strength of the joints manufactured out of the exact material in published research.
2. Investigation of the FSW parameter window.
    - Five tool rotational speeds and three feed rates were selected to form a testing matrix of fifteen various FSW parameter combinations, all with different welding rates.
    - The assessment of the welds were completed based on welding temperature and forging force (which were monitored during welding) material loss, joint quality, ductility and static strength and efficiency of the joints.
    - The FSW parameter combinations all displayed various effects associated to the selected parameters. With the majority of the higher welding rates being the most successful welds.
3. Optimisation of the FSW process through the application of a multi-objective optimisation strategy.
    - Using the data obtained in the completion of objective 3 and the application of modeFRONTIER, a multi-objective optimisation process was developed to fully explore the FSW parameter window.
    - The optimum FSW parameters specified by the optimisation simulation was a tool rotational speed of 1433 RPM, a feed rate of 196 mm/min and a welding rate of 7.3 rev/mm. These parameters were specific to this to configuration and thickness of the welding sheets and Aluminium alloy. Due to the fixed gearing of the CNC FSW machine the closest tool rotation to the optimum value was 1600 RPM.
4. Define a robust FSW procedure for introducing controlled and constant LOP defects.
    - Controlled LOP defects were introduced into the FSW joints by controlled tool offsets in the normal and lateral positions relative to the joint line of the butting welding plates.
    - The offsetting of the tool had very little influence on the process outcomes such as the welding temperature and the forging force. The largest variations that were noted were due to the normal position variations but the forging force was constant across

all varying lateral positions. This indicated that the any discrepancy or variation in the performance of the joints would be due to the presence of the root defect.

- These defects were shown to be consistent in size, positon and inclination along the full welding track.
- The tool offsets created a number of LOP defects which originated from the root surface of the weld and extended to several depths through the thickness of the joints.

5. Characterisation of the effects of the LOP defects on the mechanical behaviour on the flawed FSW joints.
    - The LOP defect size greatly influenced the structural strength of the FSW joints under both tensile and bending applied loads.
    - As the length of the defect increase the static strength of the joints decreased.
    - A number of the tool offsets resulted in a reduction in the fatigue life of the FSW joints in both the high and low cycle fatigue. The non-defective optimised joint exhibited a low cycle fatigue life comparable to that of the base material.
6. Investigation of the LSP parameter window.
    - Two major LSP parameters, power intensity and coverage were initially varied at multiple levels in order to provide a wide range of tested parameters. After identification of a more suitable parameter window, through deflection and material saturation analysis.
    - Four power intensities and coverages were further investigated to identify the parameter combination effects on the base and FSW AA6082-T6.
    - The investigation took into account the processing quality, air breakdown effects on the efficiency of the energy transmission, sample deflection, surface roughness, strain hardening effects and the fatigue life improvements of the base material.
    - The results of the investigations showed that the higher peak pressures associated to the higher power intensities tended to influence the material the most.
7. Optimisation of the LSP parameters through the application of a multi-objective optimisation strategy.
    - Using the data obtained in the completion of objective 6 and the application of modeFRONTIER, a multi-objective optimisation process was developed to fully explore the LSP parameter window.
    - The optimisation simulation of the LSP process indicated that the process could be optimised to achieve two specific goals, these were parameters to maximise component fatigue or to maximise the depth of penetration of the effects of the LSP process.

- A set of optimum parameters were suggested which attempted to be the best mix of both optimisation goals of maximising the fatigue life and the penetration depth of the effects of LSP. The simulation specified a power intensity of 3.33GW/cm^2 and coverage of 1067 spots/cm^2.

8. Combination of the most suitable FSW and LSP parameters.
    - LSP was a suitable technique of introducing a state of compressive residual stress within a FSW joint.
    - The optimum welding process created a tensile residual stress state within the near surface of the root of the joint. An average tensile stress of 100 MPa was measured across the joint.
    - Application of LSP to the root surface of the joint altered the tensile state to a fully compressive residual stress state in the near surface. The average measured residual stress varied from approximately -150 to 200 MPa over the three measured depths.
    - LSP improved the defective FSW joint (defect length of 175μm) by 20%.
    - LSP improved the defect free FSW joints fatigue life by as much as 68%.
    - LSP improved the consistency of failure of a number of tool offset samples

11 Presentation of Work

The accepted abstracts can be found in Appendix G.

- Leering M.P., Polese C., (2015*), Laser Shock Peening to Recover Fatigue Life of Flawed Friction Stir Welded Joints*. 5th International Conference on Laser Shock Peening and Related Phenomena. Cincinnati, Ohio, USA, 10-15 May 2015.
- Leering M.P., Polese C., (2015), *Laser Shock Peening to Recover Fatigue Life of Flawed Friction Stir Welded Joints for Aerospace Applications*. 1st International Metallic Materials and Processes: Industrial Challenges. Deauville, France, 25-27 November 2015.

References

[1] J. A. Al-jarrah, "Optimization of Friction Stir Welding Parameters for Joining Aluminum Alloys Using RSM," *Adv. Theory Appled Mech.*, vol. 6, no. 1, pp. 13–26, 2013.

[2] D. Furfari and M. Pacchione, "Laser Shock Peening (LSP) in Friction Stir Welded (FSW) Joints with Lack of Penetration (LOP)," Airbus Germany, Hamburg, 2008.

[3] J. W. Olcott, "Eclipse Aviation: Changing the Way People Travel," *Aircraft Owners and Pilots Association*, 2004.

[4] The Aluminum Association Inc., "Aluminum Standards and Data 2000 and/or International Alloy Designations and Chemical Composition Limits for Wrought Aluminum and Wrought Aluminum Alloys," no. Revised. 2001.

[5] L. G. J. Gooren, "A pilot study into microstructural aspects of fatigue in AA6082-T6 and AA2024-T3," Technische Universiteit Eindhoven, 2005.

[6] P. Mazal and P. Liskutin, "Experimental Evaluation of Fatigue properties of Wrought AL Alloys EN AW - 6082 and EN AW-7075," *Met. 2010*, pp. 1–6, 2010.

[7] T. Khaled, "An Outsider Looks at Friction Stir Welding," *FAA Rep. number ANM-112N-05-06*, pp. 1–71, 2005.

[8] A. U. Fehrenbacher, A. U. Duffie, A. Neil, A. U. Ferrier, J. Nicola, A. U. Pfefferkorn, and E. Frank, "Toward Automation of Friction Stir Welding Through Temperature Measurement and Closed-Loop Control," *J. Manuf. Sci. Eng.*, vol. 133, no. 5, 2011.

[9] Y. Sato, "Friction stir welding of poor-weldable structural materials," 2013. [Online]. Available: http://www.rpip.tohoku.ac.jp/seeds/profile/125/lang:en/.

[10] P. Vilaça and W. Thomas, “Friction Stir Welding Technology,” *Adv Struct Mater*, vol. 8, no. April, pp. 85 – 124, 2011.

[11] R. Mishra, “Friction stir welding and processing,” *Mater. Sci. Eng. R Reports*, vol. 50, no. 1–2, pp. 1–78 w.m th, Aug. 2005.

[12] Y. N. Zhang, X. Cao, S. Larose, and P. Wanjara, “Review of tools for friction stir welding and processing,” *Can. Metall. Q.*, vol. 51, no. 3, pp. 250–261, Jul. 2012.

[13] A. Meilinger and I. Torok, “THE IMPORTANCE OF FRICTION STIR WELDING TOOL Ákos Meilinger , Imre Török,” *Prod. Process. Syst.*, vol. 6, no. 1, pp. 25–34, 2013.

[14] D. Correia, C. Polese, and I. Correia, “Design of Friction Stir Welding Parameters for Longitudinal Aluminium Friction Stir Welded Joints,” University of the Witwatersrand, 2011.

[15] P. Prasanna, C. Penchalayya, and D. Anandamohana Rao, “Effect of tool pin profiles and heat tre...pdf,” *Am. J. Engineeing Res.*, vol. 2, no. 1, pp. 7–15, 2013.

[16] J. Adamowski, M. Szkodo, and A. Energia, “Friction Stir Welds (FSW) of aluminium alloy AW6082-T6,” *J. Achiev. Mater. Manuf. Eng.*, vol. 20, pp. 403–406, 2007.

[17] L. Wan, Y. Huang, Z. Lv, S. Lv, and J. Feng, “Effect of self-support friction stir welding on microstructure and microhardness of 6082-T6 aluminum alloy joint,” *Mater. Des.*, vol. 55, pp. 197–203, Mar. 2014.

[18] L. Svensson, L. Karlsson, H. Larsson, B. Karlsson, M. Fazzini, and J. Karlsson, “Microstructure and mechanical properties of friction stir welded aluminium alloys with special reference to AA 5083 and AA 6082,” *Sci. Technol. Weld. Join.*, vol. 5, no. 5, pp. 285–296, 2000.

[19] S. Muthukumaran and S. K. Mukherjee, “Multi-layered metal flow and formation of onion rings in friction stir welds,” *Int. J. Adv. Manuf. Technol.*, vol. 38, pp. 68–73, 2008.

[20] R. R. Ambriz and D. Jaramillo, “Mechanical Behavior of Precipitation Hardened Aluminum Alloys Welds,” in *Intech*, .

[21] D. Correia, “Investigation into the Friction Stir Welding of Aeronautical Grade Aluminium Alloys Using Standard and Innovative Tooling,” The University of the Witwatersrand, 2014.

[22] D. Trimble, J. Monaghan, and G. E. O’Donnell, “Force generation during friction stir welding of AA2024-T3,” *CIRP Ann. - Manuf. Technol.*, vol. 61, no. 1, pp. 9–12, 2012.

[23] P. Cavaliere, a. De Santis, F. Panella, and a. Squillace, “Effect of welding parameters on mechanical and microstructural properties of dissimilar AA6082-AA2024 joints produced by friction stir welding,” *Mater. Des.*, vol. 30, no. 3, pp. 609–616, 2009.

[24] Ø. Frigaard, Ø. Grong, and O. T. Midling, “A process model for friction stir welding of age hardening aluminum alloys,” *Metall. Mater. Trans. A*, vol. 32, no. 5, pp. 1189–1200, 2001.

[25] P. A. Colegrove, H. R. Shercliff, and R. Zettler, “Model for predicting heat generation and temperature in friction stir welding from the material properties,” *Sci. Technol. Weld. Join.*, vol. 12, no. 4, pp. 284–297, 2007.

[26] M. Z. H. Khandkar, J. a. Khan, and a. P. Reynolds, “Prediction of temperature distribution and thermal history during friction stir welding: input torque based model,” *Sci. Technol. Weld. Join.*, vol. 8, no. 3, pp. 165–174, 2003.

[27] A. P. Reynolds, W. Tang, Z. Khandkar, J. a. Khan, and K. Lindner, “Relationships between weld parameters, hardness distribution and temperature history in alloy 7050 friction stir welds,” *Sci. Technol. Weld. Join.*, vol. 10, no. 2, pp. 190–199, 2005.

[28] D. H. Santiago, G. Lombera, S. Urquiza, A. Cassanelli, and L. A. De Vedia, “Numerical Modeling of Welded Joints by the ‘ Friction Stir Welding ’ Process,” vol. 7, no. 4, pp. 569–574, 2004.

[29] C. Hamilton, S. Dymek, and a Sommers, “Characteristic Temperature Curves for Aluminum Alloys during Friction Stir Welding,” *Weld. J.*, vol. 89, no. 9, p. 189s–194s, 2010.

[30] J. De Backer and G. Bolmsjö, “Thermoelectric method for temperature measurement in friction stir welding,” *Sci. Technol. Weld. Join.*, vol. 18, no. 7, pp. 558–565, 2013.

[31] W. Tang, X. Guo, J. C. McCLURE, L. E. Murr, and a. Nunes, “Heat Input and Temperature Distribution in Friction Stir Welding,” *J. Mater. Process. Manuf. Sci.*, vol. 7, no. 2, pp. 163–172, 1998.

[32] W. J. Arbegast and P. J. Hartley, “Friction Stir Weld Technology Development at Lockheed Martin Michoud Space Systems - An Overview,” in *The Fifth International Conference on Trends in Welding Research*, 1998, p. 541.

[33] T. Hashimoto, S. Jyogan, K. Nakata, Y. G. Kim, and M. Ushio, “FSW joints of high strength aluminum alloy,” in *1st International Symposium on Friction Stir Welding*, 1999.

[34] A. Fehrenbacher, N. a Duffie, N. J. Ferrier, F. E. Pfefferkorn, and M. R. Zinn, “Effects of tool – workpiece interface temperature on weld quality and quality improvements through temperature control in friction stir welding,” pp. 165–179, 2014.

[35] W. J. Arbegast, “Friction Stir Joining : Characteristic Defects,” South Dakota School of Mines and Technology, 2003.

[36] H. Zhang, S. B. Lin, L. Wu, J. C. Feng, and S. L. Ma, “Materials & Design Defects formation

procedure and mathematic model for defect free friction stir welding of magnesium alloy," vol. 27, pp. 805–809, 2006.

[37] A. P. Reynolds, "Defect Formation in Friction Stir Welds," *Model. Defects - Underst. Prev. I*, p. 4.

[38] M. N. James, D. G. Hattingh, H. Lombard, I. Wedderburn, D. L. H. Bulbring, A. Els-Botes, and A. Steuwer, *Failure mechanisms of advanced welding process*. woodhead Publishing Limited, 2010.

[39] A. S. Babu, "An Overview of Friction Stir Welding," *Int. J. Res. Mech. Eng. Technol.*, vol. 5762, pp. 259–265, 2013.

[40] O. Hatamleh, "The Effects of Laser Peening and Shot Peening on Mechanical Properties in Friction Stir Welded 7075-T7351 Aluminum," vol. 77058, no. 281, pp. 1–23.

[41] C. Mandache, D. Levesque, L. Dubourg, and P. Gougeon, "Non-destructive detection of lack of penetration defects in friction stir welds," *Sci. Technol. Weld. Join.*, vol. 17, no. 4, pp. 295–303, May 2012.

[42] C. Zhou, X. Yang, and G. Luan, "Effect of root flaws on the fatigue property of friction stir welds in 2024-T3 aluminum alloys," *Mater. Sci. Eng. A*, vol. A418, pp. 155–160, 2006.

[43] T. Dickerson, "Fatigue of friction stir welds in aluminium alloys that contain root flaws," *Int. J. Fatigue*, vol. 25, no. 12, pp. 1399–1409, Dec. 2003.

[44] J. K. Paik, Y. V. S. Kumar, and J. M. Lee, "Ultimate strength of cracked plate elements under axial compression or tension," *Thin-Walled Struct.*, vol. 43, pp. 237–272, 2005.

[45] D. G. Kinchen and G. P. Adams, "Lack of Penetration in Friction Stir Welds: Effects on Mechanical Properties and NDE Feasibility," in *AeroMat 2000 Conference and Exposition Friction Stir Joining: Session 4*, 2000.

[46] S. Gopi and K. Manonmani, "Study of friction stir welding parameters in conventional milling machine for 6082-T6 aluminium alloy," *Aust. J. Mech. Eng.*, vol. 10, no. 2, pp. 129–141, 2012.

[47] K. Mroczka and A. Pietras, "FSW characterization of 6082 aluminium alloys sheets," *Int. Sci. J.*, vol. 40, no. 2, pp. 104–109, 2009.

[48] J. Karlsson, B. Karlsson, H. Larsson, L. Karlsson, and L. Svensson, "Microstructure and Properties of Friction Alloys," *Joints Alum. - Ina. 1998 7th Int. Conf.*, pp. 1–5, 1998.

[49] P. M. G. P. Moreira, T. Santos, S. M. O. Tavares, V. Richter-trummer, P. Vilaça, and P. M. S. T. De Castro, "Mechanical and metallurgical characterization of friction stir welding joints of AA6061-T6 with AA6082-T6," *Mater. Des.*, vol. 30, pp. 180–187, 2009.

[50] P. Staron, M. Koçak, S. Williams, and a Wescott, “Residual stress in friction stir-welded Al sheets,” *Phys. B Condens. Matter*, vol. 350, no. 1–3, pp. E491–E493, Jul. 2004.

[51] a. Steuwer, M. J. Peel, and P. J. Withers, “Dissimilar friction stir welds in AA5083–AA6082: The effect of process parameters on residual stress,” *Mater. Sci. Eng. A*, vol. 441, no. 1–2, pp. 187–196, Dec. 2006.

[52] M. Ericsson, “Influence of welding speed on the fatigue of friction stir welds, and comparison with MIG and TIG,” *Int. J. Fatigue*, vol. 25, no. 12, pp. 1379–1387, Dec. 2003.

[53] A. Cirello, G. Buffa, L. Fratini, and S. Pasta, “AA6082-T6 Friction Stir Welded Joints Fatigue Resistance: Influence of Process Parameters,” *Proc. Inst. Mech. Eng. Part B J. Eng. Manuf.*, vol. 220, no. 6, pp. 805–811, Jan. 2006.

[54] A. H. Clauer, “Laser Shock Peening for Fatigue Resistance,” *Surf. Perform. Titan.*, no. 1996, pp. 217–230.

[55] K. Ding and L. Ye, *Laser shock peening Performance and process simulation*. Cambridge England: woodhead Publishing Limited, 2006.

[56] P. Peyre, P. Merrien, H. P. Lieurade, R. Fabbro, and a Bignonnet, “Optimization of the residual stresses induced by laser shock treatment and fatigue life improvement of 2 cast Aluminium alloys,” *The Fifth International Conference on Shot Peening, ICSP 5*. pp. 301–310, 1993.

[57] A. M. Korsunsky, J. Liu, D. Laundy, M. Golshan, and K. Kim, “Residual elastic strain due to laser shock peening: synchrotron diffraction measurement,” *J. Strain Anal. Eng. Des.*, 2006.

[58] R. K. Nalla, I. Altenberger, U. Noster, G. Y. Liu, B. Scholtes, and R. O. Ritchie, “On the influence of mechanical surface treatments deep rolling and laser shock peening on the fatigue beha v ior of Ti Á 6Al Á 4V at ambient and ele v ated temperatures,” *Mater. Sci. Eng.*, vol. 355, pp. 216–230, 2003.

[59] V. Cahmpagne, S. Grendahl, R. Tenaglia, and D. Lahrman, “Laser Peening for U.S. Army Helicopters,” Army Research Laboratory, LSP Technologies, Aberdeen Proving Ground, 2007.

[60] Y. Hu, C. Gong, Z. Yao, and J. Hu, “Investigation on the non-homogeneity of residual stress field induced by laser shock peening,” *Surf. Coatings Technol.*, vol. 203, no. 23, pp. 3503–3508, 2009.

[61] L. Berthe, R. Fabbro, P. Peyre, and E. Bartnicki, “Wavelength dependent of laser shock wave generation in the water confinement regime,” *J. Appl. Phys.*, vol. 85, no. 11, pp. 7552–7555, 1999.

[62] D. Glaser and C. Polese, “Laser Shock Peening for Integral Airframe Structures Applications,” University of the Witwatersrand, 2013.

[63] Y. Cao, Y. C. Shin, and B. Wu, “Parametric Study on Single Shot and Overlapping Laser Shock Peening on Various Metals via Modeling and Experiments,” *J. Manuf. Sci. Eng.*, vol. 132, no. 6, 2010.

[64] Y. Zhang, J. You, J. Lu, C. Cui, Y. Jiang, and X. Ren, “Effects of laser shock processing on stress corrosion cracking susceptibility of AZ31B magnesium alloy.,” *Surf. Coat. Technol.*, no. 204, pp. 3947 – 3953, 2010.

[65] Y. Hu and Z. Yao, “Fem simulation of residual stresses induced by laser shock with overlapping laser spots,” *Acta Metall. Sin. (English Lett.*, vol. 21, no. 2, pp. 125–132, 2008.

[66] N. Hfaiedh, P. Peyre, H. Song, I. Popa, V. Ji, and V. Vignal, “Finite Element analysis of Laser Shock Peening of 2050-T8 aluminum alloy,” *Int. J. Fatigue*, vol. 70, pp. 480–489, 2014.

[67] J. Ocatia, M. Morales, C. Molpeceres, J. Porro, J. Grum, and M. Zupancic, “LASER SHOCK PROCESSING AS A METHOD FOR SURFACE PROPERTIES MODlFICATlON OF METALLIC MATERIALS,” *Conf. Proc. ICSP-9*, pp. 466–471, 2005.

[68] M. Obata, Y. Sano, N. Mukai, M. Yoda, S. Shima, and M. Kanno, “Effect of Laser Peening on Residual Stress and Stress Corrosion Cracking for type 304 Stainless Steel,” in *The Seventh International Conference on Shot Peening*, 1991.

[69] J. Noack and A. Vogel, “Laser-induced plasma formation in water at nanosecond to femtosecond time scales: calculation of Thresholds, Absorption Coefficients and Energy Density,” *IEEE J. Quantum Electron.*, vol. 35, no. 8, pp. 1–12, 1999.

[70] D. X. Hammer, R. J. Thomas, G. D. Noojin, B. a Rockwell, P. K. Kennedy, and W. P. Roach, “Experimental Investigation of Ultrashort Pulse Laser-indeuced Breakdown Thresholds in Aqueous Media,” *IEEE J. quantum Electron.*, vol. 32, no. 4, p. 670, 1996.

[71] M. I. C. Curtiss Wright, “Laser Shock Peening (LSP).” [Online]. Available: http://www.metalimprovement.co.uk/laser-peening.html.

[72] S. S. Harilal and B. Harilal, “Diagnostics of Laser Induced Spark in Air Using Fast ICCD Photography Diagnostics of Laser Induced Spark in Air using fast ICCD Photography,” San Diego, 2002.

[73] A. Vogel, K. Nahen, D. Theisen, and J. Noack, “Plasma formation in water by picosecond and nanosecond Nd:YAC laser pulses .1. Optical breakdown at threshold and superthreshold irradiance,” *IEEE J. Sel. Top. Quantum Electron.*, vol. 2, no. 4, pp. 847–860, 1996.

[74] U. Trdan, M. R. Hill, and J. Grum, “Residual stress variations due to strain hardening effect after Laser Shock Peening,” in *9th International Congress on Thermal Stresses*, 2011, no. 3, pp. 3–6.

[75] P. Peyre, P. Merrien, and H. P. Lieurade, “Laser shock peening processing of aluminium alloys: application to high cycle fatigue behavior,” *Mater. Sci. Eng.*, vol. A210, pp. 102–13, 1996.

[76] Y. Sano, K. Masaki, T. Gushi, and T. Sano, “Improvement in fatigue performance of friction stir welded A6061-T6 aluminum alloy by laser peening without coating,” *Mater. Des.*, vol. 36, pp. 809–814, Apr. 2012.

[77] O. Hatamleh, “A comprehensive investigation on the effects of laser and shot peening on fatigue crack growth in friction stir welded AA 2195 joints,” *Int. J. Fatigue*, vol. 31, no. 5, pp. 974–988, May 2009.

[78] M. Iordachescu, A. Valiente, L. Caballero, D. Iordachescu, J. L. Ocaña, and J. A. Porro, “Laser Shock Processing influence on local properties and overall tensile behavior of friction stir welded joints,” *Surf. Coatings Technol.*, vol. 206, no. 8–9, pp. 2422–2429, Jan. 2012.

[79] Investopedia, “Pareto Efficiency,” 2014. [Online]. Available: http://www.investopedia.com/terms/p/pareto-efficiency.asp.

[80] Esteco, “modeFRONTIER 4 User Manual.” p. 4.

[81] D. R. Askeland and P. P. Fulay, *Essentials of Material science and engineering*, Second edi. Cengage Learning, 2010.

[82] D. Broek, *Elementary Engineering Fracture Mechanics*. Martinus Nijhoff Publishers, 1982.

[83] F. Kienhofer, “MECN 2009 Mechanical Engineering Design course notes.” The University of the Witwatersrand, pp. 48–76, 2010.

[84] T. Materia, “Linear Elastic Fracture Mechanics (LEFM): Part Two.” p. 2010, 2010.

[85] Faculty of Computing Engineering and Mathematical Science, “Fatigue and Fracture Mechanics,” Universtiy of West England, 2002.

[86] M. E. Fitzpatrick, A. T. Fry, P. Holdway, F. A. Kandil, and L. Suominen, *Determination of Residual Stresses by X-ray Diffraction - Issue 2*, no. 52. 2005.

[87] Elettra Sincrotrone Trieste, “Elettra’s Beamlines,” 2012. .

[88] Kistler, “Multicomponent Force Link Set - Data Sheet for 9366CC0,5,” 2010.

[89] FLIR, “FLIR T640 - Data Sheet.”

[90] L. M. Simelane, “Static Testing and Fracture Surface Characterisation of Friction Stir Welded Aluminium Joints,” 2013.

[91] M. Ahmad, I. Tuene, E. Kim, and A. Shukla, “Logarithmic Spiral,” pp. 1–5, 2008.

[92] Quntra-Ray, “Quntra-Ray Pro Series Pulsed Nd:YAG Laser User’s Manual,” no. June. California, p. 2006, 2006.

[93] OPHIR Photonics, “190-1100 nm USB Silicon CCD Camera.” pp. 142–143, 2014.

[94] Z. Loftus and W. J. Arbegast, “NASA / CR- Friction Stir Weld Tooling Development for Application on the 2195 AI-Cu-Li Space Transportation System External Tank,” *Lockheed Martin Michoud Sp. Syst. Adv. Programs Technol.*, pp. 1–5.

[95] H. J. Liu, H. Fujii, M. Maeda, and K. Nogi, “Tensile properties and fracture locations of friction-stir-welded joints of 2017-T351 aluminum alloy,” *J. Mater. Process. Technol.*, vol. 142, no. 3, pp. 692–696, 2003.

[96] D. Glaser, “Laser Shock Peening for Integral Airframe Structures Applications,” University of the Witwatersrand, 2013.

[97] E. Maawad, Y. Sano, L. Wagner, H.-G. Brokmeier, and C. Genzel, “Investigation of laser shock peening effects on residual stress state and fatigue performance of titanium alloys,” *Mater. Sci. Eng. A*, vol. 536, pp. 82–91, 2012.

[98] A. Gujba and M. Medraj, “Laser Peening Process and Its Impact on Materials Properties in Comparison with Shot Peening and Ultrasonic Impact Peening,” *Materials (Basel).*, vol. 7, no. 12, pp. 7925–7974, 2014.

[99] M. A. Rahim, “Effects of Laser Shot Peening on Friction Stir Welding,” no. October. 2014.

[100] C. Cellard, D. Retraint, M. François, E. Rouhaud, and D. Le Saunier, “Laser shock peening of Ti-17 titanium alloy: Influence of process parameters,” *Mater. Sci. Eng. A*, vol. 532, pp. 362–372, 2012.

[101] O. Hatamleh and A. DeWald, “An investigation of the peening effects on the residual stresses in friction stir welded 2195 and 7075 aluminum alloy joints,” *J. Mater. Process. Technol.*, vol. 209, no. 10, pp. 4822–4829, Jun. 2009.

[102] Y. Liao, S. Suslov, C. Ye, and G. Cheng, “The mechanisms of thermal engineered laser shock peening for enhanced fatigue performance. Acta Mater. 2012, 60, 4997 – 5009.,” *Acta Mater.*, vol. 60, pp. 4997–5009, 2012.

[103] O. Hatamleh, “The Effects of Laser Peening and Shot Peening on Mechanical Properties in Friction Stir Welded 7075-T7351 Aluminum,” *J. Mater. Eng. Perform.*, vol. 77058, no. 281,

pp. 1–23, 2008.

[104] D. Booth and I. Sinclair, “Fatigue of friction stir welded 2024-T351 aluminium alloy,” *Mater. Sci. Forum*, vol. 396–4, no. 3, pp. 1671–1676, 2002.

[105] H. Aydin, A. Bayram, M. T. Yildirim, and K. Yi??it, “Influence of welding parameters on the fatigue behaviours of friction stir welds of 3003-O aluminum alloys,” *Medziagotyra*, vol. 16, no. 4, pp. 311–319, 2010.

A. Appendix A – Apparatus Specifications

A.1 MAHO MH-C700 CNC Milling Machine

Table A.1 lists the possible rotational speeds of the tool spindle achievable on this CNC machine.

Table A.1 - Fixed Gearing Rotational Speeds of Tool Spindle

Rotational Speeds [RPM]		
500	1000	2000
630	1250	
800	1600	

Table A.2 provides a detailed breakdown of the specifications of the milling machine used to complete all FSW presented in this research [21].

Table A.2 - Specifications of MAHO MH-C 700 CNC Milling Machine

Working Capacity:	Longitudinal table traverse, X axis	500 mm
	Vertical table traverse, Y axis	400 mm
	Spindle head cross traverse, Z axis	400 mm
Drives/consumption:	Milling spindle brake motor	4 kW
	DC feed motors	2.2 kW
	Hydraulics and central lubrication	0.8 kW
	Coolant pump	0.12 kW
Horizontal and vertical milling spindle:	Speed range 50/60 Hz	40 – 2000 RPM (Sliding gear box)
	Spindle nose hydraulic tool clamping	ISO 40
Main Transmission:	Sliding gear box, geometric ratio 1.25, Number of speeds	18
Feeds:	Infinitely variable on all axes	1 – 2000 mm/min
Rapid Traverse Rate:	Constant	3 m/min
Measuring System:	Photo-electric linear traverse measuring system for X/Y/Z	0.001 mm

	axis	
Control Unit:	CNC Contouring control NC 6600 with operators panel in the control station	
Weight of machine:	Including control cabinet vertical milling head, universal table	2500 kg
Fixed Table:	Clamping area	800 x 400 mm
	Number of T-slots 14 H 7	8
	Distance between slots	45 mm
	Approx. Weight	160 kg
Indexing Table 72 x 5:	Table with fixed support. Clamping for rotary movement hydro mechanical	
	Indexing performed by AC motor via H-function control	
	Working area	F720 x 420 mm
	Centre bore diameter	300 mm H7
	Number of T-slots 14 H 7	9
	Distance between slots	45 mm
	Approx. Weight	200 kg
Circular table in NC Execution:	Circular movement locked and unlocked hydro mechanical	
	Table is designed so that the circular movement of the table plate is controlled as the 4^{th} axis (B-axis) of control	
	Adaption of measurement directly on circular axis with 0.01 resolution	
	Circular movement via DC motor	
	Circular speed	1 /min-1680 /min 0-4.4/rpm
	Working surface	F720 x 420 mm
	Centre Bore	30 mm H7
	Number of T-slots 14 H 7	9

	Approx. weight	200 kg
Universal Built in Rotary table 72 x 5:	Clamping for circular movements	
	Clamping area	F720 x 420 mm
	Centre bore diameter	300 mm H7
	Number of T-slots	7
	Distance between T-slots	45 mm
	Table circular movement	360
	Worm drive ratio	0.125
	Direct indexing, indirect indexing	72 x 5
	Number of hole circles	18
	Scale drum 1 rev	3
	1 graduation	2’
	Swivel range about trans. axis	30
	Inclining range about long axis	30
	Approx. weight	230 kg

A.2 Quanta Ray Pro-270 Specifications

Table A.2 below provides the specifications of the Quanta Ray Pro-270 Nd:Yag laser used in the completion of all LSP samples.

Table A.3 - Specifications of Quanta Ray Pro-270 Nd:Yag Laser

Power Specifications:	Model	PRO-270
	Rep. Rate	10 Hz
	Wave length	1064 nm
	Energy	1 -1750 mJ/p
Performance (wavelength of 1064 nm):	Pulse width	8 – 12 ns
	Short term energy stability	±2%
	Long term power drift	< 3%
Mode:	Beam diameter, Pro -200 range	<10 mm
	Spatial mode profile, standard fit, near field (1m)	> 70%
	Spatial mode profile, standard fit, far field (	>95%

	Spatial mode profile, standard fit, Modulation	<40%
Pulse:	Line width, standard	<1.0 /cm
	Line width, injection seeded	<0.003 /cm
	Timing jitter	<0.5 ns
BeamLok Specifications:	Pointing stability	<± 50 µrad
	Beam divergence	< 0.5 mrad
	Lamp lifetime	30 million pulses
	Remote control	Analogue

A.3 Kistler Multicomponent Force Link Set Type: 9366CC0.5 Specifications

Table A.3 below provides the specifications of the Kistler multicomponent force link set type: 9366CC0.5 used in the monitoring and capture of force data during FSW [88].

Table A.4 - Kistler Multicomponent Force Link Set Type: 9366CC0.5 Specifications

Force Measuring Ranges:	Longitudinal table direction, F_x	-25 to 25 kN
	Vertical table direction, F_y	-25 to 25 kN
	Spindle head direction, with mounted steel plate on top, F_z	-25 to 60 kN
Temperature	Operational temperature ranges	-20 to 70 °C
Measurement Capability	Force directions	F_x, F_y, F_z
	Moment directions	M_x, M_y, M_z

A.4 FLIR T640 Thermal Camera Specifications

Table A.4 lists the detailed specifications of the FLIR T640 thermal imaging camera [89].

Table A.5 – FLIR T640 Thermal Camera Specifications

Imaging and Optical Data:	Field of view	25° x 19° / 0.25 m
	Spatial resolution	0.68 mrad
	Thermal sensitivity	<40mK @ +30°C
	Image frequency	30 Hz
	Focus	Automatic or manual

	Zoom	1-8x
	IR resolution	640 x 480 pixels
Measurement:	Temperature ranges	-40 to +150 °C +100 to 650 °C +300 to +2000 °C
	Accuracy	±2°C or ±2% of reading
Measurement Analysis:	Reference temperature	Manually set or captured from any measurement function
	Emissivity correction	Variable from 0.01 to 1 or selected from materials list

A.5 Coherent Field Max II – Top Laser Energy/Power Meter

Table A.5 lists the detailed specifications of the Coherent Field Max II – Top Laser Energy/Power Meter.

Table A.6 – Coherent Field Max II – Top Laser Energy/ Power Meter

Electrical and Mechanical:	Analogue output	1, 2, or 5V full-scale 100 ohm source impedance
	Calibration accuracy	± 1%
	Digital tuning needle	100 mS 20 Hz
	Pyroelectric input (maximum voltage input)	18 V
	Measurement resolution	± 0.1% of full scale
Ranges:	Measurement range (full scale, sensor-dependent) Energy Mode	

	Power Mode	3 nJ to 300 kJ 3 nW to 300 kW
	Rep rate	± 1Hz (accuracy) 300 Hz (maximum) 1 Hz (resolution)
Physical Characteristics:	Dimensions (h x w x d)	20 cm x 10 cm x 4 cm
	Display	58x 73 mm fixed –segment LCD with backlight
	Weight	0.5 kg

A.6 Coherent EnergyMax J-10GE-LE Photodiode

Table A.6 lists the detailed specifications of the Coherent EnergyMax J-10GE-LE photodiode.

Table A.7 - Coherent EnergyMax J-10GE-LE Photodiode Specifications

Measuring Capabilities:	Energy range	200 pJ to 400 nJ (@ 1064 nm)
	Noise equivalent energy	< 8 pJ (@ 1064 nm)
	Wavelength range (nm)	800 to 1700
	Maximum average power	15 mW
	Maximum repartition rate	10000 pulse/s
	Maximum pulse width	1 µs
Sensor:	Active area diameter	10 mm
	Sensor material	Germanium

B. Appendix B – Engineering Drawings

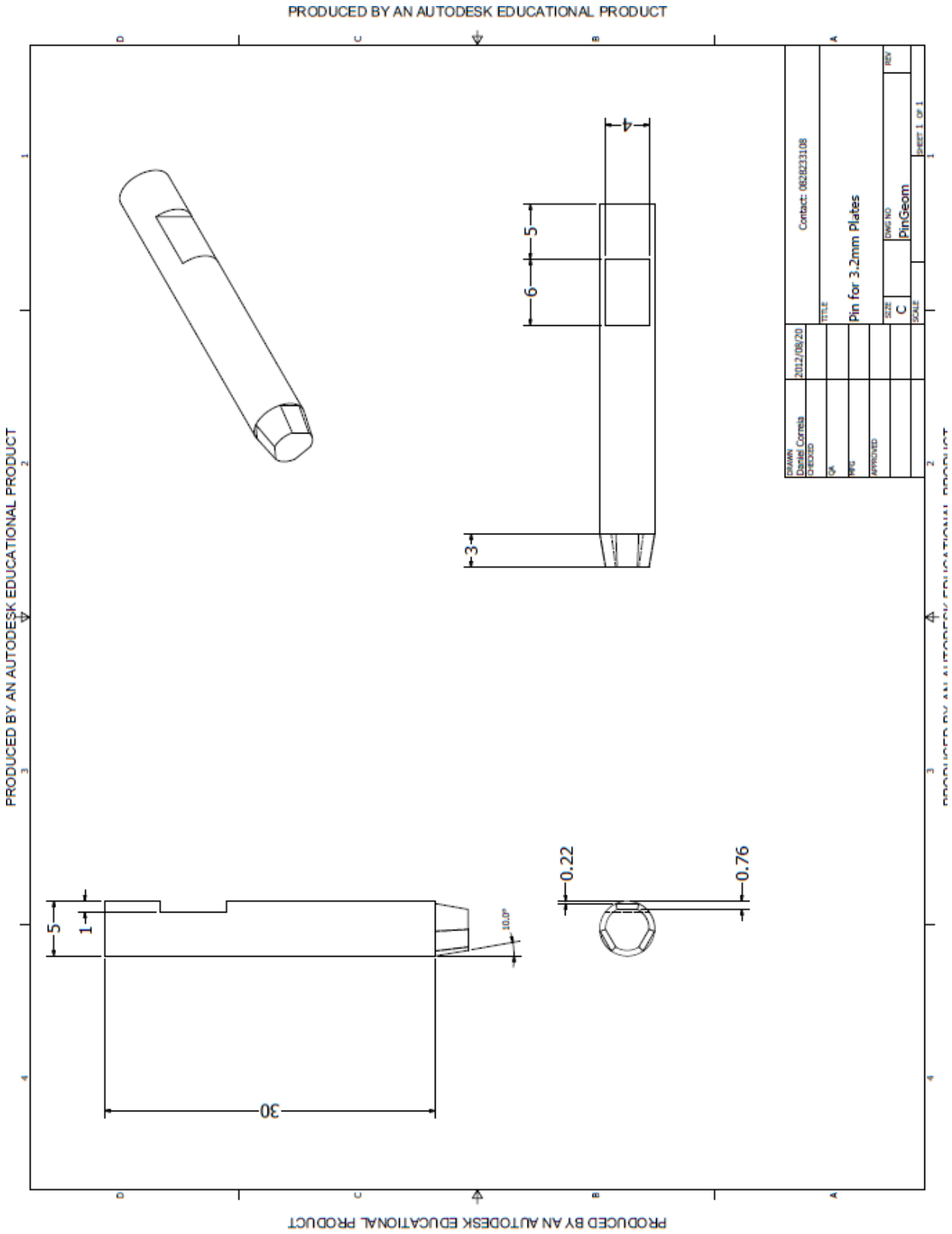

Figure B.1 - Engineering Drawing of Welding Pin

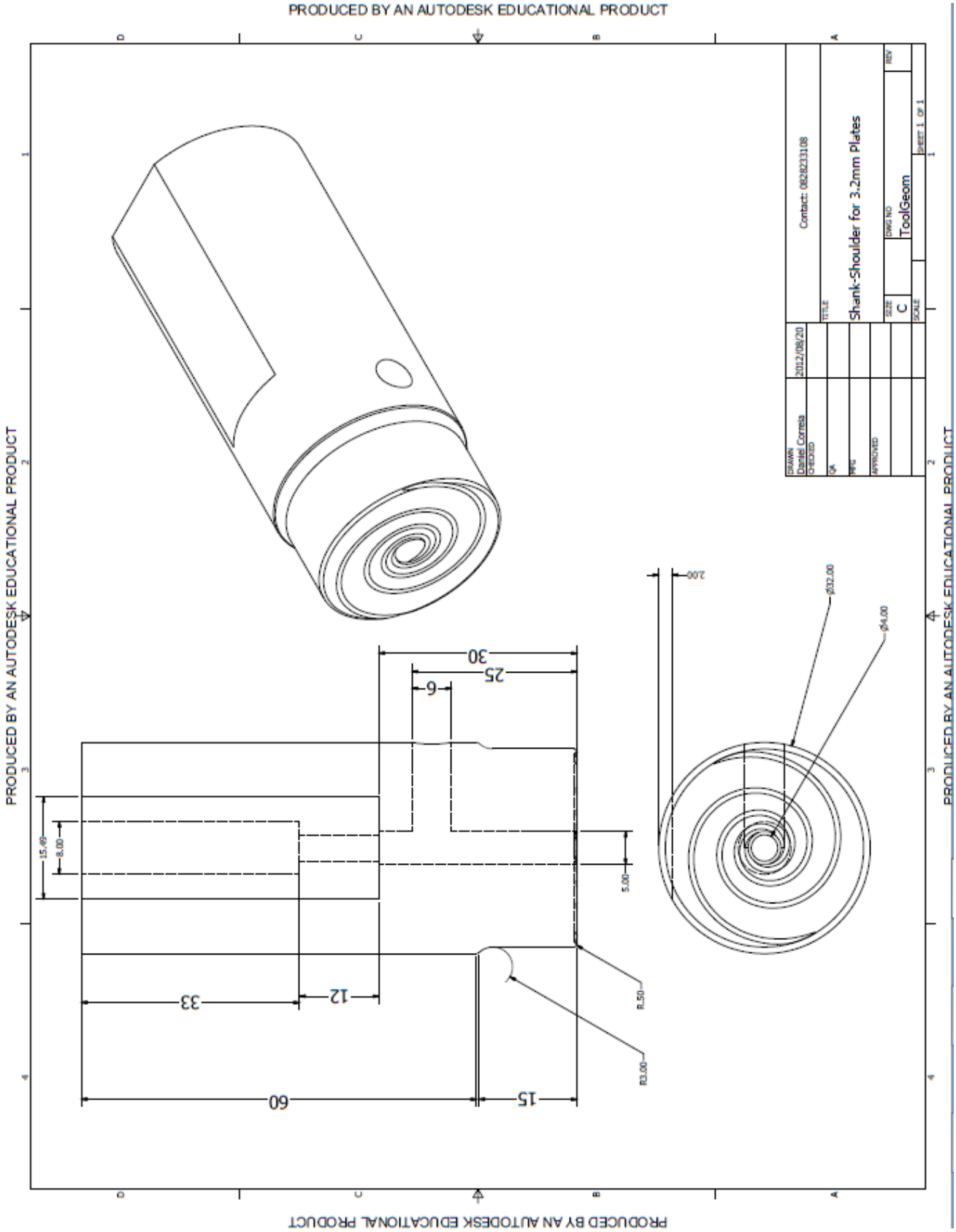

Figure B.2 - Engineering Drawing of Welding Shoulder

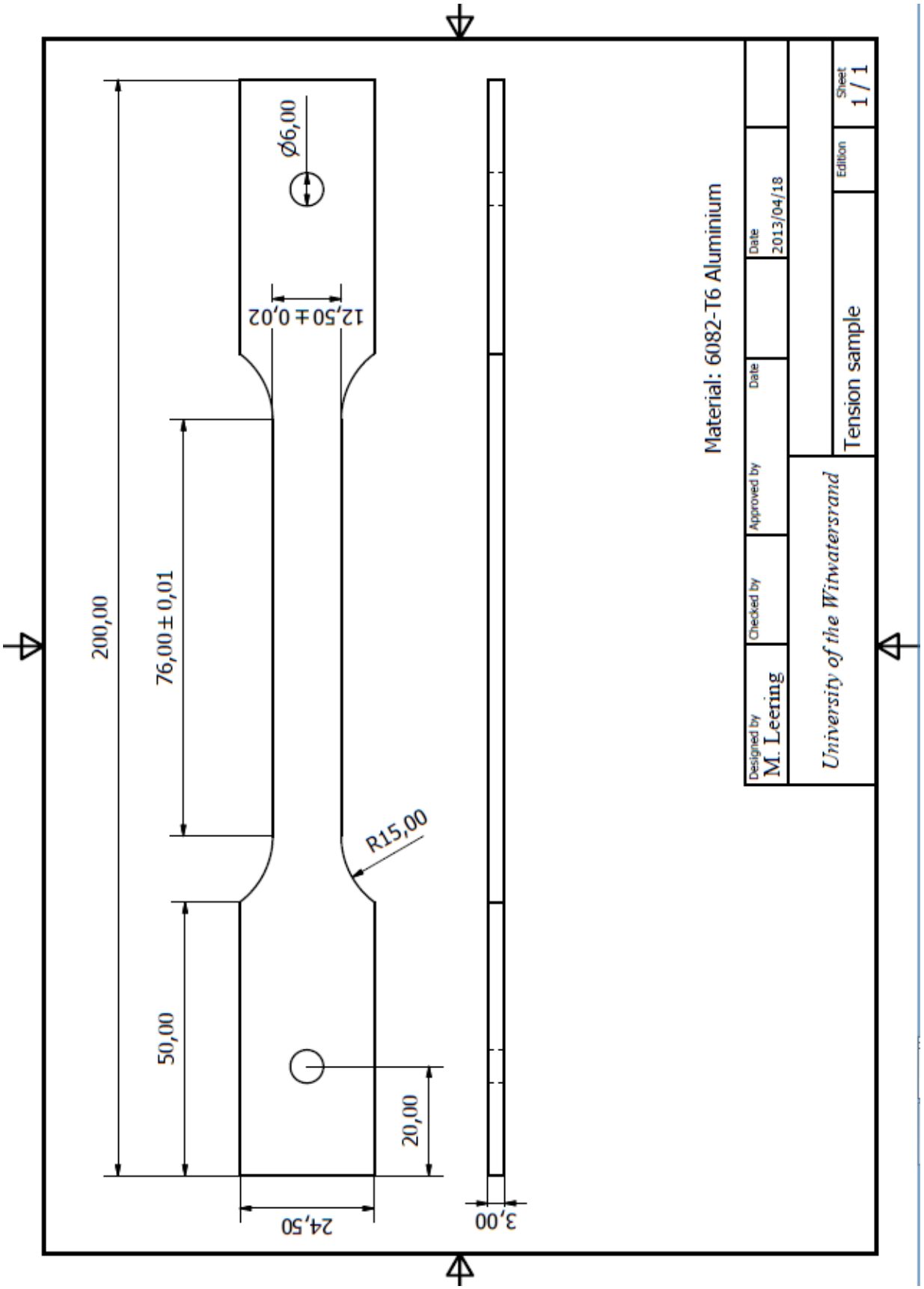

Figure B.3 - Tensile Test Dog Bone Drawing

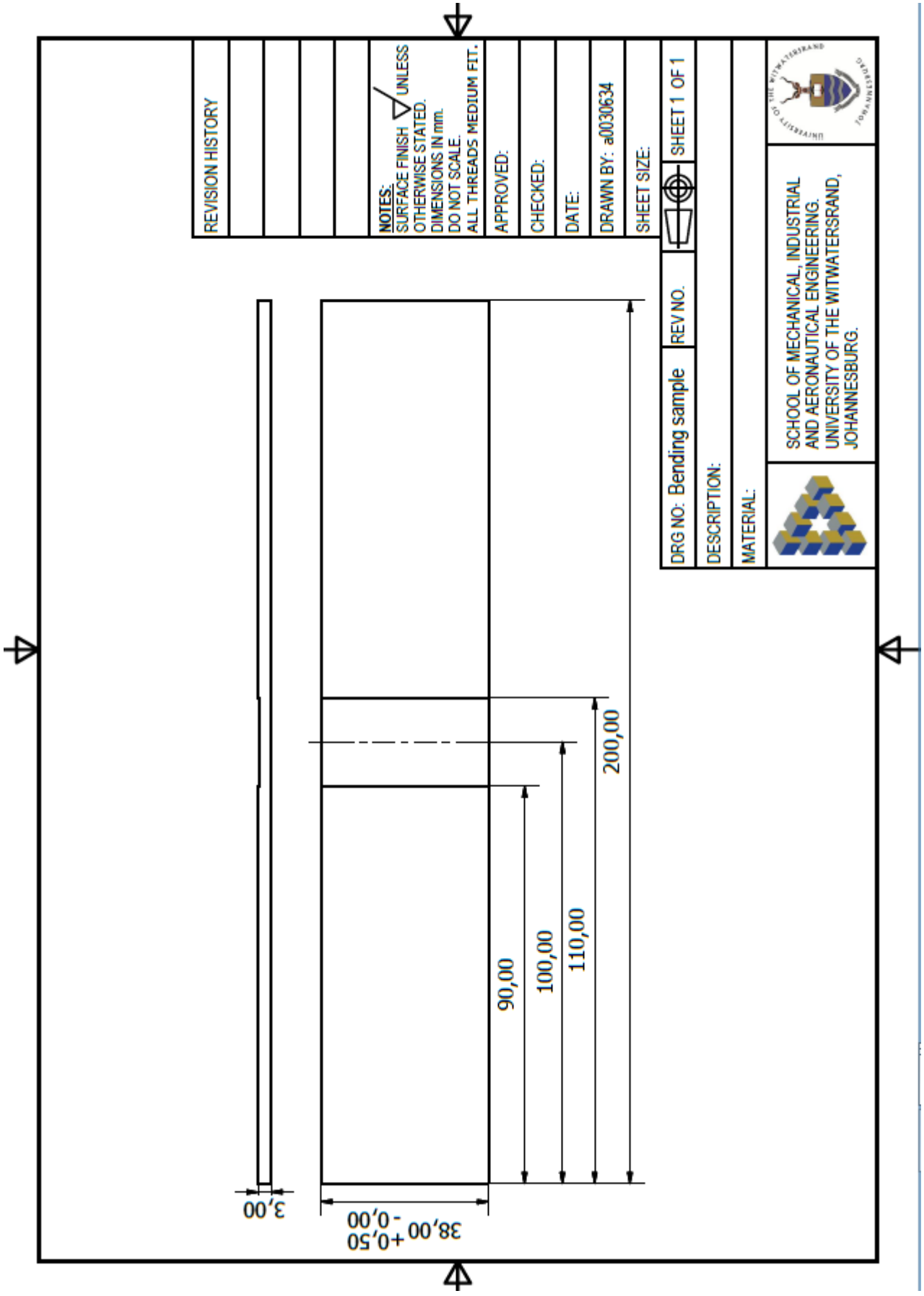

Figure B.4 – Three Point Bending Coupon

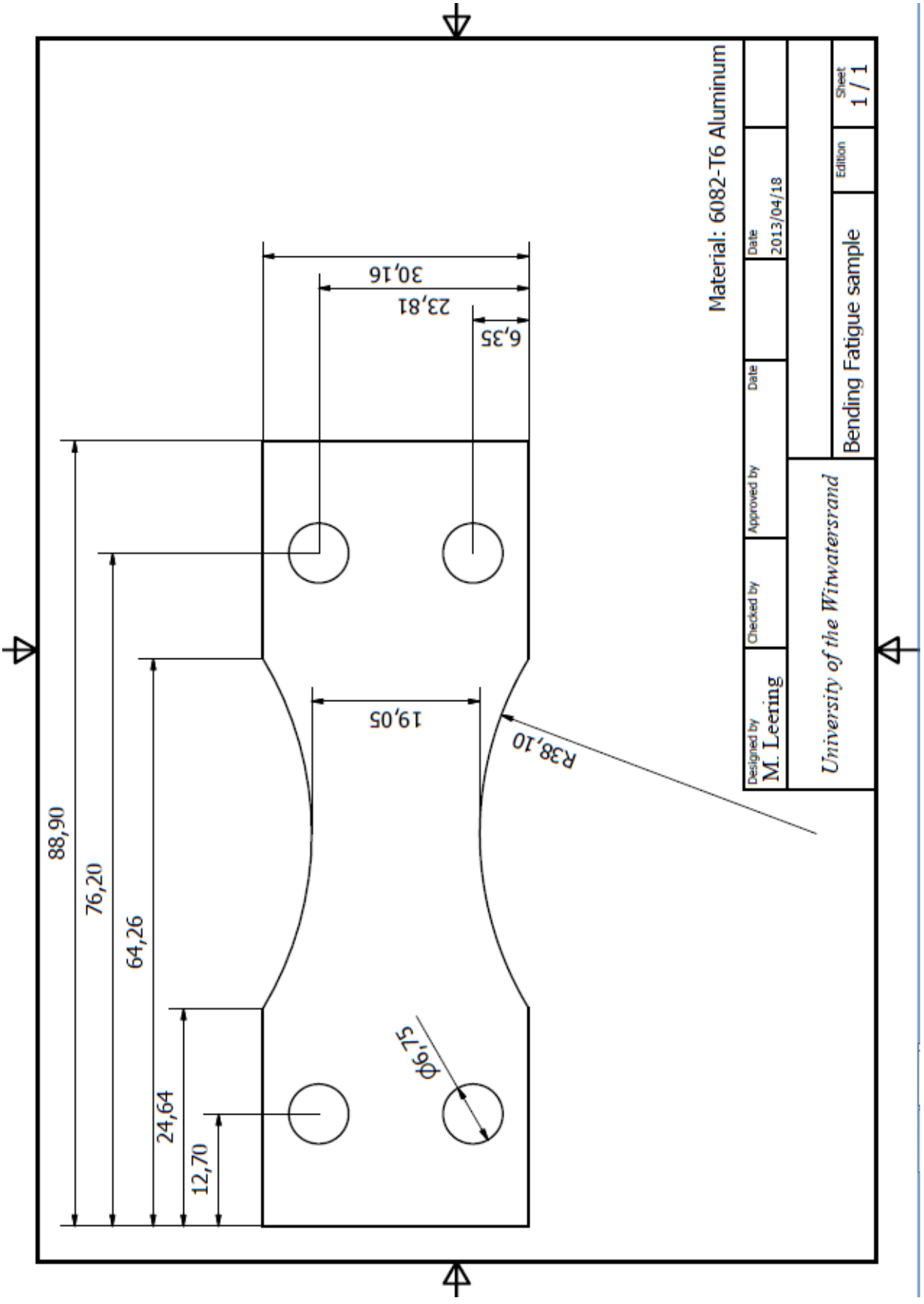

Figure B.5 –Bending Fatigue Coupon Dimensions

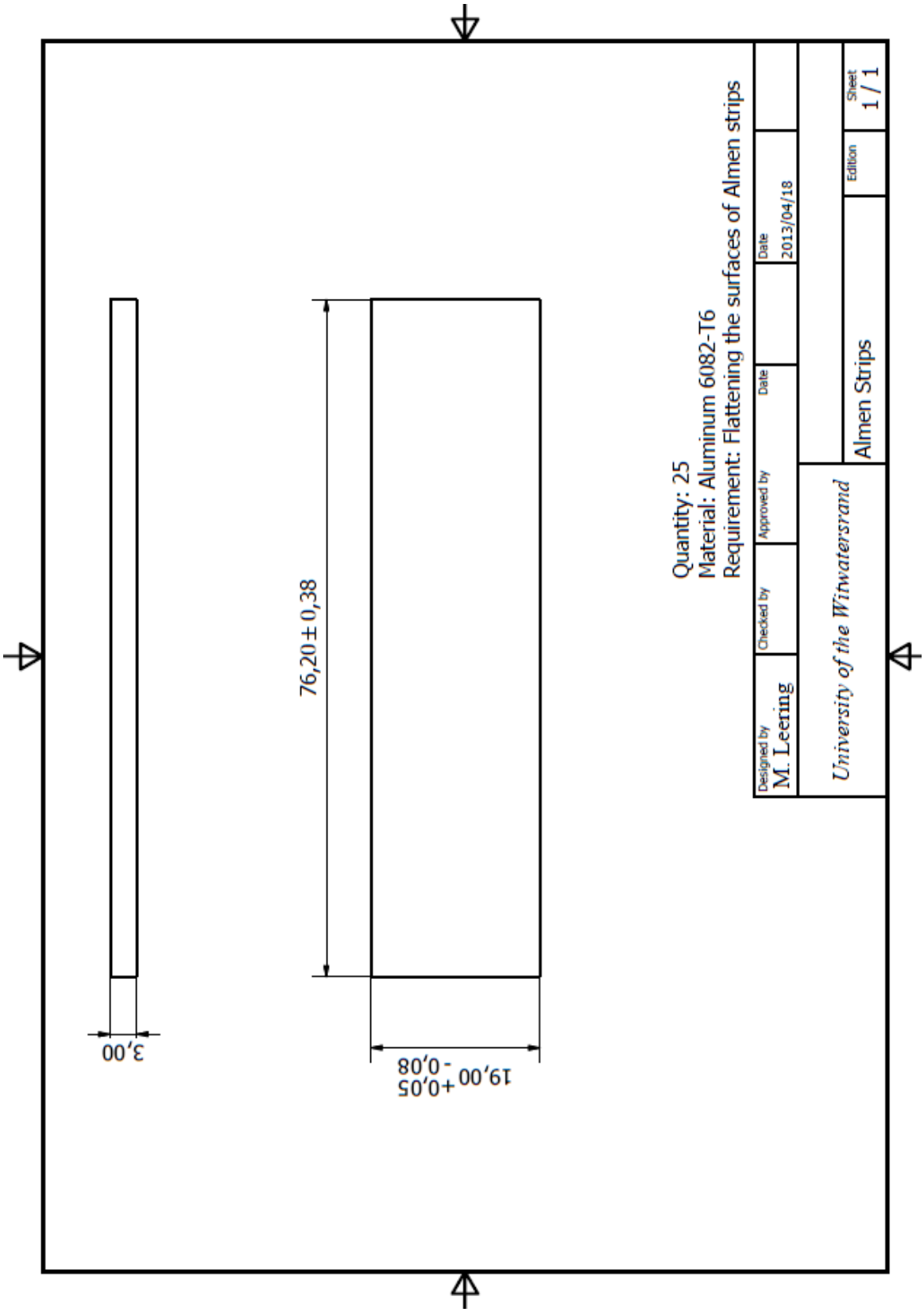

Figure B.6 - Almen Strip Geometry

C. Appendix C – Additional Data

This portion of this document holds any addition data or information pertaining to this research which was deemed not critical to the progression of the report but was still referred to in the text.

C.1 Additional Data for Force Monitoring during Friction Stir Welding

Table C.1 lists the maximum loads achieved during the plunge portion of the weld. The effects of feed rate did not influence the magnitude of these forces due to the tool only traversing in the normal direction. Figure C.1 and Figure C.2 shows the approximately similar magnitudes of the maximum forces recorded during the interaction of the pin and shoulder of the tool whilst welding. Increasing the spindle speed reduced the magnitudes of the recorded forces.

Table C.1 – Maximum Vertical Forces caused by Friction Stir Welding Pin and Shoulder during Plunge

RPM		**630**		**800**		**1000**		**1250**		**1600**	
Forces [N]		**Max Pin**	**Max Shldr.**	**Max Pin**	**Max Shldr.**	**Max Pin**	**Max Shldr.**	**Max Pin**	**Max Shldr.**	**Max Pin**	**Max Shldr.**
Feed Rate [mm/min]	**200**	6954.4	14589.8	4993.9	14727.8	3891.6	12266.8	3372.8	11171.9	2861.3	9950.0
	400	6413.6	13984.4	4929.2	14808.3	3989.3	12584.2	3236.1	11154.8	2700.2	9814.5
	600	6666.3	14227.3	5015.9	14044.2	4176.0	12454.8	3463.1	11024.2	3250.7	10388.2

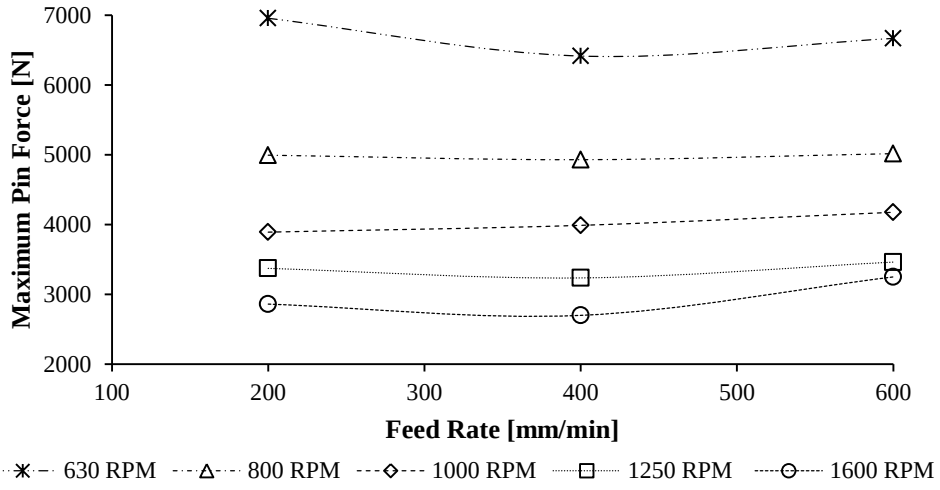

Figure C.1 – Maximum Pin Loads variation With Friction Stir Welding Parameters

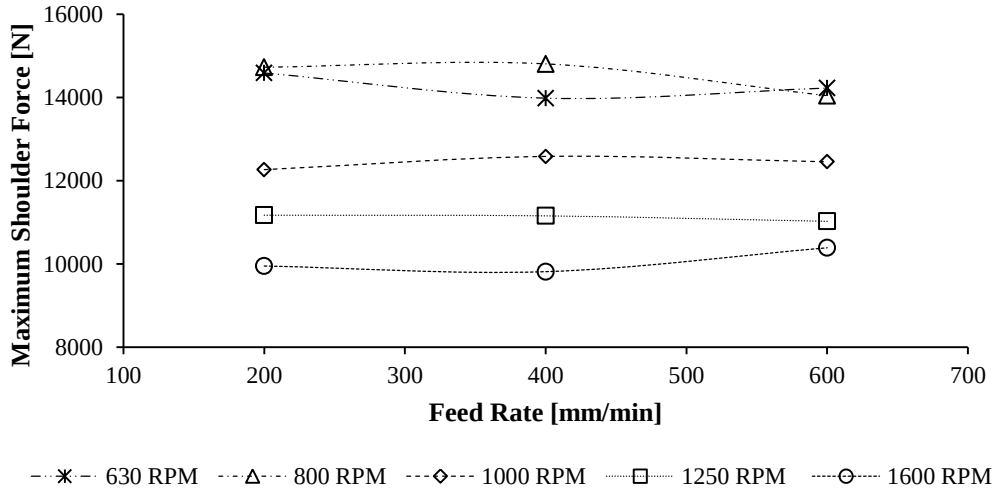

Figure C.2 -Maximum Shoulder Load variation With Friction Stir Welding Parameters

C.2 Additional Thermal Data pertaining to the Friction Stir Welding Process

This portion of this document holds any addition data or information pertaining to thermal effects of the Friction Stir Welding process.

Figure C.3 indicates the change in temperature due to the reduction in welding force [30]. Figure C.4 in Appendix C.2 shows the probe positions, the temperature history of each probe, the temperature surface over the length of the weld and the temperature surface during the feed stage for the various welding parameter combinations that were investigated.

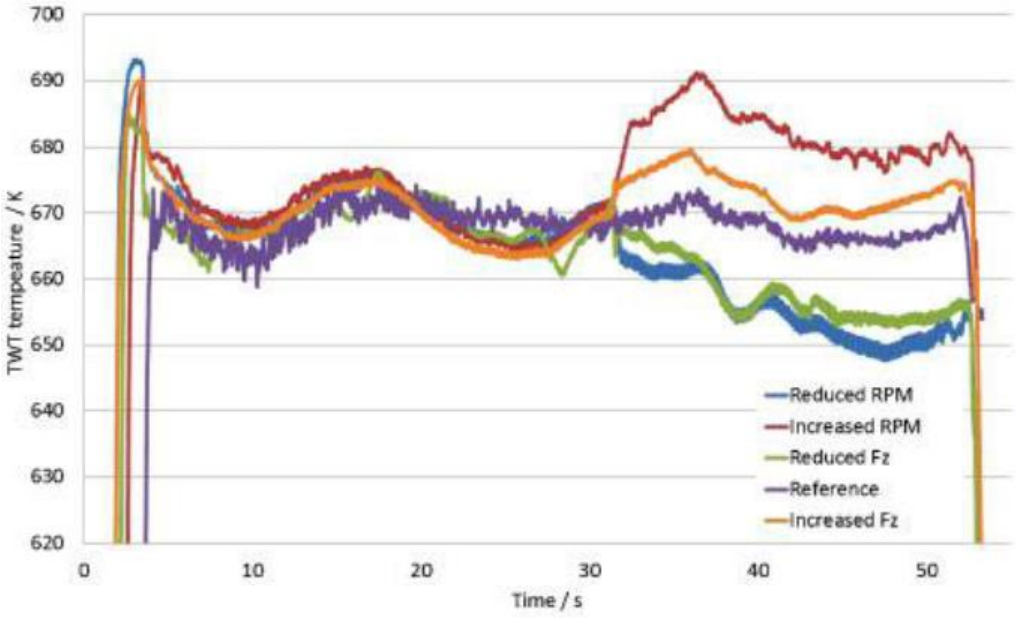

Figure C.3 – Variation in Welding Temperature due to Changing Friction Stir Welding Normal Force

Figure C.4 – Influence of Friction Stir Welding Parameter Change on Welding Temperature

Weld Parameters	Probe Positions (All images at x5 zoom)	Full Weld Temperature Surface	Temperature Surface during Feed
630 RPM 200 mm/min 0 - 660°C	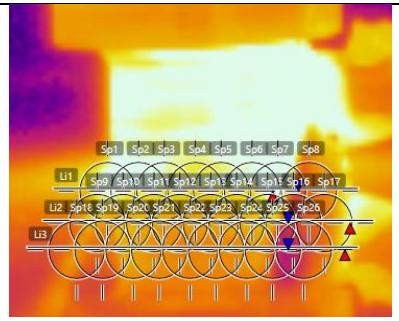	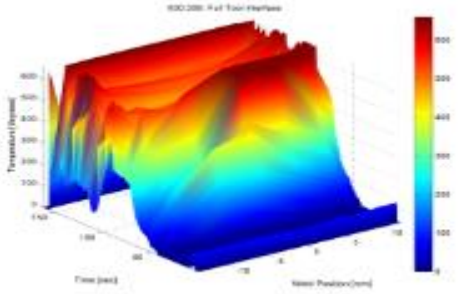	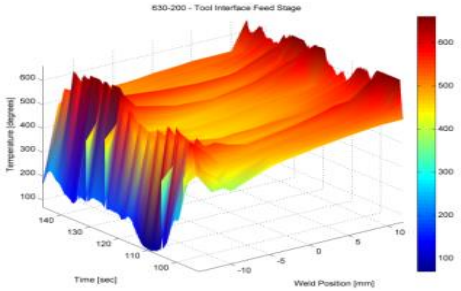
630 RPM 400 mm/min 0 - 660°C	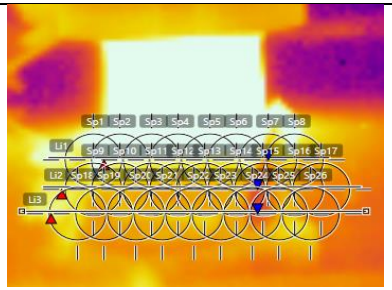	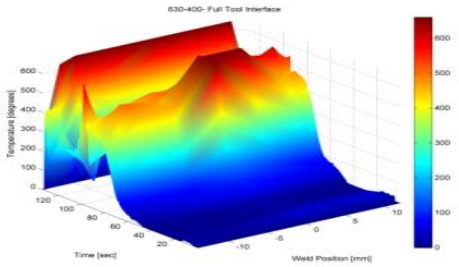	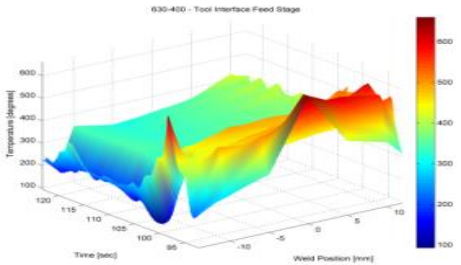
630 RPM 600 mm/min 0 - 660°C	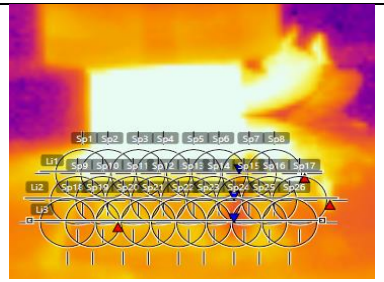	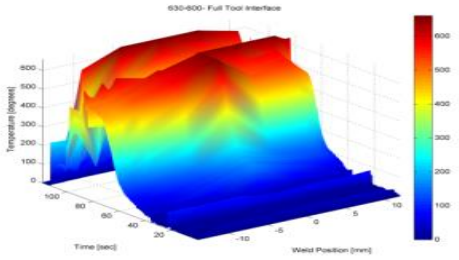	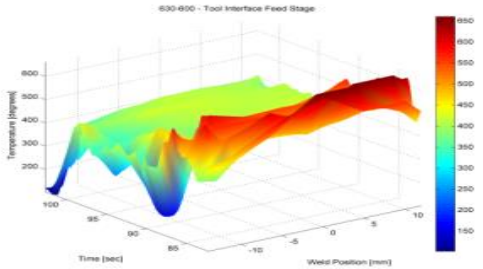

800 RPM 200 mm/min 0 - 660°C	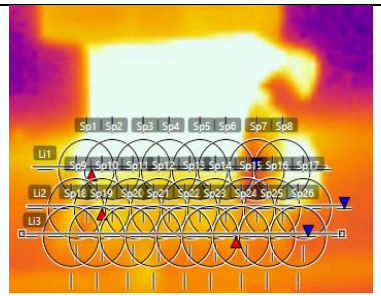	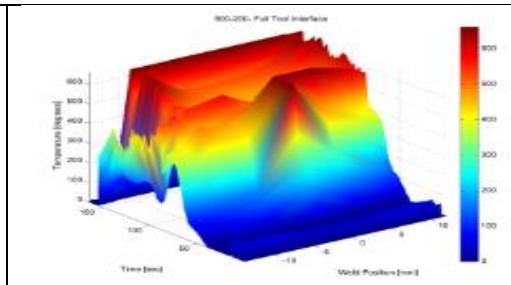	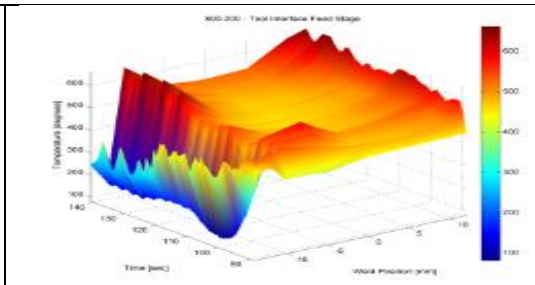
800 RPM 400 mm/min 0 - 660°C	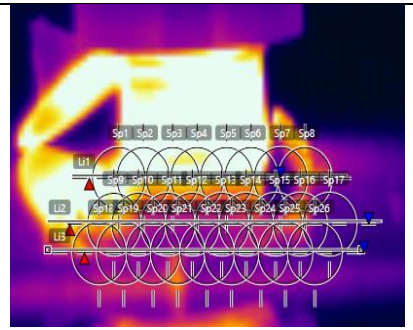	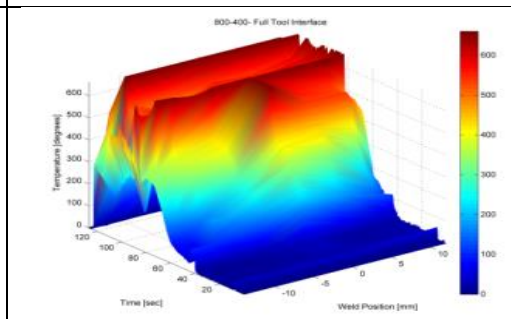	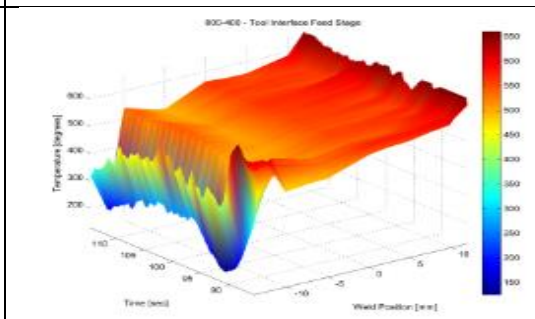
800 RPM 600 mm/min 0 - 660°C	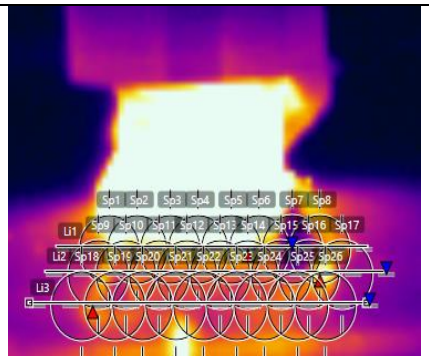	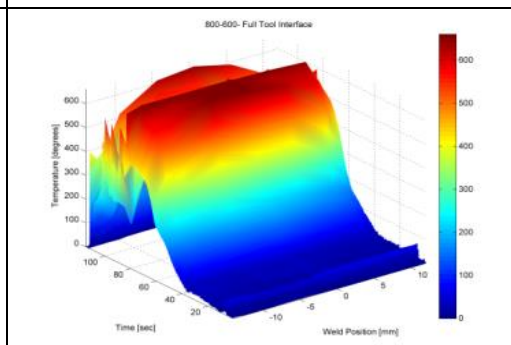	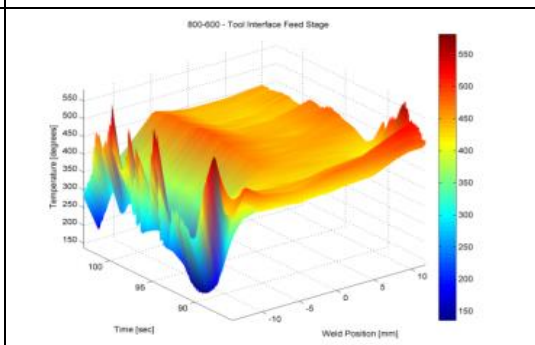

1000 RPM 200 mm/min 0 - 660°C	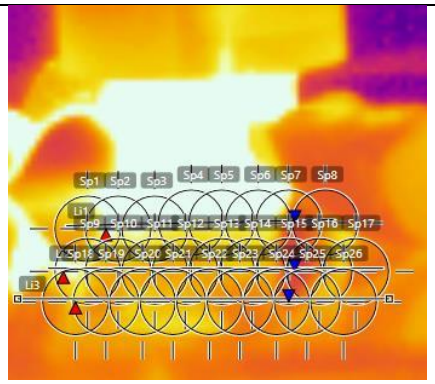	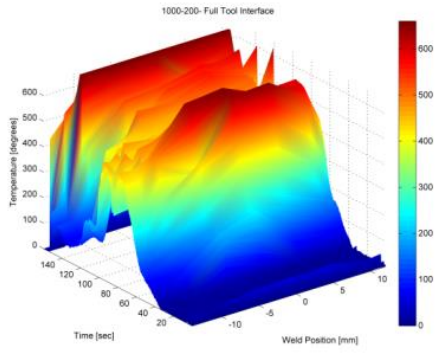	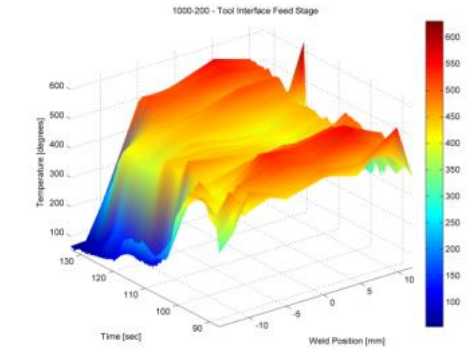
1000 RPM 400 mm/min 0 - 660°C	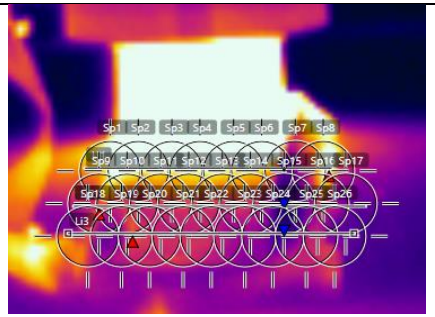	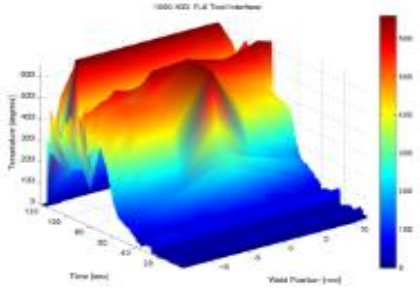	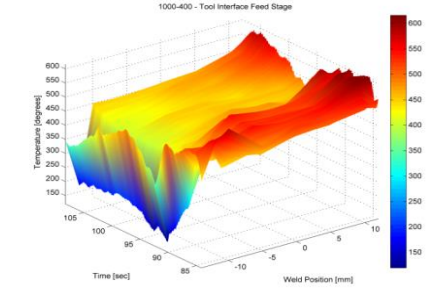
1000 RPM 600 mm/min 0 - 660°C	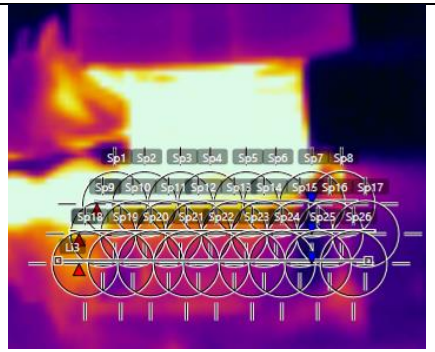	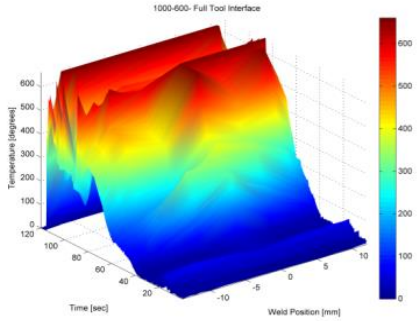	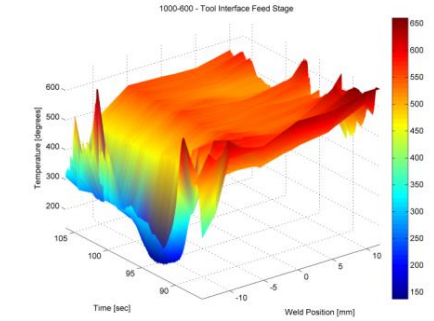

1250 RPM 200 mm/min 0 - 660°C	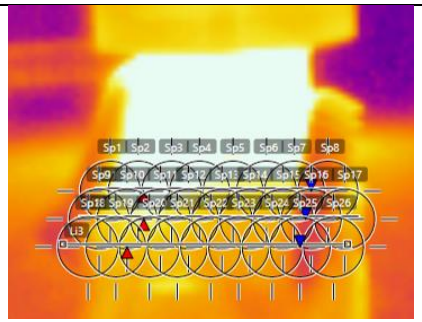	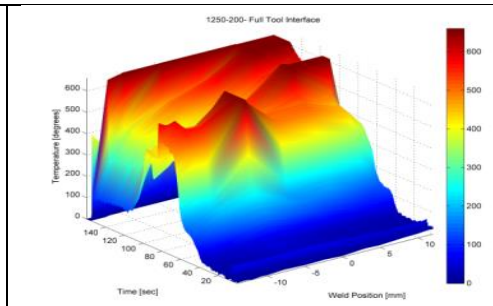	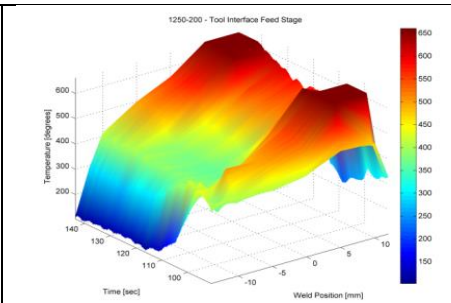
1250 RPM 400 mm/min 0 - 660°C	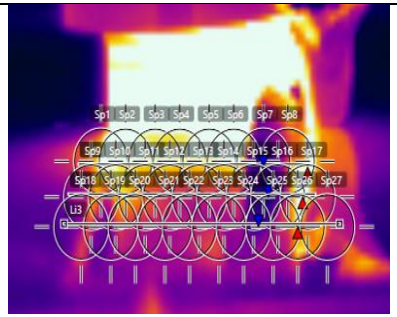	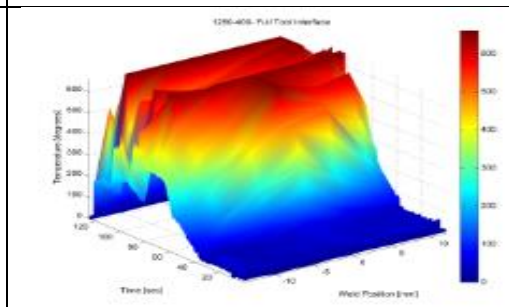	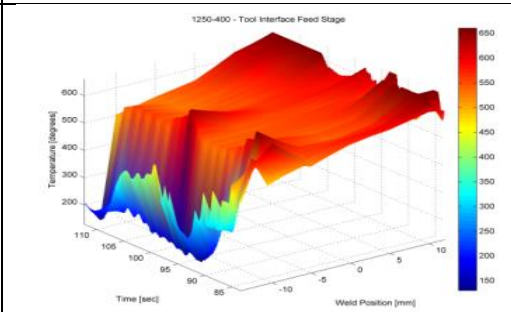
1250 RPM 600 mm/min 0 - 660°C	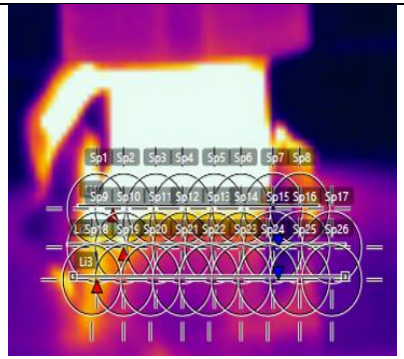	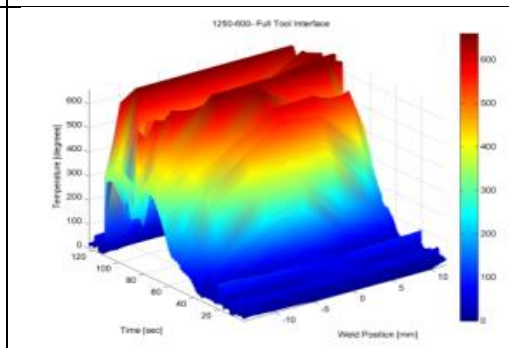	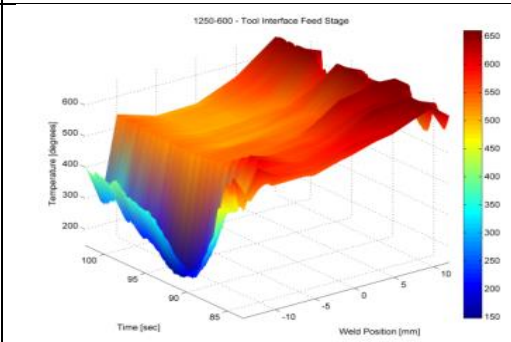

1600 RPM 200 mm/min 0 - 660°C	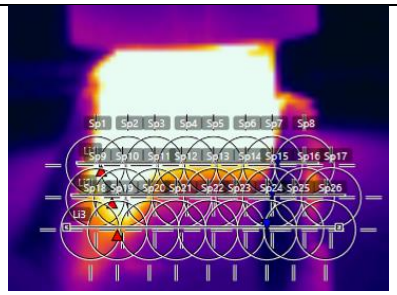	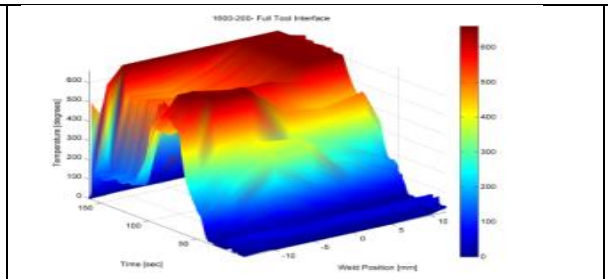	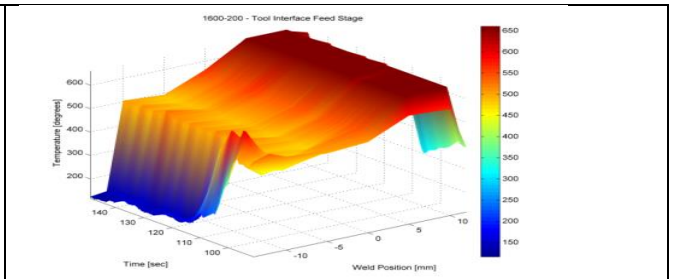
1600 RPM 400 mm/min 100 – 3000°C	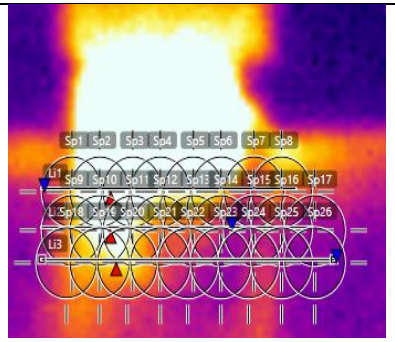	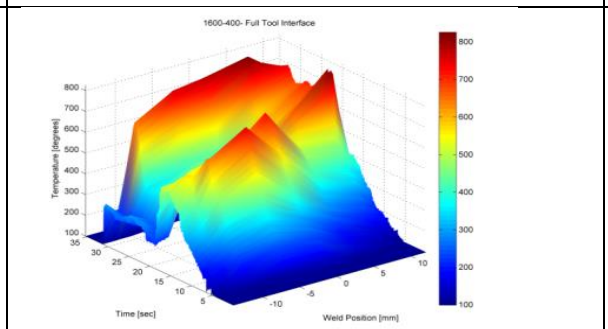	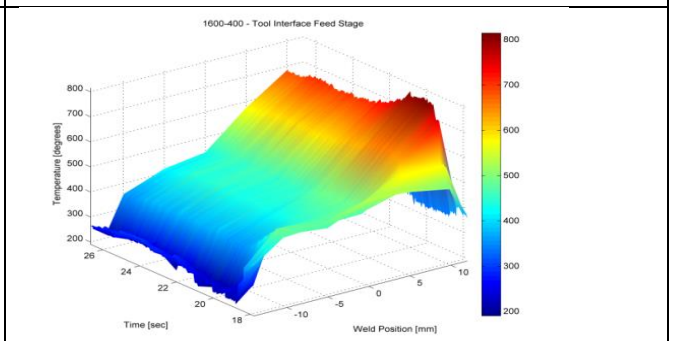
1600 RPM 600 mm/min 0 - 660°C	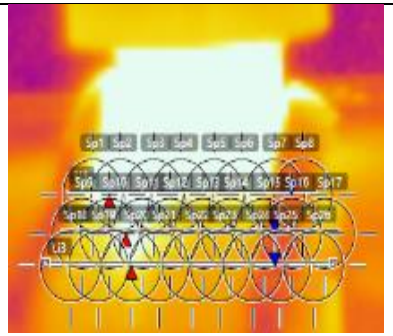	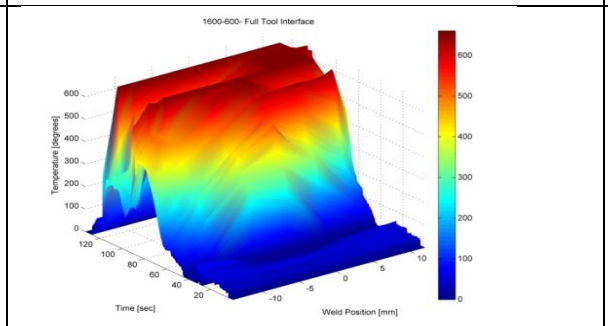	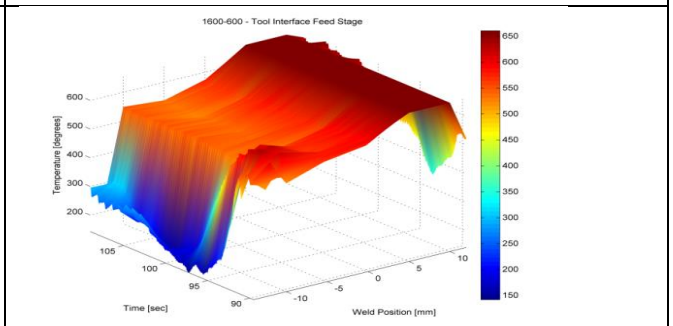

C.3 Additional Strength of Friction Stir Welded Joints Data

This section covers all additional information regarding the static testing of the Friction Stir Welded joints.

C.3.1 Additional Data on Tensile Testing of Friction Stir Welded Joints

Figure C.5 illustrates the engineering stress and strain curves of the reaming tool rotations that were investigated.

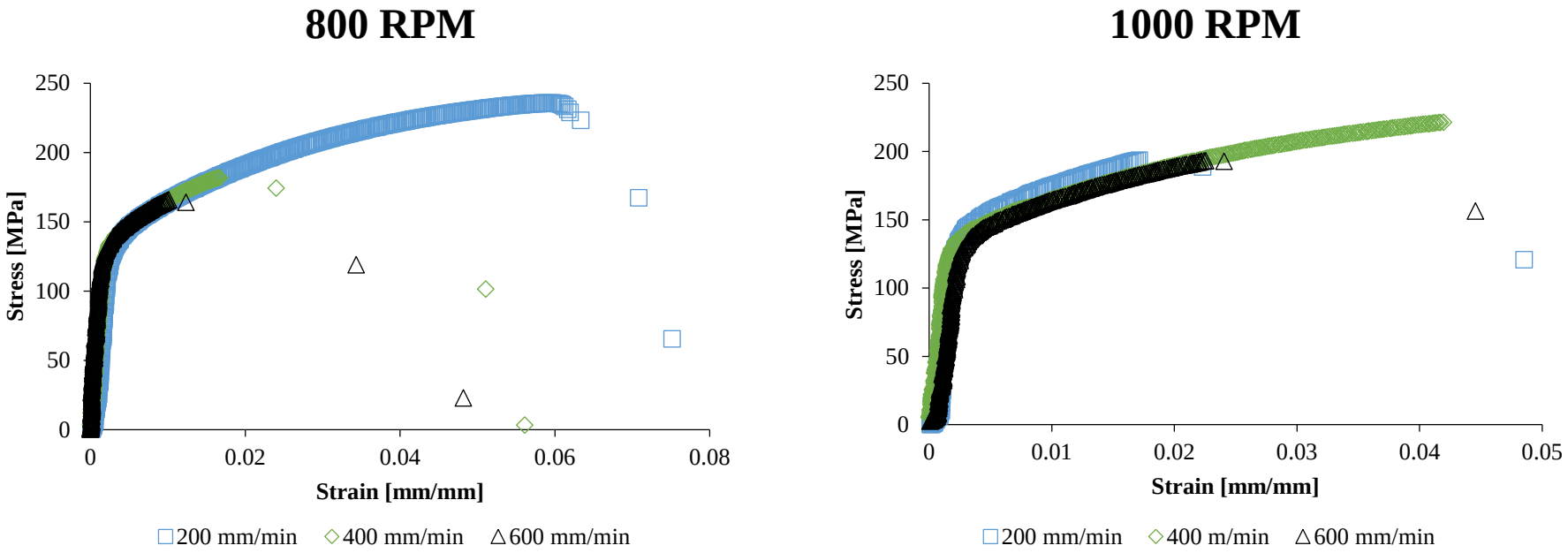

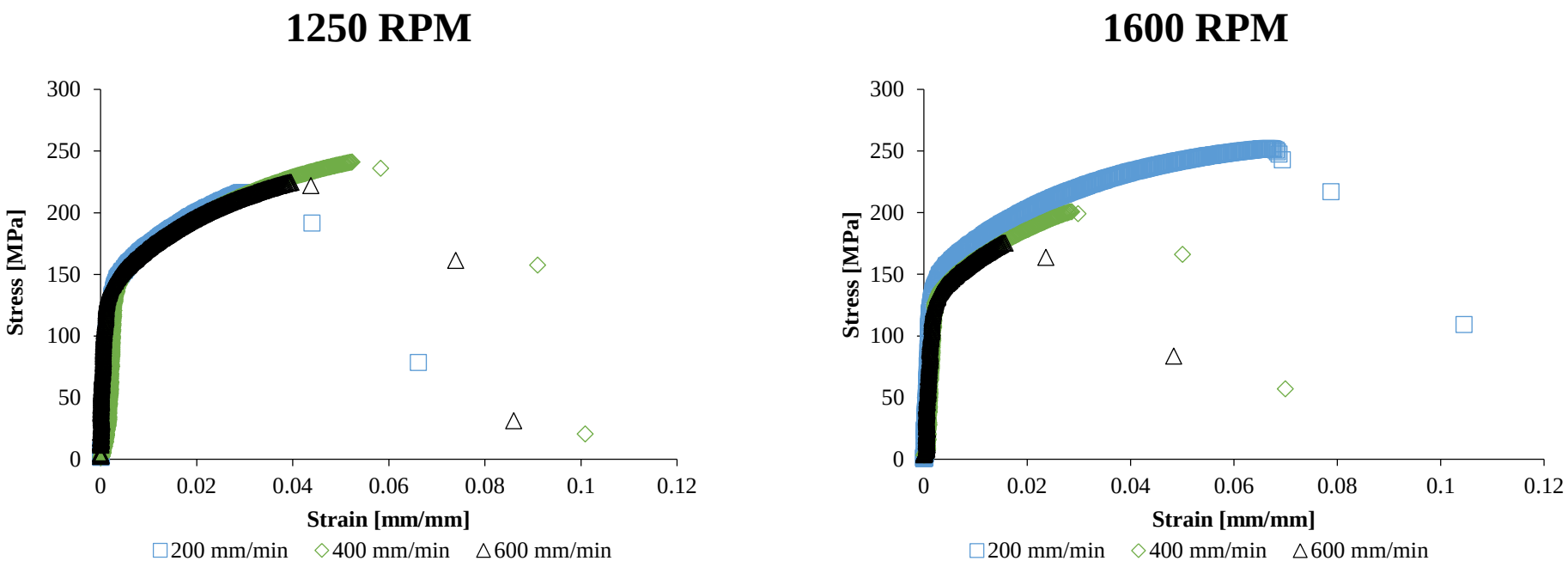

Figure C.5 - Additional Engineering Stress-Strain Plots for Various Tool Rotational Speed

C.3.2 Additional Data on Bending Testing of Friction Stir Welded Joints

Figure C.5 illustrates the engineering stress and strain curves of the reaming tool rotations that were investigated.

Parameters	Force – Displacement Plot	Parameters	Force – Displacement Plot
630 RPM 200 mm/min	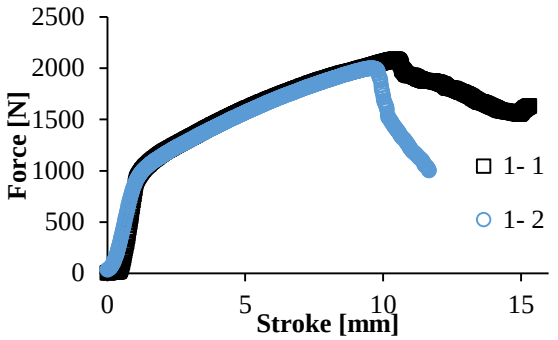	630 RPM 400 mm/min	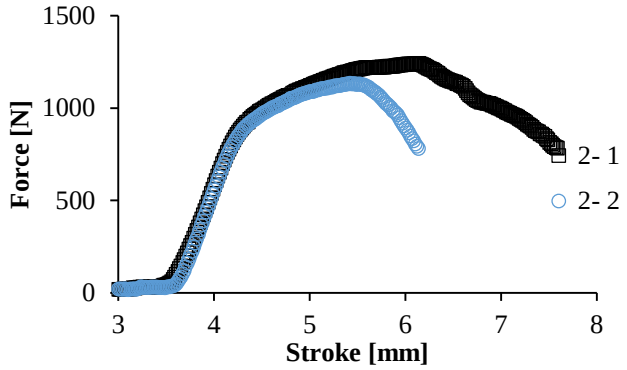
630 RPM 600 mm/min	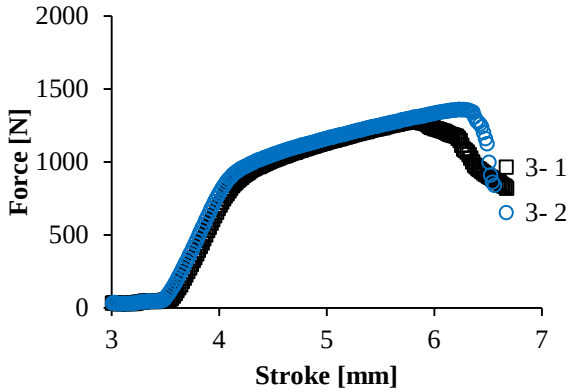	800 RPM 200 mm/min	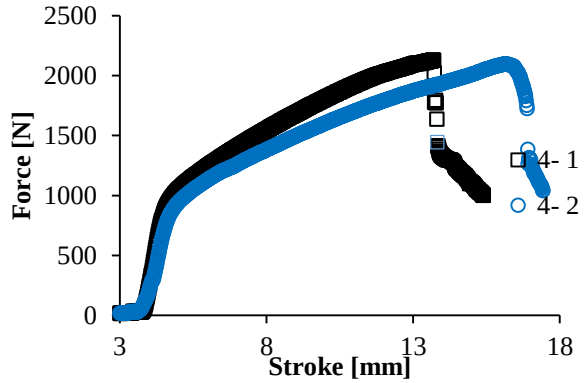

800 RPM 400 mm/min	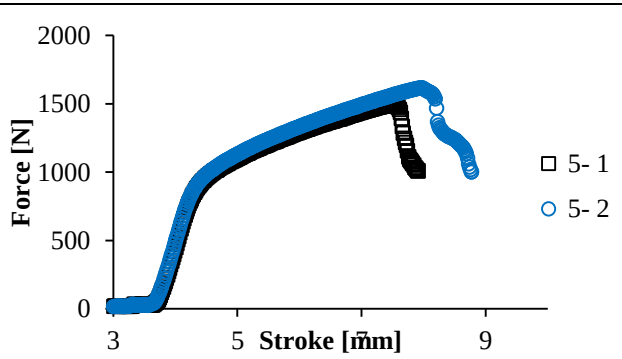	800 RPM 600 mm/min	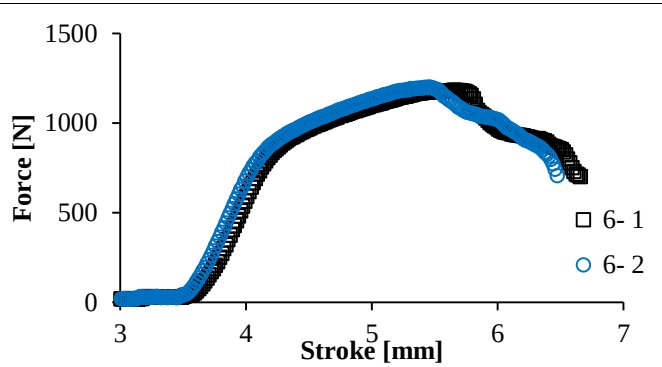
1000 RPM 200 mm/min	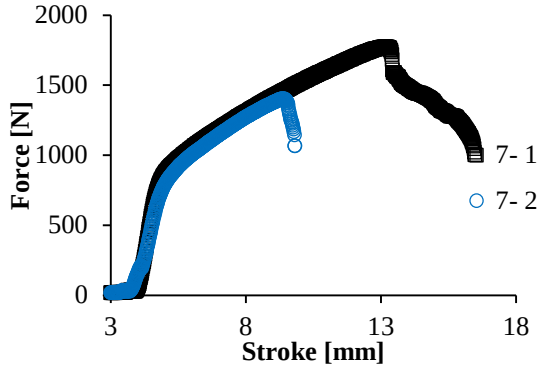	1000 RPM 400 mm/min	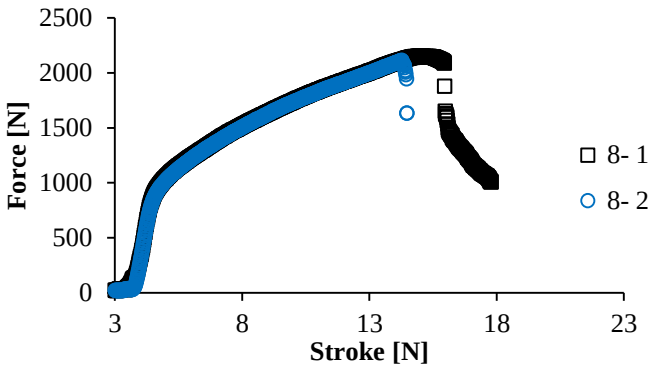
1000 RPM 600 mm/min	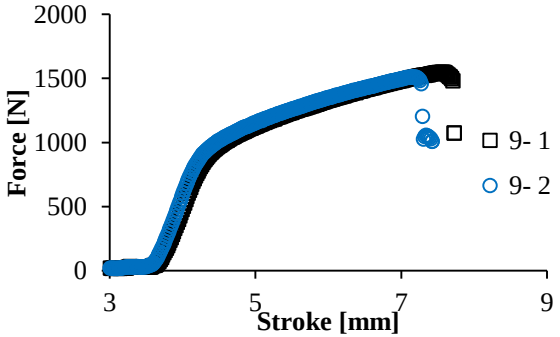	1250 RPM 200 mm/min	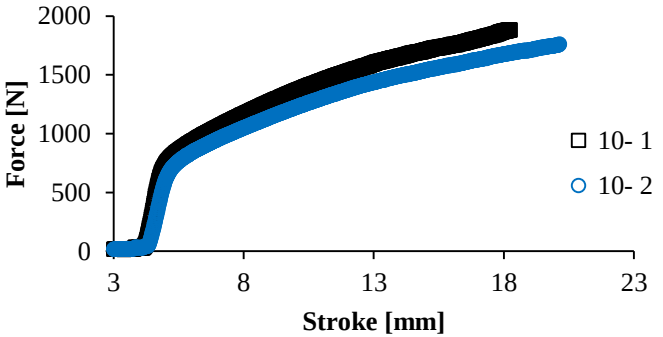

1250 RPM 400 mm/min	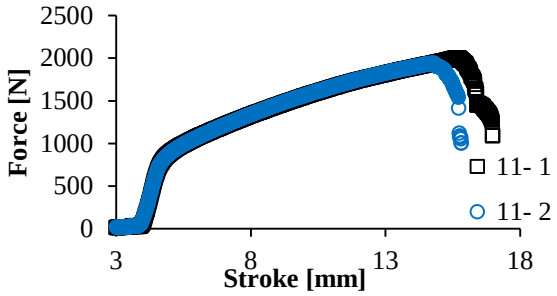	1250 RPM 600 mm/min	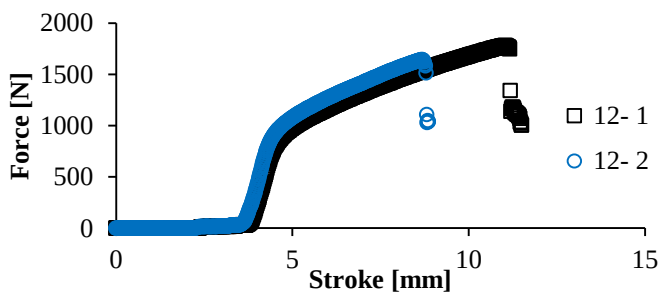
1600 RPM 200 mm/min	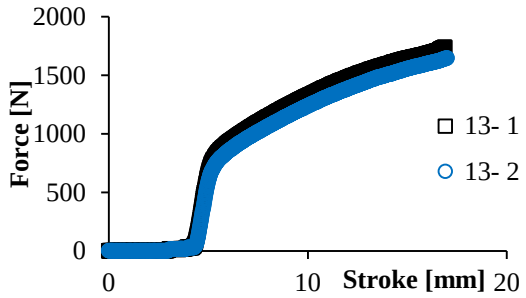	1600 RPM 400 mm/min	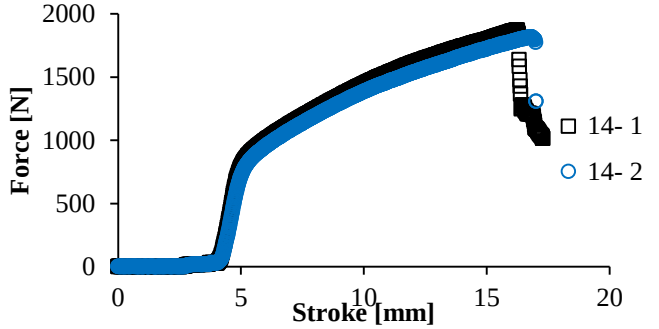
1600 RPM 600 mm/min	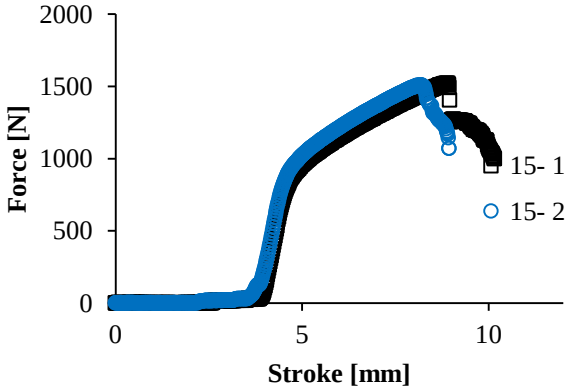		

Figure C.6 - Measured Output of Bending Force with Plunger Stroke for Three Point Bending Tests

C.4 Additional Data on Penetration Depth of the Effects of Laser Shock Peening

This section covers all additional information regarding the measurement of the variation in hardness of a FSW joint which has been LSP processed under a variety of processing parameter combinations. The region in which the hardness profiles become linear was the depth at which the effects of LSP were no longer seen. Figure C.7 to Figure C.9 illustrate the measured hardness profiles from the root surface to the crown of the peened FSW joints at various laser power intensities.

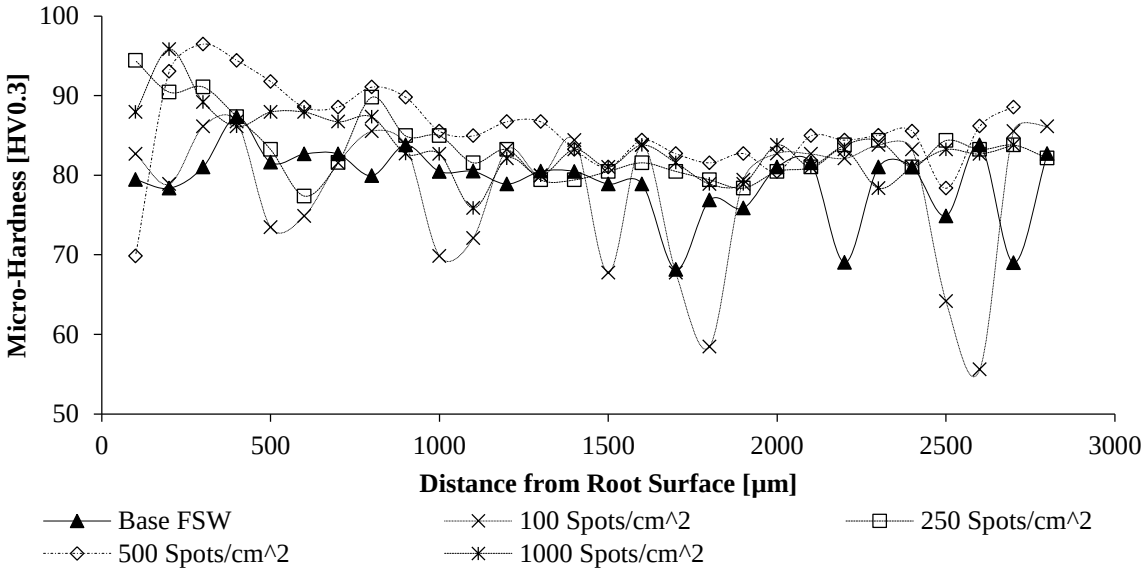

Figure C.7 – Micro-Hardness through the thickness of the Friction Stir Welded Joint which had been Laser Shock Peened at a Power Intensity of 1 GW/cm^2

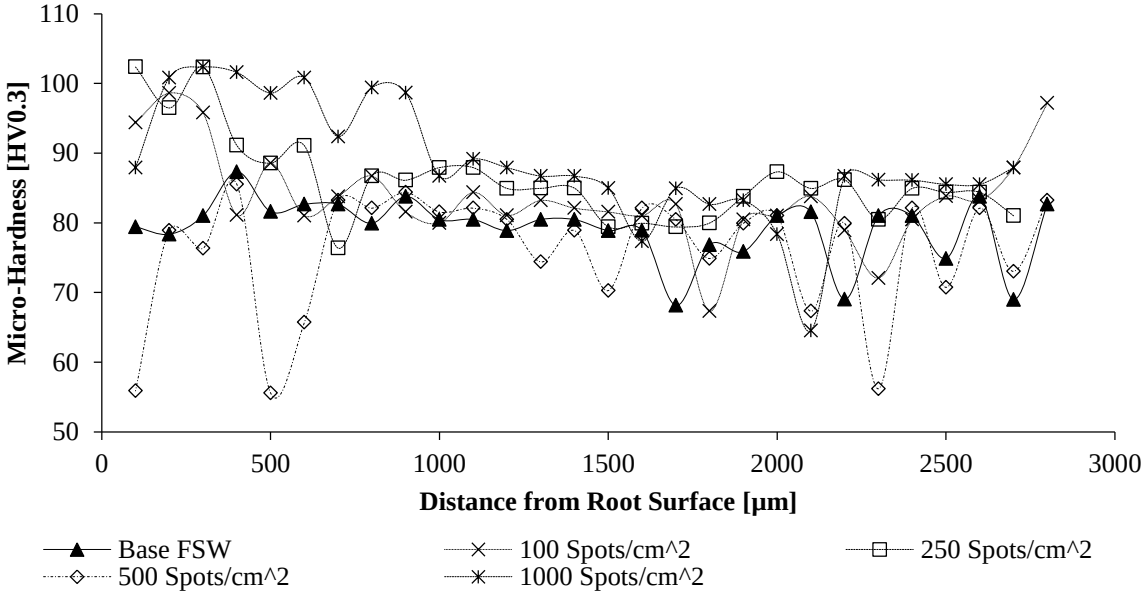

Figure C.8 - Micro-Hardness through the thickness of the Friction Stir Welded Joint which had been Laser Shock Peened at a Power Intensity of 2 GW/cm^2

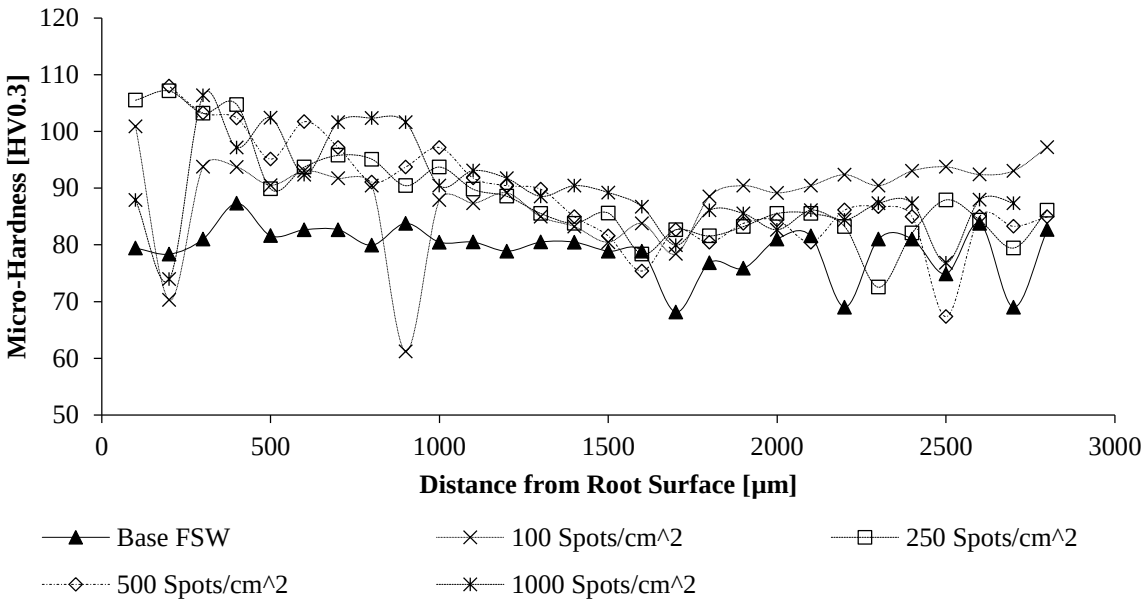

Figure C.9- Micro-Hardness through the thickness of the Friction Stir Welded Joint which had been Laser Shock Peened at a Power Intensity of 3.5 GW/cm^2

C.5 Additional Data for Effects of Offsets on the Thickness of the Joints

This section lists the additional data pertaining to the thickness variations due to the offset joints. Table C.2 lists the thickness variations of the offset FSW joints.

Table C.2 - Thickness of Offset Friction Stir Welded Joints with Lack of Penetration

Lateral Offset [mm]	Normal Offset [mm]	Location	Avg base thick [mm]	Avg weld thick [mm]	Percentage Reduction [%]
0	0.05	Centre	3.02	2.24	25.77
0	0.15	Centre	2.98	2.58	13.45
0	0.25	Centre	2.95	2.55	13.31
0	0.35	Centre	2.95	2.77	6.00
1.25	0.05	Advancing	2.97	2.40	19.28
0.5	0.05	Advancing	2.95	2.39	18.83
1.25	0.05	Retreating	2.94	2.45	16.80
0.5	0.05	Retreating	2.97	2.44	17.89
2.5	0.35	Advancing	2.98	2.73	8.49
2.5	0.35	Retreating	2.99	2.68	10.47
0.5	0.25	Advancing	2.97	2.68	9.68
0.5	0.25	Retreating	2.97	2.62	11.57

D. Appendix D – AA6082-T6 Aluminium

In order to get a greater idea of the working material, tensile test were performed to experimentally determine the mechanical properties of the material. Table D.1 lists the experimentally determined mechanical properties of the working material used for this research. It must be noted that there was roughly a 40 MPa deference between the experimentally determined yield and ultimate stress to that of the published equivalents.

Table D.1 - Experimentally Determined Mechanical Properties of AA6082-T6 Working Material

Property	Value	Units
Ultimate Tensile Strength	348.83	MPa
Yield Tensile Strength	303.72	MPa

Figure D.1 provides the plot of the experimentally tested base material, 3 mm thick AA AA6082-T6 Aluminium. The 0.2% yield intercept has also been indicated showing the yield strength of the material.

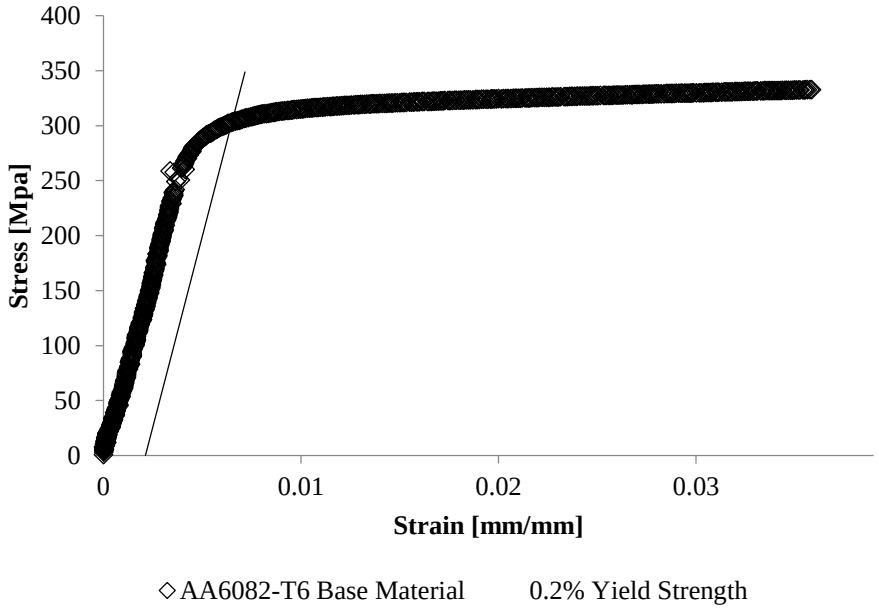

Figure D.1 - Experimental Stress Strain plot for AA AA6082-T6 Aluminium indicating the 0.2% Yield Strength

provides the comparison of the experimental fatigue data achieve through testing of the base AA6082-T6 Aluminium at a number of stress intensities to that of published results for the same material [6].

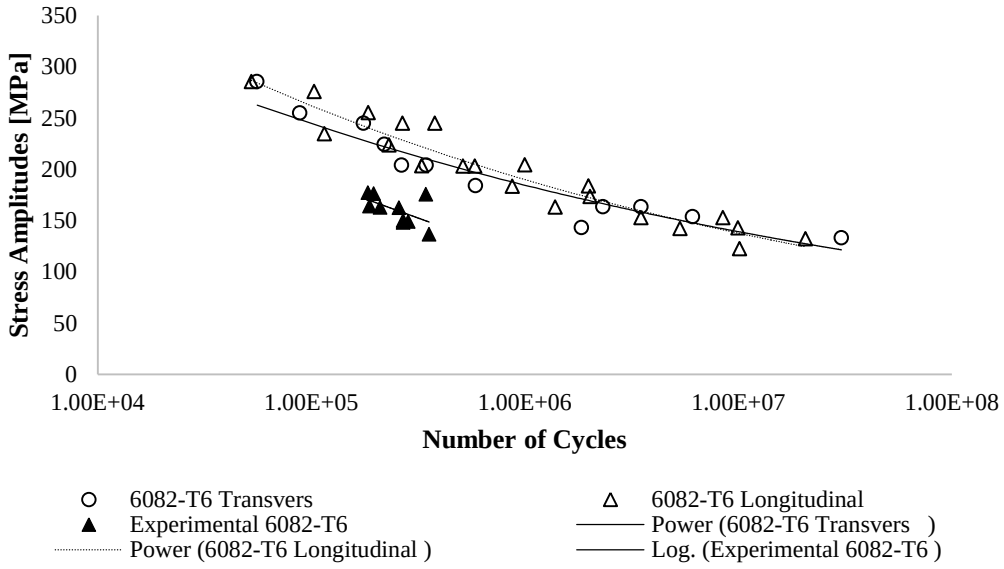

Figure D.2 - AA6082-T6 Bending Fatigue Comparison of Experimental versus Published Fatigue Life

130-140 MPa *140-150 MPa* *160-170 MPa* *170-180 MPa*

Figure D.3 - Fatigue Fracture Position of Base Material Coupons

Table D.2 lists all test data pertaining to the fatigue testing of the base material.

Table D.2 – Fatigue Test Data of Base Material (AA 6082-T6 3mm thick)

Sample Name	Meas. Max Stress [MPa]	Meas. Min Stress [MPa]	Stress Amp [MPa]	R	No. cycles	Meas. Max Stress After [MPa]	Meas. Min Stress After [MPa]	R_after	Ave Stress [MPa]	Ave R	Ave Cycles
Base Set 1_1	177.03	-174.16	175.60	-1.02	139160.00	160.93	-190.54	-0.84			
Base Set 1_2	176.68	-177.80	177.24	-0.99	140580.00	172.41	-179.97	-0.96			
Base Set 1_3	176.33	-176.33	176.33	-1.00	156200.00	179.97	-173.95	-1.03	176.39	-1.00	145313.33
Base Set 2_1	161.70	-163.17	162.44	-0.99	171820.00	159.67	-165.97	-0.96			
Base Set 2_2	163.24	-162.40	162.82	-1.01	184600.00	165.34	-163.10	-1.01			
Base Set 2_3	163.80	-164.22	164.01	-1.00	177500.00	162.33	-162.33	-1.00	163.09	-1.00	177973.33
Base Set 3_1	148.26	-148.33	148.30	-1.00	254180.00	145.60	-154.56	-0.94			
Base Set 3_2	150.50	-149.87	150.19	-1.00	255600.00	149.45	-149.31	-1.00			
Base Set 3_3	149.45	-148.82	149.14	-1.00	259860.00	152.88	-145.53	-1.05	149.21	-1.00	256546.67
Base Set 4_1	136.78	-136.22	136.50	-1.00	377720.00	133.77	-138.67	-0.96	136.50	-1.00	377720.00

Figure D.4 illustrates the base material fracture surface of the bending fatigue coupons tested at various stress amplitudes.

170-180 MPa *160-170 MPa*

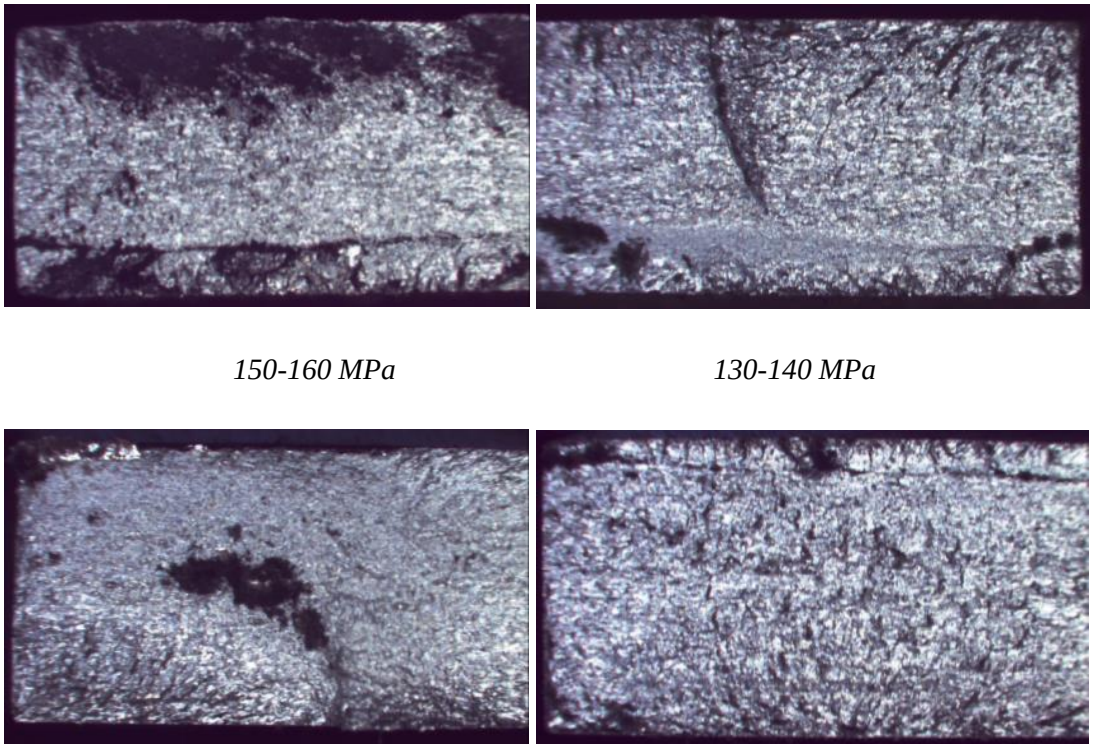

150-160 MPa *130-140 MPa*

Figure D.4 - Fracture Surface of the Base Material run at Various Stress Amplitudes

E. Appendix E - Experimental Methodology

This section will cover the experimental methods employed in completing the FSW, LSP and other general testing methods.

E.1. Friction Stir Welding Methodology

This section covers the procedures of all actions required to be under taken to complete FSW safely and according to an acceptable and repeatable method.

E.1.1. Running of Friction Stir Welding Machine

This section outlines the procedure for completing a full friction stir weld.

1. Switch on main switch at back of machine.

2. Turn emergency stop switch to on position.

3. Press on button and once machine control screen is on press the reset button.

4. Reference machine by pressing 0 button, R and cycle start.

5. Complete steps covered in section 4.2 or ensure that backing bar support and clamping devices are firmly attached to machine.

6. Complete steps covered in section 4.3.

7. Complete steps covered in section 4.4.

8. Complete steps covered in section 4.5.

9. Place welding plate on missing side of backing bar closest to user, place extrusion on top of plate, push against aligned plate and tighten clamps.

10. Complete steps covered in section 4.6.

11. Ensure nothing is obstructing the movement of the tool stock or table.

12. Mode select, button 1 Automatic.

13. Start the recording of the force plate and thermal camera.

14. On CNC control unit press cycle start, the machine will engage it's gearing to the set user spindle speed, press cycle start again.

15. Once weld is complete stop thermal camera and force plate.

16. Unclamp welded plates.

17. Redo steps as required to complete further welds.

18. Once completed press emergency stop button, then off button and switch the main black power switch off at the back of machine.

Precautions:

The following are a number of precautions which need to be considered at all times.

• If needed all processes speeds can be decreased or increased using machine throttle.

• Make sure all clamps are secured before beginning the welding process.

• Ensure the emergency stop button can be pressed in an emergency.

E.1.2. Moving of Force Plate

1. Remove backing plate and clamps.

2. Insure that force plate is fully unbolted from the table of the FSW machine.

3. Remove input cable (cable in metallic sleeve) at the back of DAQ, the plug has clasp that is required to be pushed forward and held before removing it from the back of the DAQ.

4. Using the engine host, appropriate sling, eyelet and D shackle from the lab. The eyelet must be fastened directly to the top of the force plate with the D shackle and sling connecting the plate to the host.

5. Slowly host the plate and move appropriately.

6. Fasten to the table of the FSW once moving is completed.

Precautions:

The following are a number of precautions which need to be considered at all times.

• Kistler plate is extremely expensive thus care must be taken in moving it.

• All health and safety rules must be followed accordingly.

• The assembly of the plate is extremely heavy thus avoid moving it without it being connected to the host.

• Add Cooper Slip (can be asked for in stores) to every threaded hole before tightening the connecting bolts.

E.1.3. Setting the Plunge Distance

Assuming this procedure is beginning from the tool post is at the home position.

1. Ensure that welding tool is inserted into the tool post and is seated correctly.

2. Move the tool post out to the middle of the backing bar area.

3. Safely move the machine table up towards the bottom of the pin of the welding surface.

4. Once the distance of the pin to the backing bar is close enough move in finer increments.

5. Using an engineering shims of known thickness, reduce the distance between the table and pin.

6. Place shim between the table and pin and close distance until the pin JUST pushes against the shim holding it on the table.

7. Once the shim is held that Z distance must be read directly from the machine display.

8. The Z distance must be either kept or must be corrected for the plunge distance that the user requires.

9. Push mode select, button 6, T and set Z distance accordingly.

10. Return the tool post to the home position.

Precautions:

The following are a number of precautions which need to be considered at all times.

• When moving the tool post ensure that welding tool will not come into contact with anything.

• Ensure that the welding tool does not come into contact with the backing bar.

• Ensure that the thickness of the engineering shim is of a known dimension.

E.1.4. Setting the Edge of Welding Plate Parallel to the Travel of the Tool

This section outlines the steps required to align the welding plates with the travel of the welding tool.

1. Place first plate on the further half of the backing bar.

2. Place steel extrusion on plate.

3. A line the edge of the plate as parallel as possible by eye.

4. Slightly tighten the clamps on the extrusion so that the plate is held just.

5. If tool holder containing clock gauge is not in the tool post remove respective tool and replace it with clock gauge.

6. Place the machine into neutral this is done by selecting mode select, button 3 (Programme), toggle through program till block N0010 (CNC code M40 should be displayed), select cycle start and finally physically rotate the tool post by hand to check that gear selection has been completed.

7. Move the tool post using course movements until the tip of clock gauge is close to edge of plate.

At this point the user must use fine movements using the hand wheel. Move edge finder in Y-direction until clock gauge begins to read a deflection. Place in the tip at roughly the middle of thickness of the plate.

8. Run the gauge in the X-direction along the plate reading the deflections as appropriate.

9. Adjust welding plate as required.

10. Once the plates are within a range of no more than 0.02 mm tighten the clamps, secure the plate by tightening the clamps.

Precautions:

The following are a number of precautions which need to be considered at all times.

• Do not move the table or post in large movements as to avoid over travelling or running the clock gauge into a part of the table.

• Do not over exceed the deflections of the clock gauge at any stage.

• Do not complete this section without putting the machine into neutral.

E.1.5. Centring the Welding Tool on Welding Line

This section outlines the steps required to align the welding tool on the centre of the welding line.

1. Ensure that the tool holder with the 10 mm edge finder is inserted into the tool stock.

2. Make sure steps covered in section 4.3 have been completed.

3. Set the spindle speed to no more than 500 RPM, mode select, button 3 and toggle to step 17 (block N0011) and select cycle start to engage gearing.

4. Mode select, button 0 to jog the machine and using the x,y and z controls move the edge finder to the edge of the plate, leave a small gap in the y direction between the edge finder and plate.

5. Ensure that the spindle is set to spin at no more than 500 RPM, press the Spindle start button to get the spindle to begin spinning.

6. Using the hand wheel, moving the y direction at 0.02 mm an increment, move the edge finder towards the edge of plate.

7. At the point where the edge find moves off to one side then the plate and the finder have made contact, stop moving the tool completely.

8. Stop the spindle.

9. Record the y position reading on the control unit.

10. Subtract half the diameter from the reading shown.

11. Input that calculated values into the Fixture positioning, mode select, button 6, button E, Y and value.

This method may be used to find the edge of the x position as well.

Precautions:

The following are a number of precautions which need to be considered at all times.

• The edge finder is designed for a maximum rpm of 500, if this exceeded the spring inside the finder will be damaged.

• If the finder is over extended the spring will be damaged.

• Depending on the location of the x and y position it is likely that either half the diameter might have to be added or subtracted to the read values in the respective axis.

• When inputting values make sure to put the correct signs (+/-).

E.1.6. Setting of Welding Parameters

The settings of welding parameters are done by changing the previously set parameters within the programme. The only plunge rate, dwell, welding feed rate and spindle speed can be varied.

1. Mode select button, button 3 and move through the programme using the next button.

2. Toggle to block 4 to set spindle speed (RPM), press S button and the value required.

3. Toggle to block 9 to set plunge rate, press F button and the value required.

4. Toggle to block 10 to set dwell time, press L button and the value required.

5. Toggle to block 12 to set feed rate and x position to feed to, pressing the F and X button and the values require.

6. Toggle to block 13 to set the end dwell time, press symbol and the value required.

Precautions:

The following are a number of precautions which need to be considered at all times.

• When setting spindle speed ensure that the required rpm is possible with the machines gearing system.

• Ensure to end all values with a decimal so that the control will read the exact values required.

• Every time a value is inputted make sure to put the correct + or – in front of the value.

E.2. Laser Shock Peening Methodology

This section covers the procedures of all actions required to be under taken in the completion of LSP, in a safely, acceptable and repeatable method.

E.2.1. Processing of Samples

This section outlines the steps required to process a variety of samples with LSP.

1. Follow laser start procedure outlined by the CSIR NLC.
2. Follow steps described in section 0 in ensuring correct alignment of the laser path is correct from the laser exit to the target surface.
3. Follow steps described in section 0 to ensure the position of the target surface to obtain the correct spot diameter.
4. Set the laser to Q-Switch and optimise the energy of the laser to the required amount by altering the oscillation and amplitude settings.
5. Turn of X-Y table at control box and begin the start-up of controller PC.
6. Replace deionised water in sump with clean new water at the beginning of processing period, a processing period was typically one week long.
7. Secure required sample holder to X-Y table.
8. Secure test piece into sample holder and ensure that the component is level and target surface is free of obstructions.
9. Verify distance of target surface to lens. The distance between target and lens must be set to the dimension specified in section 0 for the required beam spot diameter.
10. Program X-Y table control program with desired stepping and scanning speed. These speeds correlate to a specific spot coverage and overlapping rate, required speeds are listed in Table

5.5. Set the dimensions of the area of the component which needs to be processed, the program requires the length and breadth of the intended processed area.

11. Set the laser path at the starting point on the target surface. A zero x and y coordinate is required to be found so that correct processing of the area is completed.
12. Turn on water pump and alter the position of the water applicator nozzle to encompass the area of the sample which is being processed.
13. Turn on compressed air which is connected to the air knife.
14. Remove beam stop which should be in front of the laser exit.
15. Simultaneously begin the program on the X-Y table control pc and start pulsing of the laser by setting it to repetition triggering.
16. Allow for the full execution of the program.
17. Cease fire of the laser at the instant were the program completes and the X-Y table begins to return to the zero position.
18. Place beam stop in front of laser exist.
19. Turn off water pump, ceasing water flow.
20. Turn off compressed air.
21. In the event of multiple processing areas occurring on a single sheet of material the new zero position for the next target area needs to be set, repeat steps 7 through 16 for remaining samples. If the processing of the sheet is complete remove from the sample holder.

Precautions:

The following are a number of precautions which need to be considered at all times.

- Whenever the laser is not in operation a beam stop must be placed in front of the laser exist.
- When the laser is in operation all operators are required to wear all safety equipment.
- Do not cross the laser beam path at any point along its travel.
- Ensure that water layer over the sample is laminar and of a constant thickness.
- Excessive splashing and mist build up must be mitigated were possible.
- Monitor N_2 levels and make sure that the flow on the gas into the laser does not drop below 2.5 units.
- Ensure that the exterior laser warning light is on, indicating that the laser processing is being conducted.
- The compressed air must not be operational whenever any laser processing is in operation.
- Ensure that the laser cannot propagate further than the target area.
- Ensure that all splash shields are in place.
- Ensure that all optics are clean and free of any dirt.
- All correct protective wear and protocols must be used during this operation.

E.2.2. Alignment of Optics

This section outlines the steps required to align all optics to ensure the correct propagation of the laser beam from the laser beam outlet to the target surface.

1. Place required mirrors and lens in there desired positions along the intended path of the laser.
2. Set the laser to Long Pulse setting.
3. Place beam stops in the general area of anticipated laser trajectory along its path. A beam stop must be placed in front of the lens to prevent no accidental beams are passed through the lens and become higher energy focused beams.
4. Remove the laser beam stop at the outlet of the beam.
5. Using a laser flash card and beginning at the laser beam output fire singular shots on to the flash card. With each shot move the card position further and further away from the output and closer to the first mirror.
6. Align the mirror so that it reflects the majority of the beam energy 90° to the laser. The beam should hit the mirror roughly in the centre of the optic.
7. Repeat step 4 to 5 between mirrors 1 and 2.
8. Position the second mirror in order to bend the beam 90° vertically.
9. Repeat steps 4 to 5 for the distance between mirror 2 and 3.
10. Repeat steps 4 to 5 for the distance between mirror 3 and the lens.
11. Using flash paper, in a clear plastic bag, align the focused beam through the splash guards.
12. Fire the laser whilst placing the flash paper at the anticipated target distance from the lens to ensure that the beam is not clipping and is perfectly aligned.
13. Replace the laser beam stop at the output of the laser.

Precautions:

The following are a number of precautions which need to be considered at all times.

- Make sure that all optics are placed in the holders correctly. They all have a specific surface which is capable of interactions with the laser. If the optic is placed in the holder incorrectly the optic will be certainly damaged and will have to be replaced.
- Ensure that all optics are clean. The surface of the optic must be free of dust or objects in order to prevent damage to the optic.
- Ensure that the laser beam does not clip any sides of the optical holders or splash guards.
- All correct protective wear and protocols must be used during this operation.
- Monitor N_2 levels and make sure that the flow on the gas into the laser does not drop below 2.5 units.

- Ensure that the lens is set at a slight angle to prevent the laser beam being reflected off the target surface back in the direction of the initial laser path.

E.2.3. Measuring of Beam Spot Size

This section outlines the steps required to obtain the distance at which the target surface needs to be positioned relative to the lens in order to obtain the correct beam diameter.

1. The user must have an idea of the desired spot diameter, power intensity and the pulse duration of the laser in order to roughly calculate, using equation 2.2, an estimate of the required beam energy to match the required power intensity.
2. Set the laser setting to Long Pulse.
3. Place a stand for the holder of the ND Filters. The stand must be placed before the lens.
4. Remove the beam stop in front of the laser output.
5. Align the ND Filter holder so that the beam passes roughly through the centre of the holder.
6. Place the CCD camera on a fine scale moveable z stage, this is done so that small adjustments in the cameras position can be made.
7. Set the laser control to Q- Switch.
8. Build a stack of ND filters and place them in the holder.
9. Connect the CCD camera to the Q-Switch trigger on the laser and the laptop.
10. Before removing the protective cap of the CCD camera ensure the beam hits the camera lens roughly in the middle.
11. Set the BeamGage program accordingly.
12. Fire a single shot and check the intensity of the beam profile. One should never saturate the camera as this means that there are insufficient ND filters and damage to the camera will occur if the saturation is too high. Red-orange colours indicate regions of high intensity and need to be avoided in the laser spot size measurements.
13. Optimise the ND filters to get the correct intensity of the profile.
14. Fire the laser, record the beam profile and spot size and measure the straight line distance from the reference position of the lens to the reference position of the CCD camera. This distance in which the focused laser beam has converged to whilst propagating.
15. Place the CCD camera at a location that the indicated spot size is below the required value. Record the distance and save the laser profile and properties on the laptop.
16. Move the CCD camera to the position which roughly gives the required dimension of the spot size. Record the distance and properties of the laser profile.
17. Move the CCD camera to a position in which the dimension of the measure beam spot size is greater than that of the required spot. Record the distance and the properties of the beam.
18. Plot the measured distances versus the measured spot sizes. A straight line will be created. Select the distance which indicates the correct required spot size for processing of samples.

19. Replace the beam stop in front of the beam output.

Precautions:

The following are a number of precautions which need to be considered at all times.

- Do not touch the surfaces of any ND filters.
- Ensure that all filters and oriented correctly.
- Handle the CCD camera with great care.
- Do not use insufficient ND filter so that the CCD camera is over saturated.
- Do not use the repetition mode whilst using the ND filters as this will destroy the optics.
- Always use the same reference points on the lens and camera in the measurement of the distances.
- All correct protective wear and protocols must be used during this operation.

E.3. General Testing Methodology

This section covers the procedures of all actions required to be under taken in the completion of the respective tests, in a safely, acceptable and repeatable method.

E.3.1. Tensile Testing

This section outlines the steps required to complete a standard tensile test. This method was applied for all samples which were required to be tensile tested.

1. Check that 20 kN load cell and grips are secured in the machine.
2. Turn on Shimadzu controller unit and computer.
3. Set up controller program to run a tensile test with the correct amount of samples and subsamples.
4. Deburr edges of tensile sample with either fine grit sand paper or special tools.
5. Write relevant sample data on both advancing and retreating sides of the sample.
6. Place retreating side of the sample in the fixed jaw. Tighten the jaw, making sure that the sample is not bent or skew in anyway.
7. Lower the movable jaw until the clamp has roughly 50 mm of the tensile sample length within the clamp. Tighten the clamp.
8. Check that both clamps are tight and that the sample is firmly secured in the clamps. No slipping of the sample should occur.
9. Set the cross head position and measured force to zero.
10. Ensure that cross head speed is correctly set to 10 mm/min.
11. Begin test, wait till fracture of the sample.
12. Unclamp each of the broken pieces of the tensile sample.

13. Tap the two ends together ensuring that the fracture surfaces do not come into contact.
14. Place them in an airtight bag with a Silicon gel bag.
15. Return the movable clamp to its home position.
16. Repeat steps 4 to 15 for all tensile samples.
17. Save data and complete processing according to section 5.4.7.

Precautions:

The following are a number of precautions which need to be considered at all times.

- Never allow for the cross head to over travel its limits.
- Never allow for the fixed and moving jaws to come into contact with one another.
- Do not bend the sample when tightening jaws.
- Ensure that the sample is straight as other loading such as bending and torsion will be introduced during the test.
- The speed of the cross head resets after each test thus it needs to be set after each run to ensure constant testing parameters.
- The fracture surface of the sample may be sharp, do not touch the fracture surface.

E.3.2. Three Point Bending Testing

This section outlines the steps required to complete a standard three point bending test. This method was applied for all samples which were tested under three point bending.

1. Check that 20 kN load cell and respective three point bending support and plunger are secured in the correct positions.
2. Set the distance between the rollers according to ASTM E 190-92.
3. Turn on Shimadzu controller unit and computer.
4. Set up controller program to run a three point bending test with the correct amount of samples and subsamples.
5. Deburr edges of bending sample with either fine grit sand paper or special tools.
6. Write relevant sample data on both advancing and retreating sides of the sample.
7. Place the sample so that the welded section is directly in the middle of the two rollers.
8. Lower the plunger so that it just comes into contact with the centre of the sample.
9. Set the cross head position and measured force to zero.
10. Ensure that cross head speed is correctly set to 10 mm/min.
11. Begin test, wait till fracture of the sample or the bent sample to slip off the rollers.
12. Return the movable plunger to its home position.
13. Repeat steps 5 to 12 for all tensile samples.
14. Save data and complete processing according to section 5.4.7.

Precautions:

The following are a number of precautions which need to be considered at all times.

- Never allow for the cross head to over travel its limits.
- Never allow for the plunger and roller support to come into contact with one another.
- Ensure that the sample is straight and perpendicular to the plunger during the test to ensure correct loading of the sample.
- The speed of the cross head resets after each test thus it needs to be set after each run to ensure constant testing parameters.

E.3.3. Fatigue Testing

This section outlines the steps required to complete a bending fatigue test. This method was applied for all samples which were required to be fatigue tested.

1. Visually inspect that all wiring of the calibration sample to the DAQ is in order.
2. Turn on DAQ and allow to warm up for approximately 30 minutes.
3. Set the eccentric to the required setting, this should be done according to Figure 5.41.
4. Select the correct combination of support pads to align the calibration sample centroid with that of the machines.
5. Place the calibration sample into the sample holder of the fatigue machine.
6. Secure the calibration sample with the required four washers and nuts which should be tightened to 10 N.m.
7. Turn on PC and open LabVIEW software.
8. Perform shunt calibration for the strain gauges mounted on the calibration sample.
9. Begin recording of the strains.
10. By hand, turn over the motor by rotating the eccentric and allow for a number of full cycles to be completed.
11. Stop the recording and obtain the maximum and minimum recorded strains.
12. If the maximum and minimum strains are almost approximately equal then the setting of the motor height is correct. If these values are not close then adjust the motor height in order to balance the strains and repeat steps 8 to 10.
13. Ensure that all bolts are secured sufficiently.
14. Measure the thickness of the fatigue sample, select the correct combination of support pads to align the centroid of the sample with the central load application line of the machine.
15. Place the test sample into the sample holder of the fatigue machine.
16. Secure the test sample with the required four washers and nuts which should be tightened to 10 N.m.

17. Set up the software for the digital camera, which needs to be placed above the sample to ensure that a clear view of the test sample is captured every 60 seconds.
18. As soon as the first image is captured begin the fatigue test.
19. Once fracture occurs turn off the fatigue machine. Allow for an image of the fractured sample to be taken.
20. Carefully, remove the fractured sample.
21. Repeat steps 5 through 11. Recording what the final setting of the machine was after the completion of the test.
22. Repeat steps 12 through 21 for the remaining samples.

F. Appendix F - Uncertainty Analysis

This section has been dedicated to the calculation of the uncertainty of the experimental data.

The uncertainty of the ultimate tensile strength was calculated according to following:

$$\Delta F = \pm 1\%\ of\ 20kN = 200\ N$$

$$\Delta L = \Delta T = 0.05\ mm$$

$$\sigma_{ulti} = \frac{F}{L \cdot T}$$

$$\Delta\sigma_{ulti} = \sqrt{\left(\frac{\partial\sigma_{ulti}}{\partial F} \cdot \Delta F\right)^2 + \left(\frac{\partial\sigma_{ulti}}{\partial L} \cdot \Delta L\right)^2 + \left(\frac{\partial\sigma_{ulti}}{\partial T} \cdot \Delta T\right)^2}$$

$$\Delta\sigma_{ulti} = \sqrt{\left(\frac{200}{L \cdot T}\right)^2 + \left(\frac{-0.05F}{T \cdot L^2}\right)^2 + \left(\frac{-0.05F}{L \cdot T^2}\right)^2}$$

Figures in which this equation was applied to calculate the uncertainty in the ultimate tensile strength:

- Figure 5.7
- Figure 6.37
- Figure 6.39
- Figure 6.43
- Figure 7.16
- Figure 7.18

The uncertainty of the percentage reduction of the FSW joint thickness to the base material thickness was calculated according to the following:

$$\Delta T_{weld} = \Delta T_{base} = 0.05\ mm$$

$$\%\ Reduction = \frac{T_{weld}}{T_{base}} \times 100\%$$

$$\Delta\%Reduction = \sqrt{\left(\frac{\partial\%Red.}{\partial T_{weld}} \cdot \Delta T_{weld}\right)^2 + \left(\frac{\partial\%Red.}{\partial T_{base}} \cdot \Delta T_{base}\right)^2}$$

$$\Delta\%Reduction = \sqrt{\left(\frac{100}{T_{base}} \cdot 0.05\right)^2 + \left(\frac{-100 \cdot T_{weld}}{{T_{base}}^2} \cdot 0.05\right)^2}$$

- Figure 6.40
- Figure 7.15

The uncertainty of the ultimate efficiency of the welded joints to that of the base material, shown in Figure 6.40, was calculated according to the following:

$$\Delta\sigma_{ulti\ weld} = \sqrt{\left(\frac{200}{L \cdot T}\right)^2 + \left(\frac{-0.05F}{T \cdot L^2}\right)^2 + \left(\frac{-0.05F}{L \cdot T^2}\right)^2}$$

$$\Delta\sigma_{ulti\ base} = \sqrt{\left(\frac{200}{L \cdot T}\right)^2 + \left(\frac{-0.05F}{T \cdot L^2}\right)^2 + \left(\frac{-0.05F}{L \cdot T^2}\right)^2}$$

$$\%\ Eff_{ulti} = \frac{\sigma_{ulti\ weld}}{\sigma_{ulti\ base}} \cdot 100\%$$

$$\Delta\%Eff_{ulit} = \sqrt{\left(\frac{\partial\%Eff_{ulti}}{\partial\sigma_{ulti\ weld}} \cdot \Delta\sigma_{ulti\ weld}\right)^2 + \left(\frac{\partial\%Eff_{ulti}}{\partial\sigma_{ulti\ base}} \cdot \Delta\sigma_{ulti\ base}\right)^2}$$

$$\Delta\%Eff_{ulit} = \sqrt{\left(\frac{100\Delta\sigma_{ulti\ weld}}{\sigma_{ulti\ base}}\right)^2 + \left(\frac{-100 \cdot \sigma_{ulti\ weld} \cdot \Delta\sigma_{ulti\ base}}{{\sigma_{ulti\ base}}^2}\right)^2}$$

Table F.1 lists the calculated uncertainty for a number of sets of data which could not be clearly shown on the respective figures.

Table F.1 – Uncertainty of Tensile Test Data

Spindle Speed [RPM]	Feed Rate [mm/min]	Δ Ultimate Stress [MPa]	Δ Yield Stress [MPa]	Δ Joint Efficiency [%]
630	**200**	7.66	6.70	2.74
	400	6.80	6.40	2.34
	600	6.37	5.99	2.13
800	**200**	7.37	6.55	2.61
	400	7.08	6.39	2.48
	600	6.57	6.21	2.24
1000	**200**	8.01	7.25	2.70
	400	7.86	6.73	2.80
	600	6.79	6.20	2.39
1250	**200**	8.92	7.77	3.03
	400	8.37	7.26	2.92
	600	7.75	6.83	2.72
1600	**200**	9.18	7.91	3.12
	400	8.43	7.58	2.82
	600	7.94	7.06	2.73

The uncertainty of the power intensity of the laser was calculated according to the following, shown in Figure 6.59:

$$\Delta E = 0.0005\, J$$

$$\Delta \tau = 0.05\, ns$$

$$\Delta d = 0.005\, mm$$

$$I = \frac{400E}{\pi \tau d^2}$$

$$\Delta I = \sqrt{\left(\frac{\partial I}{\partial E} \cdot \Delta E\right)^2 + \left(\frac{\partial I}{\partial \tau} \cdot \Delta \tau\right)^2 + \left(\frac{\partial I}{\partial d} \cdot \Delta d\right)^2}$$

$$\Delta I = \sqrt{\left(\frac{400}{\pi \tau d^2} \cdot \Delta E\right)^2 + \left(\frac{-400E}{\pi \tau^2 d^2} \cdot \Delta \tau\right)^2 + \left(\frac{-800E}{\pi \tau d^3} \cdot \Delta d\right)^2}$$

The uncertainty associated to the micro-hardness measurements was calculated according to the following:

$$\Delta F_{ind} = 0.5g$$

$$\Delta L_{dia1} = \Delta L_{dia2} = 0.005\mu m$$

$$HV = \frac{1854\, F_{indentation}}{L_{diagonal1} \times L_{diagonal2}}$$

$$\Delta HV = \sqrt{\left(\frac{\partial HV}{\partial F_{ind}} \cdot \Delta F_{ind}\right)^2 + \left(\frac{\partial HV}{\partial L_{dia1}} \cdot \Delta L_{dia1}\right)^2 + \left(\frac{\partial HV}{\partial L_{dia2}} \cdot \Delta L_{dia2}\right)^2}$$

$$\Delta HV = \sqrt{\left(\frac{1854}{L_{dia1} \cdot L_{dia2}} \cdot \Delta F_{ind}\right)^2 + \left(\frac{-1854 \cdot F_{ind}}{{L_{dia1}}^2 \cdot L_{dia2}} \cdot \Delta L_{dia1}\right)^2 + \left(\frac{-1854 \cdot F_{ind}}{L_{dia1} \cdot {L_{dia2}}^2} \cdot \Delta L_{dia2}\right)^2}$$

Each indentation had some uncertainty defined by the above equation. This lead to a large number of uncertainty calculations. The uncertainty ranged was listed in Table F.2 was calculated from the minimum to the maximum measured hardness value

Table F.2- Calculated Hardness Uncertainty Range

	Hardness [$HV_{0.3}$]	Uncertainty [$HV_{0.3}$]
Minimum Hardness	55.58	0.28
Maximum Hardness	115.04	0.58

The uncertainty associated to the fatigue testing present in section 6.2.6, was calculated according to the following:

It was assumed that the Young's modulus varied by ±1GPa.

$$\Delta E = \pm 1\ GPa$$

$$\Delta\varepsilon_{measured} = 5 \times 10^{-6}$$

$$\Delta no.of\ cycles = 1420$$

Measured bending stress uncertainty:

$$\sigma_{bending} = E_{young's} \times \varepsilon_{measured}$$

$$\Delta\sigma_{bending} = \sqrt{\left(\frac{\partial\sigma_{bending}}{\partial E_{young's}} \cdot \Delta E_{young's}\right)^2 + \left(\frac{\partial\sigma_{bending}}{\partial\varepsilon_{measured}} \cdot \Delta\varepsilon_{measured}\right)^2}$$

$$\Delta\sigma_{bending} = \sqrt{\left(\varepsilon_{measured} \cdot \Delta E_{young's}\right)^2 + (E \cdot \Delta\varepsilon_{measured})^2}$$

Stress ratio uncertainty:

$$\Delta\sigma_{max} = \Delta\sigma_{min} = \sqrt{\left(\varepsilon_{measured} \cdot \Delta E_{young's}\right)^2 + (E \cdot \Delta\varepsilon_{measured})^2}$$

$$R = \frac{\sigma_{min}}{\sigma_{max}}$$

$$\Delta R = \sqrt{\left(\frac{\partial R}{\partial\sigma_{min}} \cdot \Delta\sigma_{min}\right)^2 + \left(\frac{\partial R}{\partial\sigma_{max}} \cdot \Delta\sigma_{max}\right)^2}$$

$$\Delta R = \sqrt{\left(\frac{1}{\sigma_{max}} \cdot \Delta\sigma_{min}\right)^2 + \left(\frac{-\sigma_{min}}{{\sigma_{max}}^2} \cdot \Delta\sigma_{max}\right)^2}$$

Stress range uncertainty:

$$\Delta\sigma_{max} = \Delta\sigma_{min} = \sqrt{\left(\varepsilon_{measured} \cdot \Delta E_{young's}\right)^2 + (E \cdot \Delta\varepsilon_{measured})^2}$$

$$\sigma_r = \sigma_{max} - \sigma_{min}$$

$$\Delta\sigma_r = \sqrt{\left(\frac{\partial\sigma_r}{\partial\sigma_{max}} \cdot \Delta\sigma_{max}\right)^2 + \left(\frac{\partial\sigma_r}{\partial\sigma_{min}} \cdot \Delta\sigma_{min}\right)^2}$$

$$\Delta\sigma_r = \sqrt{(\Delta\sigma_{max})^2 + (-\Delta\sigma_{min})^2}$$

Stress amplitude uncertainty:

$$\Delta\sigma_{max} = \Delta\sigma_{min} = \sqrt{\left(\varepsilon_{measured} \cdot \Delta E_{young's}\right)^2 + (E \cdot \Delta\varepsilon_{measured})^2}$$

$$\sigma_m = \frac{\sigma_{max} - \sigma_{min}}{2}$$

$$\Delta\sigma_m = \sqrt{\left(\frac{\partial\sigma_m}{\partial\sigma_{max}} \cdot \Delta\sigma_{max}\right)^2 + \left(\frac{\partial\sigma_m}{\partial\sigma_{min}} \cdot \Delta\sigma_{min}\right)^2}$$

$$\Delta\sigma_m = \sqrt{\left(\frac{\Delta\sigma_{max}}{2}\right)^2 + \left(\frac{-\Delta\sigma_{min}}{2}\right)^2}$$

The uncertainty associated to the fatigue data listed in Table 6.20 has been list in Table F.3

Table F.3 - Uncertainty Associated to the Fatigue Testing of the Base and Base with Laser Shock Peening

Sample Name	**$\Delta\sigma_{max}$ [MPa]**	**$\Delta\sigma_{min}$ [MPa]**	**ΔR**	**$\Delta\sigma_r$ [MPa]**	**$\Delta\sigma_m$ [MPa]**
Base Set 1_1	2.55	2.51	0.0201	3.58	1.79
Base Set 1_2	2.55	2.56	0.0205	3.61	1.81
Base Set 1_3	2.54	2.54	0.0204	3.60	1.80
Base Set 2_1	2.34	2.36	0.0206	3.32	1.66
Base Set 2_2	2.36	2.35	0.0203	3.33	1.66
Base Set 2_3	2.37	2.37	0.0205	3.35	1.68
Base Set 3_1	2.15	2.15	0.0205	3.04	1.52
Base Set 3_2	2.18	2.17	0.0204	3.07	1.54
Base Set 3_3	2.16	2.15	0.0204	3.05	1.53
Base Set 4_1	1.99	1.98	0.0204	2.80	1.40

Continuation of Table F.3

Sample Name	**$\Delta\sigma_{max}$ [MPa]**	**$\Delta\sigma_{min}$ [MPa]**	**ΔR**	**$\Delta\sigma_r$ [MPa]**	**$\Delta\sigma_m$ [MPa]**
Base+LSP_5_1	2.38	2.37	0.0203	3.36	1.68
Base+LSP_5_2	2.40	2.39	0.0203	3.39	1.70
Base+LSP_5_3	2.39	2.38	0.0204	3.37	1.69
Base+LSP_3.5_1	2.39	2.37	0.0203	3.36	1.68
Base+LSP_3.5_2	2.40	2.39	0.0204	3.39	1.70
Base+LSP_3.5_3	2.39	2.38	0.0203	3.38	1.69
Base+LSP_2_1	2.38	2.38	0.0205	3.37	1.68
Base+LSP_2_2	2.39	2.39	0.0204	3.38	1.69
Base+LSP_2_3	2.41	2.38	0.0202	3.39	1.69
Base+LSP_1_1	2.40	2.41	0.0205	3.40	1.70
Base+LSP_1_2	2.41	2.40	0.0203	3.40	1.70
Base+LSP_1_3	2.41	2.40	0.0203	3.40	1.70

The calculation of the uncertainty associated to the normalised stress, shown in Figure 7.18, was completed according to the following:

$$\Delta\sigma_{max} = 7.63\ MPa\ (calculated)$$

The uncertainty for the ultimate stress was calculated using the equations listed above.

Table F.4 – Calculated Uncertainty of the Ultimate Tensile Stress for Friction Stir Welded Joints manufactured with offset Tool Positions

Tool Positions	Uncertainty [MPa]
0mm Cntr 0.15mm	9.35
0mm Cntr 0.25mm	7.59
0mm Cntr 0.35mm	7.86
1.25mm Adv. 0.05mm	8.21
0.5mm Adv. 0.05mm	7.24
1.25mm Ret. 0.05mm	7.87
0.5mm Ret. 0.05mm	8.32
2.5mm Adv. 0.35mm	8.22
2.5mm Ret. 0.35mm	6.01
0.5mm Adv. 0.25mm	7.13
0.5mm Ret. 0.25mm	7.43
0mm Cntr 0.05mm	7.63

$$\sigma_{normalised} = \frac{\sigma}{\sigma_{max}}$$

$$\Delta\sigma_{normalised} = \sqrt{\left(\frac{\partial\sigma_{normal}}{\partial\sigma}\cdot\Delta\sigma\right)^2 + \left(\frac{\partial\sigma_{normal}}{\partial\sigma_{max}}\cdot\Delta\sigma_{max}\right)^2}$$

$$\Delta\sigma_{normalised} = \sqrt{\left(\frac{1}{\sigma_{max}}\cdot\Delta\sigma\right)^2 + \left(\frac{-\sigma}{{\sigma_{max}}^2}\cdot\Delta\sigma_{max}\right)^2}$$

Due to the variation in thickness of the skimmed fatigue samples, an added level of uncertainty had to be taken into account in calculating the uncertainty associated to the fatigue testing of the skimmed samples. The uncertainty was calculated according to the following:

It was assumed that the Young's modulus varied by ±1GPa.

$$\Delta E = \pm 1\ GPa$$

$$\Delta\varepsilon_{measured} = 5 \times 10^{-6}$$

$$\Delta no.of\ cycles = \pm 1420$$

Measured bending stress uncertainty:

$$\sigma_{bending} = E_{young's} \times \varepsilon_{measured}$$

$$\Delta\sigma_{bending} = \sqrt{\left(\frac{\partial\sigma_{bending}}{\partial E_{young's}}\cdot\Delta E_{young's}\right)^2 + \left(\frac{\partial\sigma_{bending}}{\partial\varepsilon_{measured}}\cdot\Delta\varepsilon_{measured}\right)^2}$$

$$\Delta\sigma_{bending} = \sqrt{\left(\varepsilon_{measured} \cdot \Delta E_{young's}\right)^2 + (E \cdot \Delta\varepsilon_{measured})^2}$$

The angle of the stress triangle:

$$\Delta\sigma_{up} = \Delta\sigma_{down} = \sqrt{\left(\varepsilon_{measured} \cdot \Delta E_{young's}\right)^2 + (E \cdot \Delta\varepsilon_{measured})^2}$$

$$\Delta T = 0.05mm$$

$$\theta_{up} = \tan^{-1}\left(\frac{\sigma_{up\_measured}}{T/2}\right)$$

$$\Delta\theta_{up} = \Delta\theta_{down} = \sqrt{\left(\frac{\partial\theta_{up}}{\partial\sigma_{up}} \cdot \Delta\sigma_{up}\right)^2 + \left(\frac{\partial\theta_{up}}{\partial T} \cdot \Delta T\right)^2}$$

$$\Delta\theta_{up} = \Delta\theta_{down} = \sqrt{\left(\frac{2T}{4{\sigma_{up}}^2 + T^2} \cdot \Delta\sigma_{up}\right)^2 + \left(\frac{-2\sigma_{up}}{4{\sigma_{up}}^2 + T^2} \cdot \Delta T\right)^2}$$

Calculated Stress at the surface of the skimmed sample was completed using similar triangles in order to make the calculation easier:

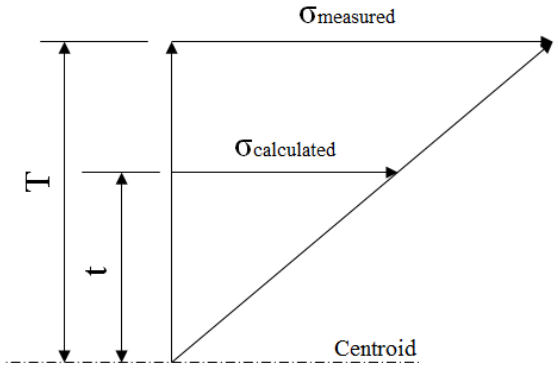

$$\Delta\sigma_{bending} = \sqrt{\left(\varepsilon_{measured} \cdot \Delta E_{young's}\right)^2 + (E \cdot \Delta\varepsilon_{measured})^2}$$

$$\Delta T = \Delta t = 0.05mm$$

$$\frac{\sigma_{measured}}{\sigma_{cal}} = \frac{T}{t}$$

$$\sigma_{cal} = \frac{t\sigma_{measured}}{T}$$

$$\Delta\sigma_{cal} = \sqrt{\left(\frac{\partial\sigma_{cal}}{\partial\sigma_{meas.}} \cdot \Delta\sigma_{meas.}\right)^2 + \left(\frac{\partial\sigma_{cal}}{\partial t} \cdot \Delta t\right)^2 + \left(\frac{\partial\sigma_{cal}}{\partial T} \cdot \Delta T\right)^2}$$

$$\Delta\sigma_{cal} = \sqrt{\left(\frac{t}{T} \cdot \Delta\sigma_{meas.}\right)^2 + \left(\frac{\sigma_{meas.}}{T} \cdot \Delta t\right)^2 + \left(\frac{-t\sigma_{meas.}}{T^2} \cdot \Delta T\right)^2}$$

Stress ratio uncertainty:

$$\Delta\sigma_{max} = \Delta\sigma_{min} = \sqrt{\left(\frac{t}{T} \cdot \Delta\sigma_{meas.}\right)^2 + \left(\frac{\sigma_{meas.}}{T} \cdot \Delta t\right)^2 + \left(\frac{-t\sigma_{meas.}}{T^2} \cdot \Delta T\right)^2}$$

$$R = \frac{\sigma_{min}}{\sigma_{max}}$$

$$\Delta R = \sqrt{\left(\frac{\partial R}{\partial\sigma_{min}} \cdot \Delta\sigma_{min}\right)^2 + \left(\frac{\partial R}{\partial\sigma_{max}} \cdot \Delta\sigma_{max}\right)^2}$$

$$\Delta R = \sqrt{\left(\frac{1}{\sigma_{max}} \cdot \Delta\sigma_{min}\right)^2 + \left(\frac{-\sigma_{min}}{{\sigma_{max}}^2} \cdot \Delta\sigma_{max}\right)^2}$$

Stress range uncertainty:

$$\Delta\sigma_{max} = \Delta\sigma_{min} = \sqrt{\left(\frac{t}{T} \cdot \Delta\sigma_{meas.}\right)^2 + \left(\frac{\sigma_{meas.}}{T} \cdot \Delta t\right)^2 + \left(\frac{-t\sigma_{meas.}}{T^2} \cdot \Delta T\right)^2}$$

$$\sigma_r = \sigma_{max} - \sigma_{min}$$

$$\Delta\sigma_r = \sqrt{\left(\frac{\partial\sigma_r}{\partial\sigma_{max}} \cdot \Delta\sigma_{max}\right)^2 + \left(\frac{\partial\sigma_r}{\partial\sigma_{min}} \cdot \Delta\sigma_{min}\right)^2}$$

$$\Delta\sigma_r = \sqrt{(\Delta\sigma_{max})^2 + (-\Delta\sigma_{min})^2}$$

Stress amplitude uncertainty:

$$\Delta\sigma_{max} = \Delta\sigma_{min} = \sqrt{\left(\frac{t}{T} \cdot \Delta\sigma_{meas.}\right)^2 + \left(\frac{\sigma_{meas.}}{T} \cdot \Delta t\right)^2 + \left(\frac{-t\sigma_{meas.}}{T^2} \cdot \Delta T\right)^2}$$

$$\sigma_m = \frac{\sigma_{max} - \sigma_{min}}{2}$$

$$\Delta\sigma_m = \sqrt{\left(\frac{\partial\sigma_m}{\partial\sigma_{max}} \cdot \Delta\sigma_{max}\right)^2 + \left(\frac{\partial\sigma_m}{\partial\sigma_{min}} \cdot \Delta\sigma_{min}\right)^2}$$

$$\Delta\sigma_m = \sqrt{\left(\frac{\Delta\sigma_{max}}{2}\right)^2 + \left(\frac{-\Delta\sigma_{min}}{2}\right)^2}$$

G. Appendix G – Presentation of Work

Laser Shock Peening to Recover Fatigue Life of Flawed Friction Stir Welded Joints

M. Leering[1], C. Polese[1, 2]

[1]*School of Mechanical, Industrial and Aeronautical Engineering,* [2]*DST-NRF Centre of Excellence in Strong Materials, University of the Witwatersrand, 1 Jan Smuts Avenue, Johannesburg, 2000, South Africa*

Mitchell.Leering@wits.ac.za

Friction Stir Welding (FSW) is a solid state thermo-mechanical joining process which is a novel welding technique utilised on materials such as aluminium, steel and titanium. During this process, a rotating welding tool is plunged between two sheets, locally heating the material and further stirs them together forming a solid bond once cooled. A possible flaw which may occur during this welding is known as Lack of Penetration (LOP). LOP can occur due to slight misalignment of the welding tool, variations in sheet thickness and inaccuracies in assembly tolerances which are possible issues in the industrial domain [1]. These flaws are commonly recognised as cracks, which originate from the root of the weld. An example of extreme LOP is shown in Fig. 1a. The effects of LOP were investigated by intentionally introducing controlled offsets of the welding tool whilst FSW occurs using aluminium alloy AA6082-T6, 3mm thick sheets. LOP was found to reduce the tensile load carrying capability by as much as 20%, depending on the magnitude and position of the crack.

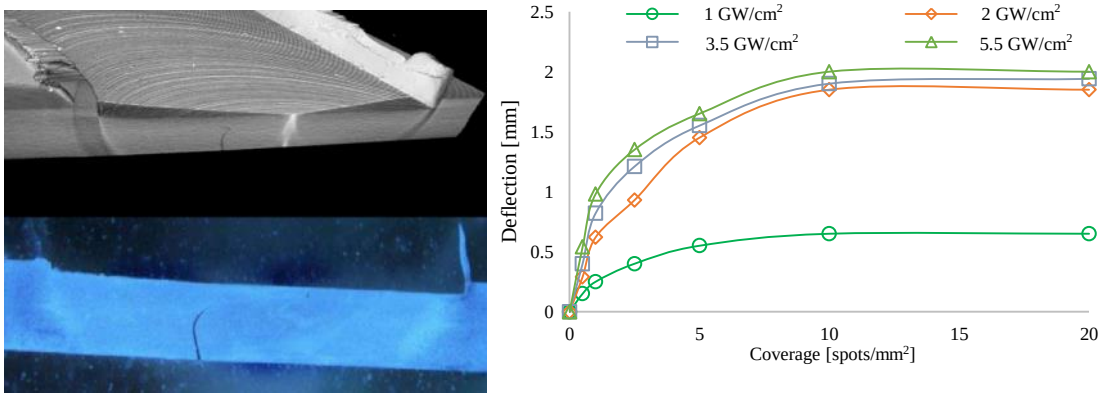

Fig.1. (a) Micro CT scan of FSW with 2.5mm horizontal tool offset. (b) Deflection of aluminium samples, with varying LSP parameters.

Laser Shock Peening (LSP) is a process whereby a pulsing laser interacts with the surface of a metal material resulting in compressive residual stresses being introduced into the component. LSP has already been utilised in the mitigation of unfavourable tensile residual stress, characteristic of FSW, and showed to improve the fatigue performance of the unflawed joints [2, 3]. LSP was used in the present work to alter the tensile residual stress in controlled flawed FSW joints, in order to reduce the rate at which the initiated cracks (LOP) propagate throughout the weld. This ideally rectifies the detrimental effects of LOP on the fatigue life and general strength of the FSW joints. LSP parameters were initially optimised by investigating the effects of varying laser power intensities (1-5.5 GW/cm^2) and processed coverage (0.5-20 spots/mm^2) on the deflection, hardness, and residual stress of both base and FSW materials, as for example shown in Fig. 1b for the measured deflection of the LSP base material. Static testing, bending fatigue testing, and fracture surface analysis were then used to show that LSP has a beneficial effect on these flawed joints. Successful demonstrations of using LSP for this purpose would result in a reduced need for strict material quality control, welding assembly tolerances, post-welding testing and the eventual scrapping of irrecoverable welds.

[1] C. Mandache, D. Levesque, "Non-destructive detection of lack of penetration defects in friction stir welds", Science and Technology of Welding and Joining, vol. 17, 295-303 (2012).
[2] Y. Sano, K. Masaki, "Improvement in fatigue performance of friction stir welded AAA6061-T6 aluminum alloy by laser peening without coating", Materials & Design, vol. 36, 809-814 (2012).
[3] O. Hatamleh, "A comprehensive investigation on the effects of laser and shot peening on fatigue crack growth in friction stir welded AA AA2195 joints," International Journal of Fatigue, vol. 31, 974-988 (2009).

Laser Shock Peening to Recover Fatigue Life of Flawed Friction Stir Welded Joints

M. Leering[1], C. Polese[1, 2]

[1]*School of Mechanical, Industrial and Aeronautical Engineering,* [2]*DST-NRF Centre of Excellence in Strong Materials, University of the Witwatersrand, 1 Jan Smuts Avenue, Johannesburg, 2000, South Africa*

Mitchell.Leering@wits.ac.za

Friction Stir Welding (FSW) is a solid state thermo-mechanical joining process which is a novel welding technique utilised on materials such as aluminium, steel and titanium. During this process, a rotating welding tool is plunged between two sheets, locally heating the material and further stirs them together forming a solid bond once cooled. A possible flaw which may occur during this welding is known as Lack of Penetration (LOP). LOP can occur due to slight misalignment of the welding tool, variations in sheet thickness and inaccuracies in assembly tolerances which are possible issues in the industrial domain [1]. These flaws are commonly recognised as cracks, which originate from the root of the weld. An example of extreme LOP is shown in Fig. 1a. The effects of LOP were investigated by intentionally introducing controlled offsets of the welding tool whilst FSW occurs using aluminium alloy AA6082-T6, 3mm thick sheets. LOP was found to reduce the tensile load carrying capability by as much as 20%, depending on the magnitude and position of the crack.

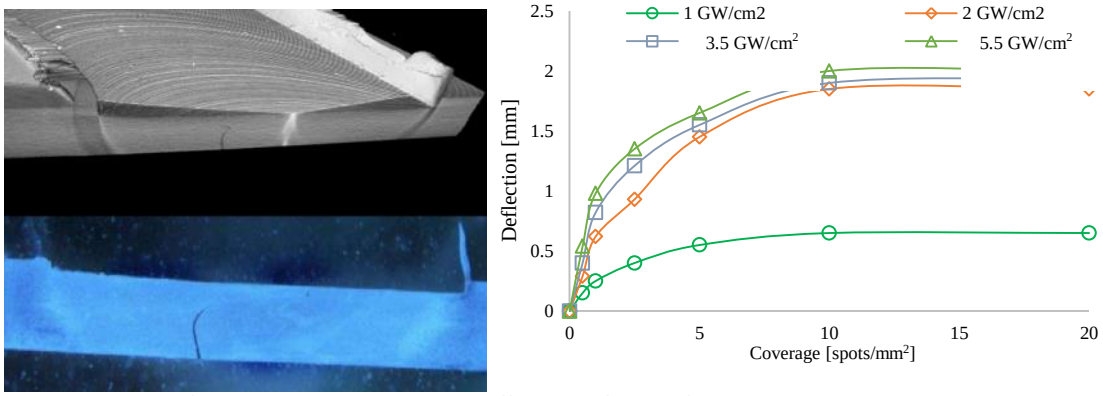

Fig.1. (a) Micro CT scan of FSW with 2.5mm horizontal tool offset. (b) Deflection of aluminium samples, with varying LSP parameters.

Laser Shock Peening (LSP) is a process whereby a pulsing laser interacts with the surface of a metal material resulting in compressive residual stresses being introduced into the component. LSP has already been utilised in the mitigation of unfavourable tensile residual stress, characteristic of FSW, and showed to improve the fatigue performance of the unflawed joints [2, 3]. LSP was used in the present work to alter the tensile residual stress in controlled flawed FSW joints, in order to reduce the rate at which the initiated cracks (LOP) propagate throughout the weld. This ideally rectifies the detrimental effects of LOP on the fatigue life and general strength of the FSW joints. LSP parameters were initially optimised by investigating the effects of varying laser power intensities (1-5.5 GW/cm^2) and processed coverage (0.5-20 spots/mm^2) on the deflection, hardness, and residual stress of both base and FSW materials, as for example shown in Fig. 1b for the measured deflection of the LSP base material. Static testing, bending fatigue testing, and fracture surface analysis were then used to show that LSP has a beneficial effect on these flawed joints. Successful demonstrations of using LSP for this purpose would result in a reduced need for strict material quality control, welding assembly tolerances, post-welding testing and the eventual scrapping of irrecoverable welds.

[1] C. Mandache, D. Levesque, "Non-destructive detection of lack of penetration defects in friction stir welds", Science and Technology of Welding and Joining, vol. 17, 295-303 (2012).
[2] Y. Sano, K. Masaki, "Improvement in fatigue performance of friction stir welded AAA6061-T6 aluminum alloy by laser peening without coating", Materials & Design, vol. 36, 809-814 (2012).
[3] O. Hatamleh, "A comprehensive investigation on the effects of laser and shot peening on fatigue crack growth in friction stir welded AA AA2195 joints," International Journal of Fatigue, vol. 31, 974-988 (2009).